Proceedings of the

Fifth Conference on Physics at the LHC PLHC2010

June 7–12, 2010
Hamburg, Germany

Editors: Markus Diehl, Johannes Haller, Thomas Schörner-Sadenius, Georg Steinbrück

Verlag Deutsches Elektronen-Synchrotron

Impressum

Proceedings of the Fifth Conference on Physics at the LHC (PLHC2010) June 7–12, 2010, Hamburg, Germany

Conference homepage
`http://plhc2010.desy.de/`

Slides at
`http://indico.desy.de/conferenceDisplay.py?confId=1964`

Online proceedings at
`http://plhc2010.desy.de/proceedings`

Editors:
Markus Diehl, Johannes Haller, Thomas Schörner-Sadenius, Georg Steinbrück
December 2010
DESY-PROC-2010-01
ISBN 978-3-935702-43-0
ISSN 1435-8077

Published by
Verlag Deutsches Elektronen-Synchrotron
Notkestraße 85
22607 Hamburg
Germany

Committees

Conference Chairs: Guenakh Mitselmakher (Florida) and Joachim Mnich (DESY)
Scientific Secretary: Thomas Schörner-Sadenius (DESY)

International Advisory Board

Ž. Antunović (Split), S. Asai (Tokyo), S. Bertolucci (CERN), M. Cavalli-Sforza (IFAE Barcelona), H.S. Chen (IHEP Beijing), M. Danilov (ITEP), D. Fournier (LAL Orsay), F. Gianotti CERN), G. Giudice (CERN), N. Glover (Durham) , A. Golutvin (IC London/CERN/ITEP), D. Green (FNAL), R.-D. Heuer (CERN), P. Jenni (CERN), Y.-K. Kim (Chicago/FNAL), P. Maettig (Wuppertal), M. Mangano (CERN), T. Mueller (Karlsruhe), T. Nakada (EPFL Lausanne), R. Petronzio (INFN Rome), C. Quigg (FNAL), P. Schleper (Hamburg), J. Schukraft (CERN), A. Sissakian (JINR), B. Spaan (Dortmund), M. Spiro (CNRS Paris), J. Stachel (Heidelberg), G. Tonelli (Pisa), M. Tuts (Columbia), J. Virdee (IC London)

Programme Committee

D. Denegri (Saclay, Chair), K. Jakobs (Freiburg, Chair), F. Antinori (Padova), M. Carena (FNAL), R. Forty (CERN), C. Grojean (CERN), J. Incandela (UCSB), T. LeCompte (Argonne), A. Nisati (Rome), G. Rolandi (CERN), K. Safarik (CERN), O. Schneider (EPFL Lausanne), P. Sphicas (CERN), S. Tapprogge (Mainz), D. Zeppenfeld (Karlsruhe)

Local Organizing Committee

A. Brandes (DESY, Conference Secretary), C. Potter (CERN, Conference Secretary), K. Borras (DESY), M. Brehmer (DESY), M. Diehl (DESY), V. Gülzow (DESY), J. Haller (Hamburg), M. Medinnis (DESY), M. Mende (DESY), S.-O. Moch (DESY), K. Mönig (DESY), G. Steinbrück (Hamburg), G. Weiglein (DESY), P. Wegner (DESY)

Preface

The conference “Physics at the LHC 2010” took place at DESY in Hamburg, Germany, from 7–12 July 2010. It was the fifth conference of the PLHC series, which started in Prague in 2003 and continued in Vienna (2004), Cracow (2006) and Split (2008). The rich programme covered all fields of LHC physics and attracted more than 270 participants, demonstrating the vivid interest by both experimentalists and theorists.

In this first large conference at which 7 TeV collision data from the LHC were discussed, special emphasis was put on first experience with the operation of the LHC detectors, on detector performance studies and on early physics results. The main message of the conference was that the LHC is in good shape, with data taking by the experiments going smoothly, triggers and reconstruction working well, and detector understanding progressing quickly. It was shown that already now many performance goals of the detectors are either achieved or within close reach. These results document that the experiments are well prepared for their future tasks: discoveries at the TeV scale, for which prospects and expectation were also presented at the conference.

The participants noted with satisfaction that the German funding bodies expressed their keen interest to further support the LHC. This was confirmed in the welcome messages of Georg Schütte, State Secretary in the German Ministry for Education and Research, and Bernd Reinert, State Council for Science and Education of the state of Hamburg.

It is a pleasure to thank our colleagues from the DESY IT and Public Relations departments and from the technical support team for their tremendous efforts and their ceaseless attention to detail in the preparation of the conference. Equally, we thank all involved staff and students from DESY and Hamburg University for their support during and between the sessions and for their help in preparing the proceedings volume. Special thanks go to the administrative and secretarial team for their tireless work before and during the conference week: Antje Brandes, Michaela Grimm, Cristina Guerrero, Martina Mende and Natalia Potylitsina-Kube. Further invaluable support came from Birgit Breetzke, Sylvie Faverot-Spengler, Alla Grabowsky, Iris Kerkhoff, Steffi Killough, Sabine Krohn, Petya Lilova and Andrea Schrader. We also thank the members of the Advisory and Programme Committees for their efforts, especially the conference chairs Guenakh Mitselmakher (Florida) and Joachim Mnich (DESY) and the Programme Committee chairs Daniel Denegri (Saclay) and Karl Jakobs (Freiburg). We acknowledge financial support from DESY, the Deutsche Forschungsgemeinschaft (DFG), the University of Florida, the Association of Friends and Supporters of DESY, the Helmholtz Alliance “Physics at the Terascale” and the Sonderforschungsbereich 676 “Particles, Strings and the Early Universe”.

The organisers are very much looking forward to the results of the future high-statistics and high-energy runs at the LHC and to the next “Physics at the LHC” conference, to be held in Perugia, Italy, from 6–11 June 2011.

Hamburg, December 2010
Markus Diehl, Johannes Haller, Thomas Schörner-Sadenius, Georg Steinbrück

Contents

1 Opening talk and summary 1

The LHC and Beyond - Past, Present and Future 3
Rolf-Dieter Heuer

Experimental summary and outlook 10
Peter Jenni

2 Machine and detectors: status, performance and outlook 13

Near and medium term LHC machine prospects 15
Mike Lamont

Status and initial operation of ALICE 23
Jürgen Schukraft

LHCf: Status and short term prospects 29
Gaku Mitsuka

Strip Tracker of CMS: Operation and performance in first 7 TeV collisions 34
Natale Demaria

Tracking and Alignment in LHCb 39
Florin Maciuc

Alignment of the CMS tracker and track reconstruction with collision data in CMS 43
Alessio Bonato

Alignment of the Inner Detector and of the Muon Spectrometer of the ATLAS experiment 47
Igor Potrap

ALICE silicon tracker alignment and performance 51
Marcello Lunardon

The commissioning of ALICE's TPC 55
Magnus Mager

Operational experience and performance of the CMS pixel detector during the first LHC beams **59**
Valeria Radicci

ATLAS inner detector material studies **63**
Kerstin Tackmann

Performance of muon identification and reconstruction in ATLAS **67**
Thijs Cornelissen

CMS muon spectrometer, muon reconstruction and identification performance **71**
Luca Scodellaro

Performance of the Missing Transverse Energy Reconstruction in the first ATLAS Data at 7 TeV **75**
Adam Yurkewicz

LHCb commissioning and operation **79**
Dirk Wiedner

Particle Identification in LHCb **83**
Fúnaì Xíng

Commissioning and performance of the ATLAS trigger with proton collisions at the LHC **87**
Iwona Grabowska-Bold

Reconstruction and selection of physics objects in the ATLAS high level trigger **91**
Rasmus Mackeprang

3 First results and Standard Model physics **95**

ALICE first physics results **97**
Andrea Dainese

First CMS Results **107**
Valerie Halyo

Physics with first LHCb data **119**
Olivier Schneider

Top physics at the Tevatron **128**
Julia Thom

Status of (N)NLO calculations **134**
Thomas Gehrmann

Monte Carlo for the LHC **147**
Michael H. Seymour

Charged particle multiplicities in inelastic pp interactions with ATLAS and the ATLAS Minimum BiasTune 1 **157**
Gerhard Brandt

Transverse momentum and pseudorapidity distributions of charged hadrons at CMS **160**
Yen-Jie Lee

Identified particle production in inelastic pp scattering with ATLAS **164**
Jedrzej Biesiada

Perspectives of strangeness measurements at LHC with ALICE **168**
Antonin Maire

Cluster properties from two-particle angular correlations in pp collisions at CMS **173**
Elisabetta Gallo

First results on particle correlations in ALICE **177**
Dariusz Miśkowiec

Measurement of Bose-Einstein correlations in the first LHC-CMS data **181**
Ezio Torassa

Event-shape variables at hadron colliders **186**
Andrea Banfi

Response of single isolated hadrons in the first ATLAS data at $\sqrt{s}$ = 900 GeV **190**
Pier-Olivier DeViveiros

Minimum Bias and Underlying Event Developments in Herwig++ **194**
Stefan Gieseke, Simon Plätzer, Andrzej Siodmok, Christian Röhr

NLO matrix elements and truncated showers **199**
Stefan Höche, Frank Krauss, Marek Schönherr, Frank Siegert

NLO and parton showers: the POWHEG − BOX **204**
Simone Alioli

Underlying event studies in inelastic pp collision events with the ATLAS detector **209**
Markus Warsinsky

The underlying event in pp collisions at 900 GeV in CMS **214**
Giuseppe B. Cerati

Baryon–antibaryon asymmetry in the central region at $\sqrt{s} = 0.9$ and 7 TeV with ALICE **219**
Michal Broz

Observation of diffraction and measurement of the forward energy flow with the CMS detector **223**
Benoît Roland

Electron performance with the ATLAS detector with J/ψ, W and Z **227**
Nicolas Kerschen

Observation of W and Z boson candidates with the CMS experiment **232**
Emanuele Di Marco

Jet commissioning and dijet physics in CMS **237**
Maxime Gouzevitch

Observation of energetic jet production in pp collisions at $\sqrt{s} = 7$ TeV using the ATLAS experiment at the LHC **241**
Eric Feng

Performance of the particle flow algorithm in CMS **246**
Daniele Benedetti

Improving the present precision of the electroweak parameters at the LHC: a forlorn hope? **250**
Mieczyslaw Witold Krasny

Four-top events at the LHC **254**
Géraldine Servant

4 Higgs physics and physics beyond the Standard Model **259**

Theory of dark matter **261**
Graciela B. Gelmini

Higgs and electroweak symmetry breaking **267**
J. Espinosa, C. Grojean and M. Mühlleitner

Prospect for Higgs searches in CMS with 1 fb^{-1} at 7 TeV and CMS performance validation with early data **271**
Alberto Graziano

BSM Higgs physics at the LHC in the forward proton mode **275**
Sven Heinemeyer, Valery A. Khoze, Misha G. Ryskin, Marek Tasevsky, Georg Weiglein

Hidden Higgs Scenarios: new constraints and prospects at the LHC **279**
Radovan Dermíšek

Commissioning of Leptons and Prospects for Searches of Leptoquarks, W' and Z' in CMS **284**
Kerstin Hoepfner

Early searches with jets with the ATLAS detector at the LHC **288**
Victor Lendermann

Discovering SUSY in the first LHC run **291**
Sven Heinemeyer

Sparticle masses from transverse mass kinks at the LHC: The case of Yukawa unified SUSY GUTs **295**
Diego Guadagnoli

SUSY parameter determination **299**
Takanori Kono

CP-violation in SUSY cascades at the LHC **303**
Jamie Tattersall, Gudrid Moortgat-Pick, Krzysztof Rolbiecki

Missing energy commissioning in CMS and prospects for supersymmetry searches with 1 fb^{-1} **307**
Robert Schöfbeck

Drell-Yan production of heavy vectors in Higgs-less models **311**
Oscar Catà, Gino Isidori, Jernej F. Kamenik

5 Flavour physics **315**

B Physics (Experiment) **317**
Michal Kreps

Flavour theory and the LHC era **325**
Andrzej J. Buras

Review of charm physics: a theory perspective **342**
Thomas Mannel

An updated measurement of the B_s^0 mixing phase $\sin(2\beta_s)$ at CDF **350**
Elisa Pueschel

Towards the measurement of the J/ψ cross section at $\sqrt{s} = 7$ TeV in LHCb **354**
Julien Cogan

b and c physics with early ATLAS data **358**
Nir Amram

Results and prospects for di-muon final states at LHCb **362**
Justine Serrano

Prospects for CP violation at LHCb **366**
Géraldine Conti

6 Heavy ion physics **371**

Heavy ion collisions: puzzles and hopes **373**
Jean-Paul Blaizot

Heavy ion physics with the ATLAS detector **379**
Helena Santos

7 Posters **383**

Unnatural origin of fermion masses for technicolor **385**
Matti Antola, Matti Heikinheimo, Francesco Sannino, Kimmo Tuominen

Collider signatures related to quark flavour violation in the MSSM **388**
Björn Herrmann

ATLAS high-level calorimeter trigger algorithms performance with first LHC pp collisions **391**
Pavel Ježˇ

Three-loop predictions for the light Higgs mass in the MSSM **394**
Philipp Kant

Alignment of the ATLAS Inner Detector tracking system **397**
Thomas Loddenkoetter

Forward Λ_b production in pp collisions at LHC **400**
Gennady I. Lykasov, Denis A. Artemenkov, Vadim A. Bednyakov

On the phenomenology of a two-Higgs-doublet model with maximal CP symmetry at the LHC: synopsis and addendum **403**
Markos Maniatis, Andreas von Manteuffel, Otto Nachtmann

Performance of the ATLAS liquid argon calorimeter **406**
Zhaoxia Meng

Neutral MSSM Higgs and Z boson associated production at the LHC **409**
Caesar P. Palisoc, Bernd A. Kniehl

Performance of the ATLAS inner detector trigger algorithms in p-p collisions at $\sqrt{s} = 900$ GeV and $\sqrt{s} = 7$ TeV **412**
Andrea Ferretto Parodi

MSSM Higgs Boson Production via Gluon Fusion **415**
Margarete Mühlleitner, Heidi Rzehak, Michael Spira

Inclusive and associated b-quark production in the Regge limit of QCD **418**
Bernd A. Kniehl, Vladimir Saleev, Alexandera Shipilova

Physics potential of the CMS CASTOR forward calorimeter **421**
Dmytro Volyanskyy

The sensitivity of the ATLAS detector to the Standard Model Higgs boson in the four lepton final state **424**
Craig Wiglesworth

Tile calorimeter at work in the collision era **427**
Tibor Zenis

Recent performance results with the ATLAS Muon Spectrometer **430**
Giovanni Zevi Della Porta

Opening talk and summary

The LHC and Beyond - Past, Present and Future

Rolf-Dieter Heuer

CERN, CH-1211 Geneva 23, Switzerland

DOI: http://dx.doi.org/10.3204/DESY-PROC-2010-01/1

This paper presents CERN's scientific plans for the LHC and outlines options for high-energy colliders at the energy frontier for the years to come. The immediate plans include the exploitation of the LHC at its nominal design luminosity and energy as well as upgrades to the LHC and its injectors. This may be followed by a linear electron-positron collider, based on the technology being developed by the Compact Linear Collider and by the International Linear Collider, or by a high-energy electron-proton machine, the LHeC. This paper describes the past, present and future directions, all of which have a unique value to add to experimental particle physics, and concludes by outlining key messages for the way forward.

1 Introduction - The Physics

The Large Hadron Collider (LHC) [1] is primarily a proton-proton collider (see Figure 1) with a design centre-of-mass energy of 14 TeV and nominal luminosity of $10^{34}\ cm^{-2}s^{-1}$, and will also be operated in heavy-ion mode. The high 40 MHz collision rate and the tens of interactions per crossing result in an enormous challenge for the detectors and for the collection, storage and analysis of the data.

By colliding unparalleled high-energy and high-intensity beams, the LHC will open up previously unexplored territory at the TeV scale in great detail, allowing the experiments to probe deeper inside matter and providing further understanding of processes that occurred very early in the history of the Universe.

Of central importance to the LHC is the elucidation of the nature of electroweak symmetry breaking, for which the Higgs mechanism and the accompanying Higgs boson(s) are presumed to be responsible. In order to make significant inroads into the Standard Model Higgs Boson search, sizeable integrated luminosities of several fb^{-1} are needed. However, even with 1 fb^{-1} per experiment, discovery of the Standard Model Higgs Boson is still possible in certain mass regions beyond the lower limit of 114.4 GeV from direct searches at LEP2. At a centre-of-mass energy of 7 TeV and for 300 pb^{-1} per experiment, combining the results from ATLAS and CMS would provide a 3 σ sensitivity for a Standard Model Higgs Boson mass of 160 GeV, and will exclude the Standard Model Higgs Boson between 145 GeV and 180 GeV for 1 fb^{-1} per experiment. Exclusion of the full mass range down to the LEP2 lower limit requires 1.5 fb^{-1} per experiment at 14 TeV centre-of mass-energy, while the discovery of a Standard Model Higgs Boson at the LEP2 lower limit requires 10 fb^{-1} per experiment at 14 TeV centre-of-mass energy.

The reach for new physics at the LHC is considerable already at LHC start-up. In Supersymmetry (SUSY) theory, due to their high production cross-sections, squarks and gluinos can

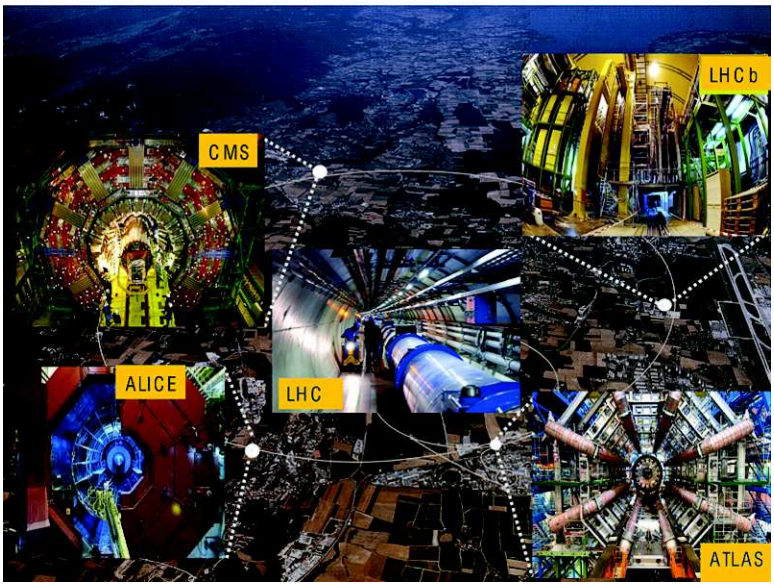

Figure 1: The LHC accelerator and the ALICE, ATLAS, CMS and LHCb experiments. There are also three smaller experiments - LHCf, MoEDAL and TOTEM.

be produced in significant numbers even at modest luminosities. This would enable the LHC to start probing the nature of dark matter. The LHC discovery reach for SUSY particles is up to a mass of about 400 GeV for 100 pb^{-1} and up to 800 GeV for 1 fb^{-1} per experiment at 7 TeV centre-of-mass energy. The discovery reach for the new heavy bosons Z' and W' is 1.5 TeV and 1.9 TeV, respectively, for 1 fb^{-1} per experiment at 7 TeV centre-of-mass energy.

The LHC will also provide information on the unification of forces, the number of space-time dimensions and on matter-antimatter asymmetry. With the heavy-ion collision mode, the LHC will probe the formation and the properties of the quark-gluon plasma at the origin of the Universe.

2 The LHC Programme

2.1 The Past

The start-up of the LHC on 10 September 2008 was a great success for both the accelerator and the experiments. Circulating beams were established rapidly and the beams were captured by the radiofrequency system with optimum injection phasing and with the correct reference. The incident of 19 September 2008, caused by a faulty inter-magnet bus-bar splice, resulted in significant damage in Sector 3-4 of the accelerator. Actions were taken immediately to repair the damage and to introduce measures to avoid any re-occurrence. The damaged thirty-nine main dipole magnets and fourteen quadrupole magnets were removed and replaced. Fast pressure release valves (DN200) were added on the main magnets, an improved anchoring on the vacuum barriers was introduced around the ring, and an enhanced quench protection system was implemented. This has resulted in a significant amount of work and any remaining risks

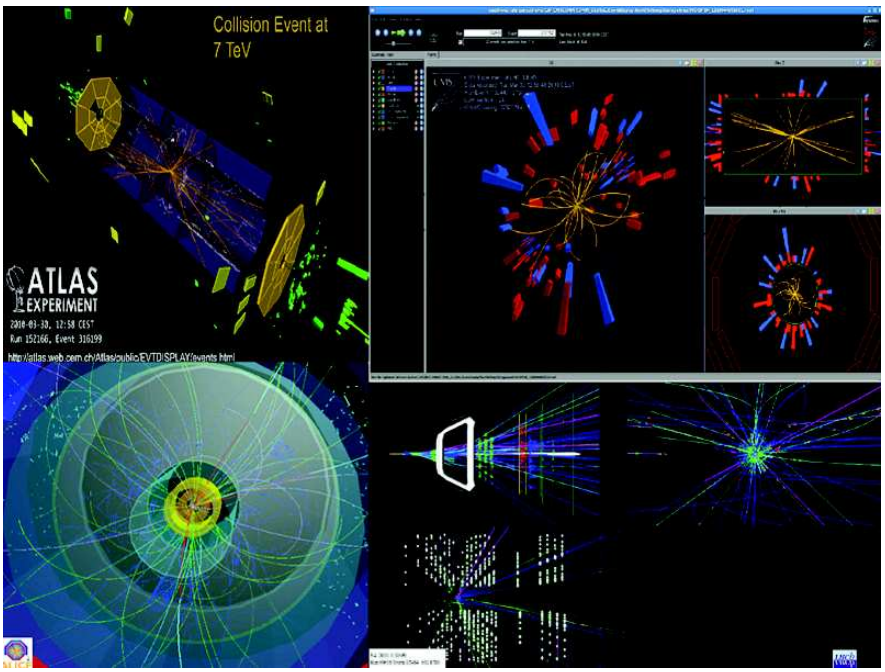

Figure 2: First collisions at 7 TeV centre-of-mass energy.

to the LHC, due to the shortcomings of copper-stabilizer joints of the main LHC magnets, are minimized by limiting the top beam energy in the first years of LHC operation.

Excellent progress was made in the above-mentioned repair, consolidation and improvement work, and first collisions at the LHC were recorded by the experiments on 23 November 2009 at a centre-of-mass energy of 900 GeV. During this first physics run at the end of 2009, the LHC accelerator performed exceptionally and the readiness of the experiments and the computing was excellent, resulting in impressive preliminary results provided already at an open seminar held at CERN on 18 December 2009 and the prompt publication of the first physics results by year's end.

2.2 The Present

First LHC beams for 2010 were available on 27 February for commissioning the accelerator with beam. This was followed by first physics collisions at 7 TeV centre-of-mass energy on 30 March (see Figure 2) and by the first physics runs with a stronger focusing at the interaction points. During the 2009 and 2010 LHC physics runs, data has been collected at 900 GeV, 2.36 TeV and 7 TeV centre-of-mass energies with increasing instantaneous luminosities.

CERN has taken the following decisions that will allow the LHC to provide substantial physics in 2010-2011 and be technically capable of operating at the design energy and high intensities as of 2013:

- The LHC will be operated at 3.5 TeV/beam during 2010 and 2011, with a target integrated luminosity of 1 fb^{-1} and with a heavy-ion run at the end of both years.

- This extended operations period will be followed by a long shutdown (of the order of at least 12 months) in 2012 to repair and consolidate the inter-magnet copper-stabilizers to allow for safe operation at 7 TeV/beam for the lifetime of the LHC.
- In the shadow of the inter-magnet copper stabilizer work, the installation of the fast pressure release valves will be completed and between two and five magnets which are known to have problems for high energy will be repaired or replaced. In addition, SPS upgrade work will be carried out.

2.3 The Future

The coming years will lay the foundation for the next decades of high-energy physics at CERN. The research programme until around 2030 is determined by the full exploitation of the LHC physics potential, consisting of the design luminosity and the high-luminosity upgrade (HL-LHC), together with focused R&D for a Linear Collider (machine and detectors) and for superconducting higher-field magnets for a higher-energy proton collider (HE-LHC), if necessitated by the physics. These initiatives will position CERN as the laboratory at the energy frontier. The strategy for the LHC for the coming years is the following:

- exploitation of the physics potential of the LHC up to design conditions in the light of running experience and by optimizing the schedule for physics;
- preparation of the LHC for a long operational lifetime through appropriate modifications and consolidation to the machine and detectors and through the build-up of an adequate spares inventory;
- improvement to the reliability of the LHC through the construction of LINAC4 [2], which will reduce the risk to LHC operation by replacing the ageing LINAC2, which first came into operation in 1978;
- the R&D and subsequent implementation necessary for a significant luminosity increase of the LHC beyond the design luminosity, i.e. HL-LHC, if necessitated by the physics and/or running experience; in particular it includes the focusing elements in the interaction regions and the upgrades of the injector chain;
- LHC detector modifications to make optimal use of the design LHC luminosity;
- the detector R&D necessary for the luminosity upgrade HL-LHC and the corresponding modifications of the existing LHC experiments.

This strategy is also driven by the necessity to bring the LHC injector chain and the technical and general infrastructure up to the high standards required for a world laboratory in order to ensure reliable operation of the CERN complex.

The ambitious longer-term plans aim at a total integrated luminosity of the order of 3000 fb^{-1} (on tape) by the end of the life of the LHC around 2030. This implies an annual luminosity of about 250-300 fb^{-1} in the second decade of running the LHC. It also calls for a new strategy to optimize the integrated luminosity useful for physics. Therefore, the LHC operation schedule will henceforth be over a two-year cycle, with a short technical stop around Christmas at the end of the first year and a longer shutdown following the end of the second year. Such a schedule is more efficient for the operation of a superconducting accelerator.

In light of the above developments, the following strategy has been introduced:

- The Chamonix LHC Performance Workshop in January 2010 identified the need for a complete refurbishment of all copper-stabilizer joints of the main LHC magnets for safe running at 7 TeV/beam. The copper-stabilizer repair is scheduled throughout 2012 (long shutdown).

- To ensure reliable operation of the LHC in the coming years, there is a need to consolidate intensively the existing LHC injector chain. This is due to the fact that even if approved soon, the low-power superconducting proton linac LP-SPL and PS2 would realistically be available in 2020 at the earliest.

- In order to optimize the strategy towards the HL-LHC, with the goal of maximizing the integrated luminosity useful for physics, CERN has set up a task force. A preliminary recommendation from this task force is to delay the inner triplet replacement to a single HL-LHC upgrade around 2020. The complete HL-LHC upgrade needs a much clearer definition of implementation objectives based on the requirements of the experiments, such as the use of crab cavities, in order for the LHC to operate reliably at luminosities of about $5 \times 10^{34}\ cm^{-2}s^{-1}$. This may include the option of luminosity leveling to ensure a high luminosity lifetime.

- Furthermore, the bottlenecks of the injector chain need to be tackled and hence upgrades are being studied with a view to increasing the extraction energy of the PS Booster as well as upgrades to the SPS, the latter currently being a significant bottleneck for increasing the LHC intensity beyond design.

3 The Way Forward and the European Strategy for Particle Physics

The LHC will provide a first indication of any new physics at energies of the TeV scale. Many of the open questions left by the LHC and its upgrades may be addressed best by an electron-positron collider, based on technology developed by the Compact Linear Collider (CLIC) [3] and International Linear Collider (ILC) [4] collaborations. Moreover, the option of a high-energy electron-proton collider (LHeC) [5] is being considered for the high-precision study of QCD and of high-density matter.

Great opportunities are in store at the TeV scale and a fuller understanding of Nature will come about through a clearer insight at this energy level. As in the past, there is a synergy between collider types proton-proton, electron-positron and electron-proton. The discovery of the Standard Model over the past few decades has advanced through the synergy of hadron-hadron (e.g. SPS and the Tevatron), lepton-hadron (HERA) and lepton-lepton colliders (e.g. LEP and SLC). Such synergies should be continued in the future and thus a strategy has been developed along these lines. An upgrade to the LHC will not only provide an increase in luminosity delivered to the experiments, but will also provide the occasion to renew the CERN accelerator complex. The ILC could be constructed now whereas further R&D is needed for CLIC. There is a drive to converge towards a single electron-positron linear collider project. The above effort on accelerators should advance in parallel with the necessary detector R&D. First results from the LHC will be decisive in indicating the direction that particle physics will take in the future.

European particle physics is founded on strong national institutes, universities and laboratories, working in conjunction with CERN. The increased globalization, concentration and scale of particle physics require a well-coordinated European strategy. This process started with the establishment of the CERN Council Strategy Group, which organized an open symposium in Orsay in 2006, a final workshop in Zeuthen in May 2006 and with the strategy document being signed unanimously by Council in July 2006 in Lisbon [6]. CERN considers that experiments at the high-energy frontier to be the premier physics priority for the coming years. This direction for future colliders at CERN follows the priorities set in 2006 by the CERN Council Strategy Group. The European Strategy for Particle Physics includes several key areas of research, all in line with CERNs plans for the future directions. The years 2010 and 2011 are seeing the start of the LHC physics exploitation leading to important input for the update of the European strategy for particle physics planned for 2012.

4 Key Messages

Particle physics will need to adapt to the evolving situation. Facilities for high-energy physics (as for other branches of science) are becoming larger and more expensive. Funding for the field is not increasing and the timescale for projects is becoming longer, both factors resulting in fewer facilities being realized. Moreover, many laboratories are changing their missions. All this leads to the need for more co-ordination and more collaboration on a global scale. Expertise in particle physics needs to be maintained in all regions, ensuring the long-term stability and support through-out. It would be necessary to engage all countries with particle physics communities and to integrate the communities in the developing countries. The funding agencies should in their turn provide a global view and synergies between various domains of research, such as particle physics and astroparticle physics, should be encouraged.

Particle physics is now entering a new and exciting era. The start-up of the LHC allows particle physics experiments at the highest collision energies. The expectations from the LHC are great, as it could provide revolutionary advances in the understanding in particle physics and a fundamental change to our view of the early Universe. Due to the location of the LHC, CERN is in a unique position to contribute to further understanding in particle physics in the long term.

Results from the LHC will guide the way in particle physics for many years. It is expected that the period of decision-making concerning the energy frontier will be in the next few years. Particle physics is now in an exciting period of accelerator planning, design, construction and running and will need intensified efforts in R&D and technical design work to enable the decisions for the future course and global collaboration coupled with stability of support over long time scales.

The particle physics community needs to define now the most appropriate organizational form and needs to be open and inventive in doing so, and it should be a dialogue between the scientists, funding agencies and politicians. It is mandatory to have accelerator laboratories in all regions as partners in accelerator development, construction, commissioning and exploitation. Furthermore, planning and execution of high-energy physics projects today require world-wide partnerships for global, regional and national projects, namely for the whole particle physics programme. The exciting times ahead should be used to establish such partnerships.

5 Fascinating Science

With the largest and most complex scientific equipment, the LHC accelerator and experiments are today attracting immense attention and the LHC is possibly the most-watched scientific endeavour. The LHC is in the spotlight of not only the scientific community but also of the general public and the international media. It has become so due to its fascinating and forefront science, which addresses long-standing questions of human-kind with vanguard technologies. Moreover, the LHC stimulates general interest, increases knowledge, educates and trains the scientists and engineers of tomorrow and drives innovation and technology. This current interest should be used to promote the field of particle physics.

6 Conclusions

In this paper we have provided a description of the driving factors for the LHC physics programme and for future proton and lepton colliders. In the coming years, the ordered priorities are the full exploitation of the LHC, together with preparation for a possible luminosity upgrade and the consolidation and optimization of the CERN infrastructure and the LHC injectors. It will be necessary to keep under review the physics drivers for future proton accelerator options and it will be necessary to compare the physics opportunities offered by proton colliders with those available at a linear electron-positron collider and an electron-proton collider. The R&D associated with future colliders should continue in parallel.

7 Acknowledgements

I would like to thank the organizers for the invitation to make this contribution and for the excellent organization of the very interesting conference, which included first results from the LHC. I would also like to thank Emmanuel Tsesmelis for his assistance is preparing this contribution.

References

[1] LHC Design Report, Volumes I, II and III, http://lhc.web.cern.ch/lhc/LHC-DesignReport.html

[2] http://linac4.web.cern.ch/linac4/

[3] http://clic-study.web.cern.ch/CLIC-Study/

[4] http://www.linearcollider.org/

[5] http://lhec.web.cern.ch/lhec

[6] The European Strategy for Particle Physics, http://council-strategygroup.web.cern.ch/council-strategygroup/Strategy_Statement.pdf

Experimental summary and outlook

Peter Jenni

CERN, 1211 Genève 23, Switzerland

DOI: http://dx.doi.org/10.3204/DESY-PROC-2010-01/12

For the first time at a 'Physics at the LHC' conference real collision data and results were presented from the LHC. Selected samples from the huge amount of commissioning studies have been described in this talk, all of which illustrate how impressively well the LHC experiments are ready for physics. Alongside, the Tevatron collider and its experiments continue to deliver efficiently a rich harvest of physics results, and only a few highlights could be emphasised. A roadmap of expected physics to come from the two hadron colliders has been sketched.

1 Introduction

The LHC began high-energy operation on 30th March 2010, with 7 TeV centre-of-mass pp collisions. This marks clearly the beginning of a new era in particle physics, the eagerly awaited journey into new territory at the energy frontier can start. The two most important messages of this conference can simply be summarized as: This is the first 'Physics at the LHC' conference with the LHC running, and the LHC experiments presenting real data from collisions, and the data presented demonstrate that the experiments are extremely well prepared for producing fast high quality physics results.

The progress of the LHC collider has been outstanding over the past months, and at the time of writing (end of July 2010) the data samples accumulated and analysed by the experiments have superseded the ones shown at the conference by more than an order of magnitude. Furthermore, as all the sophisticated analyses will be documented in these proceedings in detail, and 'first-hand' by those directly involved in the work, the experimental summary talk will not be reproduced here. It will be limited to a few general comments.

2 Commissioning the LHC experiments

It is impressive to note that the four large LHC detectors (ALICE, ATLAS, CMS and LHCb) are already operated, only a couple of months into the run, with very high efficiencies for data taking. For example the large, complex general purpose detectors ATLAS and CMS reported for all their subsystems typically more than 98% of the readout channels working, and overall data taking efficiencies above 90%. Even though they did not yet have to stress-test their trigger schemes with the luminosities reached so far at this stage by the LHC, very detailed studies with unbiased data allowed them to verify an accurate understanding of rates and threshold behaviours.

A huge variety of performance studies were reported by all experiments using the minimum bias data collected during the 900 GeV run end of last year and with the 7 TeV data from the current run over the last two months. These performance studies culminate in 'rediscovering' many classical resonance signals, charmed meson mass peaks, as well as the J/ψ decaying into lepton pairs. The resolutions are approaching already in many cases the design values, and detailed features like for example hit distributions, particle identification capabilities and energy distributions are almost perfectly well described by Monte Carlo simulations. It is not exaggerated to state that never in the past experiments have been ready to such a great extent when starting up operation with beams. This is certainly only possible thanks to a long history of test beam studies, which condition the detector simulations, combined with exploiting the huge amounts of cosmics data from the last couple of years. The collision data is now already used to 'fine-tune' the understanding of the detectors.

LHCf, one of the two small dedicated forward experiments, has been accumulating data of high quality since the start, whereas TOTEM has demonstrated its readiness to join running soon when conditions will permit.

A special comment is due to the smooth performance of the computing and software chains. The experiments have been able to efficiently handle large amounts of date, distributed worldwide in the collaborations, and to very quickly analyse them and produce results within days. The WLCG as backbone to all these operations has been crucial, and delivered reliably the expected performance.

3 Understanding the environment: minimum bias events at LHC

The first LHC physics publications cover basic features like differential and global charged particle multiplicity and transverse momentum distributions. All four experiments showed new results, allowing one to make detailed comparisons with Monte Carlo predictions. There is clearly a need for tuning the latter in order to get satisfactory descriptions of the pp event environment at the new energies of LHC. Further results addressed more detailed aspects, like the structure of the underlying events, distributions of identified particle types, and multiparticle correlations.

An important ingredient for the quantitative understanding of LHC physics will be the knowledge of parton distribution functions. The final HERA structure function results presented at this conference are of particular relevance in this respect.

4 Physics and outlook

Whereas the LHC is just entering the scene, the Tevatron Collider at Fermilab is continuing to perform in a superb way. The CDF and D0 collaborations operate with high efficiency their well understood detectors, and exploit them with highly developed analysis skills. No doubt that they have still a major potential for great physics in the near future. During that time the LHC experiments will continue to 'rediscover' the known particles from the Standard Model and make first basic measurements at 7 TeV. At this conference ATLAS and CMS have shown the first handful of W and Z events, again demonstrating that the detectors work well, and they are eagerly preparing for the Top as a next step.

Both CDF and D0 have shown a rich harvest of physics results which are discussed in many excellent summary talks, as well as the most topical ones in dedicated expert presentations. Combining their data they will remain certainly at the forefront for the Higgs search still for a couple of years, and in precision measurements, like the W mass measurement, it will take the LHC experiments still several years to match them. Owing to the high collision energy, the LHC is expected to take leadership in the coming year for searches of heavy mass objects like for example SUSY particles and W' or Z'. For the Higgs, combining ATLAS and CMS, a definite statement about its existence or not should be possible around 2015 when the LHC will have accumulated some $10\,\mathrm{fb}^{-1}$ or more at 14 TeV.

It is interesting to note that early hints for New Physics beyond the Standard Model could well come from the Heavy Flavour physics in the first years at LHC.

The turn-on of the LHC opens a great era for our community; exciting times are ahead of us!

Machine and detectors: status, performance and outlook

Near and medium term LHC machine prospects

Mike Lamont for the LHC team

CERN, Geneva, Switzerland

DOI: http://dx.doi.org/10.3204/DESY-PROC-2010-01/8

The challenges facing the LHC machine as it nears the end of its initial commissioning period are recalled. With these in mind projections are made for the coming two years' operation. The foreseen shutdowns for the following years are briefly outlined and estimates for the potential luminosity and integrated luminosity cautiously presented.

1 Introduction

The LHC is drawing to the close of a successful initial commissioning period. The machine has proven to be magnetically and optically well understood and there is excellent agreement with model and machine. It is magnetically reproducible; this is important because it means optics and thus set-up remains valid from fill to fill. The aperture is clear and as expected. There has been excellent performance from instrumentation and controls, and key subsystems are performing well, namely: injection; the beam dump systems; collimation and machine protection.

The ramp and squeeze are, in general, under control and the LHC routinely injects, ramps and squeezes multiple bunches and brings them into stable beams conditions allowing data taking by the experiments. It has also proved possible to keep these conditions for extended periods of time. The maximum fill length is a remarkable 30 hours - impressive for a machine at this stage of commissioning. Nominal bunch intensities have been injected, successfully ramped and brought into collisions at 3.5 TeV.

This progress has been made in the face of the daily challenge of operating an immensely complex machine with the omnipresent concern for machine safety. Operations is dependent on some huge supporting systems, for example: cryogenics, quench protection systems, powering, access, and vacuum and also dependent on a large number of critical sub-systems: RF, synchronization, timing, transverse feedback, orbit and tune feedback, beam instrumentation with huge distributed systems, controls infrastructure, software, databases. Most of these are performing well but there are clearly some features left to iron out and commissioning to finish.

The problems posed by the above systems eat into machine availability and some of them give pause when considering machine safety. The scale of the dangers that the machine faces has been well documented. The 11 GJ of energy stored in the magnets at 7 TeV are sufficient to heat and melt around 15 tons of Copper. The 360 MJ stored in the nominal beam correspond to around 80 kg of TNT. The damage potential of a mere 2 to 3 MJ beam has already been amply demonstrated in extraction tests of the LHC beam from the SPS.

Two points are to be made here: firstly, the LHC has a way to go before it is ready to handle the dangers of beams with stored energies of tens of mega-Joules or higher; secondly it

will always be faced with an enormously complex infrastructure and the attendant problems. Even a cursory glance at the evolution of accelerators like HERA, the Tevatron, and LEP show that ramping up luminosity production takes time. LHC has started well, and to be credible in face of expectations, it had to.

2 Machine protection issues

A brief reminder of the main machine protection issues is given below. Full mastery of these dictates the ability of the ramp up in peak luminosity and motivates the cautious, staged increase in total beam current outlined later.

- **The Beam Interlock System (BIS)** of the LHC uses 16 beam interlock controllers (BIC) distributed around the ring to gather about 140 user permits [1]. All systems for protection during beam operation have an interface with the BIS, for example: beam dumping system, collimators, beam dilutors, beam monitors, powering interlock systems, RF system, vacuum system, access safety system, and the LHC experiments. The LHC BIS provides a beam permit signal based on the status of the above inputs, and also on the status of the mask settings and the LHC setup beam flag. When the LHC beam permit signal changes from true to false, injection into the LHC is inhibited, and the LHC beam dump system is triggered within 3 turns to remove safely any circulating beam.

- **The LHC beam dump system (LBDS)** is designed to perform fast extraction of beam from the LHC in a loss free way [2]. For each beam a system of 15 horizontal kicker magnets (MKD), 15 vertically deflecting magnetic septa (MSD) and 10 diluter magnets (MKB) is installed. After the kickers the beam sees an additional deflection when traversing the Q4 quadrupole. The MSD deflect the beam vertically before it is further swept in the horizontal and vertical planes in a spiral shape by the MKB kickers. After several 100 m. of beam dump line the beam is absorbed by the dump block (TDE). To protect the septa from mis-kicked beams a special fixed 8 m long graphite protection device (TCDS) is placed just in front of the MSD.

- For nominal operations the MKD rise time should always be accurately synchronised with the 3 μs **abort gap**, so that no beam is swept across the aperture. However some failures can occur which lead to an asynchronous dump. In addition stray particles may also be present in the abort gap. To protect the LHC aperture from these eventualities, a movable single-jawed 6 m long graphite protection device (TCDQ) is installed upstream of Q4, supplemented by a two-jaw 1 m long graphite secondary collimator (TCSG) and a 2 m long fixed iron mask (TCDQM).

- The primary purpose of **the LHC collimation system** is beam halo cleaning [3]. During LHC operation, proton losses must be kept under control in order to avoid quenches of the superconducting magnets. Almost 100 collimators and absorbers with alignment tolerances of less than 0.1 mm ensure that over 99.99% of stray protons are intercepted. The primary and secondary collimators are made of reinforced graphite and are regarded as robust; the tertiary collimators are made of tungsten are regarded as non-robust.

The hierarchy that exists between primary, secondary, tertiary collimators and the protection devices must be respected. It is thus imperative that the collimators and protection devices

are in the correct position at all times. The collimators and protection devices are positioned with respect to the closed orbit and therefore the closed orbit must be in tolerance at all times. This includes the ramp and squeeze and orbit feedback becomes mandatory during these phases. Failure to enforce these strictures will exposed the machine to damage; it will take some time to ensure this categorically.

3 Looking ahead

3.1 Operational schedule

In future it is planned to operate the accelerator complex on a two year basis. Within a two years running period there will be regular six weekly technical stops to solve non-conformities and perform preventive maintenance. There will be a short mid-period Christmas break to perform essential maintenance activities in both the LHC and the injectors.

An operational year within the two year period will include:

- 4 days technical stop and recovery every 6 weeks;
- at least 2 days machine development per month;
- 4-5 week ions run per year;
- other experiment requests for special running conditions e.g. Totem.

The machine availability will, optimistically, be in the order of 50 to 60% during the time dedicated to physics production. Any integrated luminosity estimates should of course take into account the impact of the above on time available to the delivery of luminosity. The two-yearly cycle will be punctuated by relatively long shutdowns, the drivers for which are enumerated below.

3.2 Foreseen long shutdowns

The main drivers for the upcoming major shutdowns [4] are summarized in table 1. From a machine perspective the three major tasks foreseen are:

- **Splice consolidation:** to be 100% sure that the LHC can go safely to 7 TeV per beam, full eradication of the well documented splice issues requires a complete warm-up and long shutdown (2012) during which all interconnect splices will be equipped with mechanical clamping and electrical shunts [5].
- **Collimation phase II** represents the necessary upgrades of the collimation system to allow operation with nominal and ultimate intensities. The upgrades target limitations in efficiency, impedance and other issues. They will consist of two main phases: the warm leg which foresees additional secondary collimators and scrapers into IR3 and IR7 warm regions; and the cold leg which sees installation of collimators in the super-conducting dispersion suppressors in IR7, IR3 and IR2. The latter upgrade is a huge exercise involving moving superconducting magnets. The aim is to do the first part of the exercise (IR3) in the 2012 shutdown [7].

Table 1: Main LHC shutdown activities foreseen in the next 10 years.

Year	Main driver	Secondary activities
2012	Splice consolidation	Collimation phase 2 IR3
15 months		Helium relief valves
		LHC experiments - consolidation
		Radiation to electronics
2016	LINAC4	Booster upgrade
12 months	Collimation phase 2	RF cryogenics upgrade
	LHC experiments consolidation	Radiation to electronics
		Possible crab cavity installation
2020	Preparation for LHC high luminosity	
	Experiments upgrades	

- **LINAC4** represents stage one of the LHC Luminosity upgrade program. The existing proton LINAC - LINAC2 - presents serious reliability and sustainability worries with persistent vacuum problems and an obsolete RF tube design. Instead of an intensive consolidation program the decision has been made to replace it with a new LINAC using modern technologies for better injection and reduced losses (H- injection). LINAC4 will require 7 months to link up with the booster and commission during which time no protons will be available to the accelerator complex.

4 Looking ahead - luminosity

4.1 2010

The clear priority in 2010 is to lay the foundations for 2011 and the eventual delivery of 1 fb^{-1} by the end of 2010/2011. By July 2010 the remaining main objectives of the LHC commissioning with beam program were:

- finish commissioning of some critical sub-systems such as abort gap monitoring, abort gap cleaning, and the transverse damper;
- consolidation and routine physics at stored beam energy of over 1 MJ for an extended period with machine development periods as required;
- gain solid operational experience of faultlessly injecting, ramping, squeezing and establishing stable beams;
- perform a safe, phased increase in intensity with validation and a running period at each step.

Machine protection is clearly hypercritical once the safe beam limit is passed, as is fault free operations and operational procedures. The pre-requisites and detailed planning for increasing intensity are in place and will essentially cover: a full verification of aperture, orbit and optics; full verification of beam dump, protection devices, collimation, injection protection; guaranteed beam quality from injectors; a fully tested beam interlock system including transmission of safe

Table 2: Projected intensity increases and associated performance in 2010 with around nominal bunch intensity (1.1×10^{11}). All numbers approximate.

N_b	N_c	I_{tot}	Energy per beam [MJ]	Peak Luminosity [$cm^{-2}s^{-1}$]	Days	Int. Lumi [pb^{-1}]	Approx. date
3	1	3×10^{11}	0.2	2.5×10^{29}	5	0.03	W4 June
4	2	4×10^{11}	0.2	5.1×10^{29}	5	0.07	W1 July
8	4	8×10^{11}	0.4	1.0×10^{30}	5	0.13	W2 July
20	10	2×10^{12}	1.1	2.5×10^{30}	10	0.6	W3/4 July
24	16	2.4×10^{12}	1.5	4.9×10^{30}	20	1.7	August
48	32	4.8×10^{12}	3.0	9.8×10^{30}	10	1.7	September
96	96	9.6×10^{12}	5.9	2.9×10^{31}	10	5.1	September
144	144	1.4×10^{13}	8.9	4.4×10^{31}	10	7.6	October
192	192	1.9×10^{13}	11.8	5.9×10^{31}	10	10.1	October
240	240	2.4×10^{13}	14.8	7.3×10^{31}	10	12.7	November

machine parameters; fully tested hardware interlock systems; and all required feedback systems operational and appropriate interlocks fully tested.

This list is not exhaustive. Resolution of all procedural, operation, controls, machine protection system, instrumentation, and hardware issues must all have been addressed. It is clear that above will not happen overnight and that a full and careful program of tests and checks is required. An extended operational running period with all prerequisites in place should be pursued. This will allow confirmation that all operational procedures, controls, and instrumentation are fully functional.

Near nominal bunch intensities have been pushed into physics successfully and the resulting outline of the planned increase in beam intensity in 2010 is shown in table 2. The key issue here is the staged increase to and above 1 MJ which is seen as as the damage threshold. An extended running period over summer at around 1.4 MJ is foreseen. This will allow thorough testing of the operations' procedures, and extended verification of the full gamut of machine protection issues before moving on.

4.2 2010 - heavy ion run

A five week lead ion run is scheduled for 2010 with ion set-up starting in the LHC at the beginning of November. It is hoped to leverage the experience gained with protons to rapidly push through the ion commissioning program - the magnetic machine will be near-identical to that used for protons. Ions in the injector chain will have been commissioned in the weeks before they are brought to the LHC.

The early ion parameters that will be applicable to the 2010 run are shown in table 3 and quoted directly from [8]. The initial interaction rate will be around 100 Hz of which 10 Hz will be central collisions with an impact parameter between 0 and 5 fm. In month one might hope to see around 10^8 interactions.

4.3 2011

The present schedule sees a restart of the LHC on 4th February 2011 after a two month technical stop spanning the Christmas period and January. The year foresees 9 months of proton running

Table 3: Parameter list for early (2010/2011) and nominal ion running.

Parameter	units	Early	Nominal
$\sqrt{s}$ per nucleon	TeV	2.76	5.5
Initial luminosity	$cm^{-2}s^{-1}$	1.25×10^{25}	1×10^{27}
Number of bunches		62	592
Bunch spacing	ns	1350	99.8
β^*	m	2	0.5
Pb ions per bunch		7×10^7	7×10^7
Transverse norm. emittance	μm	1.5	1.5
Luminosity half life (1,2,3 expts.)	hours	$3< \tau_{IBS} <70$	8, 4.5, 3

Table 4: Possible 2011 ball-park scenarios with 1.1×10^{11} protons per bunch.

N_b	β^* [m]	Energy per beam [MJ]	Peak Luminosity [$cm^{-2}s^{-1}$]	Int. Lumi per month [pb^{-1}]
432	3.5	27	1.3×10^{32}	61
432	2.5	27	1.8×10^{32}	85
796	3.5	49	2.4×10^{32}	113
796	2.5	49	3.4×10^{32}	157

and a 4 weeks lead ion run. The clear aim during the physics running period is to run flat out above 1×10^{32} $cm^{-2}s^{-1}$ and accumulate an integrated luminosity of 1 fb^{-1} .

The exact parameters for the run will be established given the experience gained in 2010 but ballpark scenarios are shown in table 4. Assuming nominal bunch intensity and nominal transverse emittance, the key parameters in play become β^* and the number of bunches.

- The limit for β^* at 3.5 TeV with the crossing angle on is taken to be 2.5 m. [9].
- Constraints from the collimation system limit the total intensity to around 20% of nominal [3].
- The 796 nominal bunches option shown in table 4 represents about 25% of the nominal intensity and represents an optimistic upper limit for operations in 2011.
- A Hübner factor of 0.2 is assumed for a 27 day month.

4.4 2013 to 2015

4.4.1 Constraints

The beam energy of the LHC will be limited to 3.5 TeV until after splice consolidation in 2012. The consolidation should open the way to 6.5 and eventually 7 TeV. Here it is assumed that it will take around 2 years at 6.5 TeV before the necessary training of the dipoles to 7 TeV is completed [6].

At higher energy, estimates of the limits from collimation phase 1 state that the maximum acceptable intensity is 40% of nominal into a perfect machine [3]. This number drops if imperfections are taken into account. To go beyond this limit the collimation system must include

Table 5: Possible 2013 -2015 beam parameters and associated integrated luminosity

Year	Months	Energy [TeV]	$\beta*$ [m]	N_b	Peak Luminosity [$cm^{-2}s^{-1}$]	Int. Lumi per month [fb^{-1}]
2013	6 (+1)	6.5	1.0	720	1.4×10^{33}	0.7
2014	9	6.5	1.0	1404	2.8×10^{33}	1.3
2015	8	7.0	0.55	2808	1×10^{34}	4.7

collimators, at minimum, in the dispersion suppressors down stream of IR3 and appropriate repartitioning of the existing cleaning configuration [7]. The successful completion of stage one of the collimator upgrade - the installation of collimators in the dispersion suppressors of IR3 in the 2012 shutdown - would open the way towards nominal intensity; the full scheme should allow nominal and ultimate intensities.

4.4.2 Performance

In exploiting 6.5 TeV there will be a move up another learning curve and a stepped increase in total intensity and a possible squeeze to a conservative β^* of 1 m. and finally to 0.55 m. At least a month should be allowed for recommissioning after the long shutdown. The resultant peak luminosities and integrated total per month and per year are shown in table 5. A nominal bunch intensity of 1.15×10^{11} protons is assumed. The β^* and number of bunches will of course be tuned given operational experience and it must be noted that the table show illustrative, ball-park figures. With the usual provisos one might hope to hit nominal energy and luminosity in 2015.

4.5 2017 and beyond

Coming back from a long 2016 shutdown one would hope that:

- the booster, the PS at increased injection energy together with LINAC4 are good to deliver the ultimate bunch intensity (after a suitable commissioning period) to the SPS;
- following an upgrade program, the ultimate intensity can be handled by the SPS;
- the LHC by this stage can handle the ultimate intensity.

The ultimate intensity is very challenging for the LHC. Many systems will be at their technological limits with little or no margin [10]. Given this, the way to 2020 would be steering the LHC between two options: running at or around nominal intensity delivering something like 40 - 50 fb^{-1} in a 9 month year; pushing over one or two years towards ultimate intensity which could eventually deliver around 100 fb^{-1} in a 9 month operational year.

5 Conclusions

The LHC has seen impressive initial commissioning. Further increases in total beam intensity must be accompanied by careful validation of all aspects of machine protection. Short and medium term luminosity estimates are presented. In the short term the objectives are clear and realistic i.e. 1 fb^{-1} by the end of 2011. After a long shutdown for splice consolidation, three

years running at 6.5/7 TeV are envisaged. Installation of stage 1 of the phase 2 collimation system in 2012 should open the way for a push to nominal intensity in the years 2013 - 2015. Progress after a long shutdown in 2016 will be dependent on what is learnt in the previous years and could include: running steady at a nominal production rate; or pushing intensities towards ultimate.

The luminosity estimates presented here are biased towards the optimistic and assume that the LHC can achieve 21st century Hübner factors. The errors bars are big and numbers should be treated with a modicum of circumspection, particularly after 2012.

References

[1] B. Puccio, R. Schmidt, J. Wenninger, Beam interlocking strategy between LHC and its injectors, 10th ICALEPCS Int. Conf. on Accelerator and Large Expt. Physics Control Systems. Geneva, 10 - 14 Oct 2005, PO2.037-3 (2005).

[2] T. Kramer, B. Goddard, M. Gyr, A. Koschik, J. Uythoven, T. Weiler, Apertures in the LHC beam dump system and beam losses during beam abort, Proceedings of EPAC08, Genoa, Italy.

[3] R. Assmann, Intensity limits from phase-1 collimation, Minutes LHC Machine Committee meeting No. 6, March 2009.

[4] K. Foraz, S. Myers, LHC and injectors schedule for the next decade, CERN-ATS-2010-075, July 2010.

[5] F. Bertinelli, Scenarios for consolidations intervention, Proceedings of the LHC performance workshop, Chamonix 2010.

[6] E. Todesco, Dipoles retraining for 7 TeV, Proceedings of the LHC performance workshop, Chamonix 2010.

[7] R. Assmann, Summary of the collimation upgrade plans, Proceedings of the LHC performance workshop, Chamonix 2010.

[8] J. Jowett, Ions in the LHC, Proceedings of Chamonix 2009 workshop on LHC Performance.

[9] W. Herr, Separation and crossing scheme, minimum beta star, Proceedings of Evian beam commissioning workshop, January 2010.

[10] R. Assmann, Implications of higher intensities in the LHC, Proceedings of the LHC performance workshop, Chamonix 2010.

Status and initial operation of ALICE

Jürgen Schukraft for the ALICE Collaboration

CERN, 1211 Geneva, Switzerland

DOI: http://dx.doi.org/10.3204/DESY-PROC-2010-01/7

After close to 20 years of preparation, the dedicated heavy ion experiment ALICE took first data with proton collisions at the LHC at the end of 2009. This article recalls the main design choices made for the detector and summarizes initial operation and performance of ALICE at the LHC; first physics results are covered elsewhere in these proceedings.

1 The first 18 months: design choices

ALICE, which stands for A Large Ion Collider Experiment, is very different in both design and purpose from the other experiments at the LHC. Its main aim is the study of matter under extreme conditions of temperature and pressure, i.e. the Quark-Gluon Plasma, in collisions between heavy nuclei. Data taking with pp (and later p-nucleus) is required primarily to collect comparison data for the heavy ion program. However, given the specific and complementary capabilities of ALICE, a number of measurements concerning soft and semi-hard QCD processes are of interest in their own in these more elementary collisions and are part of the initial physics program [1, 2].

Designing a dedicated heavy ion experiment in the early 90's for use at the LHC almost 20 years later posed some significant challenges: In a field still in its infancy – with the SPS lead program starting only in 1994 – it required extrapolating the conditions to be expected by a factor of 300 in energy and a factor of 7 in beam mass. The detector therefore had to be both, 'general purpose' – able to measure most signals of potential interest, even if their relevance may only become apparent later – and flexible, allowing additions and modifications along the way as new avenues of investigation would open up. In both respects ALICE did quite well, as it included a number of observables in its initial menu whose importance only became clear after results appeared from RHIC (e.g. secondary vertexing for heavy quarks, particle identification up to large transverse momentum), and various major detection systems where added over time to match the evolving physics, from the muon spectrometer in 1995, the transition radiation detector (TRD) in 1999, to a large jet calorimeter (EMCAL) added as recently as 2008.

Other challenges relate to the experimental conditions expected for nucleus-nucleus collisions at the LHC. The most difficult one to meet is the extreme number of particles produced in central collisions, which could be up to three orders of magnitude larger than in typical proton-proton interactions at the same energy, and a factor two to five still above the highest multiplicities measured at RHIC. The tracking of these particles was therefore made particularly safe and robust by using mostly three-dimensional hit information with many points along each track (up to 200) in a moderate magnetic field (B = 0.5 T) to ease the problem of

tracking. In addition, a large dynamic range is required for momentum measurement, spanning more than three orders of magnitude from tens of MeV to well over 100 GeV. This is achieved with a combination of detectors with very low material thickness (to reduce scattering of low momentum particles) and a large tracking lever arm L of up to 3.5 m, which gives a figure of merit for momentum resolution, BL^2, quite comparable to those of the other LHC experiments. In addition, the vertex detector with its six silicon planes, four with analogue read-out, can work as a standalone spectrometer with momentum and PID information to extend the low momentum range for particles that do not reach the outer tracking detectors.

And finally, Particle Identification (PID) over much of this momentum range is essential, as many phenomena depend critically on either particle mass or particle type. ALICE therefore employs essentially all known PID techniques in a single experiment, including energy loss in silicon and gas detectors, Cherenkov and transition radiation, time-of-flight, electromagnetic calorimeters, as well as topological decay reconstruction.

As the LHC luminosity with heavy ion beams is rather modest, with interaction rates of order 10 kHz or less with Pb beams, rather slow detectors can be employed like the TPC and silicon drift detectors. Only moderate radiation hard electronics and trigger selectivity are required and most of the read-out is not pipelined but uses 'track and hold'. However, because the event size in heavy ion interactions is huge (up to 100 Mbyte/event) and the statistics has to be collected in a short time (1 month/year), the DAQ has been designed for very high bandwidth of over 1 Gbyte/s to permanent storage, larger than the throughput of all other LHC experiments combined.

The layout of the ALICE detector and its various subsystems is described in detail in [3].

2 The next 18 years: R&D and construction

The ALICE design evolved from the Expression of Interest (1992) via a Letter of Intent (1993) to the Technical Proposal (1996) and was officially approved in 1997. The first ten years were spent on design and an extensive R&D effort. Like for all other LHC experiments, it became clear from the outset that also the challenges of heavy ion physics at LHC could not be really met (nor paid for) with existing technology. Significant advances, and in some cases a technological break-through, would be required to build on the ground what physicists had dreamed up on paper for their experiments. The initially very broad and later more focused, well organised and well supported R&D effort, which was sustained over most of the 1990's, has lead to many evolutionary and some revolutionary advances in detectors, electronics and computing [4]. One example is given in the following for the 'heart' of ALICE, the Time Projection Chamber (TPC) [5].

The need for efficient and robust tracking has led to the choice of a TPC as the main tracking detector. By providing highly redundant information (up to 159 space points per track), it has to deliver reliable performance with tens of thousands of charged particles within the geometrical acceptance. In order to enhance the two-track resolution and reduce space charge distortions, a rather unusual Neon/CO_2 based drift gas mixture is used: the CO_2 reduces diffusion whereas the Neon has a low primary ionisation and large ion mobility, therefore limiting the built-up of space charge currents. The wire readout chambers are adapted to this gas with a narrow gap, as low as 2 mm, between anode wires and the pad plane. Special attention was also paid to minimise the amount of material and therefore the four cylinders of 5 m length and diameter up to 5.6 m, which make up the TPC vessel, are made of lightweight composite materials. The total amount

of material traversed by a particle from the vertex through the silicon detectors to the outer part of the active TPC volume was thus kept to about 10% of a radiation length, with the TPC operating gas a non-negligible part of the total. The second innovation is the readout electronics: a preamplifier/signal shaper, operating at the fundamental thermal limit of noise, is followed by a specially developed readout chip, the ALICE TPC Read Out (ALTRO) chip. It processes digitally the signals for optimized performance at high collision rates, including a programmable digital pulse shaping circuit and zero suppression/baseline restoration algorithms.

As usual, optimisation involves compromises, and there is a price to pay for the specific choices made: The 'cool' drift gas requires a rather high drift field gradient (400 V/cm); the drift velocity depends very sensitively on temperature (which is kept constant and homogeneous to about 100 mK), pressure, electric field, and gas composition; the chambers have to be constructed with tight geometrical tolerances; the lightweight field cage easily deforms under stress or even gravitation and needs to be kept essentially force-free. In particular the drift velocity needs to be known and constantly calibrated with 10^{-4} accuracy; this is done with several independent methods including a laser system and a special drift velocity detector, while final precision is achieved after several passes using track matching with the vertex detectors.

3 The last 18 weeks: operation

The very first pp collisions where observed in ALICE on November 23, 2009, when the LHC slipped in, on very short notice, an hour of colliding beams for each of its four large experiments during the very early commissioning phase. Such was the penned up energy and enthusiasm about 'real data', after years of simulation exercises, that this first harvest of some 300 events, significantly less than the number of ALICE collaborators, was analysed right away and made it into a physics publication only five days later [6]; well before stable beams were declared on 6 December and sustained data taking could start. It took 20 years to built the experiment, one hour to take the first data, 2 days to get the first result and 3 days to finalise the author list: all of this a clear sign that physics exploitation had started for good!

The many years of preparation, analysis tuning with simulations, and detector commissioning with cosmics during much of 2008/9 paid of quickly and handsomely with most of the detector components working with collisions 'right out of the box' and rather close to performance specifications. Within days all experiments could show first qualitative results and the first phase of LHC physics, often referred to as the 'rediscovery of the standard model', was getting under way [7]. The various members of the 'particle zoo' created in pp collisions made their appearance in ALICE in rapid succession, from the easy ones ($\pi, K, p, \Lambda, \Xi, \phi, \ldots$) in 2009 to the more elusive ones when larger data sets were accumulated early 2010 (K*,Ω, charmed mesons, $J/\Psi, \ldots$).

However, precise results and small systematic errors need more than large statistics and a good detector performance; they require a precise *understanding* and detector simulation as well. The next months were therefore spent on 'getting to know' the experiment in greater detail, including calibration, alignment, material distribution and detector response which are all crucial ingredients for the analysis and correction procedures.

An illustration of the detective work required to accurately measure the material distribution in the central part of ALICE is visible in Figure 1. It shows the distribution of reconstructed photon conversion points in a projection transverse to the beam direction; they sample in great detail the material distribution inside the detector with different structures (beam pipe,

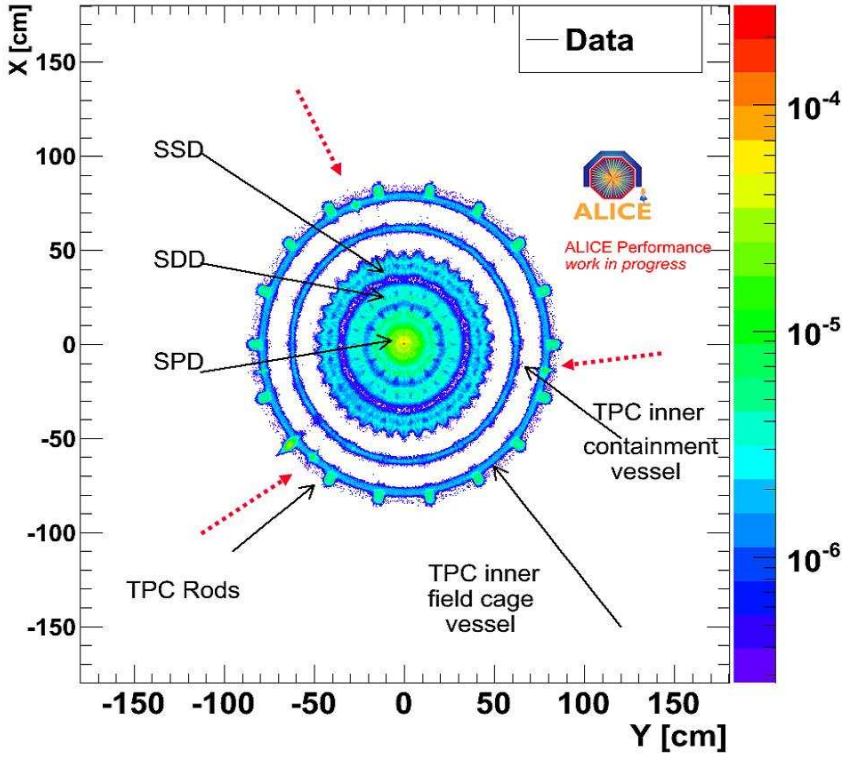

Figure 1: Reconstructed conversion points transverse to the beam direction, showing the material distribution between the vertex and the innermost two vessels of the TPC. The red dashed arrows are explained in the text.

silicon detector layers, TPC vessels etc.) easily discernible. The outermost ring corresponds for example to the TPC inner field cage, with 18 'peaks' corresponding to 18 rods which support the field defining conductive aluminium strips. However, three additional peaks (marked by red dashed arrows) in the data had no known correspondence in the actual detector geometry description, and the baseline between the peaks was slightly higher than expected. After several weeks of consulting construction drawings, and, more important, the people who actually built the detector, it turned out that the additional structures were in the position where the three pieces of the field cage were joined together with a 'generous helping' of glue, whereas the increased thickness corresponded to a last minute change in thickness of the carbon fibre layers, which did not make it into the final drawings. Designing a thin detector is one thing, knowing precisely what was actually built quite another! After similar investigations in other parts of the detector, the material thickness had slightly increased overall but is now known to better than 5% relative accuracy (i.e. 0.5% X/X_0 absolute). Such accuracy is important for example for the measurement of the antiproton to proton ratio, where annihilation of antiprotons in the detector material is one of the limiting factors in reducing the systematic error [8].

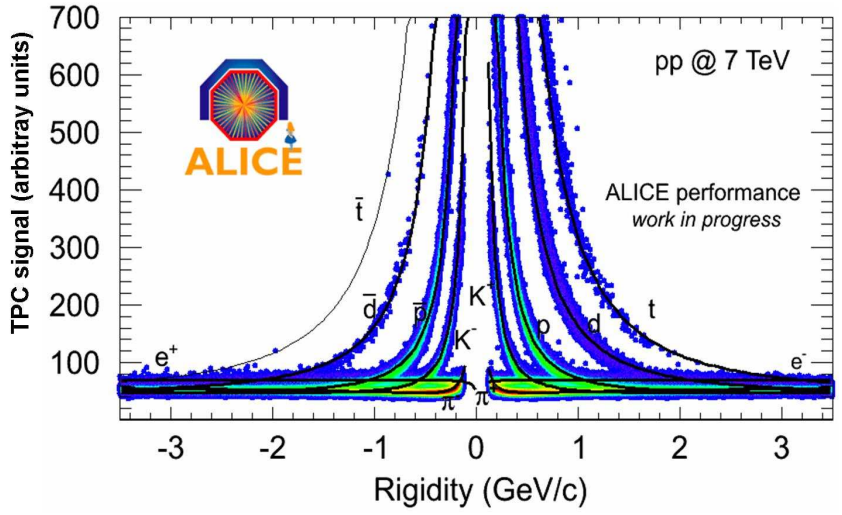

Figure 2: Energy loss distribution versus rigidity for primary and secondary particles reaching the TPC. The lines overlaid on the distribution correspond to the expected energy loss for different particle species.

4 Detector status and data taking

Most of the 18 different ALICE detector systems are fully installed, commissioned and operational, with the exception of the two systems (TRD and EMCAL) which were added more recently and are only now nearing the end of construction. Both systems have currently about 40% of their active area installed and will be completed during the long shutdown in 2012.

Detector alignment, which started with cosmics and continues with beam, is essentially completed for the silicon pixel (SPD) and silicon drift (SDD) vertex detectors (residual misalignment < 10 μm), and has reached about 100 μm for the SDD (where geometrical alignment and drift velocity calibration are coupled). The TPC geometry is aligned to 200–300 μm, approaching the specifications, and the outer detectors are at the mm level required for track matching. This work is still ongoing for the muon spectrometer, which could not be prealigned with cosmics given its vertical orientation along the beam line.

Accurate gain and pulse height calibrations, which are needed in particular for the detectors used for dE/dx particle identification, is essentially complete with the TPC dE/dx resolution having reached its design value about 6% for long tracks. The energy loss distribution in the TPC is shown in Figure 2 versus rigidity, separately for positive and negative charges, demonstrating the clear separation between particle species reached in the non-relativistic momentum region. Note that in this plot tracks are not required to point precisely back towards the vertex and therefore many secondaries produced in the detector material are included.

The TPC drift velocity is measured precisely and continuously (with a time granularity of less than 30 min) to $< 10^{-4}$ using the collision data. The momentum resolution has reached 1% (7%) at 1 (10) GeV. Further calibration, in particular to correct for higher order effects of the electric and magnetic fields (ExB, local E field distortions,..), are ongoing in order to

extend the accessible momentum range towards 100 GeV, where the design resolution is $< 10\%$, including the information from the vertex detectors. Also the performance of the TOF is reaching design with a detector resolution of about 90 ps. The tight construction schedule for the electromagnetic calorimeters PHOS and EMCAL did not allow for calibration with test beams and is therefore currently done with beam data with the help of reconstructed π^0 decays.

Data taking in ALICE during 2010 will focus on collecting a large sample ($> 10^9$) of minimum bias collisions which are needed as comparison sample for the heavy ion run later this year. By end of May, some 200 million MB events and 0.6 M events triggered with a single low p_t trigger in the muon spectrometer have been recorded. The data taking efficiency is slightly above 80%, limited somewhat by the careful and slow procedure to switch on the sensitive gas detectors after beams are brought into collisions; a procedure which was put in place as a precautionary measure during this initial LHC running. Data are automatically reconstructed shortly after data taking, and offline reconstruction as well as analysis work very satisfactory, making extensive use of the LHC computing GRID.

After two decades of design, R&D, construction, installation, commissioning and simulations, the ALICE experiment has 'hit the ground running' since LHC started its operation at the end of 2009. The detector is in good shape (and of the correct weight!), most systems are fast approaching design performance, and physics analysis has started and produced the first results (see elsewhere in these proceedings). While heavy ion physics will be its main subject, the collaboration has started to explore the 'terra incognita' at LHC with pp collisions, along the way gaining experience and sharpening its tools in anticipation of the first heavy ion run later this year.

References

[1] F. Carminati *et al.* [ALICE Collaboration], J. Phys. G **30** (2004) 1517.

[2] B. Alessandro *et al.* [ALICE Collaboration], J. Phys. G **32** (2006) 1295.

[3] K. Aamodt *et al.*[ALICE Collaboration], J. Instrum. **3**, S08002 (2008)

[4] J. Schukraft and C. Fabjan in L. Evans (Editor), "The Large Hadron Collider: A marvel technology," *Lausanne, Switzerland: EPFL (2009) 251 p*

[5] J. Alme *et al.*, arXiv:1001.1950 [physics.ins-det].

[6] K. Aamodt *et al.* [ALICE coll.], Eur. Phys. J. C **65** (2010) 111.

[7] LHC status reports, CERN, 18 December 2009, http://indico.cern.ch/conferenceDisplay.py?confId=76398

[8] A. K. Aamodt *et al.* [ALICE Collaboration], arXiv:1006.5432.

LHCf: Status and short term prospects

Gaku Mitsuka for the LHCf Collaboration

Nagoya University, Chikusa-ku Furo-cho, Nagoya, Japan

DOI: http://dx.doi.org/10.3204/DESY-PROC-2010-01/30

The LHC forward experiment (LHCf) is the dedicated experiment for the measurements of the cross section and energy spectrum of neutral pions and neutrons in the very forward region ($\eta > 8.4$) at the Large Hadron Collider (LHC) at CERN. The first physics data LHCf has taken on December 2009 at $\sqrt{s} = 900$ GeV. Data taking at $\sqrt{s} = 7$ TeV has been continued since March 2010. In this paper, analysis results with the first limited sample of data at 900 GeV and 7 TeV are presented.

1 Introduction

There have been highest energy cosmic-ray observations in the last decade which have dramatically improved the quality and quantity of the observation data [1, 2]. However, no consistent description is available about the nature of the very high-energy cosmic-rays among each observations. This still unsolved puzzle is mostly originated in the uncertainty of the interaction of primary cosmic ray off nuclei above 10^{18} eV where no experimental data is available from accelerators.

Even in the existing accelerator data, there have not been adequate measurements of the spectra of very forward secondary particles that are necessary to understand the air shower development. Among many hadron collider data, such information is obtained only from UA7 [3] for π^0 at $\sqrt{s} = 630$ GeV and ISR data [4] for neutrons at $\sqrt{s} = 70$ GeV. However, LHC makes it possible to study hadron interactions at $\sqrt{s} = 14$ TeV, corresponding to 10^{17} eV in a fixed target system. LHCf is designed for measurements of the spectra and cross section of very forward ($\eta > 8.4$) secondary neutral pions and neutrons at the LHC. These measurements can provide the stringent limits on many parameters unavoidable in hadron interaction models and set an anchor to extrapolate a description at low energies to the highest energy end.

2 The LHCf experiment

The LHCf detectors are installed in the slot of the TANs (target neutral absorbers) located ± 140 m away from the ATLAS interaction point (IP1) and measure secondary neutral particles arriving from the IP1. Inside the TAN, the beam vacuum chamber makes a Y shaped transition from the single copper beam-pipe facing the IP1 to the two separate beam pipes joining to the arcs of LHC. Charged particles from the IP1 are swept aside by the D1 dipole magnet before reaching the TAN. At this unique location the pseudo-rapidity η ranges from 8.4 to infinity (zero degrees).

The LHCf detector is a pair of two independent calorimeters, called *Arm1* and *Arm2* installed at the IP8 side and the IP2 side from the IP1, respectively. Both detectors consist of a combination of small sampling and imaging calorimeters, which is called a *tower*, essentially 16 layers of plastic scintillators (3 mm thickness) interleaved with tungsten absorber (7 mm for the first 11 layers and 14 mm for the rest), and 4 layers of position sensitive detectors. The longitudinal size of the sensitive area to neutral particles is 230 mm or $44X_0$ (1.7λ) in units of radiation length (hadron interaction length). The transverse size of each tower is 20 mm×20 mm and 40 mm×40 mm in Arm1, and 25 mm×25 mm and 32 mm×32 mm in Arm2. The smaller tower is designed to cover the range to zero degrees, and the detector position can be adjusted using the vertically movable manipulators. Four X-Y layers of position sensitive detectors, scintillating fiber (SciFi) belts in Arm1, and micro-strip silicon sensors in Arm2, are inserted at 6, 10, 30, and $42X_0$ to determine the incident shower position. The schematic views of the detectors are shown in Figure 1.

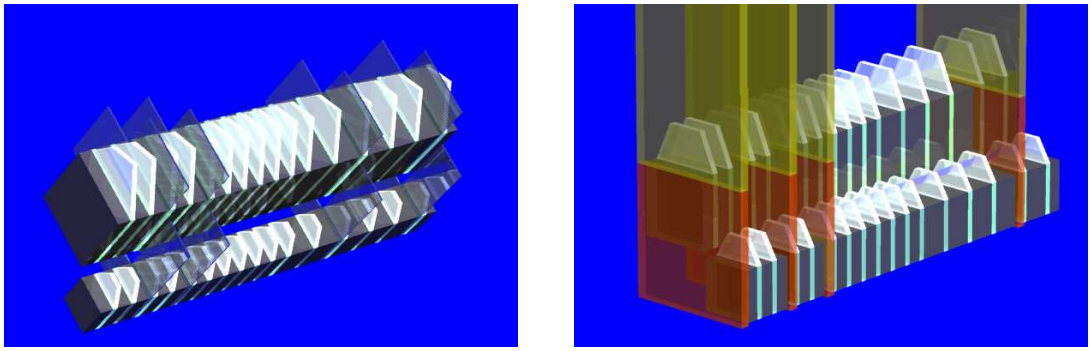

Figure 1: Schematic views of the LHCf detectors (Arm1 in the left panel and Arm2 in the right panel). Plastic scintillators (light green) are interleaved with tungsten layers (dark gray). Four layers of position sensitive layers (SciFi in Arm1 indicated by light gray and silicon strip detector in Arm2 indicated by brown) are inserted.

The calorimeters are designed to have energy and position resolutions better than 5% and 0.2 mm, respectively, for electromagnetic showers with energies above 100 GeV. Thanks to the small aperture of a tower, the multiplicity of secondary particles in a single tower is reduced to a reasonable level even at $\sqrt{s} = 14$ TeV. The two towers are positioned to detect a gamma-ray pair from the π^0 decay with one electromagnetic shower in each towers. By reconstructing the invariant mass of gamma-ray pairs, π^0 can be identified among gamma-like events and hence the energy spectrum of π^0 is measured. Even with a short operation at the commissioning of LHC, statistically sufficient physics data can be recorded to deeply investigate the existing interaction models on the market. Please see other documents for the scientific goal and the details of the detectors [5, 6].

3 Operations in 2009 and 2010

LHC has succeeded first physics collisions (*stable beams*) on 6 December 2009 at $\sqrt{s} = 900$ GeV. They provided a total of 0.5M collisions at IP1 in 2009. After a winter shutdown, the LHC

succeeded to have collisions at $\sqrt{s} = 7$ TeV on 30 March 2010 and is gradually increasing the luminosity. The integrated luminosity reached ~ 14 nb^{-1} at the end of May. Meanwhile the LHC provided 15 times more collisions at $\sqrt{s} = 900$ GeV than 2009. LHCf has successfully started data taking at the first collisions and is accumulating data at all runs with stable beam conditions.[1] LHCf has accumulated 113k and 100M high energy shower events (approximately above 10 GeV) at 900 GeV and 7 TeV collisions, respectively. The trigger of the LHCf detectors is based on the signals from one of the beam monitors (BPTX) and the existence of a high energy shower in any of the calorimeters. During the 2009–2010 runs, the LHC was always operated with at least one non-crossing bunch (having no pair bunch in the other beam) in both beams. Any high energy particles associated with passage of such bunches at IP1 are thought to be collision products of the beam and residual gas in the beam pipe, thus background in our measurement.

4 Analysis

4.1 Event reconstruction and particle identification

One half of the secondary particles reaching the TAN is expected to be from gamma rays and the rest is from hadrons (mainly neutrons). Here a parameter called "$L_{90\%}$" is introduced to identify whether an incident particle of a shower is a gamma or a hadron. $L_{90\%}$ is defined as the longitudinal position of the first tungsten layer in units of radiation length where 90% of the total energy is deposited.

4.2 Analysis results at $\sqrt{s} = 900$ GeV

Energy spectra of gamma-ray-like and hadron-like events after applying the particle ID criteria are shown in Figure 2. The data is from the Arm1 detector after combining the results of two towers. With this limited statistics, no significant difference is found between Arm1 and Arm2. Considering the statistical error and the conservative systematic uncertainty related to the energy scale, the measured spectra and the prediction by QGSJET2 [7] have a good agreement.

4.3 Analysis results at $\sqrt{s} = 7$ TeV

The energy spectra of gamma-ray-like and hadron-like events are shown in Figure 3. Here the spectra measured in the Arm2 detector are separated in the results of two different towers. The red (upper) and blue (lower) squares are events associated with the crossing and non-crossing bunches, respectively. The contamination of the beam-gas background was two orders of magnitude below the signal level and can be neglected in the analysis. A comparison of the spectra between each tower shows the harder spectra in the small tower (covering the range to zero degrees) in gamma-ray like and hadron like spectra. This tendency indicates a strong beaming of the high energy very forward particles that was not observed in the 900 GeV data.

Furthermore, in the case of 7 TeV collisions, gamma-ray pairs from π^0 decays may hit two towers in the same event due to the small opening angle. Using the energy and position

[1] LHCf has finished operation at this energy in the middle of July 2010 and removed the detectors from the LHC tunnel.

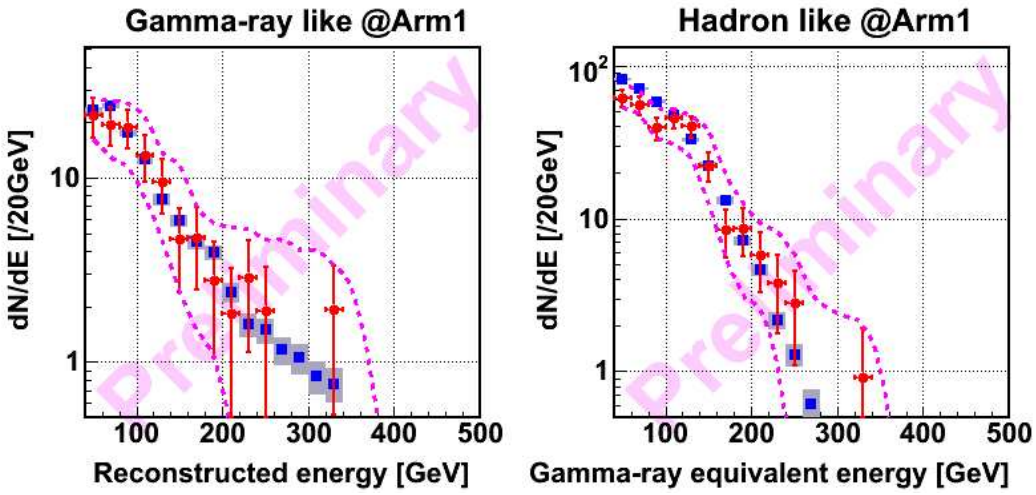

Figure 2: Energy spectra at $\sqrt{s} = 900$ GeV. The red points indicate the data taken in 2009 and its statistical error. The blue squares and the gray hatched area indicate the MC simulation with QGSJET2 and its statistical error, respectively. The systematic uncertainty related to the energy scale is drawn as a dashed curve (+15%, −10%).

information of these gamma-rays and assuming that its vertex is IP1, the invariant mass of the gamma-ray pairs can be reconstructed. The observed π^0 mass is reasonably distributed around 135 MeV.

5 Conclusions

No significant trouble has happened at the operation of LHC since last year and data taking has been stably continued.

As for the analysis at 900 GeV, the energy spectra of the data taken in 2009 seem to be agreeable with QGSJET2 although they have small statistics and a large statistical and systematic uncertainty.

The analysis at 7 TeV indicates harder spectra in the small tower than in the large tower even with the limited number of events. This can be understood by strong beaming of high energy secondary particles.

References

[1] J. Abraham *et al.*, Phys. Rev. Lett. **101** (2008) 061101
[2] J. Abraham *et al.*, Phys. Rev. Lett. **104** (2010) 091101
[3] E. Pare *et al.*, Phys. Lett. B, **242** (1990) 531
[4] W. Elauger and F. Monnig *et al.*, Nucl. Phys. B, **109** (1976) 347
[5] O. Adriani *et al.*, JINST **5** (2010) P01012
[6] H. Menjo *et al.*, Astropart. Phys. submitted.
[7] S. Ostapchenko, Nucl. Phys. B Proc. Suppl., 151(2006), 147-150.

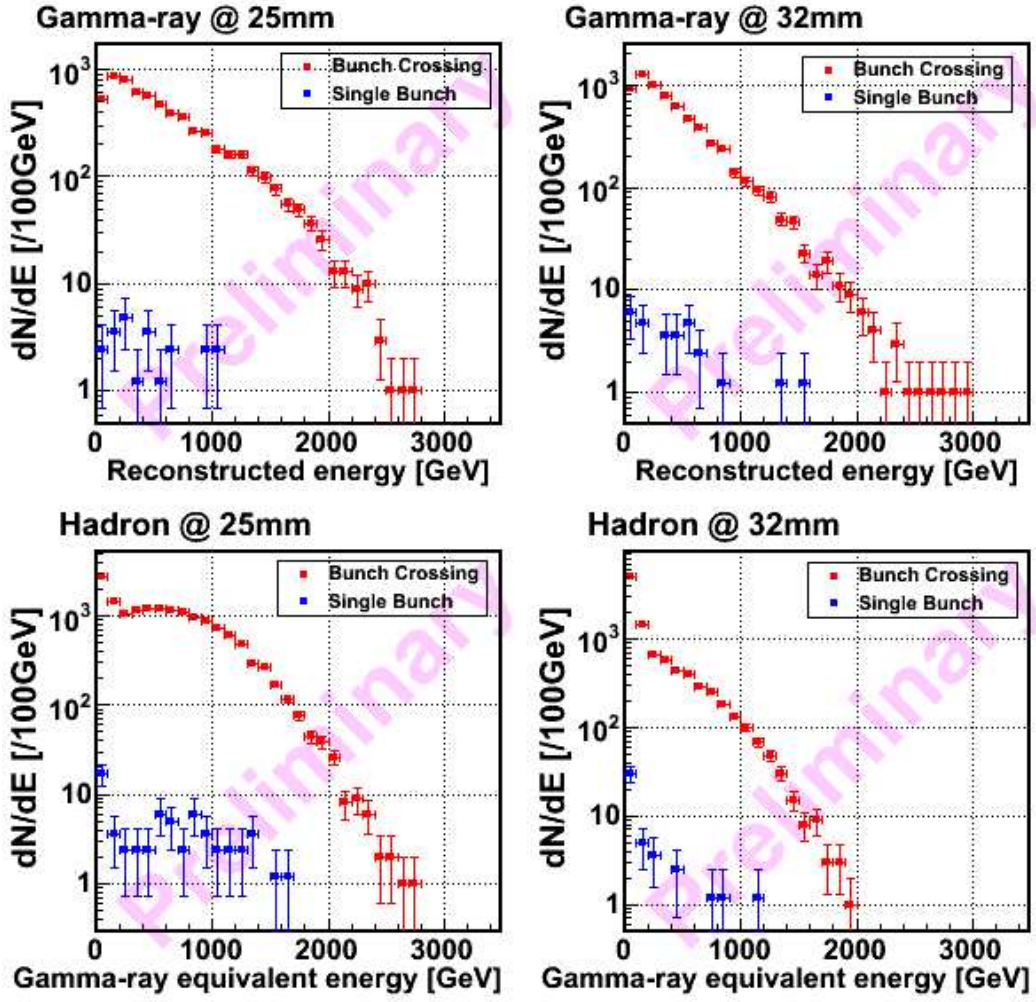

Figure 3: Energy spectra at $\sqrt{s} = 7$ TeV. The red (upper) squares indicate the crossing bunch data and its statistical error, while the blue (lower) squares show non-crossing bunch data.

Strip Tracker of CMS: Operation and performance in first 7 TeV collisions

Natale Demaria

INFN Torino, v. P.Giuria 1, 10125 Torino, Italy

DOI: http://dx.doi.org/10.3204/DESY-PROC-2010-01/186

The Strip Tracker of CMS has been run in deconvolution mode in 2010 during the first high energy collisions of the LHC. This paper describes the operational state and the detector performance.

1 Introduction

The CMS Tracker [1] is the main tracking detector of the CMS experiment at the CERN Large Hadron Collider. It contains two systems based on silicon sensor technology, one employing pixels and another using silicon microstrips.

The Silicon Strip Tracker (SST), the subject of this paper, surrounds the pixel system and consists of: the Inner Barrel (TIB) with 4 layers, three Inner Disks on each side (TID), an Outer Barrel with 6 layers (TOB) and two End Caps with nine disk each (TEC). It is the largest silicon detector ever built, with 9.3 million sensor channels covering a surface area of 198 m^2. The SST was designed to measure charged particles with high efficiency and spatial resolution over a wide range of momenta, and to operate with minimal intervention for the nominal LHC lifetime of 10 years.

The Tracker was thoroughly tested already before and after the installation in the experimental cavern, using cosmics rays [2]. The first collisions at CMS were recorded in December 2009 at energy of $\sqrt{s} = 900\,GeV$ and 2.36 TeV with the front end electronics configured in *peak mode*, with a 50 ns integration time. In 2010, the SST was commissioned with the front end electronics configured in *deconvolution mode*, characterized by a faster signal, approximately gaussian with a sigma of 11 ns allowing the identification of the LHC bunch: this mode is the baseline for running at higher luminosity where pile-up events start to play a role.

The first section of this paper describes briefly the commissioning and running of SST while the second section illustrates the performance results obtained at the new high energy regime of the LHC.

2 Detector running and commissioning

The SST was proven during 2010 to be a very solid, reliable and stable detector, determining only 0.4% of down time of CMS during LHC collisions and negligible dead time. Important steps have been the commissioning of the detector and achieving good stability of the detector systems.

2.1 Commissioning

The key elements in the front end readout electronics are: the chip (APV25), providing analog readout signal serialized for 128 channels; the multiplexer serializing 256 signals and the Linear Laser Driver (LLD). This sends the data to the back end electronics via a 30 to 50 meters long optical fiber connected to the Front End Detector (FED). The FED digitalizes the signal, subtracts on an event by event basis the common mode noise and makes the zero suppression, sending to the CMS DAQ only the signal for those channels forming clusters well above the baseline.

In order to bring the SST detector into an operational state suitable for data-taking, several commissioning procedures are required to configure, calibrate, and synchronise the various hardware components of the control and readout systems. The full commissioning sequence of the SST is explained in [3]. It is mostly based on calibrations done without an external trigger and consists of the following sequence: internal synchronization of all analog signals from front end chips to the FED; gain equalization of all LLDs transferring out the signal via optical fibers; optimization of the average baseline at the FED; adjustment of the pulse shape of each chip and finally the measurement of the average baseline (pedestal) and of the noise of each channel. The pedestal and noise measured are then uploaded to the FED and used to perform the zero suppression of data. In the absence of a real signal, the SST is very quiet: occupancy due to noise is of the other of 10^{-5} in deconvolution and 10^{-6} in peak mode, to be compared with about 1-4% occupancy during collisions at full luminosity. Gain, pedestal and noise have been monitored by taking periodically timing and pedestal runs and they have been confirmed to be very stable: updates were done only occasionally due to minor hardware interventions done during LHC technical stops.

Detector parts that are malfunctioning are mainly detected during SST commissioning. Only good alive channels are selected to be readout and for the year 2010 they constitute 98.1% of the SST, distributed in: 96.3% (TIB/TID), 98.3% (TOB), 98.8% (TEC+) and 99.1% (TEC-). The major contribution to the bad channels comes from two sets of modules that are sharing, each one, the same power supply line for the digital power to the front end (for trigger, clock and I_2C bus): the cable has a short at the level of a patch panel inside CMS. These two shorts are responsible for 1.1% of the bad channels and will be recovered at the next LHC shutdown in 2012. Other missing parts are due to: HV lines missing (0.1%); HV lines shorts (0.3%); bad fibers and other problems (0.4%).

It has to be remembered that the SST was designed with very high redundancy and can accept a high level of dead channels before tracking performance is affected.

2.2 Detector systems

The SST is cooled by two cooling plants distributing C_6F_{14} liquid at 4 °C via 180 lines. Only 2 lines (for 0.6% of front end) are closed due to substantial leaks, but the associated detector modules are powered on and fully working, despite a nearly 20% higher temperature. Still one cooling plant is leaking at a non negligible level in other two lines and further investigations are under way.

The SST uses 2000 power supply units and has reached a failure rate of 1% per year. During 2010 the replacement of the power supply unit was normally done at the first opportunity of down time of the LHC.

The SST readout has been running stably. The only interventions required have been: the

early replacement of 5% of VME-PCI boards due to failures in the opto-receiver; the recent replacement of one FED out of 440 due to a bad temperature probe that was causing one FED to eventually stop working.

2.3 Detector running with beams

The SST was included in the readout of CMS at all times, but was giving sensible data only during Stable Beams: as a safety precaution the high voltage needed to deplete the silicons was switched on only when LHC declared stable beams and they were switch off again when LHC was declaring a handshake to go to other states like beam dump or adjust. In order to send little or no data to CMS when the high voltage was off, the FEDs were set automatically by the DAQ with a high threshold.

Recently the SST spy channel readout has been introduced in the standard running during stable beams. It allows to readout synchronously from VME all the FED data at a frequency of about 0.1 Hz. This will allow to monitor on-line the data and therefore measure pedestals and noise while taking collisions data.

3 Performance

The signal in deconvolution mode is very fast and therefore a precise timing with respect the trigger is necessary. A preliminary scan with 20 steps of 2 ns each was done already during 2009 with 2.36 TeV collisions but was repeated in early April 2010 scanning in each subdetector separately. Only one layer per subdetector is scanned while the other layers are set in peak mode and used as a telescope to extrapolate tracks to the measured layer. Results of this scan are shown on left of Fig. 1: the line indicates the settings found in 2009; a difference of up to 4 ns was found and new settings have been used since then. In the figure is visible the quick signal provided by the deconvolution mode of the front end chip. The signal over noise ratio of

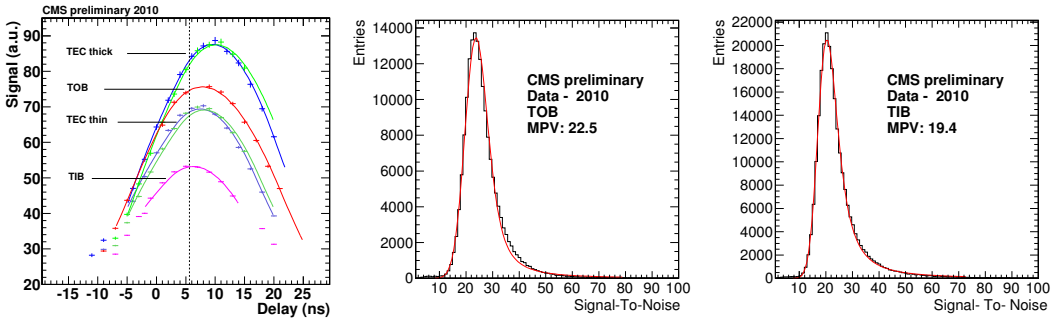

Figure 1: Results in deconvolution mode: on left the signal versus the delay of trigger; in the middle and right plots, the ratio of signal over noise for the TOB and TIB respectively.

the SST in deconvolution mode is very good and fits with expectations. The value normalized to tracks perpendicular to the silicon sensor of the most probable value of the Landau has been measured of 18.5, 19.4, 23.9, 19.4 and 22.5 respectively for TID, TEC thin, TEC thick, TIB

and TOB subdetectors modules. Results for TOB and TIB are shown respectively in the center and right plots of Fig. 1.

Given a good track crossing a layer, the presence or absence of a hit in that layer measures its hit detection and reconstruction efficiency. Cuts have been applied, avoiding crossing the layer at the border of the acceptance region, given the extrapolation error of the track and known bad modules have been excluded. The overall measured efficiency is 99.9%: this analysis has revealed eight additional inefficient modules that are currently under investigation.

The hit resolution was measured using tracks crossing overlaps regions. The small distance and amount of material between the overlapping modules makes the comparison of local coordinates of the two modules a good estimate of the hit resolution. The measurement is almost insensitive to local misalignment, except for uncertainties on the relative angles between the two modules that have a negligible contribution to first order. The study has been done for different track inclinations with respect the module surface and results are in good agreement with simulation. For example a resolution of 14, 18 and 28 μm was measured for pitches of 80, 120, 180 μm and a track crossing angle of 10-20^o with respect to the normal to the module. For each track the SST provides not only a measurement of momentum, but also a multiple

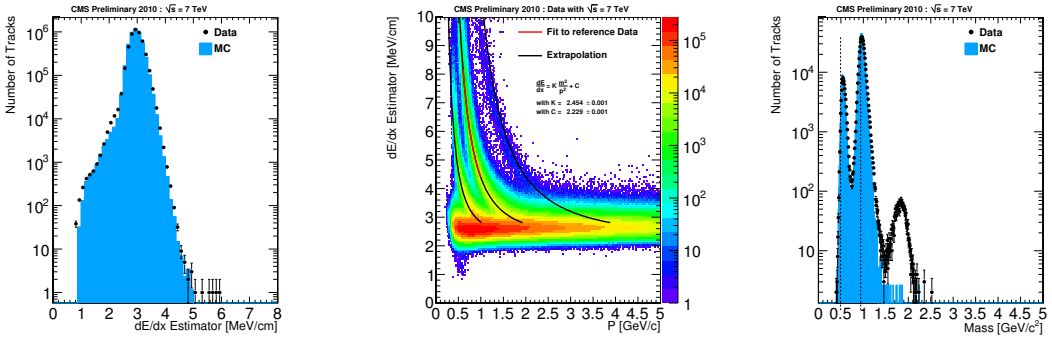

Figure 2: Left: dE/dx; center: dE/dx vs momentum; right: mass plot for $p < 2\,\mathrm{GeV/c}$, $\mathrm{dE/dx} > 5\,\mathrm{MeV/cm}$ (see more in text).

measurement of dE/dx and therefore provides some particle identification capabilities. A barrel track can count on at least 10 independent measurements from the SST: a harmonic mean with power -2 has been preferred instead of the median or the truncated mean and is therefore reported here. Data and simulation are in very good agreement as is shown on the left of Fig. 2. The results of dE/dx versus the momentum can be seen in the middle of Fig. 2: the lines of kaons, protons and deuterons are visible. The lines reported are a fit to an approximated formula as shown in the picture. For small momentum this formula can be reversed, so the mass can be computed from the dE/dx and the momentum. The plot of the mass abundance on the right of Fig. 2, together with simulation expectations, shows how well the presence of protons and kaons is described by simulation, whereas deuterons are not well reproduced.

4 Conclusions

The Silicon Strip Tracker of CMS was running during 2010 collisions in deconvolution mode, showing excellent S/N, cluster reconstruction efficiency and resolutions, dE/dx performances,

achieved thanks to the detector commissioning and the calibration procedures. The detector ran efficiently with almost no downtime thanks to the stability of all detector systems, in particular cooling, power supply and back end electronics linked to DAQ.

This results are an excellent milestone for the 2010-2011 long physics data taking with LHC collisions at 7 TeV center of mass energy.

References

[1] The CMS Collaboration, *The CMS experiment at the CERN LHC*, **JINST 803** (2008) S08004.
The CMS Collaboration, *CMS: The Tracker Project Technical Design Report*, **CERN-LHCC-98-06** (1998).
The CMS Collaboration, *Addendum to CMS Tracker TDR*, **CERN-LHCC-2000-016** (2000).

[2] The CMS Collaboration, *Commissioning and Performance of the CMS Silicon Strip Tracker with Cosmic Ray Muons* **J. Instrum. 5** (2010) T03008.
W.Adam, N.Demaria et al., *Performance studies of the CMS Strip Tracker before installation* **J. Instrum. 4** (2009) P06009.

[3] W.Adam, N.Demaria et al., *Commissioning and performance of the CMS silicon strip tracker with cosmic ray muons* **J. Instrum. 5** (2010) T03008.

Tracking and Alignment in LHCb

Florin Maciuc for the LHCb Collaboration

Max Planck Institut für Kernphysik, Saupfercheckweg 1, D-69117 Heidelberg, Germany

DOI: http://dx.doi.org/10.3204/DESY-PROC-2010-01/188

This paper reports on the status of tracking and alignment for the LHCb detector. Topics covered are: tracking efficiency, primary vertex precision, impact parameters, and software alignment of the tracking sensors. Special emphasis is placed on the agreement between data and Monte Carlo. The first physics results are discussed in relation to the alignment and tracking quality, and the LHCb tracking detectors and sensor types are described.

1 LHCb Detector

The LHCb - Large Hadron Collider beauty - detector is optimized for precision measurements of CP violation and rare decays of B-mesons. At a collision energy of 14 TeV and nominal luminosity of $2 \times 10^{32} cm^{-2} s^{-1}$, the expected production rate of $b\bar{b}$ pairs is 10^5 Hz, leading to about $10^{12}\, b\bar{b}$ pairs produced per year.

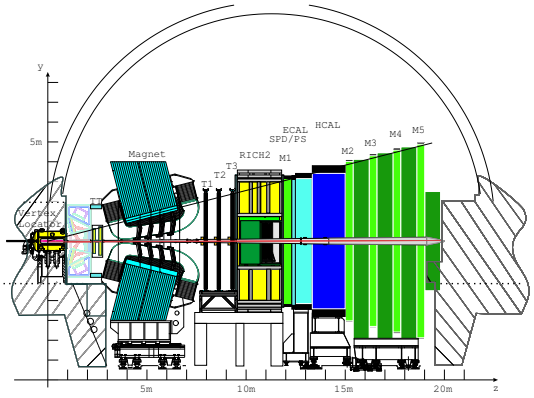

Figure 1: LHCb spectrometer

LHCb is a single-arm forward spectrometer with an angular coverage close to the beam between 15 to 300 mrads in the magnet bending plane and 15 to 250 mrads in the transverse plane. The setup is schematically given in Fig. 1, with the Primary Vertex (PV) inside the VErtex LOcator (VELO) to the extreme left. The tracking detectors of LHCb are: VELO, Inner Tracker (IT), Outer Tracker (OT) and Tracker Turicensis (TT), with the latter just before the magnet. The most precise LHCb tracking detector is the VELO, a silicon strip detector with the pitch varying between 38 to 102 μm. This subdetector is split in two halves - to the right and left of the beam - which are retractable. The retracting of the VELO halves allows to protect the silicon sensors during beam injections and during the times when the LHC beams do not have the desired stability.

The OT is a straw tube detector with an estimated hit resolution close to 200 μm. Behind the magnet, both IT and OT have 3 stations, T1-T3, with stereo layers of sensors. The stereo angle sequence of $0^0, -5^0, 5^0, 0^0$ per each station, means the measurement of a trajectory is most precise in the x direction, where the xz plane is the bending plane, z the beam direction and y the main magnetic field component direction. Similarly to VELO, the IT and TT are silicon strip detectors with a pitch of 196 μm and 183 μm, respectively. The IT has sensors that

span the LHCb acceptance closest to the beam where the particle occupancy is the highest, and its acceptance is roughly complementary to the OT acceptance.

To obtain an estimate for the particle momentum, the track before the magnet of VELO+TT is matched with its equivalent behind the magnet, which is a particle track in OT or IT. The bending in the particle trajectory gives a precise momentum estimate. This report quotes values based on the 2010 early LHCb data at 7 TeV center of mass collision energy, with low luminosity and closed VELO.

2 Primary Vertex and Impact Parameter Resolutions

To obtain a value for the primary vertex (PV) resolution, for each event the VELO track sample is split in two and the PV position is obtained for each subsample. The difference between these positions gives a distribution with an RMS that approximates the sought resolution. The agreement between Monte Carlo (MC) and data was improved with respect to the first reconstruction, however overall there is a residual disagreement persisting. Remaining misalignments between VELO sensors at a level of 4 μm account for half of the previous discrepancy, with the other half generated by a difference in the hit error estimates between data and MC. The origin of the last effect is explained in more detail in the end of Sec.3, when discussing the IT hit resolution. The PV resolution is given in Tab.1 for each coordinate, when 25 VELO tracks were used.

The Impact Parameter (IP) is the distance of the closest approach to the PV for a track. This parameter is essential in tagging prompt particles and for vertexing. Causes that lead to a finite IP resolution are the random scattering of particles in the VELO and residual misalignments. In addition, as before for the PV resolution, the different VELO hit resolution in data and in MC explains half of the difference in the IP resolution values that are given in Tab.2. The remaining difference is mostly due to misalignments.

$r(\mu m)$	MC	Data
Δx	11.5	15.8
Δy	11.3	15.2
Δz	57	91

Table 1: PV resolutions

	$\Delta\,(IP_X)$ (μm)	$\Delta\,(IP_Y)$ (μm)
Data	$16.2 + 24.6/p_T$	$15.7 + 24.4/p_T$
MC	$11.2 + 19.9/p_T$	$11.9 + 19.3/p_T$

Table 2: Table with IP resolutions

3 Alignment

The nominal geometry of the trackers was first changed to account for the optical survey values. Subsequently, the software alignment uses the survey geometry as the starting geometry, and obtains alignment corrections to the sensors positions. The alignment was done for each detector: VELO, TT, IT and OT, and the final alignment precision of the relevant coordinate was estimated to be much lower than the intrinsic hit resolution - e.g., the residual misalignment in x for an IT sensor is estimated to be about 15 μm, less than the intrinsic hit resolution of 50-60 μm for IT. We have already seen that the VELO alignment is precise to 4 μm, and TT has similar alignment precision to IT's.

The quality of alignment can be inferred directly from the distribution of the measurement residuals. These are given for two detectors in Figs.2 and 3. The observed differences between MC residuals and data residuals obtained for the aligned geometry, are mostly the result of

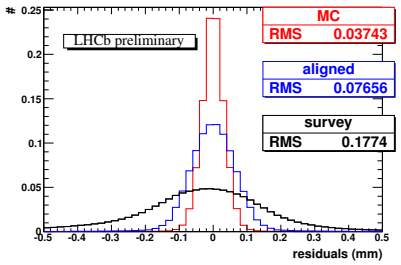

Figure 2: IT residuals

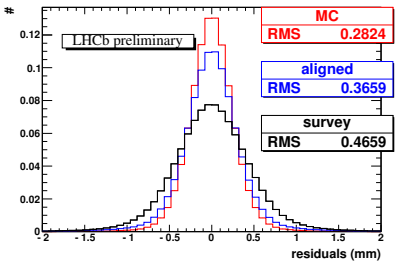

Figure 3: OT residuals

unresolved misalignments. For IT the disagreement appears larger, however in this case the main cause is not the persistent misalignment, but the overestimation in the MC of the charge sharing between the strips. This effect is described in the next paragraphs.

As the other silicon detectors of LHCb, the IT has silicon-strip sensors. The measured position, and implicitly the track coordinate, is given by a cluster of strips on the surface of the silicon sensor. The resolution of the measurement is directly correlated with the number of strips in the cluster. A charge sharing between adjacent clusters increases the number of strips for a measurement, and hence generally increases the measurement precision. In the past, the charge sharing was overestimated, and as a consequence in the silicon trackers the hits are more precise in the MC when compared to real data. The MC was using an average IT hit resolution value close to 40 μm, however, in data it was found out that a more realistic value is about 55 μm. After correcting the hit resolution in the MC, the average was found to be close to 52 μm. TT exhibits the same problem, with almost the same degree of severity. The same problem, but much less severe, was found for the VELO, which explains in part the difference between MC and data for the IP and PV resolutions. After the measurement resolutions were corrected in the MC, the data and MC results look similar. Yet, at the level of alignment there are still problems with some less constrained degrees of freedom, e.g., for IT the alignment in the beam direction poses a problem as this degree of freedom is weakly constrained by the measurements, which are mostly x measurements.

4 Tracking Efficiency

We define the tracking efficiency as the probability for a particle to have a corresponding reconstructed track, when the particle is emitted into the detector acceptance and remains within this acceptance all the way till the last tracking station. This definition includes the hit efficiency and the track reconstruction efficiency, but it does not include any acceptance related efficiency. Because usually the tracks are required to have a precise momentum estimate, we restrict the following topic to the sample of *"Long"* tracks with segments in both regions before and after the magnet. To estimate the tracking efficiency we have used mainly two methods. The first method uses the K_S signal and its two-pion final state. Here, a selection of K_S candidates is done and the final sample is split in two types of candidates:
- candidates with two Long tracks of opposite charge as final state pions;
- candidates with a Long track and a VELO track with an associate calorimeter cluster.
The calorimeter hit behind the last tracking station, insures that the second pion is within acceptance, and provides a way to better estimate the momentum. In Fig.4, the signals for the

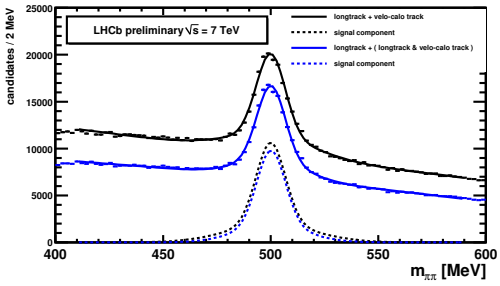

Figure 4: K_S signal for two samples, the dashed lines are after background subtraction

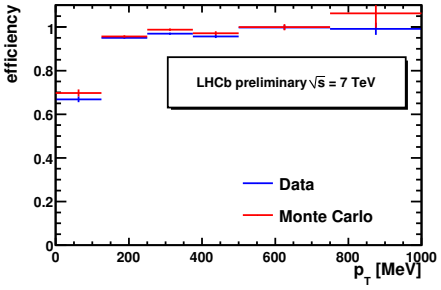

Figure 5: Tracking efficiency vs p_T of K_S

two subsamples are compared. The difference is given by the probability to have a reconstructed track segment in IT, OT respectively, for the second pion. In Fig.5 the close agreement between data and MC is highlighted in a plot of efficiency versus the transverse momentum of the parent.

The second method is based on matching calorimeter clusters and VELO segments, and extracting the tracking efficiency after the magnet by finding the number of tracks which have the corresponding segments after the magnet in IT (OT). The fraction of Long tracks to the total gives an estimate of the efficiency. As the combinatoric background is very large for this method, a cut must be imposed on the number of calorimeter clusters and VELO segments for a given event. The results of both methods are close, with overall efficiency numbers:
1. First method, for data $92.3 \pm 0.3\%$, for MC $93.0 \pm 0.5\%$, ratio 0.99 ± 0.01;
2. Second method, for data $92.8 \pm 1.6\%$, for MC $93.9 \pm 1.3\%$, and the ratio 0.99 ± 0.02.

5 Conclusions

LHCb early data analyses have shown that, overall, tracking leads to similar results in MC and in data. Many problems were fixed, as it is the case with the silicon strip tracker error estimates, missing materials in MC, and alignment of trackers to precision better than the intrinsic hit resolution.

Some disagreements persist - e.g., though MC and data values are close, primary vertex and impact parameter resolutions are different. However, the tracking tools and the present status of the alignment have already allowed very precise measurements. One such measurement is highlighted by the Λ mass peak in Fig.6 where the width of the signal is 2.8 MeV and the mass value within 50 KeV of the Particle Data Group (PDG) value. Other particle masses were found to agree with their corresponding PDG values on the percent level, or better. The physics results of the early data showed that the tracking and alignment quality is sufficient. Additional tuning of the MC and tracking tools is ongoing. The alignment quality is monitored, and we hope to achieve an even better alignment than we have right now.

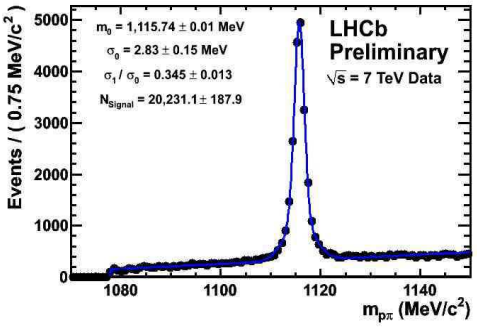

Figure 6: Angular distribution for $b\bar{b}$ pair.

Alignment of the CMS tracker and track reconstruction with collision data in CMS

Alessio Bonato for the CMS Collaboration

CERN, Geneve 23, 1211 Geneva, Switzerland

DOI: http://dx.doi.org/10.3204/DESY-PROC-2010-01/190

The CMS all-silicon tracker was aligned using more than three million cosmic rays particles. The positions of the modules were determined with respect to cosmic ray trajectories to a precision of $3-4$ μm in the barrel and $3-14$ μm in the endcap in the most sensitive coordinate. The trajectories of charged particles produced in the LHC collisions were reconstructed and their momenta were measured in the 3.8 T solenoidal magnetic field. Reconstructed tracks are used to determine the position of the primary interaction vertex in the event and to monitor the position of the colliding beams. The tracks have been used further to reconstruct the hadronic decays of several mesons, including K^0_S, $D*$, Λ, and ϕ. The performance of track reconstruction has been measured in the data and is compared to the expectation from simulation.

1 Introduction

The Compact Muon Solenoid (CMS) [1] detector is one of the multi-purpose experiments developed for data taking at the Large Hadron Collider (LHC). The main goals of the experiment range from the measurement of Standard Model parameters to the potential discovery of physics beyond the Standard Model. For all these tasks, it is required a precise measurement of the momentum of the charged particles generated in the collisions. The main component of CMS dedicated to the tracking is the silicon Tracker (TK) [2] positioned in a solenoidal magnetic field of 3.8 T. This is the largest tracker ever built with Si-based detectors. Two detector technologies are used: 1440 Si-pixel modules, organized in one barrel (BPIX) and two forward (FPIX) sub-assemblies, and 15148 Si microstrip modules composing the Silicon Strip Tracker (SST). The operation and calibration of the pixels and the SST were carried out successfully during the early LHC data taking [3]. In order to achieve the desired performances, a careful alignment of the modules must be carried out. The uncertainty related to the module position has to be negligible when compared to the intrinsic hit resolution (typically $10-20$ μm for pixel detectors and $20-60$ μm in SST). The performance of the tracking must be monitored in order to assess the quality of the reconstruction algorithms and to spot any potential problem in the alignment and calibration. A review of the status of the alignment of the TK, the tracking performances - controlling both the kinematic properties of the tracks and those of known resonances - and the b-tagging is presented after the very early stage of the LHC run at $\sqrt{s} = 7$ TeV.

2 Alignment of the Si Tracker

Two different statistical methods were used: the *Hit and Impact Point* (HIP) algorithm [4] and *MillePede II* (MP) algorithm [5]. The inputs to the algorithms were cosmic rays recorded shortly before the start of the LHC operations and tracks from minimum bias events with $\sqrt{s} = 7$ TeV. The statistics were chosen to be approximately the same: 2M cosmic rays and 1.7M minimum bias events (corresponding to $\approx 1\ nb^{-1}$). The selected tracks had to pass requirements on the momentum, $p > 2$ GeV (4 GeV for cosmic rays), length and normalised χ^2. The hits given as input to the algorithms had to pass several selections in order to be used, including signal-over-noise ratio in the SST and cluster shape in the pixels. The compatibility of the two data sets used was checked by means of the Primary Vertex (PV) residuals validation tool. This validation looks at the distributions of the Impact Parameter (IP) of the tracks respect to the PV refitted without that track. The mean of these distributions must be zero for an unbiased geometry. Figure 1 shows the result of this test on minimum bias tracks using a TK geometry aligned using only the cosmic rays sample. No large deviations from zero are observed. A MC simulation with an artificially introduced displacement of the two halves of BPIX is also presented. Such a displacement is mechanically allowed in the pixel detector, the plot shows the sensitivity to it of this validation tool.

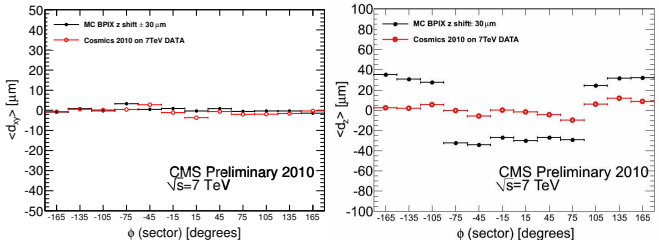

Figure 1: Result of the validation on minimum bias tracks using the residuals of the track impact parameter with respect to the Primary Vertex. The means of the distribution of the PV residuals in the transverse (left) and longitudinal planes (right) are presented for both data (open circles) and MC (full dots).

The alignment using only cosmic tracks achieved excellent results [6]. The inclusion of the minimum bias events in the alignment of the TK brought significant improvements in the precision of the alignment of the modules in the endcap region. This holds in particular for the FPIX modules that were poorly aligned using only cosmics due to the lack of statistics related to its small geometrical acceptance for vertical tracks. The comparison with the MC simulation exhibits a remarkable agreement when using a geometry in simulation that realistically reproduces the expected level of alignment precision after a cosmics-only alignment (STARTUP scenario). In Figure 2 the MC simulation using both a perfectly aligned geometry and the STARTUP scenario geometry is compared to data. The distribution of the normalized χ^2 and the distribution of the median of the residuals for every module in FPIX (that collected more than 30 hits) are presented as they are obtained from the validation of 1M minimum bias events. The performance in data surpasses that of the STARTUP in FPIX and gets close to the performance predicted with a perfectly aligned TK.

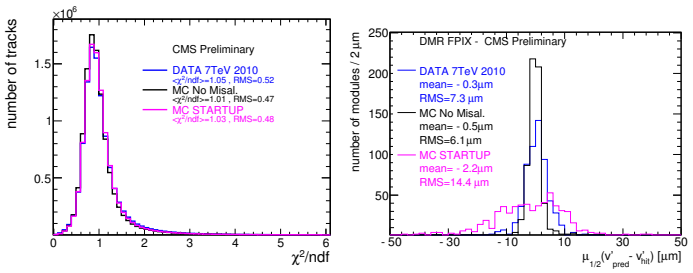

Figure 2: Distribution of the normalized χ^2 of the tracks (left) and of the median of the residuals of hits collected in FPIX (right). The distribution from real data is compared to two different MC distributions obtained fitting the same tracks with a perfectly aligned geometry and a realistic misalignment scenario of the Tracker before the alignment with collision tracks.

3 Tracking performance

The performance of the TK has been analyzed starting from the study of the resolution and efficiency in reconstructing the PV and the track parameters. Studies have been carried out at both $\sqrt{s} =$ 900 GeV [7] and $\sqrt{s} = 7$ TeV [8]. The efficiency in reconstructing the PV is $> 99.9\%$ if at least four tracks are used in the fit. The PV resolution depends strongly on the number of tracks used in the fit and their p_T. It is measured as a function of the number of tracks in the events and their average p_T. The tracks used in the former fit are divided randomly in two smaller collections, each of them used for recalculating the PV. The distribution of the difference in position between the two new PV are fitted with a single Gaussian distribution. The standard deviation of the fitted Gaussian gives the resolution. For the minimum bias events at 7 TeV with more than 30 tracks, the resolution on the PV is found to be 20 μm (25 μm) in both the x and y (z) direction. The distribution of the basic track parameters like p_T, pseudorapidity, and IP are well described by the MC (Pythia 8 Tune 1).
A higher level of validation of the TK performance is to look at the reconstruction of the resonances decaying in charged particles. Figure 3 presents a study of reconstruction of $D*$ mesons decaying in the chain $D* \rightarrow D^+(\rightarrow K\pi)\ \pi_s$. The excess over the combinatorial background due to the $D*$ is evident in the distribution of the difference between the invariant masses of the $K\pi\pi$ and $K\pi$ systems. The invariant mass of the $K\pi$ combinations exhibits a clear peak corresponding to the D^+ mass. These plots give an example of the capability of the TK in reconstructing in a precise and unbiased way the invariant mass peak of low-mass resonances. It also shows the readiness of the commissioning of the TK and of the tracking tools. Similar performances are observed for many other resonances like K^0_s, Λ, ϕ, Ω. Overall the value of the mass of the resonances agrees with the PDG value at level of few per mille. The lifetimes of the K^0_s and Λ are measured to be well compatible with the world averages.

The TK is the main device for carrying out the rich b-physics program at CMS. In order to have a b-tagging with high efficiency and purity, a very high quality of the alignment is mandatory, as well as a precise estimation of the errors sourcing from the alignment. The commissioning of the b-tagging performance is described more in detail in [9]. The first b-tagging algorithms being commissioned rely essentially on the measurement of the significance of the IP of the tracks and of displaced vertexes. The precision achieved by the CMS TK is a few tens of microns. The agreement with the STARTUP MC is very good.

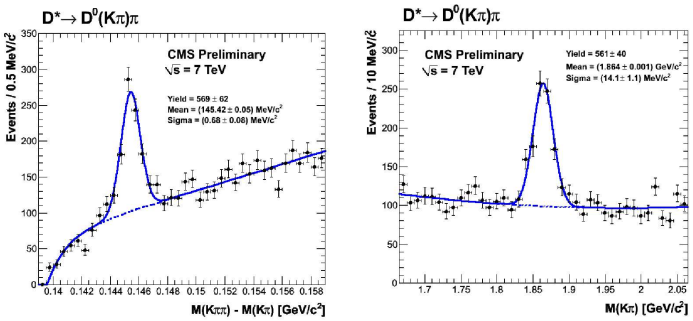

Figure 3: Distribution of the difference between the invariant masses of the $K\pi\pi$ and $K\pi$ systems (left) and of the reconstructed invariant mass of the $K\pi$ system (right). The error bars are presenting only the statistical uncertainty.

References

[1] CMS Collaboration, *The CMS experiment at the CERN LHC*, JINST 0803 (2008) S08004

[2] CMS Collaboration, *The CMS tracker system project: technical design report*, CERN/LHCC 98-006 (1998); CMS Collaboration, *The CMS tracker: addendum to the technical design report*, CERN/LHCC 2000-016 (2000).

[3] N. Demaria, *CMS Silicon Strip tracker operation*, these proceedings;
V. Radicci, *Operational experience and performance of the CMS pixel detector during the first LHC beams*, these proceedings.

[4] V. Karimaki, T. Lampen, and F. P. Schilling, *The HIP algorithm for track based alignment and its application to the CMS pixel detector*, CMS Note 2006/018 (2006).

[5] V. Blobel, *Software alignment for tracking detectors*, Nucl. Instrum. Meth. A566 (2006) 513;
G. Flucke, P. Schleper, G. Steinbruck, and M. Stoye, *CMS silicon tracker alignment strategy with the Millepede II algorithm*, JINST 3 (2008) P09002.

[6] CMS Collaboration, *Alignment of the CMS Silicon Tracker during Commissioning with Cosmic Rays*, 2010 JINST 5 T03009 [arXiv:hep-ex/0910.2505] .

[7] CMS Collaboration, *Tracking and Vertexing Results from First Collisions*, CMS-PAS-TRK-10-001.

[8] CMS Collaboration, *Tracking and Primary Vertex Results in First 7 TeV Collisions* , CMS-PAS-TRK-10-005.

[9] CMS Collaboration, *Commissioning of b-jet identification with pp collisions at sqrt(s) = 7 TeV* , CMS-PAS-BTV-10-001.

Alignment of the Inner Detector and of the Muon Spectrometer of the ATLAS experiment

Igor Potrap for the ATLAS Collaboration

Max-Planck-Institut für Physik, Munich, Germany

DOI: http://dx.doi.org/10.3204/DESY-PROC-2010-01/191

The ATLAS experiment at the Large Hadron Collider at CERN is equipped with two tracking systems: the Inner Detector and the Muon Spectrometer. To achieve the desired tracking performance, these subdetectors have to be aligned with the precision of better than 10 micrometers for the Inner Detector and of better than 30 micrometers for the Muon Spectrometer. Track based alignment approaches in combination with optical sensor measurements are used to fulfil these requirements. The alignment corrections have been successfully applied to the LHC collision data. The results show that the precision of current alignment already allows for a good tracking performance.

1 Alignment of the ATLAS Inner Detector

The Inner Detector is the main part of the ATLAS tracking system. It consists of three subdetectors enclosed inside a superconducting solenoid magnet. The Pixel Detector, the innermost one, consists of silicon modules with the intrinsic resolution of 10 μm in the precision coordinate ($r\phi$). The Semiconductor Tracker (SCT) consists of double-layer silicon microstrip modules with the combined resolution of 17 μm. The Transition Radiation Tracker (TRT) is constructed of straw drift tubes. Relatively low tube resolution of 130 μm is compensated by the large number of tube layers in the TRT detector.

Several track-based alignment algorithms have been developed for the Inner Detector. Two of them, *Global* χ^2 and *Local* χ^2, are based on least-square minimization of track residuals. The *Global* χ^2 algorithm takes into account all correlations between alignment parameters, but it requires inversion of a single huge (about 36 000 x 36 000) matrix. The *Local* χ^2 algorithm requires inversion of a large number of small (6 x 6) matrices which takes much less computing resources. In this case the correlations between different modules are lost. Many iterations of the alignment procedure are needed to restore these correlations. There so-called *Robust* alignment algorithm is based on shifting modules according to their observed residual offsets. All three independent approaches were tested and have shown consistent results.

1.1 Performance with collision data

The first alignment results for the Inner Detector have been produced with cosmic data collected during the ATLAS commissioning period [1]. The alignment of the Inner Detector is performed at different levels of granularity: starting from large structures such as the alignment of the whole subdetectors with respect to each other, then continuing with the alignment of the barrel

layers and the end-cap disks and ending with the alignment of each individual module. Due to the poor illumination of the end-caps with cosmic rays, only the barrel part of the inner detector was aligned at the individual module level. With the start of LHC collisions, the first reliable alignment of the end-caps became available. The combination of collision and cosmic ray data has been used to produce alignment corrections for 7 TeV collision data. The use of cosmic tracks helps to cure some weak modes of the alignment. Unbiased residuals for Pixel, SCT and TRT detectors in the barrel and in the end-cap regions produced with 7 TeV collision data are presented in Figure 1 in comparison with the results from the perfectly aligned simulation. The distributions are very close to the simulated ones. The results show that current alignment already provides good tracking performance.

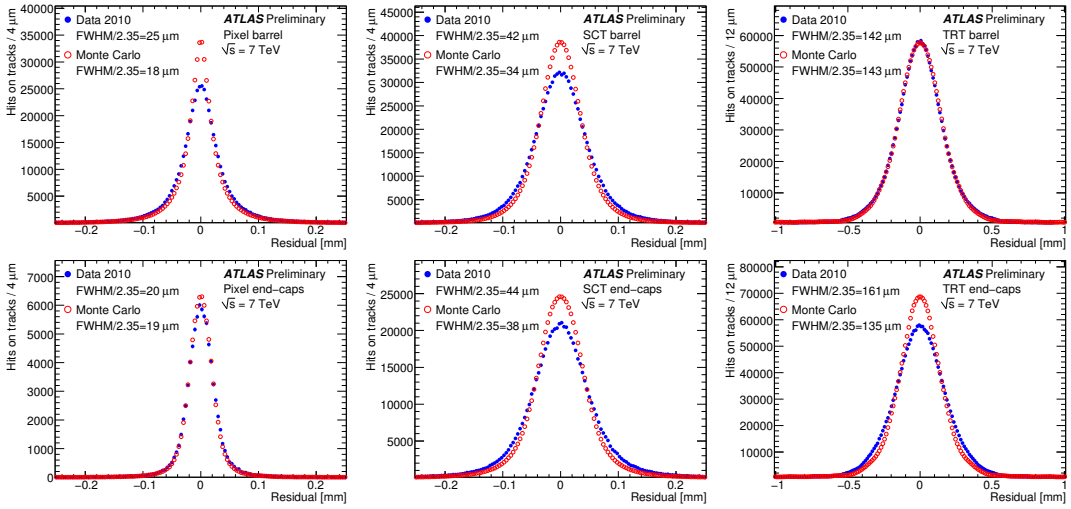

Figure 1: Unbiased residual distributions produced in the barrel (top plots) and in the end-cap (bottom plots) regions of the Pixel, SCT and TRT detectors using 7 TeV collision data.

2 Alignment of the ATLAS Muon Spectrometer

The Muon Spectrometer of the ATLAS experiment is designed to measure muon momenta of up to 1 TeV with a resolution of better than 10% [2]. It consists of three layers of precision drift tube chambers located in a toroidal field of superconducting air-core magnets. To achieve the desired momentum resolution with the 3-point track sagitta measurement, the muon chambers have to be aligned with an accuracy of better than 30 micrometers in the track bending plane. The muon optical alignment system [3] is designed to continuously monitor muon chamber positions and deformations with time. It is based on optical sensors forming two independent subsystems in the barrel and in the end-caps of the Muon Spectrometer. Apart from the optical alignment there are also several alignment tasks which require track based approaches. Those are alignment of the *small* barrel sectors with respect to the *large* ones [1], alignment of the barrel

[1] The barrel part of the Muon Spectrometer consists of the *large* and the *small* sectors with the toroid magnet coils located inside the *small* sectors.

part of the Muon Spectrometer with respect to the end-cap part and alignment of the whole Muon Spectrometer with respect to the Inner Detector. Also, initial chamber positions have to be determined with straight muon tracks from cosmic rays and from proton-proton collisions in a dedicated run of the ATLAS detector with the toroid magnets switched off.

2.1 End-cap performance

The end-cap optical alignment system is designed to provide the accuracy on track sagitta measurement of about 40 μm. In Figure 2 the sagitta distributions for straight cosmic tracks in the end-cap region are shown for the cases of the nominal detector geometry and the geometry including alignment corrections. The sagitta of straight tracks is expected to be zero. The mean value of the distribution with alignment corrections is compatible with zero while the width of it is dominated by multiple scattering.

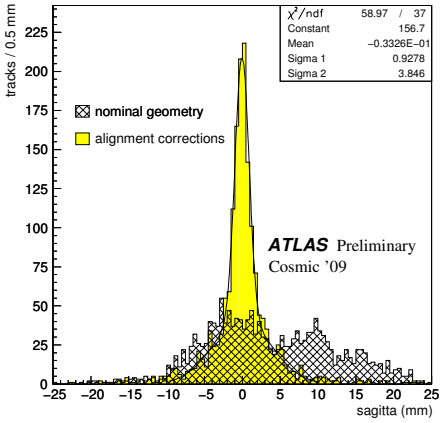

Figure 2: End-cap sagitta distribution for straight cosmic tracks reconstructed using alignment corrections (filled histogram) in comparison with nominal geometry results (hashed histogram).

2.2 Barrel performance

The barrel optical alignment system can monitor geometry changes leading to track sagitta measurement degradation of about 10–20 μm while the absolute accuracy on sagitta measurements is expected to be at the level of 100–200 μm only. The problem comes from the uncertainties on the optical sensors positions due to the precision of the optical sensors mounting and calibrations. To solve this problem, alignment with straight tracks is used to determine the initial geometry. Once it is determined, the optical alignment system monitors all chamber movements with the desired accuracy.

The performance of the alignment procedure in the barrel part of the Muon Spectrometer has been checked with straight cosmic tracks. Special cosmic runs with toroidal magnet field switched off but solenoidal field switched on were used to perform sagitta resolution studies as a function of muon momentum measured inside the Inner Detector. The widths of track sagitta distributions determined in each momentum bin are plotted as a function of muon momentum in Figure 3 for the *large* and the *small* barrel sectors separately.

There are two contributions to sagitta resolution: from multiple scattering and from the intrinsic resolution of the Muon Spectrometer. The contribution from multiple scattering decreases with muon momentum. It is about a factor of two larger for the *small* sectors because of the presence of the toroid magnet coils. The intrinsic resolution has contributions from the drift tube resolution, the muon chamber alignment and non-ideal internal chamber geometry which was not yet taken into account. The intrinsic resolution term was determined to be at the level of 80 μm inside the *large* barrel sectors and at the level of 100 μm inside the *small* barrel sectors.

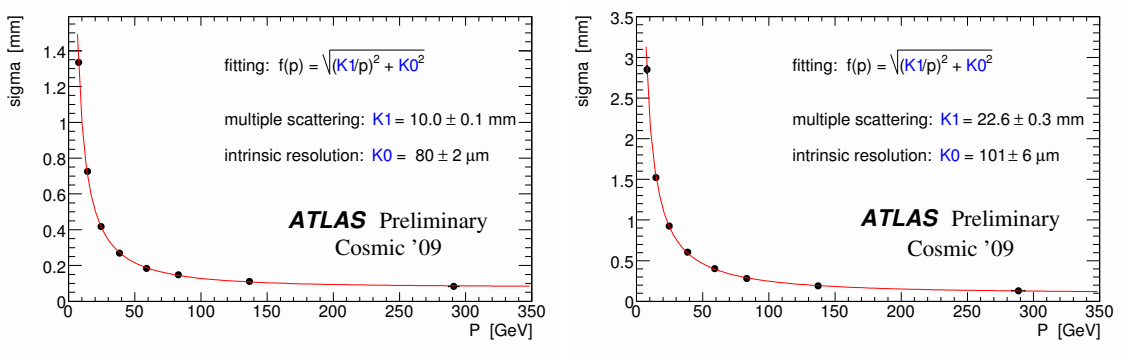

Figure 3: The track sagitta resolution measured inside the *large* (left plot) and inside the *small* (right plot) barrel sectors of the Muon Spectrometer as a function of the muon momentum.

3 Summary

Alignment of the ATLAS tracking systems was well prepared for the first LHC collisions. The distributions of unbiased residuals are very close to the ideal geometry simulations for each of the Inner Detector subsystems. The current alignment precision already provides good tracking performance. Improvements are expected for the Inner Detector alignment with larger statistics and with better treatment of weak modes. The optical alignment system is used to continuously monitor chamber positions of the ATLAS Muon Spectrometer. The results produced with cosmic ray tracks show that the combination of track-based and optical alignment procedures allows to achieve the required level of accuracy. Special runs of proton-proton collisions with the magnetic field switched off are planned to improve the alignment of the ATLAS Muon Spectrometer in the regions which are poorly illuminated by cosmic ray tracks.

References

[1] ATLAS Collaboration, *The ATLAS Inner Detector commissioning and calibration*, arXiv:1004.5293v2 [physics.ins-det].

[2] ATLAS Collaboration, *ATLAS muon spectrometer*, Technical Design Report, CERN/LHCC/97-022.

[3] ATLAS muon alignment PDR (2001), Available at: http://atlas-muon-align.web.cern.ch/atlas-muon-align/PDR/pdr_doc.html.

ALICE silicon tracker alignment and performance

Marcello Lunardon for the ALICE Collaboration

University of Padova and INFN, via Marzolo 8, 35131 Padova, Italy

DOI: http://dx.doi.org/10.3204/DESY-PROC-2010-01/192

The Inner Tracking System (ITS) is the detector of the ALICE central barrel located closest to the beam axis and it is therefore a key detector for tracking and vertexing performance. It consists of six cylindrical layers of silicon detectors with three different technologies: two layers each of pixel, drift and strip detectors. We present here the results obtained for the ITS alignment using charged tracks from cosmic rays and the first *pp* collision data, including the validation of survey measurements, the analysis of the track-to-track and point-to-track residuals as a tool for determining the residual misalignment and monitoring the global alignment of the system. A first look at the track impact parameter resolution extracted from the data is also presented.

1 Alignment of the Inner Tracking System

The ALICE experiment [1] at the Large Hadron Collider at CERN is dedicated to the study of the properties of hot and dense strongly-interacting matter produced in Pb-Pb collisions at $\sqrt{s_{NN}} = 5.5$ TeV. The large Time Projection Chamber (TPC) and the Inner Tracking System (ITS) [2] are the main track reconstruction devices in the ALICE central barrel.

The ITS consists of six cylindrical layers of silicon detectors with almost 2200 active modules and a total surface of 6.3 m^2. Three different technologies are used: 240 modules of pixels in two layers at a distance of 3.9 and 7.6 cm from the beam axis (the Silicon Pixel Detector, SPD), 260 modules of silicon drifts at 15 and 24 cm (Silicon Drift Detector, SDD), and 1698 modules of double-sided strips at 38 and 43 cm (Silicon Strip Detector, SSD).

The ITS was designed with the aim to improve the position, angle, and momentum resolution for tracks reconstructed in the TPC, to identify the secondary vertices from the decay of hyperons and heavy flavoured hadrons, and to reconstruct the interaction vertex with a resolution better than 100 microns. ITS is also used for low momentum tracking (below 200 MeV/c) and for recovering the high momentum tracks that are lost in the dead zones between the TPC sectors.

In order to achieve the required high precision on the track parameters, the relative position (location and orientation) of every module needs to be determined precisely. The number of parameters to be determined in the spatial alignment of the 2198 sensor modules of the ITS is about 13000, with a target alignment precision well below 10 microns in some cases (pixels).

The alignment procedure uses the optical and mechanical survey measurements as a starting point for the realignment. Survey information about the sensor positions on ladders (linear assemblies of sensors at the same azimuthal angle) are currently available for both SSD and SDD. Also positions of the SSD ladders with respect to the supporting cones have been measured.

The final alignment precision can be reached using reconstructed tracks. Two different algorithms for the minimization of the point-to-track residuals are used to determine the most probable position of the modules in the ALICE reference frame: Millepede [3] and an iterative module-by-module approach. The current strategy includes the use of both cosmic ray and proton-proton collision tracks, with and without magnetic field. In the case of drift detectors (SDD), Millepede is also used to help the calibration procedure, because of the strong interplay between alignment and calibration parameters (drift velocity).

The level of the alignment is checked by looking at several benchmark variables: for both *pp* collision tracks and cosmic ray tracks we evaluate the mean values and widths of the distributions of "unbiased" local residuals (i.e. the distribution of distances in the module reference frame between a given point and the track fitted without using that point) and the point-to-track distance for clusters in the overlapping regions between modules of the same layer (thereafter referred to as "extra clusters"). For cosmic ray tracks we also look at the track-to-track distance between two half-tracks reconstructed in the top and bottom halves of the detector. The track-to-track distance is measured both as angular distance and as linear distance for tracks passing close to the beam line. In the latter case, the width of the distribution provides a direct measurement of the resolution on the track impact parameter in the transverse direction (often indicated as d_0), one of the key detector performance figures in the scope of the ALICE heavy-flavour physics program.

The first alignment of the ITS using a sample of about 10^5 cosmic ray tracks collected in 2008 is extensively described in Ref. [4]. The recorded tracks allowed the alignment of most of the SPD, the validation of the SSD survey measurements and a first global alignment of the SPD+SSD system, while they did not allow a satisfactory alignment of the SDD modules, mainly because of the interplay of the alignment parameters and the calibration parameters.

A new alignment using about 2×10^7 *pp* collision tracks at 7 TeV and a few 10^4 cosmic ray tracks collected in 2009−2010 was performed this year and used in the extraction of the first physics results of ALICE [5].

As in the first case, the alignment procedure starts by applying the survey corrections available for SSD and SDD modules. Thanks to the large *pp* collision statistics available, a complete validation of the alignment of SSD using extra clusters over the full azimuthal angle and as a function of the transverse momentum has been performed. The widths of the point-to-track distributions of extra clusters confirm that the residual misalignment is compatible with the nominal precision of the survey measurements (i.e. less than 5 μm RMS for modules on the same ladders and less than 20 μm RMS for modules on different ladders), as already verified in [4] for the top and bottom regions of the detector.

The SPD modules were then aligned with Millepede, keeping the SSD modules fixed and using cosmic ray tracks and *pp* collision tracks with magnetic fields B=0, B=+0.5 T and B=-0.5 T at the same time. With respect to Ref. [4] a better alignment especially on the horizontal sides of the detectors was achieved. As shown in the left panel of Figure 1, the mean values of "unbiased" local residual distributions for SPD modules on both layer 1 and layer 2 are of the order of a few microns over the full azimuthal angle (except for a few modules with poor or null statistics because of functioning problems). We verified also that the point-to-track distributions of extra clusters for *pp* data at 7 TeV (not used for the alignment) are compatible with the MC simulation with a residual misalignment of about 8 μm RMS.

A preliminary alignment of a subset of SDD modules with good calibration and uniform drift velocity was also performed. For these modules a special implementation in Millepede of the drift time initial value and the drift speed as extra alignment parameters has been used.

The width of the "unbiased" local residual distributions for SDD modules in layer 4 is shown in the right panel of Figure 1 as a function of the transverse momentum. A final systematic uncertainty (calibration + alignment) of about 60 μm in the $r\phi$ plane can be extracted. The current value, even if still large, starts to be comparable with the intrinsic resolution of the detector (about 35 μm), showing the possibility to get close to the nominal performance of the detector in the near future.

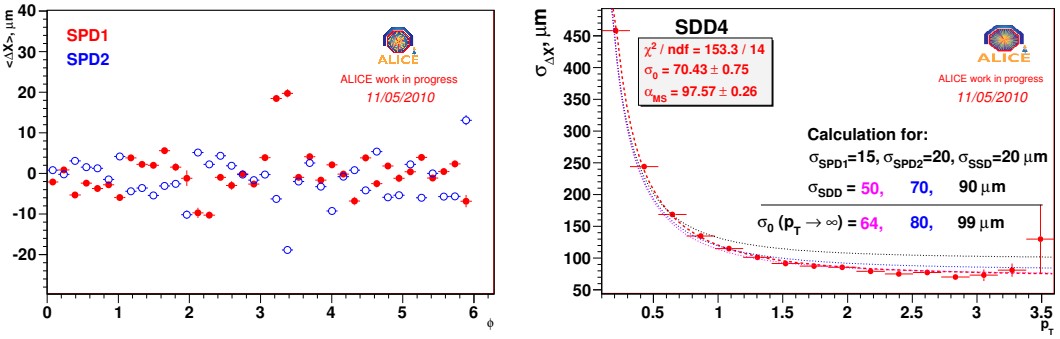

Figure 1: Mean values of the "unbiased" local residual distributions for SPD modules (left panel) and widths of the "unbiased" local residual distributions for SDD modules in layer 4 (right panel) – see text for details.

2 Tracking prolongation efficiency and track impact parameter resolution

As already mentioned at the beginning of this paper, a good ITS performance is required in order to accomplish the rich heavy flavour physics program of ALICE. We report here the TPC-to-ITS tracking prolongation efficiency and a first evaluation of the transverse track impact parameter resolution as a function of the transverse momentum, two of the main performance figures for the Inner Tracking System. The latter, in particular, is strongly correlated with the level of alignment reached in the first 2 layers of pixel detectors.

In the left panel of Figure 2 we show the probability for a track reconstructed in the TPC to be prolonged inside the ITS. The considered TPC tracks are requested to meet minimum quality requirements (number of TPC clusters > 70, χ^2/cluster < 4, $|\eta| < 0.8$, ellipsoidal cut on the distance of closest approach (DCA) using the TPC-only track parameters, with main axes $|DCAxy| < 2.4$ cm and $|DCAz| < 3.2$ cm). Two cases of ITS points selection are shown here: at least two points in ITS (dark squares) and at least one point in SPD (light circles). In the first case an efficiency greater than 96% on the full p_T range was reached, while in the second case the efficiency is reduced because a significant fraction of SPD modules were inactive during the considered data taking. In both cases a good agreement between data (filled markers) and MC simulation (open markers) was found.

The right panel of Figure 2 shows a first estimate of the transverse impact parameter resolution as a function of the transverse momentum. The above mentioned quality cuts in

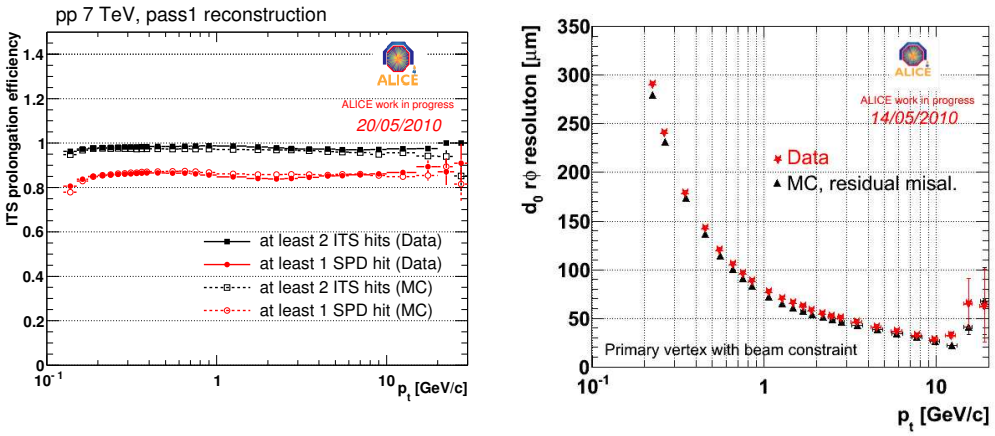

Figure 2: TPC-to-ITS prolongation probability (left panel) and transverse impact parameter resolution (right panel). See text for details.

TPC and a requirement of two points in SPD have been applied for track selection. The impact parameter of each track was estimated with respect to the primary vertex reconstructed using the other tracks in the same event and the beam constraint. An agreement within a few percent between data and MC was found.

3 Conclusions

The status of the alignment and first performance figures for the ALICE Inner Tracking System have been presented. Using the large *pp* collision data sample collected in 2009−2010 we could validate the SSD survey measurements and complete the SPD alignment on the full azimuthal angle. A first preliminary alignment of SDD has been performed as well. The overall ITS performance is now within 10% of the MC target. Further studies are ongoing to address possible correlated alignment effects and to understand the current data-to-MC differences, e.g. possible material budget effects.

References

[1] K. Aamodt et al., ALICE collaboration, JINST **3** S08002 (2008).

[2] G. Dellacasa et al., CERN/LHCC 99-12 (1999).

[3] V. Blobel, *Linear least squares fits with a large number of parameters*, http://www.desy.de/∼blobel, (2000).

[4] K. Aamodt et al., ALICE collaboration, JINST **5** P03003 (2010).

[5] A. Dainese, *ALICE first physics results*, these proceedings.

The commissioning of ALICE's TPC

Magnus Mager for the ALICE Collaboration

CERN, 1211 Genève 23, Switzerland

DOI: http://dx.doi.org/10.3204/DESY-PROC-2010-01/193

ALICE exploits a large volume time projection chamber (TPC) as its main tracking detector. After ten years of construction it was installed in its final location in 2008 and has been continuously running with cosmic data ever since. This extensive data collection led to a well calibrated detector at "day zero".

As soon as the LHC collided beams for the first time at $\sqrt{s} = 900\,\text{GeV}$ in November 2009, the TPC was a key sub-detector in the ALICE data taking stream. During the following period of $\sqrt{s} = 7\,\text{TeV}$ collisions in April 2010 it recorded more than 30 million *pp* events within the first 5 days of integrated running time. Excellent performance and a thorough understanding of the detector were achieved.

1 Introduction and system overview

After having been completely assembled in 2006, installed in the cavern in 2007 and commissioned with cosmic rays in 2008 the ALICE Time Projection Chamber (TPC) took its first *pp* collision data on December, 6th 2009 at $\sqrt{s} = 900\,\text{GeV}$ shortly after the first collisions were delivered by the LHC. With the confidence gained from the first days of operation, the $\sqrt{s} = 7\,\text{TeV}$ data taking started directly on March, 30th 2010 and is continuing since.

The ALICE-TPC [1] is built out of a huge gas filled hollow cylinder with active radial and transverse dimensions of $848 < r < 2466\,\text{mm}$ and $|z| < 2497\,\text{mm}$, respectively (see Fig. 1). The electric field is orientated along the z-axis, aligned with the beams and the magnetic field. It is defined by a high voltage electrode at 100 kV in the $z = 0$ plane as well as a field cage made of aluminised Mylar strips that are held at the correct potential by a voltage divider network.

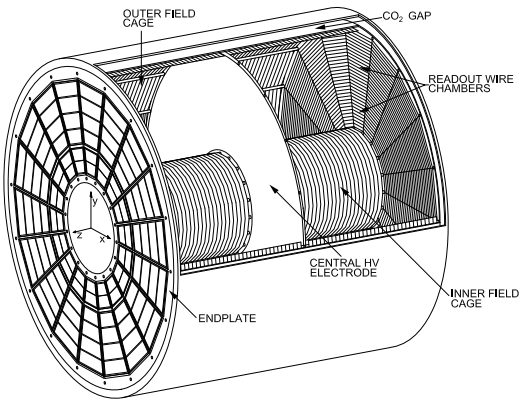

Figure 1: The TPC field cage.

The gas used is a Ne–CO_2–N_2 mixture in a ratio of [85.7–9.5–4.8], which is highly purified, cleaned from Oxygen (down to 1 ppm), and kept at a fixed humidity ($50 - 60\,\text{ppm}$ of H_2O) to avoid the drying-out of glue. In addition radioactive Krypton may be injected into the gas for calibration purposes. At nominal conditions this gas mixture yields a drift velocity of $2.6\,\text{cm}/\mu\text{s}$ and thereby defines the TPC acquisition time to be around $96\,\mu\text{s}$. 72

multi-wire proportional read-out chambers (18 inner and 18 outer on each side) provide the necessary gas amplification and signal read-out.

The read-out is performed by 557,568 pads connected to custom made electronics, which samples the signal with 10 MSPS resulting in 960 units in drift direction at nominal conditions. The channels are distributed over 4,536 front-end cards (FECs) housing 128 complete analog and digital data acquisition chains each. The FECs are grouped into 216 read-out partitions (two on each inner and four on each outer read-out chamber), which provide the interfaces to the ALICE Trigger, detector control system (DCS) and data acquisition (DAQ). Custom made chips "PASA" (Pre-Amplifier and Shaping Amplifier) and "ALTRO" (ALICE TPC Read-Out, digitisation, signal processing and multiple-event buffering) housing 16 channels each are used to acquire and process the signals on-detector in order to achieve a good noise figure and the necessary data reduction (without zero-suppression an event has a size of about 700 MByte) to fit a high event rate into the available bandwidth.

2 Calibration

The TPC is equipped with three dedicated calibration sub-systems:

- a calibration pulser that injects electrical pulses onto the cathode wires of the read-out chambers,
- a radioactive Krypton source that can be attached to the gas system, and
- a laser system that shoots 336 narrow, intense (40 μJ in 10 ns), 266 nm wavelength beams into the TPC volume (see Fig. 2).

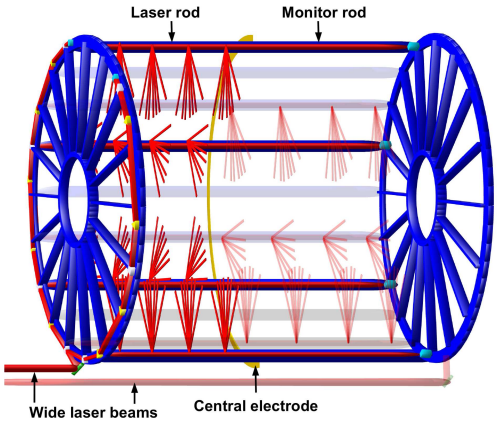

Figure 2: The laser calibration system.

The laser system is activated interleaved with collision data taking in order to capture time (and space) dependent variations of the drift velocity, while the Krypton calibration is repeated only once a year in a dedicated session.

Moreover data from cosmic rays and collisions are used to calibrate the detector. This led to a well calibrated detector in advance of the first collisions [1, 2, 3]. The complementary topology (in particular important for alignment) of collision events and their high abundance further improved the calibration.

Noise. The detector RMS noise stabilised at an average level of 700 electrons (0.7 LSB). It has a smooth spacial variation throughout the pad plane with only a few hot spots next to the high voltage feed-throughs. It is very stable in time, which allows us to adjust the zero-suppression scheme in the on-detector electronics accordingly and leads to an average empty event (no tracks) size of only 30 kByte.

Gain. The gain of the TPC read-out chambers and electronics is precisely measured by using decays from injected radioactive Krypton gas and the calibration pulser, respectively, and shows fluctuations of the order of 20%. No attempt was made to equalise the gain by adjusting the high voltage of the gas amplification, but the different gains are taken into account in the offline reconstruction.

The Krypton measurement was repeated at different gain levels to choose the best trade-off between chamber stability and loss of signal.

***E* × *B*.** The inhomogeneities of the magnetic field (about 1%) lead to a spacial distorition of up to 7 mm in the transverse plane for maximum drift. Before the detectors were inserted into the magnet the magnetic field had been carefully measured, which allowed us to correct for the $E \times B$ effect due to B-field inhomogeneities.

In addition to the B-field inhomogeneity also the E-field is not perfectly homogeneous, which is mostly caused by slightly misaligned read-out chambers and not precisely tuned reference voltages at the chambers. Recent calculations helped to tune the voltages and to apply mechanical forces to reshape the field cage. Moreover the B- and E-fields' principle axes are not perfectly aligned which gives an additional contribution to the $E \times B$ effect.

Recent analysis taking into account the E-field inhomogeneities and the angle between the fields allows to correct for the distortions down to 1 mm. Additional refinements of the models and methods to obtain their parameters indicate that this can be improved further in the near future.

3 Performance results

3.1 Operation

Stability. The detector runs in a fully automated way and is remotely operated by the ALICE-wide DCS. The TPC has proven to work in a very stable fashion. However, occasionally the field cage and read-out chambers trip. While the precise reason is still under investigation there is a clear correlation with LHC beam losses.

Speed. Designed for high multiplicity heavy-ion collisions, looking at single *pp* events the TPC is essentially empty. This has a crucial impact on its performance as protocol overhead of empty channels become an issue. A special mode of operation "sparse read-out" was employed to partly overcome these restrictions but required us to waive the derandomising multiple event buffering feature. The mean event size of 300 kByte for minimum bias 7 TeV *pp* collisions leads to a read-out time of about 500 μs, which is defined by the slowest read-out partition. The latter is one housing a track, and is about ten times slower than the average partition. A summary is given in Tab. 1 together with an estimate for *PbPb* based on the real *pp*-rates.

event type	size	read-out time
empty	30 kByte	280 μs
7 TeV min. bias	300 kByte	500 μs
PbPb central	70 MByte (est.)	2.3 ms (est.)

Table 1: Event sizes and read-out times.

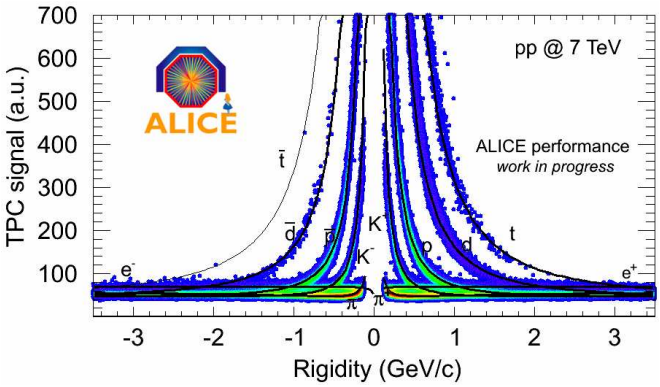

Figure 3: The dE/dx-spectrum for 7 TeV data.

3.2 Observables

$p_\perp$ resolution. The transverse momentum resolution of the TPC is obtained by looking at cosmic rays that cross the whole TPC and go through the inner tracking system. These tracks have a topology similar to two back-to-back particles emerging from a collision and are tracked as such. Their mismatch in reconstructed momentum yields the $p_\perp$ resolution, which can be expressed as: $(\sigma_{p_\perp}/p_\perp)^2 = (0.01)^2 + (0.007\,\mathrm{GeV}^{-1} \cdot p_\perp)^2$.

dE/dx resolution. The PID information collected by the TPC is based on the specific ionisation loss of the traversing particles. Trained by extensive cosmic ray studies, the spectrum obtained shortly after the first collisions clearly shows the good PID properties of the detector. Figure 3 depicts the obtained 7 TeV spectrum. The current resolution for minimum ionising pions is 5%.

Tomography. Photon in e^+e^- conversions are used to identify the material content of the inner detectors. This includes the inner tracking system as well as the inner field cage of the TPC. Figure 4 shows the comparison to Monte-Carlo estimations based on the material distribution given by the technical drawings. The study shows both, the accuracy of the tracking, and the understanding of the material budget, which is in radial direction: 1.367% (inner field cage), 0.607% (gas) and 2.153% (outer field cage).

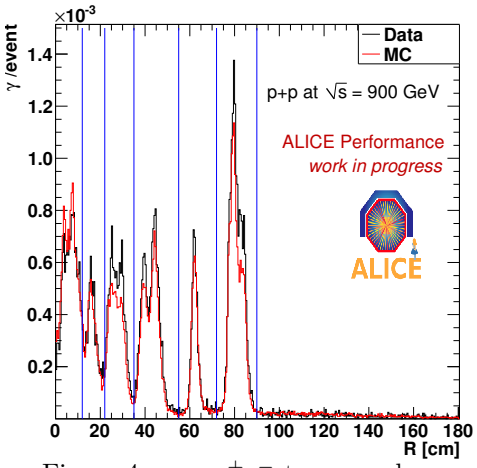

Figure 4: $\gamma \rightarrow e^+e^-$ tomography.

References

[1] J. Alme *et al.*, arXiv:1001.1950 [physics.ins-det].

[2] J. Wiechula [ALICE TPC Collaboration], Nucl. Phys. A **830** (2009) 531C [arXiv:0907.4257 [nucl-ex]].

[3] D.T. Larsen [ALICE TPC Collaboration], Nucl. Inst. Meth. A **617** (2010) 35C.

Operational experience and performance of the CMS pixel detector during the first LHC beams

Valeria Radicci for the CMS Collaboration

The University of Kansas, Lawrence, Kansas 66045, US

DOI: http://dx.doi.org/10.3204/DESY-PROC-2010-01/194

The CMS pixel detector is a complex system consisting of 66M pixels of 100×150 μm size with the main goal of high resolution reconstruction of charged particle tracks. It took almost 10 years of design, construction and commissioning before operation with LHC beams. After the installation in July 2008, the pixel detector was commissioned and calibrated with cosmic muons and the first proton collisions. This paper describes the operational experience, the calibration, and the performance of the pixel detector.

1 Introduction

The silicon pixel tracker is the core of CMS and the closest detector to the interaction point. It is a complex system with 66M pixel channels covering an area of approximately 1 m^2 designed to provide three high precision hits for charged particle tracks in the CMS 3.8 T magnetic field [1].

After 10 years of design and construction it was inserted in CMS in July 2008, and then calibrated and commissioned for more than one year with cosmic muons while awaiting beams. This long period of cosmic runs was useful for the detector understanding and calibration. The cosmic data were used for setting the operating parameters as well as for the time and space alignment [2], [3]. In fall 2009 the operation with colliding beams started, these data were used to complete the calibration procedure and to evaluate the detector performance.

In this paper the results obtained with p-p collisions at center-of-mass energies of 0.9, 2.3, and 7 TeV are shown. A short introduction of the pixel system and operating conditions is given at the beginning, then the status of the present detector is discussed. The calibration and commissioning phases are presented: timing calibration, threshold optimization, bias scan, and Lorentz angle measurement. In the final section, the pixel detector performance with first beams is shown focusing on comparison of data and Monte Carlo, hit detection efficiency, and hit resolution measurements.

2 The CMS pixel detector status

The silicon pixel detector consists of three barrel layers with radii of 4.4, 7.3, 10.2 cm, respectively, and two end-cap disks placed on each side of the barrel at a distance in z of 35.5 and 48.5 cm from the interaction point, respectively.

The basic element of the detector is a module composed of a silicon pixel sensor bump-bonded to a readout chip (PSI-46 ROC) placed on carbon fiber supports. The 4160 pixel cells

of the ROC are arranged in a 52 column and 80 row matrix. In each cell the charge produced in the sensor is amplified, formed, and compared to a threshold. The charge over the threshold, together with a time stamp, is stored in a buffer at the ROC periphery waiting for the accepted LHC level 1 trigger [4]. The technology chosen for the silicon sensor is $n+$, 100×150 μm pixels on n substrate. Slightly different sensor thicknesses and pixel isolation techniques are used: 285 μm p-spray for the barrel and 270 μm p-stops for the end caps [5].

During data taking with beams the operating conditions are not changed from the cosmic runs in order to take advantage of the calibration already performed. The coolant temperature is at 7.4°C[1] and the bias voltage is 150 V in the barrel and 300 V in the end caps.

Currently 98.3% of the pixel detector is in operation: 98.9% of the barrel and 96.8% of the endcaps. The main reasons for failures are broken wire bonds or missing high voltage connections. The number of dead pixels is very low: less then 0.02% in the barrel and less then 0.1% in the endcaps, consistent with the observation during the module test. The number of noisy pixels is negligible, the total fraction is less than 5×10^{-6} [2].

3 Detector calibration

Before operating the system each component of the analog readout chain has to be adjusted: the ROC, the analog optical hybrid and the front end opto-receiver. The optimization procedure is repeated for each channel using an internal calibration signal (V_{cal}) created by the ROC at the pixel preamplifier input [2].

An important calibration to be performed is the optimization of the comparator thresholds. The particle position reconstruction in the pixel detector relies not only on the charge measured by a single pixel but also on the charge shared between pixels and the analog interpolation of the charge between neighboring channels. In order to improve the spatial resolution, the pixel detector has to be sensitive to smaller charges and the pixel charge response has to be uniform. For this purpose an iterative procedure is implemented to lower the ROC threshold to find the minimum value at which the pixels are still 100% efficient. Trim bits at the comparator are also tuned to reduce the pixel to pixel threshold variations. In Figure 1(a), the distribution of the final thresholds is shown, the mean value is 2457. Due to time walk, small signals can take more than a bunch crossing to fire the comparator, and can be associated with a wrong bunch crossing. The minimum hit signal that fires the discriminator threshold in time with the trigger bunch crossing is higher than the absolute threshold and can be estimated comparing the observed cluster size with that expected from MC. The minimum charge that can be correctly readout is approximately 3200 e^-.

Another calibration performed is the timing alignment. The CMS clock must arrive at the correct time for the 25 ns window to be associated correctly to the signal produced by the particles. The best delay maximizes the cluster charge, size, and detection efficiency. A first timing alignment was performed using the fiber lengths. Later, a coarse scan was performed measuring the cluster charge and size with early beams and an accurate timing optimization was achieved measuring the efficiency with beams at 7 TeV.

The high voltage bias scan was also performed with beams at 7 TeV. In Figure 1(b), the efficiency measured in the barrel as a function of bias voltage is shown. At the operating point, 150 V, the efficiency is over 99% and the detector is over depleted. The efficiency curve is

[1]The sensor temperature is around the coolant temperature plus 6°C.

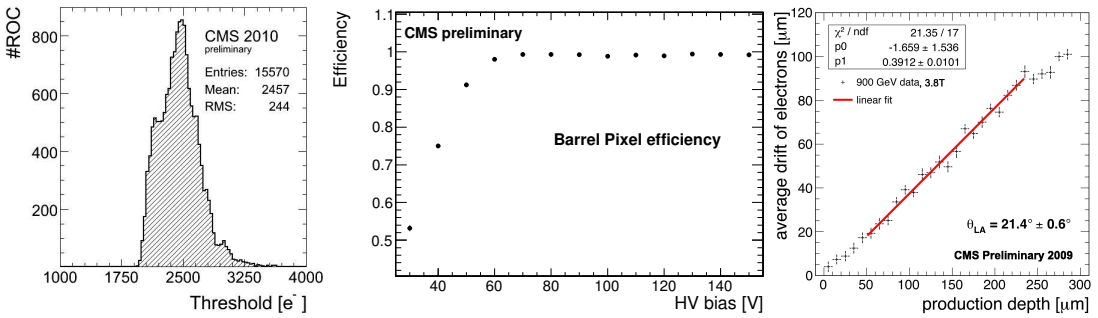

(a) (b) (c)

Figure 1: (a) Distribution of the thresholds in barrel and end caps; (b) detector efficiency vs bias voltage in the barrel; (c) Lorentz angle measurement with the *grazing angle method*.

expected to change in the future due to aging and radiation effects and will be continually re-measured to monitor the operating voltage.

The charge sharing is enhanced in the magnetic field by the Lorentz force on the charge deposited by ionization. The Lorentz angle (θ_{LA}) has to be measured to correct the hit position. Two methods are used to measure θ_{LA}. The *minimum cluster size* method, more suited to use with cosmic data, measures the cluster size as a function of the track angle. The minimum size is observed when the charges are produced along the Lorentz drift direction: $\theta_{LA} = 22.2° \pm 0.1°$. The second method, the *grazing angle* method, selects reconstructed tracks nearly parallel to the surface which create long clusters. The average drift distance of the electrons is measured as a function of the estimated production depth Fig. 1(c). The slope of the linear fit is $\theta_{LA} = 21.4° \pm 0.6°$. The two techniques agree within the errors.

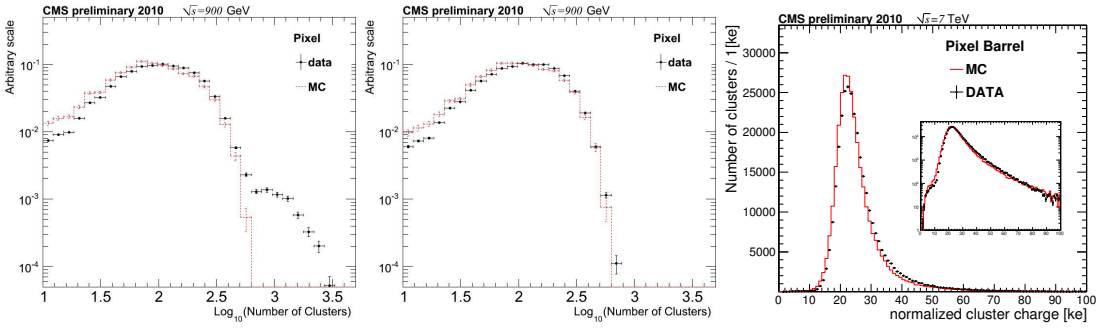

(a) (b) (c)

Figure 2: (a) Distribution of the number of clusters in minimum bias events; (b) distribution of the number of clusters after the background event cut; (c) normalized cluster charge in the barrel.

4 Performance with first LHC beams

The distribution of the number of clusters in minimum bias events observed with colliding beams at 900 GeV is shown in Fig 2(a), the data (dots) are compared with the simulated

events (line) [6]. A good agreement between data and MC is clear in the region with low numbers of clusters, but an excess of large multiplicity events is observed in data. Events with high occupancy have been seen since first collisions both in pixels and in strips. Typically these background events are characterized by a large number of long clusters in the barrel. Asymmetry in the r-ϕ plane suggests that the source is beam-gas interactions. A beam-gas veto, or combined cuts on the cluster shape and track quality, removes the background events as shown in Fig 2(b).

The cluster charge distribution, in the pixel barrel, normalized by the track path length to the thickness of the silicon sensor is shown in Fig 2(c), the measured distribution (dots) is in good agreement with expectation (line) [7].

The intrinsic position resolution is evaluated using tracks traversing the barrel in the overlapping regions where modules on the internal and external part of the same layer overlap by a few millimeters and are close together ($\simeq 4$ cm). The difference between the hit positions in two consecutive modules is evaluated and subtracted from the difference between the two track impact points.

The double difference is more precise than the simple difference between the extrapolated and the measured hit and moreover it is independent of the translational misalignment of the modules. Final results compared with simulation are reported in Table 1[2]. The simulated resolutions agree reasonably well with the measured ones [7].

Data	(12.7 ± 2.3) μm	along x
	(28.2 ± 1.9) μm	along y
Simulation	(14.1 ± 0.5) μm	along x
	(24.1 ± 0.5) μm	along y

Table 1: Position resolutions.

5 Conclusion

The pixel detector has been commissioned during one year of cosmic runs. This long period of commissioning ensured that the pixel detector started data-taking with 98.3% of the modules in operation and over 99% hit efficiency. The thresholds are optimized to be sensitive up to 3200 e^- and the hit resolution is (12.7 ± 2.3) μm along x. The detector behaves as expected: Data and MC show a general good agreement. New data from collisions will allow further improvement in the alignment precision and calibrations. Periodical calibrations are foreseen to monitor the aging of the detector and the effects of radiation, for example, the increase of the depletion voltage and the degradation of the spatial resolution.

References

[1] R. Adolphi *et al.* [CMS Collaboration], JINST **3** (2008) S08004.

[2] S. Chatrchyan *et al.* [CMS Collaboration], JINST **5** (2010) T03007 [arXiv:0911.5434 [physics.ins-det]].

[3] S. Chatrchyan *et al.* [CMS Collaboration], JINST **5**, T03009 (2010) [arXiv:0910.2505 [physics.ins-det]].

[4] W. Erdmann [CMS Collaboration], Nucl. Instrum. Meth. A **549**, 153 (2005).

[5] Y. Allkofer *et al.*, Nucl. Instrum. Meth. A **584**, 25 (2008) [arXiv:physics/0702092].

[6] A. Moraes, C. Buttar and I. Dawson, Eur. Phys. J. C **50**, 435 (2007).

[7] V. Khachatryan *et al.* [CMS Collaboration], submitted to the European Physical Journal C.

[2]The resolution is given both in x (r-ϕ plane) and in y (z axis); the pixel dimensions are 100 and 150 μm, respectively

ATLAS inner detector material studies

Kerstin Tackmann for the ATLAS Collaboration

CERN, 1211 Geneva 23, Switzerland

DOI: http://dx.doi.org/10.3204/DESY-PROC-2010-01/195

A good understanding of the material budget of the ATLAS Inner Detector is crucial for physics analyses at ATLAS. This note describes three complementary studies of the material located inside of the ATLAS electromagnetic calorimeter, using converted photons, uniformity of the energy flow in the electromagnetic calorimeter, and reconstructed K_S mass variations.

1 Introduction

An accurate and high-granularity map of the ATLAS Inner Detector (ID) material is necessary for a precise reconstruction of high-energy photons and electrons. The ID material affects both the track trajectories (especially through bremsstrahlung effects) and the electromagnetic shower development (because of the magnetic field and the energy lost in the ID material). The data taken with the ATLAS detector, described in detail in [1], in the last months of 2009 at a center-of-mass energy of $\sqrt{s} = 900\,\text{GeV}$ and since April of 2010 at $\sqrt{s} = 7\,\text{TeV}$ have allowed for a range of studies, which are complementary in both the reconstruction techniques and the location of the material that is probed.

2 Inner detector studies with converted photons

Reconstruction of converted photons in the ID Low-p_T neutral mesons provide an abundant source of converted photons. They are reconstructed from two oppositely charged tracks with transverse momentum $p_T > 500\,\text{MeV}$, which have a significant fraction of high-threshold hits in the Transition Radiation Tracker (TRT) as expected for electrons [2]. Several geometric selection criteria and a requirement on the fit quality of the conversion vertex are imposed to remove combinatorial background, while retaining a high signal efficiency.

Material studies To achieve a very high purity, photon conversions are required to have a small vertex fit χ^2, $\chi^2_{\text{vtx}} < 5$, and both tracks are required to have at least 4 hits in the silicon Pixel and SemiConductor Tracker (SCT) and at least 90% probability to be electrons, as determined using high-threshold radiation in the TRT. The expected purity from simulation is well above 90% in most regions of the ID and the radial resolution for the vertex position is around 4 mm. About 85000 photon conversion candidates are reconstructed in the $500\,\mu\text{b}^{-1}$ that are used for this study. The distribution of photon conversion vertices can be used to map the distribution of material in the ID. Fig. 1 shows clearly the beam pipe ($R = 34.3\,\text{mm}$), the three barrel Pixel layers ($R = (50.5, 88.5, 122.5)\,\text{mm}$) and the first two SCT barrel layers

($R = (299, 371)$ mm), together with the Pixel Support Tube ($R = 229$ mm) and various other support structures. In the xy projection, the cooling pipes on the Pixel detector modules and the overlap regions in the first SCT layer are visible. A clear shift in the simulated radial positions is observed for the Pixel Support Tube and global Pixel supports (around $R = 200$ mm) (see Fig. 1 (right)), while the overall amount of material seems to be in good agreement.

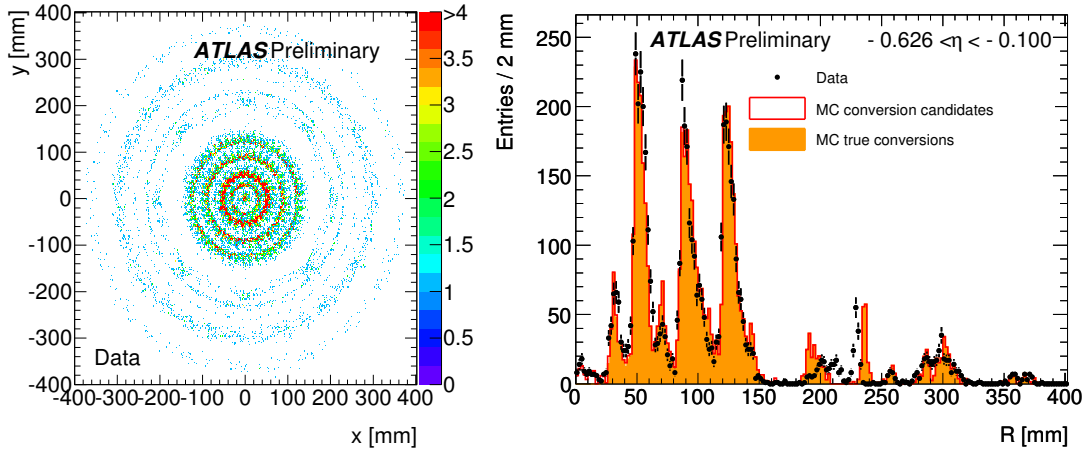

Figure 1: Distribution of reconstructed photon conversion vertices in the xy projection, restricted to $|\eta| < 1$ (left) and radial distribution of reconstructed photon conversion vertices for $-0.626 < \eta < -0.1$ (right).

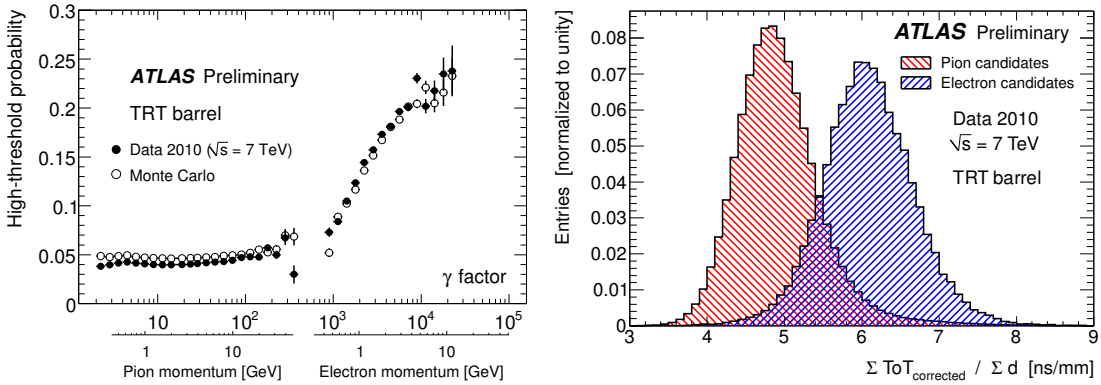

Figure 2: High-threshold onset curve for the barrel region of the TRT (left) and normalized time-over-threshold distributions for electron and π candidates in the TRT barrel region.

Electron identification with the transition radiation tracker Photon conversions can serve as a clean source of electrons for studying the particle identification capabilities of the TRT. The high-threshold radiation onset curve (Fig. 2 left) is determined using a tag-and-probe approach, where, after requiring $\chi^2_{\text{vtx}} < 5$ and at least 4 silicon hits on both tracks, one of the daughter tracks is required to have a fraction of high-threshold hits of more than 0.12, while

the other track is used to extract the rise and the upper plateau of the onset curve. The lower plateau is extracted from generic tracks depleted in electron candidates by requiring a hit in the innermost Pixel layer and vetoing tracks overlapping with photon conversion candidates. The measured time-over-threshold (ToT), normalized to the transverse track length in the straws, yields separation between electrons and hadrons due to the higher ionization energy loss, and hence longer pulses above threshold, of electrons, as shown in Fig 2 (right). Using only low-threshold hits for determining the ToT allows for additional electron-hadron separation independent of the high-threshold information. Electron candidates for this study are supplied by photon conversions with the same selection as used for the material studies.

Cross checking of the beam pipe material using π^0 Dalitz decays Making use of the well-measured branching fraction of the π^0 Dalitz decay, $\pi^0 \rightarrow e^+e^-\gamma$, the radiation length in a certain volume can be determined by comparing the number of photon conversions in that volume with the number of π^0 Dalitz decays. In particular, this can be used to check the radiation length of the beam pipe, where the efficiency to reconstruct converted photons is almost identical to the efficiency of reconstructing the e^+e^- pairs of Dalitz decays. The relative amount of reconstructed Dalitz decays and photon conversions on the beam pipe is in good agreement between the data and the simulation (see Fig. 3), which gives confidence in the description of the beam pipe in the simulation. In the future, the estimation of the radiation length of the ID material will be done relative to the well-known radiation length of the beam pipe.

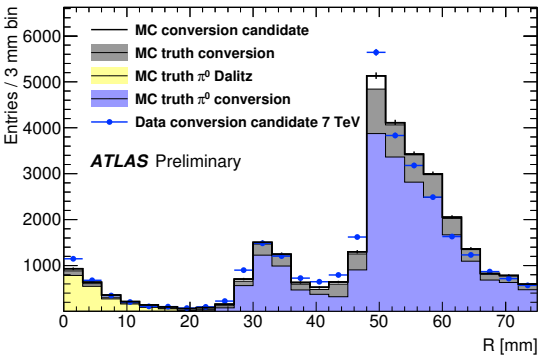

Figure 3: Radial distribution of reconstructed Dalitz decay e^+e^- pairs and photon conversion vertices in the the full η range, $|\eta| < 2.5$.

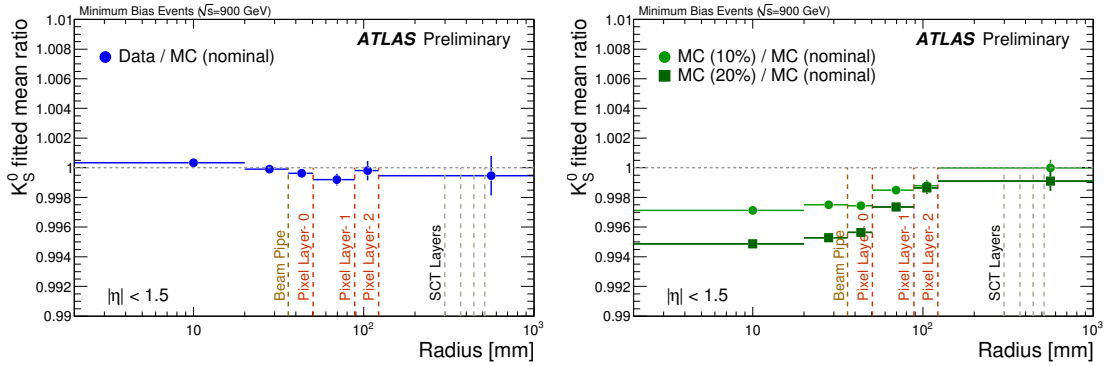

Figure 4: Mean value of the reconstructed K^0_S mass (normalized to its value reconstructed in the simulation) as a function of the decay radius in data (left) and in simulation samples with additional material (right), which demonstrates the sensitivity of this method.

3 Inner detector material studies with K^0_S

The reconstructed mass of K^0_S mesons decaying to $\pi^+\pi^-$ is sensitive to the amount of material traversed by the π tracks through their interaction with the detector material through ionization. Flaws in the modeling of the material will result in biased track momenta and hence a biased reconstructed mass of the K^0_S. By studying the dependence of the reconstructed K^0_S on the K^0_S vertex position in radius, η and ϕ, the material in different detector regions can be constrained. Using the $\sqrt{s} = 900\,\text{GeV}$ data taken in 2009, no evidence for unaccounted for material in the Pixel detector up to $|\eta| < 2$ is found and the nominal detector model is found to be a good description of the data [3] (see Fig 4).

4 Probing the material in front of the calorimeter using energy flow in minimum bias events

The occupancy in the electromagnetic (EM) calorimeter is sensitive to the total amount of material in front of the calorimeter. In particular, material outside of the reach of the ID-based methods can be studied with this method. This study [4] uses about $100\,\mu\text{b}^{-1}$ collected at $\sqrt{s} = 7\,\text{TeV}$. The occupancy is defined as the fraction of events with a channel energy above a fixed threshold, which corresponds to about 5 times the electronic noise. Material localized in regions of ϕ can be seen by studying occupancy variations in ϕ at constant η. The amount of material in SCT and TRT services running at constant ϕ and amounting to about $0.2X_0$ is found to be in good agreement between data and simulation. Up to $1X_0$ of material missing in the simulation is observed in the regions around the rails that support the ID, as shown in Fig. 5.

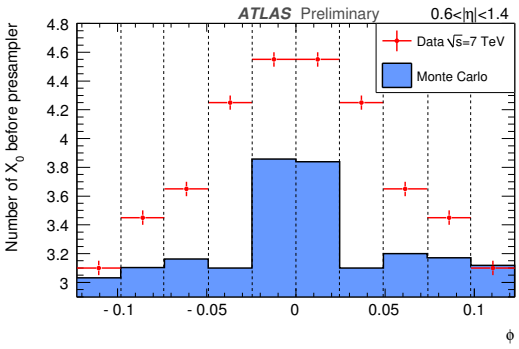

Figure 5: Average number of radiation length X_0 in front of the the EM calorimeter per bin in ϕ ($\Delta\phi = 2\pi/256$, given by the granularity of the cells in the second layer of the EM calorimeter).

5 Conclusions

Multiple complementary methods are used to understand the material budget of the ATLAS Inner Detector. In general, the simulation is found to be in good agreement with the data, with a few localized disagreements.

References

[1] G. Aad *et al.* [ATLAS Collaboration], JINST **3**, S08003 (2008).
[2] G. Aad *et al.* [The ATLAS Collaboration], arXiv:0901.0512 [hep-ex].
[3] The ATLAS Collaboration, ATLAS-CONF-2010-019.
[4] The ATLAS Collaboration, ATLAS-CONF-2010-037.

Performance of muon identification and reconstruction in ATLAS

Thijs Cornelissen for the ATLAS Collaboration

INFN Sezione di Genova, Via Dodecaneso 33, 16146 Genova, Italy

DOI: http://dx.doi.org/10.3204/DESY-PROC-2010-01/196

Muon final states provide clean signatures for many physics processes at the LHC. The performance of the ATLAS muon reconstruction and identification was studied with up to 0.6 nb^{-1} of LHC pp collision data at $\sqrt{s} = 7$ TeV collected with a minimum bias trigger. Measured detector efficiencies, hit multiplicities, muon isolation, and residual distributions of reconstructed muon tracks are well reproduced by the Monte-Carlo simulation.

1 Data and simulation samples and event selection

The performance of the muon reconstruction was studied [1] using up to 0.6 nb^{-1} of integrated luminosity recorded by the ATLAS detector at a center-of-mass energy of 7 TeV. Stable beam operation as well as proper functioning of all the subdetectors was required in the event selection. In addition, to reduce the background from cosmic events, at least three tracks in the inner detector with at least one pixel hit and six SCT hits were required. For triggering the Minimum Bias Trigger Scintillator (MBTS) was used [2]. Compared to the dedicated muon triggers, the MBTS allows an unbiased study of the muon performance without a momentum cutoff.

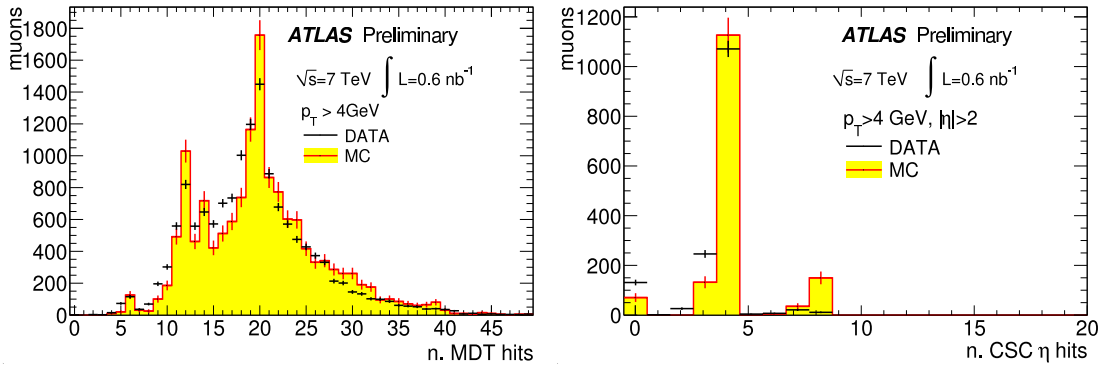

Figure 1: Comparison of the measured distributions of the number of MDT hits (left plot) and CSC hits in the bending plane (right plot) on the combined muon tracks with the Monte-Carlo predictions.

Several different types of reconstructed muon objects are available in ATLAS: *stand-alone*

muons, *combined muons*, *segment tagged muons*, *calorimeter tagged muons*. The highest quality category of muons are combined muons, i.e. muons that are formed by combining an inner detector track with a muon spectrometer track. Unless stated otherwise, we will only consider combined muons in this article, as these have a very low contamination from cosmic ray events.

2 Validation of the muon Monte-Carlo simulation

The predictions of the muon Monte-Carlo simulation are validated first by studying elementary distributions, like the number of hits per reconstructed track and the distribution of the reconstructed track parameters. The tracking performance of the inner detector is well described by the Monte-Carlo simulation, more details can be found in Ref. [3]. The distributions of the number of MDT and CSC hits, which measure the position of the track in the bending plane in the muon spectrometer, are shown in Fig. 1. Reasonable agreement between the data and simulation is observed, the relative lack of tracks with eight CSC hits (in the overlaps between adjacent CSC chambers) in the data is expected to be solved with updated alignment constants. Larger discrepancies were observed for the distributions of the number of muon trigger hits per track, due to known inefficiencies of the trigger chambers that were not simulated.

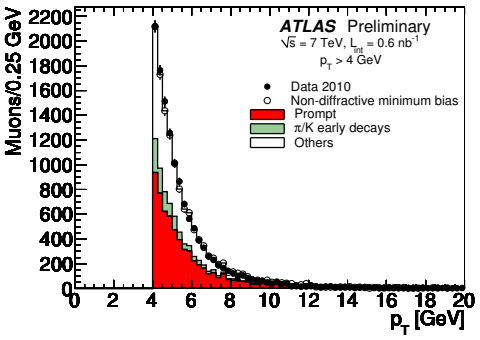

Figure 2: p_T spectrum of the reconstructed combined muons.

The distributions of the reconstructed track parameters were also studied, as shown in Fig. 2 where the p_T spectrum is shown for the data and the simulation. According to the simulation, the spectrum is dominated by light meson decays at low p_T, while the contribution from prompt muons becomes more important at high momentum.

3 Validation of muon energy deposits in the calorimeters

Muons inside jets tend to be produced by hadron decays, therefore a powerful tool for selecting prompt muons is the requirement that the muon is isolated. The isolation can be performed in two ways: by cutting on the energy deposited in a cone around the muon (subtracting the energy deposited by the muon itself), or by cutting on the sum of the transverse momenta of the tracks in a cone around the muon. The size of the cone is typically $0.2 \leq \Delta R \leq 0.4$ ($\Delta R = \sqrt{\Delta\eta^2 + \Delta\phi^2}$). In Fig. 3 the distribution of the track isolation is shown for the data and the simulation, with a cone of size $\Delta R = 0.3$. As before reasonable agreement between the measured and simulated distributions is achieved.

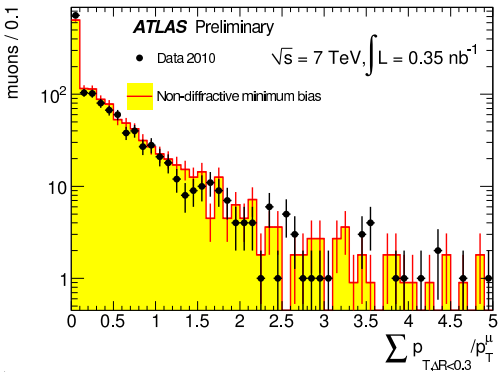

Figure 3: Measured sum of the transverse momenta of tracks around a combined muon in a cone of $\Delta R < 0.3$.

One can conclude that the ATLAS Monte-Carlo simulation can be used to optimize muon isolation criteria.

4 Measurement of relative efficiency and momentum resolution

Investigation of the relative efficiencies of the muon reconstruction algorithms provides a study of the predictive power of the Monte-Carlo simulation at a higher level of complexity. For instance, the efficiency of the combined muon reconstruction algorithm can be measured for muons that are reconstructed in the inner detector and that are both segment tagged and calorimeter tagged (tagged muons). This latter category of muons is used because it has a high purity and a high efficiency (90% according to MC). Fig. 4 shows the efficiency of reconstructed combined muons measured with respect to tagged muons for collision data and for Monte-Carlo simulation. The combined muon reconstruction efficiency in simulation, measured using only muons identified in the simulation as true muons, is also shown in the figure (as the star-shaped symbols labeled as MC truth). The relative efficiency for data is on average a few percent lower than predicted by simulation, indicating either a lower purity of the tagged muon sample in data than in simulation or a lower efficiency of combined muon reconstruction in data than simulation. The relative efficiency predicted for simulation is also a bit lower than the efficiency of combined muon reconstruction in simulation, due to some contamination of the tagged muon sample by inner detector tracks that are mistagged as muons.

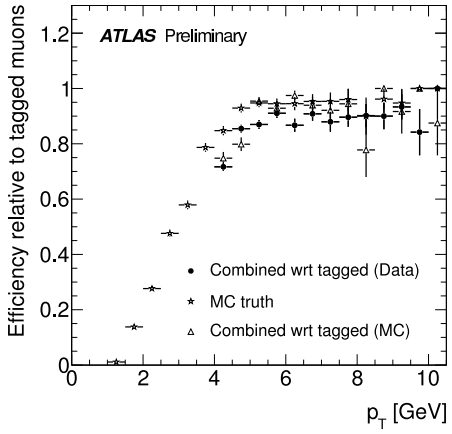

Figure 4: Efficiency of the combined reconstruction relative to the segment and calorimeter tagged muons.

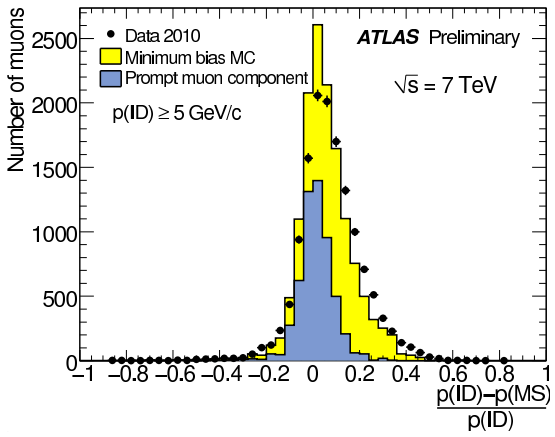

Figure 5: Relative difference between the inner detector and stand-alone muon momentum.

The inner detector momentum resolution for muons with 6 GeV $< p_T <$ 20 GeV is dominated by multiple scattering. A fractional momentum resolution of $\lesssim 2\%$ is reached in the barrel region which increases to about 5% in the forward end-cap region [4][5]. The stand-alone muon momentum resolution is dominated by energy loss fluctuations for $p_T \lesssim 10$ GeV and by multiple scattering above 10 GeV. A fractional stand-alone momentum resolution of $\gtrsim 5\%$

is expected for muons with $p_T \lesssim 10$ GeV [4]. The distribution of the difference of the muon momentum measured in the inner detector and the stand-alone muon momentum therefore provides an estimate of the stand-alone muon momentum resolution. Fig. 5 shows the distribution of this difference divided by the momentum measured in the inner detector. The distribution has a narrow core and a tail to positive values. The shape of the distribution is similar in the Monte-Carlo simulation. According to the Monte-Carlo simulation, the tail of the distribution to positive values is caused by muons from pion and kaon decays-in-flight. There is a larger tail in the measured than in the simulated distribution, the origin of which was found to be remaining misalignments in one of the endcaps of the inner detector, which has already been improved at the time of writing.

5 Conclusions

The first half inverse nb of pp collision minimum bias data at $\sqrt{s} = 7$ TeV has been used to validate the muon Monte-Carlo simulation. The measured relative efficiencies of the muon reconstruction algorithms are well predicted by the Monte-Carlo simulation. The same level of agreement between simulation and experimental measurement is observed in the energy deposition in the calorimeters for isolated and non-isolated muons. The ATLAS muon Monte-Carlo simulation has shown to be a reliable tool for muon performance studies.

References

[1] ATLAS Collaboration, *"Muon Performance in Minimum Bias pp Collision Data at $\sqrt{s}$ = 7 TeV with ATLAS"*, ATLAS-CONF-2010-036

[2] ATLAS Collaboration, *"Charged-particle multiplicities in pp interactions at $\sqrt{s} = 900$ GeV measured with the ATLAS detector at the LHC"*, Phys Lett **B** 688 (2010) 21.

[3] T. Kuhl, *"Performance of track / vertex reconstruction and B tagging of the ATLAS inner detector"*, these proceedings.

[4] ATLAS Collaboration, *"Expected performance of the ATLAS Experiment - Detector, Trigger and Physics"*, `arXiv:0901.0512 [hep-ex].`

[5] ATLAS Collaboration, *"The ATLAS Inner Detector commissioning and calibration"*, `arXiv:1004.5293 [physics.ins-det]`

CMS muon spectrometer, muon reconstruction and identification performance

Luca Scodellaro for the CMS Collaboration

Instituto de Física de Cantabria, Avda de los Castros, 39005 Santander, Spain

DOI: http://dx.doi.org/10.3204/DESY-PROC-2010-01/197

The design of the CMS muon identification and reconstruction is presented, as well as its performance on cosmic-rays and collision data. Efficiencies of various trigger, identification, and reconstruction algorithms have been measured for a broad range of muon momenta. Using the cosmic-ray data, CMS has measured the charge asymmetry of cosmic muons, as a function of the muon momentum from 3 GeV/c to 1 TeV/c. For muon momenta below 100 GeV/c the flux ratio is measured to be a constant 1.2766 ± 0.0032 (stat) ± 0.0032 (syst), the most precise measurement to date.

1 Design of the CMS muon spectrometer

The Compact Muon Solenoid [1] (CMS) is a multi-purpose detector designed to exploit the high discovery potential provided by the Large Hadron Collider (LHC). Muons are a distinctive signature for many of the most interesting physical processes at CMS. The purposes of the CMS muon spectrometer are muon identification, momentum measurement and trigger. It is based on three different technologies of gaseous detectors (see Figure 1): the Drift Tubes (DT), the Cathode Strip Chambers (CSC) and the Resistive Plate Chambers (RPC).

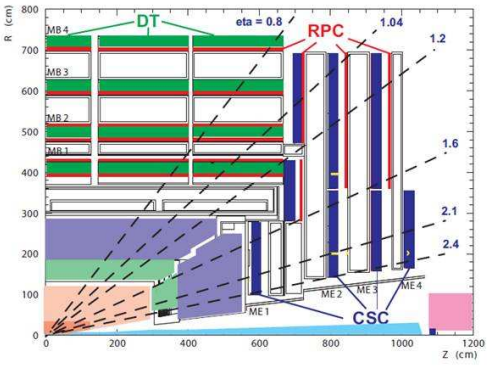

Figure 1: Layout of the CMS muon system.

1.1 Drift tubes

A set of 250 drift tubes chambers cover the barrel region ($|\eta| < 1.2$), where the neutron-induced background is small and the muon rate is low. The chambers are arranged in five wheels, each with four stations forming concentric cylinders along the beam line. They are made of staggered cell layers: two set of four layers measure the bending coordinate $r\phi$ with a precision of about 100 μm. Another set of four layers measure the z (θ) coordinate in the three innermost stations. The DT chambers can trigger on track segments with bunch-crossing identification at level 1.

DT performance has been tested during the commissioning of the detector using cosmic-rays [2, 3]. The efficiency of hit reconstruction has been measured to be greater than 98% over a large part of the drift volume, yielding a segment reconstruction efficiency greater than 99%. The resolution on single hit position is of the order of 260 μm in all chambers. Finally, level 1 trigger reaches a 95% efficiency for muon tracks in the fiducial volume of the chambers.

1.2 Cathode strip chambers

Cathode strip chambers have been chosen to detect muons in the endcap region ($|\eta| < 2.4$), which is characterized by a large and varying magnetic field, and by a higher particle rate. A total of 468 chambers have been arranged in four disks per endcap. Each disk is in turn divided in rings with a varying number of chambers. Each chamber is composed by six gaps with a layer of staggered cathode strips and one of anode wires. The bending coordinate ϕ is measured by the strip centroid with a design resolution of about 150 μm (75 μm for chambers in the innermost ring). The signal from the wires provides a measurement of the radial position, and its fast response is used for bunch-crossing identification at trigger level.

CSC performance has been measured with cosmic-rays [3, 4]: the spatial resolution for local reconstruction has been found to vary between 47 and 243 μm, while the reconstruction efficiency is above 99% both for hits and segments. Finally, for muons with transverse momentum $p_T > 20$ GeV/c the trigger efficiency results greater than 99%.

1.3 Resistive plate chambers

The CMS muon spectrometer is completed by a system of resistive plate chambers designed to improve the muon trigger efficiency: 480 chambers arranged in six stations in the barrel, and 432 chambers ordered in three stations in the endcap (up to $|\eta| < 1.6$), provide a fast response (~ 2 ns) for unambiguous bunch-crossing identification at level 1.

The level 1 trigger efficiency has been measured to be between 80 and 90% for muons in the the fiducial volume of the chambers during the commissioning of the detector [3, 5].

2 Muon reconstruction performance in cosmic-ray events

The reconstruction performance of the CMS muon spectrometer has been studied in a large sample of cosmic-ray events collected during the 2008 [6]. The efficiency of various reconstruction and identification algorithms has been measured through cosmic-ray muons crossing all the detector: good quality muons reconstructed in one hemisphere are selected and the corresponding track in the opposite hemisphere is searched within $|\Delta\phi| < 0.3$ and $|\Delta\eta| < 0.3$ around the reference track. A minimum transverse momentum $p_T > 10$ GeV/c is required to ensure the muon cross all the detector. To test algorithms developed for collision data, cuts are applied on the distance of the point of closest approach of track to the nominal interaction point: $r < 4$ cm and $|\Delta z| < 10$ cm. Figure 2 shows the measured efficiencies for muon tracks reconstructed using information from the tracker system only (*tracker tracks*), from the muon system only (*standalone muons*), and from all the sub-detectors (*global muons*). Also shown are the efficiencies for two main algorithms of muon identification: in the *compatibility* approach, after that a tracker track has been extrapolated to the muon system and matched to local segments, cuts are applied on related variables computed on the base of calorimeter and

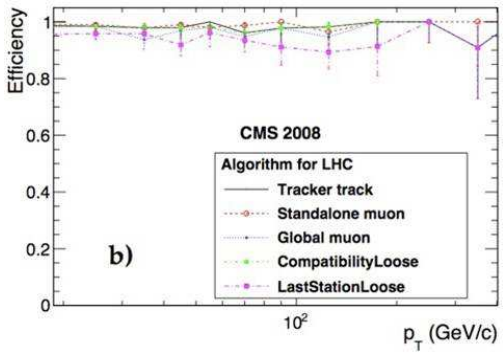

Figure 2: Muon reconstruction and identification efficiencies as a function of the muon transverse momentum p_T.

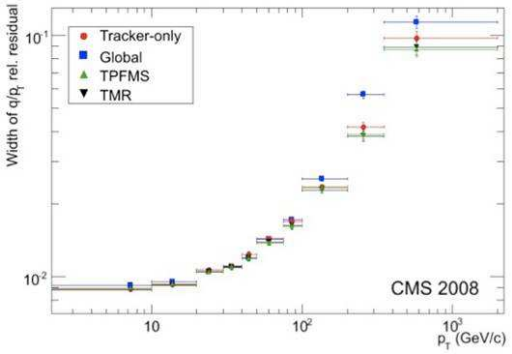

Figure 3: Width of the relative residual distributions for different muon reconstruction algorithms.

muon system information. In the *last station* algorithm, a well matched segment is required in the outermost station.

The resolution on the muon momentum measurement is estimated by the width of the distribution of the relative residuals, $R(q/p_T)$:

$$R(q/p_T) \quad = \quad \frac{(q/p_T)^{upper} - (q/p_T)^{lower}}{\sqrt{2}(q/p_T)^{lower}}, \tag{1}$$

where $(q/p_T)^{upper}$ and $(q/p_T)^{lower}$ are the ratio of the track charge to the transverse momentum for muons reconstructed in the upper and lower detector hemisphere, respectively. Figure 3 shows the momentum resolution for tracker tracks, global muons, and for other two reconstruction algorithms which combine tracker information to hits found in the innermost muon station only.

3 Measurement of the charge asymmetry of atmospheric muons

The CMS collaboration has recently measured the flux ratio of positive to negative muons in cosmic-rays as a function of the muon momentum [7]. The measurement combines data samples collected during the 2006 magnet test and the extended data taking period of 2008, and information both from global and standalone muons. The raw charge ratio measured in CMS has to be corrected for several effects such as energy loss crossing the earth surface to the detector cavern, momentum resolution and mis-assignment of the charge. Final results are shown in Figure 4 for a broad range of muon momentum (3 GeV/c to 1 TeV/c). For momenta below 100 GeV/c, the flux ratio is measured to be a constant 1.2766 ± 0.0032 (stat) $\pm$ 0.0032 (syst). For higher momenta, an increase of the charge asymmetry is observed, in agreement with theoretical model of muon production in cosmic-ray showers, and with previous measurements.

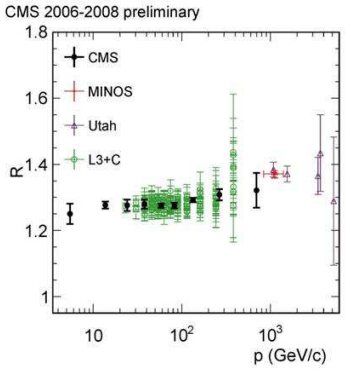

Figure 4: Flux ratio of positive to negative muons in cosmic-rays.

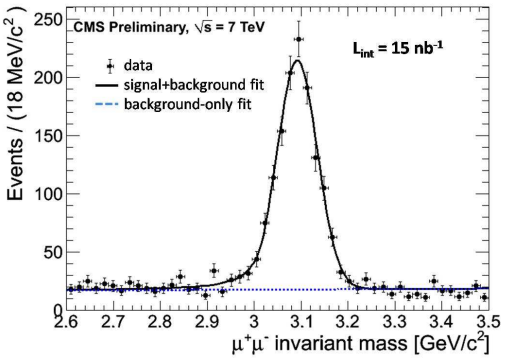

Figure 5: $J/\psi \to \mu^+\mu^-$ reconstructed invariant mass spectrum.

4 First results with collision data

The CMS muon spectrometer is starting to show its potential for detecting and reconstructing particle decays into muons. With 15 nb^{-1} of collision data at a center-of-mass energy of 7 TeV, a narrow J/ψ resonance has been measured in the $\mu^+\mu^-$ invariant mass spectrum (see Figure 5). First candidate $W \to \mu\nu$ and $Z \to \mu^+\mu^-$ decays have also been reconstructed.

5 Conclusions

The design of the CMS muon spectrometer and its performance on cosmic-rays has been presented. Efficiency of trigger, identification and reconstruction algorithms have been measured. The CMS muon system proved to improve the momentum resolution of reconstructed tracks at high transverse momentum. The CMS collaboration has measured the charge asymmetry of cosmic muons in the momentum range between 3 GeV/c to 1 TeV/c. For muon momenta below 100 GeV/c, the flux ratio is measured to be a constant 1.2766 ± 0.0032 (stat) $\pm$ 0.0032 (syst), which is the most precise measurement to date. First muons have been detected in proton-proton collisions at a center-of-mass energy of 7 TeV. In particular, a clear $J/\psi \to \mu^+\mu^-$ resonance has been measured, and first vector boson candidates have been reconstructed.

References

[1] CMS Collaboration, JINST **3** (2008) S08004.

[2] CMS Collaboration, JINST **5** (2010) T03015 [arXiv:physics.ins-det/09114855].

[3] CMS Collaboration, JINST **5** (2010) T03002 [arXiv:physics.ins-det/09115422].

[4] CMS Collaboration, JINST **5** (2010) T03018 [arXiv:physics.ins-det/09114992].

[5] CMS Collaboration, JINST **5** (2010) T03017 [arXiv:physics.ins-det/09114045].

[6] CMS Collaboration, JINST **5** (2010) T03022 [arXiv:physics.ins-det/09114994].

[7] CMS Collaboration, CMS PAS MUO-10-001 [arXiv:hep-ex/10055332].

Performance of the Missing Transverse Energy Reconstruction in the first ATLAS Data at 7 TeV

Adam Yurkewicz for the ATLAS Collaboration

Stony Brook University, Nicolls Road, Stony Brook, NY 11794-3800, United States of America

DOI: http://dx.doi.org/10.3204/DESY-PROC-2010-01/243

In April 2010, the ATLAS experiment collected over 43M collision events at a center-of-mass energy of 7 TeV. These data are used to test the performance of the missing transverse energy reconstruction with up to 250 GeV total transverse energy accumulated per event. The resolution and tails of the missing transverse energy distributions are in good agreement with the simulation.

1 Data and Monte Carlo Simulation Samples and Event Selection

The performance of the missing transverse energy ($E_{\mathrm{T}}^{\mathrm{miss}}$) reconstruction was studied [1] using 43M proton-proton collision candidate events recorded by the ATLAS detector at a center-of-mass energy of 7 TeV under nominal magnetic field conditions.

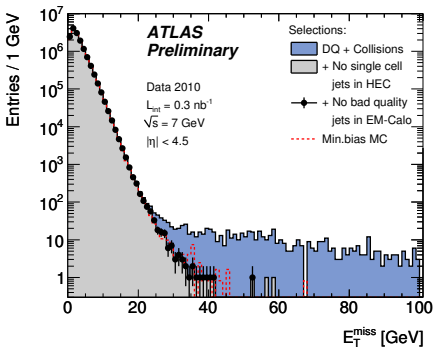

Figure 1: $E_{\mathrm{T}}^{\mathrm{miss}}$ distribution for collision events from 7 TeV data, after successive selections. The corresponding distribution from Monte Carlo simulation is overlaid.

Only those luminosity blocks (periods corresponding to about two minutes of data-taking) satisfying data quality (DQ) criteria for inner detector, calorimeters and jet and missing transverse energy reconstruction were analyzed [2]. The integrated luminosity of the sample after all data quality criteria applied was about 0.3 nb^{-1}.

Selected "minimum bias" events, triggered by the Minimum Bias Trigger Scintillators (MBTS) located on the Liquid Argon (LAr) calorimeter cryostat walls covering the pseudorapidity range $2.1 < |\eta| < 3.8$ [3], and passing additional timing criteria constitute a final data sample of about 14.4 million collision events.

About 18 million minimum bias events were generated using the PYTHIA Monte Carlo program [4], tuned with data from previous hadron colliders [5]. These events were passed through a full Geant4 [6] detector simulation with a detailed description of geometry and material.

Jets are reconstructed with the anti-k_T algorithm [7] with a distance parameter $R = 0.4$ and full four-momentum recombination. For this study, events were rejected if any jet in the event with transverse momentum $p_{\mathrm{T}} > 10$ GeV at the electromagnetic scale fell into any of the following three categories:

- Fake jet caused by sporadic noise bursts in the Hadronic Endcap (HEC) calorimeters.
- Fake jet caused by noise bursts in the electromagnetic calorimeter causing large coherent noise in neighboring cells
- Jet reconstructed from large out-of-time energy deposits in the calorimeter

This requirement removed only a fraction of about 1.0×10^{-4} of all selected collision events.

The $E_{\mathrm{T}}^{\mathrm{miss}}$ distribution before and after cleaning cuts, is shown in Figure 1. The data are well described by the Monte Carlo simulation and no significant tails are observed after cleaning cuts are applied.

2 Reconstruction of $E_{\mathrm{T}}^{\mathrm{miss}}$

$E_{\mathrm{x}}^{\mathrm{miss}}$, $E_{\mathrm{y}}^{\mathrm{miss}}$, $E_{\mathrm{T}}^{\mathrm{miss}}$, and the total transverse energy ($\sum E_{\mathrm{T}}$) are defined as:

$$E_{\mathrm{x}}^{\mathrm{miss}} = -\sum_{i=1}^{N_{\mathrm{cell}}} E_i \sin\theta_i \cos\phi_i \quad , \quad E_{\mathrm{y}}^{\mathrm{miss}} = -\sum_{i=1}^{N_{\mathrm{cell}}} E_i \sin\theta_i \sin\phi_i$$

$$E_{\mathrm{T}}^{\mathrm{miss}} = \sqrt{(E_{\mathrm{x}}^{\mathrm{miss}})^2 + (E_{\mathrm{y}}^{\mathrm{miss}})^2} \quad , \qquad \sum E_{\mathrm{T}} = \sum_{i=1}^{N_{\mathrm{cell}}} E_i \sin\theta_i$$

where E_i, θ_i and ϕ_i are the cell energy, polar angle and azimuthal angle, respectively, and $E_{\mathrm{T}}^{\mathrm{miss}}$ is reconstructed over the range $|\eta| < 4.5$ using only calorimeter information.

All cell energies are calibrated at the electromagnetic scale. The electromagnetic scale gives the correct energy scale for the energy deposited in electromagnetic showers, while it does not correct for the lower hadron response in non-compensating calorimeters.

Only cells belonging to three-dimensional topological clusters (topoclusters) [8] are used. These topoclusters are seeded by cells with $|E_i| > 4\sigma_{\mathrm{noise}}$ (σ_{noise} is the Gaussian width of the cell energy distribution measured in randomly triggered events), and are built by iteratively adding neighboring cells with $|E_i| > 2\sigma_{\mathrm{noise}}$ and, finally, by adding all direct neighbors of the accumulated secondary cells.

3 $E_{\mathrm{T}}^{\mathrm{miss}}$ Performance

Figure 2 shows the $E_{\mathrm{x}}^{\mathrm{miss}}$ and $E_{\mathrm{y}}^{\mathrm{miss}}$ distributions for collision events from 7 TeV data, after data quality selections with the corresponding distributions from Monte Carlo simulation overlaid. The shift of 0.35 GeV of the average $E_{\mathrm{T}}^{\mathrm{miss}}$ in the data with respect to the simulation is caused by a displacement of the actual beam spot with respect to the calorimeter center, together with a small misalignment of the LAr forward calorimeters (FCal), neither of which is perfectly modeled in the Monte Carlo simulation.

A more quantitative evaluation of the $E_{\mathrm{T}}^{\mathrm{miss}}$ performance can be obtained from a study of the $E_{\mathrm{x}}^{\mathrm{miss}}$ and $E_{\mathrm{y}}^{\mathrm{miss}}$ resolutions as a function of $\sum E_{\mathrm{T}}$. The resolutions are expected to increase

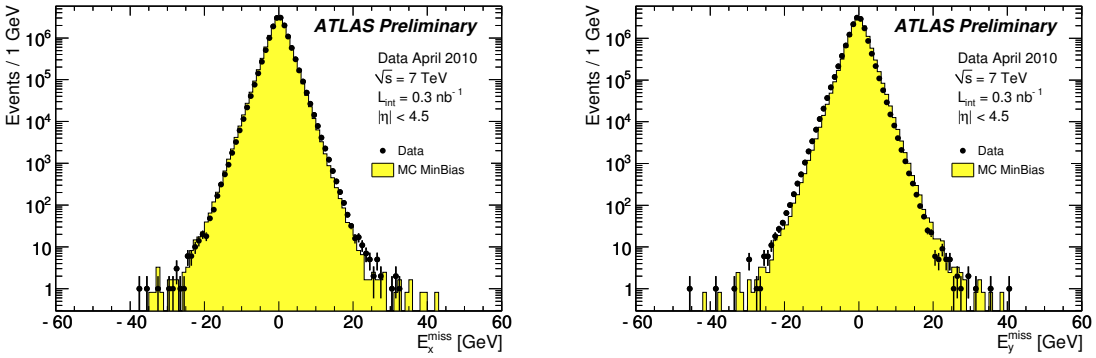

Figure 2: $E_{\mathrm{x}}^{\mathrm{miss}}$ and $E_{\mathrm{y}}^{\mathrm{miss}}$ distributions for data and Monte Carlo simulation.

proportionally with $\sqrt{\sum E_{\mathrm{T}}}$, as can be seen for ATLAS data and Monte Carlo in Figure 3. A good fit to the resolution as a function of $\sum E_{\mathrm{T}}$ is obtained with σ ($E_{\mathrm{x}}^{\mathrm{miss}}$, $E_{\mathrm{y}}^{\mathrm{miss}}$)=0.41 $\times$ $\sqrt{\sum E_{\mathrm{T}}/[\mathrm{GeV}]}$ for the data and with σ ($E_{\mathrm{x}}^{\mathrm{miss}}$, $E_{\mathrm{y}}^{\mathrm{miss}}$)=0.43 $\times$ $\sqrt{\sum E_{\mathrm{T}}/[\mathrm{GeV}]}$ for Monte Carlo simulation.

4 $E_{\mathrm{T}}^{\mathrm{miss}}$ Refined Calibration

A more refined calculation of $E_{\mathrm{T}}^{\mathrm{miss}}$ is being commissioned in which the calorimeter cells associated with each of the different types of reconstructed 'physics' objects (electrons/photons, τ-lepton, jets, muons) will be separately and independently calibrated. Also, cells belonging to topoclusters not associated with any such objects [9] are added as a last step of the refined calculation. For minimum bias events only two terms contribute significantly to the calculation of $E_{\mathrm{T}}^{\mathrm{miss}}$: the main contribution is from cells in topoclusters not associated to any reconstructed object (CellOut) and a lesser contribution comes from cells belonging to jets (RefJet). Such jets are reconstructed at the electromagnetic energy scale using the same anti-k$_T$ algorithm with the same configuration mentioned earlier, but with a lower p_{T} threshold of 7 GeV to test the ability of the Monte Carlo simulation to describe the detector response.

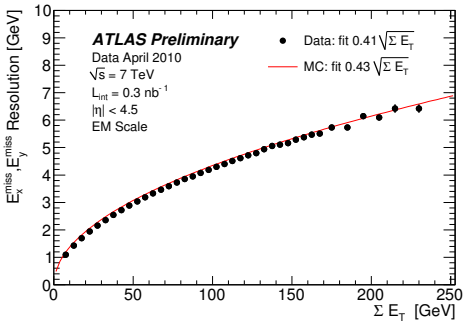

Figure 3: The $E_{\mathrm{x}}^{\mathrm{miss}}$, $E_{\mathrm{y}}^{\mathrm{miss}}$ resolutions as a function of the $\sum E_{\mathrm{T}}$ for data and Monte Carlo simulation.

The contributions to $E_{\mathrm{T}}^{\mathrm{miss}}$ given by these two terms is shown in Figure 4. The RefJet term is non-zero for only a small percentage of events, at 4% and 5% in data and MC respectively. The RefJet contribution tends to be small because the most frequent occurrence is di-jet events,

which are nearly back-to-back in ϕ and closely matched in p_{T}.

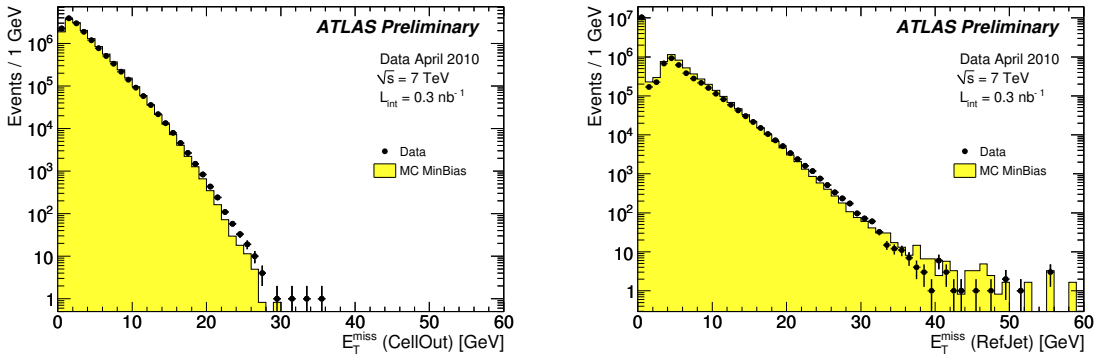

Figure 4: Distribution of $E_{\mathrm{T}}^{\mathrm{miss}}$ computed with cells from topological clusters not in reconstructed objects (CellOut) (left) and distribution of $E_{\mathrm{T}}^{\mathrm{miss}}$ computed with cells from topological clusters in Jets (RefJet) (right) for data (dots) and Monte Carlo simulation (histograms). The number of events in Monte Carlo simulation are normalized to the number of events in data.

5 Conclusions

The missing transverse energy reconstruction has been studied in the first minimum bias collisions at a center-of-mass energy of 7 TeV. No large tails are observed in the $E_{\mathrm{T}}^{\mathrm{miss}}$ distributions after cleaning cuts are applied, and the measured $E_{\mathrm{T}}^{\mathrm{miss}}$ resolution is in reasonable agreement with the Monte Carlo simulation.

A more refined calculation of $E_{\mathrm{T}}^{\mathrm{miss}}$ is being commissioned that will allow the full exploitation of the detector capability.

References

[1] ATLAS Collaboration, *"Performance of the Missing Transverse Energy Reconstruction in Minimum Bias Events at $\sqrt{s}$ of 7 TeV with the ATLAS Detector"*, ATLAS-CONF-2010-039.

[2] ATLAS Collaboration, *"Data-Quality Requirements and Event Cleaning for Jets and Missing Transverse Energy Reconstruction with the ATLAS Detector in Proton-Proton Collisions at a Center-of-Mass Energy of $\sqrt{s} = 7$ TeV"*, ATLAS-CONF-2010-038.

[3] ATLAS Collaboration, *Charged-particle multiplicities in pp interactions at $\sqrt{s} = 900$ GeV measured with the ATLAS detector at the LHC*, Phys Lett **B** 688 (2010) 21.

[4] T. Sjostrand, S. Mrenna and P. Skands, *PYTHIA 6.4 Physics and Manual*, JHEP **05** (2006) 026.

[5] ATLAS Collaboration, *ATLAS Monte Carlo Tunes for MC09*, ATL-PHYS-PUB-2010-002.

[6] S. Agostinelli *et al.*, *GEANT4: A simulation toolkit*, NIM **A 506** (2003) 250.

[7] M. Cacciari, G. P. Salam, and G. Soyez, *The anti-k_T jet clustering algorithm*, JHEP **04** (2008) 063, 68 ArXiv:0802.1189.

[8] W. Lampl *et al.*, *Calorimeter clustering algorithms: Description and performance*, ATL-LARG-PUB-2008-002.

[9] ATLAS Collaboration, *Expected Performance of the ATLAS Experiment - Detector, Trigger and Physics (Jet and $E_{\mathrm{T}}^{\mathrm{miss}}$ chapter)*, CERN-OPEN-2008-020, ArXiV:0901.0512.

LHCb commissioning and operation

Dirk Wiedner for the LHCb Collaboration

CERN, Route de Meyrin 385, CH-1211 Geneva 23, Switzerland

DOI: http://dx.doi.org/10.3204/DESY-PROC-2010-01/245

The LHCb detector was commissioned with beam in November and December 2009. The time alignment was performed and data for space alignment taken both with and without magnetic field. When data taking was restarted in 2010, a second iteration on time and space alignment was performed. The resulting detector performance lead amongst others to good invariant mass resolution, as could be demonstrated in the Λ measurement yielding m$=1115\pm2.5\,\mathrm{MeV/c^2}$. This article will report on procedures used and progress in commissioning the detector for the first LHC physics run.

1 Introduction

The Large Hadron Collider beauty (LHCb) experiment [1] (Fig. 1) is a dedicated experiment for the precision measurements of rare and CP-violating decays of B-mesons. The experimental techniques applied allow for a highly efficient sampling of beauty events. Since the $b\bar{b}$ production in pp collisions at 7-14 TeV is strongly favored in the forward/backward region, LHCb has been constructed as a single arm forward spectrometer.

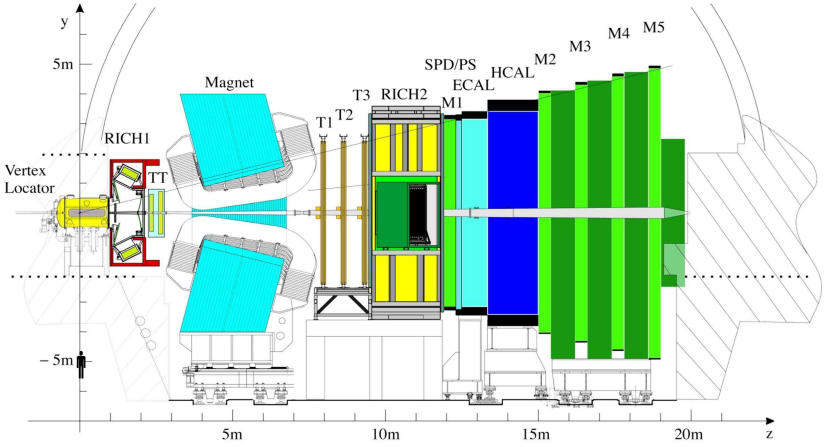

Figure 1: The Large Hadron Collider beauty experiment (LHCb)

The detector surrounding the pp collision point is a silicon strip detector known as the Vertex Locator, VELO. The VELO is positioned, during data taking, with active silicon only 8 mm from the LHC beam. The VELO location, extremely close to the interaction point,

and its high resolution leads to excellent impact parameter performance, critical for B decay identification. Inclusion of the impact parameter measurement in the trigger system leads to early and efficient selection of B decays. The momentum and invariant mass measurement is performed with a dipole magnet and the VELO, together with the Tracker Turicensis (TT) (before the magnet), the silicon Inner Tracker (IT), and the drift tube Outer Tracker (after the magnet).

The particle ID is performed by the RICH, calorimeters and muon systems. The K-π and K-p separation is achieved by two Ring Imaging Cerenkov detectors: RICH1, located after the VELO, has two different radiators, aerogel and gaseous C_4F_{10}, to cover the lower (up to $\approx$10 GeV/c) and middle momentum range (10$\leq$p$\leq$60 GeV/c); RICH2, behind the tracking stations, covers the highest momentum range (16$\leq$p$\leq$100 GeV/c) using CF_4.

After the RICH2 come the LHCb calorimeters identifying photons, electrons and hadrons by converting them into showers. They supply the hardware (Level 0) trigger for high E_T electrons, photons and hadrons. The rejection of a high background of charged pions requires longitudinal segmentation of the electromagnetic shower detection, a preshower detector (PS), followed by the main section of the ECAL. The electron trigger must also reject a background of π^0s with high E_T, provided by a scintillator pad detector (SPD) plane in front of the PS. The thickness of the ECAL is 25 radiation lengths for optimal energy resolution, while the hadronic colorimeter has 5.6 interaction lengths.

The muon system, furthest away from the interaction point, is used for the muon identification and is included in the Level 0 trigger to select high-p_T muons. It is composed of five stations of wire chambers (M1-M5). In M1 GEMs are used in the inner region.

The trigger system has two stages. The Level 0 (L0) trigger is implemented in hardware and selects events with high p_T (μ, e, γ, h) at a rate of 1 MHz (input rate 40 MHz). The higher level trigger is implemented in software; after L0 confirmation, it associates L0 objects with large impact parameter tracks and performs inclusive and exclusive selections. The rate to storage is 2 kHz at an event size of 35 kB.

2 Commissioning steps

2.1 Commissioning without beam

After installation, the commissioning started for all sub-systems in parallel. The first round of commissioning made use of electrical test pulses for the tracking systems and optical LED and laser pulsing systems for the calorimeters and RICH detectors. This allowed to verify the correct channel connectivity, the testing of the data acquisition and the building of the control software. With the help of test pulses an internal time alignment of sub-detectors with a precision of $\approx$1 ns was achieved.

In 2008 the data taking with cosmic events started. Despite the forward geometry of LHCb it was possible to acquire 4 million cosmic particle shower events and perform a global time alignment between calorimeters [2], muon stations [3][4], Outer Tracker [5], Inner Tracker [6] and RICH detectors.

2.2 Commissioning with non colliding proton beam

Located very close to the injection line of LHC beam 2, LHCb was able to use particles produced during LHC injection tests. The proton beam coming from the SPS at an energy of 450 GeV was

dumped on the injection line beam stopper 350 m downstream of LHCb. This created a particle shower hitting the LHCb detector from the back. These dense particle showers allowed for an initial time and space alignment of LHCb. This was especially useful for the VELO [7] and the Silicon Trackers which, due to their small sizes, could not profit from cosmic particle shower events. Interactions between single proton beams circulating in the LHC and the residual gas in the beam pipe provided particle tracks with less density, suitable for the Outer Tracker time alignment and vertex studies.

2.3 Commissioning with proton-proton collisions

The final step in the commissioning of LHCb began with the first proton-proton collisions at 450 GeV energy per beam in 2009. All sub-detectors and the L0 trigger were used to record about 300 000 collision events at 450 GeV before the winter stop. This data was used to achieve better spatial [8] and time alignment but also to start particle reconstruction, leading amongst others to the measurement of K_s, Λ and ϕ decays.

3 Operation

In March 2010 routine detector operation with proton-proton collisions at 3.5 TeV per beam started. For the VELO this further step in energy was of vital importance as only now the beam crossing angle allowed the closing of the VELO. During proton beam injection and energy ramping the VELO stays at a distance of 28 mm from its nominal position, when the LHC beam is stable, it can be moved in close to the beam. The VELO closure during stable beam operation was first achieved on the 1^{st} of April 2010 and currently takes less than 15 minutes. The reproducibility of the closed position relative to the beam is a few μm in the x-direction. The IT and TT have shown the expected signal to noise ratio and unbiased tracking residuals of 65 μm. The corresponding figure for the Outer Tracker is about 270 μm. Both Silicon Trackers and the Outer Tracker have less than 1 % of dead channels. The good performance of all tracking detectors has lead to a high tracking efficiency and in turn good invariant mass resolution. The reconstructed mass of the Λ with the first 65 μb^{-1} is 1115$\pm$2.5 MeV/c^2 (PDG: 1115.683$\pm$0.006 MeV/c^2), see Figure 2.

The particle identification (PID), which is crucial for the analysis of hadronic B-decays, strongly relies on the performance of the RICH detectors. As Figures 3 and 4 show, the $\phi \to K^+K^-$ selection power with RICH particle identification is excellent in comparison to the same data set without RICH PID.

The calorimeter works very effectively, providing the first level trigger at LHCb. The energy calibration provides a π^0 mass of 135.16$\pm$0.02 MeV/c^2 with σ=6.06 Mev/c^2, in agreement with the PDG value (134.9766$\pm$0.0006) MeV/c^2. The good performance of the muon system has lead to the reconstruction of more than 2000 J/Ψs from di-muon events in the first 12.8 nb^{-1}.

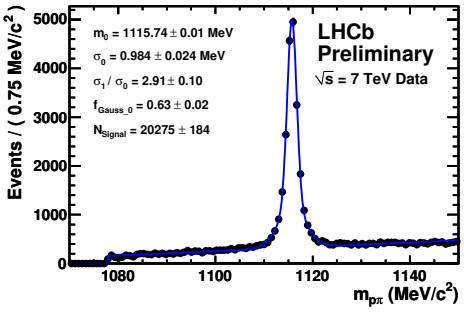

Figure 2: Mass of the Λ

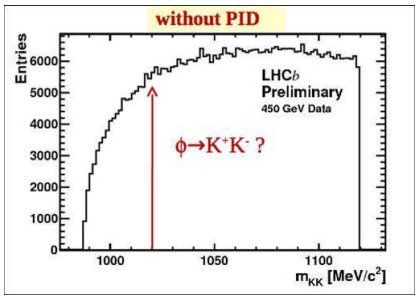

Figure 3: $\phi \to K^+K^-$ selection without RICH detectors

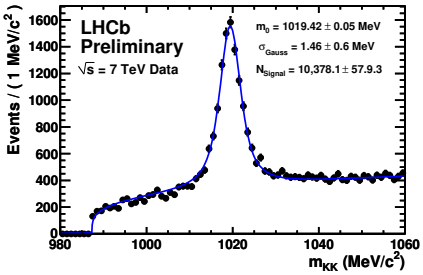

Figure 4: $\phi \to K^+K^-$ selection using RICH detectors

The central run control allows the shift leader to steer the detector from only two panels. The first panel controls the high voltage settings of all detectors in accordance with the LHC machine state. The second is the central data acquisition control panel. In addition to the shift leader, a data manager is the only other person needed to run LHCb; he/she checks the online data quality through histograms for each sub-system.

4 Conclusions and outlook

With $14\,\mathrm{nb}^{-1}$ of acquired integrated luminosity the LHCb detector has proven to be fully ready for data taking. This was achieved by careful preparation, utilizing test pulses and cosmic showers. First collisions were used to conclude commissioning and high statistics data are currently used to fine tune calibrations. Ahead lies an intense and exciting physics programme based on an expected integrated luminosity of $1\,\mathrm{fb}^{-1}$ by the end of 2011 with many channels to look at [10]: the tree-level determination of γ, charmless charged two-body B-decays, measurement of mixing-induced CP violation in $\mathrm{B}_s^0 \to J/\Psi\phi$, analysis of the decay $\mathrm{B}_s \to \mu^+\mu^-$, analysis of the decay $\mathrm{B}^0 \to K^{*0}\mu^+\mu^-$, analysis of $\mathrm{B}_s^0 \to \phi\gamma$ and other radiative B-decays.

References

[1] A. A. Alves *et al.* [LHCb Collaboration], JINST **3** (2008) S08005.

[2] M. Calvi *et al.*, CERN-LHCb-PUB-2010-015.

[3] M. Frosini *et al.*, CERN-LHCb-PUB-2009-028.

[4] S. Furcas *et al.*, CERN-LHCb-CONF-2009-025.

[5] A. Pellegrino *et al.*, LHCb-TALK-2010-013.

[6] J. van Tilburg *et al.*, CERN-LHCb-CONF-2010-004.

[7] S. Borghi *et al.*, Nucl. Instrum. Meth. A **618** (2010) 108.

[8] M. Deissenroth [LHCb Collaboration], J. Phys. Conf. Ser. **219** (2010) 032035.

[9] M. Adinolfi *et al.*, Nucl. Instrum. Meth. A **603** (2009) 287.

[10] B. Adeva *et al.* [The LHCb Collaboration], arXiv:0912.4179 [hep-ex].

Particle Identification in LHCb

Fúnaì Xíng for the LHCb Collaboration

University of Oxford, United Kingdom

DOI: http://dx.doi.org/10.3204/DESY-PROC-2010-01/247

Particle identification (PID) is a fundamental requirement for LHCb. It is provided by RICH, Muon and Calorimeter sub-detectors. To maintain the integrity of the LHCb physics performance, it is essential to measure and monitor the PID efficiencies and mis-ID fractions over time. This can be done by using specific decays of certain particles, such as $K^0_s, \phi, \Lambda, J/\psi$ and D^{*+}, for which pure samples can be isolated using only kinematic quantities. These samples can then be used to calibrate the PID performance from data. This report presents preliminary PID results from early 2010 LHC runs at $\sqrt{s} = 7$TeV.

1 Introduction

The LHCb experiment [1] is designed to make precision measurements of CP-violation and rare decays of B and D hadrons at the Large Hadron Collider (LHC). LHCb is a forward spectrometer (Fig. 1). Its design is optimised to accept the decay products of b and $\overline{b}$ hadrons, which are preferentially produced with a strong angular correlation in the forward−backward directions.

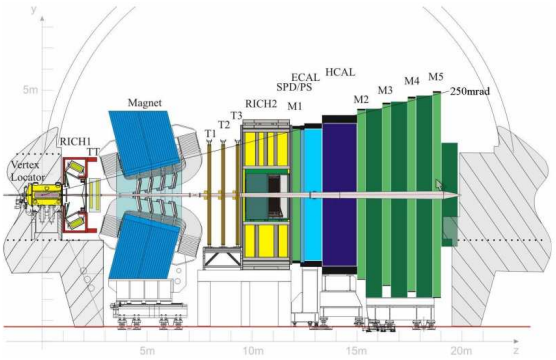

Figure 1: LHCb Detector. Of particular importance for this report are the RICH detectors (RICH 1 and RICH 2), the calorimeter system (SPD-PS, ECAL and HCAL) and the muon system (M1-M5). The tracking is provided by the vertex locator and the stations TT and T1-T3.

LHCb aims to search for evidence of new physics through precise measurements in the flavour sector. Measurements of particular importance are as follows [2]:

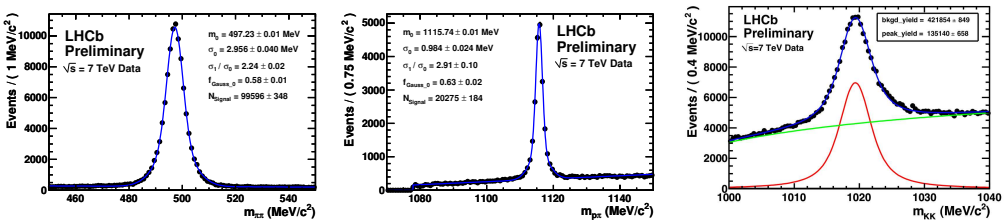

Figure 2: K^0_s(a), Λ^0(b) and ϕ(c) samples selected with kinematic properties alone for RICH calibration. In (c), the lower line indicates the signal component. RICH PID information is used to identify one daughter kaon.

1. Measuring CP-violation in B^0_s-mixing with $B^0_s \to J/\Psi\phi$;
2. Searching for the very rare decay $B^0_s \to \mu^+\mu^-$;
3. Measuring the angular distribution in the decay $B^0_d \to K^*\mu^+\mu^-$;
4. Precision measurement of γ angle in both tree and loop processes. This involves the reconstruction of channels such as $B^+ \to D^0K^+$ and $B^0_s \to hh'(h, h' = \pi, K)$ respectively;
5. Photon polarisation measurements in $B^0_s \to \phi\gamma$ and $B^0_s \to K^*\gamma$;
6. Mixing and CP-violation measurements in the D-meson systems.

It can be seen that all the above measurements require particle ID, whether it be of muons, neutrals in the final state, or discrimination between different hadron species. In LHCb, particle ID is provided by the Ring Imaging Cherenkov (RICH), muon and calorimeter sub-detectors.

2 RICH

LHCb possesses 2 RICH detectors, which utilise 3 radiators (silica aerogel, C_4F_10 and CF_4) to perform π/K/p separation from 2 to 100 GeV/c. The polar angular acceptance of the upstream RICH 1 detector, in the spectrometer bending plane, is 25 $\to$ 300 mrad, while that for the downstream RICH 2 is 15 $\to$ 120 mrad. Pixel Hybrid Photon Detectors (HPDs) have been developed to detect and reconstruct the Cherenkov rings. A total of 484 HPDs cover the $3 \times 3m^2$ total photon detection area, consisting of 196 HPDs in RICH 1 and 288 in RICH 2.

To calibrate the PID performance of the RICH, pure samples of π, K, p have to be identified independent of RICH PID. Specific decays (Fig. 2) can be used due to their clean kinematic signatures. For example $K^0_s \to \pi^-\pi^+$ is used to select a π sample, $\Lambda^0 \to \pi^-p^+$ is used to provide both p and π samples. In $\phi \to K^-K^+$, RICH PID information is used to identify one kaon, which leaves the other kaon as an unbiased source for calibration. In using this sample it is important to subtract off the effects of the non-negligible background lying under the peak. At higher luminosity, $D^{*+} \to D^0(K^-\pi^+)\pi^+$ will be the main particle source for kaon calibration.

The RICH PID performance from 2010 data is illustrated in Fig. 3. These results are for a particular cut on the log likelihood information from the RICH pattern recognition. A tighter cut can be used to suppress the mis-ID rate to a lower level. These plots show that the RICH system already has excellent performance over the typical track momentum range of the B/D meson decays, from 2 to 100 GeV/c. Though the performance is very good, it is not yet at the level found in the Monte Carlo. Improvements are underway in terms of mirror alignment and calibration of the radiator refractive indices.

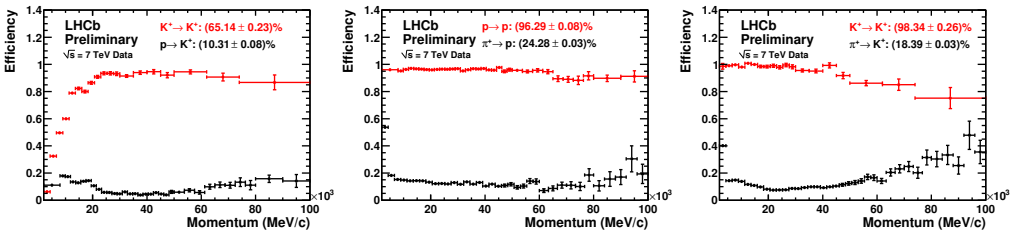

Figure 3: RICH PID performance from collisions data. The kaon identification efficiency versus $p \to K$ mis-ID rates is shown in (a). (b) shows the equivalent curve for proton identification and $\pi \to P$ mis-ID, and (c) for kaon identification and $\pi \to K$ mis-ID.

3 Muon System

The muon system is designed to identify muons with high efficiency and purity. It consists of 5 tracking stations, each subdivided into 4 regions with different granularities. It incorporates two types of tracking technologies: Multi Wire Proportional Chambers (MWPCs) and Gas Electron Multipliers (GEMs). The total thickness of the LHCb hadron absorber, which acts as shielding for the muon system, is 23λ.

Calibration of the muon ID efficiency can be performed using $J/\psi \to \mu^-\mu^+$, where one μ is identified with the Muon system and the other μ with information from the calorimeters only. The results are shown in Fig. 4. The average efficiency is measured to be $\epsilon = 97.3 \pm 1.2\%$. This is in good agreement with Monte-Carlo simulations.

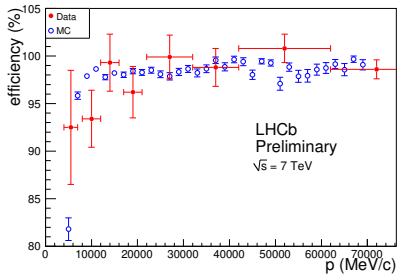

Figure 4: Muon ID efficiency using $J/\psi \to \mu^-\mu^+$, over a momentum span of around 5-70 GeV/c. Data and MC are shown in filled and empty circles, respectively.

The μ mis-ID rates can be estimated using $K^0_s \to \pi^-\pi^+$ (for $\pi \to \mu$ mis-ID) and $\Lambda^0 \to \pi^- p^+$ (for $p \to \mu$ mis-ID). The results are shown in Fig. 5. As can be seen the mis-ID rates fall with momentum and there is good agreement seen between data and Monte-Carlo. Misidentification in the pion sample arises from decays in flight, whereas for the protons it comes about from misassociation of hits or punch-through. Additional variables, which quantitify the agreement of the position of the hits in the muon system with the expected trajectory, can be used to suppress the mis-ID rate further.

htb

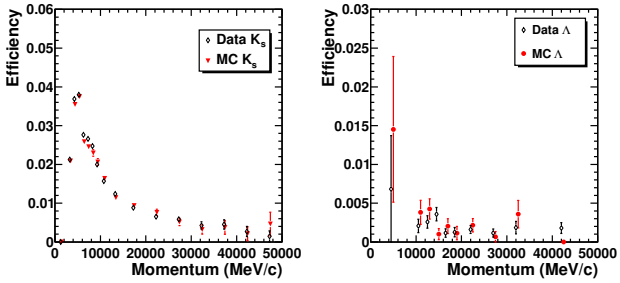

Figure 5: $\pi - \mu$ (a) and p - μ (b) mis-ID rate, with data in empty circles and MC in filled shapes.

4 Calorimeter System

The calorimeter system consists of scintillator pad detector (SPD), pre-shower detector (PSD), electromagnetic calorimeter (ECAL) and hadron calorimeter (HCAL). They provide identification of e, γ and neutral hadrons/resonances, as well as the measurement of their energies and positions. Figure 6 shows examples of the neutral resonances ($\pi^0 \to \gamma\gamma$ and $\rho, \omega \to \pi^-\pi^+\pi^0$) identified by the calorimeter system.

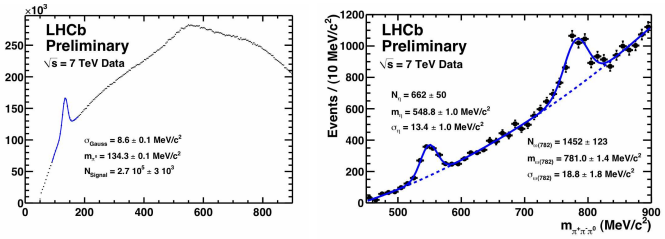

Figure 6: Neutral resonances $\pi^0 \to \gamma\gamma$ (a) and $\rho, \omega \to \pi^-\pi^+\pi^0$ (b) identified by calorimeter.

5 Conclusions

Particle identification is essential for achieving the physics goals of LHCb. The RICH, muon and calorimeter sub-system are all fully operational and have already provided useful PID information for physics analysis. The muon ID performance already is the same as for the Monte-Carlo. With ongoing work in the detector calibration and alignment, the RICH PID performances are approaching the Monte-Carlo expectations.

References

[1] [The LHCb Collaboration], "The LHCb Detector at the LHC," 2008 JINST 3 S08005, doi: 10.1088/1748-0221/3/08/S08005

[2] [The LHCb Collaboration], "Roadmap for selected key measurements of LHCb," arXiv:0912.4179.

Commissioning and performance of the ATLAS trigger with proton collisions at the LHC

Iwona Grabowska-Bold for the ATLAS Collaboration

University of California, Irvine, USA and University of Science and Technology, Kraków, Poland

DOI: http://dx.doi.org/10.3204/DESY-PROC-2010-01/247

The ATLAS trigger has been used successfully to collect cosmic ray and single-beam events, and collision data during the 2009–2010 LHC running at center-of-mass energies of 900 GeV and 7 TeV. The three levels of the ATLAS trigger have been extensively exercised under different conditions and many of its components have been commissioned to be ready for active event selection. We describe the status for the commissioning of the trigger selections using first LHC data collected in the ATLAS experiment. Plans for the evolution of the trigger during the forthcoming LHC running are also briefly discussed.

1 Introduction

The ATLAS experiment [1] is one of the two general-purpose detectors at the Large Hadron Collider (LHC). It collected proton-proton collisions at the end of 2009 at a center-of-mass energy of 900 GeV and continues to accumulate data at $\sqrt{s} = 7$ TeV since March 2010. The proton-beam running was preceded by many months of collecting cosmic-ray data, which allowed for exercising the ATLAS trigger system and eased its commissioning with beam.

In the following sections, a brief overview of the ATLAS trigger system is given, which is followed by a discussion on the commissioning status and performance of calorimeter and tracking-based triggers. Complementary information on the performance of electron, photon, tau, muon, jet, and missing-energy trigger signatures can be found in [2].

2 ATLAS trigger system

The ATLAS trigger system [1] consists of three levels:

- The Level 1 (L1) trigger is purely hardware based. It uses coarse granularity detector data from the calorimeters and muon trigger chambers only to impose a fast (latency $<$ 2.5 μs) trigger decision and define Regions of Interest (RoI) with large energy deposits or potential muon tracks, respectively. Its maximum output rate is about 75 kHz, out of 40 MHz of collision input. If the event is accepted, the detector data are passed from their front-end electronics to Read Out Buffers (ROB) to be later accessed by subsequent trigger levels.

- The Level 2 (L2) trigger is software based and is run on a large farm of processors. It is seeded by L1 and only information of those RoIs which pass certain configurable thresholds

is processed. The detector information is available with full granularity within the RoIs, for which dedicated, fast reconstruction algorithms are executed (average execution time per event about 40 ms). The maximum output rate of L2 to the next trigger level is about 3 kHz. If the event is accepted, the data fragments from all ROBs are sent to the Event Builder. It synchronizes and combines this information to build the complete event and forwards it to the PC farm of the next trigger level.

- The Event Filter (EF) is also software based. It is seeded by L2 and the complete detector data for the event processing are available. Given the larger available resources for reconstruction at the EF (about 4 s per event), offline-like algorithms are used for a better trigger object determination. Its average output rate is about 200 Hz, sufficient for the offline data storage system to handle.

The L2 and EF are collectively referred to as the High Level Trigger (HLT).

3 Commissioning of the L1 trigger

The initial timing synchronization of the ATLAS detectors and triggers made use of so called *splash events*, where a proton beam was steered into a collimator, thereby producing an approximately plane shower of charged particles over most of the ATLAS detector. This allowed quick timing calibration of many trigger inputs with respect to the beams with an accuracy of ± 5 ns. The final L1 calorimeter synchronization adjustments are based on collision data which can be timed to a precision of 2 ns.

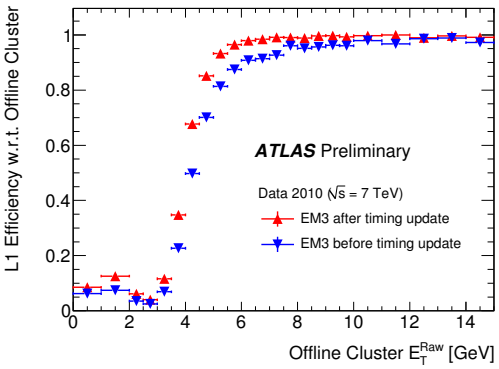

Figure 1: L1 efficiency for the electromagnetic trigger with a 3 GeV threshold (EM3) as a function of the uncalibrated offline cluster E_T for two timing settings.

The good performance of the first level calorimeter trigger during 7 TeV running can be inferred from the behavior of the trigger turn-on curves. An example is shown in Fig. 1. The figure was made using p-p collision data from 2010 and shows the efficiency of the electromagnetic calorimeter trigger with a 3-GeV-threshold (EM3) as a function of the transverse energy calculated offline, using uncalibrated clusters. It shows the improvements in the turn-on behavior after timing adjustments have been made. The L1 efficiency is rapidly approaching the plateau at 100%.

The first level muon trigger is a real time system which uses dedicated trigger detectors. The system uses information from two types of detectors: Resistive Plate Chambers (RPC) in the central region ($|\eta| < 1.05$) and Thin Gap Chambers (TGC) in the forward region ($1.05 < |\eta| < 2.4$) [1]. The RPC and TGC triggers were earlier commissioned with cosmic rays and splashes, and are now being fine tuned with the ongoing p-p collision runs at 7 TeV. The higher rate of muon triggers in the forward region has allowed accurate timing calibration of the TGC system within 3 ns. Synchronization of the RPC trigger is still ongoing as an insufficient data volume has been collected in the central region so far.

4 Performance of the HLT reconstruction

The HLT commissioning strategy consists of several steps. During the first data-taking period with low luminosity, the HLT algorithms were disabled online to ensure no impact on data taking. They were running offline in quasi-real time instead to check against possible errors, crashes and timeouts. Once no problems have been found they were deployed online.

In the second phase, data were selected by the L1 trigger and subsequently processed online by the HLT. However, all events were accepted independent of the HLT decision for further studies as low luminosities allowed the trigger to be based solely on L1. The HLT performance was studied offline in detail. Once it was fully understood and turned out to be satisfactory w.r.t. the offline requirements and at the same time peak luminosities exceeded $O(10^{29})$ cm^{-2}s^{-1}, the HLT rejection was turned on for first low-E_T thresholds to reduce the output rate and provide higher purity events.

The HLT reconstruction is based on the calorimeters and the muon spectrometer which made use of tracking information from the inner detector where appropriate. Final physics objects are built then from calorimeter clusters and tracks which constitute electrons, photons, muons, taus, and jets.

The details of the calorimeter trigger reconstruction and performance are described in [3]. Figure 2 shows the E_T spectrum as reconstructed at L2 for electromagnetic clusters for ~ 9 μb^{-1} of stable beam data collected with 900 GeV collisions and ~ 400 μb^{-1} of stable beam data collected with 7 TeV collisions. Also a comparison with the minimum bias MC is overlaid which shows a very good agreement with the data.

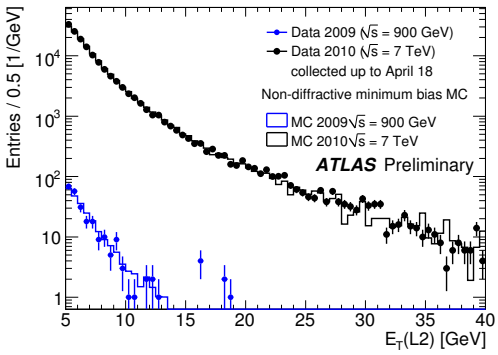

Figure 2: E_T spectrum of reconstructed clusters for data collected with 900 GeV and 7 TeV collisions. A comparison with a minimum bias MC is also shown.

The performance of the HLT track reconstruction has been assessed using data from running periods where the LHC delivered stable beam collisions during which time the ATLAS inner detector components were powered and read out. The events were selected online by the minimum bias trigger as described in [4], without using any information on HLT tracks. In the early low luminosity running period, the low track multiplicity allowed us to reconstruct all tracks at the HLT as the rate of RoI-based tracks was insufficient for these studies. Those trigger tracks were then matched geometrically to the more precise offline reconstructed ones as a reference for assessing their performance. Details of the tracking analysis are described in [5, 6]. The efficiency of the trigger tracking algorithms is defined as the percentage of offline reconstructed tracks that are matched to a trigger track and is flat for a reasonable p_T cut, as shown in Fig. 3.

The details of the HLT muon trigger reconstruction are described in [7]. Figure 4 shows the efficiency of L2 muon tracks reconstructed using the muon spectrometer alone relative to offline reconstructed muons with a nominal threshold set to 4 GeV as a function of the transverse momentum p_T measured by the offline reconstruction. Data were collected at $\sqrt{s} = 7$ TeV. A requirement of a L1 muon trigger has been imposed on the trigger selection, while the offline selection requires a reconstructed muon with a cut $p_T > 2$ GeV, momentum $p > 4$ GeV with

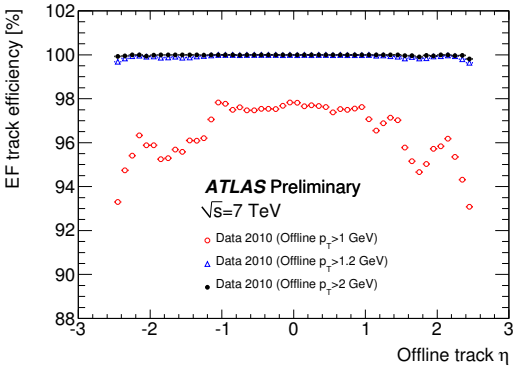

Figure 3: Integrated EF track-finding efficiency for three p_T thresholds.

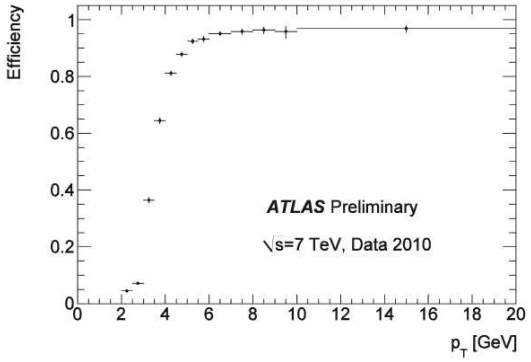

Figure 4: Efficiency of reconstructing a L2 muon in the muon spectrometer w.r.t. offline muons.

the number of hits in the inner detector to be larger than five. Also a match with a L1 RoI was required.

5 Summary

The commissioning of the ATLAS trigger with the first proton-proton collisions is ongoing. The HLT has been exercised and validated in the online running at event output rates low enough for writing to tape all L1-triggered events i.e. at instantaneous luminosities up to $O(10^{29})$ cm^{-2}s^{-1}. At higher luminosity conditions, the HLT has gradually been enabled to provide the additional rejection needed to keep the total output data rate to tape to around 200 Hz. As of now, the peak luminosity at which ATLAS has operated is $O(10^{30})$ cm^{-2}s^{-1} and the lowest-p_T electron, photon, tau, muon, and missing E_T triggers are providing additional HLT rejection. Over the next months, the LHC luminosity is expected to rise by more than two orders of magnitude and most of the HLT is supposed to be in active selection mode by then.

References

[1] G. Aad *et al.* [The ATLAS Collaboration], "Expected Performance of the ATLAS Experiment - Detector, Trigger and Physics," arXiv:0901.0512 [hep-ex].

[2] The ATLAS Collaboration, R. Mackeprang, "Reconstruction and selection of physics objects in the ATLAS high level trigger", these proceedings.

[3] The ATLAS Collaboration, "ATLAS High Level Calorimeter Trigger Software Performance for First LHC Collision Events", ATLAS-CONF-2010-030.

[4] The ATLAS Collaboration, "Performance of the Minimum Bias Trigger in p-p Collisions at $\sqrt{s}$ = 900 GeV", ATLAS-CONF-2010-025.

[5] The ATLAS Collaboration, "Performance of the ATLAS Inner Detector Trigger algorithms in p-p collisions at $\sqrt{s}$=900 GeV", ATLAS-CONF-2010-014.

[6] The ATLAS Collaboration, A. Ferretto, "Performance of the ATLAS Inner Detector trigger algorithms in p-p collisions at center-of-mass energies of 900 GeV and 7 TeV", these proceedings.

[7] The ATLAS Collaboration, "ATLAS Muon Trigger Performance in cosmic rays and pp collisions at $\sqrt{s}$ = 900 GeV", ATLAS-CONF-2010-013.

Reconstruction and selection of physics objects in the ATLAS high level trigger

Rasmus Mackeprang for the ATLAS Collaboration

Discovery, center for particle physics,
Niels Bohr Institute, Blegdamsvej 17, 2100 København Ø, Denmark

DOI: http://dx.doi.org/10.3204/DESY-PROC-2010-01/258

We give an overview of the performance of the ATLAS trigger selections based on extensive online running during LHC collisions and describe the progress towards fully commissioning the individual triggers. Distributions of key selection variables are shown, calculated at the different trigger levels and compared with offline reconstruction. We include examples of triggering on Standard Model physics such as candidate W-boson decays. Comparisons between data and simulations are shown for important selection variables, already illustrating a good level of understanding of the detector and trigger performance. Finally, we give a brief overview of plans for the evolution of trigger selections.

1 The ATLAS trigger

The collision environment of the Large Hadron Collider (LHC) is expected to reach luminosities hitherto unprecedented for hadron colliders in the coming years. Among the experimental challenges facing the detectors installed is the fact that a bunch crossing rate of 40 MHz along with the high total cross section for proton proton collisions will give very high rates of events dominated by soft QCD. To ensure an efficient and unbiased reconstruction of TeV-scale physics, the ATLAS detector is equipped with a tree level trigger system described in detail in [1].

- Level 1 (L1) is a hardware-based trigger that takes decisions, based on calorimeter and muon spectrometer information, to bring down the rate from 40 MHz to below 75 kHz.
- Level 2 (L2) performs a partial reconstruction in the geometrical area (or *Region of Interest*, RoI) where the L1 trigger found candidate physical objects (electrons, jets, muons). Its task is to reduce the event rate to 3 kHz within an average time budget of 40 ms.
- The Event Filter (EF) Reads out the full detector and performs reconstruction with methods very close to those used in the offline reconstruction. The final output rate of the EF is approximately 200 Hz and the time budget is 4 s.

The L2 and EF trigger levels are collectively referred to as the high level trigger (HLT).

2 Performance of physics selections

A common trait for the L2 and EF trigger levels is that they utilize variables defined in the same way as in the offline reconstruction. A crucial point in understanding the trigger performance

is thus the comparison of selection variables between the different HLT levels and the offline reconstruction.

An example is shown in Figure 1 for the muon trigger algorithms running on 7 TeV collision data. The muon reconstruction performs tracking both in the muon spectrometer and in the Inner Detector. Tracks are then matched and refitted. The transverse momentum referred to in the figure is thus the refitted transverse momentum of the combined muon track. The figure shows a clear linear correlation between the trigger and the offline reconstruction.

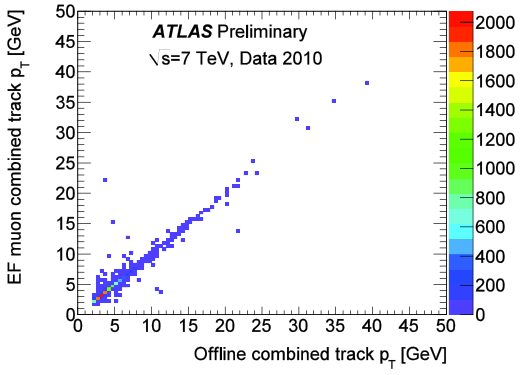

Figure 1: Reconstructed transverse muon momentum calculated in the EF vs the offline calculation.

Similar comparisons are carried out for all physics objects targeted by the ATLAS trigger. For details on these studies, we refer to references [2]. Studies in these notes are carried out for 900 GeV collisions, but the methods remain valid at other centre of mass energies. The performance of the trigger as such is detailed in [3]. In the following sections, we first present the evaluation of the e/γ trigger selections (Sec. 3). Then we present selected plots for various types of signatures (Sec. 4).

3 Electrons and photons

Electrons and photons (e/γ) are important objects to trigger on for many physics studies. Low-energy electrons allow us to study quarkonia, which can be used as standard candles. These are used for many analyses. Medium energy electrons give access to electroweak physics, while high energy electrons will be a good channel for many types of physics beyond the Standard Model. Photons ranging in energy from very low energies up to several hundreds GeV also serve a variety of calibration and signal purposes. For instance, $H \rightarrow \gamma\gamma$ is a central Higgs discovery channel in many scenarios.

Both types of signatures seed off an L1 electromagnetic (EM) RoI. Clustering of EM calorimeter cells is then performed and cuts are applied on the shape of the shower in the calorimeter. Electron signatures furthermore perform tracking in the inner detector and match any tracks found to the EM cluster. All of this is done inside the cone defined by the RoI.

Key parameters in the e/γ selection are shown in Figure 2. The shower shape parameter R_η, shown in Figure 2(a), is calculated in the second layer of the EM calorimeter as the ratio of the energy deposited in a block of $\eta \times \phi = 3 \times 7$ calorimeter cells divided by the energy deposited in 7×7 cells centered around the shower position. A progressively better agreement with offline reconstruction is observed comparing L2 to EF, while Figure 2(b) shows good agreement between data and Monte Carlo in thread with other performance plots not shown in this paper.

On April the 5th 2010, the first W-candidate event was recorded in ATLAS, triggering an electron trigger with a transverse momentum threshold of 10 GeV. Agreement was good between trigger and offline reconstructed quantities and the event was seen to be consistent

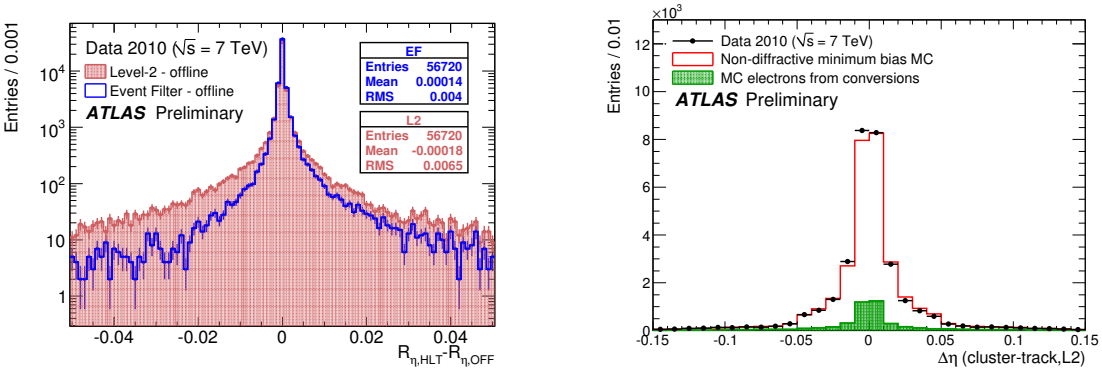

(a) Comparison of R_η as calculated in the HLT and offline.

(b) Track/cluster matching in η at L2 compared to Monte Carlo.

Figure 2: Performance plots for e/γ trigger algorithms.

with a $W^+ \to e^+\nu_e$ decay. For details on the W/Z observation analysis, please see [4].

4 Jets and $\not\!\!E_T$

Giving a complete overview of all types of trigger signatures exceeds the scope of this paper. Here, however, it seems appropriate to show a few selected plots. Figure 3(a) shows the resolution of the EF jet algorithm relative to that of the offline reconstruction. It is worth noting that there is an apparent consistency in this plot despite the fact that different jet algorithms are employed. In the EF, a k_T algorithm is used, while the offline has migrated to being anti-k_T-based.

While the missing transverse energy is well described in the trigger with respect to the offline reconstruction, it is also a sensitive variable to the combined understanding of the detector. It is therefore good to see the agreement observed in Figure 3(b) between collision data and Monte Carlo.

5 Conclusion and outlook

The "trigger menus" (list of trigger signatures) of the first half of 2010 have been focused on the commissioning needs of the ATLAS detector. The triggering has been driven by L1 alone with the HLT running online *without* rejecting any events. This has allowed for a comprehensive validation of the combined trigger/DAQ software.

As the LHC increases luminosity, active HLT selection has been enabled for low-threshold signatures. The consistency demonstrated by the ATLAS trigger in reproduction of offline quantities as well as a generally good description of the data provided by the Monte Carlo has built confidence in the selections to the point where active rejection has been enabled for the HLT. The evolution from here is driven by physics requirements as luminosity increases beyond 10^{30} cm^{-2}s^{-1}. The planned evolution is shown in Table 1. The strategy for dealing with

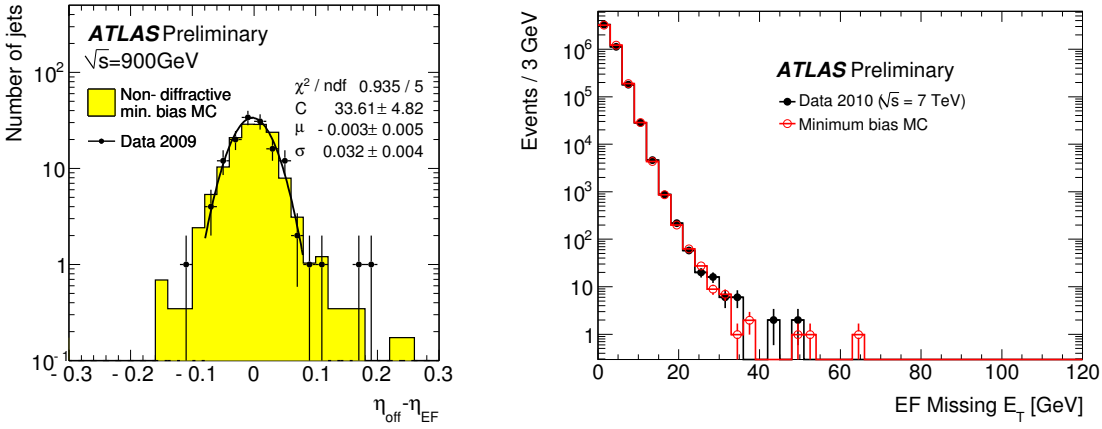

(a) Spatial resolution in the EF with respect to offline and comparison with Monte Carlo.

(b) Data / Monte Carlo comparison of the missing E_T as calculated in the EF.

Figure 3: Performance plots for jets and $\not{E}_T$.

$\mathcal{L}(\mathrm{cm}^{-2}\mathrm{s}^{-1})$	10^{30}	10^{31}	10^{32}
Photons & Electrons	10 GeV γ	20 GeV γ	30 GeV γ (tight)
	10 GeV e	10 GeV e (medium)	15 GeV e (medium)
Taus	29 GeV τ	50 GeV τ	84 GeV τ
	12 GeV τ + 20 GeV $\not{E}_T$	12 GeV τ + 20 GeV $\not{E}_T$	16 GeV τ + 25 GeV $\not{E}_T$
Muons	10 GeV	10 GeV	13 GeV

Table 1: Evolution of primary trigger transverse momentum thresholds with luminosity. The electron, photon and tau triggers are using loose cuts where nothing else is noted. This distinction is not relevant for the muon signatures.

higher luminosities is comprised of three elements: Tightening cuts to increase purity, raising thresholds as commissioning needs diminish and applying prescales to bring down the rate. Many selections exist in "loose", "medium" and "tight" versions to facilitate this progression. Prescaling is generally not used on primary physics triggers.

References

[1] G. Aad *et al.* [ATLAS Collaboration], "The ATLAS Experiment at the CERN Large Hadron Collider," JINST **3** (2008) S08003.

[2] The ATLAS Collaboration, ATLAS-CONF-2010-013, ATLAS-CONF-2010-014, ATLAS-CONF-2010-021, ATLAS-CONF-2010-022, ATLAS-CONF-2010-026, ATLAS-CONF-2010-025, ATLAS-CONF-2010-028, ATLAS-CONF-2010-030.

[3] Iwona Grabowska-Bold,"Commissioning and performance of the ATLAS trigger with proton collisions at the LHC", in these proceedings.

[4] The ATLAS Collaboration, "Observation of $W \to \ell\nu$ and $Z \to \ell\ell$ production in proton-proton collisions at $\sqrt{s} = 7$ TeV with the ATLAS detector," ATLAS-CONF-2010-044.

First results and Standard Model Physics

ALICE first physics results

Andrea Dainese for the ALICE Collaboration

INFN – Sezione di Padova, via Marzolo 8, 35131 Padova, Italy

DOI: http://dx.doi.org/10.3204/DESY-PROC-2010-01/264

ALICE is the dedicated heavy-ion experiment at the Large Hadron Collider. The experiment has also a broad program of QCD measurements in proton–proton (pp) collisions, which have two-fold interest: the study of particle production at the highest energy frontier, and the definition of references for the corresponding measurements in the upcoming Pb–Pb run. We present the first results on the pseudorapidity and transverse-momentum dependence of charged particle production in pp collisions at LHC energies, on the $\bar{\mathrm{p}}$/p ratio and on the Bose–Einstein particle correlations. As an outlook, we report on the status of the ongoing analyses for strangeness and heavy-flavour production measurements.

1 Introduction

The ALICE experiment [1, 2] will study nucleus–nucleus and proton–proton collisions at the Large Hadron Collider, with the main goal of investigating the properties of the high-density state of QCD matter that is expected to be formed in Pb–Pb collisions [3, 4]. The detector was designed in order to provide tracking and particle identification, for all particle species, over a large range of momenta (from tens of MeV/c to over 100 GeV/c), low material budget and excellent vertexing capabilities. These features have been tailored to reach a detailed characterization of the state of matter produced in Pb–Pb collisions, with particular attention to global event properties and hard probes. However, they also provide unique capabilities for carrying out a program of QCD measurements in pp collisions.

This report is organized as follows. In section 2, the ALICE experimental setup is described, with emphasis on the detectors that were used for the results presented here, along with the data collection and event classification. The two most fundamental measurements that characterize inclusive particle production are reported in sections 3 and 4: the charged particle multiplicity density and multiplicity distribution at $\sqrt{s} = 0.9$, 2.36 and 7 TeV [5, 6, 7, 8], and the charged particle transverse momentum (p_{t}) distribution and mean transverse momentum as a function of event multiplicity at 0.9 TeV [9, 8]. In section 5 the measurement of the midrapidity antiproton over proton ratio, which allows to address the mechanisms that transfer the baryon number from beam to central rapidity, at 0.9 and 7 TeV is described [10, 11]. In section 6 the measurement of the Bose–Einstein two-pion correlation, that allows to characterize the spatial extension of the particle emitting source, is described [12, 13]. Finally, in section 7, an outlook is given on the ongoing analyses on strangeness [14] and heavy-flavour production.

2 ALICE detector, data collection and event classes

The ALICE apparatus is described in [1]. It consists of two main parts: a central detector, placed inside a solenoidal magnet providing a field of up to 0.5 T, where charged and neutral particles are reconstructed and identified in the pseudorapidity range $|\eta| < 0.9$, and a forward muon spectrometer covering the range $-4 < \eta < -2.5$. The apparatus is completed by a set of smaller detectors in the forward areas, for triggering, charged particle and photon counting, and event classification.

The main results presented in this report (sections 3–6) were obtained using the following ALICE detectors: the VZERO scintillators, the Inner Tracking System (ITS), the Time Projection Chamber (TPC).

The two forward scintillator hodoscopes (VZERO) are segmented into 32 scintillator counters each, arranged in four rings around the beam pipe. They cover the pseudorapidity ranges $2.8 < \eta < 5.1$ and $-3.7 < \eta < -1.7$, respectively.

The ITS [16] is composed of high resolution silicon tracking detectors, arranged in six cylindrical layers at radial distances to the beam line from 3.9 to 43 cm. Three different technologies are employed: Silicon Pixel Detectors (SPD) for the two innermost layers, Silicon Drift Detector (SDD) for the two intermediate layers, and Silicon Strip Detector (SSD) for the two outermost layers. The design spatial resolutions of the ITS sub-detectors ($\sigma_{r\phi} \times \sigma_z$) are: 12×100 μm^2 for SPD, 35×25 μm^2 for SDD, and 20×830 μm^2 for SSD. The SPD and SSD detectors were aligned using survey measurements, cosmic muon data [15] and collision data to an estimated accuracy of 10 μm for the SPD and 15 μm for the SSD [16]. No alignment corrections are applied to the positions of the SDD modules, for which calibration and alignment are in progress. The estimated misalignment of the SDD modules is about 100 μm.

The TPC [17, 18] is a large cylindrical drift detector with cathode pad readout multiwire proportional chambers at the two edges. The active volume is $85 < r < 247$ cm and $-250 < z < 250$ cm in the radial and longitudinal directions respectively. At the present level of calibration, the transverse momentum resolution achieved in the TPC is given by $(\sigma_{p_\mathrm{t}})/p_\mathrm{t})^2 = (0.01)^2 + (0.007\, p_\mathrm{t})^2$, with p_t in GeV/c. The transverse momentum resolution for $p_\mathrm{t} > 1$ GeV/c is measured in cosmic muon events by comparing the muon momenta reconstructed in the upper and lower halves of the TPC [17]. For $p_\mathrm{t} < 1$ GeV/c, the Monte Carlo estimate of $\sigma(p_\mathrm{t})/p_\mathrm{t} \simeq 1\%$ was cross-checked using the measured K^0_S invariant mass distribution. The $\mathrm{d}E/\mathrm{d}x$ resolution is estimated to be about 5% for full-length tracks [17].

All data presented in this report were collected with a magnetic field of 0.5 T. The analyses with pp collisions at $\sqrt{s} = 0.9$ and 2.36 TeV are based on data collected in November and December 2009, while the analyses at $\sqrt{s} = 7$ TeV are based on data collected in April and May 2010. The data at 0.9 TeV and 7 TeV were collected with a trigger requiring a hit in the SPD or in either of the VZERO counters; i.e. essentially at least one charged particle anywhere in the 8 units of pseudorapidity. At 2.36 TeV, the VZERO detector was turned off; the trigger required at least one hit in the SPD ($|\eta| < 2$). The events were selected in coincidence with signals from two beam pick-up counters (BPTX), one on each side of the interaction region, indicating the passage of proton bunches. Control triggers taken (with the exception of the 2.36 TeV data) for various combinations of beam and empty-beam buckets were used to measure beam-induced and accidental backgrounds. Most backgrounds were removed as described in [6]. The remaining background in the sample is typically of the order of 10^{-4} to 10^{-5} and can be neglected.

The total inelastic pp cross section is commonly subdivided into contributions from diffrac-

tive and non-diffractive processes. At 0.9 TeV, we perform our analyses for two classes of events: inelastic (INEL) and non-single-diffractive (NSD) pp collisions. The INEL sample is selected using the minimum-bias trigger condition described above (signal in SPD or in either of the VZERO counters). For the NSD analyses, a subset of this sample is selected offline by requiring a coincidence between the two VZERO detectors. This condition suppresses a significant fraction of the single-diffractive (SD) events. The fractions of the different process types contributing to the selected event samples are estimated by a Monte Carlo simulation. The process fractions of single-diffractive and double-diffractive (DD) events in the event generators are scaled to match the cross section in $\mathrm{p\bar{p}}$ at $\sqrt{s} = 0.9$ TeV measured by the UA5 experiment [19]. The selection efficiency for INEL and NSD events is approximately 96% and 93%, respectively. Since the 2.36 TeV data sample was triggered by at least one hit in the SPD, this selection was used for both INEL and NSD analyses. At 7 TeV, there is no experimental information available about diffractive processes; therefore, we chose an event class requiring at least one charged particle in the pseudorapidity interval $|\eta| < 1$ (INEL > 0), minimizing the model dependence of the corrections. For the comparison of the multiplicity measurements at all LHC energies, we analyzed the data at 0.9 TeV and 2.36 TeV also in this event class.

3 Results on charged particle multiplicity at $\sqrt{s} = 0.9$, 2.36, and 7 TeV

ALICE has measured the charged particle multiplicity density $\mathrm{d}N_{\mathrm{ch}}/\mathrm{d}\eta$ and the multiplicity distribution $\mathrm{d}N_{\mathrm{events}}/\mathrm{d}N_{\mathrm{ch}}$ at $\sqrt{s} = 0.9$, 2.36, and 7 TeV in $|\eta| < 1.3$ (1.0 at 7 TeV) [5, 6, 7]. The analysis is based on using hits in the two SPD layers to form short track segments, called tracklets. A tracklet is defined by a hit combination, one hit in the inner and one in the outer SPD layer, pointing to the reconstructed vertex. The tracklet algorithm is described in [5, 6]. For this analysis, the position of the interaction vertex is reconstructed by correlating hits in the two silicon-pixel layers [20]. The vertex resolution achieved depends on the particle multiplicity, and is typically 100–300 μm in the longitudinal (z) and 200–500 μm in the transverse direction. Primary charged particles are defined as the particles produced in the collision, excluding the weak decays of strange hadrons. Their multiplicity is estimated by counting the number of SPD tracklets, corrected for: geometrical acceptance, detector and reconstruction efficiencies; contamination from weak-decay products of strange particles, gamma conversions, and secondary interactions; undetected particles below the 50 MeV/c transverse-momentum cut-off, imposed by absorption in the material; combinatorial background in tracklet reconstruction. Two different event generators, PYTHIA [21] (tune Perugia-0 [22]) and PHOJET [23], were used to evaluate the corrections, using the PYTHIA results as central value and the PHOJET results to define an asymmetric systematic error. Other systematic uncertainties were estimated as detailed in [6]. The main error sources that were considered are: detector material description, SPD residual misalignment, particle composition in the generators, fraction of particle below the low-momentum cut-off, relative fraction of non-diffractive, single-diffractive and double-diffractive events.

The pseudorapidity density of primary charged particles in the central pseudorapidity region $|\eta| < 1$ are presented in Table 1 and compared to models. The measured values are higher than those from the models considered, except for PYTHIA tune ATLAS-CSC [25] for the 0.9 TeV and 2.36 TeV data, and PHOJET for the 0.9 TeV data, which are consistent with the data. At 7 TeV, the data are significantly higher than the values from the models considered, with the

Energy (TeV)	ALICE	PYTHIA [21] (109) [24]	PYTHIA [21] (306) [25]	PYTHIA [21] (320) [22]	PHOJET [23]
Charged-particle pseudorapidity density					
0.9	$3.81 \pm 0.01^{+0.07}_{-0.07}$	3.05	3.92	3.18	3.73
2.36	$4.70 \pm 0.01^{+0.11}_{-0.08}$	3.58	4.61	3.72	4.31
7	$6.01 \pm 0.01^{+0.20}_{-0.12}$	4.37	5.78	4.55	4.98
Relative increase (%)					
0.9–2.36	$23.3 \pm 0.4^{+1.1}_{-0.7}$	17.3	17.6	17.3	15.4
0.9–7	$57.6 \pm 0.4^{+3.6}_{-1.8}$	43.0	47.6	43.3	33.4

Table 1: $\mathrm{d}N_{\mathrm{ch}}/\mathrm{d}\eta$ at central pseudorapidity ($|\eta| < 1$), for inelastic collisions having at least one charged particle in the same region (INEL> 0), at three centre-of-mass energies [7]. For ALICE, the first uncertainty is statistical and the second is systematic. The relative increases between the 0.9 TeV and 2.36 TeV data, and between the 0.9 TeV and 7 TeV data, are given in percentages. The experimental measurements are compared to the predictions from models. For PYTHIA the tune versions are given in parentheses. The correspondence is as follows: D6T tune (109), ATLAS-CSC tune (306), and Perugia-0 tune (320).

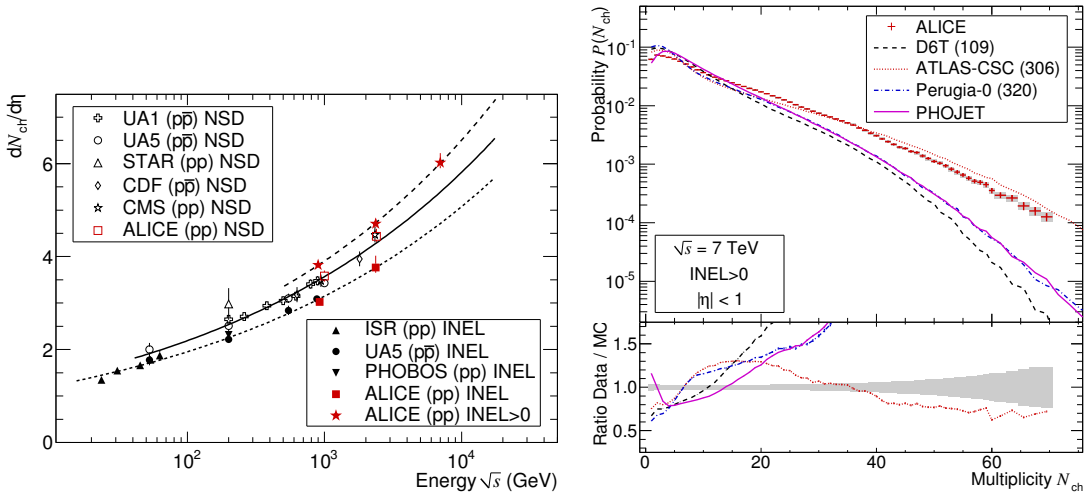

Figure 1: Left: Charged-particle pseudorapidity density in the central pseudorapidity region $|\eta| < 0.5$ for inelastic and non-single-diffractive collisions, and in $|\eta| < 1$ for inelastic collisions with at least one charged particle in that region (INEL>0), as a function of the centre-of-mass energy [7]. The lines indicate the fit using a power-law dependence on energy. Right: multiplicity distribution at 7 TeV in $|\eta| < 1$ for the INEL>0 event class [7]. The error bars for data points represent statistical uncertainties, the shaded areas represent systematic uncertainties. The data are compared to models: PHOJET (solid line), PYTHIA tunes D6T (dashed line), ATLAS-CSC (dotted line) and Perugia-0 (dash-dotted line). In the lower part, the ratios between the measured values and model calculations are shown with the same convention. The shaded area represents the combined statistical and systematic uncertainties.

exception of PYTHIA tune ATLAS-CSC, for which the data are only two standard deviations higher. We have also studied the relative increase of pseudorapidity densities of charged particles (Table 1) between the measurement at 0.9 TeV and the measurements at 2.36 TeV and 7 TeV. We observe an increase of $57.6\% \pm 0.4\%\,(stat.)^{+3.6}_{-1.8}\%\,(syst.)$ between the 0.9 TeV and 7 TeV data, compared with an increase of 47.6% obtained from the closest model, PYTHIA tune ATLAS-CSC. Therefore, the measured multiplicity density increases with increasing energy significantly faster than in any of the models considered. In Fig. 1 (left), the centre-of-mass energy dependence of the pseudorapidity density of charged particles is shown for the INEL > 0, INEL and NSD classes. Note that INEL > 0 values are higher than inelastic and non-single-diffractive values, as expected, because events with no charged particles in $|\eta| < 1$ are removed. The energy dependence is well described by a power-law with $\mathrm{d}N_{\mathrm{ch}}/\mathrm{d}\eta \propto \sqrt{s}^{\alpha}$ ($\alpha \simeq 0.2$) and extrapolates to the design LHC energy of 14 TeV with values that range from 5.7 for INEL to 7.4 for INEL > 0.

The multiplicity distributions $\mathrm{d}N_{\mathrm{events}}/\mathrm{d}N_{\mathrm{ch}}$ were measured at the three energies. The raw measured distributions were corrected for efficiency, acceptance, and other detector effects, using a method based on unfolding with a detector response matrix from Monte Carlo simulations [6]. The unfolding procedure applies χ^2 minimization with regularization. The multiplicity distribution at 7 TeV is shown in Fig. 1 (right) A comparison with models shows that only the PYTHIA tune ATLAS-CSC is close to the data at high multiplicities ($N_{\mathrm{ch}} > 25$). However, it does not reproduce the data in the intermediate multiplicity region ($8 < N_{\mathrm{ch}} < 25$). At low multiplicities, ($N_{\mathrm{ch}} < 5$), there is a large spread of values between different models: PHOJET is the lowest and PYTHIA tune Perugia-0 the highest. Similar comparisons for 0.9 and 2.36 TeV can be found in [6].

4 Results on charged particle p_{t} spectra at $\sqrt{s} = 0.9$ TeV

Charged particle tracks are reconstructed using information from the TPC and ITS detector systems. Signals on adjacent pads in the TPC are connected to particle tracks by employing a Kalman filter algorithm. The TPC tracks are extrapolated to the ITS and matching hits in the ITS detector layers are assigned to the track. The event vertex is reconstructed using the combined track information from TPC and ITS, and the measured average intersection profile as a constraint [20]. The study of the transverse momentum spectrum of charged particles in pp at $\sqrt{s} = 0.9$ TeV is reported in [9]. Tracks are selected in the pseudorapidity range $|\eta| < 0.8$. Additional quality requirements are applied to ensure high tracking resolution and low secondary and fake track contamination. A track is accepted if it has at least 70 out of the maximum of 159 space points in the TPC, and the χ^2 per space point used for the momentum fit is less than 4. Additionally, at least two hits in the ITS must be associated with the track, and at least one has to be in either of the two innermost layers, i.e., in the SPD. Tracks with $p_{\mathrm{t}} < 0.15$ GeV/c are excluded because their reconstruction efficiency drops below 50%. Tracks are also rejected as not associated to the primary vertex if their distance of closest approach to the reconstructed event vertex in the plane perpendicular to the beam axis, d_0, satisfies $|d_0| > (350 + 420\,p_{\mathrm{t}}^{-0.9})$ μm, with p_{t} in GeV/c. This cut corresponds to about seven standard deviations of the p_{t}-dependent transverse impact parameter resolution for primary tracks passing the above selection. The primary charged particle track reconstruction efficiency is about 75% for $p_{\mathrm{t}} > 0.6$ GeV/c. Below this p_{t}, the efficiency decreases and reaches 50% at 0.15 GeV/c. The contamination from secondary particles is 9% at 0.15 GeV/c and and drops

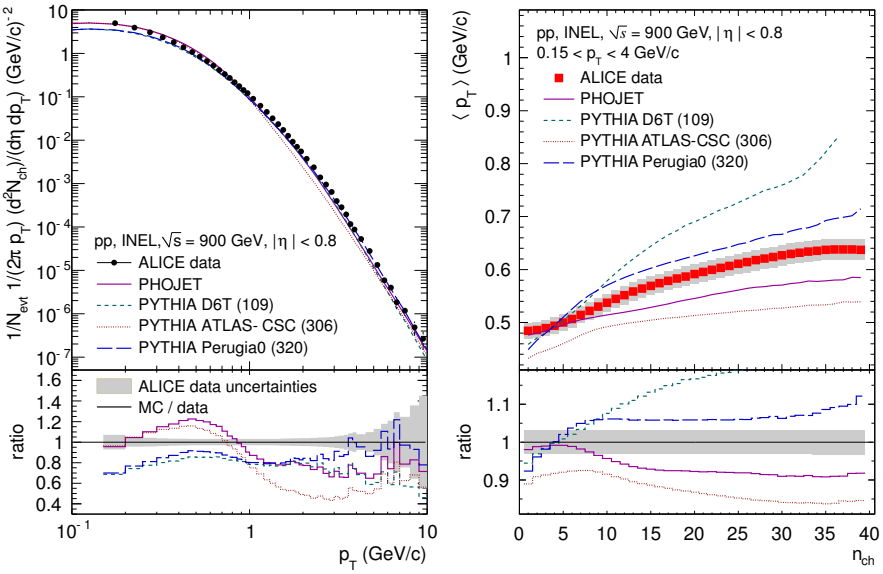

Figure 2: Left: primary charged particle $p_{\rm t}$-differential yield in INEL pp collisions at $\sqrt{s}$ = 900 GeV ($|\eta| < 0.8$), compared to results from PHOJET and PYTHIA tunes D6T [24], ATLAS-CSC [25] and Perugia-0 [22]. Right: The average transverse momentum of charged particles for $0.15 < p_T < 4$ GeV/c as a function of $n_{\rm ch}$, in comparison to models. The error bars and the shaded area indicate the statistical and systematic errors of the data, respectively. In the lower panels, the ratio Monte Carlo over data is shown. The shaded areas indicate the statistical and systematic uncertainty of the data, added in quadrature. Figures from [9].

below 3% for above 1 GeV/c [9]. The reconstruction efficiency and contamination, evaluated with the PYTHIA event generator, are converted to $p_{\rm t}$ dependent correction factors used to correct the raw $p_{\rm t}$ spectrum. For the normalization of the transverse momentum spectra to the number of events, multiplicity dependent correction factors are derived from the event selection and vertex reconstruction efficiencies for INEL and NSD events, evaluated with the PYTHIA event generator.

In Fig. 2 the results on $(1/2\pi p_{\rm t}){\rm d}^2N_{\rm ch}/{\rm d}\eta{\rm d}p_{\rm t}$ for INEL pp events at $\sqrt{s} = 0.9$ TeV [9] are shown and compared to PHOJET and different tunes of PYTHIA, D6T (tune 109), Perugia-0 (tune 320)and ATLAS-CSC (tune 306). The best agreement is found with the Perugia-0 tune, which gives a fair description of the spectral shape, but is approximately 20% below the data. The D6T tune is similar to Perugia-0 below 2 GeV/c but underestimates the data more significantly at high $p_{\rm t}$. PHOJET and the PYTHIA ATLAS-CSC tune fail to reproduce the spectral shape of the data. We note that PHOJET and ATLAS-CSC agree best with the charged particle multiplicity measurements at $\sqrt{s} = 0.9$ and 2.36, and 7 TeV, respectively (see Table 1).

The average transverse momentum $\langle p_{\rm t}\rangle$ (in the range $0.15 < p_{\rm t} < 4$ GeV/c) as a function of the acceptance and efficiency corrected multiplicity ($n_{\rm ch}$) is shown in the right-hand panel of Fig. 2 (see [9] for analysis details). A significant increase of $\langle p_{\rm t}\rangle$ with multiplicity is observed. Event generator curves are also shown and indicate that Perugia-0 and PHOJET are the closest to the data, however, none of the models gives a good description of the entire measurements.

The analysis of the transverse momentum spectra of charged particles at 7 TeV, currently ongoing, will allow to extend the $p_{\rm t}$ reach to about 50 GeV/c. Other $p_{\rm t}$ spectra analyses in progress include the identified charged hadrons (π, K, and p), using the PID capabilities of the ITS, TPC and TOF detectors, and the neutral mesons (π^0 and η), using photon pairs reconstructed via $\gamma \rightarrow e^+e^-$ conversions in the material as well as via the two ALICE electromagnetic calorimeters, PHOS and EMCAL.

5 Results on $\bar{\rm p}$/p ratio at $\sqrt{s} = 0.9$ and 7 TeV

The $\bar{\rm p}$/p ratio was measured in pp collisions at $\sqrt{s} = 0.9$ and 7 TeV in the ranges $|y| < 0.5$ and $0.45 < p_{\rm t} < 1$ GeV/c [10]. The physics motivation for this measurement is the study of the baryon transport mechanism over large rapidity intervals in high-energy proton–proton collisions. In inelastic non-diffractive proton-proton collisions at very high energy, the conserved baryon number associated with the beam particles is often called *baryon-number transport* and has been debated theoretically for some time (see references in [10]). This baryon-number transport is usually quantified in terms of the rapidity loss $\Delta y = y_{\rm beam} - y_{\rm baryon}$, where $y_{\rm beam}$ ($y_{\rm baryon}$) is the rapidity of the incoming beam (outgoing baryon). The LHC opens the possibility to investigate baryon transport over very large rapidity intervals ($\Delta y = 6.9$ and 8.9 at $\sqrt{s} = 0.9$ and 7 TeV, respectively) by measuring the antiproton-to-proton production ratio at midrapidity, $R = N_{\overline{\rm p}}/N_{\rm p}$. Most of the protons and antiprotons at midrapidity are created in baryon–antibaryon pair production, implying equal yields. Any excess of protons over antiprotons is therefore associated with the baryon-number transfer from the incoming beam. Model predictions for the ratio R at LHC energies range from unity, i.e. no baryon-number transfer to midrapidity, in models where the baryon-number transfer is suppressed exponentially with the rapidity interval Δy, down to about 0.9, in models where the baryon-number transfer does not depend on Δy.

For the analysis, the track selection described in Section 4 was used. Protons were identified using their ${\rm d}E/{\rm d}x$ signal in the TPC. In the restricted acceptance defined by $|y| < 0.5$ and $0.45 < p < 1.05$ GeV/c, the residual contamination from other hadrons and leptons is $< 0.1\%$. For the rejection of secondary protons from strange baryon decays, a $p_{\rm t}$-dependent impact parameter cut was used, specifically optimized for protons, which are detected with poorer resolution than pions. The residual secondary contamination was measured from the data, using the impact parameter distributions [10]. Since the aim of the analysis is a sensitivity on R of order 1%, special attention was placed on the evaluation of the acceptance and efficiency corrections, and in particular on the corrections for proton and antiproton elastic and inelastic (absorption) in the detector material. This was done comparing the cross sections for these processes in different particle transport models and with existing data [10].

The final $\bar{\rm p}$/p ratio R integrated within our rapidity and $p_{\rm t}$ acceptance rises from $R = 0.957 \pm 0.006(stat.) \pm 0.014(syst.)$ at $\sqrt{s} = 0.9$ TeV to $R = 0.991 \pm 0.005(stat.) \pm 0.014(syst.)$ at $\sqrt{s} = 7$ TeV [10]. The difference in the ratio, $0.034 \pm 0.008(stat.)$ is significant because the systematic errors at both energies are fully correlated. Within statistical errors, the measured ratio R shows no dependence on transverse momentum (see left panel of Fig. 3) or rapidity (data not shown). Our measurement is compatible with $R = 1$ at the highest LHC energy, thus excluding mechanisms that do not suppress the baryon-number transport over large Δy. Indeed, as seen in Fig. 3 (left), the models that implement these mechanisms, PYTHIA with Perugia-SOFT tune and HIJING/B, underpredict our result.

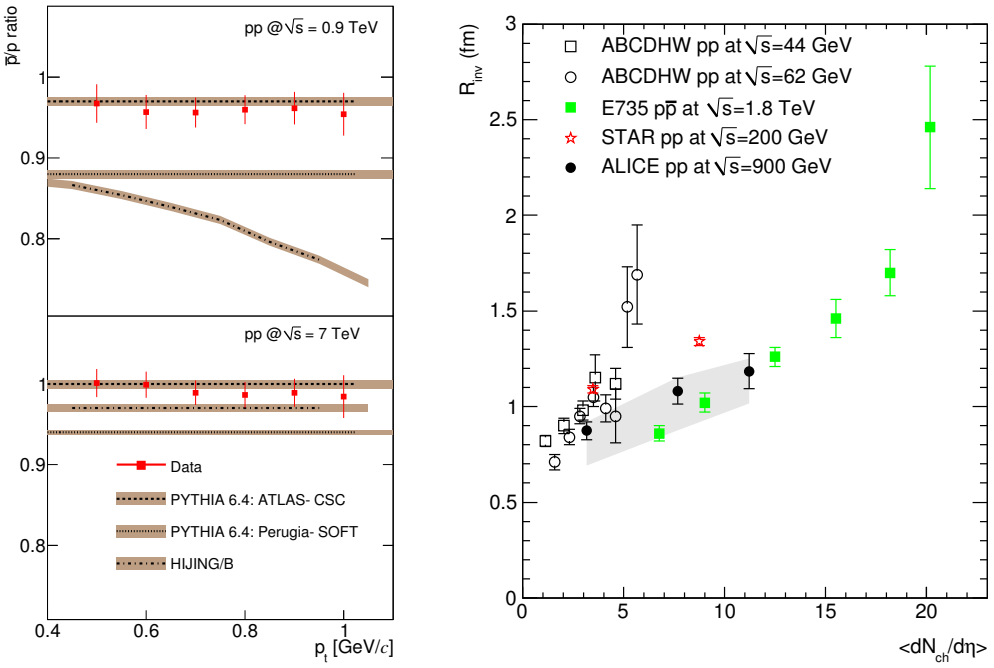

Figure 3: Left: $\bar{\mathrm{p}}/\mathrm{p}$ ratio as a function of p_{t} in $|y| < 0.5$ for pp at $\sqrt{s} = 0.9$ TeV (top) and 7 TeV (bottom) [10]. Only statistical errors are shown for the data; the width of the Monte Carlo bands indicates the statistical uncertainty of the simulation results. Right: Bose–Einstein correlation Gaussian radius, as a function of the charged-particle multiplicity at midrapidity (full dots), in pp at $\sqrt{s} = 0.9$ TeV [12]. The shaded band represents the systematic errors. For comparison, the data taken at the ISR, RHIC, and Tevatron, are shown (see references in [12]).

6 Results on Bose–Einstein correlations at $\sqrt{s} = 0.9$ TeV

Bose–Einstein enhancement of identical-pion pairs at low relative momentum allow to assess the spatial scale of the emitting source in e^+e^-, hadron–hadron, lepton–hadron, and heavy-ion collisions. Especially in the latter case, this technique, known as Hanbury Brown-Twiss (HBT) interferometry and being a special case of femtoscopy, has been developed into a precision tool to probe the dynamically-generated geometry of the emitting system. See [12] for more details and references. A systematic program of femtoscopic measurements in pp and heavy-ion collisions at the LHC will allow to investigate the nature, the similarities, and the differences of their dynamics. This program was started by measuring the two-pion correlations in pp collisions at $\sqrt{s} = 0.9$ TeV [12]. Pions tracks are reconstructed in the TPC and ITS (similar selection cuts as for the p_{t} spectrum analysis) and identified using the TPC $\mathrm{d}E/\mathrm{d}x$. The analysis of the correlation function (details in [12]) shows an increase of the extracted radius of the correlation volume with increasing event multiplicity, in line with other measurements done in particle and nuclear collisions, see Fig. 3 (right). Conversely, the strong decrease of the radius with increasing pair transverse momentum, as observed at RHIC and at Tevatron, is not manifest in our data (not shown here, see [12]).

7 Prospects for strangeness and charm production measurements at $\sqrt{s} = 7$ TeV

Several measurements of strange and heavy-flavour particle production are being prepared, using pp collision data at 0.9 and 7 TeV.

In particular, the following strange mesons and baryons are reconstructed topologically in ALICE: K^0_S, K^{*0}, ϕ, Λ, Ξ^-, Ω^-, Σ^{*-}. As examples, in the upper panels of Fig. 4, we show the signals for Λ at 0.9 TeV and Ω^- at 7 TeV.

Charm and beauty production measurements are in preparation using: at central rapidity, hadronic decays of D mesons ($D^0 \to K^-\pi^+$, $D^0 \to K^-\pi^+\pi^-\pi^+$, $D^{*+} \to D^0\pi^+$, $D^+ \to K^-\pi^+\pi^+$, $D_s^+ \to K^-K^+\pi^+$) and single electrons from D and B semi-electronic decays, identified in the TPC, TOF, Transition Radiation Detector (TRD) and EMCAL; at forward rapidity, single muons and di-muons from $c\bar{c}$ and $b\bar{b}$. Quarkonia will be reconstructed at central rapidity using di-electrons and at forward rapidity using di-muons. J/ψ signals are already well visible in the di-electron ($|y| < 1$) and di-muon ($-4 < y < -2.5$) invariant mass distributions for pp collisions at $\sqrt{s} = 7$ TeV. In the lower panels of Fig. 4, we show example signals for $D^0 \to K^-\pi^+$ and $J/\psi \to \mu^+\mu^-$ at 7 TeV.

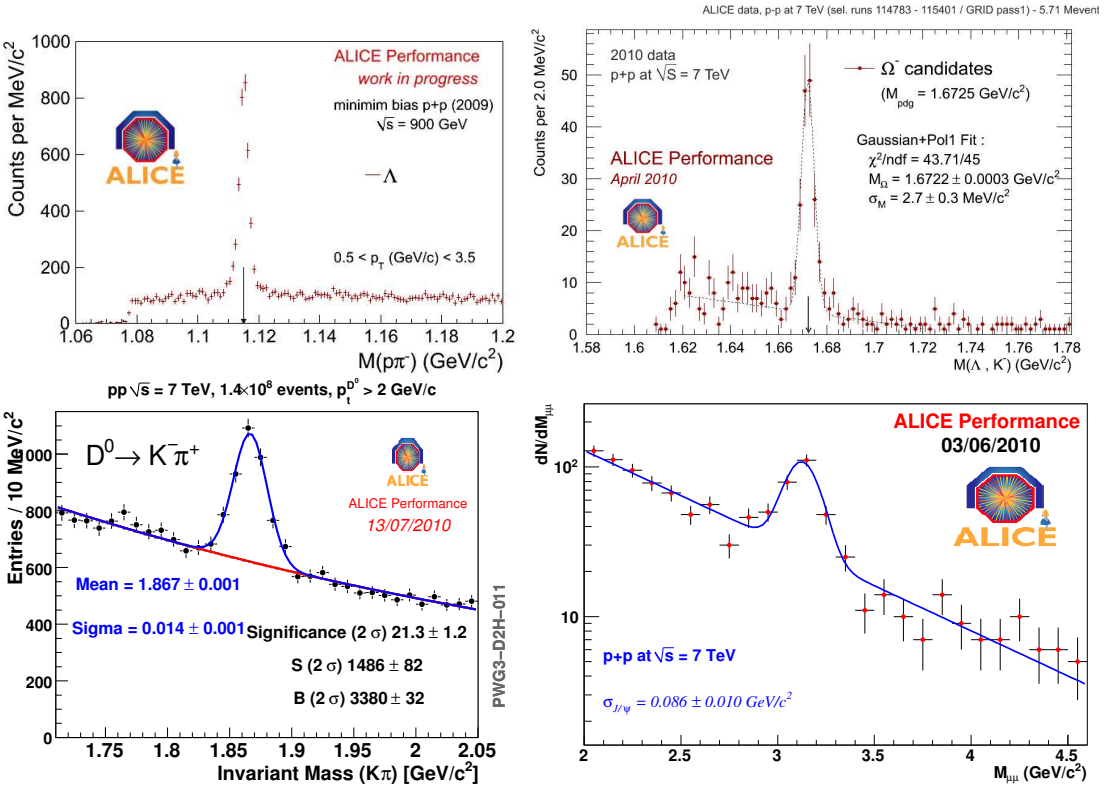

Figure 4: Example signals (invariant mass distributions) for $\Lambda \to p\pi^-$ at 0.9 TeV (top-left), $\Omega^- \to \Lambda K^-$ (top-right), $D^0 \to K^-\pi^+$ (bottom-left) and $J/\psi \to \mu^+\mu^-$ (bottom-right) at 7 TeV.

8 Summary

We have presented the first ALICE physics results for pp collisions at LHC:

- particle multiplicity at LHC increases with $\sqrt{s}$ energy significantly faster than predicted by all models;
- the mean transverse momentum evolution with event multiplicity at 0.9 TeV is not reproduced by any of the commonly used event generator tunes;
- the net baryon number at midrapity goes to unity at 7 TeV, implying that baryon number transfer over large rapidity intervals is suppressed;
- the Bose–Einstein femtoscopic measurement show that the size of the correlation volume for particle production increases with event multiplicity.

Many other analyses are ongoing, as we have shown with some examples on strangeness and charm production. ALICE has just started to deliver physics results and looks forward to the imminent LHC heavy-ion run [26].

References

[1] K. Aamodt *et al.* [ALICE coll.], J. Instrum **3** (2008) S08002.
[2] J. Schukraft [ALICE coll.], *these proceedings.*
[3] B. Alessandro *et al.* [ALICE coll.], J. Phys. G **32** (2006) 1295.
[4] F. Carminati *et al.* [ALICE coll.], J. Phys. G **30** (2004) 1517.
[5] K. Aamodt *et al.* [ALICE coll.], Eur. Phys. J. C **65** (2010) 111.
[6] K. Aamodt *et al.* [ALICE coll.], Eur. Phys. J. C **68** (2010) 89.
[7] K. Aamodt *et al.* [ALICE coll.], arXiv:1004.3514v1 (2010).
[8] P. Hristov [ALICE coll.], *these proceedings.*
[9] K. Aamodt *et al.* [ALICE coll.], arXiv:1007.0719v1 (2010).
[10] K. Aamodt *et al.* [ALICE coll.], arXiv:1006.5432v1 (2010).
[11] M. Broz [ALICE coll.], *these proceedings.*
[12] K. Aamodt *et al.* [ALICE coll.], arXiv:1007.0516v1 (2010).
[13] D. Miskowiec [ALICE coll.], *these proceedings.*
[14] A. Maire [ALICE coll.], *these proceedings.*
[15] K. Aamodt *et al.* [ALICE coll.], J. Instrum **5** (2010) P03003.
[16] M. Lunardon, *these proceedings.*
[17] J. Alme *et al.*, arXiv:1001.1950 (2010).
[18] M. Mager, *these proceedings.*
[19] G.J. Alner *et al.* [UA5 coll.], Z. Phys. C **33** (1986) 1.
[20] D. Caffarri [ALICE coll.], *these proceedings.*
[21] T. Sjöstrand, S. Mrenna, P. Skands, J. High Energy Phys. **2006** (2006) 05 026.
[22] P.Z. Skands, arXiv:0905.3418 (2009).
[23] R. Engel, J. Ranft, S. Roesler, Phys. Rev. D **52** (1995) 1459.
[24] M.G. Albrow *et al.*, arXiv:hep-ph/0610012 (2006).
[25] A. Moraes, ATLAS Note ATL-COM-PHYS-2009-119 (2009).
[26] H. Torii, *these proceedings.*

First CMS Results

Valerie Halyo for the CMS Collaboration

Department of Physics, Princeton University, Princeton, NJ 08544, USA

DOI: http://dx.doi.org/10.3204/DESY-PROC-2010-01/267

Already in 2006 with 25M muons accumulated during the Magnet Test and Cosmic Challenge with only a small fraction of the sub detector installed on the surface, CMS worked towards its first measurement of charge asymmetry of atmospheric muons that was published [8] once combined with the 270M muons accumulated during Cosmic Run at four Tesla (CRAFT) in 2008. This result was followed by the first CMS measurements of $\mathrm{dN/d}\eta$ $\mathrm{dN/d}p_T$ [3], the underlying event activity [5], two particle correlation [6], Bose-Einstein Correlations (BEC) [7], and the observation of diffractive events [4] presented in the talk. These first measurements were based on collision data taken during the successful startup at 2009 where LHC delivered about 15 μb^{-1}/ 1 μb^{-1}at collision energy of 0.9 TeV /2.36 TeV correspondingly and followed at 2010 with the first proton-proton collisions at center of mass energy at 7 TeV.

1 Introduction

The CMS experiment collected approximately 350 thousand collision events at an energy of $\sqrt{s} = 0.9$ TeV and 20 thousand events at $\sqrt{s} = 2.36$ TeV with good detector conditions and the magnet switched on at the nominal value of 3.8T. This corresponds to about 10 $\mu b^{-1}$of integrated luminosity and 0.4 μb^{-1}correspondingly. In 2010 CMS recorded the first proton proton collision at 7TeV delivered by LHC. At the time of the presentation CMS recorded about 20 n$b^{-1}$and in the eight weeks to follow LHC will deliver another 3.6 pb^{-1}. The recorded data sample is smaller than needed to do the physics studies for which CMS was designed. However, it is sufficient to assess the general quality and the proper functioning of the detector, the algorithms modeling of the detector response in the simulation and the properties of the inelastic events based on the first CMS measurement which are the primary focus of my presentation. These first measurements can be categorized into two classes consisting the primary ingredients necessary to understand inelastic collisions before proceeding to do higher level measurements. The first class of measurements [3]-[5] shed light on the understanding of the single particle properties that is essential to understand the mechanism for hadron production and the relative role of soft and hard contribution at the highest collision energy. The basic properties of charged tracks such as charged hadron multiplicities vs transverse momentum or pseudorapidity, the study of the underlying event activity and the observation diffractive process were presented. These measurements are also base line for HI physics and future measurements with pile up. The second class of measurements [6]-[7] done by CMS provides higher understanding of the correlations between the single particles leading to two studies, the two particle correlation and BEC. These measurements are also base line for Heavy Ion (HI) physics where the correlation will depend on the centrality of the event. These two fundamental categories are essential for

conforming that we understand our detector and improve our current understanding of the inelastic processes. Section 2 briefly presents the performance of the tracker, which is most relevant for the first measurements. Section 3 describes the common selection criteria for these measurements and subsection 4.1-4.5 presents briefly each of the first results presented in the talk. Section 5 draws the conclusions from the first CMS measurements [3]-[7] and summarize CMS near future plans.

2 CMS Tracker Performance

Excellent performance of the CMS silicon tracker and tracking algorithms [1] was a crucial ingredient for the first CMS measurements. Both the resolution of the primary vertices and the use of the dE/dx for particle identification were essential for the first CMS measurements and were described briefly in the talk. Beam spot and primary vertices are reconstructed with high efficiency and resolution close to the expectation from simulation. The primary vertex resolution was found to depend strongly on the number of tracks used in fitting of the vertex and the pT of those tracks. This results indicated that for momentum range and number of tracks used in these measurement we were able to reach a primary vertex resolution of about 100 μm with only few tracks, helping us to efficiently select the events. The other advantage provided by the tracker is the excellent particle identification with dE/dx used by BEC measurement [7]. Figure 1 shows the distribution of dE/dx versus momentum for particle-calibrated data. The bands departing toward high dE/dx values at low momentum are attributed to kaon, proton and deuteron tracks, respectively. The fit to the proton band restricted to the range [0.7, 1.0] GeV/c is shown as a red curve in Fig. 1, while the black curves show agreement with the fit results extracted from the proton fit results. The mass spectrum resulting by inverting the dEdx equation used the dE/dx data for tracks with dE/dx $>$ 4.15 MeV/cm and p $<$ 2 GeV/c is shown in Fig. 2. The known values of the kaon and proton masses are also indicated as vertical lines on the plot. We observe an additional peak in data which is not visible in simulation, and we attribute it to deuterons This essential particle identification tool was already prooven to be useful in one of the first measurements and is planned to be used as one of the main handles for the search for new charged long-lived particles.

3 Event Selection Common to First Measurements

Common Min Bias event selection criteria were used in most of the first CMS measurements [3]-[7]. Online, events were selected by a trigger signal in any of the Beam Scintillator Counters (BSC) scintillators, coinciding with a signal from either of the two Beam Pickups Timing eXperiment (BPTX) detectors indicating the presence of at least one proton bunch crossing the IP. From these samples, collision events were selected offline by requiring BPTX signals from both beams passing the IP, Forward Hadronic (HF) Calorimeter energy larger than 3GeV on both sides of the HF (HF $2.9 < |\eta| < 5.2$) and an analysis dependent collision vertex requirement. In addition, beam-halo muons events identified by requiring the time difference between any two hits from the BSC stations on opposite sides of the IP to be within 73 ± 20 ns were removed from the data sample. Last but not least dedicate beam background events such beam-scraping/gas events were removed from the data sample.

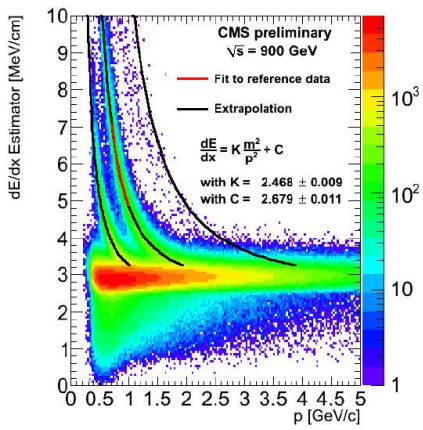

Figure 1: dE/dx versus p in data collected at 900 GeV during December 2009. red line: fit with proton mass assumption, in a restricted p range; black lines:extrapolations.

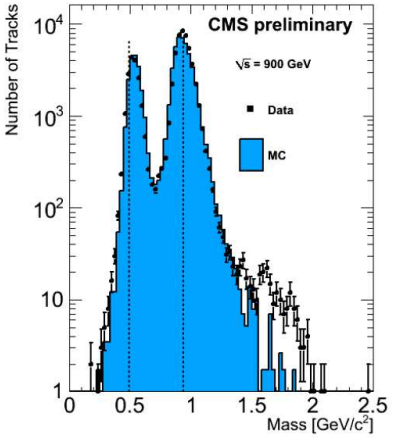

Figure 2: Mass distribution, using tracks with p < 2 GeV/c and dE/dx > 4.15 MeV/cm for 900 GeV data (dots with error bars) and simulation (solid).

4 First CMS Results

In the following a brief description of each of the first CMS results will be presented starting with the first class of measurements that aims to shed light on the understanding of the single particle properties essential to understand the mechanism for hadron production and the relative role of soft and hard contribution at the highest collision energy. The measurements belonging to this category are the transverse-momentum and pseudo-rapidity distributions of charged Hadrons at 7TeV [3], the Underlying Event Activity at 0.9TeV [5] and the observation of diffraction at 0.9TeV and 2.36TGeV [4]. The second class of measurements described in the following provides better understanding of the correlations between the single particles. The measurements in this class are the two particle correlation [6] and BEC [7].

4.1 Transverse-Momentum and Pseudorapidity Distributions of Charged Hadrons

Good understanding of the tracker performance allowed a timely publication of the first physics measurement from the first collisions data at 0.9TeV and 2.36TeV in 2009 [2] followed up with results at 7TeV from 2010 [3] collision data. In my talk I presented the measurement of the inclusive charged-hadron transverse-momentum and pseudo-rapidity distributions in proton-proton collisions at $\sqrt{s} = 7$TeV, which is the highest collision energy achieved at a particle collider to date. Measurements of $dN_{\rm ch}/dp_T$ and $dN_{\rm ch}/d\eta$ distributions and their $\sqrt{s}$ dependence are important for understanding the mechanisms of hadron production and the relative roles of soft and hard scattering contributions in the LHC energy regime. Three different methods with different sensitivity to potential systematic effects were combined in this measurement: pixel cluster counting, pixel tracklets, and full track reconstruction. The cluster counting method

correlates the observed pixel-cluster length in the z direction, expressed in number of pixels, with the expected path length traveled by a primary particle at a given η value. Background due to loopers, secondary particles and daughters of long-lived hadrons was removed. The pixel tracklets are constructed from combinations of two pixel hits in any two pixel barrel layers. The contribution from secondary particles, reconstruction efficiency and geometrical acceptance was evaluated using the PYTHIA simulations. The third method used both the pixel and the silicon strip tracker (SST) detectors to reconstruct tracks, including both barrel and endcap layers. The acceptance was limited to $|\eta| < 2.4$ to avoid edge effects. The measured yield in data was corrected, based on MC simulation and comparisons with data, for geometrical acceptance (2% correction for pT $>$ 200 MeV/c), efficiency of the reconstruction algorithm (5$-$10% for pT $>$ 300 MeV/c), fake and duplicate tracks ($<$ 1% each). The contamination of less than 2% from decay products of long-lived hadrons, photon conversions and inelastic hadronic interactions with the detector material was also subtracted. To obtain the $dN_{\rm ch}/d\eta$ result from the $p_{\rm T}$ spectrum, an extrapolation to pT = 0 was necessary, resulting in an increase of 5% in the estimated number of charged hadrons. Tracks with $|\eta| < 2.4$ and $p_T > 0.1$ GeV/c were used for the measurement of $1/(2\pi p_T) d^2N_{\rm ch}/d\eta dp_T$ as shown in Fig. 3

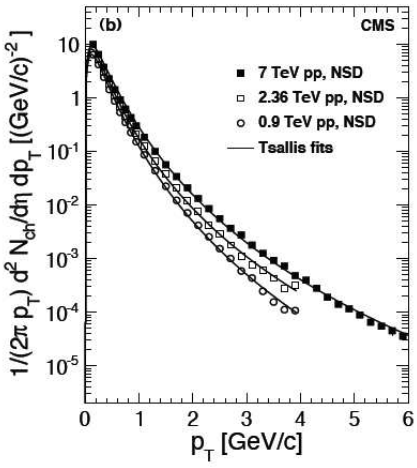

Figure 3: Measured yield of charged hadrons for $|\eta| < 2.4$ with systematic uncertainties (symbols) at 0.9, 2.36 and 7 TeV collision energy, fit with the empirical Tsallis function

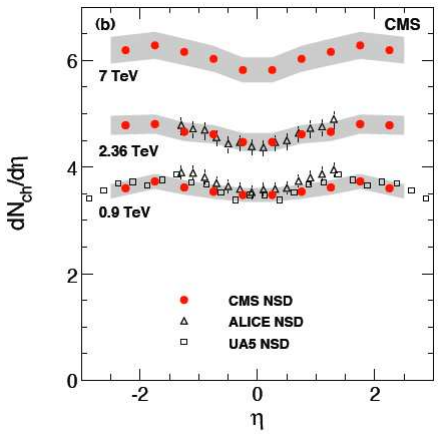

Figure 4: Reconstructed $dN_{\rm ch}/d\eta$distributions averaged over the cluster counting, tracklet and tracking methods, compared to data from the UA5 [10] (open squares) and from the ALICE [9] (opentriangles) experiments at 0.9 TeV.

The yield of charged-hadron in non-single-diffractive (NSD) events as a function of p_T was fitted by the Tsallis function which empirically describes both the low-pT exponential behavior corresponding to the beam beam remnant and the high-pT power-law behavior corresponding to the hard parton-parton collision. For the 7 TeV data, the average transverse momentum, calculated from the measured data points adding the low - and high-pT extrapolations from the fit is $\langle p_{\rm T} \rangle = 0.545 \pm 0.005$ (stat.) $\pm$ 0.015 (syst.) GeV/c. GeV/c. In addition, the measured yield

of charged hadrons at different collision energy as seen in Fig. 3 shows that the p_T spectrum gets harder at higher collision energy which is consistent with the increasing hadronic activity. The $dN_{\rm ch}/d\eta$ distribution was calculated as the weighted average of the data from the three reconstruction methods, taking into account their systematic uncertainties, and symmetrized in pseudorapidity. The averaged result is shown in Fig. 4 and is compared to measurements at the same accelerator (ALICE, [9]) and to previous measurements at the same energy but with different colliding particles (UA5, [10]). The shaded error band on the CMS data and the error bars for the data from ALICE indicates systematic uncertainties, while the error bars on the data from UA5 display statistical uncertainties only. No significant difference is observed between the $dN_{\rm ch}/d\eta$ distributions measured in pp and $p\overline{p}$ collisions at $\sqrt{s} = 0.9$ TeV. The $dN_{\rm ch}/d\eta$ distribution is found weakly eta-dependent, with a slow increase towards higher η values, and an indication of a decrease at $|\eta| > 2$. In the central region $|\eta| < 0.5$, the pseudorapidity density, $dN_{\rm ch}/d\eta$, has been measured to be 5.78 ± 0.01(stat.) $\pm$ 0.23(syst.) for non-single-diffractive events, higher than predicted by commonly used models. The relative increase in charged-particle multiplicity from $\sqrt{s} = 0.9$ to 7 TeV is 66.1% +/- 1.0% (stat) +/- 4.2% (syst). With the new measurement [3] at 7 TeV the study of particle production in pp collisions has been extended into a new energy regime.

4.2 Observation of diffraction in proton-proton collisions at 0.9 and 2.36TeV centre-of-mass energies

One of the systematics uncertainties in the measurement of inclusive charged-hadron transverse-momentum and pseudorapidity distributions for non-single-diffractive interactions [3] is the fraction of single diffractive to non diffractive events. Hence observation of single diffractive events is essential to properly describe these events in simulations. First observation of diffractive signal [4] dominated by the inclusive single diffractive (SD) reaction $pp \rightarrow Xp$ was based on 10 $\mu b^{-1}$of data collected at 0.9TeV and 0.4 μb^{-1}at 2.36TeV. Diffractive events can be described in terms of a colorless exchange with the vacuum quantum numbers (the "pomeron") and notably no color. Despite the substantial progress in the understanding of hard-diffractive events, in which a hard scale is present, in the framework of QCD (see e.g. [11]). the quantitative description of soft-diffraction still largely relies on Regge theory. The observed energy dependence of the inclusive single-diffractive cross section is however weaker than that expected by Regge theory, leading to an effect that is sometimes quantified in terms of the "rapidity gap survival probability". The acceptance of SD is high at LHC. The selection efficiency for SD events however, is model dependent and yields in about 20% according to PYTHIA and about 35% according to PHOJET; for non-diffractive (ND) events it is about 85% for both generators. In Fig. 5 we can find the distribution of the events as a function of $E \pm p_z = \sum i(E_i p_{z,i})$, where the sum runs over all calorimeter towers ($\eta < 5$). This variable would be proportional to the fractional energy loss of the scattered proton if the direction of the proton emitting the pomeron was known. The distributions are uncorrected. The bands illustrate the effect of a 10% energy scale uncertainty in the calorimeters and should be taken as a rough estimate of the systematic uncertainty due to the current imperfect understanding and simulation of the detector. At both energies, a clear diffractive contribution is evident. The data are compared with the predictions of PYTHIA (tune D6T) and PHOJET. The agreement is reasonable, with PYTHIA describing the ND part of the data better than PHOJET. To enhance the diffractive component in the data, a cut was applied to the HF energy sum. As an example, Fig. 5 shows the $E + p_z$, distributions for events in which the energy sum in HF- was $E_{HF-} < 8$ GeV (900

GeV data). This cut mainly selects single-diffractive events with a large rapidity gap (LRG) over HF- The system X is thus boosted towards the positive z direction. The data comparison to PYTHIA6 and PHOJET shows again that PYTHIA6 gives a better description of the non-diffractive component of the data, while PHOJET reproduces the diffractive contribution more accurately,

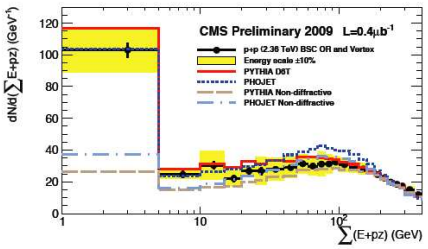

Figure 5: Distributions of the accepted events as a function of $E + pz$, 2360 GeV. The predictions of PYTHIA and PHOJET are also shown, normalised to the data. The distributions are uncorrected. The vertical bars indicate the statistical uncertainty of the data. The bands illustrate the effect of a 10% energy scale uncertainty in the calorimeters..

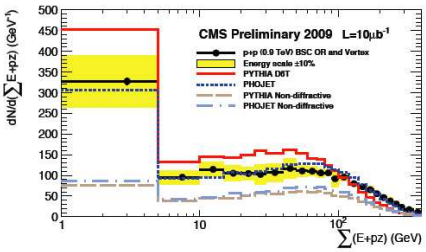

Figure 6: Distributions of $E + pz$ after the requirement of $E_{HF-} < 8$ GeV for the 900 GeV data. The distributions are uncorrected. The vertical bars indicate the statistical uncertainty of the data. The bands illustrate the effect of a 10% energy scale uncertainty in the calorimeters. The data are compared to both PYTHIA and PHOJET, normalised to the data

4.3 The Underlying Event Activity in Proton-Proton Collisions at 900 GeV

In parallel to the observation [4] of diffractive events dominated by the inclusive single diffractive CMS studied the underlying event activity [5] based on collision data at 900GeV. In the presence of a hard process the hadronic final states of hadron-hadron interactions can be described as the superposition of several contributions: products of the 2-to-2 hard parton scattering, including initial and final state radiation; hadron production in additional "multiple parton interactions"(MPI); and "beam-beam remnants" (BBR), resulting from the hadronization of the beam partonic constituents which did not participate in the hard scatter. Products of the MPI processes, which are mostly "soft", and BBR form the "underlying event" (UE). A good description of UE properties is crucial for precision measurements of Standard Model processes and for the search of physics beyond the Standard Model at the Large Hadron Collider(LHC) [12]. Predictions of several QCD models, after full detector simulation, were compared to the uncorrected data. Three distinct topological regions in the hadronic final state are thus defined in the plane transverse to the beam direction, using the angle difference, $\Delta\phi$, between the direction of the leading object and that of any charged hadron in the event. Hadron production in the "toward" region with $|\Delta\phi| < 60$ and in the "away" region with $|\Delta\phi| > 120$ is expected to be dominated by the hard parton-parton scattering and radiation. In contrast, the UE structure can be best studied in the "transverse" region with $60 < |\Delta\phi| < 120$. The analyses are performed by selecting events with a minimum value of the p_T of the leading object, which is either

a track or a track jet with $|\eta| < 2$. Requiring $p_T > 1$ GeV/c gets rid of most of the diffractive component of the collision, which sets the minimal scale for the studies. In Fig. 7 we find the average multiplicity per unit pseudorapidity for all tracks with $p_T > 0.5$ GeV. Here, the track selection is extended to $|\eta| = 2.5$. The multiplicities of particles with $p_T > 0.5$ GeV/c increase significantly with the scale fixed by the leading jet p_T. The various PYTHIA tunes describe within 10 % - 15% the overall features of the data: normalisation, η dependence and effect of the p_T cut on the leading jet. However, no description is really good, neither in normalization nor in shape. For both jet p_T cuts, the data show a significantly stronger η dependence than predicted by the PYTHIA models, although the shape description is slightly better with tunes P0 and Pro-Q20. Tune CW is too high in normalization, whereas tunes D6T, P0 and ProQ20 are generally too low, with DW being too low in the central region and too high at large $|\eta|$ values. The fact that the models underestimate activity at the lower scale it is not a surprise as the contamination from diffraction events is not well accounted in pythia. The CW tune was the last quick attempt to adjust the MPI level but overshot by a bit suggesting the correct tune is within reach.

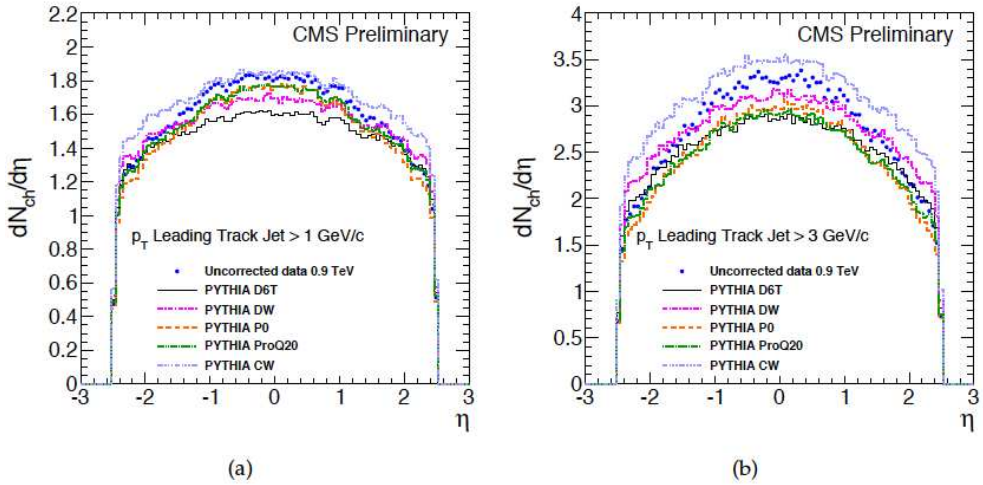

Figure 7: Average multiplicity, per unit of pseudorapidity, of charged particles with $pT > 0.5$ GeV/c, as a function of η. The leading track jet is required to have $|\eta| < 2$ and (a) $pT > 1$ GeV/c; (b) > 3 GeV/c (note the different vertical scales). Predictions from several PYTHIA MC tunes are compared to the uncorrected data.

In Fig. 8 one finds the charged particle density in transverse region versus event p_T scale. The turn on curve is correlated with the centrality of the collision, reaching head on collision at 4 GeV. The slow increase in multiplicity is related to the increase in MPI. Once again one finds that DW and CW predictions embrace the data. Similar results were seen for the multiplicity of charged particles, the sum p_T distribution and the p_T distribution of charged hadrons in the the transverse region. To summarize we find that for the 900 GeV the predictions were about 10% lower than expected however they can be tuned easily to agree with the 900GeV , 7TeV and Tevatron collision data. (see X1(Rick Field, TuneAMBT1 from Atlas.). In addition, the measurements exhibit a preference for higher values of the energy dependence, i.e. $\epsilon = 0.25$

(as in tune DW) or 0.30 (as in tune CW) and over $\epsilon = 0.16$ (original Atlas tune). Lower values of 0.16 as in tune D6T are disfavored. The analysis on 7 TeV data as well as corrections for detector effects are ongoing while in parallel an investigation of the UE with a new jet area/median approach is in progress. The goal is to produce corrected data for all center of mass and to test the UE modeling is universal: for example using Z bosons.

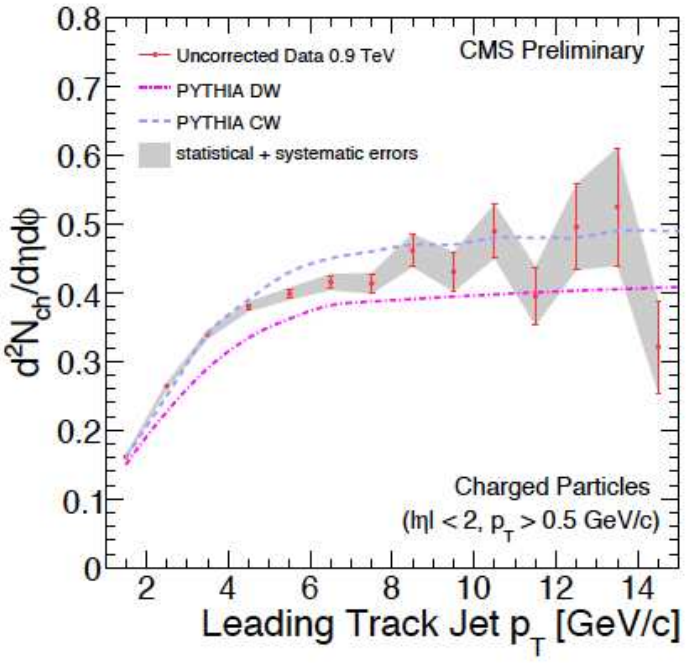

Figure 8: Average multiplicity per unit of pseudorapidity and per radian as a function of the scale provided by the pT of the leading track jet for charged particles in the transverse region, with $pT > 0.5$ GeV/c and $|\eta| < 2$. The error bars indicate the systematic error; the shaded bands correspond to the total experimental error (statistical and systematic errors added in quadrature). Predictions of the CW and DW PYTHIA MC tunes are compared to the uncorrected data.

4.4 Two-Particle Angular Correlations and Cluster Properties in pp Collisions at $\sqrt{s} = 0.9$, 2.36 and 7 TeV

Inclusive two particle correlation [6] was observed in PHOBOS [13] and UA5 [14] and exhibit an approximate Gaussian shape in the relative pseudo rapidity of between any two track with a range of $\sigma_{\Delta\eta} \approx 1$unit. Thus, these correlations have been conventionally described as "short-range". In the case of inclusive correlations, a useful ansatz is to assume that the initial interactions emit so-called "clusters". These clusters are assumed to be emitted independently (ICM) and then to subsequently decay isotropically in their own rest frame into the observed hadrons. Heavier clusters, which would emit more particles, correspond to stronger correla-

tions. This simple cluster description can, therefore, be used to quantitatively characterize this important aspect of particle production for a variety of systems and energies [15]. The observed correlation strength and extent in relative pseudorapidity between the particles are parameterized by a Gaussian distribution. The fitted parameters are the cluster multiplicity, or "size" (the average number of particles into which a cluster decays) and the decay "width" (the separation of the emitted particles in pseudorapidity). In order to measure , the pT-inclusive charged two-particle correlation function in two-particle ($\Delta\eta$,$\Delta\phi$) space, the following quantity was defined in Eq. 1.

$$R(\Delta\eta, \Delta\phi) = \left\langle (N-1)\left(\frac{S_N(\Delta\eta, \Delta\phi)}{B_N(\Delta\eta, \Delta\phi)} - 1\right)\right\rangle_N \quad (1)$$

where N represents the total track multiplicity of each event. The sample was divided into 10 bins in track multiplicity (N), each containing about 10% of all the events. At a fixed multiplicity bin, the signal distribution is the charged two-particle pair density function (normalized to unit integral). It is determined by taking particle pairs within the same event, then averaging over all events. The background distribution denotes the distribution of uncorrelated particle pairs (normalized to unit integral). It is constructed by randomly selecting two different events from the same multiplicity bin and pairing every particle from one event with the other event, representing a product of two single particle distributions. The ratio of the signal to background distribution was first calculated in each multiplicity bin. In this way, all the detector inefficiencies (e.g. tracking, non-uniform acceptance) were canceled. It is then weighted by the track multiplicity factor, $N-1$ (average multiplicity in each bin), and averaged over all the multiplicity bins to arrive at the final two-particle correlation function $R(\Delta\eta, \Delta\phi)$ 1.

$R(\Delta\eta, \Delta\phi)$ at different center of mass energy exhibit the following features: Gaussian-like shape in $\Delta\eta$ and broader at larger $\Delta\phi$. In addition, the near-side peak (small $\Delta\eta$ and $\Delta\phi$) seems enhanced at higher energy. To quantify the clustering properties with data the 2D RN distribution is projected onto relative pseudorapidity plane allowing to measure the size and with of the cluster. The results for the different center of mass energy collision data show that on average, every 2-3 charged particles are produced in a correlated fashion like a cluster. We also find the size of the cluster increasing due to higher p_T objects in the event while the width of the cluster is independent of the center of mass energy. Pythia describes well the trend as a function of the center of mass energy but under estimate the size of the cluster. It could be since Pythia does not describe well the contamination from diffraction events. Last we found by separating the near and away-side correlations that the size of the cluster increase only in the near side. This can be understood in the context of hard and soft processes in QCD. With increasing collision energy contributions from the the hard process are expected to increase and will primarily contribute to the near side where the objects are boosted.

4.5 Measurement of Bose-Einstein correlations in 0.9 and 2.36 TeV proton-proton Collisions with the CMS Experiment

Space time structure of particle emission can be studied via measurements of Bose-Einstein correlations (BEC) between identical bosons. BEC effects are made manifest by the enhanced emission of boson pairs with small relative momenta. Fourier transform of the emission region is essentially the only way to measure the size of a source at the Fermi scale. First observation of BEC occurred fifty years ago in proton-antiproton interactions [16], a number of measurements

have been produced by several experiments using different initial states [17]-[26]. Theoretically, we need to study the ratio between the joint probability of emission of a pair of bosons, and the individual probabilities. Experimentally, we have to produce the distributions of a "proximity" quantity in the data and in a reference sample (Coulomb corrected). To measure the proximity between 2 particles, we chose the difference of their 4-momentum (assuming all pions). To calculate the ratio $R = \frac{dN/dQ}{dN/dQ_{ref}}$ one should take all (charged) tracks to construct a quantity Q and repeat its calculation for the reference sample. Evidence for the effect can be seen in Fig. 9 , where we find the ratios R of the distributions of the invariant mass Q for same-charge particles and a reference sample with the same charge pairs, where one of the two particles has its three-momentum inverted (opposite hemispheres). The ratios for the MC samples with

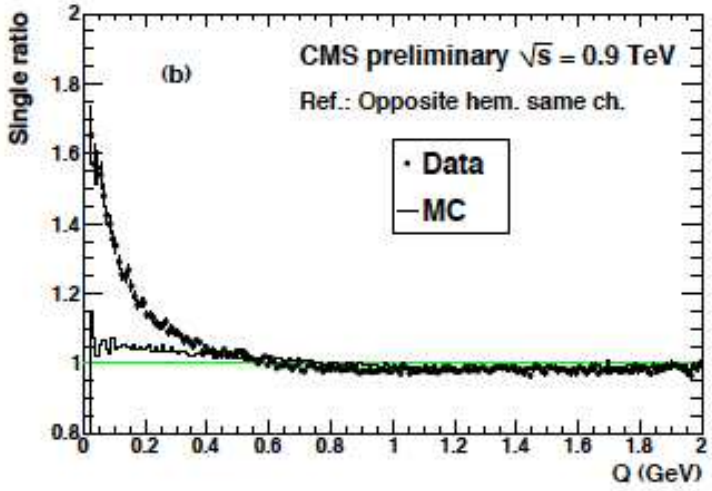

Figure 9: Ratios R of the distributions of the invariant mass Q for same-charge particles and a reference samples of same charge pairs, where one of the two particles has its three-momentum inverted (opposite hemispheres). The ratios for the MC samples with no BEC effect simulated are also shown. Lines at R = 1 are also shown in both figures.

no BEC effect simulated are also shown. To reduce the bias due to the construction of the reference samples, a double ratio $\mathcal{R}$ was defined as in Eq. 2

$$\mathcal{R} = R/R_{\mathrm{MC}} = \left(\frac{\mathrm{d}N/\mathrm{d}Q}{\mathrm{d}N/\mathrm{d}Q_{\mathrm{ref}}}\right) / \left(\frac{\mathrm{d}N/\mathrm{d}Q_{\mathrm{MC}}}{\mathrm{d}N/\mathrm{d}Q_{\mathrm{MC,ref}}}\right), \tag{2}$$

where Q_{MC} and $Q_{\mathrm{MC,ref}}$ refer to the Q distributions from the default simulation, which does not include a modeling of Bose–Einstein correlations. To perform the fit of the double-ratio spectra, the following parameterization given in Eq. 3 of R was used .

$$R(Q) = C\,[1 + \lambda\Omega(Qr)] \cdot (1 + \delta Q). \tag{3}$$

Where λ measures the strength of BEC for incoherent boson emission from independent sources, δ accounts for long-distance correlations, and C is a normalization factor. In a static

model of particle emission, the $\Omega(Qr)$ function is the Fourier transform of the emission region, whose effective size is measured by r. We found phenomenological parameterizations with an exponential shape fit the data significantly better than with a Gaussian shape. One of the subtlety is that an ideal control sample can not be constructed since we could not simply make a sample with a perfect description of the Q distribution in the absence of BEC. Therefore 7 reference samples were constructed however since none of them can be preferred or discarded a priori. Hence a systematic uncertainty is computed as the r.m.s. spread between the results obtained using the different reference samples, i.e. $\pm 7\%$ for λ and $\pm 12\%$ for r. The uncertainty related to the Coulomb corrections was determined with the opposite-charge sample, the predicted strength of the Coulomb effect being compatible with the data within $\pm 15\%$. The corresponding changes are 0.8% for r and 2.8% for λ, which are used as systematic errors. Using the combined reference sample the BEC parameters are thus measured as: $r = 1.59 \pm 0.05$(stat.) ± 0.19 (syst.) fm and $\lambda = 0.625 \pm 0.021$(stat.)$\pm 0.046$ (syst.), for 0.9 TeV data; $r = 1.99 \pm 0.18$ (stat.) ± 0.24 (syst.) fm and $\lambda = 0.663 \pm 0.073$ (stat.)± 0.048(syst.), for 2.36 TeV data. Last but not least, an increase of the parameter r with charged-particle multiplicity in the event is observed.

5 Conclusions

The CMS collaboration completed at the time of the talk its first 5 physics measurements [3]-[7] based on proton-proton collisions delivered by the LHC during 2009 and 2010 at 0.9TeV, 2.36TeV and 7TeV center of mass energy. These measurements helped shed light on on the understanding of the single particle properties and the correlation between the single particles that is essential to understand the mechanism for hadron production and the inelastic process at the highest collision energy. The performance of the detector at start-up was outstanding in particular the excellent performance of the CMS tracker essential for the first CMS measurement was demonstrated. Various other physics analyses are in progress. In addition, a preview of the up coming plans once few p$b^{-1}$of data is recorded reveal promising prospects from the CMS physics analysis groups. In particular, the B-physics finds it feasible to measure Jpsi and Upsilon di-muon decay production cross section differential in p_T and possibly in rapidity. The electroweak analysis group finds it feasible to measure the W and Z cross sections and the cross section ratio of W^+/W^- and W/Z. The first CMS results indicate that CMS can produce high quality physics measurements quickly and new exciting results will be available once more collision data is recorded at 7 TeV.

6 Acknowledgments

I would like to thank the organizers for a very pleasant conference for the many interesting talks stimulating discussions. I thank my CMS colleagues for preparing the results presented in this report,and in particular G. Tonelli, G. Rolandi, D. Acosta, A. De Roeck, R. Tenchini, B. Klima, M. Arneodo, K. Burkett, R. Field, H. Jung, W. Li, M. Mulders, K. Rabbertz and G. Veres for their helpful discussions and suggestions while preparing the talk. On behalf of CMS I also wish to congratulate our colleagues in the CERN accelerator departments for the excellent performance of the LHC machine, thank the technical and administrative staff at CERN and other CMS institutes, and acknowledge support from: FMSR (Austria); FNRS and FWO (Belgium); CNPq, CAPES, FAPERJ, and FAPESP (Brazil); MES (Bulgaria); CERN;CAS, MoST,

and NSFC (China); COLCIENCIAS (Colombia); MSES (Croatia); RPF (Cyprus);Academy of Sciences and NICPB (Estonia); Academy of Finland, ME, and HIP (Finland); CEAand CNRS/IN2P3 (France); BMBF, DFG, and HGF (Germany); GSRT (Greece); OTKA and NKTH (Hungary); DAE and DST (India); IPM (Iran); SFI (Ireland); INFN (Italy); NRF andWCU (Korea); LAS (Lithuania); CINVESTAV, CONACYT, SEP, and UASLP-FAI (Mexico);PAEC (Pakistan); SCSR (Poland); FCT (Portugal); JINR (Armenia, Belarus, Georgia, Ukraine,Uzbekistan); MST and MAE (Russia); MSTDS (Serbia); MICINN and CPAN (Spain); SwissFunding Agencies (Switzerland); NSC (Taipei); TUBITAK and TAEK (Turkey); STFC (UnitedKingdom); DOE and NSF (USA).

References

[1] The CMS Collaboration, CMS Physics Analysis Summary, TRK-10-001 (2010).

[2] The CMS Collaboration, CMS Physics Analysis Summary, QCD-09-010 (2010). JHEP 02 (2010) 041

[3] The CMS Collaboration, CMS Physics Analysis Summary, QCD-10-006 (2010). Phys.Rev.Lett. 105.022002

[4] The CMS Collaboration, CMS Physics Analysis Summary, FWD-10-001 (2010).

[5] The CMS Collaboration, CMS Physics Analysis Summary, QCD-10-001 (2010).

[6] The CMS Collaboration, CMS Physics Analysis Summary, QCD-10-002 (2010).

[7] The CMS Collaboration, CMS Physics Analysis Summary, QCD-10-003 (2010).

[8] The CMS Collaboration, CMS Physics Analysis Summary, MUO-10-00 (2010). Phys.Lett.B692:83-104,2010

[9] K. Aamodt et al.,"Charged-particle multiplicity measurement in proton-proton collisions at sqrt(s) = 0.9 and 2.36 TeV with ALICE at LHC", Eur.Phys.J.C68:89-108,2010

[10] UA5 Collaboration,"Scaling of pseudorapidity distributions at c.m. energies up", Z. Phys. C33 (1986) 1.

[11] V. Barone and E. Predazzi, High-energy particle diffraction, Springer, 2002

[12] O. S. Bruning, P. Collier, P. Lebrun et al.,"LHC Design Report" CERN, Geneva, 2004

[13] PHOBOS:Phys. Rev. C75, 054913 (2007),Phys. Rev. C81, 024904 (2010) (heavy ion)

[14] UA5: Phys.Lett.B123:361,1983

[15] UA5 Collaboration,"CHARGED PARTICLE CORRELATIONS IN ANTI-P P COLLISIONS AT C.M. ENERGIES OF 200-GEV, 546-GEV AND 900-GEV"Z. Phys. C37 1988

[16] G. Goldhaber et al., Phys. Rev. 120 (1960) 300.

[17] MARKII Collaboration, Phys. Rev. D39 (1989) 1.

[18] TASSO Collaboration, Z. Phys. C30 (1986) 355.

[19] Collaboration, Eur. Phys. J. C36 (2004) 147.

[20] DELPHI Collaboration, Phys. Lett. B286 (1992) 201.

[21] L3 Collaboration, Phys. Lett. B524 (2002) 55.

[22] OPAL Collaboration, Phys. Lett. B559 (2003) 131.

[23] UA1 Collaboration, Phys. Lett. B226 (1989) 410.

[24] NA27 Collaboration, Z. Phys. C54 (1992) 21.

[25] NA22 Collaboration, Z. Phys. C37 (1988) 347.

[26] ZEUS Collaboration, Acta Phys. Polon. B33 (2002) 3281

Physics with first LHCb data

Olivier Schneider for the LHCb Collaboration

Ecole Polytechnique Fédérale de Lausanne (EPFL), CH–1015 Lausanne, Switzerland

DOI: http://dx.doi.org/10.3204/DESY-PROC-2010-01/268

The LHCb experiment is designed for hadronic flavour physics and will look for new physics manifestations in the decay of charm and bottom hadrons abundantly produced at the LHC. All parts of the LHCb physics programme can be embarked on with the expected statistics to be collected during the first 2010–2011 physics run at $\sqrt{s} = 7$ TeV. We present first preliminary results on strangeness production, and demonstrate, using the few nb^{-1} of already collected data, the potential for initial measurements in heavy-flavour physics.

1 Physics goals and strategy

The Standard Model (SM) of particle physics cannot be the ultimate theory. It is incomplete and contains too many free parameters, such as masses and quark mixing angles. The pattern of these parameters should be governed by a hidden mechanism yet to be discovered, and so the SM is believed to be a low-energy effective theory of a more fundamental theory at a higher energy scale, anticipated to be in the TeV region and accessible at the Large Hadron Collider (LHC). This would imply new symmetries, particles, dynamics, and flavour structure.

The most exciting task of the LHC experiments will be to find this new physics, whatever it may be. This can be done either directly or indirectly. The direct approach, pursued mostly by the ATLAS and CMS experiments, aims at the observation of new particles produced in LHC's proton-proton collisions at 14 TeV. The indirect approach, on the other hand, consists in measuring quantum corrections in the decay of already known particles especially in flavour-changing neutral-current (FCNC) transitions, and looking for deviations from the SM predictions. At LHC, this will be best done by the LHCb experiment, which has been designed specifically for precise measurements of CP violation and rare decays of hadrons containing a b quark. Both approaches are complementary: while the indirect approach is sensitive to higher energy scales and may therefore sense a new effect earlier, the direct observation of any new particle is necessary to establish its unambiguous discovery as well as for measuring its main properties. New physics (NP) at the TeV scale needs to have a non-trivial flavour structure in order to provide the suppression mechanism for the already observed FCNC processes. Only indirect measurements can access the phases of the new couplings and therefore shed light on the NP flavour structure.

One of the strategies for indirect searches in hadronic decays consists of measuring as many observables as possible that can be related to the magnitudes and phases of the elements of the Cabibbo-Kobayashi-Maskawa (CKM) matrix describing the SM flavour structure in the quark sector. Any inconsistency between the interpretation of these measurements within the CKM picture will be a sign of new physics. The most awaited progress in this area is a precise NP-free

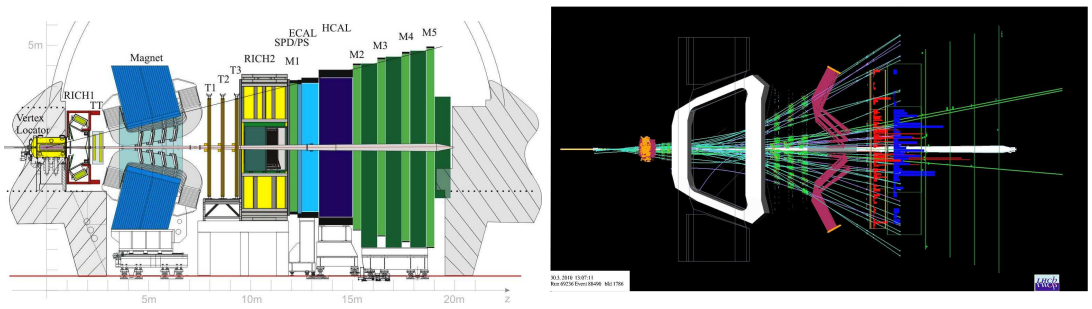

Figure 1: Left: Side view of the LHCb spectrometer, showing the Vertex Locator around the interaction region on the left, the tracking stations before (TT) and after (T1–T3) the dipole magnet, the ring-imaging Cherenkov detectors (RICH1 and RICH2), the calorimeter system (SPD/PS, ECAL, HCAL), and the muon stations (M1–M5). Right: Event display (top view, in bending plane) of one of the first recorded pp collisions at $\sqrt{s} = 7$ TeV on March 30, 2010. Reconstructed tracks, originating from the pp collision point on the left, have been reconstructed from hits in the VELO and hits (green) in the tracking stations. Cherenkov photons (mauve) are reflected on mirrors towards photo-detectors (orange). Energy depositions in ECAL (red) and HCAL (blue) as well as hits in the muon chambers (green, far right) are also visible.

determination of the CKM angle γ from tree-level processes.

Another strategy is to identify and measure single FCNC processes with good NP discovery potential, *i.e.* where NP is likely to emerge and for which a clear SM prediction can be made. Decays involving the $b \to s$ transition, which is less constrained by the current data, are good candidates. They are theoretically calculated using the Operator Product Expansion in terms of short-distance Wilson coefficients and long-distance operators describing effective vertexes such as tree diagrams, or gluon-, photon-, electroweak-, scalar- and pseudoscalar-penguin loops. New physics may both enhance some of the Wilson coefficients or introduce new operators, in particular in the right-handed sector which is suppressed in the SM.

Following these strategies, LHCb is preparing to perform rate measurements (such as the $B_s^0 \to \mu^+\mu^-$ branching fraction), determine CP-violating phases (most notably mixing-induced effects in $B_s^0 \to J/\psi\,\phi$ and $B_s^0 \to \phi\,\phi$ decays, interference between $b \to u$ and $b \to c$ transitions in tree-level $B \to DK$ decays, CP asymmetries in charmless two-body B decays), and probe the helicity structure of weak interactions (photon polarization in $B_s^0 \to \phi\,\gamma$ and other radiative decays, asymmetries in $B^0 \to K^{*0}\mu^+\mu^-$ decays). Such promising measurements are central to the core physics programme of LHCb; they have been studied in detail and are described in a recent roadmap document [1]. However, the wider programme will include many more measurements, mostly in (but not limited to) the heavy-flavor sector.

2 LHCb and first physics run

The LHCb detector [2] is a single-arm spectrometer (see Fig. 1 left) covering the forward region ($1.9 < \eta < 4.9$) where the $b\bar{b}$ production is peaked. It will rely on relatively soft $p_{\rm T}$ triggers, efficient for both leptonic B decays ($\sim 90\%$) and purely hadronic B decays ($\sim 40\%$). By design

the luminosity will be limited to an average of $\sim 2\times10^{32}$ cm^{-2}s^{-1} in order to avoid a significant fraction of events with more than one pp inelastic interaction. A nominal year (10^7 s) of running in design conditions will give an integrated luminosity of 2 fb^{-1} at $\sqrt{s} = 14$ TeV. However, in the first LHC physics run started on March 30, 2010 (see Fig. 1 right) the centre-of-mass energy is $\sqrt{s} = 7$ TeV, reducing the expected $b\bar{b}$ and $c\bar{c}$ production rates by factors ~ 2.3 and ~ 1.8, respectively, although without dramatic impact on the physics reach. The nominal instantaneous luminosity is expected to be reached in 2011, while the current lower luminosity period in 2010 allows for lower trigger thresholds, and hence better efficiencies for hadronic B decays ($\sim 75\%$). This represents also a good opportunity to collect rapidly very large samples of charm events, with a corresponding trigger efficiency boosted up from $\sim 10\%$ to $\sim 40\%$. Approximately 14 nb^{-1} of data have been collected during April and May 2010, mostly with a fully inclusive trigger requesting at least one reconstructed track in the detector. Since the last week of May, a loose High-Level Trigger is run in rejection mode to limit the output rate to a few kHz. The overall status of the experiment [3], the data-taking experience [4], and the event reconstruction performance [5, 6] obtained from the first data are described elsewhere.

The first physics measurements within reach are those of the production of known and most abundantly produced particles. LHCb is focusing initially on unstable particles which can be reconstructed through their decay into charged tracks, and therefore cleanly identified as narrow signals above some combinatorial background. So far close to 30 different mass peaks have been seen in the LHCb data, including decays involving neutrals such as $\eta \to \pi^+\pi^-\pi^0$, $\eta' \to \pi^+\pi^-\gamma$, and $D^0 \to K^-\pi^+\pi^0$. Because of the nature of the LHCb core measurements, which will most often rely on fully reconstructed decays, the understanding and modelling of the structure of minimum bias events is not of utmost importance, hence more difficult production measurements of stable particles such as charged pions, kaons, protons or tracks in general are not at the centre of the present effort. Of more direct interest are the production measurements of strange (and neutral), charm, and bottom hadrons, as well as of electroweak bosons (see Fig. 2).

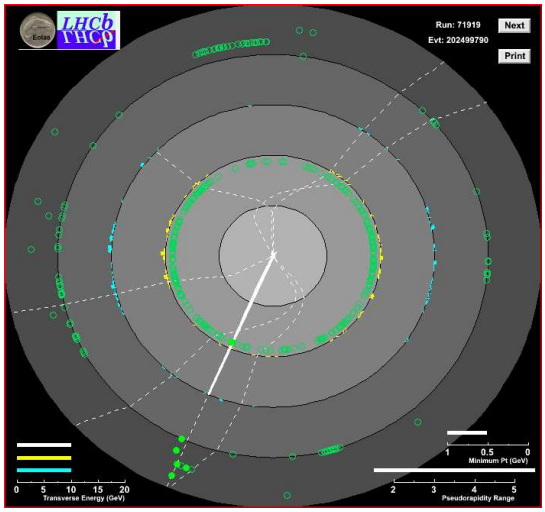

Figure 2: LHCb's first $W^+ \to \mu^+\nu$ candidate, shown in a '$z-\phi$ view' of the detector, with the Vertex Locator at the centre and muon stations at the periphery of the display. The white thick straight line represents a high p_T track ($p_T = 35.4$ GeV) with hits in the muon chambers, while the curved dotted lines are accompanying soft tracks.

Production measurements at LHCb are necessarily new since LHC is operating at an unexplored energy. In order to turn them into cross section measurements, an estimate of the luminosity is needed. The principle of a direct determination of the luminosity based on a new 'beam imaging' technique [7] has been demonstrated using the data collected during the LHC pilot run in December 2009 [8], and used for the first absolute production cross section measurement described below.

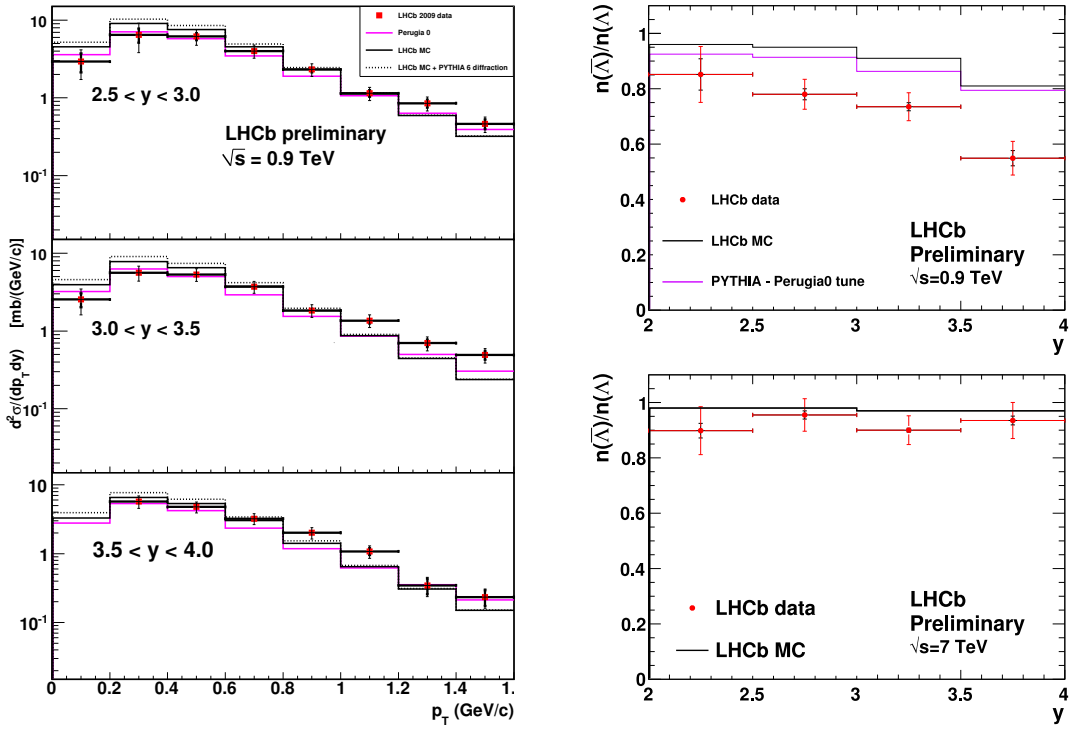

Figure 3: Left: Double-differential prompt K^0_S production cross section in pp collisions at $\sqrt{s} = 0.9$ TeV, shown as a function of K^0_S transverse momentum p_T in three different bins in K^0_S rapidity y. Right: $\bar{\Lambda}/\Lambda$ production ratio as a function of rapidity y in pp collisions at $\sqrt{s} = 0.9$ TeV (top) and 7 TeV (bottom). In all cases the red points represent LHCb data, with statistical and total uncertainties shown as vertical error bars, while the histograms are expectations from the PYTHIA 6.4 generator with different parameter settings, including the LHCb Monte Carlo (black) and the 'Perugia 0' tune [11] (purple).

3 Results on strangeness production

Strange quarks appear in the hadronization process of soft hadronic interactions, and their production is an excellent probe of the fragmentation field. In particular the measurement of strangeness production in hadronic interactions provides input for the understanding of QCD in the non-perturbative regime and for the tuning of Monte Carlo generators.

The data collected during the LHC pilot run in December 2009 at $\sqrt{s} = 0.9$ TeV were used to measure the prompt K^0_S production as a function of the K^0_S transverse momentum p_T and rapidity y in the region $0 < p_T < 1.6$ GeV/c and $2.5 < y < 4.0$ (see Fig. 3 left). At this low beam energy the beam sizes and crossing angle (induced by the LHCb dipole magnet) do not allow the complete closure of the Vertex Locator (VELO) around the interaction region. As a result the data were collected with the VELO silicon detectors retracted by 15 mm from

their nominal position, reducing significantly the azimuthal coverage provided by the VELO. However $K^0_S \to \pi^+\pi^-$ decays could still efficiently be reconstructed using tracks reconstructed in the tracking stations (TT and T1–T3). On the other hand the VELO was essential to measure pp and beam-gas interaction vertices, and determine the positions, sizes and angles of the colliding proton bunches. Together with bunch current measurements obtained from the LHC machine instrumentation, this allowed a direct determination of the integrated luminosity ($6.8 \pm 1.0\ \mu\text{b}^{-1}$) of the sample used for the K^0_S analysis. As can be seen from Fig. 3 (left), the preliminary measurements of the absolute prompt K^0_S production cross section are in fair agreement with the expectations from the PYTHIA generator, before any tuning to LHC data. These results have been finalized and published [9] since the conference.

The data collected in 2010, both at $\sqrt{s} = 0.9$ TeV and 7 TeV, were also used to study $\Lambda \to p\,\pi^-$ production. We show for the first time at this conference [10] preliminary measurements of the $\bar{\Lambda}/\Lambda$ production ratio as a function of rapidity y for the two centre-of-mass energies (Fig. 3 right). Contrary to the results at high energy, the measurements of the $\bar{\Lambda}/\Lambda$ ratio at $\sqrt{s} = 0.9$ TeV are significantly below the expectation and show a strong dependence in rapidity. Such studies are useful to investigate and understand the baryon-number transport from the beams in the more central region of the detector.

4 Charm: first look and prospects

Clean charm signals reconstructed in the first 2.7 nb^{-1} of data at $\sqrt{s} = 7$ TeV (Fig. 4) already allow to firm up exciting prospects for measurements of $D^0 - \bar{D}^0$ mixing and CP violation in the charm sector [12]. Indeed, with 0.1 fb^{-1} the statistics of (flavour-tagged) D^0 decays are expected to exceed that of the BABAR experiment by an order of magnitude. Significant contributions from LHCb are expected soon on several mixing-related observables, in particular:

- $y_{\text{CP}} = \frac{\tau(D^0 \to K^-\pi^+)}{\tau(D^0 \to K^-K^+)} - 1$ from the proper-time measurements of untagged $D^0 \to K^-\pi^+$ and $D^0 \to K^-K^+$ decays (Fig. 4 top);

- $A_\Gamma = \frac{\tau(\bar{D}^0 \to K^+K^-) - \tau(D^0 \to K^-K^+)}{\tau(\bar{D}^0 \to K^+K^-) + \tau(D^0 \to K^-K^+)}$ from the proper-time measurements of flavour-tagged $D^0 \to K^-K^+$ decays, where the flavour of the D^0 meson at production (D^0 or $\bar{D}^0$) is determined from the sign of the charged pion in the reconstructed $D^{*-} \to D^0\pi^+$ decay (Fig. 4 middle left);

- mixing parameters related to the mass and decay-width differences in the $D^0 - \bar{D}^0$ system, from the time-dependent analysis of wrong-sign flavour-tagged $D^0 \to K^+\pi^-$ decays (interference between doubly-Cabibbo suppressed decays without mixing and Cabibbo-favoured decays with mixing).

Similarly, huge statistics of charged D mesons will allow an unprecedented search for direct CP violation in charm. The most interesting modes are the singly-Cabibbo suppressed decays, governed by gluonic penguin diagrams where new physics may enter. The three-body mode $D^+ \to K^-K^+\pi^+$, together with the two Cabibbo-favoured decays $D^+_s \to K^-K^+\pi^+$ and $D^+ \to K^-\pi^+\pi^+$ to be used as control channels, offers the interesting possibility of a Dalitz plot analysis where local CP asymmetries can be probed (Fig. 4 middle right and bottom).

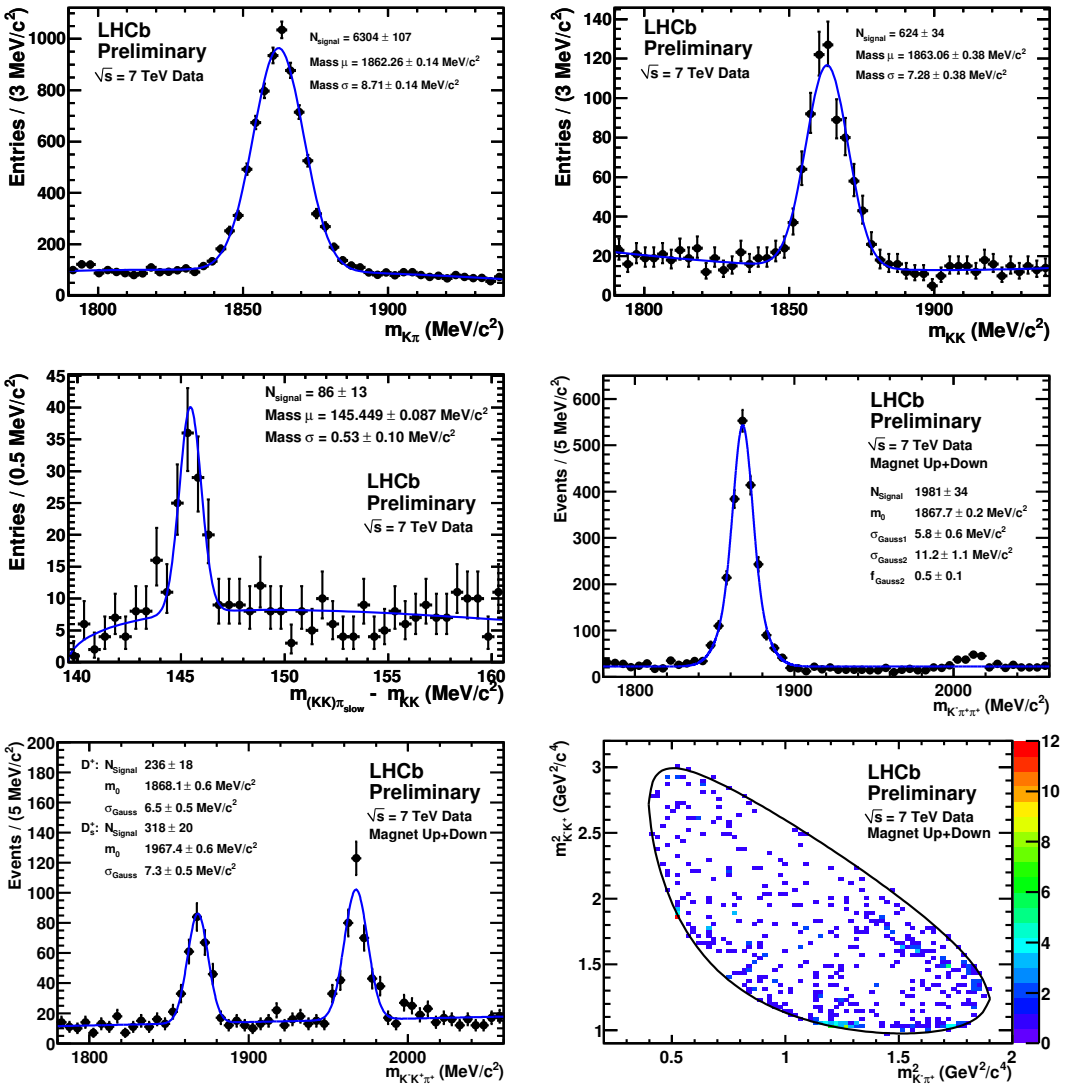

Figure 4: Some charm signals reconstructed in ~ 2.7 nb^{-1} of data at $\sqrt{s} = 7$ TeV. Top: $D^0 \to K^-\pi^+$ mass (left) and $D^0 \to K^-K^+$ (right) mass. Middle: difference between the $K^-K^+\pi^+$ and K^-K^+ masses for $D^{*+} \to D^0\pi^+ \to K^-K^+\pi^+$ candidates (left), and $D^+ \to K^-\pi^+\pi^+$ mass (right). Bottom: $K^-K^+\pi^+$ mass showing the $D^+ \to K^-K^+\pi^+$ and $D_s^+ \to K^-K^+\pi^+$ signals (left), and Dalitz plot of $D^+ \to K^-K^+\pi^+$ candidates (right).

5 First $b \to J/\psi\, X$ and $b \to D^0\mu\, X$ signals

Bottom production can easily be observed with a few nb^{-1} of data, if inclusive selections are used. Two approaches are described here, which will soon yield the first measurements of the

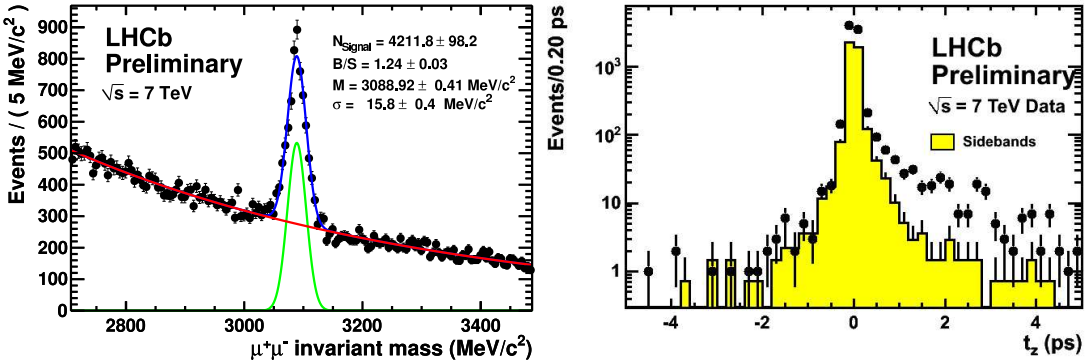

Figure 5: Left: Dimuon invariant mass distribution showing the $J/\psi \to \mu^+\mu^-$ signal in ~ 14 nb^{-1} of data at $\sqrt{s} = 7$ TeV. Right: Pseudo-proper time distribution of the J/ψ candidates in the signal window (black points) and in the sidebands (yellow histogram). The difference between the two distributions corresponds to signal J/ψ and displays a tail at large proper time indicative of $b \to J/\psi\, X$ production.

$b\bar{b}$ production cross section at $\sqrt{s} = 7$ TeV.

An important part of LHCb's physics programme is based on the selection of $J/\psi \to \mu^+\mu^-$ decays, which leave a clear signature in the detector and which can efficiently be recognized both at the trigger level and in the offline analysis. At the present level of understanding of the detector alignment and calibration, and using a very loose trigger, a signal of ~ 300 events per nb^{-1} is obtained, with a mass resolution of 16 MeV/c^2 and a signal-to-background ratio of 0.8 in a ± 45 MeV/c^2 window around the central value of the mass peak (Fig. 5 left). This abundant signal will be an important tool to further understand and improve the reconstruction performance. The two main sources of J/ψ mesons, prompt production at the pp interaction vertex and secondary production in b-hadron decays, can be separated by measuring the pseudo-proper time $t_z = (z_{J/\psi} - z_{\rm PV}) \times m_{J/\psi}/p_z$, where $z_{J/\psi}$ and $z_{\rm PV}$ are the reconstructed positions of the J/ψ decay and of the pp interaction point along the beam direction (z axis), $m_{J/\psi}$ is the nominal J/ψ mass, and p_z the z component of the reconstructed J/ψ momentum. The distribution of t_z is shown in Fig. 5 (right) for J/ψ candidates with reconstructed masses in the signal and sideband regions. The $b \to J/\psi\, X$ component of the signal is clearly visible as an exponential tail in the positive t_z region.

A similar analysis is performed by selecting $D^0 \to K^-\pi^+$ decays and using the distribution of the D^0 impact parameter (IP) with respect to the primary vertex to extract the b component. A yield of 1330 ± 350 (stat) events is obtained in ~ 3 nb^{-1}, which is the largest b-hadron signal observed so far in LHCb. In order to increase the purity an identified muon track is required in association with the D^0. If the $D^0\mu$ combination comes from a semileptonic $b \to D^0\mu^-\bar{\nu}X$ decay, the muon and the kaon from the D^0 must have equal charges ('right-sign' combination). Figure 6 shows the distributions of the D^0 mass and of the IP logarithm for both the right-sign and wrong-sign samples. Prompt D^0 production (associated with a random muon) contributes equally to both samples with small IP values, while semileptonic b-hadron decays contribute with larger IP values only to the right-sign sample. In the latter a clean and significant ($8\,\sigma$) signal of 85.3 ± 10.6 (stat) b events is extracted from a fit of the ln(IP) distribution, where the

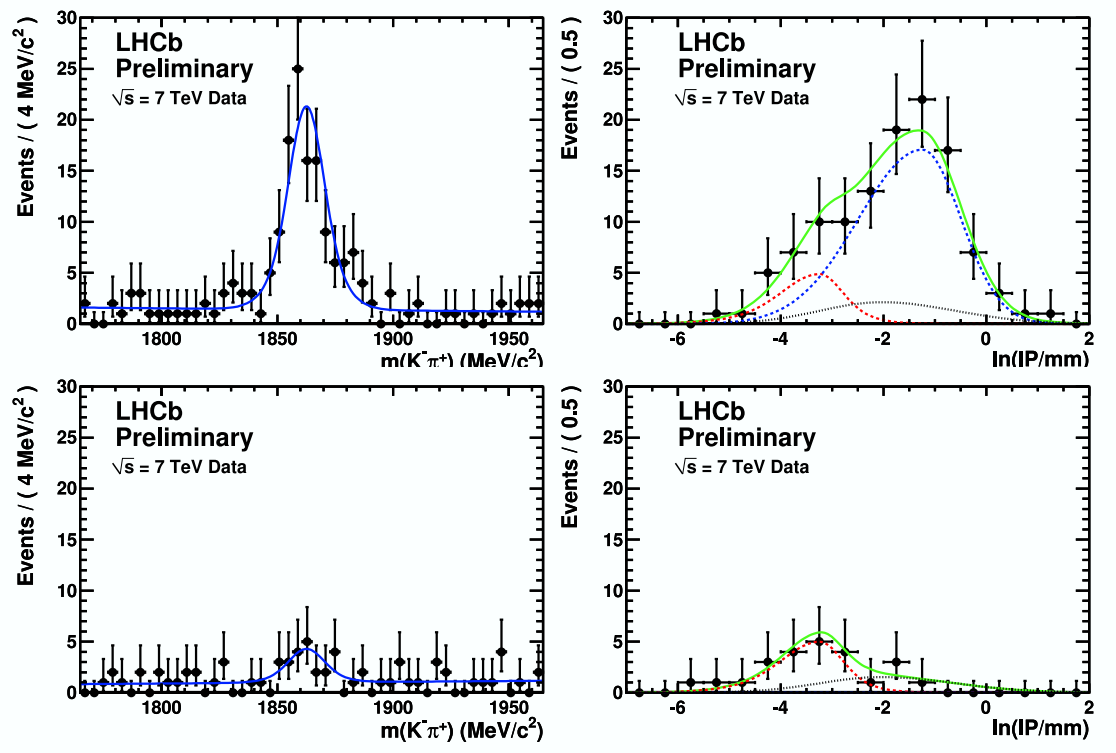

Figure 6: $D^0 \to K^-\pi^+$ invariant mass (left) and logarithm of the D^0 impact parameter in millimeters with respect to the primary vertex (right) for $D^0\mu$ candidates with 'right sign' (top) and 'wrong sign' (bottom) correlation, in ~ 3 nb^{-1} of data at $\sqrt{s} = 7$ TeV. Fit results are superimposed as curves. In the right-hand side plots, the black dotted curve represents the non-D^0 background estimated from the mass sidebands, and the blue (red) dotted curve represents the D^0 signal from b-hadron decays (prompt production).

shape of the b (prompt) component is fixed from MC (data without the muon requirement). These results have been finalized [13] since the conference.

In the future the abundant signals of semileptonic $B^0 \to D^0\mu^+\nu$ and $B_s^0 \to D_s^-\mu^+\nu$ decays are expected to play a major role in the study of CP violation in B^0 and B_s^0 mixing: Monte Carlo studies indicate that a measurement competitive with the Tevatron results can be obtained with less than 1 fb^{-1} of data, which is the statistics expected by the end of 2011.

6 Some prospects with fully reconstructed B decays

While several fully reconstructed B candidates have already been selected, the first significant mass peak has been seen by combining the $B^0 \to D^+\pi^-$ and $B^+ \to D^0\pi^+$ modes (Fig. 7). A $B_s^0 \to D_s^-\pi^+$ signal as well as $B \to DK$ Cabibbo-suppressed signals are expected soon. The main physics goal with such hadronic B decays is the determination of the CKM angle γ using the interference between $b \to c$ and $b \to u$ tree-level diagrams in $B_{(s)} \to D_{(s)}K$ decays, where

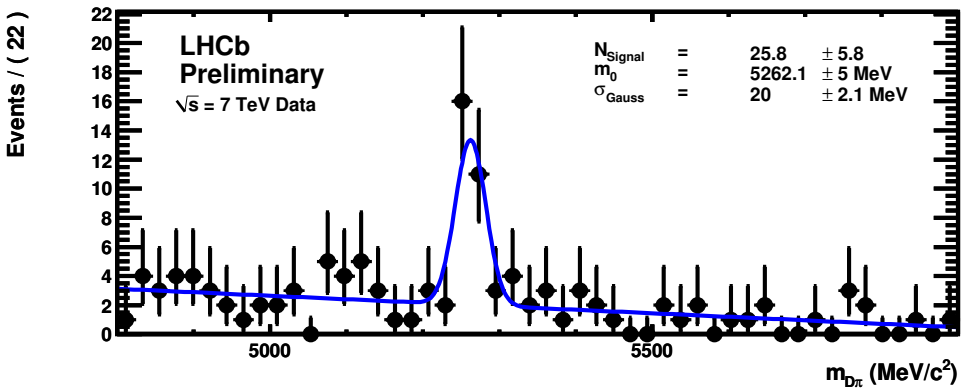

Figure 7: Sum of the $D^+\pi^-$ and $D^0\pi^+$ invariant mass distributions for ~ 13 nb^{-1} of data at $\sqrt{s} = 7$ TeV, showing the first signal of exclusively reconstructed $B \to D\,\pi$ decays.

a statistical precision of ~ 7 degrees (three times better than the current knowledge from the B factories) is expected with 1 fb^{-1} of data [1].

The current data already allow LHCb to prepare for a few key B_s^0 analyses. Amongst those, the measurement of mixing-induced CP violation in $B_s^0 \to J/\psi\,\phi$ decays and the search for the very rare $B_s^0 \to \mu^+\mu^-$ decay based on the first 0.1 fb^{-1} of data are expected to compete with Tevatron results, and may reveal hints of new physics with 1 fb^{-1} [1].

7 Summary

LHCb is taking data with success. First strangeness production measurements have been performed, and clean charm and bottom signals have been reconstructed. LHCb will embark on its core physics programme during the 2010–2011 run, where the expected integrated luminosity should already give access to heavy-flavour observables sensitive to possible new physics.

References

[1] B. Adeva *et al.* [LHCb Collaboration], arXiv:0912.4179v2 [hep-ex].
[2] A. A. Alves *et al.* [LHCb Collaboration], JINST **3** (2008) S08005.
[3] A. Golutvin [for the LHCb Collaboration], LHCb-TALK-2010-058, these proceedings.
[4] D. Wiedner [for the LHCb Collaboration], LHCb-TALK-2010-067, these proceedings.
[5] F. Maciuc [for the LHCb Collaboration], LHCb-TALK-2010-065, these proceedings.
[6] F. Xing [for the LHCb Collaboration], LHCb-TALK-2010-066, these proceedings.
[7] M. Ferro-Luzzi, Nucl. Instrum. Meth. A **553** (2005) 388.
[8] P. Hopchev [for the LHCb Collaboration], arXiv:1005.4398v1 [physics.ins-det].
[9] R. Aaij *et al.* [LHCb Collaboration], Phys. Lett. B **693** (2010) 69, arXiv:1008.3105v2 [hep-ex].
[10] W. Bonivento [for the LHCb Collaboration], LHCb-TALK-2010-063, these proceedings.
[11] P. Skands, arXiv:1005.3457v2 [hep-ph].
[12] J. Marks [for the LHCb Collaboration], LHCb-TALK-2010-062, these proceedings.
[13] R. Aaij *et al.* [LHCb Collaboration], Phys. Lett. B 694 (2010) 209, arXiv:1009.2731v1 [hep-ex].

Top physics at the Tevatron

Julia Thom for the CDF and D0 Collaborations

Laboratory for Elementary Particle Physics, Cornell University, Ithaca, NY, 14850, USA

DOI: http://dx.doi.org/10.3204/DESY-PROC-2010-01/18

Recent results on top quark physics, obtained at the Tevatron $p\bar{p}$ collider are presented. The measurements and searches were performed by the D0 and CDF collaborations, using between 3–5 fb^{-1} of Run II data at a center of mass energy of 1.96 TeV.

1 Introduction

15 years after the discovery of the top quark at the Fermilab Tevatron Collider [1, 2], CDF and D0 have collected thousands of top candidates at a center of mass energy of $\sqrt{s} = 1.96$ TeV, and have investigated top properties such as production cross sections of $t\bar{t}$ pairs and single top, top mass and decay mechanisms in detail. For example, the top quark mass has been measured with a precision less than 1%. In addition, it has become possible to perform sensitive searches for New Physics (NP) in the top sector. Many of the analysis techniques developed at the Tevatron will be of interest for the top physics program of the CMS and Atlas experiments. This paper describes only a selection of measurements and searches, done with 3–5 fb^{-1} of data, taken during Run II.

At the Tevatron, top quarks are produced predominantly in pairs, and, within the Standard Model (SM), the top quarks decay almost exclusively into a W boson and a b quark, resulting in one of the following three signatures: 'lepton+jets' (the final state includes one eletron or muon, at least 4 jets, and missing transverse energy from the undetected neutrino), 'dilepton' (two electrons or muons, at least two jets and missing transverse energy) and 'hadronic' (all jet signature). The production cross section has been measured in all three channels. The lepton+jets signature is considered the 'golden channel' because of its reasonable signal to noise ratio. The branching fraction is around 30%, and the backgrounds from QCD and W+jets can be reduced with the use of b-tagging, i.e. identification of jets originating from a b quark. This is done either through reconstruction of a secondary vertex clearly separated from the primary interaction vertex, or through association of a 'soft' lepton from semileptonic decay of a B hadron to the jet. Most results presented here use the lepton+jets signature with at least one jet tagged as coming from a b quark. In this particular channel, the dominant background is from W production with jets from heavy flavor ($b\bar{b}$ or $c\bar{c}$), which produces missing energy as well as a b tagged jets. The prediction of this background, which cannot be modeled reliably and needs correction factors extracted from the data, leads to one of the biggest systematic uncertainties.

2 Top quark pair production, and searches for new physics

The total top quark pair production cross section at $\sqrt{s} = 1.96$ TeV in $p\bar{p}$ collisions for a top quark mass of $m_t = 175$ GeV/c^2 can be calculated within the SM to be $6.7^{+0.7}_{-0.9}$ pb [3]. Deviations of the measurements from this value could indicate non-perturbative effects, or new production mechanisms beyond the SM. The recent measurements of the total top pair production cross section in all decay channels from CDF and D0 are in agreement with each other as well as the SM predictions. The combination of the CDF measurements yields a cross section of $7.50 \pm 0.31(stat.) \pm 0.34(syst.) \pm 0.15(lumi.)$ pb. The recent D0 measurements are shown in Figure 1. The top pair production cross section is now known with a relative uncertainty of less than 9% at the Tevatron center of mass energy, comparable to the theoretical uncertainty.

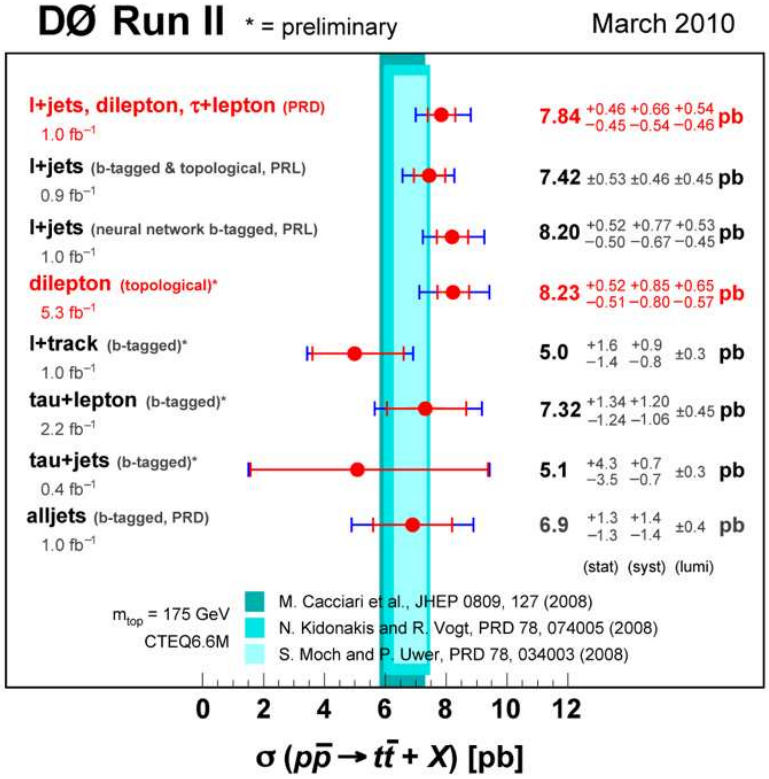

Figure 1: Recent measurements of the top quark pair production cross section at D0, in lepton+jets, dilepton and hadronic channels.

Many NP models predict the resonant production of $t\bar{t}$ pairs, and both Tevatron experiments performed searches for heavy massive resonances through the reconstruction of the invariant mass of the top quark pair. The observed spectrum is in good agreement with the SM expectation and no evidence of a resonance is found. D0, for example, has set a limit on the mass of a hypothetical massive leptophobic Z' at $m_{Z'} > 820$ GeV/c^2.

Another way that NP may be observed in $t\bar{t}$ production is through anomalies in the forward backward asymmetry. CDF has measured the asymmetry in the distribution of the top quark

rapidity in the lab frame, using 3.2 fb^{-1} of data. $t\bar{t}$ events are reconstructed in the lepton+ jets channel, where one top decays semi-leptonically and the other hadronically. The lepton charge is used to tag top versus anti-top, and the hadronic side is used to reconstruct the rapidity of the top (or anti-top) system. There is a small lab frame charge asymmetry expected in QCD at NLO, $A_{fb} = 0.05 \pm 0.015$. In NP scenarios with a Z' or an axigluon this asymmetry can be as large as $\pm 30\%$. Figure 2 shows the raw A_{fb}, showing a noticeable shift from the predictions. In order to relate this to the true underlying asymmetry, corrections for background, acceptance and smearing effects have to be applied. CDF observes $A_{fb} = 0.193 \pm 0.065(stat.) \pm 0.024(syst.)$ in the lab frame. An earlier result from D0, uncorrected and using 0.9 fb^{-1} of data, yields $A_{fb} = 0.12 \pm 0.08(stat.) \pm 0.01(syst.)$ [4].

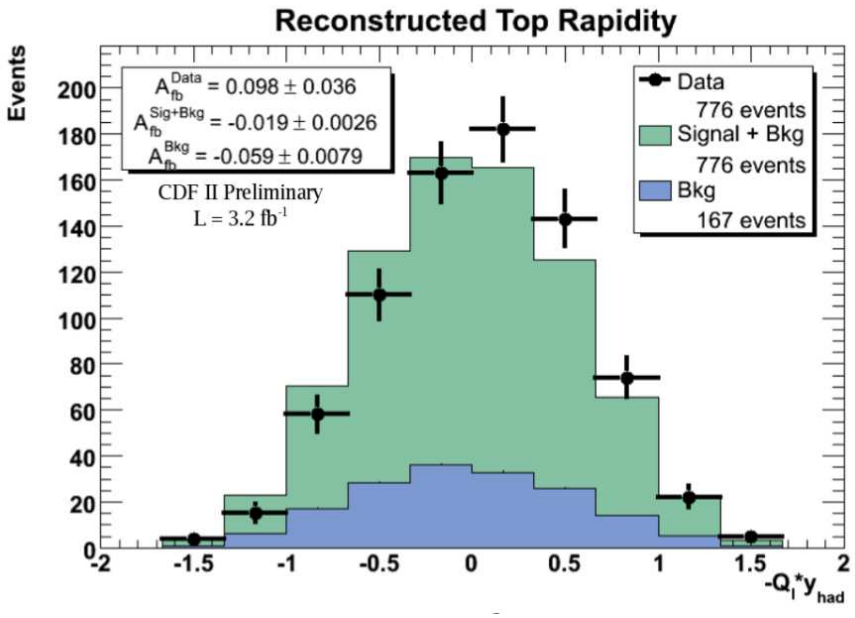

Figure 2: The reconstructed (raw) top rapidity in the lab frame, for data and simulation, as measured at CDF with 3.2 fb^{-1}.

3 Single top production

In the SM, single top quarks can be produced via electroweak interactions from the decay of an off-shell W boson ('s-channel'), or fusion of a virtual W boson with a b quark ('t-channel'). The SM prediction [5] is 0.98 ± 0.04 pb, and 2.16 ± 0.12 pb, respectively. The event selection is similar to that used in top pair production measurement, except that the final state contains two jets (instead of 4 or more). This makes the measurement of single top production extremely difficult: the background due to W+2 jet production, on the order of factor 20 over the single top production rate, is associated with large uncertainties.

The measurement of single top production is of importance as a direct probe of top weak coupling and V_{tb}, and presents a benchmark toward Higgs searches, which also have to face the

difficulty of large backgrounds from W+jets. Both D0 and CDF have presented observation of single top in sophisticated measurements that combine many channels and measurement techniques. D0 presented first evidence for single top production in 2007, using 0.9 fb^{-1} [6], and CDF in 2009 with 2.3 fb^{-1} [7]. The summary of the recent results is shown in Figure 3 . For a top quark mass of m_t=170 GeV/c^2, the combined cross section is $2.76^{+0.58}_{-0.47}$ pb. Events with single top quarks have also been used by both collaborations to directly measure the absolute value of the CKM matrix element $|V_{tb}| = 0.88 \pm 0.07$ with a 95% C.L. lower limit of $|V_{tb}| > 0.77$.

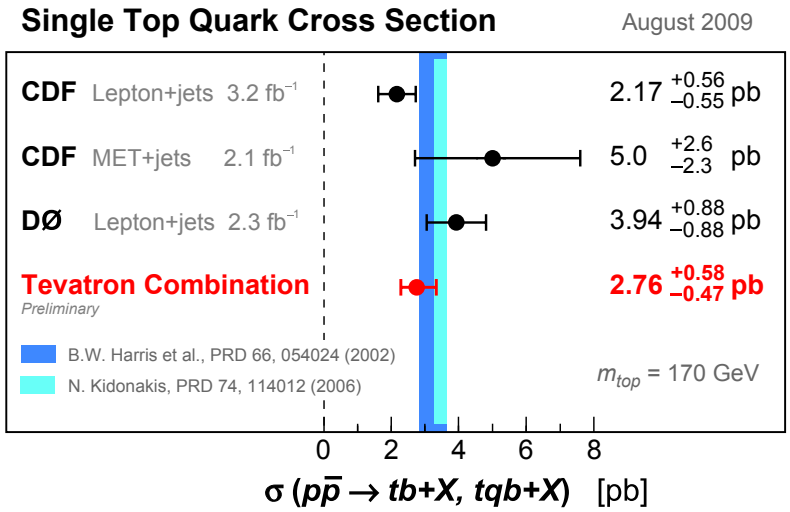

Figure 3: Tevatron combination of the single top quark cross section.

4 Top quark decay

Within the SM, the top quark decays via the $V-A$ charged-current interaction to a W boson and a b quark. New physics present in this decay could become evident in helicity measurements of the W boson originating from a top quark decay. For example, a different Lorentz structure of the Wtb interaction would alter the fractions of longitudinally (f0) and right-handed (f+) polarized W bosons from top-quark decay. The SM predicts values of 0.7 and 0, respectively. The CDF and D0 collaborations have measured these fractions using angular distributions of the charged lepton in the W rest frame measured with respect to the direction of motion of the W boson in the top quark rest-frame. CDF measured fractions of $f0 = 0.88 \pm 0.11(stat.) \pm 0.06(syst.)$ and $f+ = -0.15 \pm 0.07(stat.) \pm 0.06(syst.)$, using 2.7 fb^{-1} of data. D0 measured $f0 = 0.490 \pm 0.106(stat.) \pm 0.085(syst.)$ and $f+ = 0.110 \pm 0.059(stat.) \pm 0.052(syst.)$, using 1.2 fb^{-1} of data. All W-helicity measurements in top pair events performed at the Tevatron are compatible with the SM prediction within experimental uncertainties.

Another interesting measurement testing SM predictions associated with top quark decay is top spin determination. Top and anti-top spins are correlated, if top lifetime is short enough. The spin correlation can be measured through the angle of decay products, such as leptons

and jets, in the top rest frame with respect to a chosen quantization axis. Commonly, a spin correlation parameter C is measured, where $t\bar{t}$ is decaying with the following differential cross section and decay rate:

$$\frac{1}{\sigma}\frac{d^2\sigma}{d\cos\Theta_+ d\cos\Theta_-} = \frac{1 + C\cos\Theta_+\cos\Theta_-}{4}.$$

$\Theta_+(\Theta_-)$ denotes the angle of flight direction of $l^+(l^-)$ with respect to the quantization axis of the top (anti-top) quark. At D0, a dilepton sample is used, and the angles are measured with respect to the beam axis. The SM prediction at NLO is 0.78, and the measurement yields $C = -0.17^{+0.64}_{-0.53}(stat.+syst.)$. At CDF, the helicity basis is chosen, where the SM prediction for C at NLO is 0.4. The measured correlation parameter is $C = 0.6 \pm 0.5(stat.) \pm 0.16(syst.)$. The measurements are statistics limited and, within errors, in agreement with the SM prediction.

5 Top quark mass

The mass of the top quark is an important SM parameter, and precise top and W mass measurements are used to constrain the mass of the SM Higgs. Figure 4 shows the current constraints and their effect on the global electroweak fit and the SM Higgs mass, suggesting a light SM Higgs.

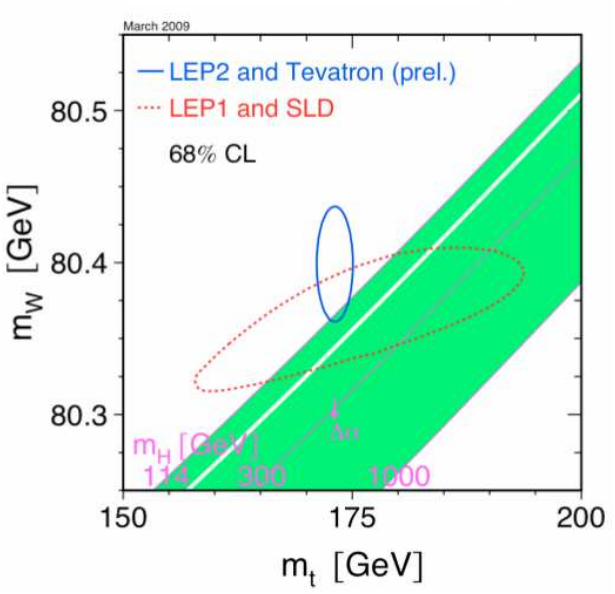

Figure 4: Current m_{top} and m_W measurements and their effect on the global electroweak fit and SM Higgs Boson.

One of the advances of Run II has been the reduction of the experimental uncertainty on the mass measurement due to the jet energy scale by an in situ calibration measurement, using hadronically decaying W bosons in the lepton+jets and the hadronic channel. The result of the combination of all decay channels from both CDF and D0 yields a top mass of $m_{top} =$

$173.1 \pm 0.6(stat.) \pm 1.1(syst.)$ GeV/c^2. Currently the most precise single top quark measurement is carried out at CDF in the lepton+jets channel, using 4.8 fb^{-1} of data, and yields a top mass of $172.8 \pm 1.3(tot.)$ GeV/c^2 [9]

6 Summary

The Tevatron has entered a new era of top quark precision measurement, and a broad program of measurements of top quark properties is underway. Already, more than twice the data presented here has been written to tape and will provide a large enough dataset to provide sensitive searches for NP in the top sector. Much of the work on background calibration can provide guidance and focus to the LHC top program and beyond.

7 Acknowledgments

I would like to thank the CDF and D0 collaborations for their help in preparing this contribution. I would like to acknowledge support from the National Science Foundation (USA). The grant number is PHY-0757894.

References

[1] F. Abe *et al.* [CDF Collaboration], Phys. Rev. Lett. **74**, 2626 (1995) [arXiv:hep-ex/9503002].

[2] S. Abachi *et al.* [D0 Collaboration], Phys. Rev. Lett. **74**, 2632 (1995) [arXiv:hep-ex/9503003].

[3] M. Cacciari, S. Frixione, M. L. Mangano, P. Nason and G. Ridolfi, JHEP **0404** (2004) 068 [arXiv:hep-ph/0303085].

[4] V.M. Abazov *et al.* [D0 Collaboration], Phys. Rev. Lett. **100**, 142002 (2008).

[5] N. Kidonakis, Phys. Rev. D **74**, 114012 (2006). [arXiv:hep-ph/0609287].

[6] V.M. Abazov *et al.* [D0 Collaboration], Phys. Rev. Lett. **98**, 181802 (2007).

[7] T. Altonen *et al.* [CDF Collaboration], Phys. Rev. Lett. **101**, 252001 (2008).

[8] Tevatron Electroweak Working Group and CDF and D Collaborations, arXiv:0808.1089.

[9] Public CDF note 10077, see http://www-cdf.fnal.gov/physics/new/top/

Status of (N)NLO calculations

Thomas Gehrmann

Institut für Theoretische Physik, Universität Zürich, CH-8057 Zürich

DOI: http://dx.doi.org/10.3204/DESY-PROC-2010-01/15

In this talk, I review recent progress on the calculation of higher order corrections to QCD observables at high energy colliders.

1 Introduction

QCD is well established as theory of the strong interaction, and its perturbation theory expansion can be used to obtain quantitative predictions for observables in high energy particle collisions. QCD effects are omnipresent in hadronic collisions, and a detailed understanding of QCD is mandatory for the interpretation of collider data, for new physics searches and for precision studies. In this talk, I review the recent progress on applications of QCD at high energy colliders.

2 Jets and Event Shapes

Hadronic jets are the final state signatures of quark or gluon production in particle collisions at high energies. As such, they are important both as tool for precision studies of QCD, and in searches for new physics effects [1]. Jets are defined through a jet algorithm (a measurement and recombination prescription to reconstruct the jet momenta from measured individual hadron momenta). Jet algorithms must fulfill infrared-safety criteria, i.e. the reconstructed jet kinematics must be insensitive to radiation of soft or collinear particles. Historically, two classes of jet algorithms were widely used at high energy colliders: cone-based algorithms and sequential recombination algorithms. Cone-based algorithms allow an intuitive understanding of the jets, and can be formulated in an infrared-safe manner [2]. Recombination algorithms are less intuitive, and their slow performance for a large number of final state particles was overcome only recently with the FastJet implementation [3]. Variants of these algorithms differ in the distance measure used to identify neighboring momenta, it turns out that the so-called anti-k_T recombination algorithm results in perfectly cone-shaped jets [4].

Much progress has been made recently in using jets as analysis tools. The concept of the jet catchment area [5] allows to obtain a geometrical interpretation of recombination algorithms, and to identify outside-jet regions, which can be used for underlying event studies. Aiming for the reconstruction of highly boosted massive particles, the study of jet substructure [6] has proven to be very promising. All decay products are first clustered in one fat jet, whose substructure is then resolved by lowering the resolution, resulting in a pronounced discontinuity once the particle decay is resolved. As one of the first results obtained using this procedure, the reconstruction of $t\bar{t}H$ (a reaction that could not be observed with standard cut-based methods

due to the large standard model background) final states appears to become feasible [7]. Many more applications are under study.

Closely related to jet observables are event shapes, which characterize the geometrical properties of a hadronic final state. Distributions in several event shape variables were measured very extensively by LEP in view of precision studies of QCD. These results have a wide variety of applications, ranging from precision measurements of α_s, tests of resummation, study of hadronization effects, and tuning of multi-purpose Monte Carlo event generators. At hadron colliders, event shapes were only studied little up to now, and their definition is more involved due to the restricted final state region usually accessible in this environment. If defined properly, they can serve as tools for model-independent searches [8], and may be complementary to jet observables [9]. An extensive classification of event shapes at hadron colliders has been made very recently [8].

3 Multiparticle production at NLO

The search for new physics signals at the CERN LHC will very often involve multi-particle final states, consisting of numerous jets, leptons, photons and missing energy. Quite in general, massive short-lived particles are detected through their decay signatures, as for example top quark pair production, which was first observed in final states with four jets, a lepton and missing energy.

Meaningful searches for these signatures require not only a very good anticipation of the expected signal, but also of all standard model backgrounds yielding identical final state signatures. Since leading-order calculations are affected by large uncertainties in their normalization and their kinematical dependence, it appears almost mandatory to include NLO corrections, which also allow to quantify the jet algorithm dependence, and effects of extra radiation. For a long time, these corrections were available only for at most three final state particles.

An NLO calculation of a n-particle observable consists of two contributions: the virtual one-loop correction to the n-particle production process, and the real radiation contribution from the $(n+1)$-particle production process. Both contributions are infrared divergent, and can be evaluated numerically only after extracting the infrared divergent contributions from the real radiation process. Several well-established and widely used methods exist for this task [10–17].

The evaluation of the one-loop multi-leg amplitudes poses a challenge in complexity (due to the large number of diagrams, and large number of different scales present) and stability (due to possible linear dependences among the external momenta). It has been known for long that any one-loop amplitude can be expressed as a linear combination of one-loop integrals with at most four external legs, plus a rational remainder. Enormous progress has been made in recent years in the systematic computation of the one-loop integral coefficients and rational terms. While previously established Feynman-diagram based techniques for tensor reduction and form factor decomposition were successfully extended [18,19] to multi-leg problems, a new arsenal of techniques was emerging from the use of unitarity and multi-particle cuts [20]. Using these, the one-loop integral coefficients of an amplitude can be inferred [21–24] without evaluation of all individual diagrams. An extension of these ideas is made by performing the reduction at the integrand level in the OPP method [25, 26]. The rational coefficients can be determined in the same framework by extending the unitarity relations from four dimensions to higher-dimensional space-time [27–29].

Given the large number of different multi-particle final states of potential interest to new

physics searches, an automation of NLO calculations is highly desirable. Based on existing multi-purpose leading order matrix element generators, the implementation of the real radiation contributions and their infrared subtraction terms is straightforward, and has been accomplished in the Sherpa [30], MadGraph [31–33] and Helac/Phegas [34] frameworks, as well as in the form of independent libraries [35,36], which complement already existing libraries in the MCFM [37, 38] and NLOJET++ [39] packages. The automation of the virtual corrections is a much larger challenge, which is currently being accomplished in several program packages based on the various available methods. A semi-numerical form factor decomposition is automated in the Golem package [40]. Unitarity and multi-particle cuts are used in the BlackHat package [41], and the OPP method is automated in CutTools [42]. Numerical D-dimensional unitarity is applied in the Rocket package [43] and the Samurai package [44]; it also forms the basis of several currently ongoing implementations [45, 46].

Several NLO calculations of $2 \to 3$ reactions at hadron colliders were completed recently. These include the production of two vector bosons and one jet [47–52], of a Higgs boson and two jets [53–56], of $t\bar{t}Z$ [57], and of three vector bosons [58–62]. Of a similar kinematical type are vector boson fusion processes, which are computed to NLO accuracy in the VBFNLO package [63]. The current frontier of complexity are NLO calculations of $2 \to 4$ reactions. Several very important processes of this type have been computed most recently.

An important channel for Higgs boson searches, and for subsequent determinations of Yukawa couplings, is the associated production of a Higgs with a heavy quark-antiquark pair, with the Higgs boson decaying into $b\bar{b}$. The QCD background processes yielding $t\bar{t}b\bar{b}$ final states were computed recently to NLO [64–67], displaying moderate but non-constant QCD corrections, which show a non-trivial dependence on the event selection cuts. A natural extension of these calculations are $t\bar{t} + 2j$ final states [68]. Extended Higgs sectors predict a sizable rate of associated production with bottom quark pairs, and the calculation of $b\bar{b}b\bar{b}$ final states is in progress [69].

The final state signature of a vector boson and three hadronic jets is often relevant in generic new physics searches. NLO corrections of $W+3j$ were obtained by two groups in the Rocket [70] and in the Blackhat+Sherpa [71,72] framework. The corrections to Z^0+3j were also obtained with Blackhat+Sherpa [73]. For both observables, corrections are moderate, and stabilize the QCD prediction to the ten per cent level, required for precision phenomenology, as can be seen in Figure 1 from [73]. Knowledge of the NLO corrections to these processes allows many phenomenological studies, such as for example the stability of final state correlations [72] under perturbative corrections, and the optimal choice of scales in multi-scale processes [72–75]. A crossing of Z^0+3j is the process $e^+e^- \to 5j$, which was measured at LEP. The NLO calculation of it is in progress.

4 Precision observables at NNLO

Few benchmark observables (e.g. jet cross sections, vector boson production, heavy quark production) are measured experimentally to an accuracy of one per cent or below. For a theoretical interpretation of these observables, an NLO description (which has a typical residual uncertainty around ten per cent) is insufficient: extractions of fundamental parameters from these observables would be limited by the theory uncertainty. For a meaningful interpretation of these observables, NNLO corrections are mandatory. Likewise, NNLO corrections are required for a reliable description of observables with potentially large perturbative corrections, like Higgs

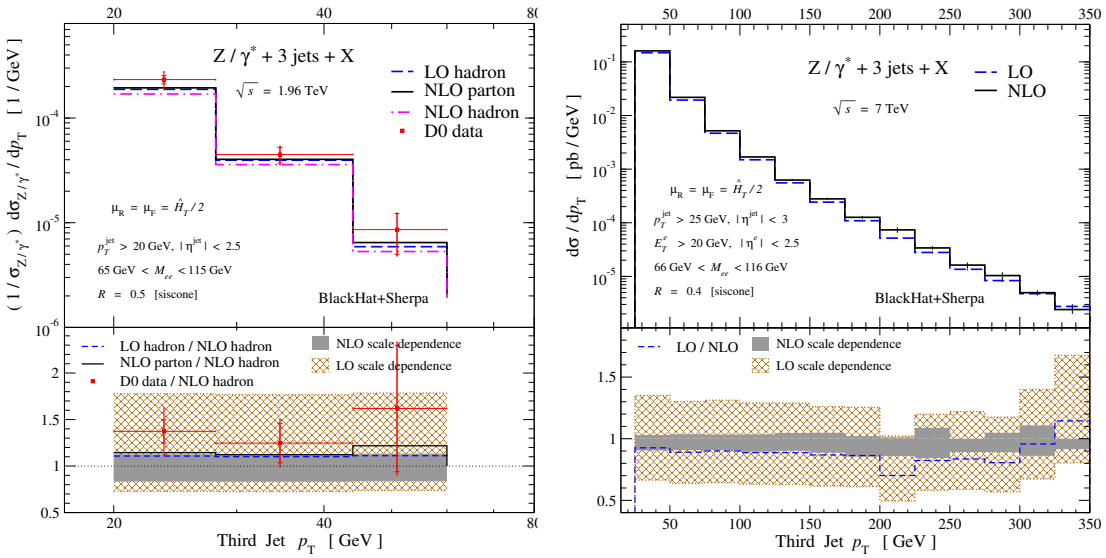

Figure 1: Transverse momentum distribution of the third-hardest jet in $Z^0 + 3j$ events at the Tevatron (left) and the LHC (right) to LO and NLO. Figure taken from [73].

boson production.

The calculation of NNLO corrections to an n-particle final state requires three ingredients: the two-loop matrix elements for the n-particle production, the one-loop matrix elements for the $(n+1)$-particle production and the tree-level matrix elements for $(n+2)$-particle production. The latter two contributions develop infrared singularities if one or two particles become soft or collinear, requiring a subtraction method to extract these infrared poles, which are then combined with the virtual corrections to yield a finite prediction. The two major challenges of NNLO calculations are the two-loop matrix elements and the handling of the real radiation at NNLO. Up to now, two types of approaches to real radiation have been applied in NNLO calculations of exclusive observables. The sector decomposition method [76–78] is based on a systematic expansion in distributions, followed by numerical integration over many different small phase space sectors. Subtraction methods search to approximate the full real radiation contribution by subtraction terms in all unresolved limits; these terms are then integrated analytically. While many subtraction methods have been worked out at NLO, only two methods have so far yielded results at NNLO: the antenna subtraction method [79] for processes in e^+e^- annihilation, and the q_T-subtraction [80] for hadron collider processes in specific kinematic configurations. Alternative approaches are under intensive development [81–83]. A combination of subtraction with sector decomposition [84] may hold the potential to become a general multi-purpose method.

The dominant Higgs boson production process is gluon fusion, mediated through a top quark loop. This process has been computed (in the infinite top mass limit) to NNLO accuracy in a fully exclusive form including the Higgs boson decay, i.e. allowing for arbitrary infrared-safe final state cuts, both using sector decomposition [85–87] and using q_T-subtraction [88, 89]. These results can be directly applied to the Higgs boson search at the Tevatron, based on a neural network combination of many different kinematical distributions [90]. Finite top mass effects at

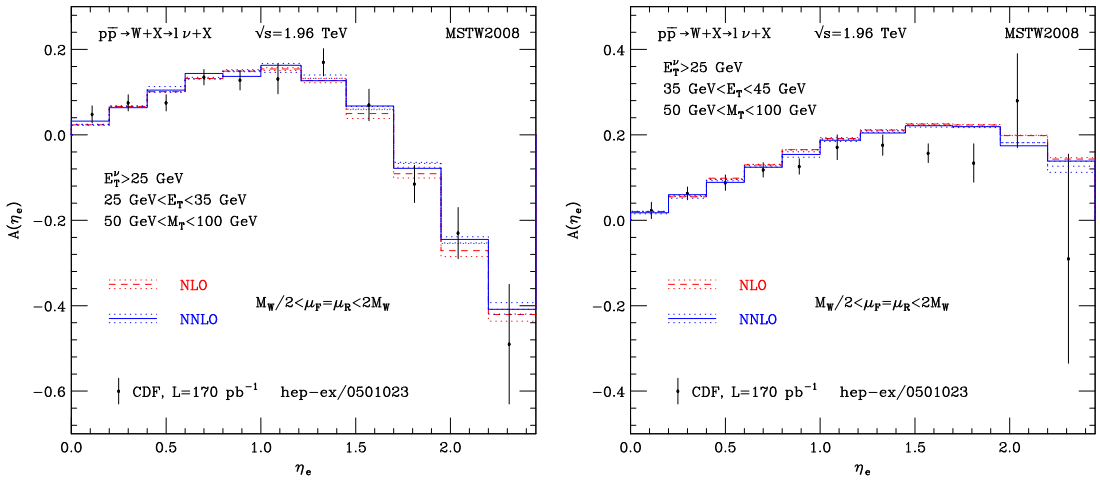

Figure 2: Lepton charge asymmetry at the Tevatron at NLO and NNLO, compared to CDF data. Figure taken from [107].

NNLO were derived most recently [91–93] for the inclusive gluon fusion cross section. At this level of precision, mixed QCD and electroweak corrections [94] become equally important. The gluon fusion reaction can be mediated through loops involving any type of massive color-charged particles, thereby offering an indirect constraint on physics beyond the standard model, such as supersymmetric particles [95–99], extra heavy quark families [100] or color-octet scalars [101].

Another very promising Higgs discovery channel is vector boson fusion. The factorizable NNLO corrections to the inclusive cross section for this process are closely related to inclusive deep inelastic scattering. They were computed very recently [102], and turn out to be rather small, resulting in a high theoretical stability of the prediction. This channel can be equally sensitive on supersymmetric contributions [103].

Fully exclusive NNLO corrections to vector boson production have equally been derived using sector decomposition [104, 105] and with q_T-subtraction [106], including the leptonic vector boson decay. Observables derived from vector boson production are very important for precision studies of the electroweak interaction, and for the determination of the quark distributions in the proton. Using the newly obtained results, the NNLO corrections (and their uncertainty) to the lepton charge asymmetry [107] can be quantified, see Figure 2, and this observable can be consistently included into NNLO fits of parton distributions.

Jet production observables have been computed to NNLO only for e^+e^- annihilation up to now. Two implementations of the NNLO corrections to $e^+e^- \to 3j$ and related observables are available [108–115], both based on antenna subtraction. The magnitude of the NNLO corrections differs substantially between different event shape observables; including these new NNLO corrections, LEP data on event shapes and jet cross sections were reanalyzed in view of an improved determination of the strong coupling constant. In general, an improved consistency among different observables was observed. To use measurements over an extended kinematical range, resummation of large logarithmic corrections in the two-jet limit is needed. This is available to next-to-leading logarithmic accuracy (NLLA) for all shape variables [116, 117], and to N^{3}LLA for thrust [118,119] and heavy jet mass [120] distributions. The by-now limiting factor

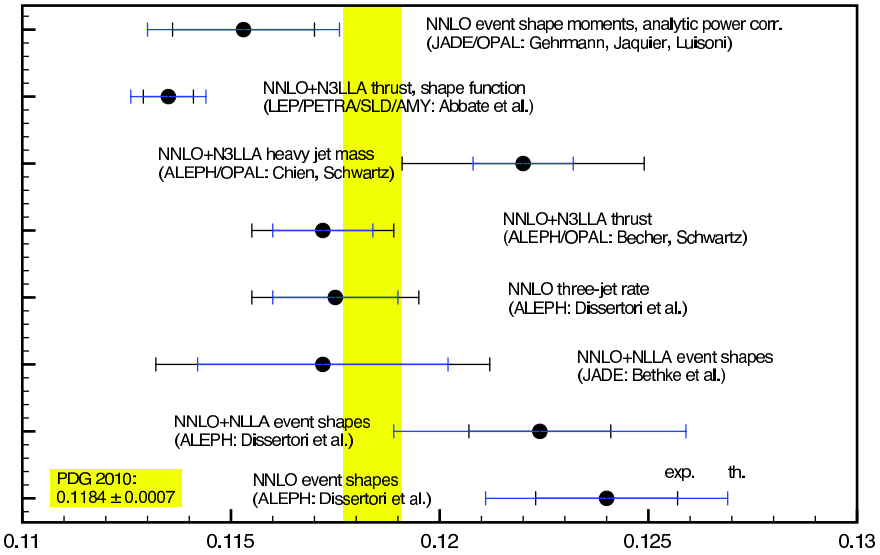

Figure 3: Determinations of α_s from event shapes and jet cross sections in e^+e^- annihilation at NNLO, compared to the Particle Data Group world average. Experimental errors are indicated in black, theoretical errors in blue.

in precision physics with event shape observables in e^+e^- annihilation is the description of the parton-to-hadron transition (hadronization), which was previously modeled from parton shower based event generators. Substantial differences are observed between the LEP-era programs and more modern generators, and to analytic approaches to hadronization, based on the shape function formalism [118–120] and on a dispersive model [121–123]. The recent determinations of the strong coupling constant from event shapes and jet cross sections at NNLO [118–120, 123–127] are summarized in Figure 3. Electroweak NLO corrections to jet observables [128–130] are potentially of the same numerical importance as NNLO QCD corrections, and could be included in future studies.

In view of the very precise jet production data from HERA and the Tevatron, the derivation of NNLO corrections to jet cross sections in hadronic collisions is of high priority. The relevant two-loop matrix elements for hadronic collisions and for deep inelastic scattering [131] are known for some time already, and substantial progress is being made to extend the antenna subtraction method to include hadrons in the initial state. The proper functioning of this method on the $gg \to 4g$ subprocess to hadronic dijet production has been demonstrated [132] most recently. The integrated forms of all antenna functions have been derived for one parton in the initial state [133], the case of two initial state partons [134] is work in progress.

The large number of top quark pairs expected to be produced at the LHC will allow for precision top quark studies, requiring NNLO accuracy on the theoretical side. The relevant two-loop matrix elements were first derived in the high energy limit [135, 136]. The exact $q\bar{q} \to t\bar{t}$ matrix element is known numerically [137], substantial parts of it have been confirmed by an analytic calculation [138, 139]. The one-loop self-interference contributions are equally known [140–142]. The matrix elements with one and two extra partons form part of the $t\bar{t}+j$ production at NLO [143–145]. Methods to handle real radiation at NNLO in the presence of massive top quarks are currently under intensive development. Generalizing the subtraction

method of [10] to NNLO and numerically integrating the relevant subtraction terms using sector decomposition [84] may provide a powerful method by combining the virtues of both approaches.

5 Infrared structure and resummation

The perturbative expansion of QCD observables in the strong coupling constant is reliable if only a single hard scale is present, it becomes problematic for observables depending on several hard scales, leading to large logarithmic corrections at all orders. In these cases, a rearrangement of the perturbative series by means of a resummation of large logarithmic corrections often appears more suitable.

Resummation of leading logarithmic corrections is accomplished by event generators [146] based on parton showers, initially based on leading order calculations. Parton showers can be combined with fixed order NLO calculations in the MC@NLO [147] or the POWHEG [148] approach. The MC@NLO event generator already covers a large number of different processes, with $W^{\pm}t$ production [149] and $H^{\pm}t$ production [150] among the most recent additions. Within POWHEG, single top production [151] and Higgs production in vector boson fusion [152] were accomplished most recently. The POWHEG box [153] provides users with a framework for implementing existing NLO calculations in this framework.

A detailed understanding of the infrared structure of QCD can be gained from the observation that infrared poles in loop amplitudes translate into large logarithms in real radiation processes and vice versa. This relation can be applied successfully in both directions: for example to predict infrared poles at two loops from resummation [154, 155] and to extract large-x resummation constants [156] from the poles of the QCD form factors. By relating the infrared poles in QCD to ultraviolet poles in soft-collinear effective theory (SCET) [157], it becomes possible to express the infrared pole structure of QCD amplitudes by a multiplicative renormalization in SCET. Based on constraints [158,159] and symmetry arguments, it becomes possible to conjecture that the infrared pole structure of massless QCD multi-loop amplitudes is uniquely determined [158–161] by the cusp anomalous dimension and the collinear anomalous dimensions of the external particles.

The resummed description of an observable consists [162, 163] of a hard coefficient, a soft function, jet functions containing final state collinear radiation and parton distributions containing initial state collinear radiation. In SCET [157], each of these elements is identified with an operator or a non-local function. The resummation [164, 165] then proceeds by computing their anomalous dimensions and solving the respective evolution equations. First applications of SCET-based resummation are the thrust [118,119] and heavy jet mass [120] distributions in e^+e^- annihilation, the inclusive Drell-Yan and Higgs production [164,166] and inclusive photon production [167]. This topic is currently under fast development, and many yet open issues, like jet production and radiation off incoming partons [168, 169] are being addressed.

Many of the constraints used to obtain the all-order conjecture for massless QCD amplitudes do not apply in the presence of particle masses. Consequently, the pole structure of massive amplitudes is more involved; in particular, it contains multi-particle correlations [170], which were absent in the massless case. Only recently, a prediction of the infrared poles to two-loop order has been accomplished [170, 171]. With these results, the resummation of the top quark pair production cross section to third logarithmic order (NNLL) could be completed. While dominant contributions at this order were known for some time [172, 173] the full corrections

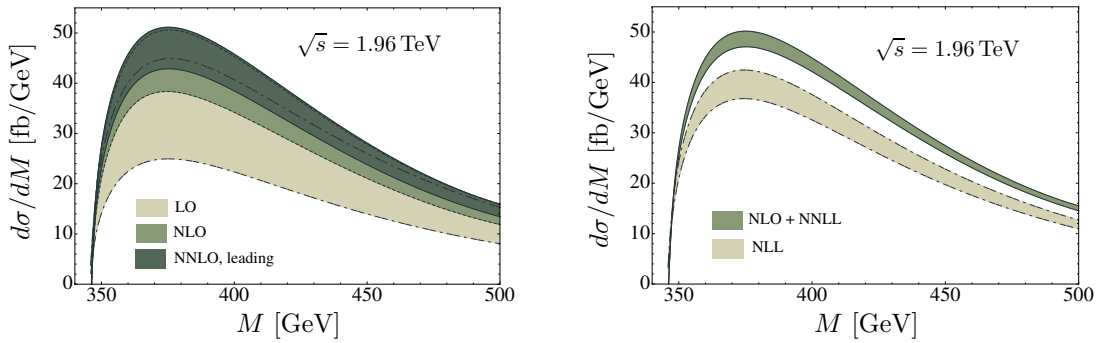

Figure 4: Top quark invariant mass distribution at the Tevatron in fixed order expansion (left) and resummation (right). Figure taken from [176].

have been obtained now in two approaches: based on massive soft anomalous dimensions [174, 175] and by using SCET [176]. The $t\bar{t}$ invariant mass distribution is compared in fixed order and resummed expansion in Figure 4, taken from [176]. It can be seen that the resummation has only moderate numerical impact on the central value, but results in a substantial reduction of the scale uncertainty. By expanding the resummed results to fixed order, one can in turn approximate the NNLO corrections to the top quark production cross section [172, 177, 178].

6 Conclusions

QCD is crucial for the success of the LHC physics programme in understanding signals and backgrounds, knowing parton distribution functions, and using jets and event shapes as analysis tools. Particle theory is getting ready for this challenge on many frontiers: with improved jet algorithms and event shape definitions, with an enormous progress on NLO calculations for multi-leg final states, with first NNLO results for precision observables, and with an emerging understanding of the all-order structure of infrared singularities.

Acknowledgments

The author gratefully ackowledges the support by the Swiss National Science Foundation (SNF) under contract 200020-126691.

References

[1] G. P. Salam, Eur. Phys. J. C **67** (2010) 637 [0906.1833].

[2] G. P. Salam and G. Soyez, JHEP **0705** (2007) 086 [0704.0292].

[3] M. Cacciari and G. P. Salam, Phys. Lett. B **641** (2006) 57 [hep-ph/0512210].

[4] M. Cacciari, G. P. Salam and G. Soyez, JHEP **0804** (2008) 063 [0802.1189].

[5] M. Cacciari, G. P. Salam and G. Soyez, JHEP **0804** (2008) 005 [0802.1188].

[6] J. M. Butterworth, A. R. Davison, M. Rubin and G. P. Salam, Phys. Rev. Lett. **100** (2008) 242001 [0802.2470].

[7] T. Plehn, G. P. Salam and M. Spannowsky, Phys. Rev. Lett. **104** (2010) 111801 [0910.5472].

[8] A. Banfi, G. P. Salam and G. Zanderighi, JHEP **1006** (2010) 038 [1001.4082].
[9] I. W. Stewart, F. J. Tackmann and W. J. Waalewijn, 1004.2489.
[10] S. Frixione, Z. Kunszt and A. Signer, Nucl. Phys. B **467** (1996) 399 [hep-ph/9512328].
[11] S. Catani and M. H. Seymour, Nucl. Phys. B **485** (1997) 291 [hep-ph/9605323].
[12] S. Catani, S. Dittmaier, M. H. Seymour and Z. Trocsanyi, Nucl. Phys. B **627** (2002) 189 [hep-ph/0201036].
[13] D. A. Kosower, Phys. Rev. D **57** (1998) 5410 [hep-ph/9710213].
[14] J. M. Campbell, M. A. Cullen and E. W. N. Glover, Eur. Phys. J. C **9** (1999) 245 [hep-ph/9809429].
[15] A. Daleo, T. Gehrmann and D. Maître, JHEP **0704** (2007) 016 [hep-ph/0612257].
[16] A. Gehrmann-De Ridder and M. Ritzmann, JHEP **0907** (2009) 041 [0904.3297].
[17] G. Somogyi, JHEP **0905** (2009) 016 [0903.1218].
[18] A. Denner and S. Dittmaier, Nucl. Phys. B **734** (2006) 62 [hep-ph/0509141].
[19] T. Binoth, J. P. Guillet, G. Heinrich, E. Pilon and C. Schubert, JHEP **0510** (2005) 015 [hep-ph/0504267].
[20] Z. Bern, L. J. Dixon, D. C. Dunbar and D. A. Kosower, Nucl. Phys. B **425** (1994) 217 [hep-ph/9403226].
[21] R. Britto, F. Cachazo and B. Feng, Nucl. Phys. B **725** (2005) 275 [hep-th/0412103].
[22] R. Britto, B. Feng and P. Mastrolia, Phys. Rev. D **73** (2006) 105004 [hep-ph/0602178].
[23] P. Mastrolia, Phys. Lett. B **644** (2007) 272 [hep-th/0611091].
[24] D. Forde, Phys. Rev. D **75** (2007) 125019 [0704.1835].
[25] G. Ossola, C. G. Papadopoulos and R. Pittau, Nucl. Phys. B **763** (2007) 147 [hep-ph/0609007].
[26] G. Ossola, C. G. Papadopoulos and R. Pittau, JHEP **0805** (2008) 004 [0802.1876].
[27] R. K. Ellis, W. T. Giele and Z. Kunszt, JHEP **0803** (2008) 003 [0708.2398].
[28] W. T. Giele, Z. Kunszt and K. Melnikov, JHEP **0804** (2008) 049 [0801.2237].
[29] R. K. Ellis, W. T. Giele, Z. Kunszt and K. Melnikov, Nucl. Phys. B **822** (2009) 270 [0806.3467].
[30] T. Gleisberg and F. Krauss, Eur. Phys. J. C **53** (2008) 501 [0709.2881].
[31] R. Frederix, T. Gehrmann and N. Greiner, JHEP **0809** (2008) 122 [0808.2128].
[32] R. Frederix, T. Gehrmann and N. Greiner, JHEP **1006** (2010) 086 [1004.2905].
[33] R. Frederix, S. Frixione, F. Maltoni and T. Stelzer, JHEP **0910** (2009) 003 [0908.4272].
[34] M. Czakon, C. G. Papadopoulos and M. Worek, JHEP **0908** (2009) 085 [0905.0883].
[35] M. H. Seymour and C. Tevlin, 0803.2231.
[36] K. Hasegawa, S. Moch and P. Uwer, 0911.4371.
[37] J. M. Campbell and R. K. Ellis, Phys. Rev. D **60** (1999) 113006 [hep-ph/9905386].
[38] J. M. Campbell and R. K. Ellis, Phys. Rev. D **65** (2002) 113007 [hep-ph/0202176].
[39] Z. Nagy, Phys. Rev. D **68** (2003) 094002 [hep-ph/0307268].
[40] T. Binoth, J. P. Guillet, G. Heinrich, E. Pilon and T. Reiter, Comput. Phys. Commun. **180** (2009) 2317 [0810.0992].
[41] C. F. Berger *et al.*, Phys. Rev. D **78** (2008) 036003 [0803.4180].
[42] G. Ossola, C. G. Papadopoulos and R. Pittau, JHEP **0803** (2008) 042 [0711.3596].
[43] W. T. Giele and G. Zanderighi, JHEP **0806** (2008) 038 [0805.2152].
[44] P. Mastrolia, G. Ossola, T. Reiter and F. Tramontano, 1006.0710.
[45] W. Giele, Z. Kunszt and J. Winter, 0911.1962.
[46] A. Lazopoulos, 0911.5241.
[47] S. Dittmaier, S. Kallweit and P. Uwer, Phys. Rev. Lett. **100** (2008) 062003 [0710.1577].
[48] S. Dittmaier, S. Kallweit and P. Uwer, Nucl. Phys. B **826** (2010) 18 [0908.4124].
[49] J. M. Campbell, R. Keith Ellis and G. Zanderighi, JHEP **0712** (2007) 056 [0710.1832].

[50] T. Binoth, T. Gleisberg, S. Karg, N. Kauer and G. Sanguinetti, Phys. Lett. B **683** (2010) 154 [0911.3181].

[51] F. Campanario, C. Englert, M. Spannowsky and D. Zeppenfeld, Europhys. Lett. **88** (2009) 11001 [0908.1638].

[52] F. Campanario, C. Englert, S. Kallweit, M. Spannowsky and D. Zeppenfeld, JHEP **1007** (2010) 076 [1006.0390].

[53] J. M. Campbell, R. K. Ellis and G. Zanderighi, JHEP **0610** (2006) 028 [hep-ph/0608194].

[54] S. Badger, E. W. Nigel Glover, P. Mastrolia and C. Williams, JHEP **1001** (2010) 036 [0909.4475].

[55] S. Badger, J. M. Campbell, R. K. Ellis and C. Williams, JHEP **0912** (2009) 035 [0910.4481].

[56] J. M. Campbell, R. K. Ellis and C. Williams, Phys. Rev. D **81** (2010) 074023 [1001.4495].

[57] A. Lazopoulos, T. McElmurry, K. Melnikov and F. Petriello, Phys. Lett. B **666** (2008) 62 [0804.2220].

[58] A. Lazopoulos, K. Melnikov and F. Petriello, Phys. Rev. D **76** (2007) 014001 [hep-ph/0703273].

[59] T. Binoth, G. Ossola, C. G. Papadopoulos and R. Pittau, JHEP **0806** (2008) 082 [0804.0350].

[60] V. Hankele and D. Zeppenfeld, Phys. Lett. B **661** (2008) 103 [0712.3544].

[61] F. Campanario, V. Hankele, C. Oleari, S. Prestel and D. Zeppenfeld, Phys. Rev. D **78** (2008) 094012 [0809.0790].

[62] G. Bozzi, F. Campanario, V. Hankele and D. Zeppenfeld, Phys. Rev. D **81** (2010) 094030 [0911.0438].

[63] K. Arnold *et al.*, Comput. Phys. Commun. **180** (2009) 1661 [0811.4559].

[64] A. Bredenstein, A. Denner, S. Dittmaier and S. Pozzorini, JHEP **0808** (2008) 108 [0807.1248].

[65] A. Bredenstein, A. Denner, S. Dittmaier and S. Pozzorini, Phys. Rev. Lett. **103** (2009) 012002 [0905.0110].

[66] A. Bredenstein, A. Denner, S. Dittmaier and S. Pozzorini, JHEP **1003** (2010) 021 [1001.4006].

[67] G. Bevilacqua, M. Czakon, C. G. Papadopoulos, R. Pittau and M. Worek, JHEP **0909** (2009) 109 [0907.4723].

[68] G. Bevilacqua, M. Czakon, C. G. Papadopoulos and M. Worek, Phys. Rev. Lett. **104** (2010) 162002 [1002.4009].

[69] T. Binoth, N. Greiner, A. Guffanti, J. Reuter, J. P. Guillet and T. Reiter, Phys. Lett. B **685** (2010) 293 [0910.4379].

[70] R. Keith Ellis, K. Melnikov and G. Zanderighi, Phys. Rev. D **80** (2009) 094002 [0906.1445].

[71] C. F. Berger *et al.*, Phys. Rev. Lett. **102** (2009) 222001 [0902.2760].

[72] C. F. Berger *et al.*, Phys. Rev. D **80** (2009) 074036 [0907.1984].

[73] C. F. Berger *et al.*, 1004.1659.

[74] K. Melnikov and G. Zanderighi, Phys. Rev. D **81** (2010) 074025 [0910.3671].

[75] C. W. Bauer and B. O. Lange, 0905.4739.

[76] T. Binoth and G. Heinrich, Nucl. Phys. B **585** (2000) 741 [hep-ph/0004013].

[77] T. Binoth and G. Heinrich, Nucl. Phys. B **693** (2004) 134 [hep-ph/0402265].

[78] C. Anastasiou, K. Melnikov and F. Petriello, Phys. Rev. D **69** (2004) 076010 [hep-ph/0311311].

[79] A. Gehrmann-De Ridder, T. Gehrmann and E. W. N. Glover, JHEP **0509** (2005) 056 [hep-ph/0505111].

[80] S. Catani and M. Grazzini, Phys. Rev. Lett. **98** (2007) 222002 [hep-ph/0703012].

[81] G. Somogyi and Z. Trocsanyi, JHEP **0808** (2008) 042 [0807.0509].

[82] U. Aglietti, V. Del Duca, C. Duhr, G. Somogyi and Z. Trocsanyi, JHEP **0809** (2008) 107 [0807.0514].

[83] P. Bolzoni, S. O. Moch, G. Somogyi and Z. Trocsanyi, JHEP **0908** (2009) 079 [0905.4390].

[84] M. Czakon, 1005.0274.

[85] C. Anastasiou, K. Melnikov and F. Petriello, Phys. Rev. Lett. **93** (2004) 262002 [hep-ph/0409088].

[86] C. Anastasiou, K. Melnikov and F. Petriello, Nucl. Phys. B **724** (2005) 197 [hep-ph/0501130].

[87] C. Anastasiou, G. Dissertori and F. Stöckli, JHEP **0709** (2007) 018 [0707.2373].

[88] M. Grazzini, JHEP **0802** (2008) 043 [0801.3232].

[89] D. de Florian and M. Grazzini, Phys. Lett. B **674** (2009) 291 [0901.2427].

[90] C. Anastasiou, G. Dissertori, M. Grazzini, F. Stockli and B. R. Webber, JHEP **0908** (2009) 099 [0905.3529].

[91] R. V. Harlander and K. J. Ozeren, JHEP **0911** (2009) 088 [0909.3420].

[92] R. V. Harlander, H. Mantler, S. Marzani and K. J. Ozeren, Eur. Phys. J. C **66** (2010) 359 [0912.2104].

[93] A. Pak, M. Rogal and M. Steinhauser, JHEP **1002** (2010) 025 [0911.4662].

[94] C. Anastasiou, R. Boughezal and F. Petriello, JHEP **0904** (2009) 003 [0811.3458].

[95] R. V. Harlander and M. Steinhauser, Phys. Lett. B **574** (2003) 258 [hep-ph/0307346].

[96] R. V. Harlander and M. Steinhauser, JHEP **0409** (2004) 066 [hep-ph/0409010].

[97] G. Degrassi and P. Slavich, Nucl. Phys. B **805** (2008) 267 [0806.1495].

[98] C. Anastasiou, S. Beerli and A. Daleo, Phys. Rev. Lett. **100** (2008) 241806 [0803.3065].

[99] M. Muhlleitner, H. Rzehak and M. Spira, JHEP **0904** (2009) 023 [0812.3815].

[100] C. Anastasiou, R. Boughezal and E. Furlan, JHEP **1006** (2010) 101 [1003.4677].

[101] R. Boughezal and F. Petriello, Phys. Rev. D **81** (2010) 114033 [1003.2046].

[102] P. Bolzoni, F. Maltoni, S. O. Moch and M. Zaro, Phys. Rev. Lett. **105** (2010) 011801 [1003.4451].

[103] W. Hollik, T. Plehn, M. Rauch and H. Rzehak, Phys. Rev. Lett. **102** (2009) 091802 [0804.2676].

[104] K. Melnikov and F. Petriello, Phys. Rev. Lett. **96** (2006) 231803 [hep-ph/0603182].

[105] K. Melnikov and F. Petriello, Phys. Rev. D **74** (2006) 114017 [hep-ph/0609070].

[106] S. Catani, L. Cieri, G. Ferrera, D. de Florian and M. Grazzini, Phys. Rev. Lett. **103** (2009) 082001 [0903.2120].

[107] S. Catani, G. Ferrera and M. Grazzini, JHEP **1005** (2010) 006 [1002.3115].

[108] A. Gehrmann-De Ridder, T. Gehrmann, E. W. N. Glover and G. Heinrich, JHEP **0711** (2007) 058 [0710.0346].

[109] A. Gehrmann-De Ridder, T. Gehrmann, E. W. N. Glover and G. Heinrich, JHEP **0712** (2007) 094 [0711.4711].

[110] A. Gehrmann-De Ridder, T. Gehrmann, E. W. N. Glover and G. Heinrich, Phys. Rev. Lett. **100** (2008) 172001 [0802.0813].

[111] A. Gehrmann-De Ridder, T. Gehrmann, E. W. N. Glover and G. Heinrich, JHEP **0905** (2009) 106 [0903.4658].

[112] S. Weinzierl, Phys. Rev. Lett. **101** (2008) 162001 [0807.3241].

[113] S. Weinzierl, JHEP **0906** (2009) 041 [0904.1077].

[114] S. Weinzierl, JHEP **0907** (2009) 009 [0904.1145].

[115] S. Weinzierl, Phys. Rev. D **80** (2009) 094018 [0909.5056].

[116] S. Catani, L. Trentadue, G. Turnock and B. R. Webber, Nucl. Phys. B **407** (1993) 3.

[117] T. Gehrmann, G. Luisoni and H. Stenzel, Phys. Lett. B **664** (2008) 265 [0803.0695].

[118] T. Becher and M. D. Schwartz, JHEP **0807** (2008) 034 [0803.0342].

[119] R. Abbate, M. Fickinger, A. H. Hoang, V. Mateu and I. W. Stewart, 1006.3080.

[120] Y. T. Chien and M. D. Schwartz, 1005.1644.

[121] Y. L. Dokshitzer, G. Marchesini and B. R. Webber, Nucl. Phys. B **469** (1996) 93 [hep-ph/9512336].

[122] R. A. Davison and B. R. Webber, Eur. Phys. J. C **59** (2009) 13 [0809.3326].

[123] T. Gehrmann, M. Jaquier and G. Luisoni, Eur. Phys. J. C **67** (2010) 57 [0911.2422].

[124] G. Dissertori, A. Gehrmann-De Ridder, T. Gehrmann, E. W. N. Glover, G. Heinrich and H. Stenzel, JHEP **0802** (2008) 040 [0712.0327].

[125] S. Bethke, S. Kluth, C. Pahl and J. Schieck [JADE Collaboration], Eur. Phys. J. C **64** (2009) 351 [0810.1389].

[126] G. Dissertori, A. Gehrmann-De Ridder, T. Gehrmann, E. W. N. Glover, G. Heinrich, G. Luisoni and H. Stenzel, JHEP **0908** (2009) 036 [0906.3436].

[127] G. Dissertori, A. Gehrmann-De Ridder, T. Gehrmann, E. W. N. Glover, G. Heinrich and H. Stenzel, Phys. Rev. Lett. **104** (2010) 072002 [0910.4283].

[128] A. Denner, S. Dittmaier, T. Gehrmann and C. Kurz, Phys. Lett. B **679** (2009) 219 [0906.0372].

[129] A. Denner, S. Dittmaier, T. Gehrmann and C. Kurz, Nucl. Phys. B **836** (2010) 37 [1003.0986].

[130] A. Denner, S. Dittmaier, T. Kasprzik and A. Muck, JHEP **0908** (2009) 075 [0906.1656].

[131] T. Gehrmann and E. W. N. Glover, Phys. Lett. B **676** (2009) 146 [0904.2665].

[132] E. W. N. Glover and J. Pires, JHEP **1006** (2010) 096 [1003.2824].

[133] A. Daleo, A. Gehrmann-De Ridder, T. Gehrmann and G. Luisoni, JHEP **1001** (2010) 118 [0912.0374].

[134] R. Boughezal, A. Gehrmann-De Ridder and M. Ritzmann, **PoS** (RADCOR2009) 052 [1001.2396].

[135] M. Czakon, A. Mitov and S. Moch, Phys. Lett. B **651** (2007) 147 [0705.1975].

[136] M. Czakon, A. Mitov and S. Moch, Nucl. Phys. B **798** (2008) 210 [0707.4139].

[137] M. Czakon, Phys. Lett. B **664** (2008) 307 [0803.1400].

[138] R. Bonciani, A. Ferroglia, T. Gehrmann, D. Maître and C. Studerus, JHEP **0807** (2008) 129 [0806.2301].

[139] R. Bonciani, A. Ferroglia, T. Gehrmann and C. Studerus, JHEP **0908** (2009) 067 [0906.3671].

[140] J. G. Körner, Z. Merebashvili and M. Rogal, Phys. Rev. D **77** (2008) 094011 [0802.0106].

[141] C. Anastasiou and S. M. Aybat, Phys. Rev. D **78** (2008) 114006 [0809.1355].

[142] B. Kniehl, Z. Merebashvili, J. G. Körner and M. Rogal, Phys. Rev. D **78** (2008) 094013 [0809.3980].

[143] S. Dittmaier, P. Uwer and S. Weinzierl, Phys. Rev. Lett. **98** (2007) 262002 [hep-ph/0703120].

[144] S. Dittmaier, P. Uwer and S. Weinzierl, Eur. Phys. J. C **59** (2009) 625 [0810.0452].

[145] K. Melnikov and M. Schulze, 1004.3284.

[146] M. Seymour, these proceedings.

[147] S. Frixione and B. R. Webber, JHEP **0206** (2002) 029 [hep-ph/0204244].

[148] S. Frixione, P. Nason and C. Oleari, JHEP **0711** (2007) 070 [0709.2092].

[149] C. D. White, S. Frixione, E. Laenen and F. Maltoni, JHEP **0911** (2009) 074 [0908.0631].

[150] C. Weydert *et al.*, Eur. Phys. J. C **67** (2010) 617 [0912.3430].

[151] S. Alioli, P. Nason, C. Oleari and E. Re, JHEP **0909** (2009) 111 [0907.4076].

[152] S. Alioli, P. Nason, C. Oleari and E. Re, JHEP **0904** (2009) 002 [0812.0578].

[153] S. Alioli, P. Nason, C. Oleari and E. Re, JHEP **1006** (2010) 043 [1002.2581].

[154] S. Catani, Phys. Lett. B **427** (1998) 161 [hep-ph/9802439].

[155] G. Sterman and M. E. Tejeda-Yeomans, Phys. Lett. B **552** (2003) 48 [hep-ph/0210130].

[156] S. Moch, J. A. M. Vermaseren and A. Vogt, Nucl. Phys. B **726** (2005) 317 [hep-ph/0506288].

[157] C. W. Bauer, S. Fleming, D. Pirjol and I. W. Stewart, Phys. Rev. D **63** (2001) 114020 [hep-ph/0011336].

[158] T. Becher and M. Neubert, Phys. Rev. Lett. **102** (2009) 162001 [0901.0722].

[159] E. Gardi and L. Magnea, JHEP **0903** (2009) 079 [0901.1091].

[160] T. Becher and M. Neubert, JHEP **0906** (2009) 081 [0903.1126].

[161] L. J. Dixon, E. Gardi and L. Magnea, JHEP **1002** (2010) 081 [0910.3653].

[162] G. Sterman, Nucl. Phys. B **281** (1987) 310.

[163] S. Catani and L. Trentadue, Nucl. Phys. B **327** (1989) 323.

[164] A. Idilbi, X. d. Ji and F. Yuan, Nucl. Phys. B **753** (2006) 42 [hep-ph/0605068].

[165] T. Becher, M. Neubert and B. D. Pecjak, JHEP **0701** (2007) 076 [hep-ph/0607228].
[166] V. Ahrens, T. Becher, M. Neubert and L. L. Yang, Eur. Phys. J. C **62** (2009) 333 [0809.4283].
[167] T. Becher and M. D. Schwartz, JHEP **1002** (2010) 040 [0911.0681].
[168] I. W. Stewart, F. J. Tackmann and W. J. Waalewijn, Phys. Rev. D **81** (2010) 094035 [0910.0467].
[169] I. W. Stewart, F. J. Tackmann and W. J. Waalewijn, 1002.2213.
[170] A. Ferroglia, M. Neubert, B. D. Pecjak and L. L. Yang, JHEP **0911** (2009) 062 [0908.3676].
[171] M. Beneke, P. Falgari and C. Schwinn, Nucl. Phys. B **828** (2010) 69 [0907.1443].
[172] S. Moch and P. Uwer, Phys. Rev. D **78** (2008) 034003 [0804.1476].
[173] N. Kidonakis and R. Vogt, Phys. Rev. D **78** (2008) 074005 [0805.3844].
[174] M. Czakon, A. Mitov and G. Sterman, Phys. Rev. D **80** (2009) 074017 [0907.1790].
[175] M. Czakon and A. Mitov, Phys. Lett. B **680** (2009) 154 [0812.0353].
[176] V. Ahrens, A. Ferroglia, M. Neubert, B. D. Pecjak and L. L. Yang, 1003.5827.
[177] M. Beneke, M. Czakon, P. Falgari, A. Mitov and C. Schwinn, Phys. Lett. B **690** (2010) 483 [0911.5166].
[178] M. Aliev, H. Lacker, U. Langenfeld, S. Moch, P. Uwer and M. Wiedermann, 1007.1327.

Monte Carlo for the LHC

Michael H. Seymour

School of Physics and Astronomy, University of Manchester, Manchester, M13 9PL, U.K.

DOI: http://dx.doi.org/10.3204/DESY-PROC-2010-01/24

I review the status of the general-purpose Monte Carlo event generators for the LHC, with emphasis on areas of recent physics developments. There has been great progress, especially in multi-jet simulation, but I mention some question marks that have recently arisen.

1 Introduction

There are three general-purpose Monte Carlo event generators designed for use at the LHC, Pythia [1], Herwig++ [2] and Sherpa [3]. The first two are built on the heritage of their fortran predecessors [4,5] while Sherpa has been constructed as a new C++ project from the beginning. Although there are of course many differences in the details of the implementations, they largely share a common approach to the structure of LHC events, which I describe briefly here to set the scene and the notation.

Most of the emphasis is on the simulation of events that contain a *hard process*, although I will return to mention minimum bias collisions later. Since the hard interaction is generally the process of interest it acts as the trigger around which the simulation of the whole event is built. In the previous generation of simulation these were almost always $2 \to 2$ processes, but one of the largest areas of development in recent years, which I will describe in detail below, has been the inclusion of higher order corrections, both in terms of multi-parton tree-level processes and also NLO corrections to the low parton multiplicity processes.

The partons involved in the hard process are coloured and, just as accelerated charges in QED radiate photons, annihilated, scattered or produced coloured partons radiate gluons. Now, however, unlike in QED, since the gluons themselves are coloured, they radiate further gluons. The hard process is therefore accompanied by an extended shower of additional radiation, which is simulated with a *parton shower* algorithm. These are formulated as a probabilistic evolution in emission scale, from the high scale of the hard interaction downwards to lower momentum scales. The outgoing partons are evolved forwards to produce a shower of accompanying radiation and the incoming partons are evolved backwards to ask, progressively, what is the probability distribution for radiation to accompany this parton on its way in to the hard interaction. Different algorithms differ in their choice of evolution variable and can generally be split into two classes: parton-based, as a sequence of $1 \to 2$ splittings with suitably-defined (respecting the coherence of radiation from different emitters) evolution variable and initial condition; and dipole-based, in which colour-connected pairs of partons emit radiation as a $2 \to 3$ splitting, with the colour structure taking care of the coherence condition.

As the parton shower is governed by perturbative emission probabilities with the strong

coupling evaluated at the evolution scale, it is not valid at scales below about 1 GeV. One therefore terminates the evolution and invokes a non-perturbative *hadronization model* for the transition from a partonic to a hadronic final state. Here again the partonic colour structure is crucial in setting the initial conditions for the hadronization and only models that respect this structure, the string (Pythia) and cluster (Herwig and Sherpa) models, are in current use.

In a hadronic collision, a partonic constituent from each hadron is involved in the hard process and its accompanying parton shower. The colliding hadrons are highly Lorentz-contracted discs and in a space-time picture completely overlap each other. They therefore have a high probability to have additional interactions, producing hadrons throughout the event, in addition to those from the hadronization of the hard process. This is known as the *underlying event* and is modelled as additional independent parton–parton interactions (multi-parton scattering models), as a soft non-perturbative interaction of the remnants as a whole (soft underlying event models), or as a mixture of the two. In fact, it is essential to include a semi-hard multi-parton interaction component to fit the HERA and Tevatron data. Recent progress in underlying event physics has focussed on the colour structure of the additional interactions and the colour connections between them and the primary process and therefore simulation of the underlying event is typically interleaved with the backward evolution of the incoming partons.

Finally, many of the hadrons produced in the hadronization of the hard and secondary processes are unstable resonances and their decays must be simulated, together with other decaying particles such as the tau lepton (decays of short-lived particles like the top, Higgs boson or SUSY particles can be thought of as part of the hard process and are typically simulated early in the event). This relatively unglamorous end of event generation has also been the subject of considerable recent progress.

Simulation of minimum bias and diffractive collisions in which there is no hard process is closely related to the underlying event and one typically uses phenomenological models to describe the total rate and its sub-division into elastic, single- and double-diffractive and inelastic components, with the multi-jet models tuned to underlying event data used to simulate the inelastic component.

In this talk I will give an outline of some of the most important areas of recent physics progress. In particular I will describe several developments in the important area of matching parton showers with higher order matrix elements, as well as a couple of question marks that have recently arisen within this area. I will describe more briefly developments in the simulation of spin correlations, of soft interactions and of secondary decays. Finally I will give brief status reports of the three general-purpose event generator projects and of the MCnet projects for generator-independent generator validation and tuning.

2 Recent physics progress

2.1 Merging parton showers with higher order matrix elements

Parton showers are built on approximations to the full QCD matrix elements for multi-parton emission, expanded around the soft and collinear limits that dominate. They therefore perform well for the bulk of emission. The colour coherence of emission between different partons in an event is crucial for this, as shown in the famous CDF Run 1 study, [6]. Three-jet events were selected with hard two-jet kinematics, with the hardest jet being above 110 GeV and a soft third jet only having to be above 10 GeV. The distributions of this third jet therefore clearly

map out the radiation of the hard $2 \to 2$ scattering system. In particular, CDF's careful study showed that coherence due to the colour connections between initial- and final-state partons was crucial to get these distributions right. HERWIG, which had this coherence built in, and a version of Pythia specially modified to include it (which subsequently became the default) were able to fit the data, while the default version of Pythia, which included colour coherence only in final-state emission, and ISAJET, which doesn't include it at all, were not even able to qualitatively describe the data. Despite the fact that this analysis is uncorrected and more than fifteen years old, it is still an extremely important one for Monte Carlo understanding and validation and we would dearly like to have an update from Run 2 as well of course as looking forward to similar analyses at the LHC.

Despite the success of modern parton shower algorithms in describing the bulk of emissions, there are many event generator applications in which multiple hard well-separated jets must be simulated well. The most obvious of these is in searches for new physics where one is often interested in final states with many jets and where, by definition, one designs the cuts to remove the bulk of emission so that all that remains is the hard well-separated tail. These regions are equally important for the top mass measurement, QCD studies of the multi-jet regime and many other applications. The rate and distribution of such jets are reasonably well described by the tree-level matrix element for the given jet multiplicity, but parton showers are needed to describe the internal structure of the jets and the full hadronic final state. Moreover it is not straightforward to merge samples with different jet multiplicities without double-counting with subsequent emission in the shower. Clearly one wishes to combine the benefits of the tree-level matrix element and parton shower approaches, and methods to do this are known as multi-jet matching.

At the same time, there are also applications where one wishes to have an event sample with next-to-leading order normalization, not least, again, for new particle searches, but also for many electroweak and top quark analyses. Attempts to match parton showers with NLO calculations are known as NLO matching.

Great progress has been made with both multi-jet and NLO matching over the last five years, as I describe in the next two sections, and practical implementations are now available for a wide variety of processes. Most recently, progress has been made in attempts to combine the two approaches together, as I will also describe more briefly.

2.1.1 Multi-jet matching

The problem of merging tree-level matrix element samples with parton showers for several jet multiplicities simultaneously was solved in principle by Catani, Krauss, Kühn and Webber (CKKW) in 2001 [7]. They introduced a matching scale, $k_{T,match}$ and showed that by using matrix elements modified by introducing Sudakov form factors above $k_{T,match}$ and parton showers modified by introducing appropriate phase space vetoes below $k_{T,match}$, one could match the two in such a way that there was no double-counting and the dependence on $k_{T,match}$ could be proved to vanish to next-to-leading logarithmic accuracy.

However, in practical implementations, for example in the study by Mrenna and Richardson [8], it was found that associated distributions typically have discontinuities at $k_{T,match}$ and that the hadron-level results were more $k_{T,match}$-dependent than the parton-level ones. Eventually this was explained as being due to the CKKW method giving the right amount of radiation, as proved, but putting some of it in the wrong place. In particular, attributing some of it to the wrong colour flow, affecting the initial conditions of the hadronization phase.

This problem was solved by Lönnblad [9] for the specific case of k_T-ordered dipole showers and more recently for the general parton shower case by the Sherpa [10] and Herwig++ [11] collaborations following an idea originally proposed by Nason [12] as part of the POWHEG approach described below. The idea is that one should run the parton shower from the lowest multiplicity configuration and to forcibly insert emissions corresponding to the exact kinematics generated by the matrix element event into the appropriate point in the ordering of the shower. The effect is to generate *truncated showers* from the internal lines of the matrix element event, as well as the external lines, and to properly populate the whole of phase space with soft radiation with the correct colour connections.

Results of this modified CKKW method have been compared with data from the Tevatron, for example the CDF W+jets [13] and Z+jets [14] data, in [10, 11]. Rates and distributions of events with up to four jets are well described and the residual matching scale dependence is shown to be very small, with a corresponding uncertainty in the total cross section of only 3%.

2.1.2 NLO matching

In a conventional Monte Carlo implementation of a next-to-leading order calculation, events in the real emission phase space have arbitrarily large positive weights, which are cancelled to give a finite cross section contribution by counter-events that have equally large negative weights but live in the phase space of the Born process. The result is finite for any infrared safe observable, but the procedure is not suitable for implementation into a parton shower, hadronization and detector simulation framework, since any arbitrarily small differences in the subsequent final state of the event and counter-event would spoil the cancellation.

Frixione and Webber showed in 2002 [15] that this problem could be solved to give Monte Carlo events with finite weight distribution, essentially by using an analytical expansion of the parton shower emission probability as the subtraction counter-event term. The result is a set of hard + either 1-jet or 0-jet events to be showered, such that there is no double-counting between the showered 0-jet and generated 1-jet events. Although the weight distributions are finite, they are not positive definite and one typically generates 'almost unweighted' events, i.e. with equal absolute values of weights, but typically around 10% of them negative. This is not a problem of principle, but can be inconvenient for some applications. A more serious problem is the fact that the analytical subtractions have to be calculated for the particular parton shower with which it will be used and, thus far, this MC@NLO method is available for a wide range of processes [16] only for use with the original HERWIG program. With a first implementation for PYTHIA reported in Ref. [17], a full version for both PYTHIA and Herwig++ is expected to appear soon.

However, a potentially more serious problem with the MC@NLO approach was noticed in Ref. [18] and explored in more detail in Ref. [19]. It is that MC@NLO distributions can inherit deficiencies in the underlying shower algorithm. This is most evident in the jet rapidity distributions in which the PYTHIA and especially HERWIG algorithms produce insufficient hard central jets. Although the MC@NLO algorithm corrects this distribution analytically to leading order, all higher orders are directly inherited from the shower. The result, especially in gluon-initiated processes such as $gg \to H$, can be rapidity distributions with significant unphysical 'notches' in them, see for example Fig. 9 of [19].

A second issue with the MC@NLO approach is that it is guaranteed to exactly reproduce the LO "+1-jet" cross section at high enough transverse momentum. This may sound like a good feature, but it turns out that processes for which the K factor is significant, so for which

one definitely wants to use a NLO matching approach, the K factor for the "+1-jet" process is also large, so that the MC@NLO result is significantly below the NLO result for the high-p_t distribution. The most extreme case is again $gg \to H$ where the difference is around a factor of two.

While in both of these cases, MC@NLO is formally correct to the order at which it is defined (NLO for the normalization and LO for the p_t distribution), phenomenologically one might prefer a solution that does not suffer from these effects. This is provided by the POWHEG method proposed by Nason [12] in 2004. It has the advantages that it provides only positive-weight events, that the distribution of hardest emission is entirely determined by the hard matrix element, without inheriting features from the parton shower, and that the entire distribution receives the K factor so, to the extent that the K factors of the inclusive and high-p_t processes are similar, the latter is well described. Finally it is independent of shower algorithm and can be used with any parton shower algorithm that is capable of producing the truncated showers discussed earlier.

The POWHEG method is implemented as a standalone program, also called POWHEG, for an increasingly wide range of processes [19–25]. It has also become the method of choice for NLO matching in the Herwig++ program, which also now comes with built-in POWHEG implementations for Drell-Yan production [26], Higgs production [27] and e^+e^- processes [28], with vector boson fusion, deep inelastic scattering and vector boson pair production including anomalous triple gauge couplings in progress. The deep inelastic scattering implementation in particular allows Herwig++ to describe the energy flow data from the HERA experiments over a wide range of x and Q^2 for the first time.

2.1.3 Towards NLO multi-jet matching

Given the success of multi-jet and NLO matching schemes, it is natural to ask whether they can be combined to produce a multi-jet sample in which each of the jet multiplicities is correct to NLO. Ideas towards this ambitious goal have been described in Ref. [29]. In Ref. [30] the first concrete implementation appeared, only for the case of e^+e^- annihilation. The extension to hadron collisions is considerably more complicated and is yet to appear as a working implementation.

Hamilton and Nason [31] took a more pragmatic approach. Motivated by the large body of validated multi-jet and NLO matching implementations in use, they examined whether it is possible to combine the POWHEG and CKKW approaches to provide a sample of multi-jet events, each calculated using the tree-level multi-parton matrix element combined with the full NLO correction for the Born configuration onto which it is mapped. They succeeded in this and studied implementations for vector boson and top pair production in hadron collisions.

With the progress made in these approaches it seems hopeful that a working NLO multi-jet matching algorithm could be achieved in the near future. It is clear that this would be a major step forward in our ability to simulate LHC final states.

2.1.4 High energy jets

I previously said that parton shower algorithms do well for the bulk of emission, but with the large step up in energy to the LHC, and the consequent opening up of phase space, we should constantly question this statement and check that we are sure. In this and the next section I mention two recent calculations that raise small question marks over our readiness.

Andersen and collaborators [32, 33] have developed a new approach to calculating multi-jet final states, which they call the high energy jet (HEJ) approach. It relies on approximating the all-order QCD matrix elements in a different limit to parton showers, namely the limit of fixed momentum transfer with available scattering energy going to infinity, the limit in which many jets have similar transverse momenta and large rapidity intervals. They show that in this limit, scattering amplitudes factorize into helicity-dependent local terms, coupled by t-channel propagators, which can be constructed in a modular way to arbitrary order. They have working implementations for pure jet processes, W/Z plus jets and Higgs plus jets and have made a thorough phenomenological analysis. As an example, see Fig. 69 of Ref. [34] in which the results are compared with the Sherpa shower with CKKW matching and the NLO calculation in MCFM, for the accompanying jet multiplicity of Higgs plus at least two jet events as a function of the rapidity separation between the two leading jets. For small separations all three calculations agree, but by $\Delta y = 4$, a typical cut used to separate this gluon fusion process from the vector boson fusion process, the HEJ approach is significantly above the other two, predicting an average number of additional jets of order 1. By $\Delta y = 6$, still within the typical region of a VBF analysis, HEJ predicts twice as many additional jets as either CKKW or NLO.

The HEJ code exists as a working Monte Carlo and work is in progress to match it properly with parton showers. It will be extremely interesting to see it further used to validate the existing parton shower and matching algorithms and to see whether it can be developed to become a fully-fledged alternative to multi-jet matching (here one could mention that it is much faster than calculating the full multi-jet matrix elements for high jet multiplicities).

2.1.5 Giant K factors

It has been known for some time that certain observables suffer from anomalously large K factors. In a recent study [36], Rubin, Salam and Sapeta considered this in more detail, isolated the origin of these giant K factors and showed how to calculate the next higher order in such cases to stabilize the perturbative series. In this section I consider the connection with parton shower algorithms.

The archetypal process in which they study this is Z+jets at high p_t (see Fig. 1 of Ref. [36]). In the Z p_t spectrum the K factor is roughly constant at about 1.5 and just about consistent with the scale variation: the LO and NLO bands just touch. However, turning to the p_t distribution of the leading jet, which is equivalent at leading order, they found a K factor that grows linearly with p_t from about 2 at 250 GeV to more than 5 at 1 TeV and that is in no way represented by the scale variation. Finally, they considered an observable that is important for search physics, the total scalar transverse momentum of all jets that accompany the Z, H_T, again equivalent at leading order. They found that the K factor grows exponentially with H_T, from about 10 at 500 GeV to 1000 at 2.5 TeV.

They argued that the large K factor in the leading jet p_t distribution is due to a new kinematic regime opening up, namely the possibility that two hard jets could be produced, accompanied by a relatively soft Z boson. It has long been known that electroweak corrections to high p_t jet production are large and negative owing to an electroweak Sudakov form factor with leading order term $\sim -\alpha_W \log^2 p_t/M_z$. Its counterpart is a real correction to dijet production $\sim +\alpha_W \log^2 p_t/M_z$ due to the emission of a Z boson. This can equivalently be seen, in our case, as a real correction $\sim +\alpha_s \log^2 p_t/M_z$ to the Z+jet process. One can easily check that this dependence is roughly linear over the p_t range considered and of the same order of magnitude as the NLO correction actually seen. Finally, this understanding also allows an understanding

of the huge K factor seen in the H_T distribution: the events with two high-p_t jets and a low-p_t Z, which occur at about the same rate as Z+one-jet events with the same jet p_t, contribute to a value of H_T a factor of two higher than p_t. Since the underlying LO p_t distribution is falling so rapidly, this factor of 2 increase in the value of the observable corresponds to a huge, exponential, increase in the value of the cross section at a given value of the observable.

In Ref. [36] an ingenious method was proposed to calculate higher order corrections to such processes. The main point is that a unitarity-type argument is used to estimate uncalculated loop corrections from calculated tree-level corrections at the same order. This process has similarities with the CKKW idea and I believe this connection could be explored further, but here I confine myself to drawing conclusions for Monte Carlo event generators.

The phase space region responsible for these large corrections corresponds to $2 \to 2$ QCD scattering events in which a Z boson is radiated from an incoming or outgoing quark or anti-quark. Such W and Z parton shower radiation is not implemented in any of the general-purpose generators, despite having been identified as important in Ref. [37]. Although this effect should be reproduced by the CKKW method, for a smooth matching, for systematic studies and for processes in which one does not have a CKKW implementation, one should include as much of the relevant physics in the shower as possible. It is clear that as we enter the LHC era the need to include electroweak boson radiation is more urgent.

2.2 Spin correlations

Spin correlations play an extremely important role in many event generator applications. For example in some searches for BSM physics one is interested in cascade decays in which the angular distributions are crucial for determining the spins of the decaying particles [38]. Sherpa [3] and Herwig++ [2] both have spin correlations built in in a flexible way. The classic example, on which both have been extensively validated, is in tau physics. For example in Higgs decays to $\tau^+\tau^-$ with both taus decaying to a single pion, one can determine whether the Higgs is a scalar or a pseudoscalar from the azimuthal correlation between the two decay planes. Both programs have been shown to reproduce the analytical result [39] well.

2.3 Underlying events/minimum bias/diffraction

These have been a traditional strength of Pythia, with highly developed multi-parton interaction and soft diffraction models. A recent development has been the inclusion of a hard diffractive component [40] into Pythia 8 along similar lines to the older standalone program Pompyt.

Herwig++ and Sherpa are also catching up in this area, with Herwig++ having a multi-parton interaction model developed from the Jimmy program, but with the addition of soft parton–parton scattering allowing simulation of minimum bias collisions for the first time [41–43]. A forthcoming version, with the further addition of colour correlation effects between the scatters, appears to be able to describe the ATLAS data [44], with detailed tuning currently in progress. Sherpa also has a new minimum bias model [3] which looks promising.

2.4 Secondary decays

Both Herwig++ [2, 45] and Sherpa [3] have implemented extensive secondary decay models, with detailed matrix elements for a wide variety of final states and interference with many intermediate resonances, and spin correlations between decays. Moreover, both include QED

corrections in the YFS scheme [46, 47]. The aim is to have at least as good a description as EVTGEN, TAUOLA and PHOTOS in all cases and thereby dispense with the need for such external packages and their results have been extensively validated against these programs.

3 Status reports

I finish my talk with very brief status reports of the main event generator projects. More detailed and up-to-date information can always be obtained from the web sites listed below.

3.1 Pythia

The fortran Pythia 6 program, which has been the workhorse of particle physics for some 25 years is still supported but is not being actively developed. All new physics developments go into the Pythia 8 program. Its core is ready and tuned, with a much more flexible structure to allow for the extensive physics model development that is now ongoing. Some features of Pythia 6 are definitely dropped, for example the old virtuality-ordered showers, and many new features added, for example hard scattering in diffraction, a significantly improved underlying event treatment and wide range of new BSMs.
`http://projects.hepforge.org/pythia`

3.2 Herwig

The current version of the fortran HERWIG program has been effectively frozen for three years, but a bug fix release will appear this summer. All development is now transferred to Herwig++, which has many physics improvements, including improved angular-ordered parton showers, with facilities built in to match with multi-jet or POWHEG hard processes, a slightly improved implementation of the cluster hadronization model, the improvements to soft modelling that allow minimum bias to be simulated for the first time and a very flexible framework for implementing new physics models. One advantage over HERWIG is the fact that each version is released with a globally-fitted parameter set. A new version release is expected this summer and should fully replace HERWIG.
`http://projects.hepforge.org/herwig`

3.3 Sherpa

Unlike the previous two generators, Sherpa was designed as a new generator in C++ from the start. In order to get started it had interfaces to external packages for some components, but by now it is a fully-fledged standalone generator. The emphasis is on multi-jet final states, with two different automated high-multiplicity matrix element generators, an automated subtraction algorithm for NLO calculations, a k_t-ordered dipole shower and built-in CKKW matching. It also has a multi-parton interaction model and a new cluster hadronization model.
`http://projects.hepforge.org/sherpa`

3.4 Tuning and validation

Within MCnet there are two other important Monte Carlo projects, Rivet [48], a generator- and experiment-independent framework for validation of generators against experiment, and

Professor [49], a generator-independent semi-automated parameter tuning tool. With Rivet, the Tevatron experiments are starting to develop a culture, which was prevalent with its predecessor HZTOOL with the HERA experiments, that all important analyses get immediately implemented to ensure that the full details of the analysis get preserved for posterity and the data can be compared to theory calculations and models on an exactly like-for-like basis for years to come. It is essential that this culture continue at the LHC, to ensure that its data gets fully preserved and exploited. As well as its important function in tuning event generator parameters, Professor provides a set of tools for visualizing the data and seeing in real time how it responds to particular combinations of parameter settings.

Both of these tools are being incorporated into the LHC experiments' software frameworks, to ensure that models tuned to the new data continue to describe the existing data, the first time any experiments have done this in such detail.

`http://projects.hepforge.org/rivet`
`http://projects.hepforge.org/professor`

4 Summary

Modern Monte Carlo event generators are highly sophisticated implementations of QCD calculations. They are reliable for a wide variety of observables over a wide range of energy scales and the model-dependent parts widely validated. But the LHC is a truly huge step into the unknown, requiring extensive tuning of soft models and validation of hard evolution. There has been a great deal of progress in describing hard emission more accurately, but, as I have shown, a few small areas where more work is needed.

Acknowledgments

I am grateful to all the other Monte Carlo authors and members of the MCnet network for discussions and input. Thanks especially to Peter Richardson, Peter Skands, Stefan Höche, Frank Siegert, Jeppe Andersen, Gavin Salam and Mathieu Rubin for contributing slides and plots to the talk. This work was supported in part by the European Union FP6 Marie Curie Research Training Network MCnet (contract MRTN-CT-2006-035606).

References

[1] T. Sjöstrand, S. Mrenna and P. Z. Skands, Comput. Phys. Commun. **178** (2008) 852 [arXiv:0710.3820 [hep-ph]].

[2] M. Bähr *et al.*, Eur. Phys. J. C **58** (2008) 639 [arXiv:0803.0883 [hep-ph]].

[3] T. Gleisberg, S. Höche, F. Krauss, M. Schönherr, S. Schumann, F. Siegert and J. Winter, JHEP **0902** (2009) 007 [arXiv:0811.4622 [hep-ph]].

[4] T. Sjöstrand, S. Mrenna and P. Z. Skands, JHEP **0605** (2006) 026 [arXiv:hep-ph/0603175].

[5] G. Corcella *et al.*, JHEP **0101** (2001) 010 [arXiv:hep-ph/0011363].

[6] F. Abe *et al.* [CDF Collaboration], Phys. Rev. D **50** (1994) 5562.

[7] S. Catani, F. Krauss, R. Kühn and B. R. Webber, JHEP **0111** (2001) 063 [arXiv:hep-ph/0109231].

[8] S. Mrenna and P. Richardson, JHEP **0405** (2004) 040 [arXiv:hep-ph/0312274].

[9] L. Lönnblad, JHEP **0205** (2002) 046 [arXiv:hep-ph/0112284].

[10] S. Höche, F. Krauss, S. Schumann and F. Siegert, JHEP **0905** (2009) 053 [arXiv:0903.1219 [hep-ph]].

[11] K. Hamilton, P. Richardson and J. Tully, JHEP **0911** (2009) 038 [arXiv:0905.3072 [hep-ph]].

[12] P. Nason, JHEP **0411** (2004) 040 [arXiv:hep-ph/0409146].

[13] T. Aaltonen *et al.* [CDF Collaboration], Phys. Rev. D **77** (2008) 011108 [arXiv:0711.4044 [hep-ex]].

[14] T. Aaltonen *et al.* [CDF Collaboration], Phys. Rev. Lett. **100** (2008) 102001 [arXiv:0711.3717 [hep-ex]].

[15] S. Frixione and B. R. Webber, JHEP **0206** (2002) 029 [arXiv:hep-ph/0204244].

[16] S. Frixione and B. R. Webber, arXiv:0812.0770 [hep-ph].

[17] P. Torrielli and S. Frixione, JHEP **1004**, 110 (2010) [arXiv:1002.4293 [hep-ph]].

[18] M. L. Mangano, M. Moretti, F. Piccinini and M. Treccani, JHEP **0701** (2007) 013 [arXiv:hep-ph/0611129].

[19] S. Alioli, P. Nason, C. Oleari and E. Re, JHEP **0904**, 002 (2009) [arXiv:0812.0578 [hep-ph]].

[20] S. Frixione, P. Nason and C. Oleari, JHEP **0711**, 070 (2007) [arXiv:0709.2092 [hep-ph]].

[21] S. Alioli, P. Nason, C. Oleari and E. Re, JHEP **0807**, 060 (2008) [arXiv:0805.4802 [hep-ph]].

[22] S. Alioli, P. Nason, C. Oleari and E. Re, JHEP **0909**, 111 (2009) [Erratum-ibid. **1002**, 011 (2010)] [arXiv:0907.4076 [hep-ph]].

[23] P. Nason and C. Oleari, JHEP **1002**, 037 (2010) [arXiv:0911.5299 [hep-ph]].

[24] S. Alioli, P. Nason, C. Oleari and E. Re, JHEP **1006**, 043 (2010) [arXiv:1002.2581 [hep-ph]].

[25] E. Re, arXiv:1007.0498 [hep-ph].

[26] K. Hamilton, P. Richardson and J. Tully, JHEP **0810** (2008) 015 [arXiv:0806.0290 [hep-ph]].

[27] K. Hamilton, P. Richardson and J. Tully, JHEP **0904** (2009) 116 [arXiv:0903.4345 [hep-ph]].

[28] O. Latunde-Dada, Eur. Phys. J. C **58**, 543 (2008) [arXiv:0806.4560 [hep-ph]].

[29] Z. Nagy and D. E. Soper, JHEP **0510** (2005) 024 [arXiv:hep-ph/0503053].

[30] N. Lavesson and L. Lönnblad, JHEP **0812** (2008) 070 [arXiv:0811.2912 [hep-ph]].

[31] K. Hamilton and P. Nason, JHEP **1006** (2010) 039 [arXiv:1004.1764 [hep-ph]].

[32] J. R. Andersen and C. D. White, Phys. Rev. D **78** (2008) 051501 [arXiv:0802.2858 [hep-ph]].

[33] J. R. Andersen and J. M. Smillie, JHEP **1001** (2010) 039 [arXiv:0908.2786 [hep-ph]].

[34] J. R. Andersen, J. Campbell and S. Höche, in [35], pp. 130–132.

[35] T. Binoth *et al.* [SM and NLO Multileg Working Group], arXiv:1003.1241 [hep-ph].

[36] M. Rubin, G. P. Salam and S. Sapeta, arXiv:1006.2144 [hep-ph].

[37] M. H. Seymour, University of Cambridge PhD thesis, 1992.

[38] C. Athanasiou, C. G. Lester, J. M. Smillie and B. R. Webber, JHEP **0608** (2006) 055 [arXiv:hep-ph/0605286].

[39] M. Krämer, J. H. Kuhn, M. L. Stong and P. M. Zerwas, Z. Phys. C **64** (1994) 21 [arXiv:hep-ph/9404280].

[40] S. Navin, arXiv:1005.3894 [hep-ph].

[41] M. Bähr, S. Gieseke and M. H. Seymour, JHEP **0807** (2008) 076 [arXiv:0803.3633 [hep-ph]].

[42] M. Bähr, J. M. Butterworth and M. H. Seymour, JHEP **0901** (2009) 065 [arXiv:0806.2949 [hep-ph]].

[43] M. Bähr, J. M. Butterworth, S. Gieseke and M. H. Seymour, arXiv:0905.4671 [hep-ph].

[44] G. Aad *et al.* [ATLAS Collaboration], Phys. Lett. B **688** (2010) 21 [arXiv:1003.3124 [hep-ex]].

[45] D. Grellscheid and P. Richardson, arXiv:0710.1951 [hep-ph].

[46] M. Schönherr and F. Krauss, JHEP **0812** (2008) 018 [arXiv:0810.5071 [hep-ph]].

[47] K. Hamilton and P. Richardson, JHEP **0607** (2006) 010 [arXiv:hep-ph/0603034].

[48] A. Buckley *et al.*, arXiv:1003.0694 [hep-ph].

[49] A. Buckley, H. Hoeth, H. Lacker, H. Schulz and J. E. von Seggern, Eur. Phys. J. C **65** (2010) 331 [arXiv:0907.2973 [hep-ph]].

Charged particle multiplicities in inelastic pp interactions with ATLAS and the ATLAS Minimum Bias Tune 1

Gerhard Brandt for the ATLAS Collaboration

DESY, Notkestraße 85, 22607 Hamburg, Germany

DOI: http://dx.doi.org/10.3204/DESY-PROC-2010-01/207

Measurements of the charged particle multiplicity produced in proton-proton collisions at the LHC at centre-of-mass energies $\sqrt{s} = 0.9$ TeV and 7 TeV recorded with the ATLAS detector are presented. Distributions are presented for events with at least one charged particle $n_{ch} \geq 1$ in the kinematic range $|\eta| < 2.5$ and $p_T > 500$ MeV. Measurements have also been made in a diffraction-limited region of phase-space $n_{\rm ch} \geq 6$ and used for the production of the first PYTHIA6 tune to LHC data, the ATLAS Minimum Bias Tune 1 (AMBT1).

We present the first measurement of the properties of charged particle production in pp collisions produced at the LHC at centre-of-mass energies of $\sqrt{s} = 0.9$ TeV (corresponding to about $12\mu\text{b}^{-1}$ of integrated luminosity) [1] and $\sqrt{s} = 7$ TeV ($6.8\mu\text{b}^{-1}$) [2]. Such measurements can be used to constrain phenomenological models of soft-hadronic interactions and for predictions at higher centre-of-mass energies. Events with at least one primary charged particle with transverse momentum $p_{\rm T} > 500$ MeV and in the pseudo-rapidity[1] range $|\eta| < 2.5$ are studied. Primary charged particles are defined as charged particles with a mean lifetime $\tau > 0.3 \times 10^{-10}$ s, directly produced in pp interactions or from subsequent decays of particles with a shorter lifetime. The distributions of tracks reconstructed in the ATLAS inner detector were corrected to obtain the particle-level distributions:

$$\frac{1}{N_{\rm ev}} \cdot \frac{{\rm d}N_{\rm ch}}{{\rm d}\eta}, \quad \frac{1}{N_{\rm ev}} \cdot \frac{1}{2\pi p_{\rm T}} \cdot \frac{{\rm d}^2 N_{\rm ch}}{{\rm d}\eta {\rm d}p_{\rm T}}, \quad \frac{1}{N_{\rm ev}} \cdot \frac{{\rm d}N_{\rm ev}}{{\rm d}n_{\rm ch}} \quad \text{and} \quad \langle p_{\rm T} \rangle \text{ vs. } n_{\rm ch},$$

where $N_{\rm ev}$ is the number of events with at least one charged particle inside the selected kinematic range, $N_{\rm ch}$ is the total number of charged particles, $n_{\rm ch}$ is the number of charged particles in an event and $\langle p_{\rm T} \rangle$ is the average $p_{\rm T}$ for a given number of charged particles.

The two most important components of the ATLAS detector [4] for this analysis are the Inner Detector (ID) to reconstruct tracks and the Minimum Bias Trigger Scintillators (MBTS) to trigger events. The 32 MBTS counters are mounted on the inner face of the endcap calorimeter cryostats, covering $2.09 < |\eta| < 3.84$. A hit in at least one of the MBTS is required to trigger an event. Coincidence in both MBTS is not required to avoid having to derive the trigger efficiency using Monte Carlo and therefore introducing a dependence on the modeling of diffraction.The

[1] The ATLAS reference system is a Cartesian right-handed co-ordinate system, with the nominal collision point at the origin. The anti-clockwise beam direction defines the positive z-axis. The polar angle θ is measured with respect to the z-axis. The pseudo-rapidity is defined as $\eta = -\ln\tan(\theta/2)$.

ID consists of a silicon pixel detector, a silicon microstrip detector (SCT) and a transition radiation tracker (TRT). Its coverage corresponds to the pseudo-rapidity range $|\eta| < 2.5$ used in this analysis. Tracks were reconstructed beginning with track seeds in the silicon detectors. Events were required to contain a primary vertex with at least two tracks having $p_T > 150$ MeV. Where available the beam-spot position was used as a constraint in the vertex reconstruction. Tracks used to measure the charged particle multiplity were selected requiring at least one pixel and at least six SCT hits as well as longitudinal and transverse impact parameters with respect to the primary vertex of $\sin\theta \cdot |z_0| < 1.5$ mm and $|d_0| < 1.5$ mm, respectively. Only events with at least one selected track were considered to avoid uncertainties stemming from the Monte Carlo description of events with no charged particles inside the kinematic region.

The track distributions were corrected back to the particle-level by using the inverse of the trigger-, vertex- and track-efficiencies as weights, where the first two were determined in data and the latter from a GEANT4-based full simulation of the ATLAS detector. The charged particle multiplicity was corrected event-by-event using iterative Bayesian unfolding and an additional analytic correction applied to correct for events lost due to trackfinding inefficiency.

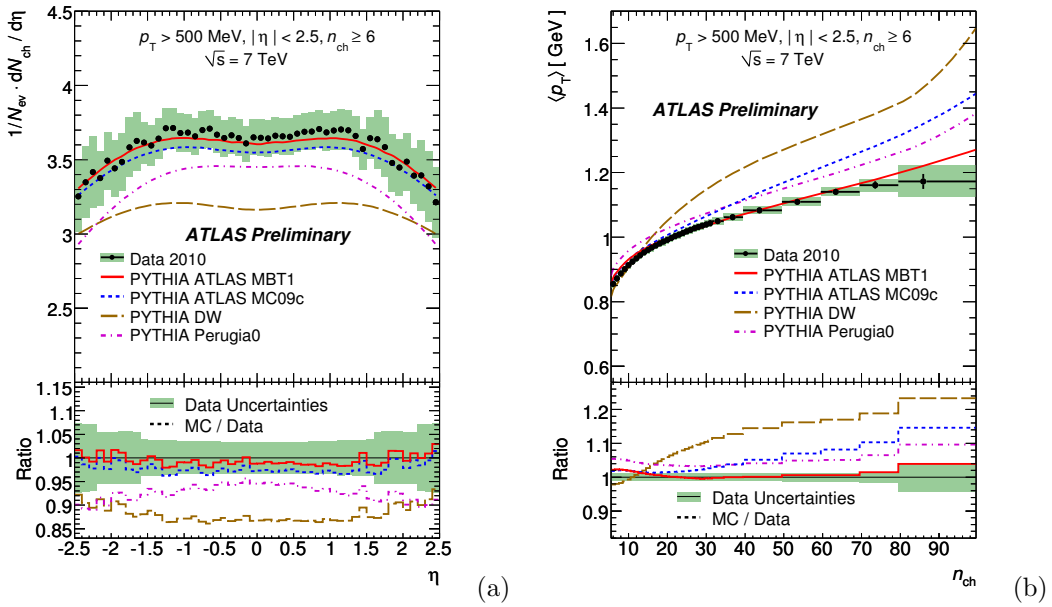

Figure 1: Charged-particle multiplicities for events with $n_{\rm ch} \geq 6$ within the kinematic range $p_T \geq 500$ MeV and $|\eta| < 2.5$. Shown is the charged-particle multiplicity as a function of pseudo-rapidity (a) and the average transverse momentum as a function of the number of charged particles in the event (b). The dots represent the data. The vertical bars represent the statistical uncertainties, while the shaded areas show statistical and systematic uncertainties added in quadrature.

In order to reduce uncertainties stemming from diffractive components in the selected sample, the measurement is further restricted to $n_{ch} \geq 6$. The charged particle multiplicity as function of pseudo-rapidity measured at $\sqrt{s} = 7$ TeV is shown in figure 1 (a) and the average transverse momentum $\langle p_T \rangle$ as function of multiplicity n_{ch} is shown in figure 1 (b). The data are

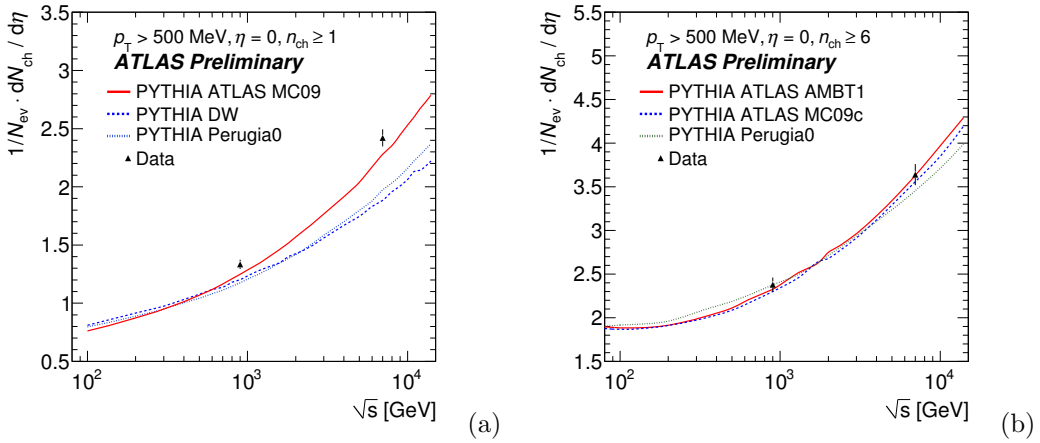

Figure 2: The average charged particle multiplicity per unit of rapidity for $\eta = 0$ for events with $n_{\rm ch} \geq 1$ (a) [2] and in a diffraction-limited phase-space $n_{\rm ch} \geq 6$ (b) [3] within the kinematic range $p_T \geq 500$ MeV and $|\eta| < 2.5$ as a function of the centre of mass energy. In (b) the new ATLAS Minimum Bias Tune 1 is already shown.

compared to predictions from Monte Carlo models, in particular the new AMBT1. This new PYTHIA6 [5] tune is based on the MC09c [6] tune. The data presented here and a measurement of the charged particle flow in different event regions relative to the leading particle [7] are used as input and the PROFESSOR [8] tool is used for the tuning. The tuned parameters are connected to multi-parton interactions and color reconnection of the hadronic final state. The dependence of the average multiplicity at central rapidity on the centre-of-mass energy is shown in figure 2 (a) for $n_{ch} \geq 1$. The measured values are observed to be higher than the predictions from Monte Carlo models. Figure 2 (b) shows the dependence in the diffraction-limited phase-space $n_{ch} \geq 6$. The agreement of data and all Monte Carlo predictions, in particular the AMBT1 tune, is much better here.

References

[1] G. Aad *et al.* [ATLAS Collaboration], "Charged-particle multiplicities in pp interactions at $\sqrt{s} = 900$ GeV measured with the ATLAS detector at the LHC," Phys. Lett. B **688**, 21 (2010) [arXiv:1003.3124 [hep-ex]].

[2] ATLAS Collaboration, "Charged-particle multiplicities in pp interactions at $\sqrt{s} = 7$ TeV measured with the ATLAS detector at the LHC", ATLAS-CONF-2010-024.

[3] ATLAS Collaboration, "Charged particle multiplicities in *pp* interactions at $\sqrt{s} = 0.9$ and 7 TeV in a diffractive limited phase space measured with the ATLAS detector at the LHC and a new PYTHIA6 tune", ATLAS-CONF-2010-031.

[4] G. Aad *et al.* [ATLAS Collaboration], "The ATLAS Experiment at the CERN Large Hadron Collider", JINST 3 (2008) S08003.

[5] T. Sjostrand, S. Mrenna and P. Z. Skands, JHEP **0605**, 026 (2006) [arXiv:hep-ph/0603175].

[6] ATLAS Collaboration, "ATLAS Monte Carlo Tunes for MC09", ATL-PHYS-PUB-2010-002.

[7] [ATLAS Collaboration], "Track-based underlying event measurements in pp collisions at $\sqrt{s} = 900$ GeV and 7 TeV with the ATLAS Detector at the LHC", ATLAS-CONF-2010-029.

[8] A. Buckley, H. Hoeth, H. Lacker, H. Schulz and J. E. von Seggern, Eur. Phys. J. C **65**, 331 (2010) [arXiv:0907.2973 [hep-ph]].

Transverse momentum and pseudorapidity distributions of charged hadrons at CMS

Yen-Jie Lee for the CMS Collaboration

Laboratory for Nuclear Science, MIT, Cambridge, MA 02139-4307, USA

DOI: http://dx.doi.org/10.3204/DESY-PROC-2010-01/208

Charged-hadron transverse-momentum and pseudorapidity distributions in proton-proton collisions at $\sqrt{s} = 7$ TeV are measured with the CMS detector at the LHC. The measured charged-hadron multiplicity per unit of pseudorapidity is $dN_{\rm ch}/d\eta|_{|\eta|<0.5} = 5.78 \pm 0.01$ (stat.) $\pm$ 0.23 (syst.) for non-single-diffractive events, higher than predicted by commonly used models. The mean transverse momentum is measured to be 0.545$\pm$0.005 (stat.)$\pm$ 0.015 (syst.) GeV/c. The results are compared with measurements at lower energies.

Introduction. Measurements of particle yields and kinematic distributions are an essential first step in exploring a new energy regime of particle collisions. Such studies contribute to our understanding of the physics of hadron production, including the relative roles of soft and hard scattering contributions, and help construct a solid foundation for other investigations. In the complicated environment of LHC pp collisions [1], firm knowledge of the rates and distributions of inclusive particle production is needed to distinguish rare signal events from the much larger backgrounds of soft hadronic interactions. They will also serve as points of reference for the measurement of nuclear-medium effects in Pb-Pb collisions at LHC. Soft interactions in pp collisions are commonly classified as elastic scattering, inelastic single-diffractive (SD) dissociation, double-diffractive (DD) dissociation, and inelastic non-diffractive (ND) scattering [2]. All results presented here refer to inelastic non-single-diffractive (NSD) interactions. The measurements reported here are of $dN_{\rm ch}/d\eta$ and $dN_{\rm ch}/dp_T$ in the $|\eta| < 2.4$ range [3] and closely follow our previous analysis at centre-of-mass energies of $\sqrt{s} = 0.9$ and 2.36 TeV [4]. The data for this study are drawn from an integrated luminosity of 1.1 μb^{-1} recorded with the Compact Muon Solenoid (CMS) experiment [5] during the first hour of the LHC operation at $\sqrt{s} = 7$ TeV. These results are the highest centre-of-mass energy measurements of the $dN_{\rm ch}/d\eta$ and $dN_{\rm ch}/dp_T$ distributions conducted at a particle collider.

Experimental methods. A detailed description of the CMS experiment can be found in Ref. [5]. The detectors used for the analysis are the pixel and silicon-strip tracker (SST), covering the region $|\eta| < 2.5$ and immersed in a 3.8 T axial magnetic field. The pixel tracker consists of three barrel layers and two end-cap disks at each barrel end. The forward calorimeter (HF), which covers the region $2.9 < |\eta| < 5.2$, was also used for event selection. The detailed Monte Carlo simulation (MC) of the CMS detector response is based on GEANT4 [6]. Any hit in the beam scintillator counters (BSC, $3.23 < |\eta| < 4.65$) coinciding with colliding proton bunches was used for triggering the data acquisition. A sample mostly populated with NSD events was selected by requiring a primary vertex (PV) to be reconstructed with the tracker [7], together with at least one HF tower in each end with more than 3 GeV total energy. Beam-halo and other beam-background events were rejected as described in Ref. [4]. The fraction of

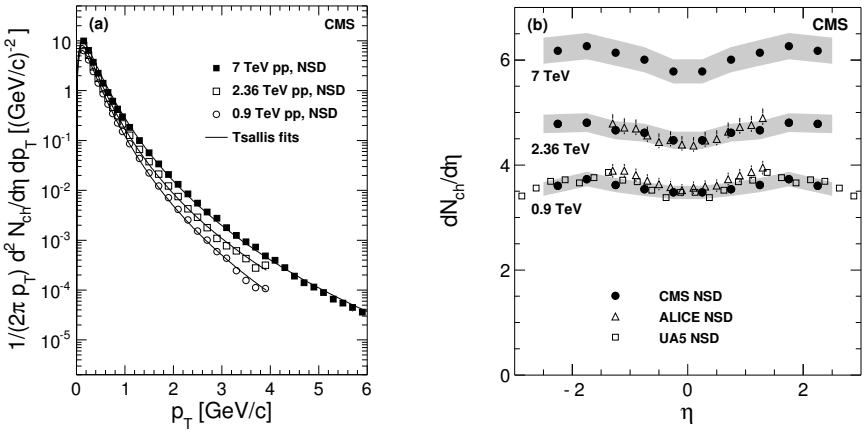

Figure 1: (a) Charged-hadron yield in the range $|\eta| < 2.4$ in NSD events as a function of p_T. (b) Distributions of $dN_{ch}/d\eta$, averaged over the three measurement methods and compared with data from UA5 [15] ($p\bar{p}$, with statistical errors only) and ALICE [17] (with systematic uncertainties). The shaded band shows systematic uncertainties of the CMS data. The CMS and UA5 data are averaged over negative and positive values of η.

background events in the data after selection is less than 2×10^{-5}. 55k events satisfying the selection criteria are selected for analysis.

The event selection efficiency was estimated with simulated events using the PYTHIA [8, 9] and PHOJET [10, 11] event generators. At $\sqrt{s} = 7$ TeV, the fraction of SD (DD) events in the selected data sample, estimated with PYTHIA and PHOJET, are 6.8% (5.8%) and 5.0% (3.8%), respectively. The overall correction for the selection efficiency of NSD processes and for the fraction of SD events remaining in the data sample lowers the measured charged-particle multiplicity by 6% compared with the uncorrected distribution.

The $dN_{\rm ch}/d\eta$ distributions were obtained with three methods, based on counting the following quantities: (i) clusters in the barrel part of the pixel detector; (ii) pixel tracklets composed of pairs of clusters in different pixel barrel layers; and (iii) tracks reconstructed in the full tracker volume. The third method also allows a measurement of the $dN_{\rm ch}/dp_T$ distribution. The three methods are sensitive to particles down to p_T values of about 30, 50, and 100 MeV/c, respectively. The measurements were corrected for the geometrical acceptance, efficiency, fake and duplicate tracks, low-p_T particles curling in the axial magnetic field, decay products of long-lived hadrons, photon conversions and inelastic hadronic interactions in the detector material. The PYTHIA parameter set from Ref. [9] was chosen to determine the corrections.

Results. For the measurement of the $dN_{\rm ch}/dp_T$ distribution, charged-particle tracks with p_T in excess of 0.1 GeV/c were used in 12 different $|\eta|$ bins, from 0 to 2.4. The Tsallis parametrization [12, 13, 14],

$$E\frac{d^3N_{\rm ch}}{dp^3} = \frac{1}{2\pi p_T}\frac{E}{p}\frac{d^2N_{\rm ch}}{d\eta\, dp_T} = C\frac{dN_{\rm ch}}{dy}\left(1+\frac{E_{\rm T}}{nT}\right)^{-n}, \qquad (1)$$

was fitted to the data. The p_T spectrum of charged hadrons is shown in Fig. 1. The average p_T (extrapolated to $p_T = 0$) is $\langle p_T \rangle = 0.545 \pm 0.005$ (stat.) ± 0.015 (syst.) GeV/c.

Experimental uncertainties related to the trigger and event selection are common to all the analysis methods. The total event selection uncertainty, including the SD fraction and the selection efficiency of the BSC and HF, was found to be 3.5%. Additional 3% and 2% uncertainties were assigned to the tracklet and track reconstruction algorithm efficiencies, respectively. All other uncertainties are identical to those listed in Ref. [4]. The $dN_{\rm ch}/d\eta$ measurements based on tracklet method were repeated on a separate data sample without magnetic field, for which almost no p_T extrapolation is needed, and gave results consistent within 1.5%. The final systematic uncertainties for the pixel counting, tracklet, and track methods were found to be 5.7%, 4.6%, and 4.3%, respectively, and are strongly correlated.

The $dN_{\rm ch}/d\eta$ distributions from the three different methods were averaged and are shown in Fig. 1. For $|\eta| < 0.5$, the average charged multiplicity density is $dN_{\rm ch}/d\eta = 5.78 \pm 0.01$ (stat.) $\pm$ 0.23 (syst.) for NSD events. The $\sqrt{s}$ dependence of the measured $dN_{\rm ch}/d\eta|_{\eta\approx 0}$ and average p_T is shown in Fig. 2. The $dN_{\rm ch}/d\eta$ results reported here show a rather steep increase between 0.9 and 7 TeV, which is measured to be 66.1% $\pm$ 1.0% (stat.) $\pm$ 4.2% (syst.). Using a somewhat different event selection, the ALICE collaboration has found a similar increase of 57.6% $\pm$ 0.4% (stat.)$^{+3.6\%}_{-1.8\%}$ (syst.) [16].

In summary, charged-hadron transverse-momentum and pseudorapidity distributions have been measured in proton-proton collisions at $\sqrt{s} = 7$ TeV. The measured $dN_{\rm ch}/d\eta$ value is higher than most predictions and provides new information to constrain ongoing improvements of soft particle production models and event generators. The mean transverse momentum are also measured in the region $|\eta| < 2.4$. These studies are the first steps in the exploration of particle production at the new centre-of-mass energy frontier, and contribute to the understanding of the dynamics in soft hadronic interactions.

Acknowledgements. We congratulate and express our gratitude to our colleagues in the CERN accelerator departments for the excellent performance of the LHC. We thank the technical and administrative staff at CERN and other CMS institutes, and acknowledge support from: FMSR (Austria); FNRS and FWO (Belgium); CNPq, CAPES, FAPERJ, and FAPESP (Brazil); MES (Bulgaria); CERN; CAS, MoST, and NSFC (China); COLCIENCIAS (Colombia); MSES (Croatia); RPF (Cyprus); Academy of Sciences and NICPB (Estonia); Academy of Finland, ME, and HIP (Finland); CEA and CNRS/IN2P3 (France); BMBF, DFG, and HGF (Germany); GSRT (Greece); OTKA and NKTH (Hungary); DAE and DST (India); IPM (Iran); SFI (Ireland); INFN (Italy); NRF and WCU (Korea); LAS (Lithuania); CINVESTAV, CONACYT, SEP, and UASLP-FAI (Mexico); PAEC (Pakistan); SCSR (Poland); FCT (Portugal); JINR (Armenia, Belarus, Georgia, Ukraine, Uzbekistan); MST and MAE (Russia); MSTDS (Serbia); MICINN and CPAN (Spain); Swiss Funding Agencies (Switzerland); NSC (Taipei); TUBITAK and TAEK (Turkey); STFC (United Kingdom); DOE and NSF (USA).

References

[1] L. Evans and P. Bryant (editors), *JINST* **3** (2008) S08001.

[2] W. Kittel and E. A. De Wolf, World Scientific, Singapore, 2005.

[3] CMS Collaboration, Phys. Rev. Lett. **105** (2010) 022002 [arXiv:1005.3299 [hep-ex]].

[4] CMS Collaboration, *JHEP* **02** (2010) 041.

[5] CMS Collaboration, *JINST* **3** (2008) S08004.

[6] Geant4 Collaboration, *Nucl. Instrum. and Methods* **A506** (2003) 250.

[7] F. Sikler, arXiv:0911.2767 [physics.ins-det].

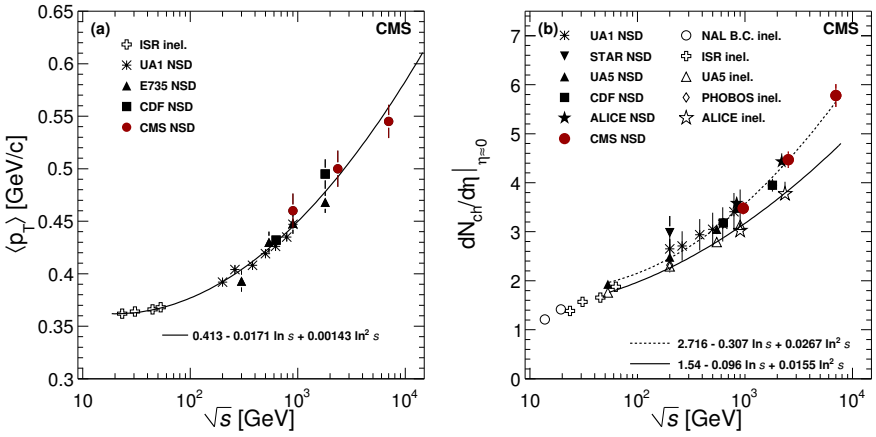

Figure 2: (a) Average p_T of charged hadrons as a function of the centre-of-mass energy. The CMS measurements are for $|\eta| < 2.4$. Also shown are measurements from the ISR [19] (pp), E735 [20] ($p\bar{p}$), and CDF [21] ($p\bar{p}$) for $|\eta| < 0.5$, and from UA1 [18] ($p\bar{p}$) for $|\eta| < 2.5$. The curve is a second-order polynomial fit to the data. The error bars on the CMS data include the systematic uncertainties. (b) Average value of $dN_{\rm ch}/d\eta$ in the central η region as a function of centre-of-mass energy in pp and $p\bar{p}$ collisions. Also shown are NSD and inelastic measurements from the NAL Bubble Chamber [22] ($p\bar{p}$), ISR [23] (pp), UA1 [18] ($p\bar{p}$), UA5 [15] ($p\bar{p}$), CDF [24] ($p\bar{p}$), STAR [25] (pp), PHOBOS [26] (pp), and ALICE [17] (pp). The curves are second-order polynomial fits for the inelastic (solid) and NSD event selections (dashed). The error bars include systematic uncertainties, when available. Data points at 0.9 and 2.36 TeV are slightly displaced horizontally for visibility.

[8] T. Sjöstrand, S. Mrenna, and P. Skands, *JHEP* **05** (2006) 026.

[9] A. Moraes, C. Buttar, and I. Dawson, *Eur. Phys. J.* **C50** (2007) 435.

[10] F. W. Bopp, R. Engel and J. Ranft, arXiv:hep-ph/9803437.

[11] R. Engel, J. Ranft, and S. Roesler, *Phys. Rev.* **D52** (1995) 1459.

[12] C. Tsallis, *J. Stat. Phys.* **52** (1988) 479.

[13] G. Wilk and Z. Włodarczyk, *Eur. Phys. J.* **A40** (2009) 299.

[14] T. S. Biró, G. Purcsel, and K. Ürmössy, *Eur. Phys. J.* **A40** (2009) 325,

[15] UA5 Collaboration, *Z. Phys.* **C33** (1986) 1.

[16] ALICE Collaboration, arXiv:1004.3514 [hep-ex].

[17] ALICE Collaboration, Eur. Phys. J. C **68** (2010) 89

[18] UA1 Collaboration, *Nucl. Phys.* **B335** (1990) 261.

[19] A. M. Rossi et al., *Nucl. Phys.* **B84** (1975) 269.

[20] E735 Collaboration, *Phys. Rev. Lett.* **60** (1988) 1622.

[21] CDF Collaboration, *Phys. Rev. Lett.* **61** (1988) 1819.

[22] J. Whitmore, *Phys. Rept.* **10** (1974) 273.

[23] Aachen-CERN-Heidelberg-Munich Collaboration, , *Nucl. Phys.* **B129** (1977) 365.

[24] CDF Collaboration, *Phys. Rev.* **D41** (1990) 2330.

[25] STAR Collaboration, *Phys. Rev.* **C79** (2009) 034909.

[26] PHOBOS Collaboration, *J. Phys.* **G30** (2004) S1133.

Identified particle production in inelastic pp scattering with ATLAS

Jedrzej Biesiada for the ATLAS Collaboration

Lawrence Berkeley National Laboratory, 1 Cyclotron Road, Berkeley, CA 94720, USA

DOI: http://dx.doi.org/10.3204/DESY-PROC-2010-01/211

We present the observation of strange and charm hadrons using tracking information from the ATLAS Inner Detector.

1 Introduction

The Large Hadron Collider at CERN is designed for discovery of new physical phenomena in high-p_T proton-proton collisions. However, accurate modeling of low-p_T processes is critical for adequate characterization of the underlying event, which is an important background in the high-p_T collisions of interest. An important ingredient in this program are identified particles containing strange and charm quarks, which can be used to tune Monte Carlo generators. Many of these particles can be identified in minimum-bias events using tracking information, and are thus important as well for evaluating tracking performance. We present here the observation of several strange and charm hadrons with the ATLAS Inner Detector [1] using a minimum-bias trigger. Data is compared with non-diffractive MC simulation, using the ATLAS MC09 tune of Pythia [2] and full GEANT4 simulation [3] of the detector. No corrections have been applied for efficiency, resolution, or other detector effects.

2 K^0_S and Λ decays

We reconstruct K^0_S and Λ decays to two charged hadrons [4] by combining pairs of tracks originating from a vertex that is well separated from the primary collision vertex. We use tracks with $p_T > 100$ MeV and simple selections on the transverse decay length, $L_{xy} > 4$ mm and $L_{xy} > 30$ mm for K^0_S and Λ decays, respectively; and the angle between the momentum direction of the reconstructed K^0_S or Λ candidate and the line connecting the primary and secondary vertices, $\cos\theta > 0.999$ and $\cos\theta > 0.9998$ for K^0_S and Λ decays, respectively. Figure 1 shows the reconstructed mass distributions in approximately 190 μb^{-1} of data; the signal and background components of the MC simulation sample are normalized separately to data. Figure 2 shows the distributions of transverse momentum and the proper decay time for K^0_S candidates, demonstrating excellent agreement between data and simulation in the proper decay time. The simulation has greater p_T on average than data; the discrepancy is under investigation.

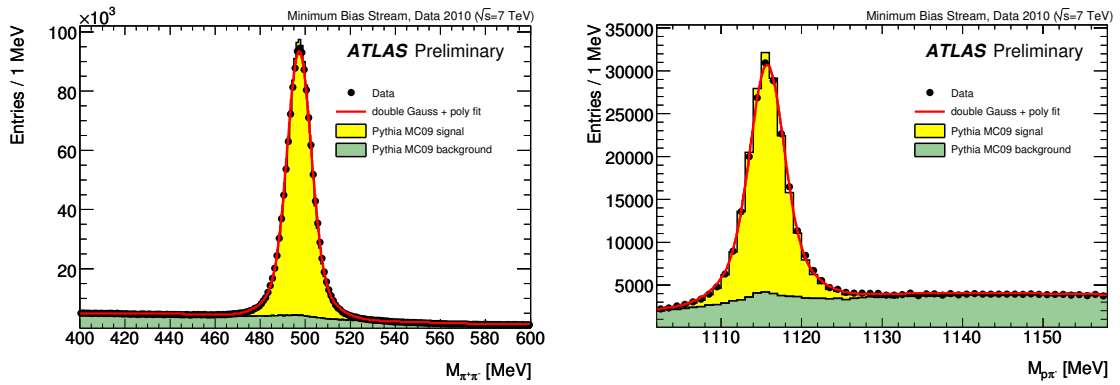

Figure 1: Comparison of measured and predicted K^0_S (left) and Λ (right) mass spectra in the barrel region of the Inner Detector. (Both tracks satisfy $|\eta| < 1.2$.) The black circles are data, while the histograms show Monte Carlo simulation (normalised to data). The solid red line is the line-shape function fitted to data.

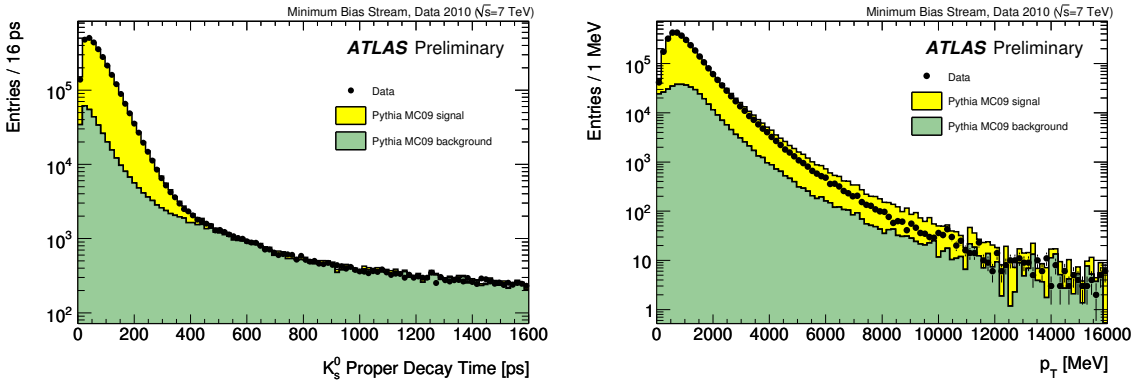

Figure 2: The proper decay time (left) and transverse momentum (right) of K^0_S candidates with reconstructed invariant mass within 20 MeV of the PDG value [5] for data and the MC sample.

3 Decays of D mesons

We reconstruct the decay $D^{*+} \to D^0(\to K^-\pi^+)\pi^+_s$ (and the charged conjugate) [6]. Since the proper decay length of the D^0 meson is approximately 123 μm, we require a positive decay length on the D^0 vertex. We exploit the relatively high energy released in charm fragmentation with the selections $p_T(D^*) > 3.5$ GeV, $p_T(K,\pi) > 1.0$ GeV, and $p_T(D^*)/\Sigma E_T > 0.02$, where ΣE_T is the total scalar transverse energy of the event as measured in the calorimeter and muon systems of the detector. Figure 3 shows a clear D^* peak in the distribution of the difference between the invariant mass of the D^* and the D^0 candidate and a clear D^0 peak in the distribution of the $K\pi$ invariant mass, with approximately 2000 signal candidates in each peak. Figure 4 shows the reconstructed mass for roughly 1700 $D^+ \to K^-\pi^+\pi^+$ signal candidates reconstructed with similar selections, but with a tighter cut of $L_{xy} > 1.3$ mm (since the D^+ meson has a

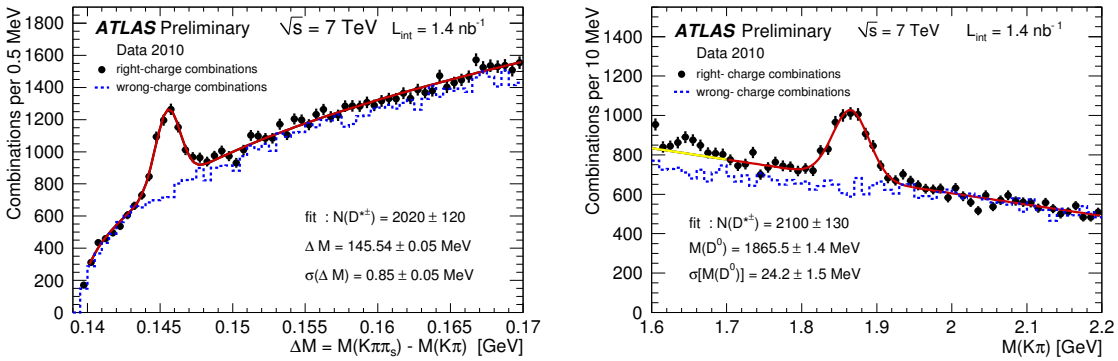

Figure 3: Left: The distribution of the mass difference, $\Delta\mathrm{M} = \mathrm{M}(K\pi\pi_\mathrm{s}) - \mathrm{M}(K\pi)$, for D^* candidates (points). Right: The $\mathrm{M}(K\pi)$ distribution for the D^0 candidates in the same D^* decay mode (points). The solid curves represent fit results, while the dashed lines show the wrong-charge combinations in data.

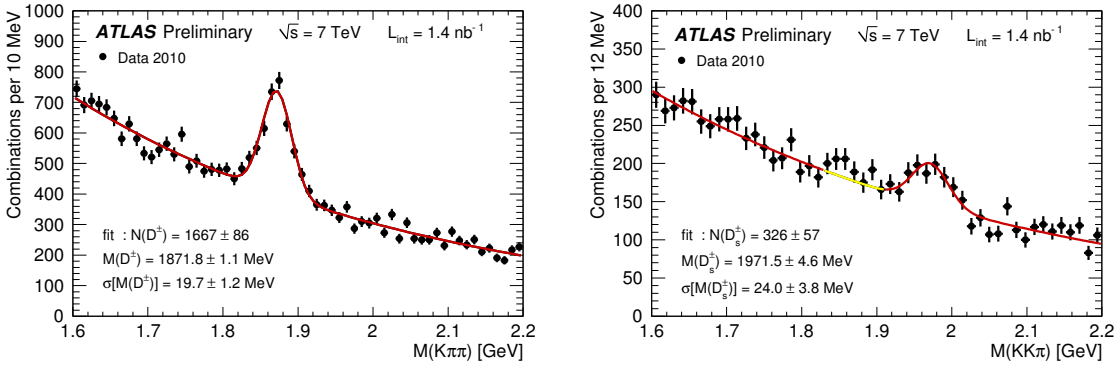

Figure 4: Left: The $\mathrm{M}(K\pi\pi)$ distribution for D^+ candidates (points). The solid curve represents a fit to the sum of a Gaussian function and an exponential background function. Right: The $\mathrm{M}(KK\pi)$ distribution for D_s candidates (points).

longer lifetime) and vetos on D^* decays and $D_\mathrm{s} \to \Phi(K^+K^-)\pi$ reflections. Figure 4 also shows roughly 330 $D_\mathrm{s} \to \Phi(K^+K^-)\pi$ signal candidates, reconstructed with additional cuts exploiting the vector nature of the Φ meson and a tighter cut of $p_\mathrm{T}(D^*)/\Sigma E_\mathrm{T} > 0.04$. The fitted positions of the mass peaks are in close agreement with the PDG values [5] for these decays.

4 Ξ and Ω Decays

We reconstruct the decays $\Xi \to \Lambda\pi$ and $\Omega \to \Lambda K$ [7]. As both the cascade baryon itself and the Λ baryon have a macroscopic proper decay length, we reconstruct the entire cascade decay chain with pointing constraints between the primary, secondary, and tertiary vertices and a

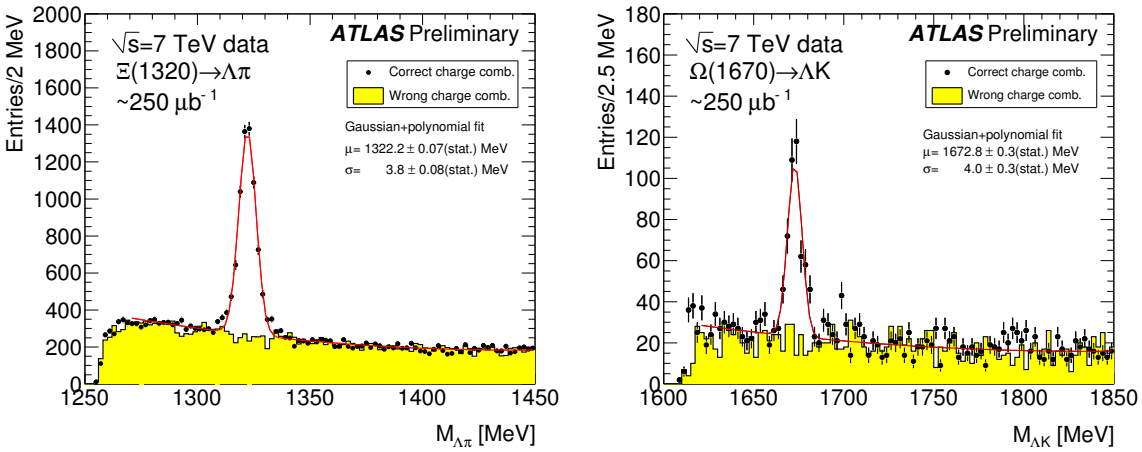

Figure 5: Left: The invariant mass of the reconstructed Ξ (left) and Ω (right) cascade-decay candidates. The red curve shows the fit result.

mass constraint on the Λ candidate. For the Ξ decay, we require that the bachelor pion have a transverse impact parameter $d_0 > 0.5$ mm and $p_{\mathrm{T}} > 150$ MeV, while for the bachelor kaon in the Ω case we require $d_0 > 1$ mm and $p_{\mathrm{T}} > 400$ MeV. For the Ξ baryon we require a flight distance of at least 4 mm, while for the Ω baryon we require a flight distance of at least 6 mm, $p_{\mathrm{T}}(\Omega) > 1500$ MeV, and a veto on Ξ reflections. In both cases we require the secondary vertex to have $\chi^2 < 7$. Figure 5 shows the reconstructed invariant mass, showing clear signal peaks for both strange baryons, in agreement with the PDG values [5] for the mass.

5 Summary

We have reconstructed several hadronic decays using the ATLAS Inner Detector. The results demonstrate excellent tracking performance and accurate MC simulation.

References

[1] The ATLAS Collaboration, "The ATLAS Experiment at the CERN Large Hadron Collider," JINST **3**, S08003 (2008).

[2] The ATLAS Collaboration, "ATLAS Monte Carlo Tunes for MC09". ATL-PHYS-PUB-2010-002.

[3] S. Agostinelli *et al.* [GEANT4 Collaboration], "GEANT4: A simulation toolkit," Nucl. Instrum. Meth. A **506**, 250 (2003).

[4] The ATLAS Collaboration: "Kinematic Distributions of K^0_{S} and Λ decays in collision data at $\sqrt{s} = 7$ TeV". ATLAS-CONF-2010-033.

[5] C. Amsler *et al.* [Particle Data Group], "Review of particle physics," Phys. Lett. B **667**, 1 (2008).

[6] The ATLAS Collaboration: "D^* mesons reconstruction in pp collisions at $\sqrt{s} = 7$ TeV". ATLAS-CONF-2010-034.

[7] The ATLAS Collaboration: "Observation of Ξ, Ω baryons and $K^*(890)$ meson production at $\sqrt{s} = 7$ TeV". ATLAS-CONF-2010-032.

Perspectives of strangeness measurements at LHC with ALICE

Antonin Maire for the ALICE Collaboration,

Institut pluridisciplinaire Hubert Curien (IPHC), 23 rue du loess - 67037 Strasbourg, France

DOI: http://dx.doi.org/10.3204/DESY-PROC-2010-01/212

In November 2009, the Large Hadron Collider produced its first proton-proton collisions at the centre of mass energy ($\sqrt{s}$) of 900 GeV. Since then, several hundred million of 7 TeV collisions have been recorded by the ALICE experiment. The low material budget of the ALICE sub-detectors in the central rapidity region and the excellent particle identification capabilities allow the extraction of transverse momentum (p_{T}) spectra for a range of identified particles. In this presentation, we report p_{T} measurements (uncorrected spectra) for strange and multi-strange particles (i.e. ϕ, $\mathrm{K}^0_{\mathrm{S}}$, Λ^0, $\overline{\Lambda}^0$, Ξ and Ω), identified via topological methods.

1 Introduction and motivation

Strange particle production in proton-proton (pp) collisions is a necessary benchmark for the physics of ultra relativistic heavy ions. This is important at the Large Hadron Collider (LHC), where the heavy-ion programme is scheduled to begin in the late 2010 [1]. Moreover, strangeness in pp collisions is interesting in itself, as it may shed light on hadron production mechanisms. While the *hard* component of the event may be described by the perturbative Quantum Chromo-Dynamics (based on parton-parton scattering and fragmentation [2, 3]), the *soft* component must be treated in a more complex manner. Currently, the soft physics is described via thermal models [4, 5] or via QCD-inspired models (relying on multi-parton processes [6] or multiple scattering [7, 8], for instance). In either case, further improvements of such phenomenological models may be spurred by confrontation with experimental measurements.

In that respect, strange and multi-strange particles (ϕ, $\mathrm{K}^0_{\mathrm{S}}$, Λ^0, $\overline{\Lambda}^0$, Ξ, Ω, ...), which are the focus of this publication, may provide the relevant insights: due to identification via decay topology reconstruction, they can be studied over a large momentum range. Starting from $p_{\mathrm{T}} \approx 0.2$ GeV/c and up to ≈ 10 GeV/c, these spectra cover the region dominated by the soft processes and reach the energy scale where hard scattering mechanisms dominate.

Some measurements have already been performed at previous and current facilities. These include both the $\mathrm{p\overline{p}}$ colliders (Sp$\overline{\mathrm{p}}$S, Tevatron) and a pp collider (RHIC), with centre of mass energies $\sqrt{s}$ ranging from 200 GeV up to 1.96 TeV [9–18]. The LHC having been in operation since November 2009, it is now possible to extend the existent 900-GeVmeasurements made by the UA1 and UA5 collaborations in $\mathrm{p\overline{p}}$, and to perform new measurements at $\sqrt{s} = 7$ TeV, beyond the Tevatron energies.

The ALICE experiment [1] is well-suited for such spectrum measurements, due to a low

p_{T} cut-off and excellent particle identification (PID) capabilities. The low p_{T} cut-off is made possible by the low magnetic field applied in the central barrel ($\leq 0.5\ T$) and the low material budget in this mid-rapidity region (13% of radiation length [19]). The PID capabilities are supplied by a set of detectors utilizing diverse techniques (energy loss, transition radiation, Cerenkov effect, time of flight).

2 Data analysis and identification methods

2.1 Data collection and detector setup

The data presented here is from the minimum bias sample collected during the Nov-Dec 2009 LHC pp run at $\sqrt{s} = 900$ GeV [20] ($\sim 3 \times 10^5$ events), and from the 7 TeV pp run that started in March 2010 and is ongoing ($> 4 \times 10^8$ events at the moment). This study makes use of the ALICE central barrel [21], covering a range in pseudo-rapidity $|\eta| < 0.9$ and the full azimuth, the whole being placed in the large L3 solenoidal magnet which provides a nominal magnetic field of $0.5\ T$.

The strangeness signals are obtained using essentially data collected by the two main tracking detectors: the Inner Tracking System (ITS), composed of 6 cylindrical layers of high-resolution silicon detectors [22], and the cylindrical Time Projection Chamber (TPC) [23].

2.2 Topological reconstruction

The strange hadron identification is performed using a combination of displaced-vertex reconstruction, invariant mass analyses as well as single track PID methods, such as energy loss in the TPC or Time-Of-Flight (TOF) in the eponymous detector. The reconstruction of the strange and multi-strange particles hinges on their respective decays. For each particle of interest, the main characteristics and utilized decay channels are listed in Tab. 1. The anti-baryons are reconstructed similarly via the channel relying on the corresponding charge conjugates.

Particles		mass (MeV/c^2)	$c\tau$	charged decay	B.R.
Mesons	$\mathrm{K}^0_{\mathrm{S}}$	497.61	2.68 cm	$\mathrm{K}^0_{\mathrm{S}} \rightarrow \pi^+ + \pi^-$	69.2%
	ϕ	1019.46	45 fm	$\phi \rightarrow \mathrm{K}^+ + \mathrm{K}^-$	49.2%
Baryons	Λ^0 (uds)	1115.68	7.89 cm	$\Lambda^0 \rightarrow p + \pi^-$	63.9%
	Ξ^- (dss)	1321.71	4.91 cm	$\Xi^- \rightarrow \Lambda^0 + \pi^-$	99.9%
	Ω^- (sss)	1672.45	2.46 cm	$\Omega^- \rightarrow \Lambda^0 + \mathrm{K}^-$	67.8%

Table 1: Main characteristics of the reconstructed particles [24].

The guidelines of the reconstruction algorithms dedicated to ϕ, V0 and cascade structures (see below) are sketched in Fig. 1, parts *a*, *b* and *c* respectively.

The identification of ϕ consists in the association of two *primary* tracks of opposite charges, identified as kaons by TPC and possibly TOF. The $\mathrm{K}^0_{\mathrm{S}}$, Λ^0 and $\overline{\Lambda}^0$ reconstruction is grounded in the secondary vertex finding, a *V0* structure built out of two *secondary* tracks of opposite charges, compatible with coming from the same vertex within one fiducial volume. In case of

Λ^0 and $\overline{\Lambda}^0$, TPC PID is required to partially remove some combinatorial background, namely for the proton (one of the two Λ decay products, known as "daughter" particles).

The Ξ^-, $\overline{\Xi}^+$, Ω^- and $\overline{\Omega}^+$ identification is based on two secondary vertices, a Λ^0 first, which is then matched with a *secondary* track, to form a typical *cascade* structure. Here again, the matching is limited to a certain fiducial volume. The TPC PID is required for each daughter track.

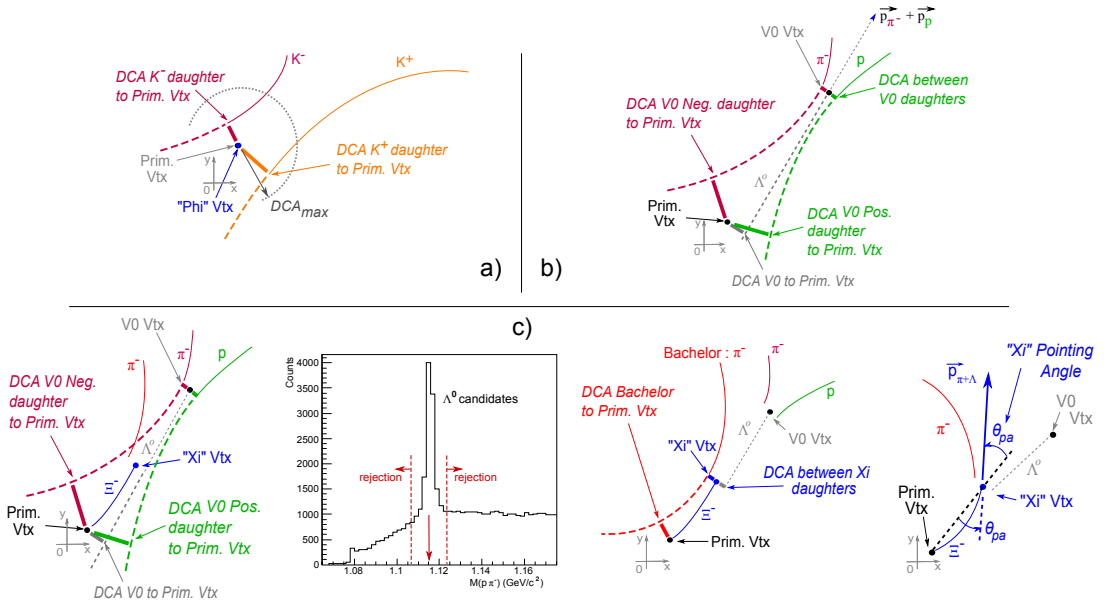

Figure 1: Reconstruction principle for (*a*) ϕ, (*b*) V0s (K^0_S, Λ^0 and $\overline{\Lambda}^0$) and (*c*) cascades (Ξ^-, $\overline{\Xi}^+$, Ω^- and $\overline{\Omega}^+$). The acronym *DCA* stands for Distance of Closest Approach.

2.3 Signal extraction

For each considered particle, we intend to extract a signal in successive p_{T} intervals. The signal extraction process using "bin-counting" method is illustrated in Fig. 2.

The signal is first approximated by a Gaussian sitting on top of a polynomial background, resulting in rough[1]estimates of the signal mean and width.

We then sample the background on each side of the signal and require both sampled regions to be more than 5σ away from the Gaussian mean. The width of the background regions varies depending on the considered particle and the transverse momentum interval chosen for the invariant mass distribution.

The sum of signal and background (S+B) is sampled in the region defined by the Gaussian mean $\pm 4\sigma$. Consequently, we make use of the areas previously sampled on the side-signal bands to assess the background B under the signal S. The signal yield $S = (S+B) - B$ is thus computed without any assumption as to its shape.

[1]The mean and width may be biased by the non-Gaussian tails of the signal. However, these quantities have the sufficient accuracy for the current purpose.

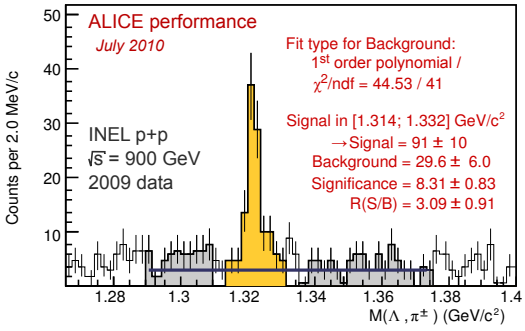

Figure 2: Signal extraction based on "bin counting" method, illustrated with the $\Xi^- + \overline{\Xi}^+$ invariant mass distribution in $1.4 < p_{\rm T}$ (GeV/c) < 2.0.

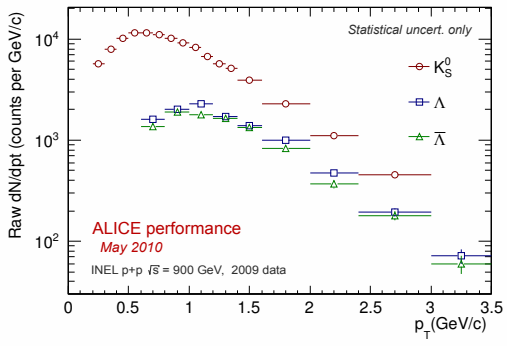

Figure 3: Raw transverse momentum spectra for $\rm K^0_S$, Λ^0 and $\overline{\Lambda}^0$ candidates (2009 data at $\sqrt{s} = 900$ GeV).

3 900 GeV and 7 TeV measurements

The results for the 2009 pp sample at 900 GeV are shown in Fig. 3 and Fig. 4. The plots show the signal counts (raw yields) for $\rm K^0_S$, Λ^0 and $\overline{\Lambda}^0$ (Fig. 3) then ϕ and $\Xi^- + \overline{\Xi}^+$ (Fig. 4), as a function of $p_{\rm T}$. The uncertainties correspond to both the statistical uncertainty related to the number of counts and the uncertainty issued from the bin-counting and fit methods needed for signal extraction.

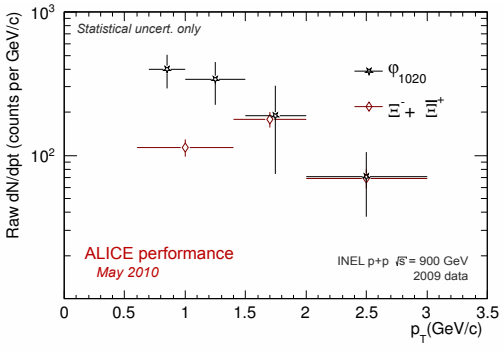

Figure 4: Raw transverse momentum spectra for ϕ and $\Xi^- + \overline{\Xi}^+$, in 2009 pp data at 900 GeV.

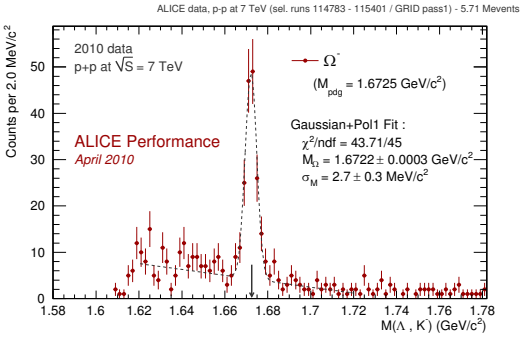

Figure 5: Invariant mass showing the Ω^- signal in 2010 pp data at 7 TeV.

A signal for the same particles can also be extracted in the pp data at 7 TeV. However, due to the available statistics, all particles and anti-particles can be studied separately and with larger counts: $\Xi^-$and $\overline{\Xi}^+$or even $\Omega^-$and $\overline{\Omega}^+$can now be discriminated, as suggested in Fig. 5.

4 Conclusion

The uncorrected spectra for strange and multi-strange hadrons are presented for the first LHC pp run at 900 GeV. Despite the limited statistics, p_{T} spectra for ϕ, $\mathrm{K}^0_{\mathrm{S}}$, Λ^0, $\overline{\Lambda}^0$ and $\Xi^- + \overline{\Xi}^+$ were obtained; the evaluation of efficiency corrections and systematic uncertainties is under finalisation.

Due to the large statistics available, the 7-TeV pp data sample enables the reconstruction of more hadron species carrying strangeness, Ω hyperons in particular as well as additional strange resonances like $\mathrm{K}^*(892)^0$ or $\Sigma^*(1385)$. This bodes well for more accurate and differential analyses such as spectra as a function of p_{T}, rapidity or event multiplicity.

References

[1] B. Alessandro (ed.) *et al.* [ALICE Collaboration], J. Phys. G **32** (2006) 1295.

[2] T. Sjöstrand, S. Mrenna and P. Z. Skands, J. High Energy Phys. 0605 (2006) 026.

[3] R. Engel, J. Ranft and S. Roesler, Phys. Rev. D**52**, (1995) 1459.

[4] F. Becattini and U. W. Heinz, Z. Phys. C**76**, (1997) 269.

[5] P. Braun-Munzinger, K. Redlich and J. Stachel, arXiv:nucl-th/0304013.

[6] T. Sjöstrand and P. Z. Skands, Eur. Phys. J. C**39**, (2005) 129.

[7] K. Werner, Nucl. Phys. Proc. Suppl. **175-176**, 81 (2008).

[8] K. Werner, I. Karpenko, T. Pierog, M. Bleicher and K. Mikhailov, arXiv:1004.0805 [nucl-th].

[9] STAR Collaboration, B. I. Abelev *et al.*, Phys. Rev. C**75**, (2007) 064901.

[10] UA5 Collaboration, R. E. Ansorge *et al.*, Nucl. Phys. B**328**, (1989) 36.

[11] UA1 Collaboration, G. Bocquet *et al.*, Phys. Lett. B**366**, (1996) 441.

[12] CDF Collaboration, F. Abe *et al.*, Phys. Rev. D**40**, (1989) 3791 RC.

[13] CDF Collaboration, D. Acosta *et al.*, Phys. Rev. D**72** (2005) 052001.

[14] UA5 Collaboration, R. E. Ansorge *et al.*, Z. Phys. C**41** (1988) 179.

[15] STAR Collaboration, J. Adams *et al.*, Phys. Lett. B**612** (2005) 181.

[16] STAR Collaboration, B. I. Abelev *et al.*, Phys. Rev. C**79** (2009) 064903.

[17] E735 Collaboration, T. Alexopoulos *et al.*, Z. Phys. C**67** (1995) 411.

[18] CDF Collaboration, public note, CDF/PUB/QCD/PUBLIC/10084 (2010), www-cdf.fnal.gov.

[19] B. Hippolyte, Eur. Phys. J. C **62** (2009) 237 [arXiv:0901.3176 [hep-ex]].

[20] L. Evans and P. Bryant, (ed.), JINST 3 **64**, (2008) S08001.

[21] K. Aamodt *et al.* [ALICE Collaboration], JINST **3** (2008) S08002.

[22] K. Aamodt *et al.* [ALICE Collaboration], JINST **5** (2010) P03003 [arXiv:1001.0502 [physics.ins-det].

[23] J. Alme *et al.* [ALICE Collaboration], arXiv:1001.1950 [physics.ins-det].

[24] C. Amsler *et al.* (Particle Data Group), Phys. Lett. B **667**, (2008) 1.

Cluster properties from two-particle angular correlations in pp collisions at CMS

Elisabetta Gallo on behalf of the CMS Collaboration

INFN Firenze, Italy

DOI: http://dx.doi.org/10.3204/DESY-PROC-2010-01/213

Results on two-particle angular correlations for charged particles are presented for proton-proton collisions data at $\sqrt{s} = 0.9, 2.36$ and 7 TeV, collected with the CMS experiment. The results are quantified in terms of a simple independent cluster parametrization and compared to previous results and to the Monte Carlo model in PYTHIA.

1 Introduction

A proton-proton collision at the LHC is a complicated process, where the hard interaction is described by perturbative QCD, but the subsequent final state radiation, hadronization process and decay and in addition multiparton interactions have to be modelled by the Monte Carlo (MC) generators. Also multiparticle correlations in the event have been studied and compared to models, in a wide range of center-of-mass (c.m.) energies, in pp, $\mathrm{p\bar{p}}$ and heavy-ion collisions.

In particular two-particle correlations have been extracted as a function of the relative pseudorapidity ($\Delta\eta$, where $\eta = -\ln(\tan(\theta/2))$ and θ is the polar angle with respect to the beam direction) and azimuthal angle ($\Delta\phi$) between the particles. The resulting two-dimensional (2-D) distribution in $\Delta\eta$-$\Delta\phi$ reveals a complicated structure, with a Gaussian peak around $\Delta\eta \simeq 0$ (see for example Ref. [1, 2, 3, 4, 5]). A simple ansatz, the Independent Cluster Model (ICM) has been used by the experiments to parametrize the correlations. In this ansatz, the clusters are assumed to be emitted independently and then decay isotropically in their own rest frame into the observed hadrons. The observed correlation strength and extent in relative pseudorapidity can be parametrized by the cluster "size" (the average number of particles into which a cluster decays) and "width" (the spread of the daughter particles in pseudorapidity).

Results from the CMS experiment were obtained in the early minimum bias data taken at $\sqrt{s} = 0.9, 2.36$ and 7 TeV [6]. The CMS tracker [7], with a coverage in pseudorapidity in the range $-2.4 < \eta < 2.4$ and full coverage in azimuth, is well suited to measure this type of correlations. In addition the tracks were selected for this analysis down to very low transverse momenta, $p_T > 0.1$ GeV/c. The trigger used for these data preferentially selected non-single-diffractive (NSD) events.

2 Analysis Technique

The approach used here is very similar to the one adopted by the previous experiments at ISR and RHIC [2, 4]. The 2-D function for the angular correlations for each pair of particles is

defined as

$$R(\Delta\eta,\Delta\phi) =< (N-1)(\frac{S_N(\Delta\eta,\Delta\phi)}{B_N(\Delta\eta,\Delta\phi)} - 1) >_{\rm N}, \quad (1)$$

where S_N and B_N are the signal and background distributions, respectively, and N is the charged track multiplicity in the event. The signal and background distributions were calculated as:

$$S_N(\Delta\eta,\Delta\phi) = \frac{1}{N(N-1)}\frac{d^2N^{\rm signal}}{d\Delta\eta\Delta\phi}, \qquad B_N(\Delta\eta,\Delta\phi) = \frac{1}{N^2}\frac{d^2N^{\rm mixed}}{d\Delta\eta\Delta\phi}, \quad (2)$$

where $\Delta\eta = \eta_1 - \eta_2$ and $\Delta\phi = \phi_1 - \phi_2$ for each pair of charged particles 1,2 in the event for the signal, while in the combinatorial background the distribution is calculated from two particles in two different events. The two events were randomly mixed in the same intervals of multiplicity and vertex longitudinal position, in order to correctly take into account the different acceptance as a function of these two variables. The ratio in Eq. (1) was also calculated in each multiplicity bin, and then averaged over all multiplicities. In the ratio, many systematic uncertainties common to the signal and background cancel out.

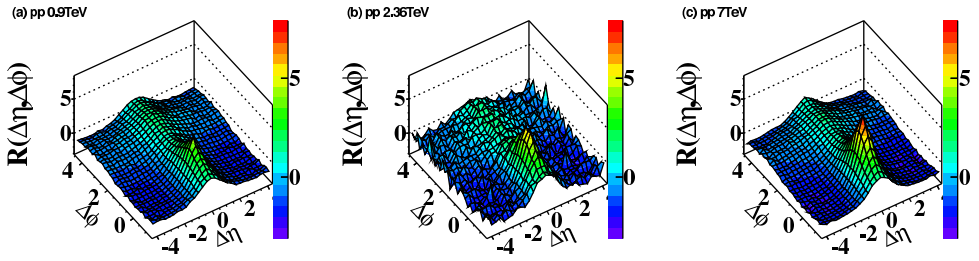

Figure 1: The 2-D two-particle correlation function $R(\Delta\eta,\Delta\phi)$ for the CMS data at the three c.m. energies.

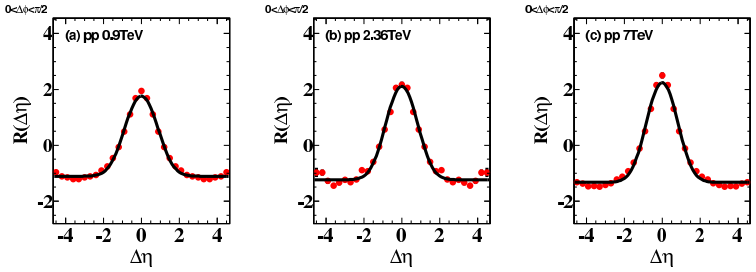

Figure 2: The two-particle correlation function $R(\Delta\eta)$ for the CMS data at the three c.m. energies. The line corresponds to the fit described in the text.

The distributions of $R(\Delta\eta,\Delta\phi)$ at the three c.m. energies are shown for the CMS data in Fig 1. One can see two main features. The first one is that the correlations present a sharp peak around $\Delta\eta,\Delta\phi \simeq 0$ and a one broader around $\Delta\eta \simeq 0, \Delta\phi \simeq \pi$, where the first one corresponds to the contribution of higher p_T clusters (hard processes like jets), while the second one to lower

p_T, soft QCD, physical objects. The second feature is that the correlations become stronger as the c.m. energy increases.

3 Results

In order to study these correlations further, the 2-D correlation function was reduced to a 1-D function in $\Delta\eta$ by integrating the signal and background distributions over $\Delta\phi$. The resulting correlation function $R(\Delta\eta)$ is shown in Fig. 2, showing the typical Gaussian shape of these correlations.

The 1-D correlation function can then be parametrized, as done by previous experiments, by:

$$R(\Delta\eta) = (K_{\rm eff} - 1)\left[\frac{\Gamma(\Delta\eta)}{B(\Delta\eta)} - 1\right], \qquad \Gamma(\Delta\eta) \propto \exp\left(-\frac{(\Delta\eta)^2}{4\delta^2}\right). \tag{3}$$

In the context of the ICM, $K_{\rm eff}$ can be interpreted as the average cluster size or multiplicity, while δ gives information on the cluster width in $\Delta\eta$. The two parameters have then been determined from a fit to the data with the function of Eq. (3), as shown in Fig. 3. The cluster size increases with the c.m. energy and on average every 2-3 particles are produced correlated, at a distance of $\Delta\eta \simeq 0.5$. The width δ remains constant with $\sqrt{s}$. The MC model PYTHIA [8] reproduces the width and the trend with $\sqrt{s}$ for $K_{\rm eff}$, but fails to predict the strength of the correlation. Different tunes in PYTHIA for multiparton interactions and the Bose-Einstein correlations cause marginal effects on the results. The HERWIG [9] MC predicts a shape for the correlation function which is very different from the one in the data.

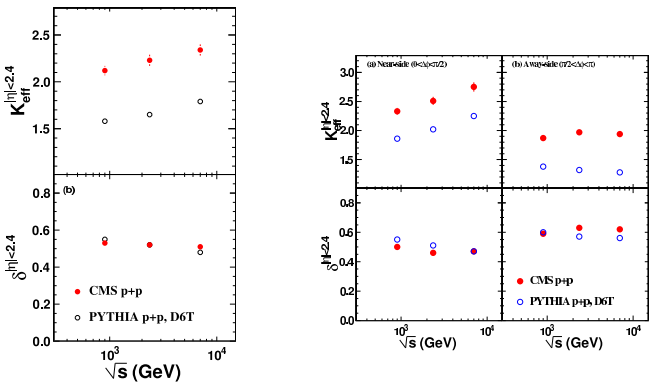

Figure 3: The two parameters $K_{\rm eff}$ and δ determined from a fit to the CMS data at the three c.m. energies. The left figure indicates the result over the whole $\Delta\phi$ range, while the right one is the result for the near- and away-side. The error bars indicate the systematic uncertainties, which are due to the tracking and event selection efficiencies and the model dependence of the corrections.

The fit was also repeated for two different ranges in $\Delta\phi$, one corresponding to the near-side, where high-p_T jets contribute, one to the away-side, for lower p_T physics. As can be seen in Fig. 3, the away-side cluster size shows no increase, while the contribution for high p_T jets increases with the c.m. energy.

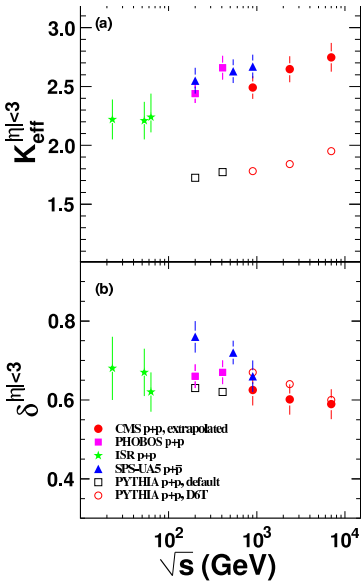

Figure 4: The two parameters $K_{\rm eff}$ and δ for the CMS data and previous results from other experiments. For this comparison the parameters have been extrapolated to the kinematic region $p_T > 0$ and $|\eta| < 3$ for the charged tracks, as explained in Ref. [6].

4 Conclusions

The results presented here are at the highest c.m. energy reached until now. It is then interesting to compare them to lowest energy data results, in pp, p$\bar{\rm p}$ and also to RHIC results. Heavy-ion experiments are particularly interesting, as this type of correlations could be modified in presence of a quark gluon plasma, so these studies are preparing the field of heavy-ion studies at the LHC. This comparison is shown in Fig. 4, where the CMS data have been extrapolated to the same kinematical region of the other experiments. The CMS result on $K_{\rm eff}$ at 0.9 TeV is lower, but compatible, with the UA5 point. The trends with $\sqrt{s}$ seen in the CMS data alone, both in the cluster size and width, are strengthened by this comparison.

References

[1] E. L. Berger, Nucl. Phys. B **85** (1975) 61.

[2] K. Eggert et al., Nucl. Phys. B **86** (1975) 201.

[3] UA5 Collaboration, Z. Phys. C **37** (1988) 191.

[4] PHOBOS Collaboration, Phys. Rev. C **75** (2007) 054913.

[5] PHOBOS Collaboration, Phys. Rev. C **81** (2010) 024904.

[6] CMS Collaboration, "Cluster-Properties from two-particle angular correlations in pp collisions at $\sqrt{s} = 0.9, 2.36$ and 7 TeV", CMS-PAS-QCD-10-002.

[7] CMS Collaboration, JINST **0803** (2008) S08004.

[8] T. Sjöstrand, S. Mrenna and P. Skands, JHEP **05** (2006) 026.

[9] M. Bahr et al., Eur. Phys. J. **C58** (2008) 639.

First results on particle correlations in ALICE

Dariusz Miśkowiec for the ALICE Collaboration

GSI, Planckstr. 1, 64291 Darmstadt, Germany

DOI: http://dx.doi.org/10.3204/DESY-PROC-2010-01/214

We report on the measurement of two-pion correlation functions from *pp* collisions at $\sqrt{s} = 900$ GeV performed by the ALICE experiment at the Large Hadron Collider. Our analysis shows an increase of the HBT radius with increasing

event multiplicity, in line with previous experiments. Conversely, the strong decrease of the radius with increasing transverse momentum, as observed at RHIC and at Tevatron, is not manifest in our data.

1 Introduction

ALICE (A Large Ion Collider Experiment) has been designed to investigate the physics of strongly interacting matter at extreme values of energy, density, and temperature in PbPb collisions [1]. These studies are to be complemented by measurements of light nuclei and *pp* collision systems. A distinguishing feature of the system created in heavy-ion collisions is the collective expansion. This view was recently challenged by the observation that at RHIC energies the transverse expansion is already manifest in the transverse momentum spectra of particles emitted in *pp* collisions, provided the energy and momentum conservation has been properly accounted for in the data analysis [2]. Moreover, dropping of the particle-source size with increasing transverse momentum – another signature of transverse expansion – was reported to be similar in *pp* and AuAu systems [3].

In this paper, we are looking for signatures of collective behavior in *pp* collisions at LHC energies by studying the size of the pion source as a function of event multiplicity and particle transverse momentum. The source size is deduced from the width of the peak representing the Bose-Einstein enhancement of identical-pion pairs at low relative momentum. This technique (Hanbury Brown - Twiss, or HBT, analysis [4, 5]) has been previously successfully applied in elementary particle [6, 7], and heavy-ion [8] collisions.

2 Data analysis and inclusive correlation functions

The results discussed here were obtained from analysis of the 250 k *pp* collision events recorded in December 2009, during the first stable-beam period of the LHC commissioning. The correlations analysis was performed using charged particle tracks registered in the ALICE Time Projection Chamber (TPC) [9]. The fiducial kinematical region was $|\eta| < 0.8$ and $0 < \phi < 2\pi$. Pion tracks were identified via the specific ionization in the TPC gas. The running conditions and the event and track selections are described in detail in Ref. [10].

The two-particle correlation function is defined as the ratio $C(\mathbf{q}) = A(\mathbf{q})/B(\mathbf{q})$, where $A(\mathbf{q})$ is the measured distribution of pair momentum difference $\mathbf{q} = \mathbf{p}_2 - \mathbf{p}_1$, and $B(\mathbf{q})$ is a similar distribution obtained via event mixing. The limited statistics available allowed us to perform a detailed analysis only for the one-dimensional two-pion correlation functions $C(q_{\rm inv})$. The $q_{\rm inv}$ is, for equal mass particles, equal to the modulus of the momentum difference $|\mathbf{q}|$ in the pair rest frame.

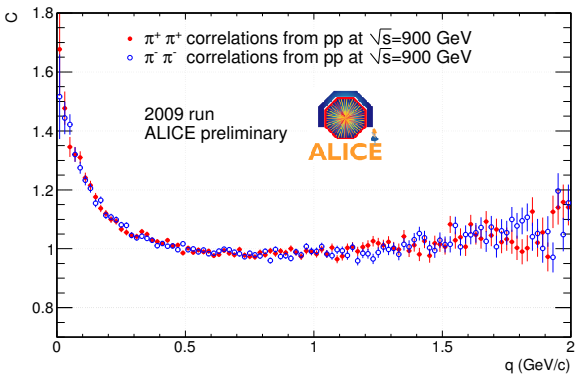

Figure 1: Correlation functions for positive (red filled dots) and negative (blue open circles) pion pairs from pp collisions at $\sqrt{s} = 900$ GeV.

Figure 1 shows the $\pi^+\pi^+$ and $\pi^-\pi^-$ correlation functions from pp collisions at $\sqrt{s} = 900$ GeV. The two functions agree within the statistical errors. The Bose-Einstein enhancement at low $q_{\rm inv}$ is clearly visible. The high $q_{\rm inv}$ part of the correlation function is not flat and it is difficult to separate the Bose-Einstein enhancement from other sources of correlations like those arising from jets or energy- and momentum conservation. The situation is different in nuclear collisions where the baseline – the underlying two particle correlation without any Bose-Einstein enhancement – is flat, and the BE peak can be clearly identified (Fig. 2).

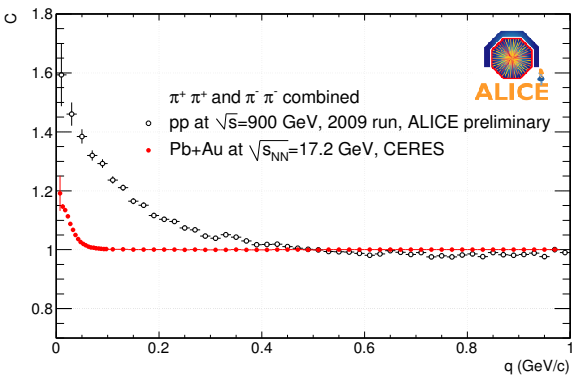

Figure 2: Comparison between the two-pion correlation functions in pp (black open circles) and PbPb collisions (red filled dots). Two-track effects, momentum resolution, and Coulomb interaction have to be corrected for in case of nuclear collisions. For hadron collisions, the non-Gaussian shape of the peak and the lack of a well defined flat baseline are the main difficulties.

In order to isolate the Bose-Einstein effect from other correlation sources, it is helpful to study the unlike-sign pion correlations for which the Bose-Einstein effect is absent. Their correlation function (Fig. 3) exhibits, in addition to the Coulomb interaction peak at low $q_{\rm inv}$ and the peaks coming from meson decays, broad structures that can be reproduced with Monte Carlo simulations using PHOJET [11] and PYTHIA [12] event generators, combined with a full simulation of the apparatus. The same calculations can thus be used to describe the baseline under the Bose-Einstein peak in the identical-pion correlation function. The fact that the structures are different for the like-sign and unlike-sign pions prevents us from using a ratio of the two correlation functions directly.

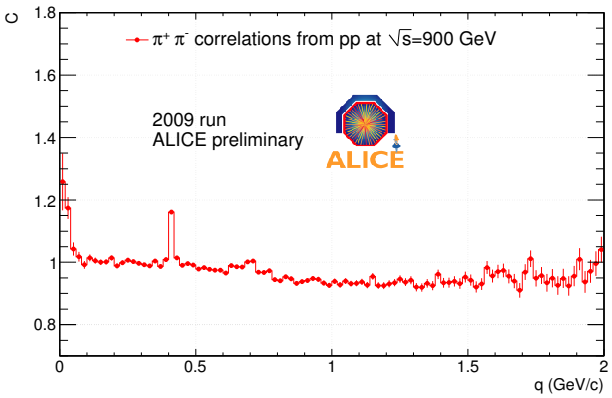

Figure 3: Correlation function for unlike-sign pion pairs from pp collisions at $\sqrt{s} = 900$ GeV.

The dynamics of the system created in the collision shows up as the dependence of the width of the Bose-Einstein peak on the multiplicity and the transverse momentum. In order to study this dependence quantitatively and to be able to compare to the existing systematics, the Bose-Einstein peak in the correlation functions was fitted by a Gaussian $G(q_{\rm inv}) = \lambda \exp(-R_{\rm inv}^2 q_{\rm inv}^2)$, with the correlation strength λ and the HBT radius $R_{\rm inv}$, sitting on a fixed baseline with the shape taken from Monte Carlo as explained before.

3 Multiplicity and transverse momentum dependence

The dependence of the HBT radius on the event multiplicity is shown in the left hand panel of Fig. 4. The tracks used in determining the multiplicity were the same as those used for the correlation analysis except that pion identification cuts were not applied. The raw multiplicity was corrected for the reconstruction efficiency and contamination, determined from a Monte Carlo simulation with the PHOJET event generator and with the full description of the ALICE apparatus. Like at RHIC and at Tevatron, the ALICE measured HBT radius increases with particle multiplicity. Such an increase is well known in nuclear collisions; its presence in hadron collisions indicates that the HBT radius is coupled directly to the final multiplicity rather than to the initial collision geometry.

The transverse momentum dependence is shown in the right hand panel of Fig. 4. The ALICE measured HBT radius is practically independent of $k_{\rm T}$ within the studied range. It should be noted that this result crucially depends on the baseline shape assumption: if the baseline is not taken from event generators but assumed to be flat then the high $k_{\rm T}$ points drop by about 30% and an apparent $k_{\rm T}$ dependence emerges. This is because the broad enhancement caused by other correlations will be attributed to Bose-Einstein correlations, giving rise to smaller radii (wider correlation function).

4 Summary

In summary, ALICE has measured two-pion correlation functions in pp collisions at $\sqrt{s} =$ 900 GeV at the LHC. Consistent with previous measurements of high-energy hadron-hadron and nuclear collisions, the extracted HBT radius $R_{\rm inv}$ increases with event multiplicity. Less consistent is the relation between $R_{\rm inv}$ and the pion transverse momentum where the ALICE measured HBT radius in minimum bias events is practically constant within our errors and

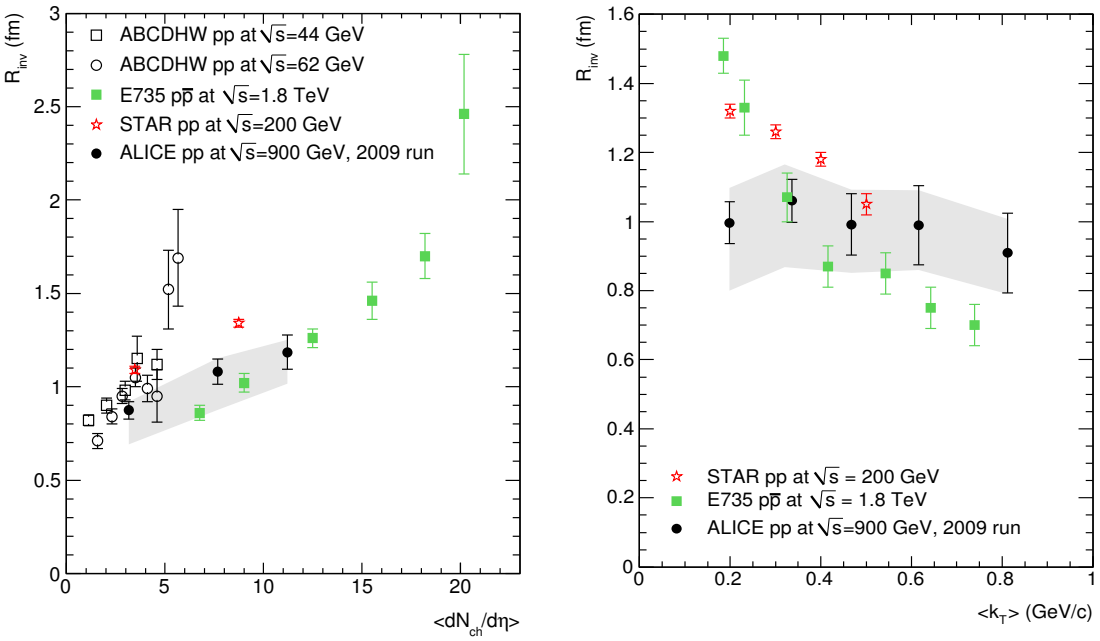

Figure 4: Dependence of HBT radius on multiplicity (left) and transverse momentum $k_{\mathrm{T}} = |\mathbf{p}_{\mathrm{T},1}+\mathbf{p}_{\mathrm{T},2}|/2$ (right). The error bars are statistical; the shaded area represents the systematic errors (for details see Ref. [10]). The ALICE results are compared to RHIC [3] and Tevatron data [13] (compilation taken from [14]).

within the transverse momentum range studied. Our data, thus, shows no signature of strong transverse expansion.

References

[1] K. Aamodt *et al.* [ALICE Collaboration], JINST **3** (2008) S08002.

[2] Z. Chajecki and M. Lisa, Phys. Rev. C **79** (2009) 034908 [arXiv:0807.3569 [nucl-th]].

[3] M. M. Aggarwal *et al.* [STAR Collaboration], arXiv:1004.0925 [nucl-ex].

[4] R. Hanbury Brown and R. Q. Twiss, Nature **178**, 1046 (1956).

[5] R. Hanbury Brown and R. Q. Twiss, Phil. Mag. **45**, 663 (1954).

[6] W. Kittel, Acta Phys. Polon. B **32**, 3927 (2001) [arXiv:hep-ph/0110088].

[7] G. Alexander, Rept. Prog. Phys. **66**, 481 (2003) [arXiv:hep-ph/0302130].

[8] M. A. Lisa *et al.* Ann. Rev. Nucl. Part. Sci. **55**, 357 (2005) [arXiv:nucl-ex/0505014].

[9] J. Alme *et al.*, arXiv:1001.1950 [physics.ins-det].

[10] K. Aamodt *et al.* [ALICE Collaboration], arXiv:1007.0516 [hep-ex].

[11] R. Engel, Z. Phys. C **66**, 203 (1995); R. Engel and J. Ranft, Phys. Rev. D **54**, 4244 (1996).

[12] T. Sjöstrand, S. Mrenna and P. Z. Skands, JHEP **0605**, 026 (2006); P. Z. Skands, arXiv:0905.3418 [hep-ph].

[13] T. Alexopoulos *et al.*, Phys. Rev. D **48**, 1931 (1993).

[14] Z. Chajęcki, Acta Phys. Polon. B **40**, 1119 (2009) [arXiv:0901.4078 [nucl-ex]].

Measurement of Bose-Einstein correlations in the first LHC-CMS data

Ezio Torassa for the CMS Collaboration

INFN Sezione di Padova, Via Marzolo 8, 35131 Padova, Italy

DOI: http://dx.doi.org/10.3204/DESY-PROC-2010-01/269

Bose–Einstein correlations have been measured using samples of proton-proton collisions at 0.9 and 2.36 TeV center-of-mass energies, recorded by the CMS experiment at the Large Hadron Collider. The signal is observed in the form of an enhancement of pairs of same-sign charged particles with small relative four-momentum. The size of the correlated particle emission region is seen to increase significantly with the particle multiplicity of the event.

1 Introduction

In particle collisions, the space-time structure of the hadronization source can be studied using measurements of Bose–Einstein correlations (BEC) between pairs of identical bosons. Since the first observation of BEC fifty years ago, a number of measurements have been made by several experiments [1]. The first measurement in pp collisions at 0.9 TeV and the highest energy measurement at 2.36 TeV is reported. Constructive interference affects the joint probability for the emission of a pair of identical bosons with four-momenta p_1 and p_2. Experimentally, the proximity in phase space between final-state particles is quantified by the Lorentz-invariant quantity $Q = \sqrt{-(p_1 - p_2)^2} = \sqrt{M^2 - 4m_\pi^2}$, where M is the invariant mass of the two particles, assumed to be pions with mass m_π. The BEC effect is observed as an enhancement at low Q of the ratio of the Q distributions for pairs of identical particles in the same event, and for pairs of particles in a reference sample that by construction is expected to include no BEC effect:

$$R(Q) = (\mathrm{d}N/\mathrm{d}Q)/(\mathrm{d}N_{\mathrm{ref}}/\mathrm{d}Q), \tag{1}$$

which is then fitted with the parameterization

$$R(Q) = C\,[1 + \lambda\Omega(Qr)] \cdot (1 + \delta Q). \tag{2}$$

In a static model of particle sources, $\Omega(Qr)$ is the Fourier transform of the spatial distribution of the emission region of bosons with overlapping wave functions, characterized by an effective size r. It is often parameterized as an exponential function, $\Omega(Qr) = e^{-Qr}$, or with a Gaussian form, $\Omega(Qr) = e^{-(Qr)^2}$ [2]. The parameter λ reflects the BEC strength for incoherent boson emission from independent sources, δ accounts for long-range momentum correlations, and C is a normalization factor.

2 Data selection, reference samples and results

The data used for the present analysis were collected by the CMS experiment [3] in December 2009 from proton-proton collisions at center-of-mass energies of 0.9 and 2.36 TeV. The events were selected by requiring activity in both beam scintillator counters [4]. A minimum-bias Monte Carlo (MC) sample was generated using PYTHIA (with D6T tune) [5] followed by full detector simulation based on the Geant4 program [6]. Additional PYTHIA MC samples were generated to simulate BEC effects with both Gaussian and exponential forms of $\Omega(Qr)$. Charged particles are required to have $p_T > 200$ MeV, which is sufficient for particles emitted from the interaction region to cross all three barrel layers of the pixel detector and ensure good two-track separation. Their pseudorapidity is required to satisfy $|\eta_{\rm track}| < 2.4$. To ensure high purity of the primary track selection, the trajectories are required to be reconstructed in fits with more than five degrees of freedom (dof) and $\chi^2/N_{\rm dof} < 5.0$. The transverse impact parameter with respect to the collision point is required to satisfy $|d_{xy}| < 0.15$ cm. The innermost measured point of the track must be less than 20 cm from the beam axis, in order to reduce electrons and positrons from photon conversions in the detector material and secondary particles from the decay of long-lived hadrons. In total 270 472 (13 548) events were selected at 0.9 (2.36) TeV center-of-mass energy. All pairs of same-charge particles with Q between 0.02 and 2 GeV are used for the measurement. The lower limit is chosen to avoid cases of tracks that are duplicated or not well separated. Coulomb interactions between charged particles modify their relative momentum distribution. This effect, which differs for pairs with same charge (repulsion) and opposite charge (attraction), is corrected for by using Gamow factors [7]. As a cross-check, the enhancement in the production of opposite-charge particle pairs with small values of Q is measured in the data and is found to be reproduced by the Gamow factors to within $\pm 15\%$. Different methods are designed to pair uncorrelated charged particles and to define reference samples used to extract the distribution in the denominator of Eq. (1). *Opposite-charge pairs*: this data set is a natural choice but contains resonances (η, ρ, ...) which are not present in the same-charge combinations. *Opposite-hemisphere pairs*: tracks are paired after inverting in space the three-momentum of one of the two particles: $(E, \vec{p}) \to (E, -\vec{p})$; this procedure is applied to pairs with same and opposite charges. *Rotated particles*: particle pairs are constructed after inverting the x and y components of the three-momentum of one of the two particles: $(p_x, p_y, p_z) \to (-p_x, -p_y, p_z)$. *Pairs from mixed events*: particles from different events are combined with the following methods: i) events are mixed at random; ii) events with similar charged particle multiplicity in the same η regions are selected; iii) events with an invariant mass of all charged particles similar to that of the signal are used to form the pairs. As an example, the ratios $R(Q)$ obtained with the opposite-hemisphere, same-charge reference samples are shown in Fig. 1 (left) both for data and simulation without BEC. A significant excess at small values of Q is observed in the data. Additional details are given in [8]. In order to reduce the bias due to the construction of the reference samples, a double ratio $\mathcal{R}$ is defined:

$$\mathcal{R}(Q) = \frac{R}{R_{\rm MC}} = \left(\frac{{\rm d}N/{\rm d}Q}{{\rm d}N_{\rm ref}/{\rm d}Q}\right) \Big/ \left(\frac{{\rm d}N_{\rm MC}/{\rm d}Q}{{\rm d}N_{\rm MC,ref}/{\rm d}Q}\right), \tag{3}$$

where the subscripts "MC" and "MC,ref" refer to the corresponding distributions from the MC simulated data generated without BEC effects. The results of fits of $\mathcal{R}(Q)$ based on the parameterization of Eq. (2) with $\Omega(Qr) = e^{-Qr}$ are given in Table 1, both for 0.9 and 2.36 TeV data. In the opposite-charge sample, the region with $0.6 < Q < 0.9$ GeV, contains a contribution of $\rho \to \pi^+\pi^-$ decays not well described by the MC. This region is therefore

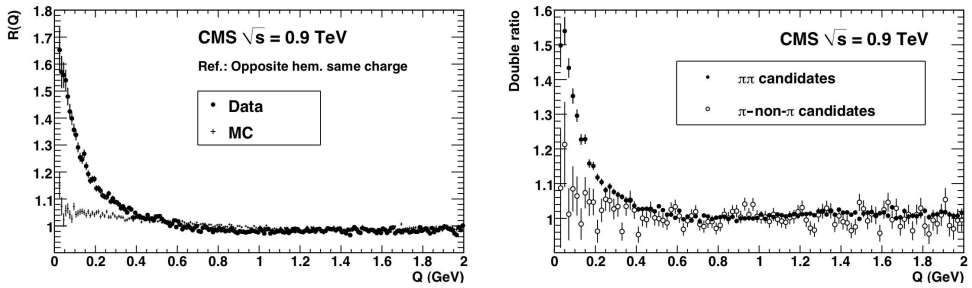

Figure 1: (Left) Ratios $R(Q)$ obtained with the opposite-hemisphere, same-charge reference samples for data (dots) and MC with no BEC effect (crosses). (Right) Double ratios $\mathcal{R}(Q)$ for the same data and reference samples using a $\mathrm{d}E/\mathrm{d}x$ measurement (dots for π-π pairs and open circles for π–not-π pairs).

excluded from the fits with this reference sample and also with the combined sample defined below. As a cross-check, the $\mathrm{d}E/\mathrm{d}x$ measurements of particles in the tracker are used to select a sample enriched in $\pi\pi$ pairs and another sample enriched in π–not-π pairs (Figure 1 right). Enhancement at small Q values is observed only in the first sample. As none of the definitions of the reference samples is preferable *a priori*, an additional, "combined" double ratio $\mathcal{R}^{\mathrm{comb}}$ is formed, where the data and MC distributions are obtained by summing the Q distributions of the seven corresponding reference samples. The distributions of $\mathcal{R}^{\mathrm{comb}}$ for 0.9 and 2.36 TeV data are shown in Fig. 2 (left), and the values of the fit parameters are given in Table 1. The leading source of systematic uncertainty on the measurements arises from the fact that none of the reference samples is expected to give a perfect description of the Q distribution in the absence of BEC. The corresponding contribution to the systematic error is computed as the r.m.s. spread between the results obtained for the different samples, i.e., $\pm 7\%$ for λ and $\pm 12\%$ for r. The systematic uncertainty related to the Coulomb corrections is computed by propagating the measured $\pm 15\%$ agreement margin, resulting in $\pm 2.8\%$ variation for λ and $\pm 0.8\%$ for r. For the 2.36 TeV data the same relative systematic uncertainties as for the 0.9 TeV results are used, in view of the reduced size of the sample and the larger statistical uncertainties of the fit results. The BEC parameters measured with the combined reference sample are: $\lambda = 0.625 \pm 0.021\,(\mathrm{stat.}) \pm 0.046\,(\mathrm{syst.})$ and $r = 1.59 \pm 0.05\,(\mathrm{stat.}) \pm 0.19\,(\mathrm{syst.})\,\mathrm{fm}$ at 0.9 TeV; $\lambda = 0.663 \pm 0.073\,(\mathrm{stat.}) \pm 0.048\,(\mathrm{syst.})$ and $r = 1.99 \pm 0.18\,(\mathrm{stat.}) \pm 0.24\,(\mathrm{syst.})\,\mathrm{fm}$ at 2.36 TeV. The fit parameters for the combined reference sample are shown in Fig. 2 (right) as a function of the track multiplicity for the 0.9 TeV data.

3 Conclusions

In summary, Bose–Einstein correlations have been measured for the first time at the LHC by the CMS experiment in pp collisions at 0.9 and 2.36 TeV center-of-mass energies. The main systematic affecting BEC measurements was studied through the use of multiple reference samples to extract the signal. For all of them an exponential shape fits the data significantly better than a Gaussian shape. An increase of the effective size of the emission region with

charged-particle multiplicity in the event has been observed.

Table 1: Results of fits to the double ratios $\mathcal{R}(Q)$ for several reference samples, using the parameterization of Eq. (2) with the exponential form, for 0.9 TeV data (left) and 2.36 TeV data (right). Errors are statistical only.

	Results of fits to 0.9 TeV data			Results of fits to 2.36 TeV data		
Reference sample	λ	r (fm)	δ (10^{-3} GeV^{-1})	λ	r (fm)	δ (10^{-3} GeV^{-1})
Opposite charge	0.56 ± 0.03	1.46 ± 0.06	-4 ± 2	0.53 ± 0.08	1.65 ± 0.23	-16 ± 6
Opposite hem. same ch.	0.63 ± 0.03	1.50 ± 0.06	11 ± 2	0.68 ± 0.11	1.95 ± 0.24	15 ± 5
Opposite hem. opp. ch.	0.59 ± 0.03	1.42 ± 0.06	13 ± 2	0.70 ± 0.11	2.02 ± 0.23	24 ± 5
Rotated	0.68 ± 0.02	1.29 ± 0.04	58 ± 3	0.61 ± 0.07	1.49 ± 0.15	58 ± 6
Mixed evts. (random)	0.62 ± 0.04	1.85 ± 0.09	-20 ± 2	0.74 ± 0.15	2.78 ± 0.36	-40 ± 4
Mixed evts. (same mult.)	0.66 ± 0.03	1.72 ± 0.06	11 ± 2	0.63 ± 0.10	2.01 ± 0.23	20 ± 5
Mixed evts. (same mass)	0.60 ± 0.03	1.59 ± 0.06	14 ± 2	0.73 ± 0.11	2.18 ± 0.23	28 ± 5
Combined	0.63 ± 0.02	1.59 ± 0.05	8 ± 2	0.66 ± 0.07	1.99 ± 0.18	13 ± 4

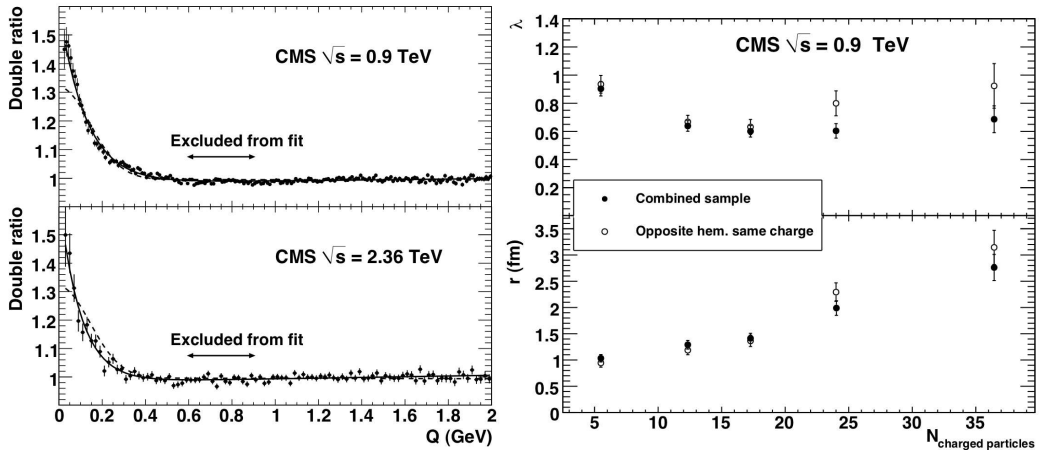

Figure 2: (Left) Fits to the double ratios $\mathcal{R}^{\mathrm{comb}}(Q)$ with exponential (solid lines) and Gaussian (dashed lines) functions, for 0.9 TeV (top) and 2.36 TeV (bottom) data. The range $0.6 < Q < 0.9$ GeV is excluded from the fits. (Right) Values of the λ (top) and r (bottom) parameters as a function of the charged-particle multiplicity for combined (dots) and opposite-hemisphere, same-charge (open circles) reference samples, at 0.9 TeV. The errors shown are statistical only.

References

[1] W. Kittel and E.A. De Wolf, World Scientific (2005) eISBN: 9789812562951.

[2] G.A. Kozlov and O. Utyuzh and G. Wilk and Z. Wlodarczyk, Phys. Atom. Nucl. **71** (2008) 1502.

[3] CMS Collaboration, JINST **3** (2008) S08004.

[4] CMS Collaboration, JHEP **2** (2010) 1.

[5] T. Sjostrand, S. Mrenna, and P. Skands, JHEP **5** (2006) 26.

[6] T. Agostinelli et al., Nucl. Instr. Meth. **A 506** (2003) 250.

[7] M. Gyulassy, S. K. Kaufmann, and L. W. Wilson, Phys. Rev. **C 20** (1979) 2267.

[8] CMS Collaboration, Phys. Rev. Lett. **105** (2010) 032001.

Event-shape variables at hadron colliders

Andrea Banfi

ETH Zurich, Wolfgang-Pauli-Straße 27, 8093 Zurich, Switzerland

DOI: http://dx.doi.org/10.3204/DESY-PROC-2010-01/248

We present precision results for distributions in global event shapes that can be measured at hadron colliders within experimental limitations. These predictions are obtained by combining exact next-to-leading order (NLO) with the all-order resummation of large logarithms of soft and collinear origin. We then discuss how event-shape measurements can be used for the tuning of Monte Carlo event generators, for tests of models of hadronisation and underlying event, and as discriminatory tools between QCD jet-like and New Physics events.

Event-shape variables are infrared and collinear safe measures of the geometrical properties of the hadronic energy-momentum flow, giving an idea on whether an event is pencil-like, planar, spherical, etc. Measurements of their mean values and distributions have played a crucial role at LEP, for precise determinations of the strong coupling α_s, for tests of analytical models of hadronisation corrections, and for validation of Monte Carlo (MC) event generators (see [1] for a recent review). In spite of the success of these studies in e^+e^- annihilation, very little attention has been devoted to their counterparts at hadron colliders [2, 3]. This was mainly because the quantities that were conveniently measured experimentally could not be accurately computed in perturbative QCD. Here I would like to present event shapes that can be measured at actual hadron colliders, and whose distributions can be computed in perturbative QCD at the accuracy needed to have a reliable estimate of the associated theoretical uncertainties.

In hadron-hadron collisions, we consider events with two hard central jets, and define event shapes that vanish in the limit of two narrow jets. For instance, given all hadrons $\{q_i\}$ in a rapidity region $\mathcal{C}$ (for instance $|\eta_i| < \eta_{\mathcal{C}}$) and using transverse momenta $\vec{q}_{\perp,i}$ only, we define the transverse thrust $T_\perp$ and the thrust minor T_m as follows

$$T_\perp = \max_{\vec{n}_\perp} \frac{\sum_{i\in\mathcal{C}} |\vec{q}_{\perp,i}\cdot\vec{n}_\perp|}{\sum_{i\in\mathcal{C}} |\vec{q}_{\perp,i}|}\,, \qquad T_m = \frac{\sum_{i\in\mathcal{C}} |\vec{q}_{\perp,i}\times\vec{n}_\perp|}{\sum_{i\in\mathcal{C}} |\vec{q}_{\perp,i}|}\,. \tag{1}$$

We can also introduce boost-invariant event shapes involving longitudinal degrees of freedom, like invariant masses or broadenings, or the three-jet resolution parameter y_3. An extensive list of hadronic event-shape definitions can be found in [4, 5].

There are three basic reasons why dijet event shapes can be studied experimentally with very first data. First, cross sections for dijet production are large both at the Tevatron and at the LHC, as shown in Table 1. From Table 1 one can also see that the flavour content of a sample can be varied by changing the leading-jet p_t-cut. Low-p_t samples (Tevatron with $p_{t1} > 50$GeV, LHC with $p_{t1} > 200$GeV) are gluon dominated, while initial-state quarks become more important for high-p_t samples (Tevatron with $p_{t1} > 200$GeV, LHC with $p_{t1} > 1$TeV). Second, event shapes are normalised quantities: experimental uncertainties associated with

	LO	NLO	$qq \to qq$	$qg \to qg$	$gg \to gg$
Tevatron, $p_{t1} > 50$GeV	60nb	116nb	10%	43%	45%
Tevatron, $p_{t1} > 200$GeV	59pb	101pb	41%	43%	12%
14TeV LHC, $p_{t1} > 200$GeV	13.3nb	23.8nb	7%	40%	50%
14TeV LHC, $p_{t1} > 1$TeV	6.4pb	10.5pb	31%	51%	17%

Table 1: Cross sections for the production of two jets in a central rapidity region ($|y_{\rm jets}| < 0.7$ at the Tevatron and $|y_{\rm jets}| < 1$ at the LHC) with a cut on p_{t1}, the transverse momentum of the leading jet. On the right it is possible to see the relative importance of each partonic subprocess.

jet-energy scale cancel between numerators and denominators, see Eq. (1). Finally, since one usually measures normalised differential distributions, like $1/\sigma\, d\sigma/dT_m$, no determination of luminosity is required.

From a theoretical point of view, event-shape distributions can be computed at NLO with NLOJET++ [6]. However, for any event shape V, both LO and NLO predictions diverge at small values of V. Only a combination of NLO and next-to-leading logarithmic (NLL) resummation (referred to as NLL+NLO) gives a distribution that is sensible for any value of V. In particular, resummation restores the correct physical behaviour at $V \to 0$, corresponding to vanishing probability of having accelerated charges without accompanying radiation. NLL resummation involves writing the *integrated* V distribution as an exponent $\Sigma(V) = \exp[Lg_1(\alpha_s L) + g_2(\alpha_s L)]$, with $L = \ln(1/V)$, $g_1(\alpha_s L)$ resumming the leading logarithms (LL, $\alpha_s^n L^{n+1}$), and $g_2(\alpha_s L)$ the NLL, $\alpha_s^n L^n$. Knowledge of $g_1(\alpha_s L)$ determines the position of the peak of the differential distribution, typically in the region $\alpha_s L \sim 1$. In the peak region $g_2(\alpha_s L)$ becomes of order one, and is therefore needed to stabilise both the position and the height of the peak.

NLL resummability is guaranteed for variables satisfying the following conditions [7]: a specific functional dependence on a single soft and collinear emission; (continuous) globalness, i.e. sensitivity to emissions in the whole of the phase space; recursive infrared and collinear (rIRC) safety, a subtle mathematical condition on the event-shape scaling properties with multiple emissions. If these conditions are satisfied, the relevant emissions that contribute to event-shape distributions at NLL accuracy are soft and collinear parton clusters widely separated in rapidity, which, due to QCD coherence, can be considered as independently emitted from hard legs. Since a similar pattern of emissions is simulated by MC event generators, one may expect that most features of rIRC safe global event-shape distributions are correctly described by these theoretical tools. Of the three constraints, the most difficult to satisfy experimentally is globalness, due to the fact that the measurement region $\mathcal{C}$ is preferably restricted to the central detector region (e.g. $|\eta| \lesssim 2.5$ at the LHC), and in any case no measurement is actually performed in the very forward regions (corresponding to a limiting rapidity $\eta_c = 5$ at the LHC). However [4], one can devise classes of global event shapes even at hadron colliders: *directly global*, where the region $\mathcal{C}$ extends up to the maximum available rapidity η_c; *exponentially suppressed*, where $\mathcal{C}$ is inside the acceptance of the central detectors (e.g. $|\eta| < 1$ at the Tevatron and $|\eta| < 1.5$ at the LHC), while outside this region we add to the event-shape definition a term that exponentially suppresses the contribution of hadrons in the forward regions; *recoil*, where measurements are performed only in a central region $\mathcal{C}$, and we add a term that is sensitive to emissions outside $\mathcal{C}$ through recoil. In the last case however a numerical breakdown of NLL resummation occurs in the region where the event shape is small.

In [5] we have performed a NLL+NLO resummation for a number of selected event shapes. Figure 1 shows predictions for the directly global thrust minor $T_{m,g}$, together with theoretical uncertainties. The latter, aimed at having an indication of missing NNLO and NNLL corrections, are estimated via: asymmetric variation of renormalisation and factorisation scales μ_R and μ_F; variation of the logarithm to be resummed $\ln(XT_{m,g})$ with $1/2 < X < 2$; variation of the matching scheme (log-R or mod-R). We observe that uncertainties are under control and within $\pm 20\%$ in a wide range of values of $T_{m,g}$. Similar results are obtained for all considered event shapes.

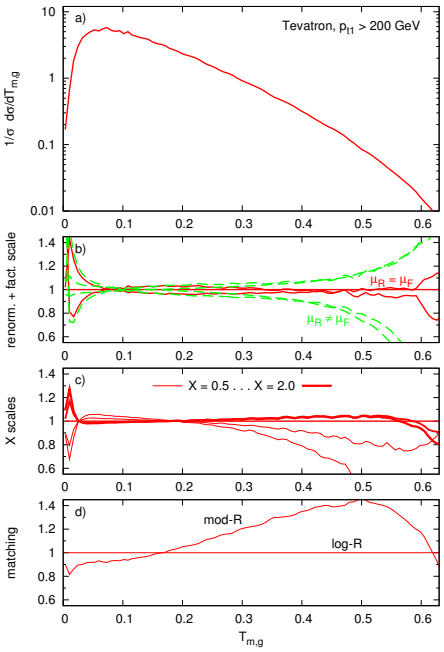

Figure 1: NLL+NLO predictions and theoretical uncertainties for $1/\sigma\, d\sigma/T_{m,g}$.

These predictions are valid at parton level only, so it is interesting to investigate the impact of hadronisation and underlying event on event-shape distributions. This can be done with MC event generators. Figure 2 shows that k_t-algorithm jet resolution parameters, for example $y_{3,g}$, are essentially not affected by hadronisation and underlying event, while event shapes, like $\rho_{T,\mathcal{E}}$, get moderate hadronisation corrections, falling as an inverse power of the jet p_t, but get a huge contribution from the underlying event. This different sensitivity shows that event-shape distributions can be exploited for the validation of MC event generators. Jet resolution parameters are better suited for tunings of parton shower parameters, while with remaining event shapes one can test models of hadronisation and underlying event.

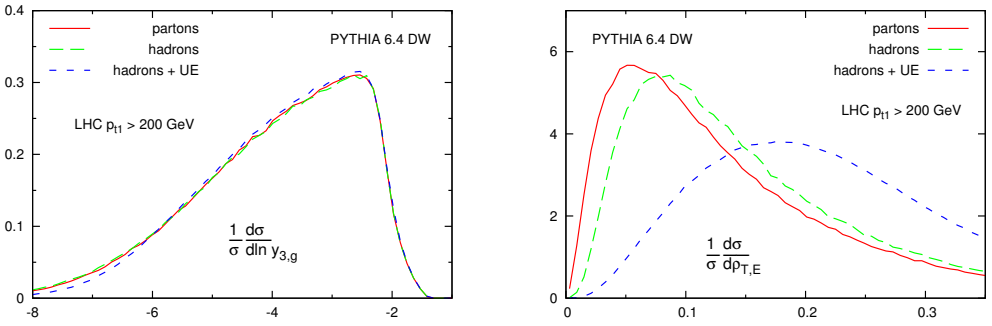

Figure 2: Distributions in directly global three-jet resolution $y_{3,g}$ (left) and exponentially suppressed total mass $\rho_{T,\mathcal{E}}$ (right), as obtained with the MC event generator PYTHIA [8] for LHC with $\sqrt{s} = 14$TeV.

A common use of event shapes is that of discriminating among events with different topologies. This is particularly important in New Physics searches, where one expects events with

massive particles to be much broader than dijet events. We have then tried to assess the performance of known hadronic event shapes for such studies. First, when considering symmetric events with an arbitrary number of particles in the transverse plane, one can only distinguish between two- and multi-jet events, irrespectively of the number of jets. One can then try to discriminate among different topologies in a sample with the same number of jets (three jets in the considered case). One then finds (see Figure 3) that infrared and collinear safe variables fare much better in this respect than unsafe ones (like the widely used transverse sphericity). We remark also that event shapes like the broadenings, which treat tranverse and longitudinal

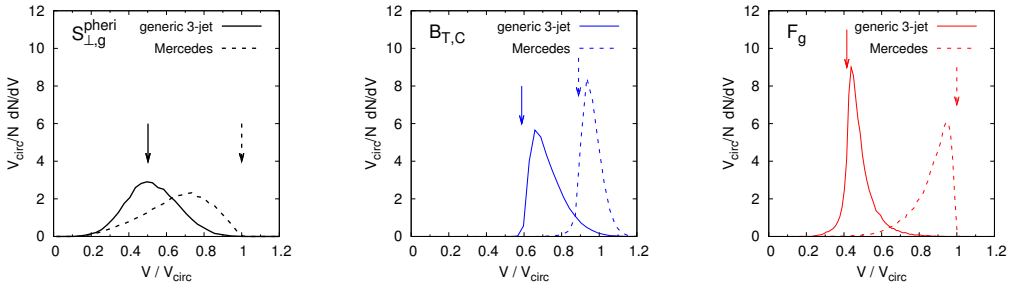

Figure 3: Distribution in the value of three different variables obtained from events with two different hard configurations dressed with parton shower. The two starting configurations are a generic three-parton and a totally symmetric (Mercedes) event in the transverse plane.

degrees of freedom on equal footing, are better suited for the identification of massive-particle decays, since their value is hardly affected by the orientation of the event plane. For practical applications, it is however desirable to have variables that are more sensitive to the spherical limit. One example presented in [5] is the *supersphero* observable which is non-zero only for events in which there are three non-coplanar particles in each of the "hemispheres" in which the event is divided by the transverse thrust axis. We believe that phenomenological applications of variables like supersphero, as well as better final-state observables for New Physics, constitute an important subject that deserves further studies.

References

[1] M. Dasgupta and G. P. Salam, J. Phys. G **30** (2004) R143 [arXiv:hep-ph/0312283].

[2] F. Abe *et al.* [CDF Collaboration], Phys. Rev. D **44** (1991) 601.

[3] I. A. Bertram [D0 Collaboration], Acta Phys. Polon. B **33** (2002) 3141 .

[4] A. Banfi, G. P. Salam and G. Zanderighi, JHEP **0408** (2004) 062 [arXiv:hep-ph/0407287].

[5] A. Banfi, G. P. Salam and G. Zanderighi, JHEP **1006** (2010) 038 [arXiv:1001.4082 [hep-ph]].

[6] Z. Nagy, Phys. Rev. D **68** (2003) 094002 [arXiv:hep-ph/0307268].

[7] A. Banfi, G. P. Salam and G. Zanderighi, JHEP **0503** (2005) 073 [arXiv:hep-ph/0407286].

[8] T. Sjostrand, S. Mrenna and P. Skands, JHEP **0605** (2006) 026 [arXiv:hep-ph/0603175].

Response of single isolated hadrons in the first ATLAS data at $\sqrt{s} = 900$ GeV

Pier-Olivier DeViveiros for the ATLAS Collaboration

University of Toronto, Department of Physics, 60 Saint George Street, Toronto M5S 1A7, Canada

DOI: will be assigned

The response of single isolated hadrons in the ATLAS calorimeters has been studied in 360 thousand collision events at 900 GeV collected during the December 2009 LHC commissioning run. Good agreement is found between the data collected and the Monte Carlo predictions. The results will be used as an input to the estimation of the Jet Energy Scale at ATLAS.

1 Introduction

The ATLAS calorimeters span a large coverage in pseudo-rapidity ($\eta < 4.9$) and are built using sampling technology [1]. The calorimeters are made from 2 sections; the electromagnetic calorimeter provides measurement of the energy of electromagnetic particles and most of the energy from hadrons while the hadronic calorimeter completes the measurement of the energy of hadronic particles. Both sections have further longitudinal segmentation to improve the resolution of the energy measurement. The calorimeters are non-compensating; the energy response of hadrons is smaller than that of electromagnetic particles.

The ATLAS tracking system is composed of pixel detectors, silicon microstrip detectors and transition radiation trackers. The system is immersed in a solenoidal magnetic field of 2 Tesla, and offers coverage up to $\eta < 2.5$. The measured curvature of the tracks can be used to measure the momentum of charged particles with an excellent resolution. The overall momentum scale of charged particles measured in the tracking system is known to better than 1%.

By combining the precise momentum measurement (p) in the tracking with the energy deposited in the calorimeters (E), the response of charged hadrons can be measured (E/p) [2]. The knowledge of this response is an important component in the estimation of the uncertainty on the Jet Energy Scale.

2 Event selection

Collision events were chosen by requiring at least one hit in either of the Minimum Bias Trigger Scintillators (MBTS), and a well-reconstructed vertex with at least 2 associated tracks. This results in a data sample of approximately 360 thousand events.

3 The observable

Energy depositions in the calorimeter cells are grouped into 3 dimensional 'topoclusters' using a noise suppression scheme [3]. The resulting topoclusters are meant to represent the energy deposits of single particles.

High quality tracks, requiring at least 1 hit in the pixel detectors, 6 hits in the silicon strips and $p_T > 500$ MeV, are selected. The tracks are further required to be matched to the event vertex, and isolated, such that no nearby track-like objects are found within a cone of $\Delta R < 0.4$, defined as:

$$\Delta R = \sqrt{(\eta_1 - \eta_2)^2 + (\phi_1 - \phi_2)^2} \quad (1)$$

The tracks are then associated to energy depositions in the calorimeter. The energy in the topoclusters is split into the different longitudinal layers of the calorimeter. The separate layers are matched with the isolated track using a cone of size R_{coll}, using the centroid of the energy deposit in each given layer. The value of R_{coll} is chosen to optimize shower containment while minimizing the contamination from the energy deposits of nearby neutral particles. Figure 1 shows the results of a Monte Carlo study of single particles versus minimum bias events. From this study, a value of 0.2 was chosen for R_{coll}, which corresponds to a shower containment of 90% and a background contamination in the order of 2%.

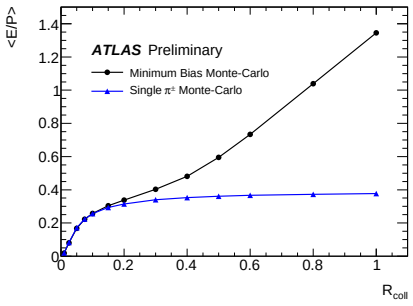

Figure 1: Monte Carlo simulation of the mean E/p value for single particles and minimum bias events in function of the matching cone size R_{coll}. The difference between the two lines is attributed to the background contamination from neutral hadrons.

4 The measurement

Figure 2 shows the distribution of E/p for two different fiducial and kinematic regions in data and Monte Carlo. The ATLAS Monte Carlo simulation consists of a combination of the PYTHIA [4] event generator and a GEANT4 [5] full detector simulation. The Monte Carlo simulations are in good agreement with the data.

4.1 Tracks not associated to any energy deposits

One of the features of the distributions is the peak at E/p values of zero. This peak corresponds to events where tracks are not associated to any energy deposits in the calorimeter. This can be due to two different effects:

1. The algorithm used to create topoclusters requires a seed cell with a ratio of signal over expected noise larger than 4. This requirement is not always fulfilled by showers from hadrons with low momentum.

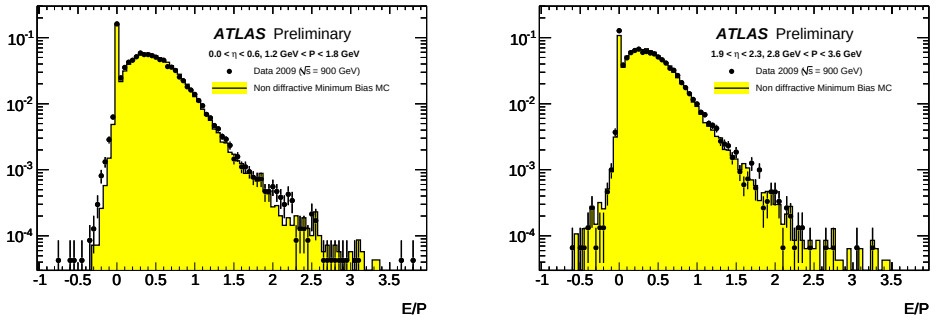

Figure 2: Distribution of E/p for data and Monte Carlo.

2. There is a probability that the particles will undergo hadronic interactions in the material in front of the calorimeter. In this case, the showers may not reach the calorimeter.

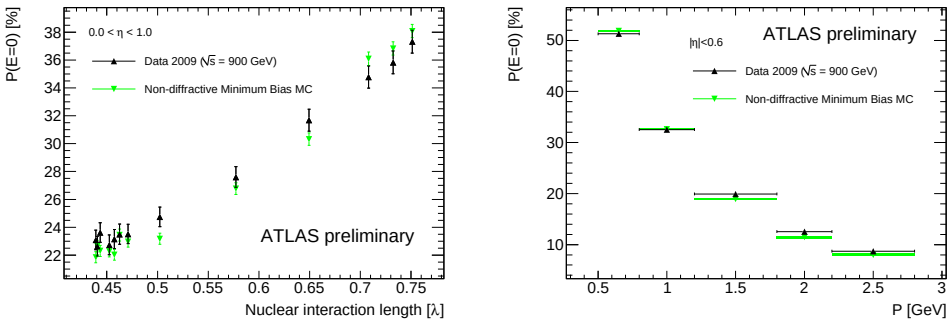

Figure 3: Probability of not having any calorimeter energy deposit associated to a isolated track as a function of the density of the dead material in front of the calorimeter and of the track p.

To study such effects, the figure of merit $P(E/p = 0)$ is used. $P(E/p = 0)$ is an estimator of the probability that a particle deposits no energy in the calorimeter, and is defined as:

$$P(E/p = 0) = \frac{N(E/p < \sigma)}{N_{total}} \tag{2}$$

where σ is the noise width of the E/p distribution, approximated by taking the width of the negative tail of the distribution in data.

Figure 3 shows the distribution of $P(E/p = 0)$ for both data and Monte Carlo as a function of both the amount of dead material in front of the calorimeter, and the particle momentum. The Monte Carlo simulations predict the behaviour of the probability well.

4.2 E/p as a function of P and η

Comparisons between the Monte Carlo and the data are shown using different bins of track momentum and track pseudo-rapidity. The results are shown in Figure 4. General agreement is found at the 5% level, with the exception of the region around $\eta = 1.7$, where the agreement is at the 10% level.

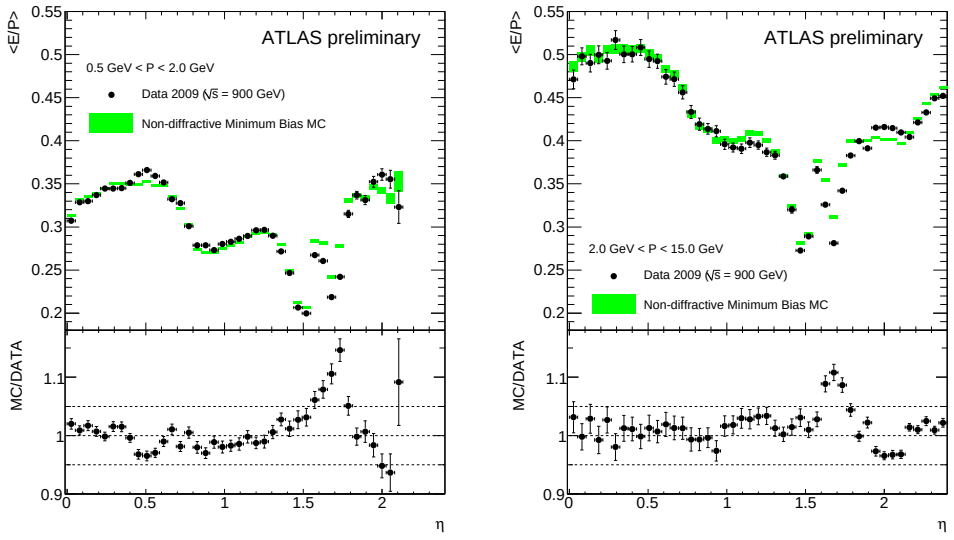

Figure 4: Mean E/p as a function of track η for two different track momentum ranges.

5 Conclusion

The mean response of single isolated hadrons in the ATLAS calorimeters has been measured using data from the December 2009 LHC commissioning run at $\sqrt{s} = 900$ GeV. General agreement has been found with the Monte Carlo predictions at the 5% level for $0.5 < p < 10$ GeV and $|\eta| < 2.3$.

References

[1] ATLAS Collaboration, *"The ATLAS Experiment at the CERN Large Hadron Collider"*, JINST **3 S08003** (2008).

[2] ATLAS Collaboration, *"Response of the ATLAS calorimeters to single isolated hadrons produced in proton-proton collisions at a center-of-mass energy of $\sqrt{s}$ = 900 GeV"*, ATLAS-CONF-2010-017

[3] W. Lampl *et al.*, *Calorimeter clustering algorithms: Description and performance*, ATL-LARG-PUB-2008-002.

[4] T. Sjostrand, S. Mrenna and P. Skands, *PYTHIA 6.4 Physics and Manual*, JHEP **05** (2006) 026.

[5] S. Agostinelli *et al.*, *GEANT4: A simulation toolkit*, NIM **A 506** (2003) 250.

Minimum Bias and Underlying Event Developments in Herwig++

Stefan Gieseke[*], *Simon Plätzer, Andrzej Siodmok, Christian Röhr*

Karlsruhe Institute of Technology, 76128 Karlsruhe, Germany

DOI: http://dx.doi.org/10.3204/DESY-PROC-2010-01/236

We briefly review the status of the multiple partonic interaction model in Herwig++. We present a comparison of some model results to ATLAS data at 900 GeV. As a result we outline how small improvements in Herwig++ result in a very reasonable description of recent minimum bias data.

1 Introduction

The underlying event model in Herwig++ [1] is based on the observation that the hard inclusive cross section for partonic $2 \to 2$ scatters,

$$\sigma^{\text{inc}}(s; p_t^{\min}) = \sum_{i,j} \int_{p_t^{\min 2}} \mathrm{d}p_t^2 f_{i/h_1}(x_1, \mu^2) \otimes \frac{\mathrm{d}\hat{\sigma}_{i,j}}{\mathrm{d}p_t^2} \otimes f_{j/h_2}(x_2, \mu^2)\,, \tag{1}$$

calculated from the usual collinear factorization ansatz, eventually exceeds the total cross section, which is expected to follow the Donnachie–Landshoff (DL)parametrization [2]. The lower limit of allowed transverse momenta is chosen to be $p_t^{\min}$, which is one of the main parameters of the model. The simplest way out is the observation that the proton is a spatially extended object, allowing for independent multiple hard interactions, which are stricly all taken into account in the calculation of the inclusive cross section. Hence, one may calculate the average number of hard interactions from an eikonal ansatz as

$$\bar{n}(\vec{b}, s) = A(\vec{b}; \mu^2)\sigma^{\text{inc}}(s; p_t^{\min})\ . \tag{2}$$

Here, the overlap function $A(\vec{b}; \mu^2)$ describes the spatial overlap of the two colliding hadrons (protons) as a function of the impact parameter $\vec{b}$. The parameter μ^2 characterizes the inverse radius of the proton. We assume a spatial distribution following the functional form deduced from the electromagnetic elastic form factor. We do allow for a different width of the distribution though, as the colour might be distributed differently than the electric charges.

The extension to soft scatterings is kept as simple as possible. First, the transverse momentum of scattered particles is extended to transverse momenta below $p_t^{\min}$. The additional soft contribution to the inclusive cross section is also eikonalized, such that we can as well calculate an average number of soft scatters from the resulting $\sigma^{\text{inc}}_{\text{soft}}$ and an overlap function $A_{\text{soft}}(\vec{b})$ for

[*]Speaker

the soft scattering centers. The functional form $A_{\rm soft}(\vec{b})$ is assumed to be the same as for the hard scatters, but we allow for a different inverse radius, $\mu^2_{\rm soft}$.

We keep this model consistent with unitarity by fixing the two additional parameters $\sigma^{\rm inc}_{\rm soft}$ and $\mu^2_{\rm soft}$ from two constraints. First, we can calculate the total cross section from the eikonal model and fix it to be consistent with the DL parametrization. In addition, using the optical theorem, we can calculate the t–slope parameter from the eikonal model as well and fix it to a reasonable parametrization.

After in a first step only the model for hard multiple partonic interactions has been introduced [3] we also studied its implications from Tevatron data and total cross section data in a simplified version [4]. Finally, the extension of the model to include soft scatters has been implemented in Herwig++ and is now the default underlying event model since version 2.3. In [5] the consistency of the model predictions with current Tevatron data has been studied in detail.

2 Herwig++ against first LHC data

Equipped with the good description of the Tevatron data we can now take a first look at the ATLAS measurements made at the 900 GeV and 7 TeV runs at the LHC [6]. We anticipate the possibility that the assumptions made in order to extend the model into the soft region may be far too simple. Nevertheless, we have been able to accommodate the detailed underlying event analyses carried out at the Tevatron. There we have come up with regions in the two dimensional parameter plane of $p_t^{\rm min}$ and μ^2 were we obtain a similarly good overall χ^2 for the underlying event data and still are consistent with our constraints from the total cross section and the elastic slope parameter. This region roughly follows a line. We now had a first look at Minimum Bias data, particularly the relatively simple distribution of charged particles in pseudorapidity.

As a first step we have varied our model parameters and compared the results against the 900 GeV data. In Fig. 1 we see the bands that result from varying the Herwig++ parameters. The blue lines indicate a favourable set of parameters. This clearly shows that, despite covering the data in the plot, the shape of the pseudorapidity distribution in Herwig++ is by far too much peaked in the forward directions. In addition, there is not enough freedom in our parameter space to describe $\langle p_\perp \rangle (N_{ch})$.

A first hint towards the possible improvement of the description is given in Fig. 2. We vary the probability that any of the additional soft scatters gets disconnected in colour space from the rest of the event and the beam remnants in particular. The value `cD` $= 1$ was used as a default, saying that the soft scatters have always been disconnected. Physically this means that there are no colour strings build up between the beam remnants and the soft particles produced in the soft underlying event. When they are build up more and more as we see when we vary the parameter towards the other extreme value 0 (always connected) we find that we produce many additional soft particles, building up an evenly filled plateau in rapidity. Having checked also other parameters, such as parton distribution functions and their behaviour at small x values we found that the effect of the colour disruption parameter was most important.

A second hint is given by the unability to describe $\langle p_\perp \rangle (N_{ch})$ which is considered to be very sensitive to the presence of non perturbative colour reconnections. So, as final additional we have considered a newly implemented model for soft colour reconnections in Herwig++. We find that only with the two latter modifications we can give a sensible description of minmum

bias events.

In order to clearify this situation quantitatively we have to take into account that there currently is no model for diffractive physics in Herwig++. In order to exclude the contribution from diffractive events, ATLAS have imposed an additional cut on the number of charged particles in a minimum bias event, $N_{\mathrm{ch}} \geq 6$ [7]. The results have been presented at this conference but are not yet publicly available. We have read off the results of this preliminary study from the available plots[1] and compared to the simulation with Herwig++ in Fig. 3. Here, we have included the variation of the colour disruption parameter and the colour reconnection model. The figure shows that a good description of minimum bias observables is indeed possible. A final version of the colour reconnection model will be available with the next release of Herwig++. In order to release the model, further consistency checks against LEP data have to be completed as this data may as well be sensitive to the colour reconnection model.

3 Conclusion

We have tested the generation of minimum bias events in Herwig++ against first data from ATLAS and found that significant improvements in the colour treatment of the Herwig++ model are needed. Taking colour reconnections and stronger colour correlations of soft scatters with the beam remnants into account we find a very good description of non–diffractive minimum bias events.

References

[1] M. Bahr *et al.*, Eur. Phys. J. C **58** (2008) 639 [arXiv:0803.0883 [hep-ph]].

[2] A. Donnachie and P. V. Landshoff, Phys. Lett. B **296** (1992) 227 [arXiv:hep-ph/9209205].

[3] M. Bahr, S. Gieseke and M. H. Seymour, JHEP **0807** (2008) 076 [arXiv:0803.3633 [hep-ph]].

[4] M. Bahr, J. M. Butterworth and M. H. Seymour, JHEP **0901** (2009) 065 [arXiv:0806.2949 [hep-ph]].

[5] M. Bahr, J. M. Butterworth, S. Gieseke and M. H. Seymour, arXiv:0905.4671 [hep-ph].

[6] G. Aad *et al.* [ATLAS Collaboration], Phys. Lett. B **688** (2010) 21 [arXiv:1003.3124 [hep-ex]].

[7] G. Brandt, this conference; ATLAS-CONF-2010-031.

[1] which is possible to sufficiently high accuracy

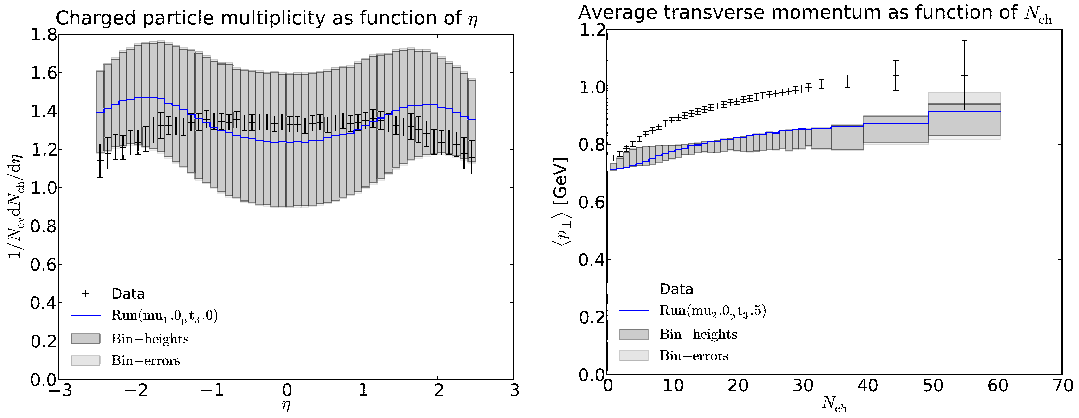

Figure 1: Pseudorapidity distribution of charged particles at 900 GeV compared to data (upper plot). $\langle p_\perp \rangle (N_{ch})$ at 900 GeV compared to ATLAS data. The grey bands indicate the variation from the unfixed parameters in Herwig++. The blue lines are some favourable choice of parameters.

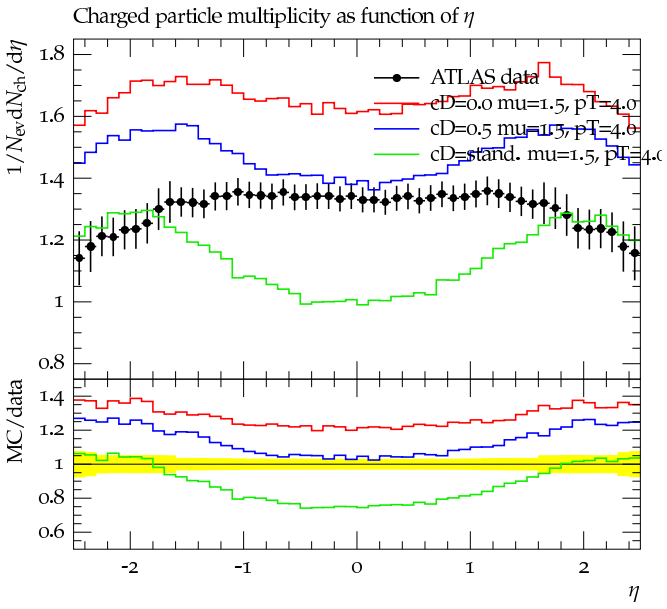

Figure 2: Pseudorapidity distribution of charged particles at 900 GeV compared to data. The lines show the sensitivity to the soft colour disruption parameter in Herwig++.

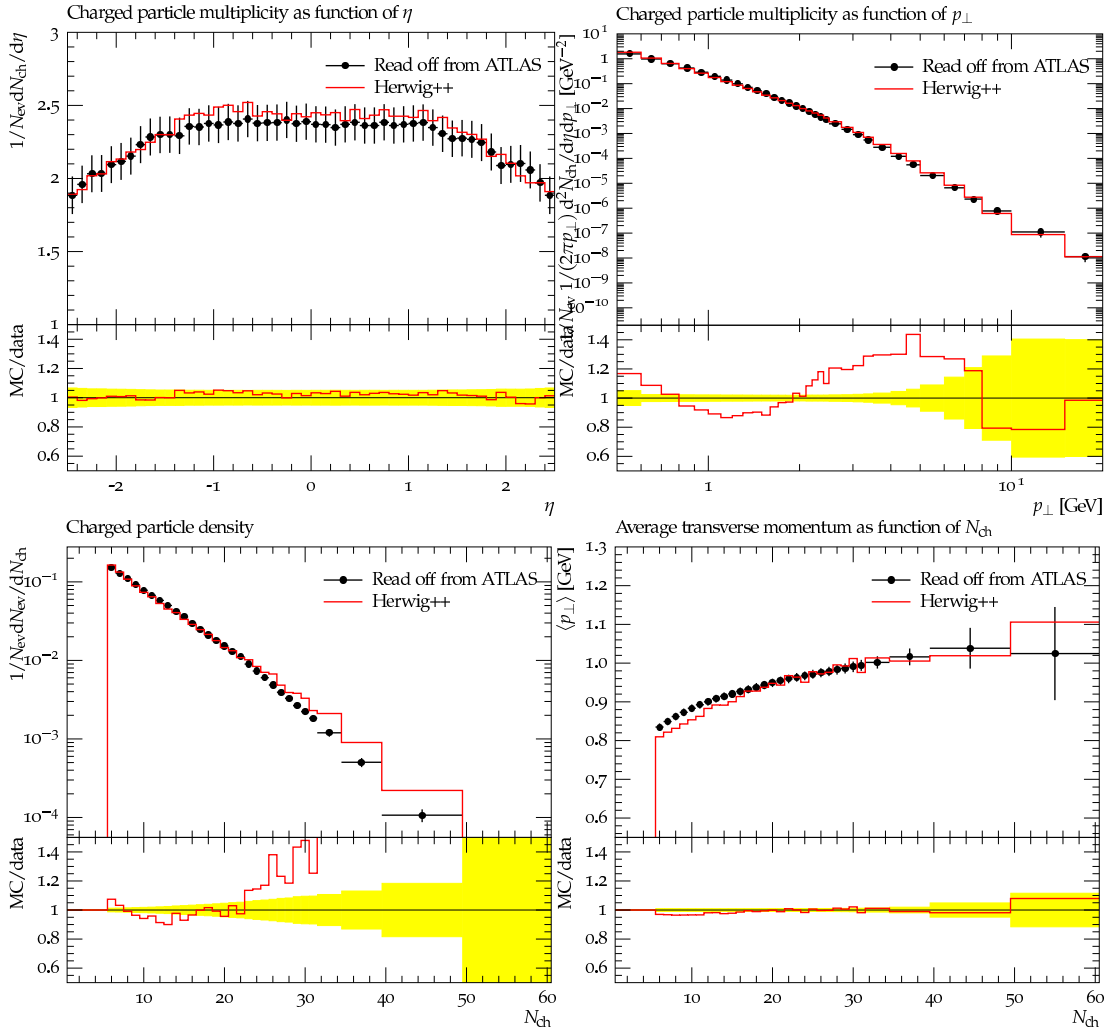

Figure 3: Various observables from the ATLAS $N_{\mathrm{ch}} \geq 6$ analysis compared to Herwig++. The data points are read off preliminary, but publically available, ATLAS figures.

NLO matrix elements and truncated showers

Stefan Höche[1],*Frank Krauss*[2,3], *Marek Schönherr*[4], *Frank Siegert*[2,5]

[1] Institut für Theoretische Physik, Universität Zürich, CH-8057 Zurich, Switzerland
[2] Institute for Particle Physics Phenomenology, Durham University, Durham DH1 3LE, UK
[3] PH-TH, CERN, CH-1211 Geneva 23, Switzerland
[4] Institut für Kern- und Teilchenphysik, TU Dresden, D-01062, Dresden, Germany
[5] Department of Physics & Astronomy, University College London, London WC13 6BT, UK

DOI: http://dx.doi.org/10.3204/DESY-PROC-2010-01/237

An algorithm is presented that combines the ME+PS approach to merge sequences of tree-level matrix elements into inclusive event samples [1] with the POWHEG method, which combines exact next-to-leading order matrix-elements with parton showers [2]. Results obtained with an implementation of this technique into the event generator Sherpa [3] exemplify the quality of the approach in Drell-Yan lepton-pair production at the Tevatron and Higgs-boson and W^+W^--production at LHC energies.

1 Introduction

Facing the huge progress at the LHC, with first data taken, and first results already published, it is crucial to have reliable tools at hand for the full simulation of Standard Model signal and background processes as well as for the simulation of signals for new physics. This task is universally handled by Monte-Carlo event generators like Sherpa [3].

One of the key features of such advanced Monte-Carlo programs is the possibility to consistently combine higher-order tree-level matrix element events with subsequent parton showers (ME+PS) [1]. This feature has proved invaluable in various recent analyses of data from previous experiments, which are sensitive to large-multiplicity final states. Despite being a tremendous improvement over pure leading-order theory, ME+PS merging still suffers from one major drawback of all tree-level calculations, which is their instability with respect to scale variations. This deficiency ultimately necessitates the implementation of NLO virtual corrections in Monte-Carlo programs. Two universally applicable methods were suggested in the past, which can perform this task, and whereof one is the so-called POWHEG algorithm [2]. This technique has been reformulated in [4], such that it can be applied in an automated manner.

Having implementations of both, ME+PS merging and the POWHEG method at our disposal, the question naturally arises, whether the two approaches can be combined into an even more powerful one, joining their respective strengths and eliminating their weaknesses. A first step into this direction was taken independently in [5] and in [6]. Here we will summarise the essence of the algorithms presented ibidem and exemplify the quality of related Monte-Carlo predictions.

2 The MENLOPS approach

A formalism allowing to describe both, the ME+PS and the POWHEG method on the same footing was introduced in [4]. To compare, and, ultimately, to combine both methods, only the expressions for the differential cross section describing the first emission off a given core process must be worked out; this is where the combination takes place.

In a simplified form, the expectation value of an observable in the POWHEG method can be described by the following master formula (for details see [2, 4])

$$\langle O\rangle^{\mathrm{POW}} = \sum_i \int \mathrm{d}\Phi_B\, \bar{\mathrm{B}}_i(\Phi_B) \Bigg[\underbrace{\bar\Delta_i(t_0)\, O(\Phi_B)}_{\text{no emission}} + \underbrace{\sum_j \int_{t_0} \mathrm{d}\Phi_{R|B}\, \frac{\mathrm{R}_j(\Phi_R)}{\mathrm{B}_i(\Phi_B)}\, \bar\Delta_i(t)\, O(\Phi_R)}_{\text{resolved emission}} \Bigg], \quad (1)$$

where $\bar{\mathrm{B}}_i(\Phi_B)$ is the NLO-weighted differential cross section for the Born phase-space configuration Φ_B and $\bar\Delta_i(t) = \exp\Big\{-\sum_j \int_t \mathrm{d}\Phi_{R|B}\, \mathrm{R_j}/\mathrm{B_i}\Big\}$ is the so-called POWHEG-Sudakov form factor. The indices i and j label parton configurations, see [4]. The parameter t is the ordering variable of the underlying parton-shower model and t_0 is the respective cutoff. Hence, t is one of the variables used to parametrise the radiative phase space $\Phi_{R|B}$.

In a similar manner, a simplified master formula for the expectation value of O in the ME+PS approach can be derived. It reads (for details see [5, 6])

$$\begin{aligned}\langle O\rangle^{\mathrm{ME+PS}} = \sum_i \int \mathrm{d}\Phi_B\, \mathrm{B}_i(\Phi_B) \Bigg[& \underbrace{\Delta_i(t_0)\, O(\Phi_B)}_{\text{no emission}} + \sum_j \int_{t_0} \mathrm{d}\Phi_{R|B} \\ & \times \Bigg(\underbrace{\Theta(Q_{\mathrm{cut}} - Q)\, \frac{8\pi\alpha_s}{t}\, \mathcal{K}_{R_j|B_i}\, \frac{\mathcal{L}_{R_j}}{\mathcal{L}_{B_i}}}_{\text{PS domain}} + \underbrace{\Theta(Q - Q_{\mathrm{cut}})\, \frac{\mathrm{R}_j(\Phi_R)}{\mathrm{B}_i(\Phi_B)}}_{\text{ME domain}} \Bigg)\, \Delta_i(t)\, O(\Phi_R) \Bigg]. \end{aligned} \quad (2)$$

The terms labelled "ME domain" and "PS domain" describe the probability of additional QCD radiation according to the real-radiation matrix elements and their corresponding parton-shower approximations, respectively. In this context, $\mathcal{K}_{R_j|B_i}$ are the parton-shower evolution kernels and $\mathcal{L}_{R_j/B_i}$ are the parton luminosities of the real-emission and the underlying Born configurations. In contrast to $\bar\Delta_i(t)$ in Eq. (1), $\Delta_i(t)$ is the uncorrected Sudakov form factor of the parton-shower model.

Combining the ME+PS method with POWHEG essentially amounts to combining the two above equations into a new master formula for the MENLOPS approach. This expression reads

$$\begin{aligned}\langle O\rangle^{\mathrm{MENLOPS}} = \sum_i \int \mathrm{d}\Phi_B\, \bar{\mathrm{B}}_i(\Phi_B) \Bigg[& \underbrace{\bar\Delta_i(t_0)\, O(\Phi_B)}_{\text{no emission}} + \sum_j \int_{t_0} \mathrm{d}\Phi_{R|B}\, \frac{\mathrm{R}_j(\Phi_R)}{\mathrm{B}_i(\Phi_B)} \\ & \times \Bigg(\underbrace{\Theta(Q_{\mathrm{cut}} - Q)\, \bar\Delta_i(t)}_{\text{PS domain}} + \underbrace{\Theta(Q - Q_{\mathrm{cut}})\, \Delta_i(t)}_{\text{ME domain}} \Bigg)\, O(\Phi_R) \Bigg]. \end{aligned} \quad (3)$$

In order to restore the POWHEG master formula, the "ME domain" term would have to be multiplied by the ratio of Sudakov form factors $\bar\Delta_i(t)/\Delta_i(t)$ only. Expanding this ratio to first order reveals that the above formula automatically yields next-to-leading order accurate predictions for any infrared and collinear safe observable O.

3 Results

In the following we present selected results obtained with an implementation of the MENLOPS algorithm in the Sherpa event generator. In particular we aim at detailing the improved description of data collected in various collider experiments.

We focus first on electron-positron annihilation into hadrons at LEP energies ($\sqrt{s}$ =91.25 GeV). Virtual matrix elements were supplied by BlackHat [7]. Figure 1 displays distributions of selected angular correlations in 4-jet production, that have been important for tests of perturbative QCD. The good fit to those data proves that correlations amongst the final-state partons are correctly implemented by the higher-order matrix elements in the MENLOPS method.

Similar findings apply in the analysis of the Drell-Yan process at Tevatron energies ($\sqrt{s}$ =1.96 TeV). Figure 2 shows the transverse momentum distribution of the reconstructed Z-boson and the multiplicity distribution of accompanying jets, constructed using the DØ improved legacy cone algorithm with a cone radius of $R = 0.5$, $p_{\perp,j} > 20$ GeV and $|\eta_j| < 2.5$. The agreement of the MENLOPS result with the respective data is outstanding.

We finally present some predictions for the production of Higgs-bosons through gluon-gluon fusion and for the production of $W^+[\to e^+\nu_e]\, W^-[\to \mu^-\bar{\nu}_\mu]$ at nominal LHC energies ($\sqrt{s}$ =14 TeV). Virtual matrix elements for these analyses have been taken from [11] and [12], respectively. Results are shown in Figs. 3 and 4. We observe very small uncertainties related to the intrinsic parameters of the MENLOPS approach. A detailed discussion is found in [6].

Acknowledgements

SH acknowledges funding by the SNF (contract 200020-126691) and by the University of Zurich (FK 57183003). MS and FS gratefully acknowledge financial support by MCnet (contract MRTN-CT-2006-035606). MS further acknowledges financial support by HEPTOOLS (contract MRTN-CT-2006-035505) and funding by the DFG Graduate College 1504. FK and MS would like to thank the theory group at CERN and the IPPP Durham, respectively, for their kind hospitality during various stages of this project.

References

[1] S. Höche, F. Krauss, S. Schumann and F. Siegert, JHEP **0905** (2009) 053 [arXiv:0903.1219 [hep-ph]].

[2] P. Nason, JHEP **0411** (2004) 040 [hep-ph/0409146];
S. Frixione, P. Nason and C. Oleari, JHEP **0711** (2007) 070 [arXiv:0709.2092 [hep-ph]].

[3] T. Gleisberg, *et al.* JHEP **0402** (2004) 056 [hep-ph/0311263];
T. Gleisberg, *et al.* JHEP **0902** (2009) 007 [arXiv:0811.4622 [hep-ph]].

[4] S. Höche, F. Krauss, M. Schönherr and F. Siegert, arXiv:1008.5399 [hep-ph].

[5] K. Hamilton and P. Nason, JHEP **1006** (2010) 039 [arXiv:1004.1764 [hep-ph]].

[6] S. Höche, F. Krauss, M. Schönherr and F. Siegert, arXiv:1009.1127 [hep-ph].

[7] C. F. Berger *et al.*, Phys. Rev. Lett. **102** (2009) 222001 [arXiv:0902.2760 [hep-ph]].

[8] G. Abbiendi *et al.* [OPAL Collaboration], Eur. Phys. J. C **20** (2001) 601 [hep-ex/0101044].

[9] V. M. Abazov *et al.* [DØ Collaboration], arXiv:1006.0618 [hep-ex].

[10] V. M. Abazov *et al.* [DØ Collaboration], Phys. Lett. B **658** (2008) 112 [hep-ex/0608052].

[11] S. Dawson, Nucl. Phys. B **359** (1991) 283;
A. Djouadi, M. Spira and P. M. Zerwas, Phys. Lett. B **264** (1991) 440.

[12] L. J. Dixon, Z. Kunszt and A. Signer, Nucl. Phys. B **531** (1998) 3 [hep-ph/9803250];
J. M. Campbell and R. K. Ellis, Phys. Rev. D **60** (1999) 113006 [hep-ph/9905386].

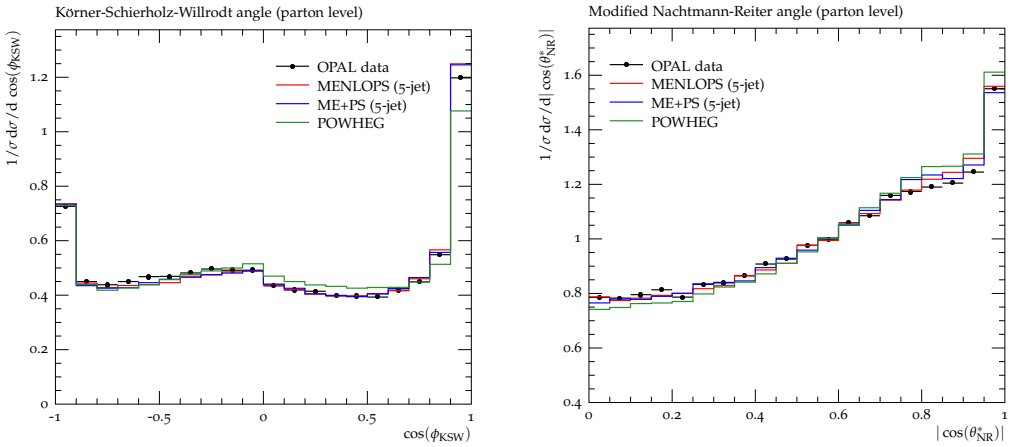

Figure 1: The Körner-Schierholz-Willrodt (KSW) angle (left) and the modified Nachtmann-Reiter (NR) angle (right) in four-jet events defined using the Durham algorithm with $y_{\rm cut} = 0.008$. Results at the parton level are compared to data from the OPAL experiment [8].

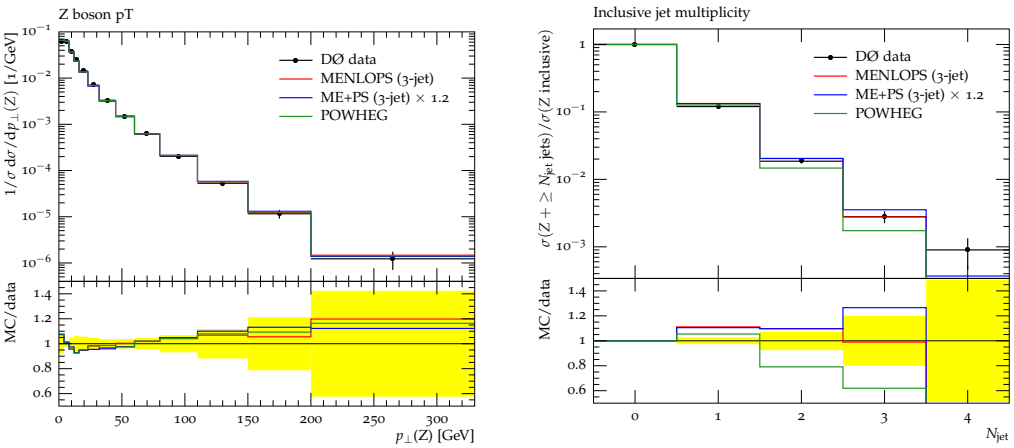

Figure 2: Left: The transverse momentum of the reconstructed Z boson in Drell-Yan events at the Tevatron ($\sqrt{s} = 1.96$ TeV). Results obtained with the MENLOPS approach are compared to data from the DØ experiment [9]. Right: Inclusive jet multiplicity in Drell-Yan events. Monte-Carlo predictions are compared to data from [10].

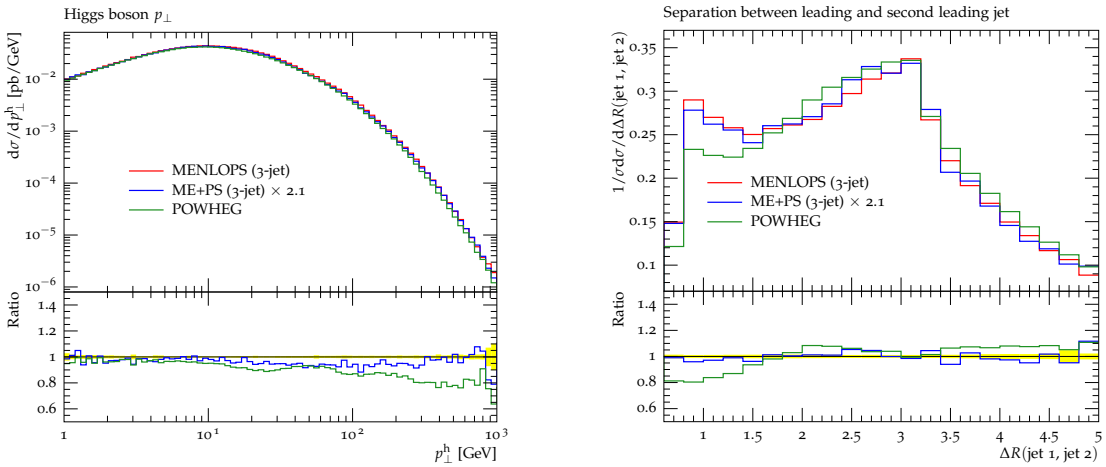

Figure 3: Left: The transverse momentum of the reconstructed Higgs boson in the gluon fusion process at nominal LHC energies (14 TeV). Right: Separation in η-ϕ space of the first and second hardest jet in Higgs-boson production via gluon fusion at nominal LHC energies.

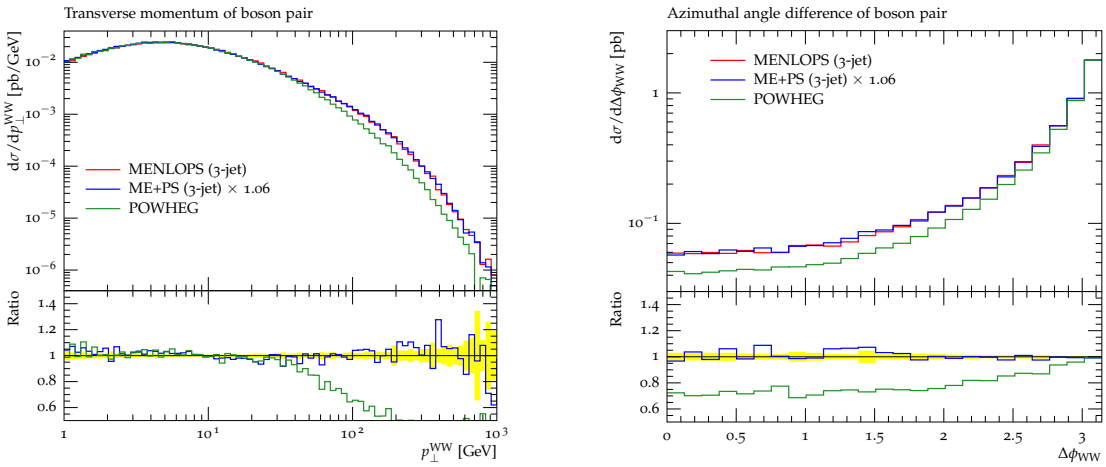

Figure 4: Left: The transverse momentum of the reconstructed W^+W^- system in $W^+[\to e^+\nu_e]\ W^-[\to \mu^-\bar{\nu}_\mu]$ events at nominal LHC energies (14 TeV). Right: Separation in η-ϕ space of the first and second hardest jet in W^+W^- production at nominal LHC energies.

NLO and parton showers: the POWHEG-BOX

Simone Alioli

DESY, Platanenallee 6, 15738 Zeuthen, Germany

DOI: http://dx.doi.org/10.3204/DESY-PROC-2010-01/238

We describe the POWHEG-BOX package, a general computer code framework for implementing NLO calculations in Shower Monte Carlo programs according to the POWHEG method. The program can be downloaded from http://powhegbox.mib.infn.it/~nason/POWHEG.

1 The POWHEG method

Next-to-leading order (NLO) perturbative QCD computations as well as *Shower Monte Carlo* (SMC) programs are fundamental tools for the present-days particle physics phenomenology. In particular, SMC programs incorporate the description of a generic high-energy hadronic collision process, starting from the collision between constituents and developing the parton shower, that increases the number of final-state particles by means of strongly ordered subsequent emissions. Eventually, the interface with a phenomenological hadronization model, enables the comparison with experimental data. For these reasons, they are routinely used by experimentalists to simulate signal and backgrounds processes in physics searches. Nevertheless, the demand for better and better predictions from high energy experiments calls for improving the precision of existing SMC's, including NLO corrections. The MC@NLO [1] method has shown first how to reach NLO accuracy for inclusive quantities, implementing the hard subprocess at NLO and developing showers within the *leading logarithmic approximation*, avoiding double counting of radiation. In this way one achieves benefits of both approaches: exclusive final states generation of SMC's and accuracy of NLO calculations.

The POWHEG method is a different prescription for interfacing NLO calculations with parton shower generators. It was first suggested in Ref. [2], and was described in great detail in Ref. [3]. This method is independent from the Monte Carlo program used for subsequent showering and generates positive weighted events only. In these respects it improves the MC@NLO approach. Until now, the POWHEG method has been successfully applied to several processes, both at lepton [4, 5] and hadron colliders [6, 7, 8, 9, 10, 11, 12, 13, 14]. In these implementations, it has been interfaced to the HERWIG [15, 16], PYTHIA [17] and HERWIG++ [18] SMC programs.

In the POWHEG method the hardest radiation[1] is generated first, independently from the following ones. Schematically[2], the hardest radiation is distributed according to

$$d\sigma = \bar{B}\left(\Phi_B\right) d\Phi_B \left[\Delta_R\left(p_T^{\min}\right) + \frac{R\left(\Phi_R\right)}{B\left(\Phi_B\right)} \Delta_R\left(k_T\left(\Phi_R\right)\right) d\Phi_{\mathrm{rad}}\right], \tag{1}$$

[1] By hardest we mean the radiation with the highest transverse momentum, either with respect to the beam for initial state radiation (ISR), either with respect to another parton for final state radiation (FSR).

[2] Here we avoid entering into the details concerning the radiation regions and the correct treatment of the associated flavour configurations [2, 3].

where $B(\Phi_B)$ is the Born contribution and

$$\bar{B}(\Phi_B) = B(\Phi_B) + \left[V(\Phi_B) + \int d\Phi_{\rm rad}\, R(\Phi_R) \right] \tag{2}$$

is the NLO differential cross section at fixed underlying Born kinematics and integrated over the radiation variables. The transverse momentum of the emitted parton, with respect to the beam or to another particle, depending on the region of singularity, is denoted by $k_T(\Phi_R)$. The lower cutoff $p_T^{\rm min}$ is necessary in order to avoid the coupling constant to reach unphysical values. $V(\Phi_B)$ and $R(\Phi_R)$ are the virtual and the real corrections and in the expression within the square bracket in Eq. (2) a procedure that takes care of the cancellation of soft and collinear singularities is understood, *e.g.* Frixione-Kunszt-Signer (FKS) [19] or Catani-Seymour (CS) [20] dipole subtraction. Then,

$$\Delta_R(p_T) = \exp\left[- \int d\Phi_{\rm rad} \frac{R(\Phi_R)}{B(\Phi_B)} \theta\left(k_T(\Phi_R) - p_T\right) \right] \tag{3}$$

is the POWHEG Sudakov, that is the probability of not having an emission harder that p_T. Equation (1) can be seen as an improvement on the original SMC hardest-emission formula, since the Born cross section is replaced with $\bar{B}(\Phi_B)$ which is normalized to NLO by construction. At small transverse momenta the POWHEG Sudakov becomes equal to a standard SMC one. However, the NLO accuracy of Eq. (1) is maintained for inclusive quantities. Moreover, the high$-p_T$ radiation region is correctly described by the real contributions

$$d\sigma \approx \bar{B}(\Phi_B)\; d\Phi_B \frac{R(\Phi_R)}{B(\Phi_B)} d\Phi_{\rm rad} \;\approx R(\Phi_R)\, d\Phi_B d\Phi_{\rm rad}\,, \tag{4}$$

since $\Delta_R \approx 1$ and $\bar{B}/B \approx 1 + \mathcal{O}(\alpha_{\rm s})$. After having generated the hardest radiation, one can interface with any available shower generator, in order to develop the rest of the shower. To avoid the double-counting, the SMC is required to be either p_T-ordered or to have the ability to veto emissions with a p_T harder than the first one[3].

2 The POWHEG-BOX

In a real collision process several colored massless partons are present, either in the initial or the final state. One thus should repeat the procedure outlined in Sec. 1 for every possible singular region, associated with any massless colored leg becoming collinear to another one, or soft. In order to do this, the full real emission cross section is decomposed into a sum of terms, each of which has at most one collinear and one soft singularities. The radiation is then generated independently in each of this regions, but only the hardest radiation is retained and the event is generated according to the flavour and kinematics associated to it. Because of this complexity, an automatic tool, the POWHEG-BOX, has been built [22], in order to help the inclusion of new processes. On the other hand, the POWHEG-BOX may also be seen as a library, where previously implemented processes are available in a common framework. The processes implemented so far and already available in the public version comprise: $W, Z/\gamma$ single vector boson production, Higgs boson through gluon and Vector Boson Fusion, single-top in $s-$ and $t-$channel.

[3] All modern SMC generators compliant with the *Les Houches Interface for User Processes* [21] should implement this last feature.

The user wishing to include a new NLO calculation must only know how to communicate the needed information to the `POWHEG-BOX`. This happens either defining the appropriate variables, either providing the necessary `Fortran` routines. The required inputs [4] are:

1. The number of legs in Born process, *e.g.* `nlegborn`$= 5$ for $pp \to (Z \to e^+e^-) + j$.

2. The list of Born and Real processes flavours, according to PDG [23] conventions[5]. Flavor is defined incoming (outgoing) for incoming (outgoing) fermion lines, *e.g.* `[5,2,23,6,3,0]` for $bu \to Ztsg$.

3. The Born phase space routine that, given random numbers in the unit `ndims`-dimensional hypercube, set the Born phase space Jacobian and returns the momenta in lab. and CM frames and the Bjorken x's.

4. The routines that performs the initialization of the couplings, and the setting of the factorization and renormalization scales.

5. The Born squared amplitude routine that, for a given set of momenta and a flavour configuration, returns $\mathcal{B} = |\mathcal{M}|^2$, summed and averaged over color and helicities as well as the color-ordered Born squared amplitudes $\mathcal{B}_{jk}$ and the helicity correlated Born squared amplitudes $\mathcal{B}_{k,\mu\nu}$, where k runs over all external gluons.

6. The real emission squared amplitude routine, that returns $\mathcal{R}$ for a given momenta and flavour list.

7. The finite part of the interference of Born and virtual amplitude contributions $\mathcal{V}_{\rm b} = 2{\rm Re}\{\mathcal{B} \times \mathcal{V}\}$, after factorizing out the common factor $\mathcal{N} = \frac{(4\pi)^\epsilon}{\Gamma(1-\epsilon)} \left(\frac{\mu_{\rm R}^2}{Q^2}\right)^\epsilon$. The routine is again defined with momenta and flavour list as input.

8. The Born color structures in the large $N_{\rm c}$ limit, set through the Les Houches interface [21].

We remark that items (1-7) are the usual ingredients needed to perform a NLO calculation in any subtraction method. Item (8) is instead needed to provide a defined color structure to the SMC generator. Internally, the `POWHEG-BOX` implements the FKS subtraction procedure in a general way. At the beginning, it automatically evaluates the combinatorics, identifying all the singular regions and the corresponding underlying Born contributions. It also performs the projection of real contributions over the singular region and computes the subtraction counterterms, from soft and collinear approximations of real emissions. Then, it builds the ISR and FSR phase space, according to the FKS parametrization of the singular region and performs the integration. Eventually, one gets the NLO differential cross section. At this stage, one can also interface to some analysis routine to obtain NLO differential distributions as a byproduct. After the integration stage, it performs the calculation of upper bounds for an efficient generation of Sudakov-suppressed events and then the generation of hardest radiation, according to the `POWHEG` Sudakov. At this point, the generated event, which contains at most only one extra radiation, has to be passed to a standard SMC program, for developing the rest

[4] For the precise definition of the following routines, we refer the reader to Ref. [22].

[5] Internally gluons are labelled 0 instead of the PDG value of 21. At the moment of writing the event on the Les Houches common block, the PDG value is restored.

of the shower. This can be done either on-the-fly or storing the events on a Les Houches events file [24]. Standard analysis routines, at partonic and hadronic level, are provided for included processes, as well as drivers for common SMC generators. Users can modify them or implement new ones.

2.1 Recent developments

Recently, thanks to this framework, the relatively complex process of $Z + 1$ *jet* production has been implemented [25]. This is a promising processes for jet calibration with the early LHC data. It is also an important source of missing energy signal as well as a background to many new physics searches. In experimental studies carried up until now, the NLO theoretical calculations were supplemented by correction factors for shower, hadronization and underlying event effects. However, these factors were evaluated by means of standard LO SMC programs. It is clear the advantage to have a SMC program which is NLO accurate, in order to ease and improve the comparisons with experimental results. We have tried a simple approach [25] to merge consistently Z and $Z + 1$ *jet* samples, in order to obtain a description as smooth and accurate as possible both in the low and high-transverse momentum regions. The results are showed in Figs. 1 and 2.

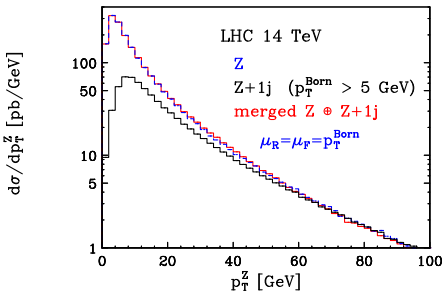

Figure 1: The p_T distribution of the Z boson in single Z production (blue dashed curve), in $Z + 1$ jet (black solid) and in the merged sample (red solid).

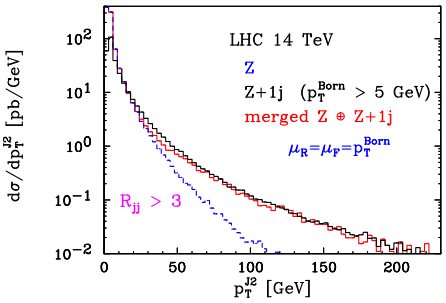

Figure 2: The p_T distribution of the *next-to-hardest* jet in single Z production (blue dashed curve), in $Z+1$ jet (black solid) and in the merged sample (red solid).

From the two figures, one can see how the merged sample models both the single Z Sudakov form factor, that plays an important role in resumming collinear/soft logarithms in the low-p_T region and the high-p_T behaviour of the next-to-hardest jet, which follows the $Z + 1$ jet distribution. In this last figure, jest are reconstructed according to the k_T algorithm, imposing also an angular separation $R_{jj} > 3$.

Acknowledgments

All results presented in this talk have been obtained in collaboration with P. Nason, C. Oleari and E. Re. This work has been supported in part by the Deutsche Forschungsgemeinschaft in SFB/TR 9.

References

[1] S. Frixione and B. R. Webber, JHEP **0206** (2002) 029 [arXiv:hep-ph/0204244].

[2] P. Nason, JHEP **0411** (2004) 040 [arXiv:hep-ph/0409146].

[3] S. Frixione, P. Nason and C. Oleari, JHEP **0711** (2007) 070 [arXiv:0709.2092 [hep-ph]].

[4] O. Latunde-Dada, S. Gieseke and B. Webber, JHEP **0702** (2007) 051 [arXiv:hep-ph/0612281].

[5] O. Latunde-Dada, Eur. Phys. J. C **58** (2008) 543 [arXiv:0806.4560 [hep-ph]].

[6] P. Nason and G. Ridolfi, JHEP **0608** (2006) 077 [arXiv:hep-ph/0606275].

[7] S. Frixione, P. Nason and G. Ridolfi, JHEP **0709** (2007) 126 [arXiv:0707.3088 [hep-ph]].

[8] S. Alioli, P. Nason, C. Oleari and E. Re, JHEP **0807** (2008) 060 [arXiv:0805.4802 [hep-ph]].

[9] K. Hamilton, P. Richardson and J. Tully, JHEP **0810** (2008) 015 [arXiv:0806.0290 [hep-ph]].

[10] A. Papaefstathiou and O. Latunde-Dada, JHEP **0907** (2009) 044 [arXiv:0901.3685 [hep-ph]].

[11] S. Alioli, P. Nason, C. Oleari and E. Re, JHEP **0904** (2009) 002 [arXiv:0812.0578 [hep-ph]].

[12] K. Hamilton, P. Richardson and J. Tully, JHEP **0904** (2009) 116 [arXiv:0903.4345 [hep-ph]].

[13] S. Alioli, P. Nason, C. Oleari and E. Re, JHEP **0909** (2009) 111 [Erratum-ibid. **1002** (2010) 011] [arXiv:0907.4076 [hep-ph]].

[14] P. Nason and C. Oleari, JHEP **1002** (2010) 037 [arXiv:0911.5299 [hep-ph]].

[15] G. Corcella *et al.*, JHEP **0101** (2001) 010 [arXiv:hep-ph/0011363].

[16] G. Corcella *et al.*, arXiv:hep-ph/0210213.

[17] T. Sjostrand, S. Mrenna and P. Z. Skands, JHEP **0605** (2006) 026 [arXiv:hep-ph/0603175].

[18] M. Bahr *et al.*, Eur. Phys. J. C **58**, 639 (2008) [arXiv:0803.0883 [hep-ph]].

[19] S. Frixione, Z. Kunszt and A. Signer, Nucl. Phys. B **467** (1996) 399 [arXiv:hep-ph/9512328].

[20] S. Catani and M. H. Seymour, Nucl. Phys. B **485** (1997) 291 [Erratum-ibid. B **510** (1998) 503] [arXiv:hep-ph/9605323].

[21] E. Boos *et al.*, arXiv:hep-ph/0109068.

[22] S. Alioli, P. Nason, C. Oleari and E. Re, JHEP **1006** (2010) 043 [arXiv:1002.2581 [hep-ph]].

[23] http://pdg.lbl.gov

[24] J. Alwall *et al.*, Comput. Phys. Commun. **176** (2007) 300 [arXiv:hep-ph/0609017].

[25] S. Alioli, P. Nason, C. Oleari, and E. Re, In preparation.

Underlying event studies in inelastic pp collision events with the ATLAS detector

Markus Warsinsky for the ATLAS Collaboration

Albert-Ludwigs-Universität Freiburg, Physikalisches Institut, Hermann-Herder-Str. 3, 79104 Freiburg, Germany

DOI: http://dx.doi.org/10.3204/DESY-PROC-2010-01/272

The first measurement of the charged particle flow in inelastic pp collision events with the ATLAS detector is described. The analysis is based on minimum-bias events collected at centre of mass energies of 900 GeV and 7 TeV. The density of charged particles and their transverse momentum sum is measured in different regions of azimuthal angle defined with respect to the leading charged particle in the event. The data show a higher underlying event activity than predicted by different Monte Carlo models and tunes.

1 Introduction

Main goals of the LHC are the search for new physics phenomena and precision measurements. In order to perform these, it is important to not only have a good description of the hard scattering process, but also of soft-QCD effects which influence the accompanying beam–beam remnants, initial and final state QCD radiation and multiple parton interactions. These effects are collectively called the underlying event (UE).

These soft physics processes cannot be derived from first principles, but instead are predicted from different phenomenological models implemented in Monte Carlo (MC) event generators. The free model parameters are adjusted to describe the available data, among these measurements of the UE activity, as well as possible. Previous measurements of the UE by the CDF experiment [1, 2] have been made at a significantly lower centre of mass energy than the LHC. It is thus important to measure the UE at LHC energies, as the extrapolation to higher centre of mass energies results in large uncertainties.

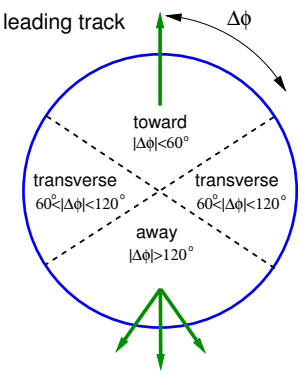

Figure 1: Azimuthal regions with respect to the leading charged particle.

For a measurement of the UE activity, it is necessary to investigate activity in a region of the event that receives only little contribution from the hard scattering process. In the following, this is accomplished by dividing the event into regions of azimuthal angle relative to the charged particle with the highest transverse momentum (called *leading* charged particle in the following), as shown in Figure 1. The transverse region is expected to receive the largest fraction from the UE and only minimal contribution from the hard

scattering process. The toward and away regions are influenced more by the dijet structure of an assumed $2 \to 2$ scattering.

2 Analysis Procedure

The ATLAS detector is described in [3]. Of relevance for the presented analysis are the minimum bias trigger scintillators (MBTS) and the inner detector (ID). The MBTS consist of scintillators mounted at $|z| = \pm 3.56\,\mathrm{m}$ and covering a pseudorapidity range of $2.09 < |\eta| < 3.84$. The ID consists of a three-layer pixel detector, a silicon strip detector and a transition radiation tracker. It covers $|\eta| < 2.5$ and is immersed in a 2 T solenoidal magnetic field. Details of the analysis can be found in [4]. The data were collected in the 900 GeV run of the LHC from December 6th to 14th 2009 and in the first run at 7 TeV on March 30th 2010. Events were triggered by requiring a signal on any side of the MBTS. The event selection in addition requires at least one reconstructed track with a transverse momentum p_T of at least 1 GeV within $|\eta| < 2.5$ and requiring transverse and longitudinal impact parameters of less than 1.5 mm. In addition a reconstructed primary vertex [5] with at least two tracks ($p_T > 100\,\mathrm{MeV}$) was required. Tracks used for the analysis were required to have $p_T > 0.5\,\mathrm{GeV}$ and the same cuts as used for the tracks to select the event. The number of events, the number of tracks and the integrated luminosity of the datasets are shown in Table 1. Beam- and cosmic-muon induced background were estimated to be negligible after this event selection.

	selected		
$\sqrt{s}$[GeV]	events	tracks	$L_{\mathrm{int}}[\mu\mathrm{b}^{-1}]$
900	202285	1540373	9
7000	265622	3474551	6.8

Table 1: Selected events, tracks and integrated luminosity.

The data were corrected to the level of primary[1] charged particles satisfying the event-level requirement of at least one primary charged particle with $p_T > 1\,\mathrm{GeV}$ and $|\eta| < 2.5$ and the selection of primary charged particles with $p_T > 500\,\mathrm{MeV}$ and $|\eta| < 2.5$. The correction procedure is described in more detail in [4, 6, 7]. To account for events lost due to the event selection, the trigger efficiency was estimated from an orthogonal trigger setup from data, the vertexing efficiency is measured in data, and lastly a correction factor to account for not reconstructing all charged primary particles with $p_T > 1\,\mathrm{GeV}$ was applied [4]. Tracks lost due to tracking inefficiency were corrected for by the track-reconstruction efficiency as estimated from the detector simulation. In addition remaining secondary particles and the fraction of primary particles corresponding to reconstructed tracks being outside the specified kinematic range were subtracted. As a final step, a bin-by-bin unfolding method is applied to account for bin-to-bin migrations and effects not covered by the other corrections. The ATLAS MC09 tune [8] of the PYTHIA6 [9] MC generator was used for this unfolding. The systematic uncertainty was estimated by using the PHOJET [10] generator as an alternative model and was found to be at most 2%, which is small compared to the systematic uncertainty of the tracking efficiency of about 5%. More detail on the systematic uncertainties can be found in [4].

[1] Primary particles are defined as having a mean lifetime $\tau > 3 \cdot 10^{-11}$ s.

3 Results

The charged particle density and the scalar p_T sum density of charged particles are shown in Figure 2 for the transverse region. The data are compared to the PYTHIA6 [9] generator using the ATLAS MC09 [8], DW [11] and the Perugia0 [12] tunes, and to the PHOJET [10] generator. While the MC models describe the basic behaviour, all predictions are lower than the data, especially at $\sqrt{s} = 7\,\text{TeV}$. The DW tune is closest to the data, while the PHOJET description is furthest off. The recently derived ATLAS AMBT1 tune [13] of the PYTHIA6 event generator, which improves the description of charged particle multiplicities in a diffraction-limited phase space gives a comparable description of the data as the ATLAS MC09 tune [13].

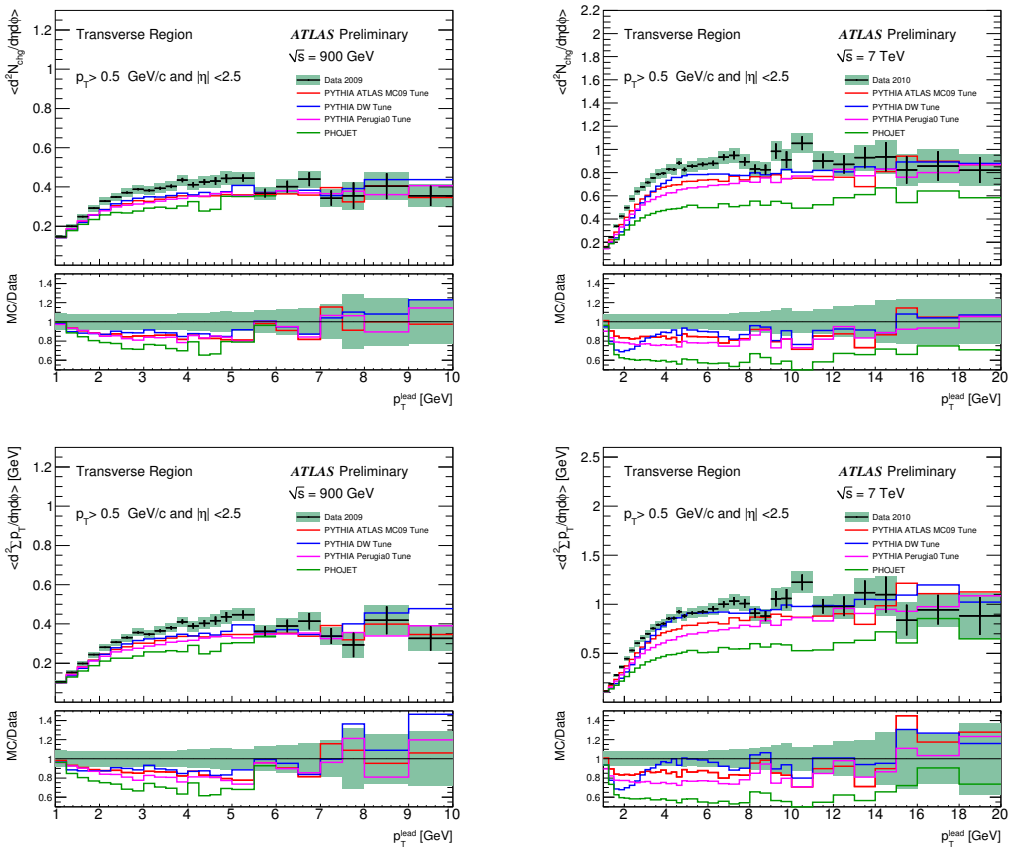

Figure 2: Observables in the transverse region. Charged particle (top row) and scalar p_T sum density (bottom row) vs. the p_T of the leading charged particle. Left column: $\sqrt{s} = 900\,\text{GeV}$, right column: $\sqrt{s} = 7\,\text{TeV}$. Black data-points: ATLAS data (shaded area total, error-bars only statistical uncertainty). Solid lines: predictions of the PYTHIA6 [9] and the PHOJET [10] MC generators.

Figure 3 shows the difference in azimuthal angle between charged particles and the leading charged particle for different cuts on the p_T of the leading charged particle. Clearly a larger

density towards and away from the leading charged particle as predicted by the MC generators is observed. This becomes more visible for higher cuts on the p_T of the leading charged particle, pointing to the emergence of a jet-like structure. The prediction of the ATLAS MC09 tune differs both in shape and normalization from the data.

Further measurements can be found in [4].

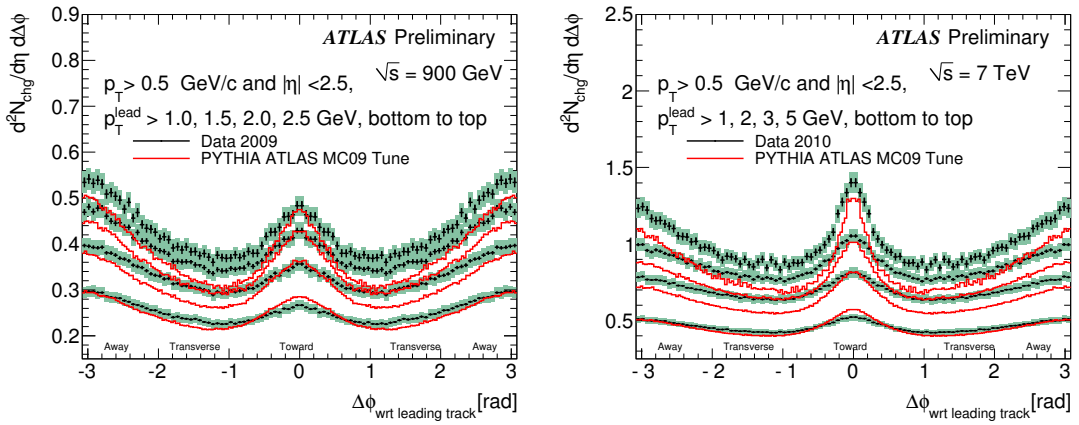

Figure 3: Azimuthal angle difference to the leading charged particle at $\sqrt{s} = 900\,\text{GeV}$ (left) and 7 TeV (right) for different transverse momentum requirements for the leading charged particle. Black data-points: ATLAS data (shaded area total, error-bars only statistical uncertainty), solid line: prediction of the PYTHIA6 MC generator with the ATLAS MC09 tune.

4 Conclusions

A first measurement of the underlying event activity at LHC energies has been presented [4]. Despite the large step in centre-of-mass, the Monte Carlo models describe the basic features of the underlying event activity, but predict slightly less activity than observed. These data will be important for constraining these models and will be used for tuning of MC event generators in the near future.

5 Acknowledgments

M. Warsinsky acknowledges the support of the Initiative and Networking Fund of the Helmholtz Association, contract HA-101 ("Physics at the Terascale").

References

[1] D. E. Acosta *et al.* [CDF Collaboration], Phys. Rev. D **70** (2004) 072002.

[2] T. Aaltonen *et al.* [CDF Collaboration], arXiv:1003.3146 [hep-ex].

[3] G. Aad *et al.* [ATLAS Collaboration], JINST **3** (2008) S08003.

[4] ATLAS Collaboration, ATLAS-CONF-2010-029.
[5] G. Piacquadio, K. Prokofiev and A. Wildauer, J. Phys. Conf. Ser. **119**, 032033 (2008).
[6] G. Aad *et al.* [ATLAS Collaboration], Phys. Lett. B **688** (2010) 21.
[7] ATLAS Collaboration, ATLAS-CONF-2010-024.
[8] ATLAS Collaboration, ATL-PHYS-PUB-2010-009.
[9] T. Sjostrand, S. Mrenna and P. Z. Skands, JHEP **0605** (2006) 026.
[10] R. Engel, Z. Phys. C **66** (1995) 203.
[11] R. Field, presentation at the Fermilab ME/MC Tuning workshop, October 2002.
[12] P. Z. Skands, arXiv:0905.3418 [hep-ph].
[13] ATLAS Collaboration, ATLAS-CONF-2010-031.

The underlying event in pp collisions at 900 GeV in CMS

Giuseppe B. Cerati for the CMS Collaboration

DOI: http://dx.doi.org/10.3204/DESY-PROC-2010-01/273

The underlying event in pp interactions at $\sqrt{s} = 900$ GeV is studied measuring the charged multiplicity density and the charged energy density in a region perpendicular to the plane of the hard 2-to-2 scattering. Two different methodologies are adopted to identify the direction and the energy scale of the hard scattering in Minimum Bias events that rely on the leading charged track and on the leading charged jet. The study allows to discriminate between various QCD Monte Carlo tunes with different multiple parton interaction schemes which correctly reproduce Tevatron underlying event data but give different predictions when extrapolated to different energies.

1 Introduction

The hard scattering in proton-proton collisions can be thought of as the sum of the hard 2-to-2 parton collision, including the initial and final state radiation, and of the underlying event (UE), given by beam-beam remnants (BBR) and multiple parton interactions (MPI). Characterising the UE is an unavoidable step towards an accurate tuning of Monte Carlo (MC) models which is crucial for the precise measurement of Standard Model processes and, consequently, for the search for physics beyond the SM. Using $\sqrt{s} = 900$ GeV collisions collected by the CMS detector [1] late 2009, UE properties at LHC energies can be compared to the predictions of several MC tunes which have been studied at Tevatron energies and inferences about MPI models can be drawn.

1.1 PHYTHIA tunes

In the work presented at this conference [2], several PYTHIA tunes are considered; they are all compatible with Tevatron data but differ in the description of parton fragmentation and multiple parton interaction. From the UE perspective, the main difference between the tunes is the value of two parameters, $p_T^0(\sqrt{s_0})$ at a reference energy $\sqrt{s_0}$ and ϵ, used by PYTHIA to regularize the $1/{p_T}^4$ divergence for final state parton $p_T \to 0$. The first is a cut-off parameter, used both for hard-scattering and MPI, while the second controls the energy dependence of the cut-off:

$$p_T^0(\sqrt{s}) = p_T^0(\sqrt{s_0}) \cdot (\sqrt{s}/\sqrt{s_0})^{\epsilon} \tag{1}$$

Among the considered tunes, *D6T* ($p_T^0(1.8\ TeV)$=1.8 GeV/c, ϵ=0.16) has the smallest ϵ value (obtained fitting UA5 Minimum Bias data at $Sp\bar{p}S$) and it is the only tune exploiting CTEQ6L pdfs; *DW* ($p_T^0(1.8\ TeV)$=1.9 GeV/c, ϵ=0.25) can be considered as the "best fit" of Tevatron data since it is compatible with the Drell-Yan p_T spectrum from CDF and

with the D0 di-jet $\Delta\phi$ distribution; both *Pro-Q20* ($p_T^0(1.8\ TeV)$=1.9 GeV/c, ϵ=0.22) and *P0* ($p_T^0(1.8\ TeV)$=2 GeV/c, ϵ=0.26) tunes make use of the Professor fit program, which exploits LEP data for the tuning of the fragmentation functions, while only P0 implements the new PYTHIA MPI model with p_T-ordered showers; the last tune, *CW*, ($p_T^0(1.8\ TeV)$=1.8 GeV/c, ϵ=0.3), was created for the sake of the present study and is intended to maximize the MPI contribution at $\sqrt{s} = 900$ GeV while still being compatible with Tevatron data.

2 Data Analysis

The predictions of these tunes after full detector simulation are compared to CMS data. Events are characterised as a function of the scale of the hard interaction, defined either by the leading track or by the leading tracker-jet; the two methods define two complementary analysis approaches. The direction of the hard interaction in the plane orthogonal to the beam direction allows to identify three equally-sized regions (Fig. 1(a)): Toward ($|\Delta\phi| < 60°$), Away ($|\Delta\phi| > 120°$) and Transverse ($60 \leq |\Delta\phi| \leq 120°$), where $\Delta\phi$ is the azimuthal angle difference between a reconstructed track and the leading object in the event. The transverse region, less sensitive to hard-scattering components and to final state radiation products, is the most convenient region to characterise the UE properties. The analysis is performed on data collected during the 2009 LHC runs at $\sqrt{s} = 900$ GeV, consisting of 250k selected events and 4.8M tracks.

2.1 Event and Track Selection

Events are selected requiring a Minimum Bias trigger [2] defined as the coincidence of both Beam Pick-up Timing for experiments with a hit in the Beam Scintillator Counters and requiring a primary vertex with at least three associated tracks. In addition, events must contain a leading object with a p_T above threshold: threshold values are 0.5, 1.0 or 2.0 GeV/c for the leading track analysis and 1.0 or 3.0 GeV/c for the leading tracker-jet. Tracks are first selected according to basic kinematic cuts tuned to obtain homogeneous tracking performance: $p_T > 0.5$ GeV/c and $|\eta| < 2$; the primary vertex compatibility is verified by requiring longitudinal and transverse impact parameter significances less than 5; finally, good quality tracks are selected demanding a p_T error less than 5% and the "highPurity" flag [2]. Both event- and track-level cut efficiencies show a good data-MC matching, with agreement at the percent level.

2.2 Systematic Uncertainties

A complete study of systematic uncertainties is carried out investigating all possible sources of data-MC disagreement. MC samples with altered descriptions of beam spot, tracker alignment, dead channels and material are analyzed and the corresponding effects evaluated. In addition, the underestimation of the rates of secondary particles in MC is accounted for and the uncertainty due to the chosen track selection is evaluated exploiting alternative sets of selection criteria. Also, the trigger uncertainty is cross-checked with the complementary forward hadron calorimeter trigger. In summary, all results are quite stable, leading to a total uncertainty O(2%) and proving that the CMS simulation is very accurate and the reconstruction algorithms very robust.

2.3 Results

The average multiplicity of charged particles per unit of pseudorapidity shows that the tunes describe the features of data within 10-15%, but none of the tunes is in satisfactory agreement. The total multiplicity depends on the interaction scale, increasing with the p_T of the leading object. As far as the shape is concerned, the best description is provided by Pro-Q20 and P0 tunes; CW is too high in normalization, D6T, P0 and Pro-Q20 are too low, while DW is high at large pseudorapidities $|\eta|$ and low at small $|\eta|$. Figure 1(b) shows the average scalar sum of charged particles transverse momenta as a function of $\Delta\phi$. In the Toward region all tunes but P0 are above data, while in the Away region only DW and CW overshoot the data. The data in the transverse region lie between the CW and DW tunes; since this region is the most sensitive to UE properties, the following results focus on this region only.

The charged multiplicity and charged energy densities as a function of the interaction scale show the same features in data and MC: a fast rise due to MPI at low p_T is followed by a slower increase due to radiation above ∼3 GeV/c and ∼5 GeV/c for leading track and jet analyses respectively. The probability distribution of track multiplicity in the transverse region is shown for events with a tracker-jet with p_T>3 GeV/c (Fig. 4): data and all tunes show a steep decrease for track multiplicity N_{ch}>2; D6T and Pro-Q20 diverge, predicting too many low multiplicity events. The track p_T distribution in the transverse region is characterised by an almost exponential spectrum, with the P0 tune close to data at high p_T and showing a flat ratio in the whole p_T range.

3 A Different Approach to the UE: Jet Area/Median

An alternative approach to studying the UE [3] is by measuring, for each jet in an event, the ratio of the jet transverse momentum and the area covered by this jet in the pseudorapidity versus azimuthal angle plane. In each event, there are hard jets that have large values of p_T/A, while most have small values and are sensitive to UE and pile up effects. The parameter $\rho = median(p_T/A)$ can be used to describe the UE activity since the median is less sensitive to the outlying hard jets.

The CMS analysis based on this method [4] makes use of track jets reconstructed with the kT algorithm with R=0.6 and defines a modified version of the ρ parameter to account for the very low detector occupancy in 900 GeV events. This analysis uses similar selections and systematic uncertainty estimation as described in the previus sections. Results comparing data with several PYTHIA tunes are compatible with those obtained with the traditional approach.

4 Conclusions

The first study of hadron production with $\sqrt{s}$ = 900 GeV LHC data at a scale provided by the leading track or the leading tracker-jet is presented. Predictions of several PYTHIA tunes, after full detector simulation, are compared to data with particular interest in the transverse region. The tunes describe CMS data within 10-15%, but, with the exception of CW, they predict too little hadronic activity in the transverse region. Data favor an energy dependence of the cut-off parameter like DW ($\epsilon = 0.25$) or even stronger ($\epsilon = 0.30$ as CW). Lower values are disfavored (i.e. D6T: $\epsilon = 0.16$). A new approach, based on the jet area, was developed and

leads to complementary results. New results, including more tunes and generator-level variables both at 0.9 and 7 TeV, are being produced and will become public in the next months.

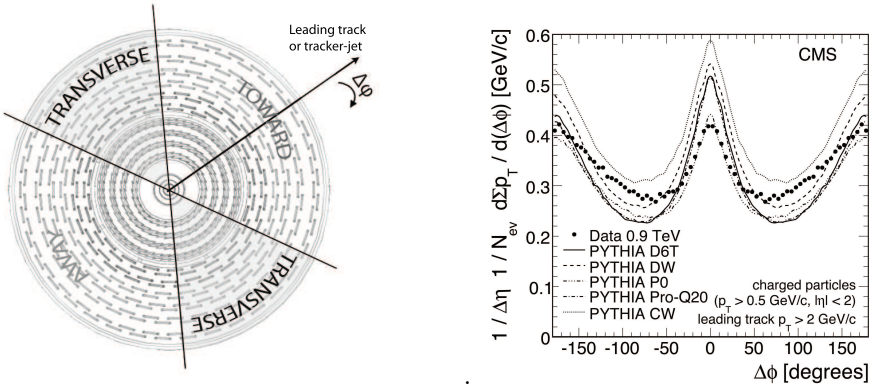

(a) (b)

Figure 1: Representation of the three regions in the the x-y view of the CMS tracker (a). Average scalar p_T sum of tracks with $p_T > 0.5$ GeV/c and $|\eta| < 2$ per unit of pseudorapidity and per radian, as a function of $\Delta\phi$; the leading track is excluded (b).

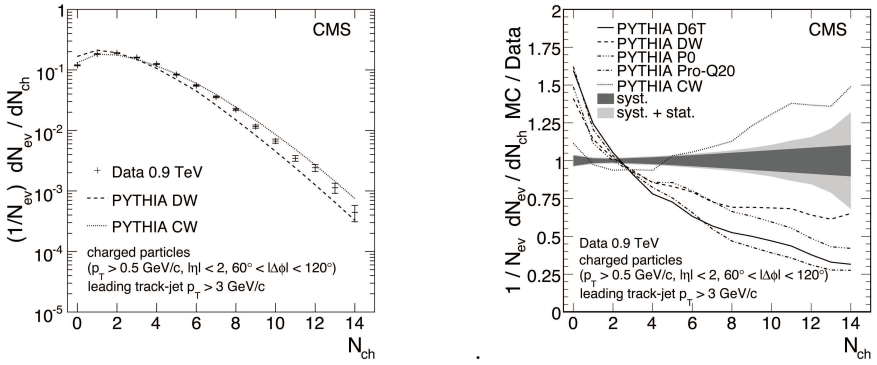

(a) (b)

Figure 2: Track multiplicity probability in the transverse region for events with a tracker-jet with p_T>3 GeV/c. (a) shows the distribution for data, DW and CW tunes; (b) shows the ratio between all tunes and data.

References

[1] CMS Collaboration, "The CMS experiment at the CERN LHC", JINST 3:S08004,2008.

[2] CMS Collaboration, "First Measurement of the Underlying Event Activity at the LHC with $\sqrt{s} = 0.9$ TeV" CMS-QCD-10-001 (2010) [arXiv:1006.2083], Submitted to the European Physical Journal C.

[3] M. Cacciari, G. P. Salam, and S. Sapeta, "On the characterisation of the underlying event", JHEP 04 (2010) 065 [arXiv:0912.4926].

[4] CMS Collaboration "Measurement of the Underlying Event Activity with the Jet Area/Median Approach at 0.9 TeV," CMS-PAS-QCD-10-005 (2010).

Baryon–antibaryon asymmetry in the central region at $\sqrt{s} = 0.9$ and 7 TeV with ALICE

Michal Broz for the ALICE Collaboration

Faculty of Mathematics, Physics and Informatics,
Comenius University Mlynská dolina 842 48 Bratislava, Slovakia

DOI: http://dx.doi.org/10.3204/DESY-PROC-2010-01/276

In this article, we discuss the results from the analysis of p+p collisions at $\sqrt{s} = 0.9$ and 7 TeV recorded by the ALICE experiment at the LHC. We concentrate on the baryon transport studies which are of great importance for the determination of the carrier of the baryon number. In particular, the rapidity and transverse momentum dependence of the $\overline{\mathrm{p}}$/p ratio is presented. The results are compared with different theoretical predictions. Finally, the energy dependence of the mid-rapidity ratios is discussed.

1 Introduction

The carrier of the baryon number (BN) is a topic that has been debated theoretically for some time [1, 2, 3, 4, 5, 6]. Based on the Quark-Gluon String Model (QGSM) [2] the BN is associated with its valence quarks. On the other hand, there are models describing the baryon structure with the picture of three strings starting at the valence quarks and joining together in the center, at a virtual point called "string junction" (J) [1, 3]. These two concepts result in a significantly different BN distribution with rapidity (BN transport), when the proton interacts inelastically at high energies. Experimentally, the BN transport over very large rapidity intervals is addressed by measuring the antiproton-to-proton production ratio at mid-rapidity, $R = N_{\overline{\mathrm{p}}}/N_{\mathrm{p}}$, or equivalently, the proton–antiproton asymmetry, $A = (N_{\mathrm{p}} - N_{\overline{\mathrm{p}}})/(N_{\mathrm{p}} + N_{\overline{\mathrm{p}}})$. In this article, we describe the measurement of the $\overline{\mathrm{p}}$/p ratio at midrapidity in pp collisions at center-of-mass energies $\sqrt{s} = 0.9$ TeV and 7 TeV ($\Delta y \approx 6.9$–8.9), with the ALICE experiment at the LHC [7].

2 Data analysis – results

Data recorded during the first LHC runs (December 2009 and March–April 2010) were used for this analysis. The trigger required a hit in one of the VZERO counters or in the SPD detector [8], in coincidence with the signals from two beam pick-up counters, one on each side of the interaction region, indicating the presence of passing bunches. The momentum as well as the particle identification relied for this analysis on the information from the TPC detector. The phase space of the analysis was restricted to the rapidity and momentum range of $|y| < 0.5$ and $0.45 < p < 1.05$ GeV/c, respectively. The corrections that are applied were the following:

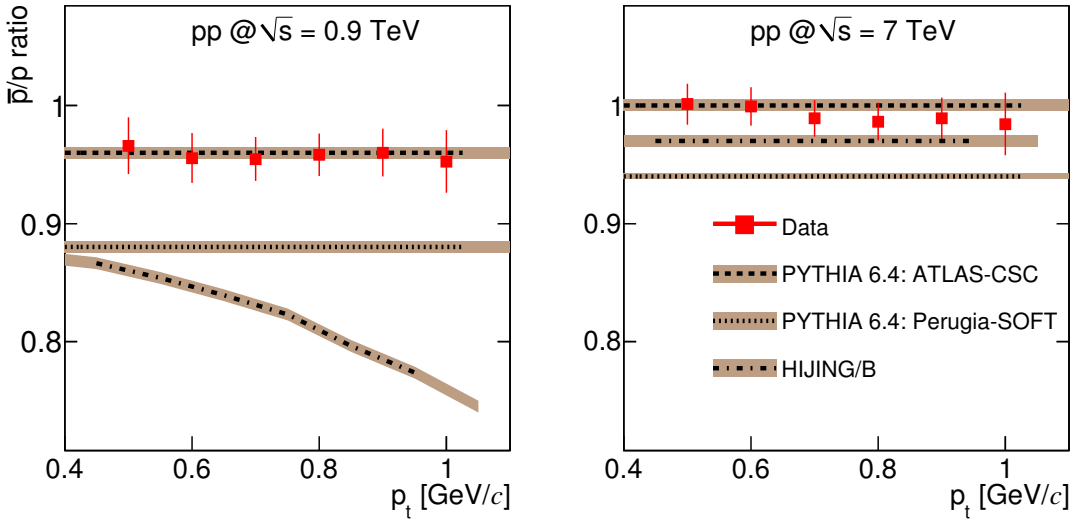

Figure 1: The p_{t} dependence of the $\overline{\mathrm{p}}/\mathrm{p}$ ratio integrated over $|y| < 0.5$ for pp collisions at $\sqrt{s} = 0.9$ TeV (left) and $\sqrt{s} = 7$ TeV (right). See also [8].

- corrections for absorption (extracted using a complete Monte Carlo production simulating the detector response with GEANT3),
- corrections for the proper p($\overline{\mathrm{p}}$)–A inelastic cross-sections (comparison between GEANT3 and FLUKA),
- corrections for background (mainly protons) and feed–down (parameterization of the distribution of the distance of closest approach– *dca* of the tracks to the primary vertex from data)
- corrections for the differences in the efficiencies of the analysis cuts for the different charges.

For more details about the corrections and the estimation of the systematic uncertainties, see [8].

The final corrected $\overline{\mathrm{p}}/\mathrm{p}$ ratio R rises from $R_{|y|<0.5} = 0.957 \pm 0.006(stat.) \pm 0.014(syst.)$ at $\sqrt{s} = 0.9$ TeV to $R_{|y|<0.5} = 0.991 \pm 0.005(stat.) \pm 0.014(syst.)$ at $\sqrt{s} = 7$ TeV. Within statistical errors, the measured ratio R shows no dependence on transverse momentum (Fig. 1) and rapidity Fig. 2 [8]. The different models studied are also independent of momentum and rapidity, with the exception of HIJING/B, which predicts a decrease with increasing p_{t} for the lower energy. The data are compared with various model predictions for pp collisions[5, 6, 9] in both Fig. 1 and Fig. 2. Two of the PYTHIA tunes [9] (ATLAS-CSC and Perugia-0) as well as the version of QGSM with the value of the string junction intercept $\alpha_{\mathrm{J}} = 0.5$ [5] describe the experimental values well, for both energies. QGSM without string junctions ($\epsilon = 0$) is slightly above the data. HIJING/B [6] underestimates the experimental results, in particular at the lower LHC energy. Also, QGSM with a value of the junction intercept $\alpha_{\mathrm{J}} = 0.9$ [5] predicts a smaller ratio, as does the Perugia-SOFT tune of PYTHIA, which also includes enhanced baryon transfer.

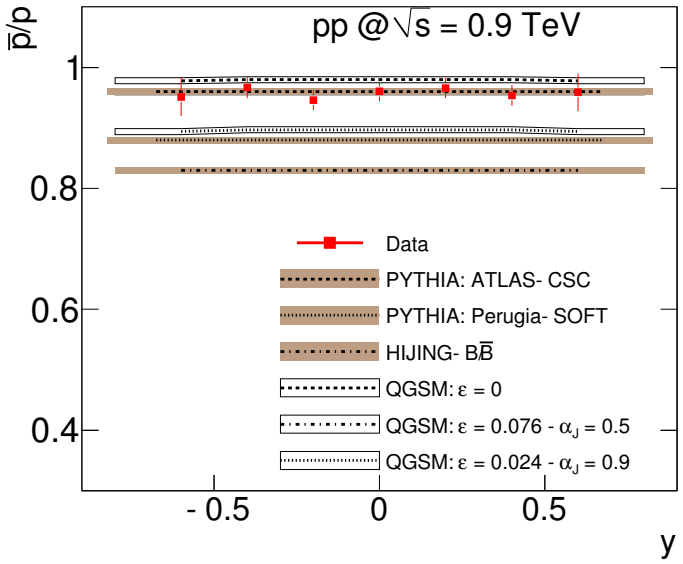

Figure 2: The $\overline{\mathrm{p}}/\mathrm{p}$ ratio as a function of the rapidity y at $\sqrt{s} = 0.9$ TeV. See also [8].

Figure 3 shows a compilation of central rapidity measurements of the ratio R in pp collisions as a function of center-of-mass energy (upper axis) and the rapidity interval Δy (lower axis). The lower energy data points are taken from [10, 11, 12]. At $\sqrt{s} = 0.9$ TeV there is still a small but significant excess of protons over antiprotons. The ratio at $\sqrt{s} = 7$ TeV is consistent with unity. The curve shown in Fig. 3 corresponds to a parameterization of the ratio taking into account that the baryon pair production at very high energy is governed by Pomeron exchange and baryon transport by string-junction exchange [4]. Following this formulation the $\mathrm{p}/\bar{\mathrm{p}}$ ratio can be described by the simple form $1/R = 1 + C\exp[(\alpha_\mathrm{J} - \alpha_\mathrm{P})\Delta y]$. The value for the Pomeron intercept is chosen to be $\alpha_\mathrm{P} = 1.2$ in accordance with the energy dependence of the rapidity density [13] and $\alpha_\mathrm{J} = 0.5$ (intercept of the Reggeon). The parameter C, which determines the relative contribution of the two diagrams, is adjusted to the measurements from ISR, RHIC, and LHC. The fit, shown in Fig. 3, gives a reasonable description of the data with only one free parameter (C), except at lower energies, where contributions of other diagrams (exchange of two junctions at both vertices) cannot be neglected [4]. The contribution of a second string junction diagram with a larger intercept [3], i.e., $1/R = 1 + C\exp[(\alpha_\mathrm{J} - \alpha_\mathrm{P})\Delta y] + C'\exp[(\alpha_{\mathrm{J}'} - \alpha_\mathrm{P})\Delta y]$ with $\alpha_{\mathrm{J}'} = 1$, is compatible with zero ($C \approx 10$, $C' \approx -0.1 \pm 0.1$).

3 Summary

In summary, we have measured the ratio of antiproton to proton production at $\sqrt{s} = 0.9$ and $\sqrt{s} = 7$ TeV. The reported values are $R_{|y|<0.5} = 0.957 \pm 0.006(stat.) \pm 0.014(syst.)$ at 0.9 and $R_{|y|<0.5} = 0.991 \pm 0.005(stat.) \pm 0.014(syst.)$ at 7 TeV. The $\overline{\mathrm{p}}/\mathrm{p}$ ratio is independent of both rapidity and transverse momentum and the results are consistent with standard models of baryon-number transport over very large rapidity intervals in pp collisions.

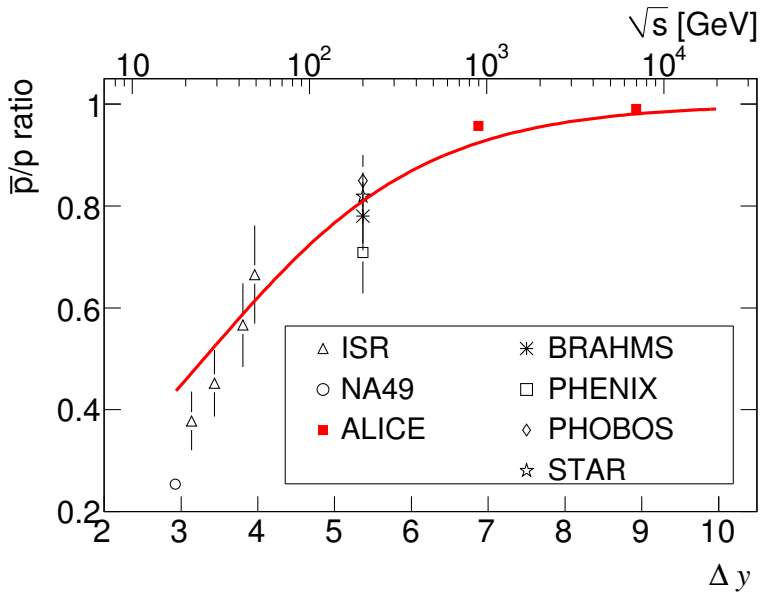

Figure 3: Central rapidity $\overline{\mathrm{p}}/\mathrm{p}$ ratio as a function of the rapidity interval Δy (lower axis) and center-of-mass energy (upper axis). Error bars correspond to the quadratic sum of statistical and systematical uncertainties for the RHIC and LHC measurements and to statistical errors otherwise. See also [8].

References

[1] G.C. Rossi and G. Veneziano, Nucl. Phys. **B123**, (1977) 507.

[2] A. Capella *et al.* Phys. Rep. **236**, 225 (1994); A.B. Kaidalov and K.A. Ter-Martirosyan, Sov. J. Nucl. Phys. **39**, 1545 (1984).

[3] B.Z. Kopeliovich, Sov. J. Nucl. Phys. **45**, 1078 (1987).

[4] D. Kharzeev, Phys. Lett. **B378**, 238 (1996).

[5] C. Merino *et al.* Eur.Phys.J. **C54** 577 (2008); C. Merino *et al.*, arXiv:0906.2659.

[6] S. E. Vance and M. Gyulassy, Phys. Rev. Lett. **83**, 1735 (1999).

[7] K. Aamodt *et al.* (ALICE Collaboration), JINST **3**, S08002 (2008).

[8] K. Aamodt *et al.* (ALICE Collaboration), arXiv:1006.5432, Accepted for publication by Phys. Rev. Lett. ; P. Christakoglou, ALICE Internal Note ALICE-INT-2010-006, 2010.

[9] T. Sjostrand, P. Skands, Eur. Phys. J. **C39**, 129 (2005); P. Skands, arXiv:1005.3457 [hep-ph] (2010), Perugia-0 (320) and Perugia-SOFT (322) tunes; A. Moraes (ATLAS Collaboration), ATLAS Note ATL-COM-PHYS-2009-119, 2009.

[10] T. Anticic *et al.* (NA49 Collaboration), Eur. Phys. J. **C65**, 9 (2010).

[11] A.M. Rossi *et al.* Nucl. Phys. **B84**, 269 (1975); M. Aguilar-Benitez *et al.* Z. Phys. **C50**, 405 (1991).

[12] B.I. Abelev *et al.* (STAR Collaboration), Phys. Rev. **C79**, 034909 (2009); I.G. Bearden *et al.* (BRAHMS Collaboration), Phys. Lett. **B607**, 42 (2005); B.B. Back *et al.* (PHOBOS Collaboration), Phys. Rev. **C71**, 021901 (2005); S.S. Adler *et al.* (PHENIX Collaboration), Phys. Rev. **C69**, 034909 (2004).

[13] A.B. Kaidalov *et al.*, Sov. J. Nucl. Phys., **44**, 468 (1986).

Observation of diffraction and measurement of the forward energy flow with the CMS detector

Benoît Roland on behalf of the CMS Collaboration

University of Antwerp, Groenenborgerlaan 171, 2020 Antwerp, Belgium

DOI: http://dx.doi.org/10.3204/DESY-PROC-2010-01/242

The observation of inclusive diffraction with the CMS detector at the LHC is presented for centre-of-mass energies $\sqrt{s}$ = 0.9 TeV and 2.36 TeV. Diffractive events are selected by the presence of a Large Rapidity Gap in the forward region of the CMS detector and uncorrected data are compared with Monte Carlo simulations based on the event generators PYTHIA and PHOJET. The measurement of the forward energy flow, in the pseudorapidity region $3.15 < |\eta| < 4.9$, is also presented at $\sqrt{s}$ = 0.9 TeV, 2.36 TeV and 7 TeV. Uncorrected data are compared with Monte Carlo simulations based on PYTHIA.

1 Observation of diffraction

A diffractive reaction in $p\,p$ collisions is a reaction $p\,p \to X\,Y$ in which the systems X and Y are separated by a Large Rapidity Gap (LRG). The final states X and Y carry the quantum numbers of the proton and may be a resonance or a continuum. Diffractive reactions are described by a colourless exchange in the t channel carrying the quantum numbers of the vacuum [1]. The two main types of diffractive processes occurring in $p\,p$ collisions are the single diffraction (SD), where one of the proton is scattered into a low-mass system, and the double diffraction (DD), where both protons dissociate. In each case the final states are characterized by an energy approximately equal to that of the incoming proton. Diffraction in the presence of a hard scale is described in perturbative QCD by the exchange of a colourless state of quarks or gluons, while soft diffraction at high energies is phenomenologically described in the Regge Theory [2] by the exchange of a Pomeron. One of the motivation to study diffraction with the early LHC data is given by the fact that a substantial fraction of the total $p\,p$ cross section – of the order of 30% – is due to diffractive reactions, while the modelling of soft diffraction is still mainly generator dependent. It is therefore essential to put further constraint on the diffractive contribution in order to improve our understanding of the collisions data and our knowledge of the pile up.

1.1 HF calorimeter and trigger subsystem

A detailed description of the CMS experiment can be found elsewhere [3] and we only describe here the subsystems used to obtain the presented results. The two Hadronic Forward calorimeters HF+ and HF-, located at ±11.2 m from the nominal interaction point (IP), cover the pseudorapidity region $2.9 < |\eta| < 5.2$. These are Cerenkov calorimeters made of radiation hard quartz fibers embedded into steel absorbers. Half of the fibers run over the full depth of the detector, the other half start at a depth of 22 cm from the front face of the calorimeter. This structure enables to distinguish showers generated by electrons or photons from those generated

by hadrons. Two subsystems, the Beam Scintillator Counters (BSC) and the Beam Pick-up Timing for the eXperiments (BPTX) were used to trigger the detector readout. The two BSCs are located at ± 10.86 m from the IP and cover the pseudorapidity region $3.23 < |\eta| < 4.65$. Each is a set of 16 scintillator tiles. The BSC elements have a time resolution of 3 ns and are designed to provide hit and coincidence rates. The two BPTXs, located around the beam pipe at ± 175 m from the IP, are designed to provide precise information on the bunch structure and timing of the incoming beam, with better than 0.2 ns time resolution.

1.2 Event selection

The $p\,p$ collision data sets collected at $\sqrt{s} = 0.9$ TeV and 2.36 TeV at the end of 2009 were used in the analysis [4]. The following conditions were imposed to select a sample with the largest acceptance for SD events while suppressing beam-related backgrounds. A signal is required in either of the BSCs in conjunction with BPTX signals from both beams passing the IP. A primary vertex was required with $|z| < 15$ cm and a transverse distance from the z axis smaller than 2 cm. It was also required that at least 3 tracks be used in the vertex fitting. Further cuts were applied to reject beam-halo event candidates and beam-scraping events. Events with large signals consistent with noise in the hadronic calorimeter were also rejected. The energy threshold in the calorimeter was 3 GeV, except for HF where 4 GeV was used. The number of events after the cuts are 207345 and 11848 at the two energies respectively [4].

1.3 Results

The events selected at $\sqrt{s} = 2.36$ TeV are plotted on the left side of Figure 1 as a function of $E + p_z$ and E_{HF+}. The variable $E \pm p_z = \sum_i (E_i \pm p_{z,i})$, where the sum runs over all calorimeter towers, approximately equals twice the Pomeron energy, with the plus (minus) sign applying to the case in which the proton emitting the Pomeron moves in the $+z$ ($-z$) direction. Diffractive events cluster at very small values of $E \pm p_z$, reflecting the peak of the cross section at small ξ, the fractional momentum loss of the proton. The variable E_{HF+} represents the energy deposition in the HF+. Diffractive events appear as a peak in the lowest energy bin of either the HF+ or the HF-, reflecting the presence of a LRG extending over one of the HFs. The uncorrected data are compared to simulated events obtained from the PYTHIA6 [5] (tune D6T) and PHOJET 1.12-35 [6, 7] event generators processed through a detailed simulation of the CMS detector based on GEANT4 [8]. The main systematic uncertainty is due to the imperfect knowledge of the calibration of the calorimeters and is estimated by a 10 % variation of the energy scale. The two left side plots of Figure 1 show that PYTHIA gives a better description of the non-diffractive part of the data. The events selected at $\sqrt{s} = 0.9$ TeV are plotted on the right side of Figure 1 as a function of $E \pm p_z$. The uncorrected distribution of $E + p_z$ is compared on the top right side to simulated events obtained from PYTHIA using the three different tunes D6T, DW [9] and CW [10] for the modelling of the Multiple Parton Interactions (MPI). The present data can not discriminate between these different tunes. To enhance the diffractive component in the data, a cut was applied to the energy deposition in HF. The uncorrected distribution of $E - p_z$ after the requirement of $E_{HF+} < 8$ GeV is compared on the bottom right side of Figure 1 to simulated events obtained from PYTHIA and PHOJET. The cut applied mainly selects SD events with a LRG extending over HF+. The system X is thus boosted towards the $-z$ direction. The plot shows that PHOJET gives a better description of the data in this region, in particular of the high mass diffractive systems.

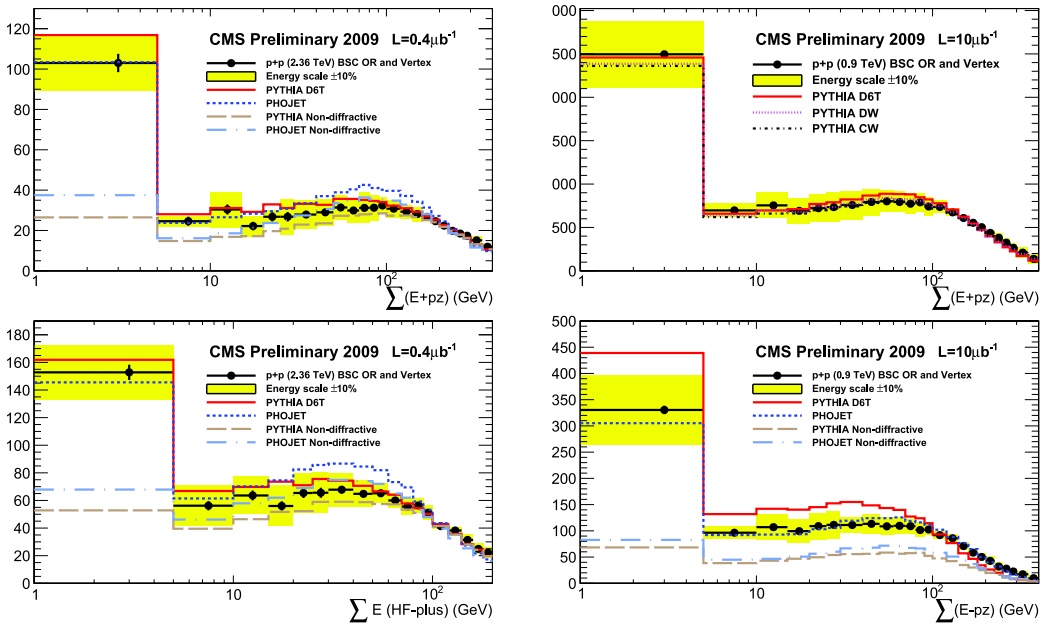

Figure 1: Distributions of the uncorrected variables $E + p_z$ and E_{HF+} for the selected events at $\sqrt{s} = 2.36$ TeV compared to the PYTHIA and PHOJET predictions (left side). Distribution of $E + p_z$ at $\sqrt{s} = 0.9$ TeV compared to the PYTHIA predictions using the tunes D6T, DW and CW (top right side). Distribution of $E - p_z$ at $\sqrt{s} = 0.9$ TeV, after the requirement of $E_{HF+} < 8$ GeV, compared to the PYTHIA and PHOJET predictions (bottom right side).

2 Measurement of the forward energy flow

Measurements in the forward region make possible to probe the small x content of the proton, in a region where the parton densities might become very large and where the probability for more than one partonic interaction per event should increase. The measurement of the forward energy flow should therefore be sensitive to the various modelling of the MPI [11] and complementary to the central region measurements to constrain their energy dependence. The collision data sets collected at $\sqrt{s} = 0.9$ TeV and 2.36 TeV at the end of 2009 and at $\sqrt{s} = 7$ TeV in March 2010 were used in the analysis [12]. The only change wrt the selection of diffractive events is relative to the use of the BSCs. Here a signal is required in both of the BSCs in conjunction with BPTX signals from both beams passing the IP. The vertex requirement and the rejection of beam-related backgrounds are the same as before. The energy flow measured in the pseudorapidity region $3.15 < |\eta| < 4.9$ is used to define the energy flow ratio:

$$R_{E\,flow}^{\sqrt{s_1},\sqrt{s_2}} = \frac{\frac{1}{N_{\sqrt{s_1}}}\frac{dE_{\sqrt{s_1}}}{d\eta}}{\frac{1}{N_{\sqrt{s_2}}}\frac{dE_{\sqrt{s_2}}}{d\eta}} \tag{1}$$

where $dE_{\sqrt{s}}$ is the energy deposition integrated over ϕ in the region $d\eta$ and $N_{\sqrt{s}}$ the number of selected events. The centre-of-mass energy $\sqrt{s_1}$ refers to either 2.36 TeV or 7 TeV, while $\sqrt{s_2}$ refers to 0.9 TeV. The two plots of Figure 2 show the ratio of the energy flows determined from

the average of the HF+ and HF- responses [12]. The pseudorapidity region is divided into 5 bins following the transverse segmentation of the HF calorimeters. Uncorrected data without systematic uncertainties are compared to simulated events obtained from PYTHIA using the tune D6T [9]. While the Monte Carlo predictions agree with the data, no conclusion on the quality of the description can be made so far due to the missing systematics. Figure 2 shows that the energy flow is increasing with increasing centre-of-mass energy and increasing η.

3 Conclusion

The observation of inclusive diffraction in pp collisions at $\sqrt{s} = 0.9$ TeV and 2.36 TeV has been presented [4]. Diffraction has been observed in two ways, as a peak at low ξ values and by the presence of a LRG. Uncorrected data have been compared to predictions from PYTHIA and PHOJET. PYTHIA describes better the non-diffractive part of the spectrum, while PHOJET gives a better description of the diffractive system. The PYTHIA tunes D6T, DW and CW give so far a similar description of the data.

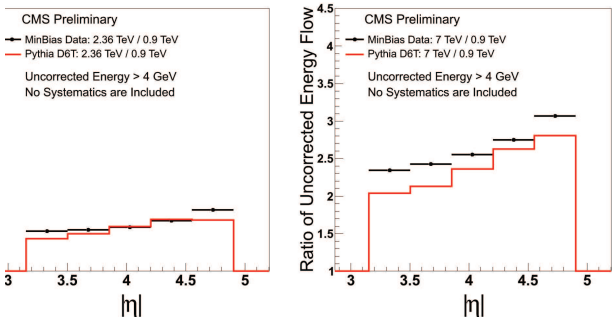

Figure 2: Energy flow ratio as a function of η. Uncorrected data are compared to PYTHIA predictions using the tune D6T.

The first measurement of the forward energy flow in the HF acceptance [12] ($3.15 < |\eta| < 4.9$) has been presented and compared to the PYTHIA predictions using the tune D6T.

4 Acknowledgments

I would like to thank M. Arneodo, A. Vilela Pereira, S. Sen and H. Jung for useful discussions, suggestions and feedback.

References

[1] M. Arneodo and M. Diehl, "Diffraction for non-believers," arXiv:hep-ph/0511047.

[2] P. D. B. Collins, "An Introduction to Regge Theory and High-Energy Physics," Cambridge University Press, Cambridge, 1977.

[3] R. Adolphi *et al.* [CMS Collaboration], "The CMS experiment at the CERN LHC," JINST **3** (2008) S08004.

[4] CMS Collaboration,"Observation of diffraction in proton-proton collisions at 900 and 2360 GeV centre-of-mass energies at the LHC," PAS-FWD-10-001 (2010).

[5] T. Sjöstrand, S. Mrenna and P. Z. Skands, JHEP **0605** (2006) 026 [arXiv:hep-ph/0603175].

[6] F. W. Bopp, R. Engel and J. Ranft, "Rapidity gaps and the PHOJET Monte Carlo," arXiv:hep-ph/9803437.

[7] R. Engel, J. Ranft and S. Roesler, Phys. Rev. D **52** (1995) 1459 [arXiv:hep-ph/9502319].

[8] S. Agostinelli *et al.* [GEANT4 Collaboration], Nucl. Instrum. Meth. A **506**, 250 (2003).

[9] P. Bartalini *et al.*, "Proceedings of the First International Workshop on Multiple Partonic Interactions at the LHC (MPI08)," Perugia, Italy, October 27-31 2008, DESY-PROC-2009-06 [arXiv:hep-ex/1003.4220].

[10] CMS Collaboration, PAS-QCD-10-001 (2010).

[11] T. Sjöstrand and M. van Zijl, Phys. Rev. D **36**, 2019 (1987).

[12] CMS Collaboration, "Energy Flow Ratios in HF at Different Collision Energies," CMS-DP-2010-007 (2010).

Electron performance with the ATLAS detector with J/ψ, W and Z

Nicolas Kerschen for the ATLAS Collaboration
CERN, CH-1211 Genève 23, Switzerland

DOI: http://dx.doi.org/10.3204/DESY-PROC-2010-01/215

We outline the electron performance of the ATLAS detector with the very first data taken at the LHC with a center of mass energy of 7 TeV. In particular, the first observation of J/ψ in the electron channel is shown as well as the first Monte-Carlo/Data comparisons of the main variables used in electron identification. Good agreement is demonstrated between observation and expectation for electron reconstruction and identification. An brief outlook on future studies to extract the electron efficiency and the calorimeter energy scale and uniformity of response using J/ψ, W and Z is also given.

1 Introduction

The electron reconstruction and identification algorithms used in ATLAS are designed to achieve both a large background rejection and a high and uniform efficiency over the full acceptance of the detector for transverse energies above 20 GeV. Isolated electrons need to be separated from hadrons in jets, from background electrons (originating mostly from photon conversions in the tracker material), and from non-isolated electrons from heavy flavour decays. The main subdetectors involved in the identification of electrons are the ATLAS electromagnetic (EM) calorimeter and the ATLAS inner detector. The ATLAS detector is described elsewhere [1]. The EM calorimeter has a fine lateral segmentation and three layers in the longitudinal direction of the showers complemented by a presampler placed in front. At high energy, most of the EM shower energy is collected in the second layer which has a lateral granularity of 0.025×0.025 in $\eta \times \phi$ space. The first layer consists of finer-grained strips in η. The fine lateral granularity extends up to $|\eta| < 2.47$. The calorimeter is divided into a barrel part and two end-caps with an overlapping region in $1.37 < |\eta| < 1.52$. The ATLAS inner detector provides precise track reconstruction over $|\eta| < 2.5$. It consists of three layers of pixel detectors close to the beam-pipe, 8 layers of silicon microstrip detectors (SCT) providing 4 space points per track at intermediate radii, and a transition radiation tracker (TRT) at the outer radii, providing about 35 hits per track (in the range $|\eta| < 2.0$). The TRT also provides substantial discriminating power between electrons and pions over a wide energy range (between 0.5 and 100 GeV). The pixel vertexing layer (also called the B-layer) is located just outside the beam-pipe at a radius of 50 mm, and provides precision vertexing and significant rejection of photon conversions (through a requirement of a track with a hit in this layer).

2 Electron reconstruction

Electron reconstruction begins with the creation of a preliminary set of clusters in the EM calorimeter. The size of these seed clusters corresponds to 3×5 cells in $\eta \times \phi$, in the middle layer of the EM calorimeter. Electron reconstruction is seeded from such clusters with $E_T > 2.5$ GeV using a sliding window algorithm over the full acceptance of the EM calorimeter. Electrons are reconstructed from the sliding window clusters if there is a suitable match with a track of $p_T > 0.5$ GeV. The "best" track is the one lying with an extrapolation closest in (η, ϕ) to the cluster barycentre in the middle EM calorimeter layer. For the barrel EM calorimeter, the optimal cluster size for electron candidates is 3×7 cells in $\eta \times \phi$, whereas it is 5×5 cells for the end-cap EM calorimeters. The cluster energy is calibrated with simulated events by parametrising, in fine η bins, the energy lost by the electron along its path as a function of the measured energy in the cluster. Figure 1 shows the linearity of the response of the EM calorimeter in simulated events, defined as the ratio between the reconstructed and the true electron energy as a function of pseudorapidity and at different energies. The deviation from linearity is less than 0.5 % at almost all values of $|\eta|$. The fractional energy resolution σ/E as a function of $|\eta|$ is shown in Fig. 1 for different energies. First studies on low energy photons from neutral pion decays indicate an overall uniformity in η better than 2 % and a unformity in ϕ better than 0.7 % for the barrel and end-cap calorimeters.

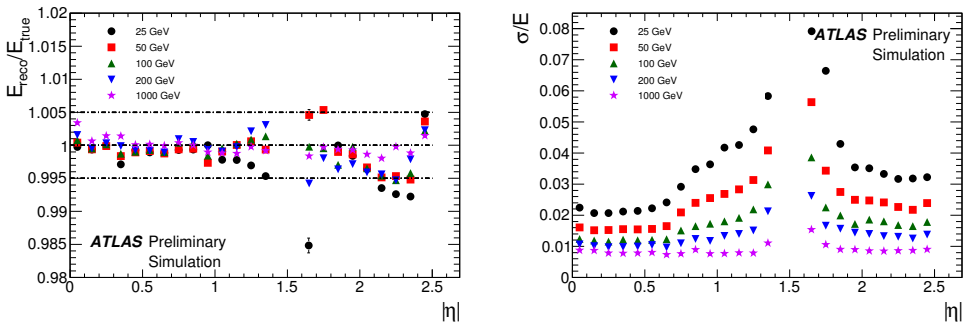

Figure 1: Linearity (left) and Resolution (right) of the EM calorimeter.

3 Electron identification

The baseline electron identification algorithms in ATLAS rely on rectangular cuts using variables which deliver good separation between isolated electrons and fake signatures from jets. These variables include calorimeter, tracker, and combined calorimeter/tracker information. Three reference sets of cuts have been defined for electrons: loose, medium, and tight. The cut values are optimised in bins of E_T and $|\eta|$. Shower shape variables of the second calorimeter layer and hadronic leakage variables are used in the loose selection. Strip cuts, track quality requirements, and track-cluster matching are added at the level of the medium selection. The tight selection adds E/p, B-layer hit requirements, and the particle identification potential of the TRT. For robustness, cut choices (including thresholds) are based on the expected level of

understanding of the detector performance at start-up.

Figure 2 shows the shower shapes for a selection of electron candidates corresponding to 1 nb^{-1} of integrated luminosity. The preselection cuts applied are: transverse energy of the cluster greater than 5 GeV, $|\eta| < 2.0$ (excluding the EM calorimeter barrel/end-caps overlapping region), number of silicon hits greater than 4 and number of TRT hits greater than 10. The shapes shown in Fig. 2 correspond to the discriminating variables used in the loose electron selection. These are: the longitudinal shower leakage (ratio of E_T in the hadronic calorimeter to E_T of the EM cluster), the ratio of cell energies in 3×7 versus 7×7 cells in $\eta \times \phi$ (R_η) and the lateral width of the shower in the second calorimeter layer (w_2). The sample of electron candidates predominantly consists of: charged hadrons faking electrons, electrons from photon conversions, and prompt electrons (mainly from b,c decays). Small shifts are observed in R_η and w_2 which remain to be understood. Fig. 3 clearly shows that the longitudinal segmentation of the electromagnetic calorimeter can be used to further separate hadrons from true electrons. The fraction of high threshold TRT hits shown in Fig. 3 after application of all other tight cuts highlights the discriminating power of the TRT.

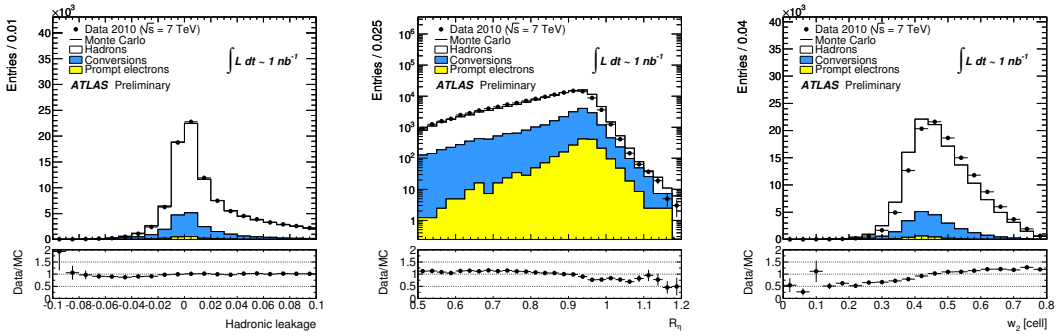

Figure 2: Hadronic leakage (left), R_η (middle) and w_2 (right) at preselection

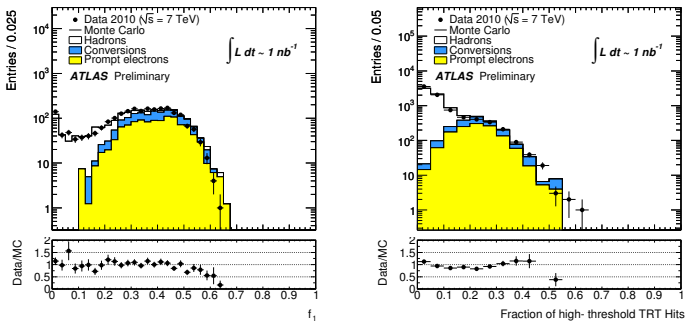

Figure 3: Fraction of energy in the first calorimeter layer, f_1 (left), fraction of high threshold TRT hits (right)

4 J/ψ observation

The J/ψ signal is the first abundant source of isolated electrons from a known resonance to be seen in the ATLAS experiment. Along with the Z boson, it is one of the few "standard candles" that will be used to calibrate the detector and assess the electron performance and identification efficiency. We present here the observation of the J/ψ in the di-electron channel. This has proved challenging in the first few nb^{-1} due to the low p_T spectrum of the J/ψ and the large hadronic background. To improve the reconstruction efficiency at low p_T, the seed finding algorithm of the standard reconstruction is replaced by a topological clustering, which is very effective at identifying low energy deposits above noise and has a very low energy threshold ($E_T > 300$ MeV). The standard fixed size clustering is then seeded from those clusters and a direct comparison with the standard reconstruction is possible. A subset of the variables from the baseline identification are used and the cuts are reoptimised to maximize the signal over the background. In particular, there is a strong reliance on f_1, the lateral shower containment in the η direction, the fraction of high threshold TRT hits and the number of hits in the silicon tracker. This allows us to have a very clean peak with very low background, as can be seen on Fig. 4. The integrated luminosity used is 6.3 nb^{-1} where calorimeter triggered events with an energy deposit greater than 3 GeV are selected. The invariant mass is computed using only track parameters and the track momenta are not corrected for Bremsstrahlung effects. The distribution is fitted with the Novosibirsk [1] function for the signal plus a straight line for the background. The yields extracted from the fit are: 52 ± 8 signal events for 6 ± 4 background events. The fitted mass is (3.05 ± 0.07) GeV which is compatible with the PDG value; the width is (0.27 ± 0.05) GeV.

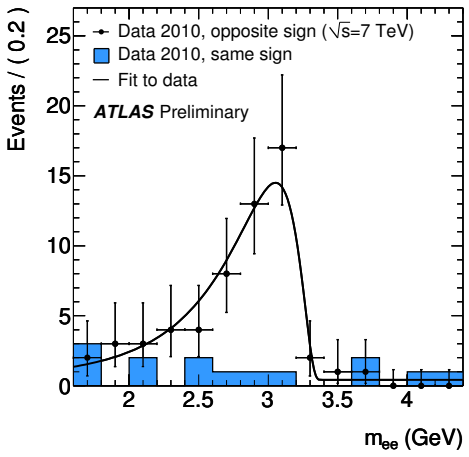

Figure 4: Invariant mass of electron-positron pairs.

[1] The Novosibirsk function is usually defined by: $f(m) = A_S \exp(-0.5\ln^2[1 + \Lambda\tau \cdot (m - m_0)]/\tau^2 + \tau^2)$, where $\Lambda = \sinh(\tau\sqrt{\ln 4})/(\sigma\tau\sqrt{\ln 4})$, the peak position is m_0, the width is σ, and τ is the tail parameter.

5 Conclusion and outlook

The assessment of the electron performance in the ATLAS experiment has started with the study of the first sample of inclusive electrons as well as the observation of the first J/ψ events. In general, their is a good agreement between data and Monte Carlo in the identification variables. Some variables do exhibit a trend which is still to be understood. An essential step towards the measurement of the electron efficiency will be the understanding of the shower shape cuts and track quality requirements commonly used in electron identification. To this effect, a tag-and-probe technique can be used to extract the shower shape and tracking distribution for probe electrons for events in a window around the J/ψ or Z mass. In addition, with the J/ψ and Z boson mass known to high accuracy, the uniformity and energy scale of the electromagnetic calorimeter will be probed and the detector inter-calibrated using the available methods that have been tested over the years in simulation and test-beams. This first look sets the stage for future studies that will benefit from the inreased luminosity expected in the future and provide a direct input to all physics measurements involving electrons.

References

[1] G. Aad *et al.* [ATLAS Collaboration], JINST **3** (2008) S08003.

Observation of W and Z boson candidates with the CMS experiment

Emanuele Di Marco for the CMS Collaboration

"La Sapienza" Università di Roma and INFN Roma, p.le Aldo Moro n. 2, 00185 Roma, Italy

DOI: http://dx.doi.org/10.3204/DESY-PROC-2010-01/216

We present the first observation of W and Z boson candidates in muon and electron decay channels in 198 nb^{-1} pp collisions at $\sqrt{s} = 7$ TeV, using the CMS detector at the LHC.

1 Introduction

The production of W and Z bosons decaying to charged leptons is an important process to measure at the LHC: it can be used to validate lepton reconstruction and identification to be used in future analyses, a precision test of perturbative QCD and the parton distribution functions of the proton (PDFs), a possible estimator of integrated luminosity for proton collisions, and the first electroweak process to be observed at the LHC. At the LHC, QCD predictions, in next-to-next-to leading order (NNLO) in the strong coupling α_s, exist for the matrix elements describing inclusive W and Z production. The cross section can be predicted with a few percent uncertainty. The production of the W and the Z in hadron collisions has been measured at several previous experiments over a range of collision energies, and Standard Model predictions have been observed to agree well with them.

2 Measurement of the $W \to \mu\nu$ and $Z \to \mu^+\mu^-$ yield

$W \to \mu\nu$ events are characterized by a high-p_T isolated muon, together with a signicant amount of missing transverse energy ($\not\!\!E_{\text{T}}$), due to the presence of a neutrino in the final state that escapes undetected. Events with high-p_T muons are recorded online using the Level-1 muon trigger and the high-level trigger (HLT), which require information from the muon chambers (Level-1, HLT) and the inner tracker (HLT). A trigger path with an HLT threshold of $p_T > 9$ GeV in the $|\eta| < 2.1$ region is chosen as the baseline of the analysis. The muon must be identified by two different algorithms, one that starts from inner tracker information ("tracker muons"), and another one that starts from segments in the muon chambers ("global muons"). Quality cuts on the inner track and on the results of the global muon fit is applied to reduce the contamination from muons produced in decays in flight of hadrons and from punch-through. We demand the presence of at least two levels of muon stations to suppress candidates which are unable to penetrate deeply in the iron yoke of CMS [1]. A full reconstruction of the W system is not possible but a mass reconstruction in the transverse plane can be performed from the measured $\not\!\!E_{\text{T}}$ and the muon momentum. This transverse mass is defined as: $M_T =$

$\sqrt{2p_T(\mu)\not{E}_T(1-\cos(\Delta\phi_{\mu,\not{E}_T}))}$, where $\Delta\phi_{\mu,\not{E}_T}$ is the azimuthal angle between muon and $\not{E}_T$ directions. The resulting M_T distribution exhibits the characteristic shape of the W Jacobian peak. Events with two high p_T muons are rejected to minimize the contribution of Drell-Yan events. The muons are required to be isolated discarding the ones with high activity in a cone around the muon in the inner tracker, electromagnetic calorimeter (ECAL) and hadronic calorimeter (HCAL). After the selection 1254 events are selected. The main sources of background are QCD events with muons coming from decays of b-hadrons, with a smaller contribution of muons from long-lived meson decays. The remaining background is $Z \to \mu^+\mu^-$, with one muon beyond the detector acceptance (3% background), $Z \to \tau^+\tau^-$ and $W \to \tau\nu$ events (2% contamination). The $t\bar{t}$ background is negligible (0.3%). The $W \to \mu\nu$ signal yield is extracted from a binned likelihood fit to the observed M_T distribution. Figure 1 (a) shows the fit to the observed M_T spectrum, together with the different templates used. The measured yield is $N_W = 818 \pm 27$ (stat.). $Z \to \mu^+\mu^-$ events are characterized by the presence of two high-p_T isolated muons forming a di-muon system with an invariant mass consistent with the Z boson mass. The expected background is very low, and therefore it is estimated from Monte Carlo. Di-muon pairs with opposite charge are selected with looser requirements than the one described for the W case if their invariant mass satisfies $60 < m_{\mu\mu} < 120$ GeV. We select 77 events: the invariant mass of these pairs is shown in Figure 1 (b). Data are compared with the Monte Carlo NLO expectations for this luminosity. The background, dominated by QCD, $t\bar{t}$ and $Z \to \tau^+\tau^-$ events, is negligible ($\approx 0.3\%$).

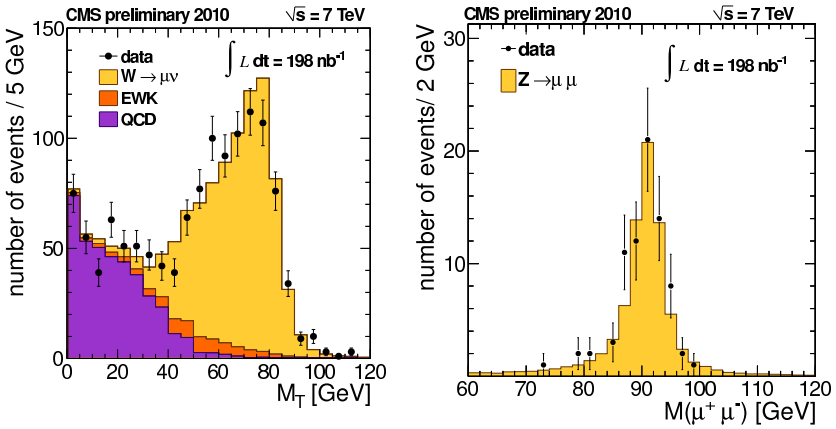

(a) (b)

Figure 1: (a) Fit to the m_T spectrum of W candidates (black points) together with the templates for the different processes. (b) Invariant mass distribution of the selected $Z \to \mu^+\mu^-$ candidates in data superimposed to the MC expectation.

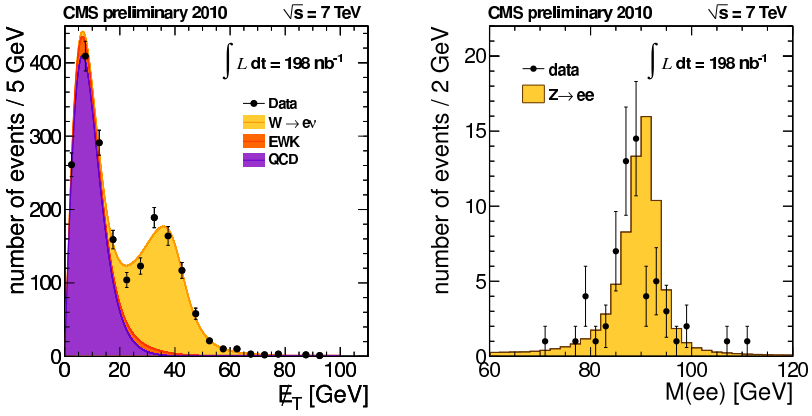

(a) (b)

Figure 2: (a) Fit to the $\not\!\!E_{\rm T}$ spectrum of W candidates (black points) together with the templates for the different processes. (b) Invariant mass distribution of the selected $Z \to e^+e^-$ candidates in data superimposed the MC expectation.

3 Measurement of the $W \to e\nu$ and $Z \to e^+e^-$ yield

Electrons are identified in the CMS detector as clusters of ECAL energy deposits matched to tracks from the silicon tracker. The ECAL covers the pseudorapidity range $|\eta| < 3.0$. Electron candidates are selected online from events that: pass a "Level 1" (L1) trigger filter, evaluated by customized hardware, which requires a coarse-granularity region of the ECAL to have $E_T > 5$ GeV; and that subsequently pass a "High Level Trigger" (HLT) software filter, requiring an ECAL cluster with $E_T > 15$ GeV, using the full granularity of the ECAL and E_T measurements calibrated to offline precision. Electron candidates require an ECAL cluster with $E_T > 20$ GeV, in the ECAL acceptance. ECAL clusters are required to match tracks using an algorithm which accounts for possible energy loss due to bremsstrahlung in the tracker layers. Particles misidentified as electrons are suppressed by: requiring the track trajectory to geometrically match the ECAL cluster; by limiting the amount of HCAL energy measured in a cone radius of $\Delta R < 0.15$ around the ECAL cluster direction; and by requiring a narrow ECAL cluster width in η. Photon conversions rejection criteria are also applied. Those identified electrons are required to be isolated requiring low activity around their direction in the tracker, ECAL and HCAL detectors. W candidates are required to have one electron, with ECAL cluster $E_T > 20$ GeV, satisfying the described identification criteria. Z events are suppressed rejecting events with a second electron candidate. This selection results in 1931 candidate events in 198 nb^{-1}. Remaining backgrounds consist of QCD di-jet events, prompt high-E_T photons, Z events, and $W \to \tau\nu$ events. The first two sources are characterized by small intrinsic $\not\!\!E_{\rm T}$, and can be separated from $W \to e\nu$ signal from an analysis of the $\not\!\!E_{\rm T}$ distribution. The last two sources can be modeled successfully by Monte Carlo simulation. The $W \to e\nu$ signal is extracted via an unbinned maximum likelihood fit to the $\not\!\!E_{\rm T}$ distribution. Figure 2 (a) shows

the $\not\!\!E_{\mathrm{T}}$ distribution of $W \to e\nu$ candidates and the results of the likelihood fit. The $W \to e\nu$ signal yield estimated from the fit is 799.7 ± 30.6 (stat.) events. Z candidates are required to have two electrons, with ECAL cluster $E_T > 20$ GeV, satisfying the criteria described above, but with a looser operating point than the W selection for electrons. The invariant mass of the electron pair is required to be between 60 and 120 GeV. This selection results in 61 candidate events in 198 nb^{-1}. Simulations of QCD di-jets estimate a background of much less than one event. Figure 2 (b) shows the mass distribution of $Z \to e^+e^-$ candidates with predictions from simulation superimposed. The data exhibit an energy scale shift relative to simulation of 1%.

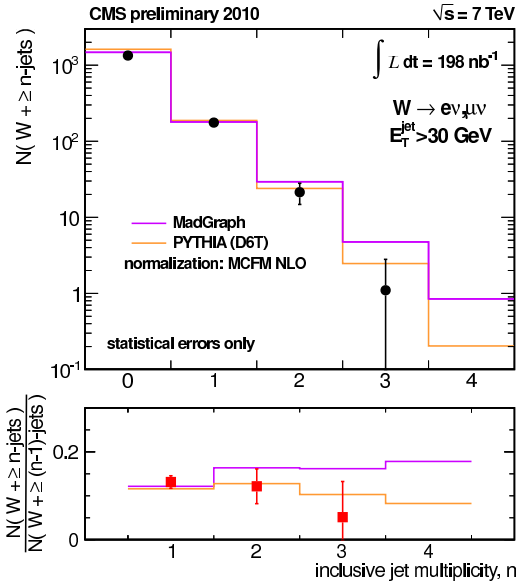

Figure 3: Number of $W \to \ell\nu$ events ($\ell = e, \mu$) containing n jets above threshold or more (top plots) and ratio $N(W \to \ell\nu,\, n \text{ jets})/N(W \to \ell\nu, \geq (n-1) \text{ jets})$ (bottom plots).

4 Production of W, Z associated with jets

We study the production of hadronic jets along with W bosons reconstructed in leptonic decay modes. The lepton selections are identical to those described in Section 2 for $W \to \mu\nu$ and in Section 3 for $W \to e\nu$. Hadronic jets are reconstructed by clustering charged and neutral hadrons and photons. The infrared-safe Anti-kt [2] jet clustering with a cone radius of $\Delta R = 0.5$ is used. We consider jets within the tracker acceptance $|\eta| < 2.5$ with an energy threshold of $E_T > 30$ GeV. Events are classified according to the number of jets above threshold in an inclusive way: the jet multiplicity bin n gathers events containing n jets or more in addition to the lepton. The $t\bar{t}$ background is sizable in jet-multiplicity bins $n \geq 3$. In the electron channel, the ratio of $t\bar{t}$ background with respect to the signal is fixed to the expectation from Monte Carlo simulation. Figure 3 presents the results $N(W \to \ell\nu + \geq n \text{ jets})$ as a function of the inclusive jet multiplicity n. Electron and muon results are combined. The rate of high

E_T jets is sensitive directly to the matrix element of the hard scattering at the parton level. Here we compare the data with predictions obtained with two different generators, PYTHIA [3] and MADGRAPH [4]. All Monte Carlo predictions are normalized to the NLO inclusive cross section prediction obtained with the MCFM generator.

5 Conclusions

First observation of W and Z (γ^*) bosons have been made using approximately 198 nb^{-1} of data taken with the CMS detector at the LHC. In addition, the W production in association with jets have been measured. Within large statistical uncertainties, no disagreements with the predictions of the Standard Model have been observed.

References

[1] R. Adolphi *et al.* [CMS Collaboration], "The CMS experiment at the CERN LHC," JINST **3** (2008) S08004.

[2] M. Cacciari, G. P. Salam and G. Soyez, "The anti-k_t jet clustering algorithm," JHEP **0804**, 063 (2008)

[3] T. Sjostrand, S. Mrenna and P. Z. Skands, "PYTHIA 6.4 Physics and Manual," JHEP **0605** (2006) 026

[4] F. Maltoni and T. Stelzer, "MadEvent: Automatic event generation with MadGraph," JHEP **0302** (2003) 027

Jet commissioning and dijet physics in CMS

Maxime Gouzevitch for the CMS Collaboration

CERN CH-1211, Geneve-23, Switzerland

DOI: http://dx.doi.org/10.3204/DESY-PROC-2010-01/220

The hadronic jets are comissionned in pp collisions by the CMS collaboration using the data produced at $\sqrt{s} = 0.9$, 2.36 and 7 TeV. Then the dijet final state is used to test the behavior of QCD at new energy scales and to search for new physics beyond the standard model.

1 Introduction

Jets are experimental signatures of the hadronisation of quarks and gluons, which are produced in high energy processes such as the hard scattering of partons in the pp collisions. Due to their large production cross section, jets are an ideal tool to probe the physics processes within and beyond the standard model. At leading order the jets are produced by pairs in a hard scattering of two partons. From one hand this process is expected to be well described by perturbative QCD with a t-channel matrix element. From the other hand the selection of dijet final states may be used to search for new resonances in parton-parton channels ($q\bar{q}$, qq, qg and gg) such as excited quarks or the presence of contact interactions.

2 Jet reconstruction at CMS collaboration

Three different types of jet reconstruction are employed by CMS [1], characterized by the way that the sub-detector inputs are used during the jet finding procedure: calorimeter jets (Calo jets), jet-plus-tracks jets (JPT jets) and particle flow jets (PF jets). Very briefly:

The calorimeter jets (Calo) are reconstructed using energy deposits in the electromagnetic and hadronic calorimeter cells, combined into calorimeter towers as inputs. A calorimeter tower consists of one or more hadron calorimeter (HCAL) cells and the geometrically corresponding electromagnetic calorimeter (ECAL) crystals.

The Jet-Plus-Tracks (JPT) algorithm corrects the energy and the direction of a calorimeter jet. It exploits the excellent performance of the CMS tracking detectors [1] to replace the calorimeter towers by tracks when they are well matched in $\eta-\phi$ space. This procedure improves significantly the resolution of calorimeter jets up to $\eta \approx 2.4$.

The Particle Flow (PF) algorithm aims to reconstruct, identify and calibrate individually each particle by combining the information from all CMS sub-detector systems. As a result of the PF reconstruction, the inputs to the jet clustering are almost fully calibrated and the resulting higher level objects (jets) require small a posteriori energy corrections.

Jet energy corrections need to be applied to account for the non-linear and non-uniform response of the CMS calorimeters. These corrections are estimated in QCD events simulated

by the PYTHIA MC generator as described in [2]. The principle consists in comparing the p_T of the reconstructed jet to the p_T of the matched generated jet taken just after the hadronisation process. The correction procedure consists of two stages: the relative correction that makes the jet response uniform in η, by calibrating, on average, to the response in the central region of the calorimeters $|\eta| < 1.3$; the absolute correction that removes the p_T dependence of the jet response. The combined correction factor $C(p_T, \eta)$ is derived as the product of the two steps. Its size is typically 2 for Calo jets at 20 GeV while it's only 1.1 for the PF jets. Additional corrections exist for pile-up and noise effects (*offset corrections*). Their importance is small with present luminosity but would increase together with the LHC performance.

The MC driven calibration procedure was checked using the data sample collected at $\sqrt{s} =$ 7 TeV using the p_T balance between two jets in the dijet data sample or the between the jet and the photon in *jet+photon* events. A conservative value of jet energy scale uncertainty of 10% (5%) was confirmed for Calo (JTP and PF) jets by comparing the difference between the jet response for data and MC.

3 Study of jet properties at $\sqrt{s} = 0.9$, 2.36 and 7.0 TeV

The CMS collaboration took advantage of the first data samples collected at $\sqrt{s} = 0.9$ (350k events) and $\sqrt{s} = 2.36$ TeV (20k events) to test our understanding of the jet kinematics and structure [3, 4]. While many jet algorithms are considered for jet reconstruction [1], it was agreed to restrict the first jet validation analyses to the anti-k_T [5] clustering algorithm with $R = 0.5$.

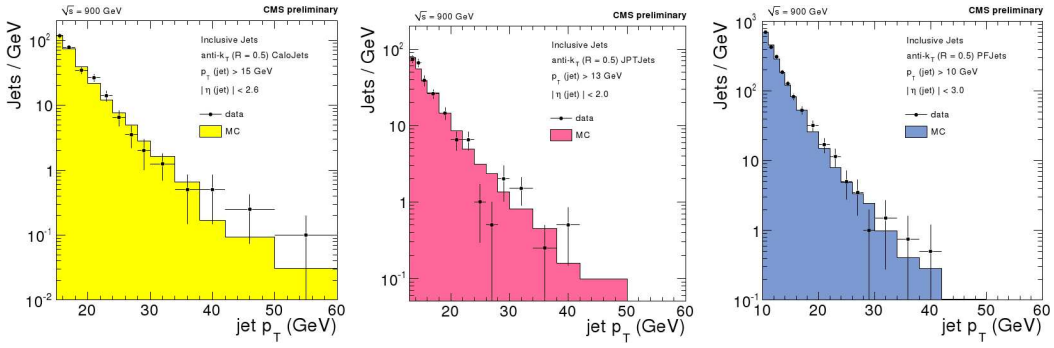

Figure 1: Comparisons of data and MC for inclusive jets p_T spectrum at $\sqrt{s} = 0.9$ TeV. From left to right: Calo, JPT and PF jets.

The inlusive jets sample was selected with relatively loose cuts: $p_T > 10 - 15$ GeV and $|\eta| < 2 - 3$ dependant on the kind of the jet [3]. A jet quality selection allowed to remove the most of the noise jets passing the kinematics cuts. Very briefly it consists in rejecting Calo or JPT jets made purely of HCAL clusters or of a single tower jet, while the PF jets are rejected if they do not contain charged hadrons. In Fig. 1 is shown the distribution of the inclusive jets spectrum for 3 kind of jets well described by MC. The jet resolution is worse in case of Calo jets and leads to a larger extension of the high p_T tail due to migrations. The good purity of

the PF jets allows to reduce the p_T down to 5 GeV in order to show that the calorimeter noise is well under control [4].

The internal composition of jets separated into electromagnetic and hadronic fraction for Calo jets is well described by MC [3]. The quality of understanding is even more striking in case of PF jets since the particle flow algorithm allow to separate between different energy fractions. The figure 2 produced in a similar analysis at $\sqrt{s} = 7.0$ TeV shows the reconstructed jets in data and MC with a striking agreement between them [6].

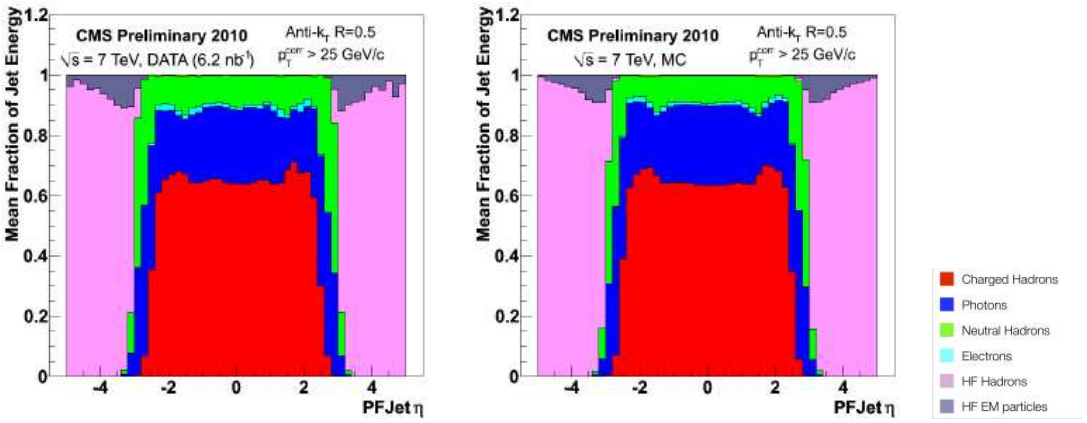

Figure 2: Reconstructed jet energy fractions as a function of pseudorapidity in the data (left) and in the simulation (right) at $\sqrt{s} = 7.0$ TeV. From bottom to top in the central region: charged hadrons, photons, electrons, and neutral hadrons. In the forward regions: hadronic deposits, electromagnetic deposits.

The dijet analysis was first carried out at lower center-of-mass energies showing a good understanding of this topology at low transverse momentum [3]. It was repeated at $\sqrt{s} = 7$ TeV with an integrated luminosity of approximatively 0.2 nb^{-1} at larger momentum by requesting a harder p_T cut above 25 GeV and a back-to-back topology [7]. The azimuthal difference $\Delta\phi = |\phi_{jet1} - \phi_{jet2}|$ is well described and peaking toward π as expected from LO QCD. To enhance the LO contribution a cut $\Delta\phi > 2.1$ is applied. The preliminary distribution of the invariant mass of two leading jets is well described by MC. Those results allow to push the investigations further to look for new physics beyond the standard model.

4 Searches for new physics

The first results presenting the search for new physics beyond the standard model in the dijet production was recently presented using 120 nb^{-1}. The first analysis [8] looks for an excess in the dijet invariant mass spectrum. Jets are selected in the central region $|\eta| < 1.3$ where the QCD background is expected to be suppressed with respect to the forward region $|\eta| > 1.3$. The search was performed for masses above 0.354 TeV where the trigger starts to be fully efficient. Statistical uncertainties are dominant at large masses while the jet energy scale is the dominant systematic uncertainty all over the mass range. The maximum observed mass range is 2.53

TeV, but no significant excess was observed as shown on the Fig. 3. On this plot the histogram bin widths are approximately equal to the expected dijet mass resolution for narrow resonances measured with calorimeter jets and gradually increase with dijet mass. The exclusion limit at 95% C.L. is drawn for string resonances with mass less than 1.67 TeV, excited quarks with mass less than 0.59 TeV and axigluons and colorons of mass less than 0.52 TeV.

The second analysis [9] was looking for the dijet centrality ratio, which is defined as the number of events with both jets in the region $|\eta| < 0.7$ divided by the number of events with both jets in the region $0.7 < |\eta| < 1.3$. Since many sources of systematic uncertainty cancel in this ratio, the dijet ratio provides a precise test of QCD and is sensitive to new physics. It is expected to be less sensitive to the mass resonances but more to an hypothetical presence of contact interactions. The first data allowed to exclude contact interactions with scale $\Lambda < 1.9$ TeV at 95% C.L.

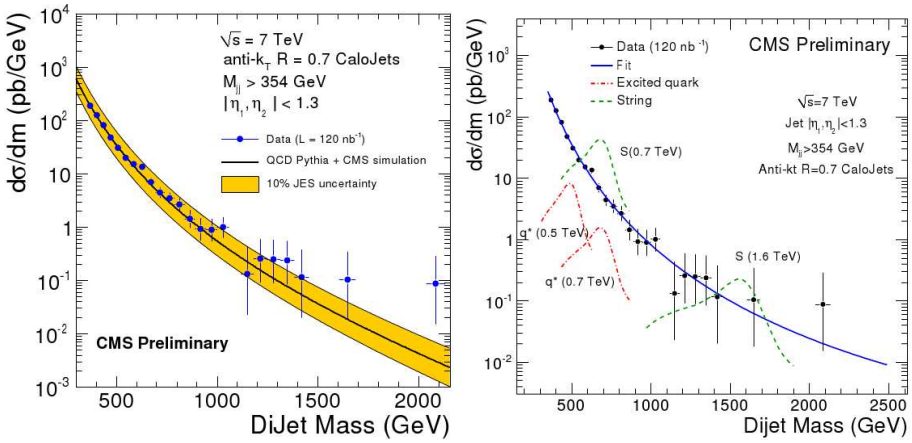

Figure 3: Left: the measured differential cross section data (points) in dijet mass are compared to a QCD MC prediction (black line). The yellow band shows the sensitivity to a 10% systematic uncertainty on the jet energy scale. Right: the dijet mass distribution (points) compared to simulations of excited quarks (dot- dashed red curves) and string resonance (green dashed curve) signals in the CMS detector.

References

[1] CMS Collaboration, "The CMS Experiment at the CERN LHC", JINST 3 (2009) S08004.
[2] CMS Collaboration, CMS PAS JME-10-003.
[3] CMS Collaboration, CMS PAS JME-10-001.
[4] CMS Collaboration, CMS PAS PFT-10-001.
[5] M. Cacciari, G. P. Salam, and G. Soyez, JHEP 0804:063 (2008).
[6] CMS Collaboration, CMS PAS PFT-10-003.
[7] CMS Collaboration, DPS-2010/014.
[8] CMS Collaboration, CMS PAS EXO-10-001.
[9] CMS Collaboration, CMS PAS EXO-10-002.

Observation of energetic jet production in pp collisions at $\sqrt{s} = 7$ TeV using the ATLAS experiment at the LHC

Eric Feng for the ATLAS Collaboration

Enrico Fermi Institute, University of Chicago, 5640 S. Ellis Ave, Chicago, IL 60637, USA

DOI: http://dx.doi.org/10.3204/DESY-PROC-2010-01/219

We report the observation of energetic jet production in proton-proton collisions at $\sqrt{s} =$ 7 TeV, based on about 1 nb^{-1} of integrated luminosity collected by the ATLAS detector. The anti $-$ k$_{\mathrm{T}}$ algorithm is used to reconstruct jets with $p_T^{jet} > 30$ GeV and $|y^{jet}| < 2.8$. Jets with p_T^{jet} up to ~ 500 GeV and events with dijet mass up to $m^{jj} \sim 1$ TeV are observed. The jet shapes and charged particle flow confirm that the observed jet signal corresponds to collimated flows of particles in the final state.

1 Introduction

The observation of energetic jets produced in pp collisions at $\sqrt{s} = 7$ TeV is reported, using about 1 nb^{-1} of data collected by the ATLAS experiment. Kinematic distributions in inclusive jet and dijet production are presented, together with internal jet structure and charged particle flow in the event. No attempt is made to correct the measurements for detector effects or account for systematic uncertainties.

These measurements were performed using the ATLAS detector, which is a general purpose, hermetic detector described in detail elsewhere [1]. The ATLAS tracking system covers the pseudorapidity range $|\eta| < 2.5$, while the electromagnetic and hadronic calorimeters cover $|\eta| < 4.9$. The data are compared to PYTHIA 6.4.21 [2], which is based on leading order $2 \to 2$ perturbative QCD matrix elements plus parton shower. The Monte Carlo (MC) uses a set of tuned parameters denoted as ATLAS MC09 [3] along with MRST LO* parton density functions [4], and the full ATLAS detector response is modeled in GEANT4 [5].

2 Event selection

The data were collected during the first LHC runs at $\sqrt{s} = 7$ TeV in March and April 2010. Events were triggered by requiring at least one hit from minimum bias trigger scintillators (MBTS) [6] that cover $2.09 < |\eta| < 3.84$. The events are required to have a reconstructed primary vertex with a z-position within 10 cm of the detector center in order to suppress beam-related backgrounds and cosmic rays. Additional quality criteria are also applied to ensure that jets are not produced by single noisy calorimeter cells or problematic detector regions [7].

3 Jet reconstruction

Jets are identified using the anti $-$ k_T jet algorithm [8] with distance parameter $R = 0.6$ by performing four-momentum recombination on topological clusters [9]. These clusters are seeded by calorimeter cells with $|E_{\rm cell}| > 4\sigma$ above the cell energy noise. All directly neighbouring cells are added, then neighbors of neighbours are iteratively added for all cells with signals above a secondary threshold $|E_{\rm cell}| > 2\sigma$.

The measured jet transverse momentum $p_T^{jet,em}$, as determined at the electromagnetic scale[1], systematically underestimates that of the hadron-level jet due to calorimeter non-compensation and dead material. Consequently an average correction $C(p_T^{jet,em}, \eta^{jet})$, determined as a function of $p_T^{jet,em}$ and $|\eta^{jet}|$ from MC simulation, is applied to obtain the corrected p_T^{jet}. No attempt is made to unfold the effects of the finite detector resolution.

Events are required to have at least one jet with (corrected) $p_T^{jet} > 30$ GeV and $|y^{jet}| < 2.8$. Preliminary studies indicate that for jets with $|y^{jet}| < 2.8$, the relative response of the calorimeter to jets in different rapidity regions is correctly modeled by MC to within $\pm 5\%$. A first determination of the energy scale for jets, using in-situ isolated tracks and calorimeter (E/p) measurements and test beam results, establishes an absolute jet energy scale uncertainty of about $\pm 7\%$.

4 Results

4.1 Inclusive jet production

Figure 1 presents the multiplicity, transverse momentum, and rapidity distributions for all jets with $p_T^{jet} > 30$ GeV and $|y^{jet}| < 2.8$. Events with six jets in the final state are observed, and jets are observed with p_T^{jet} up to $\sim$500 GeV. The MC provides a reasonable description of the distributions, but still shows some deficiencies in the observed jet rapidity distribution. The invariant mass m^{jj} of the two leading jets and their azimuthal angular separation $|\Delta\phi^{jj}|$ are presented in Fig. 2. The shape of the m^{jj} distribution at low mass reflects the limited phase space due to the thresholds applied on p_T^{jet} and y^{jet}. Above that, the observed spectrum decreases with increasing m^{jj} up to a dijet mass around 1 TeV. The observed $|\Delta\phi^{jj}|$ distribution strongly peaks at $|\Delta\phi^{jj}| \sim \pi$, indicating a dominant back-to-back dijet configuration in the final state. The shapes of the dijet mass spectrum and $|\Delta\phi^{jj}|$ distribution are described by MC simulation, though the MC underestimates the data at large $|\Delta\phi^{jj}|$.

4.2 Jet shapes and charged particle flow

The transverse momentum distribution inside the jet and the charged particle flow around the jet, which are illustrated schematically in Fig. 3, are studied in order to test our quantitative understanding of the jet properties.

The differential jet shape illustrated in Fig. 3(a) is defined as the average fraction of jet transverse momentum density within an annulus spanning $r \pm \Delta r/2$ around the jet axis:

$$\rho(r) = \frac{1}{\Delta\, r} \frac{1}{N^{jet}} \sum_{\rm jets} \frac{p_T(r - \Delta\ r/2, r + \Delta\ r/2)}{p_T(0, R)},\ 0 \le r \le R\,, \qquad (1)$$

[1]The electromagnetic scale is the appropriate scale for the reconstruction of the energy deposited by electrons or photons in the calorimeter.

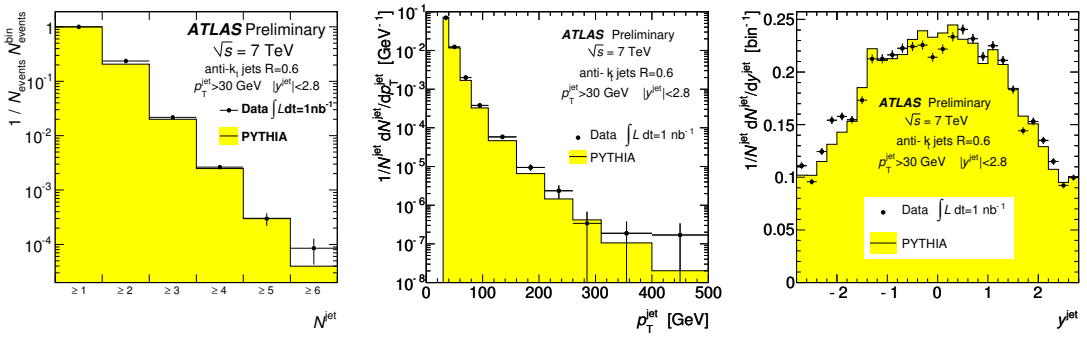

(a) (b) (c)

Figure 1: Observed inclusive jet multiplicity ($\geq N^{jet}$) distribution (left), p_T^{jet} (center), and y^{jet} (right). The distributions are normalized to unity and only statistical uncertainties are included.

where p_T denotes the scalar sum of the transverse momentum of the calorimeter clusters in a given annulus, N^{jet} is the number of jets, $R = 0.6$, and $\Delta r = 0.1$ are used. The observed jet shapes are presented in Fig. 4 for jets with $p_T^{jet} > 30$ GeV and $|y^{jet}| < 2.8$ in different regions of jet transverse momentum. The distributions peak at low r, indicating the presence of a collimated flow of particles around the jet axis. The measurements are reasonably well described by the PYTHIA MC, which tends to produce slightly narrower jets than the data.

The charged particle flow around the jet provides an independent track-based technique to confirm the calorimeter-based jet shapes and to understand the final state topology. The hadronic activity out of the jet cone is studied in inclusive dijet events using tracks, which are selected as in [10] using $p_T^{track} > 500$ MeV and $|\eta^{track}| < 2.5$. The average transverse momentum is measured as a function of the azimuthal distance to the jet axis as illustrated in Fig. 3(b) and is defined as:

$$< \frac{d^2 p_T}{|d\phi| dy} >_{jets} = \frac{1}{2R|\Delta\phi|} \frac{1}{N^{jet}} \sum_{jets} p_T(|\phi - \Delta\phi/2|, |\phi + \Delta\phi/2|), \text{with } 0 \leq |\phi| \leq \pi \,, \qquad (2)$$

where $p_T(|\phi - \Delta\phi/2|, |\phi + \Delta\phi/2|)$ is the scalar sum of the transverse momentum of the tracks at a given distance ϕ to the jet, and bins of $\Delta\phi = 0.2$ are used. Only tracks within the rapidity range spanned by the jet cone are included. The jet is required to have $p_T^{jet} > 30$ GeV and $|y^{jet}| < 1.9$ as determined by the tracking coverage of $|\eta^{track}| < 2.5$. This is performed as a function of the rapidity separation between the two leading jets $|\Delta y^{jj}|$. In Fig. 5, for $|\Delta y^{jj}| < 0.6$ the presence of two collimated jets of tracks at $|\phi| \sim 0$ and $|\phi| \sim \pi$ is observed as expected. For $|\Delta y^{jj}| > 1.2$, the jet structure for $|\phi| < 0.6$ is followed by a plateau of remaining hadronic activity as $|\phi|$ increases. The PYTHIA MC provides a reasonable description of the data, but slightly underestimates the hadronic activity away from the jet direction.

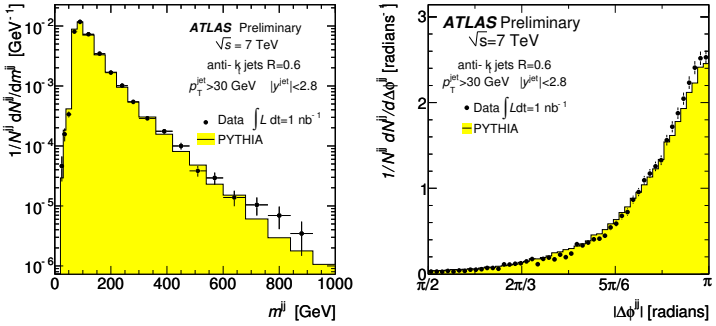

(a) (b)

Figure 2: Observed m^{jj} (left) and $|\Delta\phi^{jj}|$ (right) distributions in inclusive dijet events. Only statistical uncertainties are included and the distributions are normalized to unity.

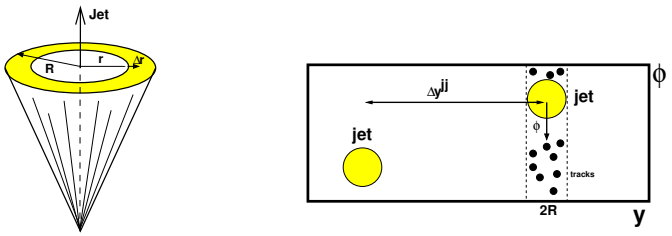

(a) (b)

Figure 3: Sketch of the jet shape as a function of the distance to the jet axis (left), and sketch of the particle flow as a function of the distance to the jet axis in the azimuthal direction (right).

5 Summary

We have reported the observation of energetic jet production in pp collisions at $\sqrt{s} = 7$ TeV, based on about 1 nb^{-1} of data collected by the ATLAS detector. The anti $-$ k$_{\mathrm{T}}$ algorithm is used to reconstruct jets with $p_T^{jet} > 30$ GeV and $|y^{jet}| < 2.8$ from calorimeter energy clusters. Jets with p_T^{jet} up to ~ 500 GeV and events with dijet mass up to $m^{jj} \sim 1$ TeV are observed. The jet shapes and charged particle flow confirm that the observed jet signal corresponds to collimated flows of particles in the final state.

6 Acknowledgments

The author is grateful for support from the NSF US LHC Graduate Student Support Award.

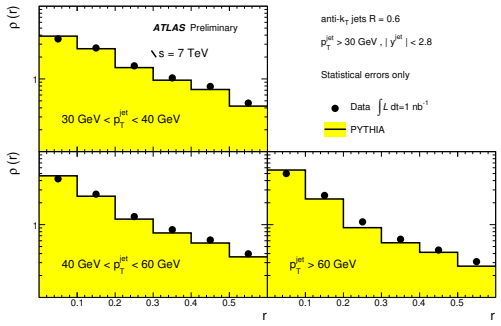

Figure 4: Observed differential jet shapes $\rho(r)$ in different regions of jet transverse momentum.

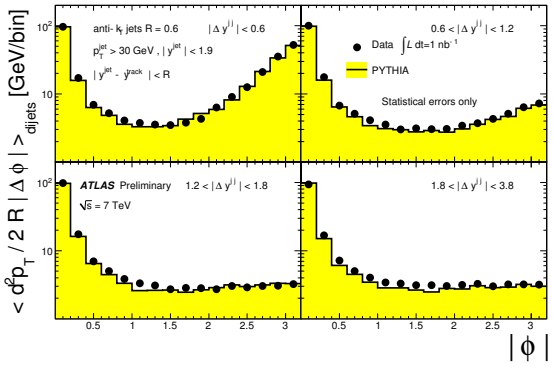

Figure 5: Observed charged particle flow in inclusive dijet events as a function of $|\phi|$ with respect to the jet direction and the rapidity separation between the two leading jets.

References

[1] ATLAS Collaboration, *The ATLAS Experiment at the CERN Large Hadron Collider*, JINST **3** S08003 (2008)

[2] T. Sjöstrand et al., *PYTHIA 6.4 Physics and Manual*, JHEP **05**, 026 (2006)

[3] ATLAS Collaboration, *ATLAS Monte Carlo tunes for MC09*, ATL-PHYS-PUB-2010-002 (2010)

[4] A. Sherstnev and R.S. Thorne, *Parton distributions for LO generators*, Eur. Phys. J. C **55**, 553 (2008)

[5] S. Agostinelli et al., *GEANT4 – a simulation toolkit*, Nucl. Instrum. Methods A **506**, 250 (2003)

[6] ATLAS Collaboration, *Performance of the Minimum Bias Trigger in p-p Collisions at* $\sqrt{s} = 900$ *GeV*, ATLAS-CONF-2010-025 (2010)

[7] ATLAS Collaboration, *Data-Quality Requirements and Event Cleaning for Jets and Missing Transverse Energy Reconstruction with the ATLAS Detector in Proton-Proton Collisions at a Center-of-Mass Energy of* $\sqrt{s} = 7$ *TeV*, ATLAS-CONF-2010-038 (2010)

[8] M. Cacciari, G. P. Salam and G. Soyez, *The anti-k_t jet clustering algorithm*, JHEP **0804**, 063 (2008)

[9] W. Lampl et al., *Calorimeter clustering algorithms: Description and performance*, ATL-LARG-PUB-2008-002 (2008)

[10] ATLAS Collaboration, *Charged-particle multiplicities in pp interactions at* $\sqrt{s} = 900$ *GeV measured with the ATLAS detector at the LHC*, Phys. Lett. B **688**, 21 (2010)

Performance of the particle flow algorithm in CMS

Daniele Benedetti for the CMS Collaboration

CERN, 1211 Geneva, Switzerland

DOI: http://dx.doi.org/10.3204/DESY-PROC-2010-01/221

The aim of the CMS particle flow algorithm is to identify and reconstruct individually each particle arising from the LHC proton-proton collision, by combining the information from all subdetectors. The resulting particle-flow event reconstruction leads to an improved performance for the reconstruction of jets and MET, and for the identification of electrons, muons, and taus.

1 The particle-flow algorithm

The CMS [1] particle-flow event reconstruction [2] combines the information from all subdetectors to identify and individually reconstruct all particles produced in the collision, namely charged hadrons, photons, neutral hadrons, muons, and electrons. The resulting list of particles can then be used to build jets, to determine the missing transverse energy ($E_{\mathrm{T}}^{\mathrm{miss}}$), to reconstruct and identify taus from their decay products, and to quantify charged lepton isolation with respect to other particles.

2 Performance of the particle-flow event reconstruction in simulated data

The typical jet energy fractions carried by charged particles, photons and neutral hadrons are 65%, 25% and 10% respectively [2]. These fractions ensure that 90% of the jet energy can be reconstructed with good precision by the particle-flow algorithm with the CMS detector, thanks to the excellent tracking efficiency and electromagnetic calorimeter resolution [1], while only 10% of the energy is affected by the poor hadron calorimeter resolution and by calibration corrections of the order of 10% to 20%. As a consequence, the jets made of reconstructed particles are expected to be much closer, in energy and direction, to jets made of Monte-Carlo-generated particles than jets made from the sole calorimeter information.

2.1 Jet energy response and resolution

Jets are reconstructed from the QCD-multijet event sample with the iterative-cone algorithm [1] with a cone size of 0.5 in the (η, ϕ) plane, from several types of inputs: all generated stable particles ("gen-jets"), particles reconstructed with the particle-flow algorithm ("particle-flow jets") and calorimeter towers ("calo-jets"). The reconstructed jets are then matched to the closest gen-jet in the (η, ϕ) plane. The jet response, defined as the Gaussian mean of the

$(p_{\mathrm{T}}^{\mathrm{rec}} - p_{\mathrm{T}}^{\mathrm{gen}})/p_{\mathrm{T}}^{\mathrm{gen}}$ distribution (where "rec" and "gen" hold for reconstructed and generated jets, respectively), is shown in Fig. 1 (left) for several p_{T} bins. The particle-flow-jet response benefits from the reconstruction of all particles in the event from a combination of all CMS sub-detectors, which ensures that little energy is lost over the whole acceptance. The particle-flow jet-energy resolutions, obtained by dividing the Gaussian width σ by the average jet response, in each p_{T} bin, are compared to the fully corrected calo-jets in Fig. 1 (right). Up to three times better resolution for jets is obtained using the particle-flow event reconstruction [2].

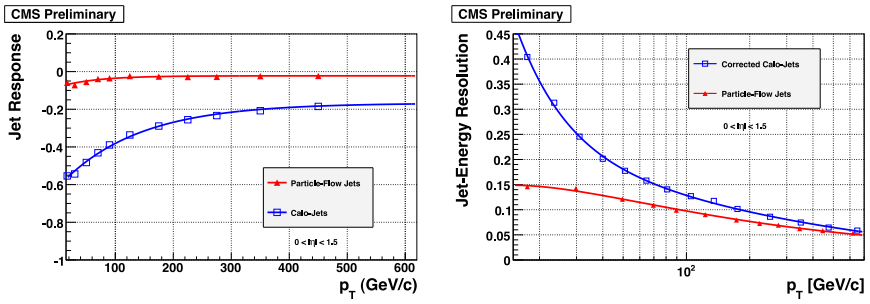

Figure 1: Jet response (left) and jet-energy resolution (right) as a function of p_{T} in the CMS barrel region ($|\eta| < 1.5$) for the particle-flow jets (triangles) and the calo-jets (squares).

3 Commissioning of the particle-flow event reconstruction with the first LHC collisions

3.1 Particles: photons, charged and neutral hadrons

The absolute photon-energy calibration and the uniformity of the electromagnetic calorimeter (ECAL) response can be checked with the abundant π^0s in the data recorded at $\sqrt{s} = 900$ GeV. The photon-pair invariant-mass distribution is shown in Fig. 2 (left) and is fit with a Gaussian for the π^0 signal added to an exponential function of the invariant mass for the combinatorial background. The agreement for the measured mass values in data and simulation with the world average of $135\,\mathrm{MeV}/c^2$ [3] to within $\pm 2\%$ demonstrates the suitability of the simulation-based absolute ECAL cluster calibration for low-energy photons in the data [4].

The energy response of the calorimeters to hadrons and its calibration is also important for the particle-flow algorithm. An improper calorimeter calibration would lead to a systematic mis-estimation of both the energy and multiplicity of neutral hadrons [4]. Consistency for the charged-hadron calibration ensures the proper energy calibration for neutral hadrons as well. To verify the calibration procedure the average calibrated calorimeter response, integrated over the pseudorapidity range $|\eta| < 2.4$, is displayed in Fig. 2 (right) as a function of the measured track momentum, from 1 to $30\,\mathrm{GeV}/c$. This figure demonstrates that *(i)* the calorimeters respond to charged hadrons as predicted from the simulation; and *(ii)* the hadron cluster calibration obtained from the simulation of the CMS detector is adequate, on average, for use of the particle-flow event reconstruction in data.

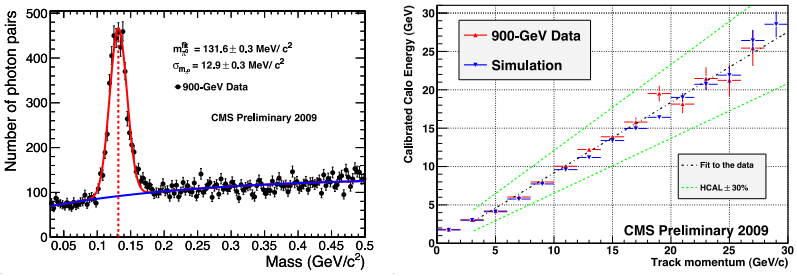

Figure 2: Left: photon-pair invariant-mass distribution in the barrel ($|\eta| < 1.0$) for the data. Right: average calibrated calorimeter response as a function of the track momentum for the 900 GeV data (light upwards triangles) and for the simulation (dark downwards triangles). The dashed lines show the same quantity when the HCAL raw response is changed by ±30%

3.2 Jets

To demonstrate the reliability of the particle-flow event description of the jet constituents, the jet energy fraction [4] as a function of pseudorapidity is shown in Fig. 3 for the data and the simulation. In the tracker-covered region, charged hadrons are found to carry on average 65% of the jet energy, photons 15% and neutral hadrons 20%. The higher fraction of neutral hadrons, with respect to the one indicated in Sec. 2, is produced by clusters arising from the hadronic calorimeter noise and due to the very low p_{T} threshold applied in this jet selection [4]. The data and simulation are found to be in good agreement.

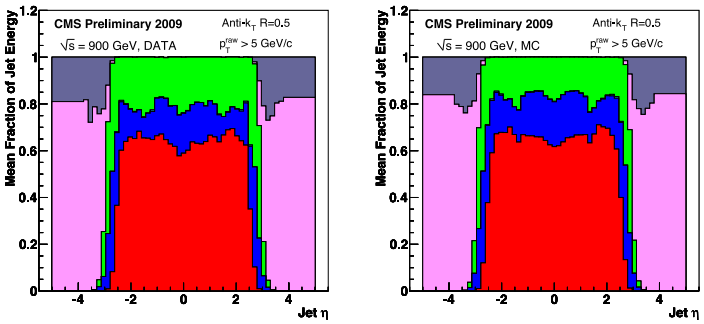

Figure 3: Reconstructed jet energy fractions as a function of pseudorapidity in the data (left), and in the simulation (right). From bottom to top in the central region: charged hadrons, photons, electrons (less than 1%), and neutral hadrons. In the forward region: hadronic deposits, electromagnetic deposits.

3.3 Missing transverse energy

The missing transverse energy allows for an indirect detection of invisible particles produced in proton–proton collisions, such as neutrinos or neutralinos. In the particle-flow event reconstruction, the missing transverse energy vector is computed as the opposite of the transverse-momentum sum of all particles reconstructed in the event, $E_{\mathrm{T}}^{\mathrm{miss}}$ is its modulus and its projections on the x and y axes are denoted $E_{\mathrm{x}}^{\mathrm{miss}}$ and $E_{\mathrm{y}}^{\mathrm{miss}}$, respectively. As a large $E_{\mathrm{T}}^{\mathrm{miss}}$ is one of the most promising signatures for new physics, it is important to ensure that experimental artifacts do not give rise to fake particles with large energies. Unlike $E_{\mathrm{T}}^{\mathrm{miss}}$, where experimental effects somewhat cancel out due to calculations involving differences in momentum, all detector effects are added up in ΣE_{T}, i.e. the scalar-sum of the transverse energies over all reconstructed particles. ΣE_{T} represents an excellent benchmark for evaluating the performance of the generator, the detector simulation, and the reconstruction algorithm.
The distribution of $E_{\mathrm{T}}^{\mathrm{miss}}/\Sigma E_{\mathrm{T}}$ is displayed for events with $\Sigma E_{\mathrm{T}} > 3$ GeV in Fig. 4 (left). Ideally, events with no expected $E_{\mathrm{T}}^{\mathrm{miss}}$ (as is the case in minimum-bias collisions) should have very low values of $E_{\mathrm{T}}^{\mathrm{miss}}/\Sigma E_{\mathrm{T}}$. This figure confirms that, for a given estimate of the ΣE_{T}, the particle-based $E_{\mathrm{T}}^{\mathrm{miss}}$ resolution is, on average, twice better than the calorimeter reconstruction [4]. Another way to visualise the improved $E_{\mathrm{T}}^{\mathrm{miss}}$ resolution is to parametrise it as a function of ΣE_{T}. To do so, the distribution of $E_{\mathrm{x}}^{\mathrm{miss}}$ and $E_{\mathrm{y}}^{\mathrm{miss}}$ was fit to a Gaussian, for several bins of ΣE_{T}. The resulting width $\sigma(E_{\mathrm{x,y}}^{\mathrm{miss}})$, shown as a function of ΣE_{T} in Fig. 4 (right), was fit by the functional form $a \oplus b\sqrt{\Sigma E_{\mathrm{T}}}$. This fit yields $a = 0.55$ GeV and $b = 45\%$ for the particle-based reconstruction.

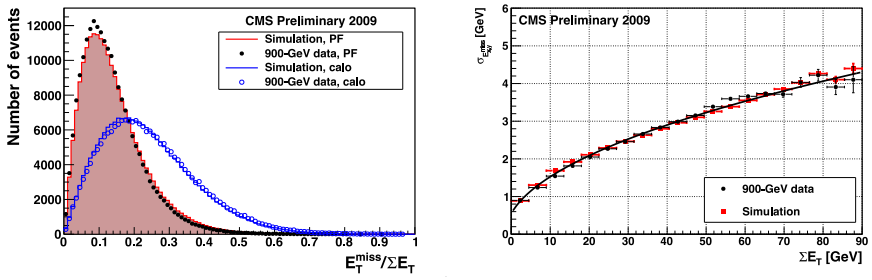

Figure 4: Left: distribution of the particle-based (solid) and calorimeter-based (hollow) $E_{\mathrm{T}}^{\mathrm{miss}}/\Sigma E_{\mathrm{T}}$ in the data (dots) and in the simulation (histogram). Right: resolution of the particle-based $E_{\mathrm{x,y}}^{\mathrm{miss}}$ as a function of the particle-based in the data (dots) and in the simulation (squares).

References

[1] CMS Collaboration, R. Adolphi *et al.*, "The CMS experiment at the CERN LHC," JINST **3** (2008) S08004.

[2] CMS Collaboration, "Particle-Flow Event Reconstruction in CMS and Performance for Jets, Taus and $E_{\mathrm{T}}^{\mathrm{miss}}$", CMS PAS **PFT-09-001** (2009).

[3] C. Amsler *et al.* [Particle Data Group], Phys. Lett. B **667** (2008) 1.

[4] CMS Collaboration, "Commissioning of the Particle-flow Event Reconstruction with the first LHC collisions recorded in the CMS detector", CMS PAS **PFT-10-001** (2010).

Improving the present precision of the electroweak parameters at the LHC: a forlorn hope?*

Mieczyslaw Witold Krasny LPNHE, Université Pierre et Marie Curie Paris 6, Université Denis Diderot Paris 7, CNRS/IN2P3, Paris, France

DOI: http://dx.doi.org/10.3204/DESY-PROC-2010-01/250

At the LHC, an improvement of the present precision of the electroweak parameters is both mandatory and difficult. In the analysis strategies proposed so far, shortcuts have been made that are justified for proton–antiproton collisions at the Tevatron, but not for proton–proton collisions at the LHC. The root of the problem lies in the inadequate knowledge of parton density functions of the proton. It is argued that more precise parton density functions of the proton are needed, and an LHC-specific analysis strategy ought to be pursued. Proposals are made on both issues.

1 Introduction

In much the same way as precise measurements of radiative corrections served to test and establish QED, precise measurements of input parameters and their use in the calculation of radiative corrections in the Electroweak Standard Model serve as benchmarks for new theoretical concepts. Therefore, besides the direct searches for new phenomena, the precision measurement of parameters of the Electroweak Standard Model[1] —e.g., the W mass—with greater precision than available from LEP and the Tevatron, is an important and indispensable part of the LHC programme.

Whilst the Z mass (M_{Z}) is well measured to ± 2.1 MeV/c^2 [1], M_{W} is measured at the Tevatron to ± 31 MeV/c^2 [2] and at LEP to ± 33 MeV/c^2 [3]. Of the three independent input parameters of the Electroweak Standard Model, M_{W}, M_{Z} and the fine-structure constant, M_{W} is by one order of magnitude less precise than M_{Z} that is second-best.

Although a precision of M_{W} that matches the precision of M_{Z} is experimentally not within reach, a much better precision than available today is desirable to exploit the full potential of the relation between M_{W} and the Fermi coupling constant G_{F} that is also well measured with a relative precision of 1×10^{-5}.

The relation between G_{F} and the three input parameters, M_{W}, M_{Z} and the fine-structure constant, is a cornerstone of the Electroweak Standard Model. Radiative corrections of this relation that depend *inter alia* on the mass of the Higgs boson, suggest a broad range for the Higgs mass that is nevertheless well within reach at the LHC. However, in case the Higgs boson will not be found, the hunt for alternative models of electroweak symmetry breaking will be

*Work done in collaboration with F. Dydak, F. Fayette, W. Płaczek, K. Rejzner and A. Siódmok, supported by the cooperation programme between the French IN2P3 and Polish COPIN Laboratories No. 05-116, and by the EU Marie Curie Research Training Network grant No. MRTN-CT-2006-035505. This note is an abbreviated version of CERN-PH-EP/2010-007 (e-Print: arXiv:1004.2597 [hep-ex])

[1] Hereafter referred to as 'electroweak parameters'.

on. Then the highest possible precision of M_{W} will be a central issue, for a better measured relation between the quantities G_{F}, M_{W}, M_{Z}, and the fine-structure constant, will put more stringent constraints on theoretical models.

In previous analyses, it was claimed that an M_{W} precision of 10 MeV/c^2 or better will be obtained at the LHC [4, 5]. This note questions such claims and argues that shortcuts have been made that are not justified, and hence the claimed measurement precision is much too optimistic. The reason is that the analysis of $p_{\mathrm{T,l}}$ spectra from leptonic W and Z boson decays in $\mathrm{p\bar{p}}$ collisions at the Tevatron—that served as template for the respective analyses at the LHC—benefits from symmetry properties that are absent in pp collisions at the LHC. A considerably better knowledge of the $u_{\mathrm{v}} - d_{\mathrm{v}}$, $s - c$, and b parton density functions (PDFs) of the proton[2] than available today is needed, together with an LHC-specific measurement and analysis programme.

No improvement of the current situation is expected unless special experimental efforts are made to obtain the missing high-precision PDFs. Two ways forward are discussed. One is to complement the pp programme of the LHC with a deuteron-deuteron collision programme. Another is to obtain missing input from a new high-precision muon–nucleon scattering experiment, and to analyze these data coherently with LHC pp and Tevatron $\mathrm{p\bar{p}}$ data.

2 The LHC precision limits

It is advocated and widely believed that the proton PDFs are precise enough not to pose a limitation for LHC data analysis. In the following, a 5% error of the x dependence of the PDFs of the u_{v} and d_{v} is considered as a realistic estimate. The present experimental uncertainty of the PDF of the c quark is at the 10% level[3]. The present experimental uncertainty of the PDF of the b quark is at the 20%

The root of the problem for the use of current proton PDFs in the analysis of W and Z production and decay at the LHC arises from 'compensating' PDF changes: a change of the PDF of one quark can be compensated by a change of the PDF of the other quark of the same family that leaves the Z rapidity distribution nearly invariant and hence escapes detection[4].

The above uncertainties of PDFs are incorporated in the simulation of p_{T} spectra from $\mathrm{W^+}$, $\mathrm{W^-}$ and Z leptonic decays. This simulation uses the LHAPDF package [7] of PDFs, and PYTHIA 6.4 [6] for the modelling of the QCD/QED initial-state parton shower and its hadronization; the transverse momentum k_{T} of quarks and antiquarks is the one incorporated in PYTHIA. The tool for event generation is WINHAC 1.31 [8], a Monte Carlo generator for single W production in hadronic collisions, and subsequent leptonic decay. WINHAC includes also neutral-current processes with γ and Z bosons in the intermediate state. The novel feature of WINHAC is that it describes W and Z production and decay in terms of spin amplitudes [9]. These involve, besides all possible spin configurations of the W and Z bosons, also the ones of the initial- and final-state fermions. The advantage of this approach is that one has explicit control over all spin states, and thus over transverse and longitudinal boson polarization amplitudes and their interferences.

[2] Throughout this paper, PDFs refer to the proton.

[3] Theoretical calculations of heavy-quark PDFs from the gluon PDF are claimed to have a smaller error margin.

[4] The condition of invariance of the Z rapidity distribution, and hence invisibility even in high-statistics data samples, is decisive: if the measured Z rapidity distribution looked differently than expected from the current proton PDFs, an appropriate change of the proton PDFs would be unavoidable.

As an example LHC detector, ATLAS is chosen. Charged leptons from W and Z decays are accepted with $p_{\mathrm{T}} > 20$ GeV/c and $|\eta| < 2.5$. The approximate range of x for W and Z production in the above kinematical region is 5×10^{-2} to 7×10^{-4}. The event statistics correspond to an integrated luminosity of 10 fb^{-1}. Both the electron- and muon decay channels of W and Z are considered. Since in pp collisions the spectra of positive and negative leptons are to be analyzed separately, it is natural to make the same distinction also for the leptons from Z decay. Along this line of reasoning, 'Z$^+$' and 'Z$^-$' lepton p_{T} spectra are generated, in analogy to 'W$^+$' and 'W$^-$' lepton p_{T} spectra[5]. All spectra are generated with various proton PDF configurations. The Z$^+$ and Z$^-$ lepton p_{T} spectra are corrected for the evolution from $Q^2 = M_{\mathrm{W}}^2$ to $Q^2 = M_{\mathrm{Z}}^2$.

From a fit of the Jacobian peaks in the p_{T} distributions and by calibrating with the known Z mass, the W$^+$ and W$^-$ masses are determined. The biases of M_{W} caused by the allowed compensating changes of the PDFs of quarks of the 1st family are at the 70 MeV/c level. The biases of M_{W} caused by the allowed compensating changes of the PDFs of quarks of the 2nd family are at the 130 MeV/c level. The biases of M_{W} caused by the allowed changes of the PDF of the b quark are at the 40 MeV/c level The conclusion is, when allowing for compensating PDF changes and a realistic PDF error margin, that there is no way to obtain M_{W} with a precision at the 10 MeV/c^2 level with the currently available proton PDFs.

There is also no way to improve, at the LHC collider, the present precision of the other electroweak parameters. For example, allowing for compensating PDF changes leads to an uncertainty of $\mathcal{O}(100)$ MeV/c^2 for M_{W} and for the difference $M_{\mathrm{W}^+} - M_{\mathrm{W}^-}$, an uncertainty of $\mathcal{O}(40)$ MeV/c^2 for Γ_{W} , and an uncertainty of $\mathcal{O}(0.001)$ for $\sin^2\theta_{\mathrm{W}}$. Already for an integrated luminosity as small as 1 fb^{-1} the errors that result from the uncertainties of today's missing input, are larger than statistical and systematic errors stemming from the LHC data.

3 Ways forward

3.1 Two-dimensional PDFs

In our view improving the present precision of the electroweak parameters requires overhauling of the analysis framework developed at the Tevatron, in particular, it requires replacing one-dimensional PDFs by the two dimensional PDFs. The differential of the two-dimensional PDF of the quark q, $\mathrm{d}q(x, k_{\mathrm{T}}; Q^2)$, denotes the number $\mathrm{d}N$ of quarks of type q with a fraction of the proton longitudinal momentum in the range $[x, x + \mathrm{d}x]$, with a transverse momentum in the range $[k_{\mathrm{T}}, k_{\mathrm{T}} + \mathrm{d}k_{\mathrm{T}}]$, at the scale Q^2.

3.2 Deuteron–deuteron collisions at the LHC

The impact of the uncertainties from missing input PDFs can be considerably reduced by operating the LHC with isoscalar beams. The natural choice is to collide deuteron beams. The deuteron beams restore isospin symmetry for the quarks of the 1st family. The four independent k_{T}-integrated PDFs $u(x)$, $d(x)$, $\bar{u}(x)$ and $\bar{d}(x)$ are reduced to two: $u(x) + d(x)$ and $\bar{u}(x) + \bar{d}(x)$. Equality of W$^+$ and W$^-$ production is restored and the spin-density matrices of W and Z

[5]This appears appropriate as a non-zero longitudinal Z polarization causes the p_{T} spectra of the positive and negative decay leptons to be slightly different, for the charge-dependent correlation of the Z spin with the emission of charged decay leptons.

produced by quarks of the 1st family are nearly the same. If the contributions from quarks of the 2nd and 3rd family could be neglected, the isospin symmetry of deuterons at the LHC would play the same role as the matter–antimatter symmetry at the Tevatron. In principle, high-statistics data from dd collisions at the LHC would be sufficient to provide electroweak parameters with the desired precision. However, caveats remain.

3.3 pp at the LHC, $p\bar{p}$ at the Tevatron, and muon–nucleon scattering combined

The concept of solving the missing-input problem by dd collisions in the LHC is elegant and technically feasible, though not realistic in the near future. Therefore, an alternative is proposed: obtaining with sufficient precision from a joint analysis of Tevatron $p\bar{p}$ data, of data from a new muon–nucleon scattering experiment, and of LHC pp data, all needed PDFs with adequate precision. The muon–nucleon scattering experiment would measure from the deep-inelastic scattering of $\mathcal{O}(100)$ GeV/c muons on stationary hydrogen and deuterium targets the asymmetry

$$\mathcal{A}_{\mathrm{DIS}}^{\mathrm{p,n}} = \frac{\sigma(\mu,\mathrm{p}) - \sigma(\mu,\mathrm{n})}{\sigma(\mu,\mathrm{p}) + \sigma(\mu,\mathrm{n})} \quad (1)$$

With the inclusion of the muon–nucleon scattering data, the problem of missing high-precision PDFs for the analysis of LHC pp data is solved. A Letter of Intent [10] for such an experiment was submitted to CERN Programme Committees. Therein, the exposure of the COMPASS detector to the muon beam of the CERN–SPS was proposed.

4 Conclusion

Unless efforts as discussed in this paper are undertaken, the precision of the W mass, and of other parameters of the Electroweak Standard Model, will not be improved at the LHC. Thus a chance may be missed towards understanding the mechanism that regularizes the unitarity problem of this Model.

References

[1] C. Amsler *et al.* (Particle Data Group), Phys. Lett. **B667** (2008) 1

[2] The Tevatron Electroweak Working Group, Updated Combination of CDF and D0 results for the Mass of the W Boson, FERMILAB–TM–2439–E, arXiv: 0908.1374 [hep-ex]

[3] The LEP Electroweak Working Group, A Combination of Preliminary Electroweak Measurements and Constraints on the Standard Model, CERN–PH–EP–2006–042, arXiv: hep-ex/0612034

[4] ATLAS Detector and Physics Performance, Report ATLAS TDR 15 (CERN/LHCC 99-15); N. Besson *et al.* (ATLAS Collaboration), Eur. Phys. J. **C57** (2008) 627, arXiv: hep-ex/0805.2093; N. Besson (for the ATLAS Collaboration), presentation at the Int. Europhysics Conference on High Energy Physics (EPS–HEP2009), Cracow (Poland), July 2009

[5] V. Buge *et al.* (CMS Collaboration), J. Phys. **G34** (2007) 995; CERN–CMS–NOTE–2006–061

[6] T. Sjostrand, S. Mrenna, and P. Skands, JHEP **05** (2006) 26

[7] M.R. Whalley, D. Bourilkov, and R.C. Group, arXiv: hep-ph/0508110

[8] W. Płaczek and S. Jadach, http://cern.ch/placzek/winhac

[9] W. Płaczek and S. Jadach, Eur. Phys. J. **C 29** (2003) 325

[10] F. Dydak, M. W. Krasny, and R. Voss, Document CERN-SPSC-2009-028 / CERN-LHCC-2009-014

Four-top events at the LHC

Géraldine Servant[1,2]

[1] CERN Physics Department, Theory Division, CH-1211 Geneva 23, Switzerland
[2] Institut de Physique Théorique, CEA/Saclay, 91191 Gif-sur-Yvette cédex, France

DOI: http://dx.doi.org/10.3204/DESY-PROC-2010-01/251

Four-top production is a spectacular final state and a sensitive probe of new physics that is relatively unconstrained by precision measurements at LEP or resonance searches at the Tevatron. Examples are models where the top quark is composite or where a new heavy particle couples strongly or exclusively to top quarks. We report preliminary results of a first detailed simulation and estimate the LHC sensitivity in the same-sign dilepton channel.

1 Introduction

Four top production occurs in the Standard Model (SM) through diagrams like the one in figure 1(a) [1]. The total $pp \to t\bar{t}t\bar{t}$ cross-section at 14 TeV is 7.5 fb in the SM and is dominated by gluon-initiated diagrams. On the other hand, in many SM extensions the top quark plays a special role. New particles X with a preference for the top quark could yield a sizeable $t\bar{t}t\bar{t}$ cross-section through processes like that depicted in Fig. 1(b). Note that this diagram involves only couplings of X to top quarks. In particular, X does not have to couple to light quarks or gluons to be produced at the LHC. If X is too heavy, the resonance is replaced by a contact interaction like in Fig. 1(c). Well-motivated examples are models where the top quark is composite [2, 3], in which the top quark acquires its large mass (after electroweak symmetry breaking) through large mixing with composite states in a new strong sector, as in 4D duals to Randall-Sundrum (RS) models. In this approach, most of the SM is fundamental but with the right-handed top quark and the Higgs that couple strongly to composite fields and the amount

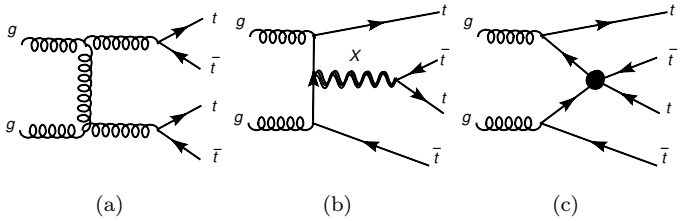

Figure 1: (a): Standard Model diagram that give rise to the $t\bar{t}t\bar{t}$ final state. (b-c): Two diagrams involving new physics, that yield to a non-zero event rate even if the new particle does not couple to light quarks. (b) represents s-channel (resonant) $t\bar{t}$ production. The effective four-top interaction in (c) can result from integrating out a heavy particle.

of composite admixture in a given SM fermion determines its mass [4].

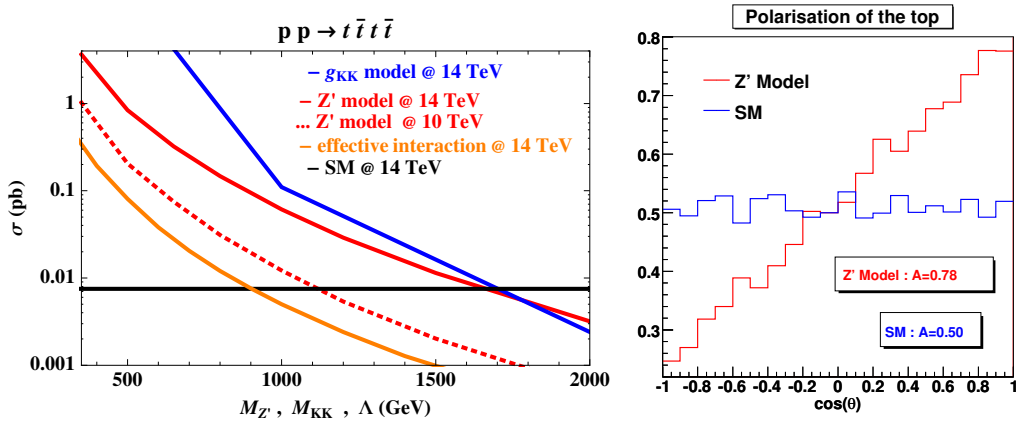

Figure 2: Left: Four-top production cross section at the LHC, mediated by a Kaluza–Klein gluon (in blue) or a Z' (in red). The orange curve refers to the effective 4-fermion interaction $(\bar{t}_R\gamma_\mu t_R)(\bar{t}_R\gamma^\mu t_R)/\Lambda^2$ leading to Fig. 1(c). Right: Angular distribution for the leptons of the top decay in the Z' model with $M_{Z'}$ =800 GeV compared to the SM.

To estimate the LHC sensitivity to this final state, we introduce a generic and very simple effective theory in which the SM is supplemented by a new heavy particle Z' having a large coupling to the right-handed (RH) top quark ($g^{Z'}_{t_R} = 3$) but suppressed couplings to the light SM fermions. In Fig. 2 we show the leading order cross section at the LHC for $t\bar{t}t\bar{t}$ production as calculated by MadGraph. In Fig. 3(a), we present the $M_{t\bar{t}}$ distributions of the $t\bar{t}$ pair emitted by a Z' with $M_{Z'} = 1.2$ TeV, of the spectator $t\bar{t}$ pair, which peaks around 500 GeV, and of the $t\bar{t}$ pair produced by the effective 4-fermion contact interaction. We compare as well with the $M_{t\bar{t}}$ from the SM four-top events, which peaks close to 600 GeV. We also display in (b) the maximum of the $t\bar{t}$ pair transverse energy distribution as a function of $M_{Z'}$.

2 Top polarisation

An interesting way to probe the properties of the top interactions relies on measuring the top polarization [3]. The SM four top production being dominated by parity invariant QCD processes, we expect to generate an equal number of left and right-handed pairs. However, in the new physics models discussed here, there is a strong bias towards RH tops. The angular distribution of the leptons from the top decays enables to analyze the polarisation of the top quarks. The differential cross section can be written as

$$\frac{1}{\sigma}\frac{d\sigma}{d\cos\theta} = \frac{A}{2}(1+\cos\theta) + \frac{1-A}{2}(1-\cos\theta) \qquad (1)$$

where θ is the angle between the direction of the lepton in the top rest frame and the direction of the top polarization. The corresponding distribution is illustrated in Fig. 2.

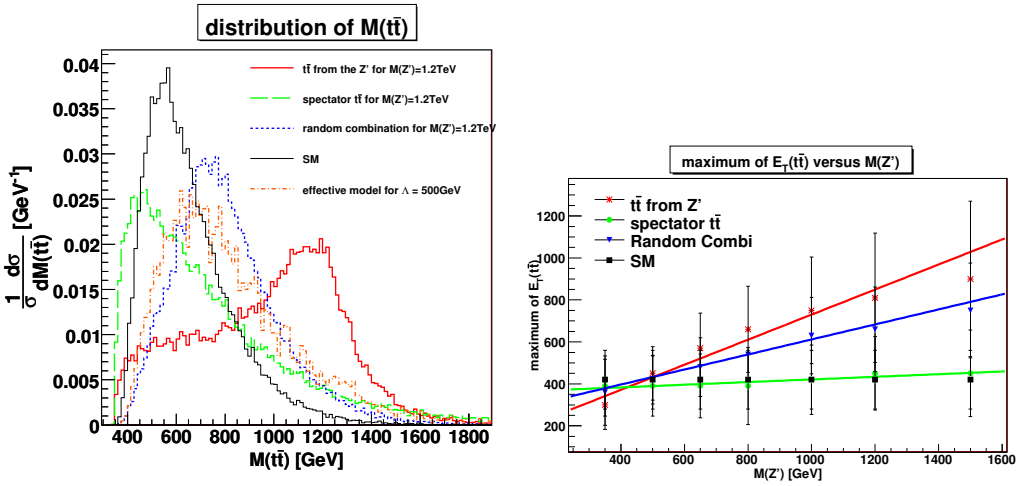

Figure 3: (a) Invariant mass distributions of the top pairs; (b) Position of the maximum of the E_T distribution of the $t\bar{t}$ pair as a function of $M_{Z'}$.

3 Same-sign dilepton channel

The strategy to extract the new physics signal from the SM background consists in requiring two leptons $e^{\pm}$ or $\mu^{\pm}$ with the same sign. Thus, $t\bar{t}$+jets production is effectively reduced. The power of selecting same-sign dilepton events to study $t\bar{t}WW$ final states from pair-production of heavy quarks was shown in detail in [5] and recently applied by CDF to put a strong bound on the mass of fourth generation down-type quarks (b') [6]. In this channel, the main backgrounds to be considered are then $t\bar{t}W$+jets, $t\bar{t}WW$+jets and $t\bar{t}$+jets where the charge of one lepton is

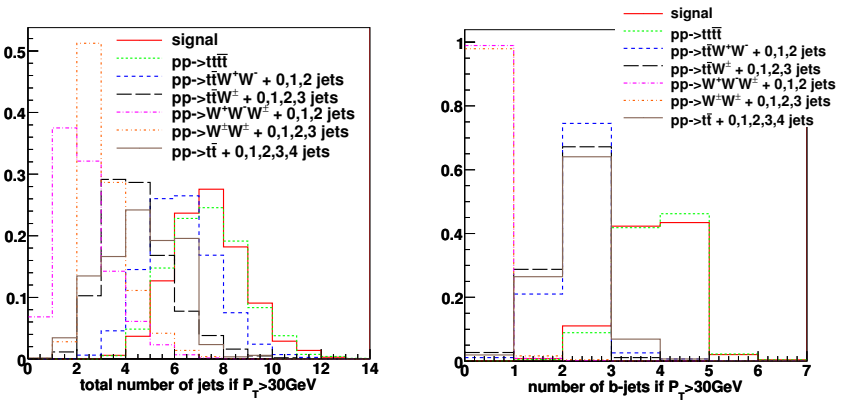

Figure 4: Fractions of signal and background events with a given number of jets with $p_T > 30$ GeV in the same-sign dilepton channel, after Pythia and jet reconstruction with a jet cone size $\Delta R = 0.4$.

misidentified. Signal and background were generated with MadGraph/MadEvent and passed through Pythia. Jets have been reconstructed using a cone size $\Delta R = 0.4$. The distribution of events with a given number of jets is represented in Fig. 4.

Given the complexity of our final state, in a first stage, the minimal approach to reconstruction is to study the scalar sum of the transverse energy of all final state objects. The H_T distribution for a 500 GeV (first panel) and 1 TeV (second and third panels) Z' are shown in Fig. 5 for respectively 10 and 100 fb^{-1} of data. For a 500 GeV mass, the signal is overwhelming after making only a very basic selection on the number of jets $n_j \geq 6$ and $p_T > 30$ GeV. A further and crucial experimental signature of the four-top final states is the large b-jet multiplicity, see Fig. 4(b), which can be used as a powerful tool to extract the signal even coming from a heavy resonance as shown in the third panel of Fig. 5. Reconstruction of (some of) the top quarks in the event can provide additional handles to reduce the background. More details and references can be found in Section 12 of [7] and in the upcoming publication [8].

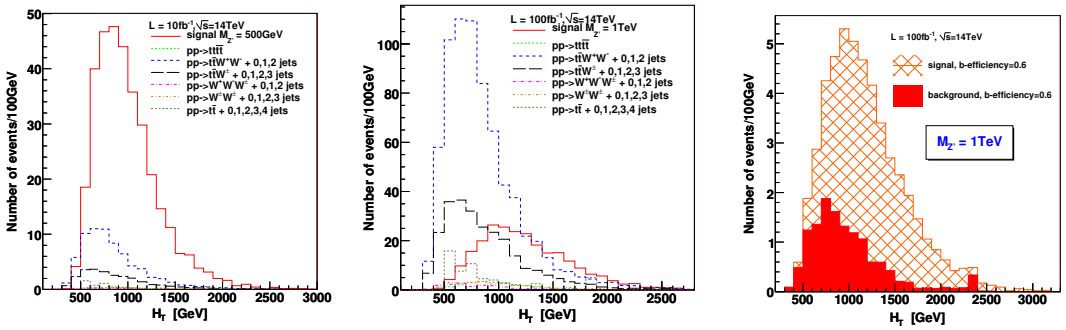

Figure 5: Total transverse energy after demanding $n_j \geq 6$, $p_T > 30$ GeV (first two plots) and in addition $n_{b-jet} \geq 3$ (third plot). In first plot, $M_{Z'} = 500$ GeV, in last two plots $M_{Z'} = 1$ TeV.

4 Acknowledgments

The work of G.S. is supported by the European Research Council Starting Grant Cosmo@LHC.

References

[1] V. D. Barger, A. L. Stange, R. J. N. Phillips, Phys. Rev. **D44**, 1987-1996 (1991).

[2] B. Lillie, J. Shu, T. M. P. Tait, JHEP **0804**, 087 (2008). [arXiv:0712.3057 [hep-ph]]; K. Kumar, T. M. P. Tait, R. Vega-Morales, JHEP **0905**, 022 (2009). [arXiv:0901.3808 [hep-ph]].

[3] A. Pomarol, J. Serra, Phys. Rev. **D78** (2008) 074026. [arXiv:0806.3247 [hep-ph]].

[4] R. Contino, T. Kramer, M. Son and R. Sundrum, JHEP **0705**, 074 (2007) [arXiv:hep-ph/0612180].

[5] R. Contino, G. Servant, JHEP **0806**, 026 (2008). [arXiv:0801.1679 [hep-ph]].

[6] T. Aaltonen *et al.* [CDF Collaboration], Phys. Rev. Lett. **104**, 091801 (2010). [arXiv:0912.1057 [hep-ex]].

[7] G. Brooijmans, C. Grojean, G. D. Kribs *et al.*, [arXiv:1005.1229 [hep-ph]].

[8] L. Gauthier, G. Servant, *in preparation.*

Higgs physics and physics beyond the Standard Model

Theory of dark matter

Graciela B. Gelmini

Department of Physics and Astronomy, University of California Los Angeles (UCLA), 430 Portola Plaza, Los Angeles, CA 90095, USA

DOI: http://dx.doi.org/10.3204/DESY-PROC-2010-01/10

The search for dark matter is a very wide and active field of research. Many potential hints of dark matter have appeared recently which led to a burst of theoretical activity and model building. I necessarily concentrate here only on some aspects of it. I review here some recent hints and some of the ways in which they could be explained.

1 Elements of a theory of dark matter

We know a lot about dark matter (DM) but we still do not have a clue of what it consists of. We know the abundance of the DM in the Universe at the level of few percent, $\Omega_{\rm CDM} = 0.232 \pm 0.013$ [1] and that it is not baryonic. We know also that the DM cannot be explained within the Standard Model (SM) of elementary particles. The bulk of the DM can only be either Cold (CDM) or Warm (WDM), namely it was non-relativistic or becoming non-relativistic at the moment galaxies should start forming in the early Universe, at temperatures $T \simeq$ keV. There are no WDM or CDM candidates in the SM, but there are many in all extensions of the SM. For example, sterile neutrinos and gravitinos can be WDM. WIMPs, Weakly Interacting Massive Particles, among others, could be CDM.

The argument showing that WIMPs are good DM candidates is old and well known. The density per comoving volume of non-relativistic particles in equilibrium in the early Universe decreases exponentially with decreasing temperature, due to the Boltzmann factor, until the reactions which change the particle number become ineffective. At this point, the WIMP number per comoving volume becomes constant. This moment of chemical decoupling or freeze-out happens later, i.e. for smaller WIMP densities, for larger annihilation cross sections σ and the present (standard) relic density is $\Omega_{\rm std} \simeq 0.2 \times [(3 \times 10^{-26}\ {\rm cm}^3/{\rm s})/\langle\sigma v\rangle]$, which for weak cross sections $\sigma \simeq 3 \times 10^{-26} {\rm cm}^{-2}$ gives the right DM density (and a temperature $T_{f.o.} \simeq m_\chi/20$ at freeze-out for a WIMP of mass m_χ). Some call this "the WIMP miracle". However, the WIMP relic density depends not only on the particle model but on the history of the Universe before Big Bang Nucleosynthesis (BBN), an epoch from which we have no data. BBN is the earliest episode (finishes 200 s after the Bang, when $T \simeq 0.8$ MeV) from which we have a trace, the abundance of light elements. WIMPs have their number fixed at $T_{f.o.}$, thus WIMPs with $m_\chi \geq 100$ MeV would be the earliest remnants and, if discovered, they would for the first time give information on the pre-BBN epoch of the Universe. At present, to compute the WIMP relic density we must make assumptions about the pre-BBN epoch. The standard relic density is derived assuming that the entropy of matter and radiation is conserved, that WIMPs are produced thermally, i.e. via interactions with the particles in the plasma, and were in kinetic

and chemical equilibrium before they decoupled at $T_{f.o.}$. WIMPs produced in this way are called "thermal WIMPs". The standard assumptions do not hold in many viable pre-BBN cosmological models, and in some of those, WIMPs can have very different relic densities (e.g. neutralinos can have the DM density in practically all supersymmetric models [2]).

Because of spontaneous symmetry breaking arguments totally independent of the DM issue, we do expect new physics beyond the SM to appear at the electroweak scale soon to be explored by the Large Hadron Collider (LHC) at CERN. Naturalness arguments imply that above the TeV scale there should be cancellations in the radiative corrections to the SM Higgs mass due to a new theory, such as supersymmetry, technicolor, large extra spatial dimensions or the Little Higgs model, for example. These extensions of the SM provide the main potential discoveries at the LHC and also DM candidates that are sometimes described as "well motivated". However, as shown in many of the recent models exclusively motivated by DM hints, the new physics needed to explain the DM may be very different. We will in the following take as a paradigm of this new physics the model ambitiously named precisely "A Theory of DM" [3]. This model is made to fit DM data, not to solve the SM hierarchy problem. Besides it provides signatures for the LHC, which depend on the particular realization of the model [4]. Thus, physics beyond the SM is required by the DM and expected at the electroweak scale, but both new physics may or may not be related. The experiments at the LHC and the searches for the DM in our galactic halo are independent and complementary.

Direct DM searches look for energy deposited within a detector by the collisions of WIMPs belonging to the dark halo of our galaxy. I will mention the DAMA modulation signal, the possible hint seen by CoGeNT and bounds from Xenon10, Xenon100 and CDMS [5]. Indirect DM searches look for WIMP annihilation (or decay) products. I will concentrate here on the positron data of PAMELA and Fermi and models to explain them.

2 Dark matter hints from direct searches

The DAMA collaboration, in the 13 years of combined data of the DAMA/NaI and DAMA/Libra experiments, has found a 8.9σ annual modulation signal [6]. compatible with the signal expected from DM particles bound to our galactic halo and a standard halo model (due to the motion of the Earth around the Sun). Are the DAMA results compatible with those of all other searches? There are many aspects to this question and I will concentrate on two possibilities: inelastically scattering DM (IDM), and light elastically scattering WIMPs.

In IDM models [7], in addition to the DM state χ with mass m_χ there is an excited state χ^*, with a small mass difference $m^*_\chi - m_\chi = \delta \simeq 100$ keV and the inelastic scattering with a nucleon N, $\chi + N \to \chi^* + N$, dominates over the elastic scattering. While the minimum WIMP velocity necessary to provide a particular recoil energy E_R in an elastic collision is $v^{el}_{min} = \sqrt{ME_R/2\mu^2}$, the minimum WIMP velocity required for an inelastic collision is higher $v^{inel}_{min} = v^{el}_{min} + \delta/\sqrt{2ME_R}$. Thus, only high-velocity DM particles have enough energy to up-scatter. v^{inel}_{min} grows as E_R decreases, so there are no low E_R events and the spectrum is very different than for elastic collisions. Besides, v^{inel}_{min} decreases with increasing target mass M, thus targets with high mass are favored (better I in DAMA than Ge in CDMS). The modulation of the signal is also enhanced (because the number of WIMPs changes more rapidly at high v), which also favors the DAMA modulation signal. For IDM with spin independent (SI) interaction with nuclei, a recent bound from the CDMS collaboration leaves very small room for compatibility with the DAMA signal, and new XENON100 bounds are expected soon. But

there are other versions of IDM which still survive all bounds from negative searches. One example is IDM with spin dependent (SD) interactions mostly coupled to protons [8]. The SD coupling with a nucleus is mainly with an unpaired nucleon, which for DAMA (as well as KIMS, COUPP and PICASSO) is a p, while for XENON, ZEPLIN, CDMS and CoGeNT is a n. Thus, while inelasticity eliminates the bounds from PICASSO and COUPP, because they have light targets, the SD coupling with p eliminates those from XENON, CDMS and CRESST.

Papers written prior to the DAMA/LIBRA results found regions of WIMP mass and cross section that reconciled all null results existing at the time with DAMA/NaI's positive signal (assuming a standard halo model, as is usual to do to compare experimental results). Light WIMPs with SI interactions in the mass range 5–9 GeV [9], and with SD interactions in the mass range 5–13 GeV [10] were found to be compatible with all existing data. The situation changed after the publication of the first DAMA/LIBRA results in 2008 (see e.g. [11] and references therein). Light WIMPs were found incompatible with other negative results, but only at the 2 or 3σ level, mostly when ion channeling as estimated by the DAMA collaboration [12] was considered. A nucleus that after a collision with a WIMP recoils along the characteristic axes or planes of the crystal structure may travel long distances without colliding with other nuclei. This channeled nucleus transfers all its energy into electrons ($Q = 1$) instead of only a fraction $Q_{Na} = 0.3$ for Na nuclei or $Q_I = 0.09$ for I nuclei, as it is the case for non-channeled recoils (Q is known as the quenching factor). A revaluation [13] of the channeling fraction in NaI has now shown that the channeling fraction is much smaller than initially estimated by the DAMA collaboration, thus the allowed DAMA/LIBRA region is insensitive to channeling up to the 5σ level [14]. Besides the DAMA data, an excess of events found recently by the CoGeNT collaboration (also hints in CRESST) generated renewed interest in light WIMPs, and a new bust of models, most having light bosons with GeV mass scale [8, 15]. CoGeNT is a 440g Ge detector with extremely low threshold, and its excess of events is compatible with a region for WIMPs with SI interaction with mass around 10 GeV close to the DAMA region due to WIMP interaction with Na (with no channeling) [8, 15]. More data in CoGeNT, CDMS and XENON100 will clarify the situation with respect to this possible signal in the near future.

3 Dark matter hints from indirect searches

The satellite INTEGRAL, launched in 2002, has confirmed the emission of 511 keV photons from the center of the galaxy, a 30 year old signal first observed by balloon born γ-ray detectors. This is a clear signal of non-relativistic positrons annihilating with electrons almost at rest. The isotropy of the emitting region, which initially seamed spherical and centered on the center of the galaxy, was one of the main reasons to consider DM annihilation as the origin of the positrons. It was argued that any astrophysical origin should show in some correlation with the visible matter distribution in the region and none had been observed until 2008, when INTEGRAL revealed an asymmetry in the emitting region, which is more extended towards the galactic plane [17]. INTEGRAL also found evidence that a population of binary stars (called low mass X-ray binaries), known potential sources of positrons, corresponding in extent to the observed cloud of antimatter. These observations have decreased the motivation to consider DM annihilation or decay as the origin of the signal, although it is yet unclear if it can be explained satisfactorily solely with astrophysics. Special DM candidates were proposed to explain this signal, since the annihilations of usual WIMPs would produce positrons with too high energies. Positrons must be produced with no more than a few MeV of energy. Thus,

these DM candidates either have masses of a few MeV (they are called LDM, Light DM [18]) or have an excited state which decays to the fundamental state releasing an energy in the MeV range, although the particle is much heavier. These are called XDM, "eXciting" DM [19]).

XDM consists of a 500 GeV mass state χ with a excited state χ^* very close in energy. This is similar to the "Inelastic DM" proposed to explain DAMA/LIBRA, but the difference in mass must be larger, $\delta = m_{\chi^*} - m_\chi \sim$ MeV and not 100 keV, so that e^+e^- are produced at rest via de-excitation of the excited state: $\chi^* \to \chi e^+ e^-$. The excitation of the χ^* state is due to collisions, which fixes the particle mass, given the characteristic speed in the galaxy, $v \simeq 10^{-3}c$. Thus $\delta \simeq (1/2) m_\chi 10^{-6} \simeq 1$ MeV which works if $m_\chi \simeq 500$ GeV.

Positrons and antiprotons, which would be produced in equal numbers as electrons and protons, are an interesting potential signal of WIMP annihilation because there is not much antimatter in the Universe. Balloon born experiments detecting positrons have found since the 1980's a possible excess over secondary cosmic ray fluxes, the so-called "HEAT excess", which already in 1998 could be explained by WIMP annihilations with WIMP masses above 200 GeV and the annihilation-rate multiplied by a "boost factor" $B > 30$. PAMELA, a satellite carrying a magnetic spectrometer launched in 2006, reported in 2008 an excess in the positron fraction $e^+/(e^+ + e^-)$ in the 10 to 100 GeV energy range [20] compatible with the "HEAT excess". Shortly after, the ATIC collaboration announced a 6σ excess in the 300-800 GeV range in the (e^++e^-) flux, with a sharp cutoff at high energies (compatible with indicating the mass of annihilating WIMPs) which was later rejected by HESS and by Fermi. Fermi measured the (e^++e^-) spectrum from 20 GeV to 1 TeV with better accuracy than all preceding experiments and found a excess of its own [22] (without a sharp cutoff). The PAMELA data on the antiproton to proton ratio and antiproton flux [21] is instead compatible with secondary cosmic rays, so whatever produces positrons should not produce an excess of antiprotons.

More than 500 papers have already been written trying to explain the PAMELA data, either with astrophysical or particle sources. The e^+ and e^- come from less than 1 kpc, so they must be produced locally. Pulsars or other supernova remnants nearby can account for the data [23]. It has also been suggested that secondary cosmic rays, such as e^+, could be accelerated at the sources of primary cosmic rays (leading to an enhancement of all secondary over primary ratios) [24], an idea that will be confirmed or rejected soon (measuring ratios such as B/C). If the source is annihilating DM particles, only very tuned models survive all constraints. A simultaneous fit to the PAMELA, Fermi and HESS data requires the DM to have mass of TeV order, to annihilate mostly into leptons of the 2nd or 3rd generation, $\tau^+\tau^-$ or 4μ or 4τ (not into e^++e^- or W pairs, because this would generate a sharp edge in the spectrum) [25]. Thus, the DM must be "leptophilic" either because the DM carries lepton number, or because of kinematics. Moreover the annihilation rate must be larger than expected for thermal WIMPs by a boost factor $B \simeq$10 to 10^3.

Astrophysical enhancements, due to nearby regions of larger DM density in the halo of our galaxy, cannot be larger than a few (< 10), which is not enough. No boost factor at all is needed if WIMPs have a large annihilation cross section, both in the early Universe and in the dark galactic halo near Earth, which would produce a too small relic abundance for thermal WIMPs but could be fine if the pre-BBN cosmology is non-standard [26]. Another possibility is that the annihilation cross section is larger in the dark halo at present, when WIMPs are more non-relativistic than in the early Universe, but it had the value necessary for thermal WIMPs to get the right relic density at the moment of freeze-out. This could be achieved if the DM annihilation cross section has a narrow resonance just below threshold, which is sampled more by low velocity particles than high velocity ones (see e.g. [27]) or by a "Sommerfeld

enhancement" of the cross section. The latter is due to the modification of the wave function of low velocity particles due to attractive long distance forces. A classical analogy is that of particles approaching with speed v a star of radius R in the presence of gravity. Since the particles are deflected towards the star, the cross section $\sigma = \sigma_0(1+v^2_{escape}/v^2)$ is larger than the geometrical cross section $\sigma_0 = \pi R^2$, and for smaller velocities $v << v_{escape}$ the enhacement is larger [3]. This mechanism works for heavy almost degenerate neutralino-chargino interactions, for which an attractive Yukawa force comes from multiple t-channel W and Z exchange [28], or in the case the Yukawa force is due to the exchange of a light gauge or scalar boson. Besides all these requirements on the DM model, constraints imposed by the annihilation of the DM in the center of our galaxy are only compatible with galactic halo models that predict a relatively small amount of DM in that region (core models as opposed to cusped ones) [25]. I should mention that also decaying DM has been considered (see e.g.[25]). It must decay mostly into leptons of the 2nd or 3rd generation, have multi-TeV mass and a very long lifetime $\tau \sim 10^{26}$ s.

Let us now present "A Theory of DM" [3]. In this model WIMPs with mass 500 to 800 GeV have excited states with mass differences between 0.1 to 1 MeV and are charged under a broken hidden gauge symmetry G_{dark} with gauge bosons ϕ ("dark photons") lighter than 1GeV. The bosons ϕ mediate new attractive forces which produce the Sommerfeld enhancement and are "leptophilic" because they are so light that can only decay into e^+e^-, $\mu^+\mu^-$ or pions. This is a model made to explain simultaneously the DAMA annual modulation signal with "inelastic" DM (IDM), the INTEGRAL data with "eXciting" DM (XDM) and the PAMELA positron fraction excess, because the DM annihilates into a pair of ϕ, each of which decays afterwords, producing as final annihilation product mostly two $\mu^+\mu^-$ pairs (or pions). Besides, the model provides signatures for the LHC (which depend on the particular realization of the model) such as GeV-dark Higgses and gauge bosons which decay into visible particles and leptons, and also the excited WIMPs that decay producing many lepton jets with GeV invariant masses [4]).

4 Summary and outlook

DM searches are independent and complementary to collider searches in multiple ways and they are advancing fast. Lots of data lead to many hints, and the data driven recent burst of model building has been due to the difficulty in accommodating all recent hints. So far, no firm DM signature has been found but the many new models have opened our imagination and expectations for things to come. The physics of DM and the physics needed at the electroweak scale may be different. In any event, in most scenarios one can think of the LHC should find at least a hint of the new physics. Whatever the LHC finds will lead to a set of possible DM candidates and reject others. Besides, DM may have several components to be found in different ways. All possibilities are still open, hopefully not for long.

References

[1] E. Komatsu *et al.*, arXiv:1001.4538 [astro-ph.CO].

[2] G. Gelmini and P. Gondolo, *Phys. Rev.* D**74**, 023510 (2006); G. Gelmini *et al.* Phys. Rev. D**74**, 083514 (2006).

[3] N. Arkani-Hamed *et al.* Phys. Rev. D **79**, 015014 (2009) [arXiv:0810.0713 [hep-ph]].

[4] N. Arkani-Hamed and N. Weiner, JHEP **0812**, 104 (2008) [arXiv:0810.0714 [hep-ph]].

[5] See the contribution of Laura Baudis at this conference.

[6] R. Bernabei *et al.*, Eur. Phys. J. C **67**, 39 (2010) [arXiv:1002.1028 [astro-ph.GA]].

[7] D. Tucker-Smith and N. Weiner, Phys. Rev. D **64**, 043502 (2001) and Phys. Rev. D**72**, 063509 (2005); S. Chang *et al.* Phys. Rev. D**79**, 043513 (2009) .

[8] J. Kopp, T. Schwetz and J. Zupan, JCAP **1002**, 014 (2010) [arXiv:0912.4264 [hep-ph]]; S. Chang *et al.* arXiv:1004.0697 [hep-ph].

[9] G. Gelmini and P. Gondolo, arXiv:hep-ph/0405278; P. Gondolo and G. Gelmini, Phys. Rev. D**71**, 123520 (2005). [arXiv:hep-ph/0504010].

[10] C. Savage, P. Gondolo and K. Freese, Phys. Rev. D**70**, 123513 (2004).

[11] C. Savage, G. Gelmini, P. Gondolo and K. Freese, JCAP**0904**, 010 (2009)

[12] R. Bernabei *et al.*, Eur. Phys. J. C**53**, 205 (2008) [arXiv:0710.0288 [astro-ph]].

[13] N. Bozorgnia, G. Gelmini and P. Gondolo, arXiv:1006.3110 [astro-ph.CO].

[14] C. Savage, G. Gelmini, P. Gondolo and K. Freese, arXiv:1006.0972 [astro-ph.CO].

[15] E. Kuflik, A. Pierce and K. Zurek, Phys. Rev. D **81**, 111701 (2010); R. Essig *et al.* arXiv:1004.0691 [hep-ph]; T. Cohen *et al.* arXiv:1005.1655 [hep-ph].

[16] D. Hooper, J. I. Collar, J. Hall and D. McKinsey, arXiv:1007.1005 [hep-ph].

[17] G. Weidenspointner *et al.*, Nature **451**, 159 (2008).

[18] C. Boehm *et al.*, Phys. Rev. Lett.**92**, 101301(2004); D. Hooper and K. Zurek, Phys. Rev. D **77**, 087302(2008).

[19] D. P. Finkbeiner and N. Weiner, Phys. Rev. D **76**, 083519 (2007).

[20] O. Adriani *et al.* [PAMELA Collaboration], Nature **458**, 607 (2009) [arXiv:0810.4995 [astro-ph]] and Astropart. Phys. **34**, 1 (2010) [arXiv:1001.3522 [astro-ph.HE]].

[21] O. Adriani *et al.*, Phys. Rev. Lett. **102**, 051101 (2009) and arXiv:1007.0821 [astro-ph.HE].

[22] A. A. Abdo *et al.* [The Fermi LAT Collaboration], Phys. Rev. Lett. **102**, 181101 (2009).

[23] F. A. Aharonian, A. M. Atoyan and H. J. Volk, Astron. Astrophys. **294** (1995) L41; D. Grasso *et al.* [FERMI-LAT Collaboration], Astropart. Phys. **32**, 140 (2009).

[24] P. Blasi, Phys. Rev. Lett. **103**, 051104 (2009); P. Blasi and P. Serpico, Phys. Rev. Lett. **103**, 081103 (2009); P. Mertsch and S. Sarkar, Phys. Rev. Lett. **103**, 081104 (2009);

[25] P. Meade *et al.* Nucl. Phys. B **831**, 178 (2010) [arXiv:0905.0480 [hep-ph]].

[26] G. Kane, R. Lu and S. Watson, Phys. Lett. B **681**, 151 (2009).

[27] M. Ibe, H. Murayama and T. T. Yanagida, Phys. Rev. D **79**, 095009 (2009).

[28] J. Hisano, S. Matsumoto and M. M. Nojiri, Phys. Rev. Lett. **92**, 031303 (2004).

Higgs and electroweak symmetry breaking

J.Espinosa[1], *C. Grojean*[2,3] *and M.Mühlleitner*[4*]

[1]ICREA, Instituciò Catalana de Recerca i Estudis Avançats, Barcelona, Spain
at IFAE, Universitat Autònoma de Barcelona, 08193 Bellaterra, Barcelona, Spain
[2]CERN, Physics Department, Theory Unit, CH–1211 Geneva 23, Switzerland
[3]Institut de Physique Théorique, CEA Saclay, F–91191 Gif-sur-Yvette, France
[4]Institute for Theoretical Physics (ITP), KIT, D-76128 Karlsruhe, Germany

DOI: http://dx.doi.org/10.3204/DESY-PROC-2010-01/198

One of the major LHC goals is the Higgs boson search. Once found measurements will be performed to establish experimentally the Higgs mechanism. In the following the composite Higgs model will be presented as an alternative to the elementary Higgs. Modifications in Higgs production and decay and implications for Higgs discovery will be discussed.

1 Introduction

In the Standard Model (SM) unitarity in the scattering of longitudinal W, Z bosons is assured by an elementary Higgs boson. The electroweak precision observables and the absence of large flavor-changing neutral currents strongly constrain departures from this minimal Higgs mechanism and support the idea of a light Higgs boson emerging as a pseudo-Goldstone boson from a strongly-coupled sector, the Strongly Interacting Light Higgs scenario [1, 2].

The effective Lagrangian in [1] should be seen as an expansion in $\xi = (v/f)^2$ where $v = 1/\sqrt{\sqrt{2}G_F} \approx 246$ GeV and f is the typical scale of the Goldstone bosons of the strong sector. It can therefore be used in the vicinity of the SM limit ($\xi \to 0$), whereas the technicolor limit ($\xi \to 1$) requires a resummation of the full series in ξ. Explicit models provide concrete examples of such a resummation. Here we refer to the Holographic Higgs models of Refs. [3, 4, 5], which are based on a five-dimensional theory in Anti-de-Sitter (AdS) space-time. The bulk gauge symmetry $SO(5) \times U(1)_X \times SU(3)$ is broken down to the SM gauge group on the UV boundary and to $SO(4) \times U(1)_X \times SU(3)$ on the IR. In the unitary gauge this leads to the following Higgs couplings to the gauge fields ($V = W, Z$) in terms of the parameter ξ

$$g_{hVV} = g_{hVV}^{SM} \sqrt{1-\xi}\,, \qquad g_{hhVV} = g_{hhVV}^{SM} (1-2\xi)\,. \tag{1}$$

The couplings to fermions depend on their embedding into representations of the bulk symmetry. In the MCHM4 model [4] the fermions transform as spinorial representations, in the MCHM5 model [5] as fundamental representations of $SO(5)$ and the Higgs fermion interactions read

$$\text{MCHM4:} \quad g_{hff} = g_{hff}^{SM} \sqrt{1-\xi} \qquad \text{MCHM5:} \quad g_{hff} = g_{hff}^{SM} \frac{1-2\xi}{\sqrt{1-\xi}}\,. \tag{2}$$

*Speaker

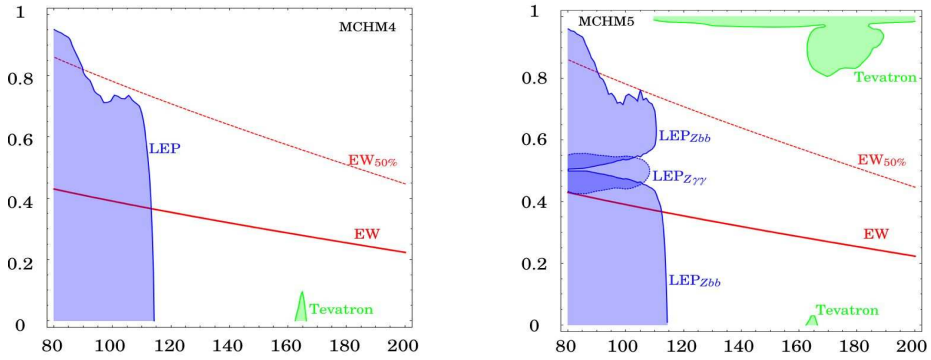

Figure 1: Limits from Higgs searches at LEP (blue/dark gray) and Tevatron (green/light gray) in the plane (M_H, ξ) for MCHM4 (left), MCHM5 (right). The red continuous line delineates the region favoured at 99% CL by EW precision data (with a cutoff scale of 2.5 TeV), the region below the red dashed line survives for an additional 50% cancellation of the oblique parameters.

2 Constraints from LEP, Tevatron and EW precision data

The (M_H, ξ) parameter region is constrained from Higgs searches at LEP and Tevatron. The excluded regions are shown in Fig.1. In both models the SM Higgs mass LEP limit $M_H \gtrsim 114.4$ GeV is lowered, since at LEP the most relevant search channel is Higgs-strahlung with Higgs decay into $b\bar{b}$ and in both models this production is suppressed compared to the SM. As in MCHM5 at $\xi = 0.5$ the Higgs fermion coupling vanishes, constraints are then set by Higgs-strahlung production with decay into $\gamma\gamma$. At Tevatron, low ξ is excluded by the Higgs decay into a W pair for $M_H \approx 160$ GeV. The exclusion region quickly shrinks to 0, since the relevant Higgs-strahlung production is suppressed compared to the SM for non-zero ξ. In MCHM5, an additional region $M_H \sim 165 - 185$ GeV can be excluded for $\xi \gtrsim 0.8$ through $H \to WW$. Close to $\xi = 1$ the exclusion is set by $H \to \tau\tau$ decays. Further constraints arise from the electroweak precision data. In our set-up they are due to the incomplete cancellation between the Higgs and gauge boson contributions to S and T and low ξ values are preferred. The upper bound on ξ is relaxed by a factor of ~ 2 if one allows for a partial cancellation of the order of 50%.

3 Branching ratios and statistical significances

The partial widths in the composite Higgs models are obtained by rescaling the Higgs couplings involved in the decay. In the MCHM4 model all couplings are multiplied by $\sqrt{1-\xi}$ so that the branching ratios are the same as in the SM. In the MCHM5 model due to different Higgs couplings to gauge bosons and fermions, the branching ratios (BRs) are modified. Fig.2 shows the BRs in the SM and the MCHM5 for three values of $\xi = 0.2, 0.5, 0.8$ in the mass range favoured by composite Higgs models. For $\xi = 0.2$ the behaviour is almost the same as in the SM. The decays into $\gamma\gamma$ and $Z\gamma$ are slightly enhanced, a behaviour which culminates at $\xi = 0.5$. Here, due to the specific Higgs fermion coupling in MCHM5 the decays into fermions and fermion-loop mediated decays into gluons are closed and the BR into $\gamma\gamma$ dominates in the low Higgs mass region. At $\xi = 0.8$ the BRs into fermions dominate at low-Higgs mass and are

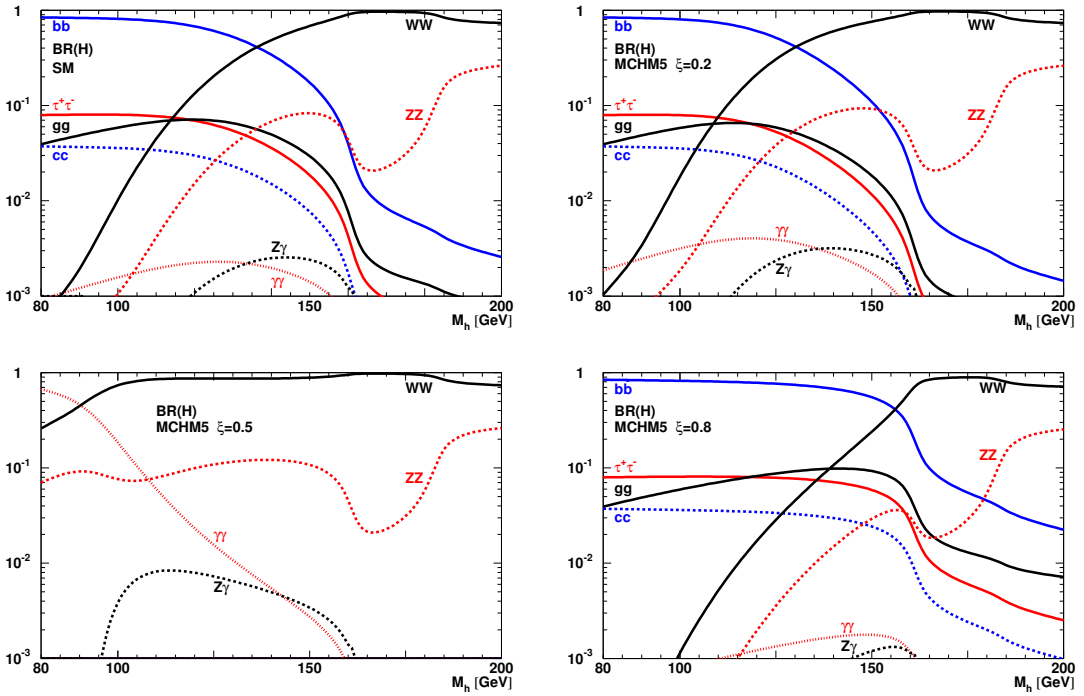

Figure 2: Higgs branching ratios as a function of the Higgs boson mass in the SM ($\xi = 0$, upper left) and MCHM5 with $\xi = 0.2$ (upper right), 0.5 (bottom left) and 0.8 (bottom right).

enhanced compared to the SM above the gauge boson threshold.

In order to study the Higgs discovery prospects, the statistical significances for different LHC search channels have been evaluated by referring to the CMS analyses [6]. The results are not significantly changed for the ATLAS analyses [7]. Assuming that only the signal but not the backgrounds rates are changed, since only Higgs couplings are affected, the significances can be obtained by applying a rescaling factor $\varkappa$ to the number of signal events. Referring to a specific search channel, it is given by taking into account the change in the production process p and in the subsequent decay into a final state X with respect to the SM, hence

$$\varkappa = \frac{\sigma_p \, BR(H \to X)}{\sigma_p^{SM} BR(H^{SM} \to X)} \, . \tag{3}$$

The number of signal events s is obtained from the SM events s^{SM} by $s = \varkappa \cdot s^{SM}$ where s^{SM} after application of all cuts is taken from the experimental analyses. With the signal events s and the background events after cuts, $b \equiv b^{SM}$, the significances in the composite Higgs model are calculated. For more details see Ref. [8]. In Figs.3 the SM significance and the MCHM5 significances for $\xi = 0.2, 0.5, 0.8$ are presented. For $\xi = 0.2$ the reduction in the production channels cannot be compensated by the enhancement in the BRs into $\gamma\gamma$ and massive gauge bosons, so that the significances are below the SM ones. This is even worse for $\xi = 0.5$ where the gluon fusion (and also $Ht\bar{t}$) production vanishes. Only for low Higgs masses the strong

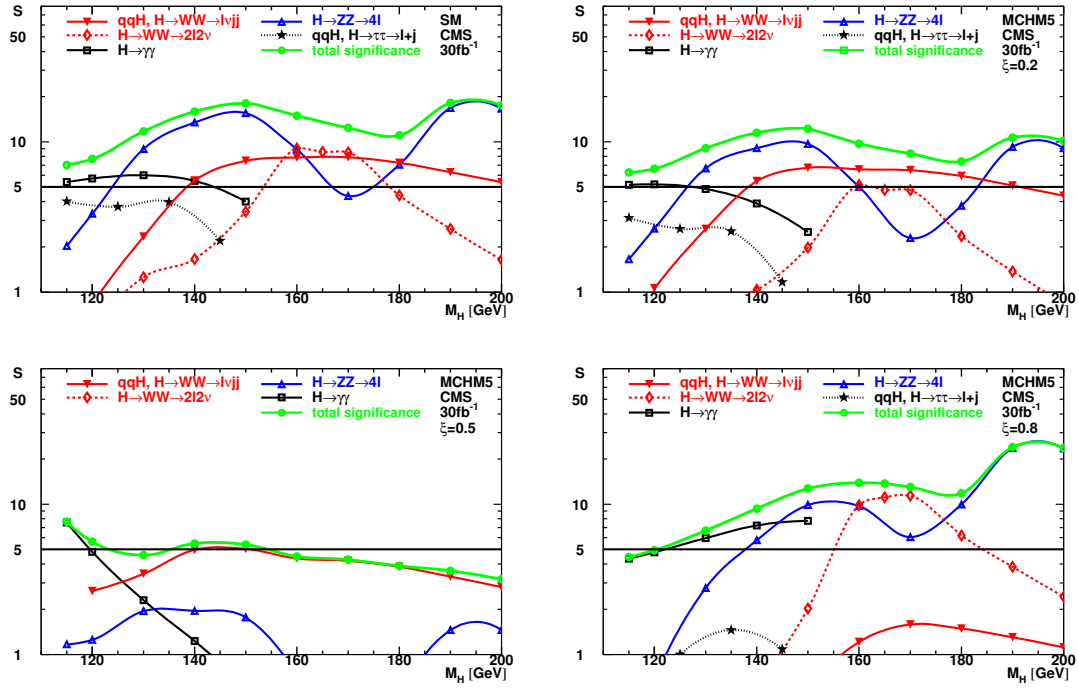

Figure 3: Significances in different channels as a function of the Higgs boson mass in the SM ($\xi = 0$) and for MCHM5 with $\xi = 0.2$, 0.5 and 0.8.

enhancement in the $\gamma\gamma$ BR can raise the significance above 5. For higher Higgs masses one has to rely on weak boson fusion with $H \to WW$ decay. For $\xi = 0.8$ the production is completely taken over by gluon fusion and leads to large significances in the massive gauge boson final states. Also $\gamma\gamma$ final states contribute for $M_H \gtrsim 120$ GeV.

References

[1] G. F. Giudice, C. Grojean, A. Pomarol and R. Rattazzi, JHEP **0706** (2007) 045 [arXiv:hep-ph/0703164].

[2] R. Contino, C. Grojean, M. Moretti, F. Piccinini and R. Rattazzi, JHEP **1005** (2010) 089 [arXiv:1002.1011 [hep-ph]]; S. Dimopoulos and J. Preskill, Nucl. Phys. B **199** (1982) 206; T. Banks, Nucl. Phys. B **243** (1984) 125; D. B. Kaplan and H. Georgi, Phys. Lett. B **136** (1984) 183; D. B. Kaplan, H. Georgi and S. Dimopoulos, Phys. Lett. B **136** (1984) 187; H. Georgi, D. B. Kaplan and P. Galison, Phys. Lett. B **143** (1984) 152; H. Georgi and D. B. Kaplan, Phys. Lett. B **145** (1984) 216; M. J. Dugan, H. Georgi and D. B. Kaplan, Nucl. Phys. B **254** (1985) 299.

[3] R. Contino, Y. Nomura and A. Pomarol, Nucl. Phys. B **671** (2003) 148 [arXiv:hep-ph/0306259].

[4] K. Agashe, R. Contino and A. Pomarol, Nucl. Phys. B **719** (2005) 165 [arXiv:hep-ph/0412089].

[5] R. Contino, L. Da Rold and A. Pomarol, Phys. Rev. D **75** (2007) 055014 [arXiv:hep-ph/0612048].

[6] G. L. Bayatian *et al.* [CMS Collaboration], J. Phys. G **34** (2007) 995.

[7] G. Aad *et al.* [The ATLAS Collaboration], arXiv:0901.0512 [hep-ex].

[8] J. R. Espinosa, C. Grojean and M. Muhlleitner, JHEP **1005** (2010) 065 [arXiv:1003.3251 [hep-ph]].

Prospect for Higgs searches in CMS with 1 fb^{-1} at 7 TeV and CMS performance validation with early data

Alberto Graziano on behalf of the CMS Collaboration

INFN & University of Turin, via Pietro Giuria 1, 10125 Turin, Italy

DOI: http://dx.doi.org/10.3204/DESY-PROC-2010-01/200

We overview the prospects for Higgs boson searches with a data sample of 1 fb^{-1} to be collected in pp-collisions at 7 TeV. We present sensitivity projections for SM-like decay modes $H \to WW \to 2\ell 2\nu$, $H \to ZZ \to 4\ell$, $H \to \gamma\gamma$ (including their combination), the MSSM-like signature $pp \to bb\Phi \to bb(\tau\tau)$ and we discuss a few other possible models/searches.

1 Introduction

The search for the Higgs boson is one of the main goals of the CMS experiment at the Large Hadron Collider. Limits on its mass have been set: LEP excluded the region $m_H < 114.4$ GeV at 95% C.L. and TeVatron recently did the same in the range $162 < m_H < 166$ GeV. Moreover, unitarity constraints require the Higgs mass to be lower than 1 TeV. The whole m_H range will therefore be explored at the LHC.

The discovery and exclusion sensitivities for Higgs searches with CMS had already been shown in a $\sqrt{s} = 14$ TeV, $L = 1 \div 30$ fb^{-1} scenario. The results presented here (see also [1]) are obtained by projecting those calculations to $\sqrt{s} = 7$ TeV, $L = 1$ fb^{-1}. Details on how this projection was performed are given.

2 Projections to $\sqrt{s} = 7$ TeV

Projections from 14 TeV to 7 TeV have been performed according to the following prescriptions.

The event yields for both the signal and the backgrounds have been rescaled by the ratio of the corresponding cross sections, $\frac{\sigma(7\ TeV)}{\sigma(14\ TeV)}$, and projected to an integrated luminosity of $L = 1$ fb^{-1}. No corrections have been applied to take into account the (up to $\sim 20\%$) higher acceptance of the detector at 7 TeV, due to the fact that particles are less forward-boosted at 7 TeV than at 14 TeV. The improvements in the detector simulation and in the reconstruction performances achieved after the 14 TeV analysis was published have not been considered either.

The systematic errors obtained from control samples have been rescaled by $1/\sqrt{N}$, where N is the number of events in the sample. Some other uncertainties, like the theoretical ones, have been left unchanged, whereas other ones have been inflated because of poorer statistics in the datasets.

The statistical analysis uses the re-evaluated event counts and uncertainties. The 95% C.L. exclusion studies have been carried out by applying the Modified Frequentist method [4], while the significances have been calculated with the Profile Likelihood method [5].

3 Projections for each search channel

3.1 Results for $H \to WW \to 2\ell 2\nu$

The signature of this channel is given by 2 isolated high-p_T leptons, along with missing E_T and the absence of jets in the central rapidity region. No Higgs mass peak can be looked for, because of the missing E_T, therefore one has to use counting experiments and the transverse mass M_T of the $2\ell 2\nu$ system.

The most important backgrounds for this channel are WW, Wt, $t\bar{t}$, WZ, ZZ and Drell-Yan processes. The WW background can be reduced by cutting on $\Delta\Phi_{\ell\ell}$, the angle between the 2 isolated leptons in the transverse plane. This angle tends to be larger for WW events than for signal ones. The Drell-Yan, WZ and ZZ backgrounds can be identified by checking if the invariant mass of the di-lepton pair is close to the Z mass peak. The $t\bar{t}$ background can be rejected by applying a 'central jet veto'.

The projection is derived using results published in [2]. Figure 1 shows the sensitivity for Higgs exclusion at 95% C.L. in this channel. The excluded m_H range is $150 < m_H < 185$ GeV. As shown in Fig. 2, a 5σ discovery is expected to be reached in the mass range $160 < m_H < 170$ GeV.

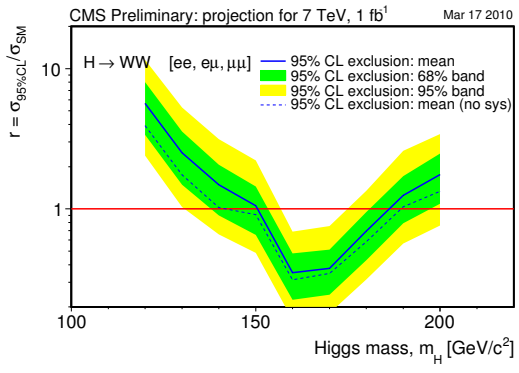

Figure 1: Exclusion plot for the $H \to WW \to 2\ell 2\nu$ channel, for $\sqrt{s} = 7\ TeV$ and $L = 1\ fb^{-1}$, assuming absence of signal.

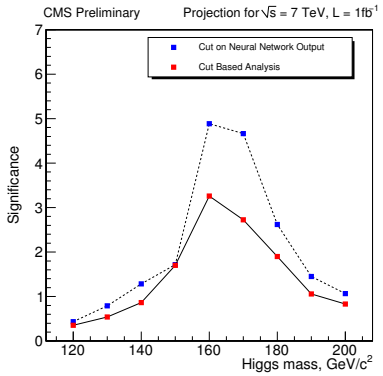

Figure 2: Expected significance for the $H \to WW \to 2\ell 2\nu$ channel as a function of m_H, for $\sqrt{s} = 7\ TeV$ and $L = 1\ fb^{-1}$.

3.2 Results for $H \to ZZ \to 4\ell$

This is the *'golden channel'* since its signature is very clear: two pairs of opposite-charge, same-flavour, high-p_T isolated leptons. Moreover, the invariant mass of the lepton pairs tends to be close to m_Z.

The main backgrounds are ZZ, $Zb\bar{b}$, $t\bar{t}$, W/Z+jets, QCD. The invariant mass $m(4\ell)$ in ZZ events does not peak around any value, therefore it is a good discriminant. The $Zb\bar{b}$ and $t\bar{t}$ backgrounds can be reduced by cutting on isolation variables and on the impact parameter significance of the leptons.

The projection is derived using results published in [3]. The plot in Fig. 3 shows that the SM Higgs exclusion is out of reach in the whole m_H range. However, in case a fourth generation of quarks exists, the Higgs boson could be excluded in the region $m_H \lesssim 420$ GeV.

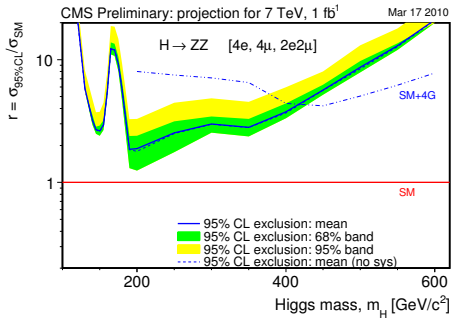

Figure 3: Exclusion plot for the $H \to ZZ \to 4\ell$ channel, for $\sqrt{s} = 7\ TeV$ and $L = 1\ fb^{-1}$.

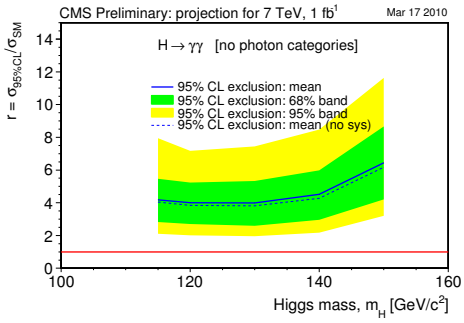

Figure 4: Exclusion plot for the $H \to \gamma\gamma$ channel, for $\sqrt{s} = 7\ TeV$ and $L = 1\ fb^{-1}$.

3.3 Results for $H \to \gamma\gamma$

The analyses in this channel require two isolated photons. The projection presented here is for a generic search for a narrow $\gamma\gamma$resonance, since nothing specific to the SM Higgs boson was used in this study. The large QCD background is estimated from sidebands.

In Fig. 4 one can see the m_H exclusion limits for this channel. The exclusion is not possible anywhere in the mass range, However, if the Higgs is *fermiophobic*, it can be ruled out in the region $m_{hf} < 110$ GeV.

3.4 Combination of the SM channels

By combining the results shown in the previous paragraphs 3.1, 3.2, 3.3 about SM Higgs, one gets the plot in Fig. 5. The expected exclusion mass range is $145 < m_H < 190$ GeV.

3.5 Results for $pp \to bb\Phi \to bb\tau^+\tau^-$

In this MSSM channel, isolated pairs of τ leptons are looked for, namely (τ_μ, τ_e), (τ_{had}, τ_e), (τ_{had}, τ_μ). The collinear approximation is applied to calculate $m(\tau\tau)$: the ν's are supposed to be collinear to the τ's. If missing E_T is there, one checks if a tagged b-jet is present and vetoes any other jets. The events are counted in a sliding $m(\tau\tau)$ window and the main backgrounds, which are $t\bar{t}$, $Zb\bar{b}$, $Zc\bar{c}$, are estimated in a data-driven way.

The plot in Fig. 6 shows the projected discovery and exclusion contours in the $(m_A,\ tan\beta)$ plane. At low m_A values, such as $m_A \sim 90$ GeV, the discovery is expected to be possible for $tan\beta > 20$ and the exclusion for $tan\beta \sim 15$.

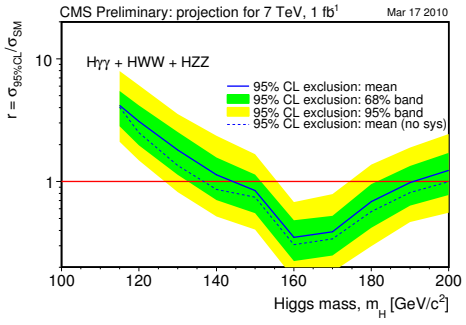

Figure 5: Expected exclusion limits for the combination of the channels, assuming absence of signal, for $\sqrt{s} = 7\ TeV$ and $L = 1\ fb^{-1}$.

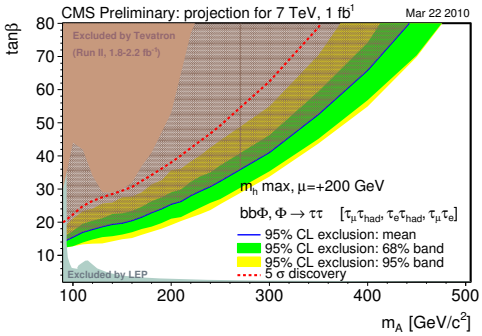

Figure 6: Expected exclusion limits for the $H \rightarrow \gamma\gamma$ channel, for $\sqrt{s} = 7\ TeV$ and $L = 1\ fb^{-1}$.

4 Conclusions

The prospects for Higgs searches with CMS have been presented in the $\sqrt{s} = 7$ TeV, $L = 1\ fb^{-1}$ scenario. A brief description of the analysis strategies in the different channels has been given and the expected reach for both exclusion and discovery has been outlined.

References

[1] The CMS Collaboration, CMS Note 2010-008

[2] The CMS Collaboration, *"Search Strategy for a Standard Model Higgs Boson Decaying to Two W Bosons in the Fully Leptonic Final State"*, CMS PAS-HIG-08-006.

[3] The CMS Collaboration, *"Search strategy for the Higgs boson in the $ZZ^{(*)}$ decay channel with the CMS experiment"*, CMS PAS-HIG-08-003.

[4] A. L. Read, "Modified frequentist analysis of search results (the CLs method)", CERN-OPEN-2000-205; also, J. Phys. G 28, 2693 (2002).

[5] e.g., Thomas Alan Severini, Likelihood methods in statistics (Oxford University Press, 2000).

BSM Higgs physics at the LHC in the forward proton mode

Sven Heinemeyer[1], *Valery A. Khoze*[2,3], *Misha G. Ryskin*[2,4], *Marek Tasevsky*[5], *Georg Weiglein*[6]

[1]Instituto de Física de Cantabria (CSIC-UC), Santander, Spain
[2]IPPP, Department of Physics, Durham University, Durham DH1 3LE, U.K.
[3]School of Physics & Astronomy, University of Manchester, Manchester M13 9PL, U.K.
[4]Petersburg Nuclear Physics Institute, Gatchina, St. Petersburg, 188300, Russia
[5]Institute of Physics, 18221 Prague 8, Czech Republic
[6]DESY, Notketraße 85, 22607 Hamburg, Germany

DOI: http://dx.doi.org/10.3204/DESY-PROC-2010-01/199

We review the prospects for central exclusive diffractive (CED) production of Higgs bosons in the SM with a fourth generation of fermions at the LHC using forward proton detectors installed at 220 m and 420 m distance around ATLAS and/or CMS. We discuss the determination of Higgs spin-parity and coupling structures at the LHC and show that the forward proton mode would provide a crucial information on the $\mathcal{CP}$ properties of the Higgs bosons.

1 Introduction

In the recent years there has been a growing interest in the possibility to complement the standard LHC searches for a Higgs boson by the options offered by forward and diffraction physics. These assume the installation of near-beam proton detectors in the LHC tunnel installed at 220 m and 420 m around ATLAS and/or CMS, see Refs. [1–6] and references therein. The combined detection of the centrally produced system and both outgoing protons can provide valuable information on the Higgs sector of MSSM and other popular BSM scenarios [3, 7–10]. Another simple example of physics beyond the SM is a model which extends the SM by a fourth generation of heavy fermions (SM4), see, for instance, [11–13]. Here it is assumed that the masses of the 4th generation quarks are (much) heavier than the mass of the top-quark. In this case, the effective coupling of the Higgs boson to two gluons is three times larger than in the SM, and all branching ratios change correspondingly.

The central exclusive diffractive (CED) processes are of the form

$$pp \to p \oplus H \oplus p \ , \tag{1}$$

where the $\oplus$ signs denote large rapidity gaps on either side of the centrally produced state. However, proving that a detected new state is, indeed, a Higgs boson will be far from trivial. In particular, it will be of great importance to determine the spin and $\mathcal{CP}$ properties of a new state and to measure precisely its mass, width and couplings.

Following [8] we consider four luminosity scenarios: "60 fb^{-1}" and "600 fb^{-1}" refer to running at low and high instantaneous luminosity, respectively, using conservative assumptions

for the signal rates and the experimental sensitivities; possible improvements of both theory and experiment could allow for the scenarios where the event rates are higher by a factor of 2, denoted as "60 fb^{-1} eff×2" and "600 fb^{-1} eff×2".

2 The Higgs boson in the SM4

A simple example of physics beyond the SM is a model, "SM4", which extends the SM by a fourth generation of heavy fermions, see, for instance, Refs. [11, 12, 14]. In particular, the masses of the 4th generation quarks are assumed to be (much) heavier than the mass of the top-quark (whereas the masses of the 4th generation leptons, which do not play a role here, are less restricted). In this case, the effective coupling of the Higgs boson to two gluons is three times larger than in the SM. No other coupling, relevant to LEP and Tevatron searches, changes significantly. Essentially, only the partial decay width $\Gamma(H \to gg)$ changes by a factor of 9 and, with it, the total Higgs width and therefore all the decay branching ratios, see for instance Ref. [13, 15]. The new total decay width and the relevant decay branching ratios can be evaluated as,

$$\Gamma_{\rm SM}(H \to gg) = {\rm BR}_{\rm SM}(H \to gg)\, \Gamma^{\rm SM}_{\rm tot}(H)\,, \tag{2}$$

$$\Gamma_{\rm SM4}(H \to gg) = 9\, \Gamma_{\rm SM}(H \to gg)\,, \tag{3}$$

$$\Gamma^{\rm SM4}_{\rm tot}(H) = \Gamma^{\rm SM}_{\rm tot}(H) - \Gamma_{\rm SM}(H \to gg) + \Gamma_{\rm SM4}(H \to gg)\,. \tag{4}$$

The Higgs boson searches at LEP [16, 17] have been re-interpreted with `HiggsBounds` [18] in the SM4. The bound on the SM Higgs boson at LEP of $M_{H^{\rm SM}} \geq 114.4$ GeV at the 95% C.L. is modified to $M_{H^{\rm SM4}} \geq 112$ GeV. On the other hand Higgs boson searches in the SM4 at the Tevatron [19] have been performed. The range 130 GeV $\lesssim M_{H^{\rm SM4}} \lesssim$ 210 GeV is found to be excluded. Combining the two analyses leaves us with a window of allowed Higgs masses in the SM4 of 112 GeV $\lesssim M_{H^{\rm SM4}} \lesssim$ 130 GeV.

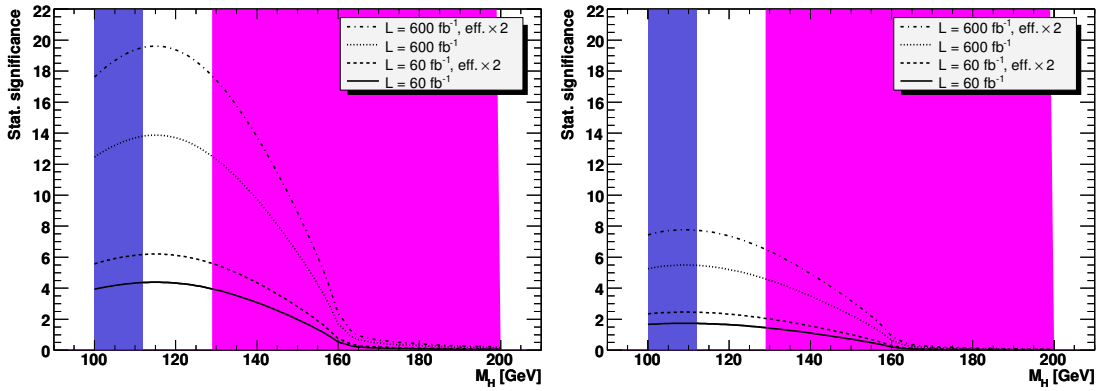

Figure 1: Significances reachable in CED Higgs production in the SM4 in the $H \to b\bar{b}$ (left plot) and $H \to \tau^+\tau^-$ (right plot) channel for effective luminosities of "60 fb^{-1}", "60 fb^{-1} eff×2", "600 fb^{-1}" and "600 fb^{-1} eff×2". The regions excluded by LEP appear as blue/light grey for low values of $M_{H^{\rm SM4}}$ and excluded by the Tevatron as red/dark grey for larger values of $M_{H^{\rm SM4}}$.

We have evaluated the significances that can be obtained in the channels $H \to b\bar{b}$ and $H \to \tau^+\tau^-$. The results are shown in Fig. 1 as a function of $M_{H^{\rm SM4}}$ for the four luminosity scenarios. The regions excluded by LEP appear as blue/light grey for low values of $M_{H^{\rm SM4}}$ and regions excluded by the Tevatron appear as red/dark grey for larger values of $M_{H^{\rm SM4}}$. The $b\bar{b}$ channel (left plot) shows that even at rather low luminosity the remaining window of 112 GeV $\lesssim M_{H^{\rm SM4}} \lesssim$ 130 GeV can be covered by CED Higgs production. Due to the smallness of BR($H^{\rm SM4} \to b\bar{b}$) at $M_{H^{\rm SM4}} \gtrsim 160$ GeV, however, the CED channel becomes irrelevant for the still allowed high values of $M_{H^{\rm SM4}}$, and we do not extend our analysis beyond $M_{H^{\rm SM4}} \leq 200$ GeV. The $\tau^+\tau^-$ channel (right plot) has not enough sensitivity at low luminosity, but might become feasible at high LHC luminosity. At masses $M_{H^{\rm SM4}} \gtrsim 220$ GeV it might be possible to exploit the decay $H \to WW, ZZ$, but no detailed analysis has been performed up to now.

3 Coupling structure and spin-parity determination

The determination of the spin and the $\mathcal{CP}$ properties of Higgs bosons using the standard methods rely to a large extent on the coupling of a relatively heavy SM-like Higgs to two gauge bosons. The first channel that should be mentioned here is $H \to ZZ \to 4l$. This channel provides detailed information about spin and $\mathcal{CP}$-properties if it is open [20]. Within a SM-like set-up it was analyzed how the tensor structure of the coupling of the Higgs boson to weak gauge bosons can be determined at the LHC [21–23]. One study for $M_{H^{\rm SM}} = 160$ GeV was based on Higgs production in weak vector boson fusion with the subsequent decay to SM gauge bosons. It was shown that the discrimination between the two extreme scenarios of a pure $\mathcal{CP}$-even (as in the SM) and a pure $\mathcal{CP}$-odd tensor structure is possible at a level of 4.5 to 5.3 σ using about 10 fb^{-1}. A discriminating power of two standard deviations at $M_{H^{\rm SM}} = 120$ GeV in the tau lepton decay mode requires an integrated luminosity of 30 fb^{-1} [23].

For $M_H \approx M_A \gtrsim 2M_W$ the lightest MSSM Higgs boson couples to gauge bosons with about SM strength, but its mass is bounded from above by $M_h \lesssim 135$ GeV [24], i.e. the light Higgs is in a mass range where the decay to $WW^{(*)}$ or $ZZ^{(*)}$ is difficult to exploit. On the other hand, the heavy MSSM Higgs bosons, H and A, decouple from the gauge bosons. Consequently, the analysis for $M_{H^{\rm SM}} = 160$ GeV cannot be taken over to the MSSM. This shows the importance of channels to determine spin and $\mathcal{CP}$-properties of the Higgs bosons without relying on (tree-level) couplings of the Higgs bosons to gauge bosons. CED Higgs production can yield crucial information in this context [2, 7, 8].

The $M_{H^{\rm SM}} = 120$ GeV analysis, on the other hand, can in principle be applied to the SUSY case. However, in this case the coupling of the SUSY Higgs bosons to tau leptons does not exhibit a (sufficiently) strong enhancement as compared to the SM case. Consequently, no improvement over the 2σ effect within the SM can be expected. The same would be true in any other model of new physics with a light SM-like Higgs and heavy Higgses that decouple from the gauge bosons.

The CED production channels may provide crucial information on the $\mathcal{CP}$ properties of Higgs-like states detected at the LHC, for instance via the J_z selection rule [25]. Thanks to this selection rule in the CED case we already know that the observed new object has even parity ($\mathcal{P} = +$), and the projection of its spin is $J_z = 0$. This knowledge will greatly simplify the determination of the detected new state.

As discussed in [7,8] it will be challenging to identify a $\mathcal{CP}$-odd Higgs boson, for instance the

A boson of the MSSM, in the CED processes. The strong suppression, caused by the P-even selection rule, effectively filters out its production. However, in the semi-inclusive diffractive reactions the pseudoscalar production is much less suppressed. As shown in a recent study [5] there are certain advantages of looking for the $\mathcal{CP}$-odd Higgs particle in the semi-inclusive process $pp \to p + gAg + p$ with two tagged forward protons and two large rapidity gaps. The amplitude of $\mathcal{CP}$-odd A boson production can be of the same order as the $\mathcal{CP}$-even boson amplitude if events with relatively hard gluons, whose energy is comparable with the energy of the whole gAg system, are selected.

4 Acknowledgments

Work supported in part by the European Community's Marie-Curie Research Training Network under contract MRTN-CT-2006-035505 'Tools and Precision Calculations for Physics Discoveries at Colliders' (HEPTOOLS).

References

[1] M. Albrow and A. Rostovtsev, arXiv:hep-ph/0009336.

[2] V.A. Khoze, A.D. Martin and M. Ryskin, *Eur. Phys. J.* **C 23** (2002) 311.

[3] M. Albrow, T. Coughlin and J. Forshaw, arXiv:1006.1289 [hep-ph].

[4] A. De Roeck, V.A. Khoze, A. Martin, R. Orava and M. Ryskin, *Eur. Phys. J.* **C 25** (2002) 391.

[5] V. A. Khoze, A. Martin, M. Ryskin and A. Shuvaev, *Eur. Phys. J.* **C 68** (2010) 125.

[6] M. Albrow et al. [FP420 R&D Collaboration], *JINST* **4** (2009) T10001.

[7] A. Kaidalov, V.A. Khoze, A.D. Martin and M. Ryskin, *Eur. Phys. J.* **C 33** (2004) 261.

[8] S. Heinemeyer, V. A. Khoze, M. G. Ryskin, W. J. Stirling, M. Tasevsky and G. Weiglein, *Eur. Phys. J.* **C 53** (2008) 231.

[9] B. Cox, F. Loebinger and A. Pilkington, *JHEP* **0710** (2007) 090.

[10] M. Chaichian, P. Hoyer, K. Huitu, V. A. Khoze and A. Pilkington, *JHEP* **0905** (2009) 011.

[11] P. Frampton, P. Hung and M. Sher, *Phys. Rept.* **330** (2000) 263.

[12] B. Holdom et al., *PMC Phys.* **A 3** (2009) 4 [arXiv:0904.4698 [hep-ph]].

[13] G. Kribs, T. Plehn, M. Spannowsky and T. Tait, *Phys. Rev.* **D 76** (2007) 075016.

[14] J. Erler and P. Langacker, *Phys. Rev. Lett.* **105** (2010) 031801.

[15] C. Anastasiou, R. Boughezal and E. Furlan, *JHEP* **1006** (2010) 101.

[16] G. Abbiendi et al. [ALEPH, DELPHI, L3, OPAL Collaborations and LEP Working Group for Higgs boson searches], *Phys. Lett.* **B 565** (2003) 61.

[17] S. Schael et al. [ALEPH, DELPHI, L3, OPAL Collaborations and LEP Working Group for Higgs boson searches], *Eur. Phys. J.* **C 47** (2006) 547.

[18] P. Bechtle, O. Brein, S. Heinemeyer, G. Weiglein and K. Williams, *Comput. Phys. Commun.* **181** (2010) 138; arXiv:0909.4664 [hep-ph]; see: `www.ippp.dur.ac.uk/HiggsBounds` .

[19] TEVNPH Working Group Collaboration for the CDF Collaboration and D0 Collaboration, CDF note 10101, DØ note 6039.

[20] V. Buescher and K. Jakobs, *Int. J. Mod. Phys.* **A 20** (2005) 2523.

[21] T. Plehn, D. Rainwater and D. Zeppenfeld, *Phys. Rev. Lett.* **88** (2002) 051801.

[22] V. Hankele, G. Klamke, D. Zeppenfeld and T. Figy, *Phys. Rev.* **D 74** (2006) 095001.

[23] C. Ruwiedel, N. Wermes and M. Schumacher, *Eur. Phys. J.* **C 51** (2007) 385.

[24] G. Degrassi, S. Heinemeyer, W. Hollik, P. Slavich and G. Weiglein, *Eur. Phys. J.* **C 28** (2003) 133.

[25] V.A. Khoze, A. Martin and M. Ryskin, *Eur. Phys. J.* **C 19** (2001) 477 [Erratum-ibid. **C 20** (2001) 599].

Hidden Higgs Scenarios: new constraints and prospects at the LHC

Radovan Dermíšek

Department of Physics, Indiana University, Bloomington, IN 47405, USA

DOI: http://dx.doi.org/10.3204/DESY-PROC-2010-01/201

We review the motivation for hidden Higgs scenarios and discuss the light CP odd Higgs scenario in the NMSSM as an example. We summarize experimental constraints including recent limits from BaBar and Aleph. The main part of the talk is the discussion of dominant decay modes of the standard model like Higgs boson, and related decay modes of the charged Higgs and heavy CP even Higgs bosons, in these scenarios with the focus on signatures and prospects for the LHC. Examples include the direct production of a light CP odd Higgs boson, and a light charged Higgs boson in top quark decays.

1 Motivation for non-standard Higgs decays

One of the most important questions in particle physics is: Where is the Higgs boson? The LEP exclusion limits, $m_h > 114$ GeV, constraints from precision electroweak data, $m_h < 157$ GeV [1], and recently also the Tevatron limits, leave a window of about 40 GeV for the standard model (SM) Higgs boson. This 40 GeV window is very interesting and there are several suggestive hints or coincidences related to it. First of all, this window overlaps with the range of Higgs masses in which the standard model can be a consistent theory all the way to the grand unification scale or the Planck scale, $m_h \simeq 125 - 175$ GeV. Another interesting coincidence is that this window also overlaps with the range of Higgs masses predicted in the minimal supersymmetric model (MSSM), $m_h \lesssim 135$ GeV. Hence, it is expected that the Higgs boson is somewhere in this window and most of the effort is focused on discovery strategies related to this possibility.

However there are also several compelling hints that the SM-like Higgs boson is below the LEP exclusion limits. First of all, electroweak symmetry breaking (EWSB) in simple supersymmetric (SUSY) extensions of the standard model, with superpartners near the electroweak (EW) scale, generically predicts the Higgs boson not heavier than about 100 GeV. Non-observation of the Higgs boson at LEP resulted in the "fine-tuning" problem in these models [2]. Second of all, the best fit to precision electroweak data is achieved for the Higgs mass of 87 GeV [1]. The third hint comes from the LEP data: the largest excess of Higgs like events at LEP corresponds to the Higgs mass of 98 GeV. It is an interesting coincidence that natural EWSB in SUSY models, precision EW data, and the largest excess of Higgs like events point to the same region. This supports the idea that the Higgs boson is light, somewhere near 100 GeV, and we missed it at LEP. How can this be?

The basic idea is very simple: if the SM-like Higgs boson decays in a different way than the Higgs boson in the standard model then the usual experimental limits do not apply. Such a

Higgs can be light, as predicted from SUSY, gives better agreement with precision electroweak data, and can even explain the largest excess of Higgs like events at LEP [3, 4, 5].

In theories beyond the SM the Higgs sector is usually more complicated and there are typically many other Higgses in addition to the SM-like Higgs boson. For example, there are five Higgs bosons in the MSSM: light and heavy CP even Higgses, h and H, the CP odd Higgs, A, and a pair of charged Higgs bosons, $H^{\pm}$; seven in the next-to-minimal supersymmetric model (NMSSM), which contains an additional singlet field: three CP even Higgs bosons, $h_{1,2,3}$, two CP odd Higgs bosons, $a_{1,2}$, and a pair of charged Higgs bosons; and there are many simple models with even more complicated Higgs sectors. Usually we explore a parameter space in which the extra Higgses are somewhat heavy – the so called decoupling limit.

The decoupling limit is not the only possibility. One of the extra Higgses can be light, for example, the singlet CP odd Higgs in the NMSSM. If it is sufficiently light, the SM-like Higgs boson can (and typically would) dominantly decay into a pair of CP odd Higgses and eventually, depending on the mass of the CP odd Higgs boson, into **four** b quarks, **four** τ leptons, **four** c quarks, **four** μ leptons, **four** electrons, **four** light quarks, or gluons [3]. Limits on these 4-body final states are weaker than limits on the SM Higgs boson (decaying into $b\bar{b}$) and currently 4τ leptons, c quarks, and light quarks or gluons final states allow the SM-like Higgs boson at ~ 100 GeV or even lighter [6, 7], as is predicted from the best theoretically motivated region of the parameter space in supersymmetric theories, and it also gives much better agreement with precision electroweak data. In addition, the subleading decay mode of the Higgs boson, $h \to b\bar{b}$, with branching ratio of $\sim 10\%$ can completely explain the largest excess (2.3σ) of Higgs-like events at LEP in the $b\bar{b}$ final state (for a reconstructed mass $M_{b\bar{b}} \sim 98$ GeV) [4].

Another, perhaps even more interesting variation of the above NMSSM scenario is the scenario with a **doublet-like** CP odd Higgs below the $b\bar{b}$ threshold. For small $\tan\beta$, $\tan\beta \lesssim 2.5$, this scenario is the least constrained (and only marginally ruled out) in the MSSM, and thus easily viable in simple extensions of the MSSM [8, 9, 10, 11]. Surprisingly, the prediction from this region is that all the Higgses resulting from two Higgs doublets: h, H, A and $H^{\pm}$ could have been produced already at LEP or the Tevatron, but would have escaped detection because they decay in modes that have not been searched for or the experiments are not sensitive to. The heavy CP even and the CP odd Higgses could have been produced at LEP in $e^+e^- \to HA$ but they would avoid detection because the dominant decay mode of H, $H \to ZA$, has not been searched for. The charged Higgs is also very little constrained although it could have been pair produced at LEP or appeared in decays of top quarks produced at the Tevatron. The dominant decay mode of the charged Higgs in this scenario is $H^{\pm} \to W^{\pm}A$ with $A \to \tau^+\tau^-$ or $A \to c\bar{c}$. In addition, the charged Higgs with properties emerging in this scenario and the mass close to the mass of the W boson could explain the 2.8σ deviation from lepton universality in W decays measured at LEP [12] as pointed out in Ref. [13].

The main idea is simple, and it can be realized in a variety of other models. For example, in specific little Higgs models the SM-like Higgs boson can dominantly decay into four c quarks [14] or four gluons [15]. Four body final states of the Higgs boson can also occur in composite Higgs models [16], and models for dark matter [17] among others. For a review of other scenarios and references, see Ref. [6].

The situation can be even more complicated if there are several lighter Higgses. In this case the SM-like Higgs boson can cascade decay into the lightest one, and eventually, depending on the mass of the lightest Higgs boson, the SM-like Higgs would decay into a large number of light jets, or a large number of muons, or a large number of electrons, or large number of soft photons [18, 19, 2]. Such events would be quite spectacular. Some of these signatures were

recently studied in Ref. [20]. An additional level of complexity arises when more Higgs boson share the coupling to the Z boson and there is not a single SM-like Higgs boson, see *e.g.* [21].

The simplest models allowing the SM-like Higgs boson at ~ 100 GeV are still those with 4-body decay modes. The NMSSM scenario with $h \to 4\tau$ has been recently studied and searched for at a variety of experiments. In the rest of this talk we will focus on this scenario.

2 Experimental searches and constraints

The first constraints on these scenarios came from CLEO [22]. The light CP odd Higgs can be produced in Upsilon decays, $\Upsilon \to A\gamma$, and the predicted branching ratio from the NMSSM model typically varies between $few \times 10^{-4}$ for the CP odd Higgs mass close to 2τ threshold, and 10^{-7} for the CP odd Higgs mass close to the Upsilon mass [23]. At present, the strongest constraints come from BaBar [24, 25] that sets limits $B(\Upsilon \to A\gamma) \lesssim 10^{-5}$ (slightly varying around this value for different masses of the CP odd Higgs boson). In order to satisfy these limits it is typically required that $m_A \gtrsim 8$ GeV for $\tan\beta > 3$. For smaller $\tan\beta$ these limits become weaker as $A \to c\bar{c}$ channel becomes more important. More details about the impact of these searches on the NMSSM parameter space can be found in Ref. [7].

Searches for $h \to aa$ were performed and are in progress at the Tevatron [26, 27]. These searches are not sensitive yet to the SM-like Higgs boson at 100 GeV. Nevertheless it is interesting to note that it is advantageous to search for a subleading decay mode of one of the CP odd Higgs bosons, $a \to \mu^+\mu^-$, as suggested in Ref. [28]. The rate for $h \to aa \to 2\tau 2\mu$ is suppressed by a factor of $\sim m_\mu^2/m_\tau^2$ compared to $h \to aa \to 4\tau$, but these events are much cleaner and one can reconstruct the mass of the CP odd Higgs boson. This search mode is very promising at the LHC where one expects about 500 events in 1 fb^{-1} of data (for 14 TeV center of mass energy) [28].

The most important constraints on this scenario come from the recent search at Aleph [29]. Naively this search rules out the SM-like Higgs that decays into four τ leptons up to 107 GeV. Note however, that this search places limits on

$$\xi^2 = \frac{\sigma(e^+e^- \to Zh)}{\sigma(e^+e^- \to Zh_{SM})} \times B(h \to aa) \times B(a \to \tau^+\tau^-)^2,$$

and thus it is very sensitive to $B(a \to \tau^+\tau^-)$, which in the NMSSM is never equal (or even close) to 100%. For large $\tan\beta$, depending on the mass of the CP odd Higgs boson, $B(a \to \tau^+\tau^-)$ is between 0.9 and 0.7 because of the sizable branching ratio of $a \to gg$. In addition, for smaller $\tan\beta$ a new decay mode, $a \to c\bar{c}$, becomes important. Folding in realistic branching ratios of $a \to \tau^+\tau^-$ one finds that Aleph limits allow the SM-like Higgs boson at 100 GeV (or slightly lighter) for any $\tan\beta > 3$ only when $m_a \gtrsim 9.5$ GeV, and generically for $\tan\beta < 2$ [7].

3 Prospects at the LHC

Recently we have been working on new ways to search for these scenarios. One question was whether we can directly observe the light CP odd Higgs (without relying on producing heavier Higgses that decay into the CP odd Higgs). The direct production cross section of the light CP odd Higgs boson in the gluon fusion channel is, depending on the mass of the CP odd Higgs boson and $\tan\beta$, between 1 and 100 nb at the Tevatron, and between 10 and 1000 nb at

the LHC [30]. In spite of the large production cross section, picking up the signal on a huge background is a serious problem. If one looks for the dominant decay mode, $a \to \tau^+\tau^-$, then it is basically hopeless, however searching for the subleading decay mode, $a \to \mu^+\mu^-$, is actually very promising. We still have to deal with huge background from Drell-Yan production of μ-pairs, and semileptonic b and c decays. Nevertheless, based on existing analyses we showed that current data sets would allow CDF and D0 to improve on limits from Babar, especially for masses of the CP odd Higgs boson close to the mass of the Upsilon [30]. At the LHC this is a very promising search mode and already the first fb^{-1} of data might provide an evidence for, or the discovery of the light CP odd Higgs. More details, and predictions for the integrated luminosity needed for the discovery as a function of the mass and couplings of the light CP odd Higgs boson can be found in Ref. [30].

Looking for subleading decay modes of the light CP odd Higgs might be also advantageous in searches for the charged Higgs. If the CP odd Higgs boson has a significant doublet component than the charged Higgs is generically light, typically lighter than the top quark. Depending on the mass of the charged Higgs and $\tan\beta$ the $B(t \to H^+b)$ can go up to 40% for $\tan\beta = 1$ and $m_{H^\pm} = 80$ GeV dropping very fast with increasing $\tan\beta$ and increasing the mass of the charged Higgs. The dominant decay mode of the charged Higgs is $H^+ \to W^+A$ and it was not previously searched for (till recently). The CDF recently performed the search and set the upper limit on $B(t \to H^+b) \times B(H^+ \to W^+A) \times B(A \to \tau^+\tau^-)$ to about 10% [31] constraining only a small region of the parameter space.

The search for the charged Higgs decaying into $W^\pm A$ will be relatively easy at the LHC which is the top quark factory. We might again look for a subleading decay mode $a \to \mu^+\mu^-$ that we cannot afford at the Tevatron because the rate would be too small. In addition, we can look for events in which one of the W bosons decays into $\mu\nu$, resulting in 3-muon events with properties that easily stand out from the background. We expect about 30 events of this type with 1 fb^{-1} of data at the LHC [32].

In conclusion, four body decay modes: 4τ, $4c$, $4q$, and $4g$ are the simplest possibilities allowing the SM-like Higgs boson at ~ 100 GeV. For the $h \to aa \to 4\tau$ scenario in the NMSSM, searching for dominant decay modes typically requires many tens of fb^{-1} of data. However, searching for the subleading decays modes is very promising with early data at the LHC. Especially searches for

- $gg \to h \to aa \to 2\tau 2\mu$ [28],
- $gg \to a \to 2\mu$ [30],
- $t \to H^+b, \quad H^+ \to W^+a, \quad a \to \mu^+\mu^-$ [32]

could lead to an evidence or discovery already with 1 fb^{-1} of data.

Acknowledgments

I would like to thank J. Gunion, H.D. Kim, E. Lunghi and A. Raval for collaboration on projects this talk is based on.

References

[1] LEP-EWWG, http://lepewwg.web.cern.ch/LEPEWWG.

[2] For a review and references, see *e.g.* R. Dermisek, Mod. Phys. Lett. A **24**, 1631 (2009) [arXiv:0907.0297 [hep-ph]].

[3] R. Dermisek and J. F. Gunion, Phys. Rev. Lett. **95**, 041801 (2005) [arXiv:hep-ph/0502105].

[4] R. Dermisek and J. F. Gunion, Phys. Rev. D **73**, 111701 (2006) [arXiv:hep-ph/0510322].

[5] R. Dermisek and J. F. Gunion, Phys. Rev. D **76**, 095006 (2007) [arXiv:0705.4387 [hep-ph]].

[6] S. Chang, R. Dermisek, J. F. Gunion and N. Weiner, Ann. Rev. Nucl. Part. Sci. **58**, 75 (2008) [arXiv:0801.4554 [hep-ph]].

[7] R. Dermisek and J. F. Gunion, Phys. Rev. D **81**, 075003 (2010) [arXiv:1002.1971 [hep-ph]].

[8] R. Dermisek, arXiv:0806.0847 [hep-ph].

[9] R. Dermisek, AIP Conf. Proc. **1078**, 226 (2009) [arXiv:0809.3545 [hep-ph]].

[10] R. Dermisek and J. F. Gunion, Phys. Rev. D **79**, 055014 (2009) [arXiv:0811.3537 [hep-ph]].

[11] K. J. Bae, R. Dermisek, D. Kim, H. D. Kim and J. H. Kim, arXiv:1001.0623 [hep-ph].

[12] [LEP Collaborations], arXiv:hep-ex/0412015.

[13] R. Dermisek, arXiv:0807.2135 [hep-ph].

[14] B. Bellazzini, C. Csaki, A. Falkowski and A. Weiler, Phys. Rev. D **81**, 075017 (2010) [arXiv:0910.3210 [hep-ph]].

[15] B. Bellazzini, C. Csaki, A. Falkowski and A. Weiler, arXiv:0906.3026 [hep-ph].

[16] B. Gripaios, A. Pomarol, F. Riva and J. Serra, JHEP **0904**, 070 (2009) [arXiv:0902.1483 [hep-ph]].

[17] J. Mardon, Y. Nomura and J. Thaler, arXiv:0905.3749 [hep-ph].

[18] R. Dermisek and J. F. Gunion, Phys. Rev. D **75**, 075019 (2007) [arXiv:hep-ph/0611142].

[19] R. Dermisek, talk given at Inaugural meeting for upgraded Belle proto-collaboration, KEK, Japan, 3-4 July, 2008.

[20] A. Falkowski, J. T. Ruderman, T. Volansky and J. Zupan, JHEP **1005** (2010) 077 [arXiv:1002.2952 [hep-ph]].

[21] R. Dermisek and J. F. Gunion, Phys. Rev. D **77**, 015013 (2008) [arXiv:0709.2269 [hep-ph]].

[22] W. Love *et al.* [CLEO Collaboration], Phys. Rev. Lett. **101**, 151802 (2008) [arXiv:0807.1427 [hep-ex]].

[23] R. Dermisek, J. F. Gunion and B. McElrath, Phys. Rev. D **76**, 051105 (2007) [arXiv:hep-ph/0612031].

[24] B. Aubert *et al.* [BABAR Collaboration], arXiv:0902.2176 [hep-ex].

[25] B. Aubert *et al.* [BABAR Collaboration], Phys. Rev. Lett. **103**, 181801 (2009) [arXiv:0906.2219 [hep-ex]].

[26] V. M. Abazov *et al.* [D0 Collaboration], Phys. Rev. Lett. **103**, 061801 (2009) [arXiv:0905.3381 [hep-ex]].

[27] S. Wilbur, CDF, in progress, presented at Pheno 2009.

[28] M. Lisanti and J. G. Wacker, Phys. Rev. D **79**, 115006 (2009) [arXiv:0903.1377 [hep-ph]].

[29] S. Schael *et al.* [ALEPH Collaboration], JHEP **1005**, 049 (2010) [arXiv:1003.0705 [hep-ex]].

[30] R. Dermisek and J. F. Gunion, Phys. Rev. D **81**, 055001 (2010) [arXiv:0911.2460 [hep-ph]].

[31] R. Erbacher, A. Ivanov, and W. Johnson, CDF, 2010, http://www-cdf.fnal.gov/physics/new/top/2009/tprop/nMSSMhiggs/.

[32] R. Dermisek, E. Lunghi and A. Raval, in progress.

Commissioning of Leptons and Prospects for Searches of Leptoquarks, W' and Z' in CMS

Kerstin Hoepfner for the CMS Collaboration

RWTH Aachen, Phys. Inst. 3A, Otto-Blumenthal-Strasse, 52074 Aachen, Germany

DOI: http://dx.doi.org/10.3204/DESY-PROC-2010-01/204

Cosmic-ray data, beam splash events, and pp collisions have been used to commission electrons and muons as physics objects suitable for searches for BSM physics with leptons in the final state. In particular, the prospects for the search for new heavy gauge bosons, like W' and Z', are presented. Searches for pair production of first and second generation scalar leptoquarks are also discussed.

1 Detection of High p_T Leptons with CMS

At present (June 2010), the CMS experiment at the LHC proton-proton collider has started recording collision data and is being commissioned for high p_T leptons. Several searches for physics beyond the Standard Model are envisaged with early data to become competitive to Tevatron experimental limits.

The CMS design has been guided by several physics channels, amongst them the potential decay of a Standard Model Higgs Boson to four leptons, yielding an optimized performance of the detector for high p_T leptons. Other new particles beyond the Standard Model are also expected to manifest themselves clearly in their leptonic decay channels as an excess at very high momenta where the known background is very low. The key components of CMS in such searches are [1]:

- A very high magnetic field of B=3.8 T provided by a solenoid for the tracker and calorimeters. The required iron return yoke is embedded in the muon system.
- An excellent momentum resolution in the tracker constructed entirely of silicon (pixels for vertexing and strip detectors for tracking) of $\Delta p/p \sim 1\%@100GeV$.
- A good and redundant muon identification with four measuring stations everywhere along the muon's path and two complementary detection technologies. It provides about 10% stand-alone momentum resolution for TeV muons, mainly limited by multiple scattering in the iron return yoke. Combined with the excellent tracker the overall momentum resolution improves significantly, thus requiring a good alignment of the tracker to the muon system.
- Very high energy resolution ($\sigma_E/E \sim 0.01/\sqrt{E(GeV)}$) for electrons and photons provided by a fully sensitive electromagnetic calorimeter made of $PbWO_4$ crystals operated inside the 3.8 T solenoid.

In addition to test beam measurements of individual subdetector components, the CMS detector has undergone several commissioning campaigns with cosmic muons and beam splash events before taking first data from proton-proton collisions. In total about 350 million cosmic triggers were recorded and used to study the performance of different muon reconstruction algorithms [2], the internal alignment of the tracker and the muon system as well as the global alignment of both subsystems with respect to each other. Using cosmic muons, the precision achieved from alignment with tracks, has already superseded the earlier expectations concerning the alignment knowledge at startup. An insufficient alignment would wash out the signal and more luminosity would be needed to achieve a sensitivity comparable to the one with ideal detector knowledge. In addition trigger performance and efficiencies were studied with cosmic muons and the trigger timing was optimized. Horizontal beam splash events, although very few, were very useful to align the two muon endcaps with respect to each other, a task which cannot be done with cosmics muons as the rate of horizontal muons is too low. Large energy depositions in the calorimeters were used to study their performance.

2 Searches for New Particles

Searches for new particles, such as new additional heavy vector bosons Z' and W' or leptoquarks would manifest themselves in the detector as an excess of events in the lepton p_T spectrum or derived quantities. Fig 1 shows examples of simulated signals for those searches:

1. The neutral heavy vector boson Z' could decay into two leptons (leptons and muons were studied), representing itself as a resonant peak in the di-electron or di-muon spectrum at very high masses. An example is shown for m(Z')=1 TeV (see Fig 1-left).

2. Assuming Standard Model-like decays, the charged vector boson W' could manifest itself as a Jacobian peak in the transverse mass spectrum reconstructed from the high p_T electron or muon and the missing transverse energy caused by the neutrino. Also here, the excess would occur at very high momenta where background due to the Standard Model is negligible (see Fig 1-middle for m(W')=1 TeV, 1.5 TeV and 2 TeV).

3. Leptoquarks, particles that carry both colour and lepton flavour, should be produced in pairs with each of them decaying into a lepton + jet. They would provide a striking signature of two isolated and high p_T leptons and two high p_T jets (see Fig 1-right). First (electrons + jets) and second (muons + jets) generation leptoquarks have been studied at CMS and early data should provide a unprecedented sensitivity.

2.1 Selection of High p_T Leptons

Using simulated data, CMS has developed strategies to efficiently select high energy electrons and high momentum muons and suppress backgrounds or derive it from data. These selections are applied to all searches discussed in this paper.

For high p_T electrons at first a standard electron identification is required, meaning a single electron trigger, formation of EM clusters and their combination with pixel hits to be confirmed by tracker hits. The electron should fulfill $E_T < 25$ GeV and $|\eta| < 2.5$ and its tracker η, ϕ coordinates should match those measured in the calorimeter. Shower shape and energy deposition have to be consistent with the EM nature of the shower and be isolated in the calorimeter and

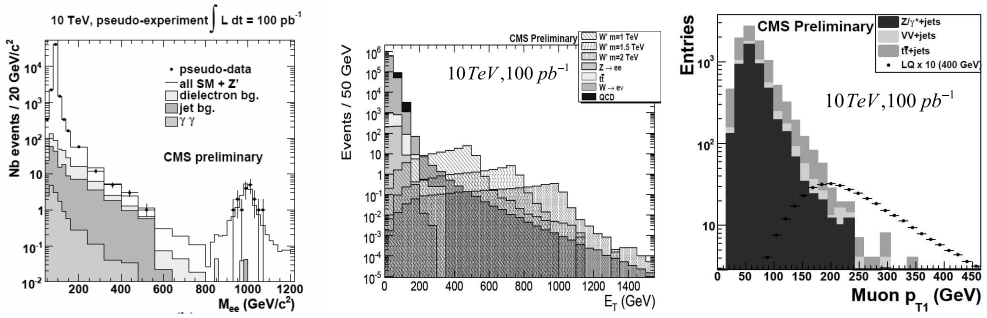

Figure 1: Examples of potential signals plotted along with their Standard Model background for three possible new particles. From the left: Z' vector bosons decaying to two leptons (electrons or muons), W' bosons deaying into an electron or muon and the corresponding neutrino, invariant mass of the lepton-quark system with an excess due to leptoquarks. All plots are for 10 TeV and 100 pb^{-1} of integrated luminosity.

the tracker. Also high p_T muons start from standard muon identification and must be triggered by the single muon trigger with the highest p_T threshold (depending on luminosity). Calorimeter energy should be consistent with a MIP signal. Calorimeter leakage is largely absorbed by the iron yoke between the muon stations. Muons can be reconstructed with hits from either the muon system or the tracker as well as a combination of both. Special reconstruction algorithms have been developed for TeV muons to treat showering and select very good quality muons. To suppress non-prompt muons isolation is required.

2.2 Search Strategies and Analyses

In the search for new, narrow resonances in the dilepton spectrum [3] with $M_{\ell\ell} > 800$GeV, the full Drell-Yan spectrum is studied from the Z-peak up to very high masses. Besides unexpected detector effects, this region should be almost free of known background processess. The signal, such as Z'-bosons or Randall-Sundrum gravitons, should manifest itself as an excess in the dilepton spectrum (left in Fig. 1). A competitive sensitivity can be reached with an integrated luminosity of about 100 pb^{-1} at 7 TeV center-of-mass energy, including systematic uncertainties due to the selection efficiency in the resonance mass region (4%), the impact on the invariant mass when extrapolating the DY background (50%) and an additional 10% uncertainty for k-factor and PDF, affecting both the signal and background.

Methods exists to check the ECAL linearity to the TeV scale. The electron efficiency will be determined from data using tag-and-probe, with ∼94% achieved for simulated data. The fake rate method will allow to measure the jet background in data (4.5 events in 100 pb^{-1} with 50% estimated systematic error).

In the muon channel additional background may be caused by mis-reconstruction and a good knowledge of alignment is essential for the invariant mass resolution. The analysis of the large cosmic muon sample has provided a sufficient basis. A small fraction of TeV-muons in the large cosmic muon sample even allowed to determine the momentum resolution (∼10% @ 1TeV) and the charge misassigment fraction (< 1.5%@1TeV). The overall muon efficiency was measured with tag-and-probe and simulated data to be (97.6±0.6)% at the Z-peak.

Potential charged heavy vector bosons, called W', would yield only one very high p_T charged lepton and E_T^{miss} [4] (see Fig. 1-middle). Also decays into jets are possible but difficult to separate from background. For leptonic channels, the signal region is almost free of background events, the few remaining ones coming from boosted (rejected by jet veto) and off-shell W-bosons (irreducible). At $\sqrt{s} = 7$ TeV a total of 11 background events is expected while a W' of 1 TeV mass would yield 43 events including trigger and reconstruction efficiencies. Three possible analysis strategies have been developed: the most advanced method uses the full kinematic information (reconstructed electron/muon and E_T^{miss}) and selects events with $0.4 < E_T^{lepton}/E_T^{miss} < 1.5$ and the angle between lepton and neutrino <2.5. In the case that E_T^{miss} is not yet fully commissioned, another search strategy relies only on the reconstructed lepton and rejects backgrounds by vetoing events with a jet of $p_T > 100$GeV in the direction opposite to the lepton. A third strategy would use MHT instead of E_T^{miss}. As the commissioning of E_T^{miss} appears to be in good shape, we plan to start with the first method. Including systematic uncertainties, such as alignment, calibration (1.5-4%), jet energy scale (7%), cross section (10%) and luminosity (10%), the existing Tevatron limit of m(W')=1 TeV can be challenged with 20-30 pb^{-1}.

Leptoquarks (LQ), being produced in pairs, would yield two very high p_T leptons (either electrons/muons or neutrinos) along with two jets [5]. In addition to the described lepton selections, jets with $p_T > 50$ GeV and $|\eta| < 3$ are selected. Both lepton-jet pairs are combined such that $\Delta M_{\ell j}$ is minimized. The scalar sum S_T of the p_T of the two leading leptons and two leading jets should fulfill $S_T > f(M_{LQ})$. Such selection would yield 39±0.15 signal and 1.5±0.3 background events in 100 pb^{-1}. Including systematic uncertainties, such an integrated luminosity would allow to search for leptoquarks with masses ranging from 250 to 500 GeV with the present experimental limit being 316 GeV.

3 Conclusions

The CMS detector is well suited to efficiently detect very high momentum leptons which may be a sign af new physics. Cosmic ray muons and beam splash events were used to align the detector, optimize triggers and reconstruction algorithms. Potential new particles, such as Z' and W' or leptoquarks would manifest themselves through an excess in single lepton or dilepton spectra. Selection criteria to select such signals were developed along with methods to quantify the background. With an integrated luminosity of 20-30 pb^{-1}, the search for W'-bosons will become competitive with the existing Tevatron limit. Further statistics will give access to searches for Z'-bosons and leptoquarks.

References

[1] CMS Coll., "The CMS experiment at the CERN LHC", JINST 3 (2008) S08004.

[2] CMS Coll., "Performance of CMS muon reconstruction in cosmic-ray events", JINST 5 (2010) T03022

[3] CMS coll., "Search for high mass resonances decaying into an electron pair in CMS at 10 TeV with 100 pb^{-1}", CMS Physics Analysis Summary, EXO-09-006

[4] CMS coll., "Discovery potential of $W' \to e\nu$ at CMS ", CMS Analysis Summary, PAS EXO-08-004

[5] CMS coll., "Search for Second Generation Scalar leptoquarks with the CMS Detector", CMS Physics Analysis Summary, PAS EXO-09-010

Early searches with jets with the ATLAS detector at the LHC

Victor Lendermann for the ATLAS Collaboration

Kirchhoff-Institut für Physik, Universität Heidelberg, Im Neuenheimer Feld 227, 69120 Heidelberg, Germany

DOI: http://dx.doi.org/10.3204/DESY-PROC-2010-01/274

First data collected with the ATLAS detector in 2010 allow us to search for new physics in various jet signatures. One of these analyses, a search for threshold effects in multi-body signatures, is presented. The results are not covered by previous collider searches.

1 Introduction

First data collected with the ATLAS detector in 2010 in pp collisions at a center-of-mass energy of $\sqrt{s} = 7\,\text{TeV}$ revealed an impressive detector performance in measurements of basic final state objects, in particular of jets [1]. The good quality of data allowed us to perform first searches for new physics beyond the Standard Model (SM) in jet signatures with the first $300\,\text{nb}^{-1}$ of data. The searches are performed for exotic dijet resonances [2], for deviations in dijet angular distributions [3], for threshold effects in multi-body signatures [4], as well as for SUSY signatures [5]. In the following, the multi-body search is discussed which is a search of a completely new type.

2 Search for new physics in multi-body signatures

High multi-jet cross-sections can be expected in particular, in models of new physics with a low scale of gravity, such as models with extra dimensions [6]. In these models, the fundamental scale of gravity, M_D, can be in the TeV range, while the Planck scale is an effective scale seen in a three-dimensional world. The lower limit from collider experiments on M_D is 940 GeV for six extra dimensions [7], while for greater than six extra dimensions it is about 800 GeV [8].

A striking prediction of such models is a continuum production of non-perturbative gravitational states, such as black holes [9], string balls [10], or p-branes [11] above the new mass threshold. Due to the lack of a UV-complete theory of quantum gravity there are few robust theoretical predictions. As gravity couples only to the energy-momentum content of matter, the decays of strong-gravitational objects should be approximately democratic to all degrees of freedom in the Standard Model. One expects high multiplicity final states dominated by jets, since quarks and gluons together include more degrees of freedom that the other SM particles.

A first search for final states of this kind is performed by ATLAS in the first $295\,\text{nb}^{-1}$ of data. One searches for a deviation from the SM prediction in the spectrum of the reconstructed invariant mass of the final state above a threshold of 800 GeV. The studied signatures include

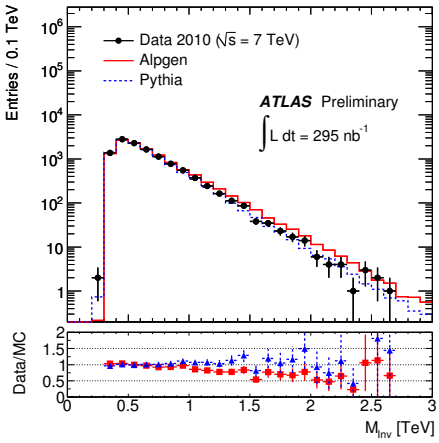

Figure 1: Invariant mass distribution for events with at least three objects and with $\sum p_T > 300\,\text{GeV}$ after normalising the background to data. The solid dots are the data, while the solid and dashed histograms are the background predictions using scaled Alpgen and Pythia, respectively.

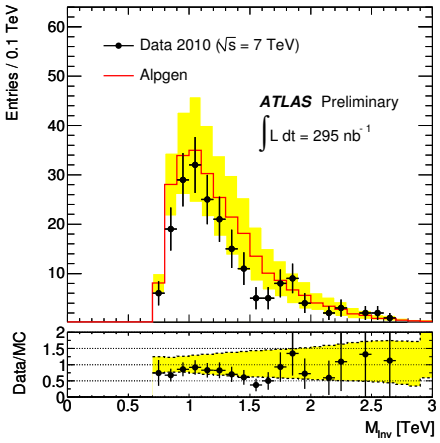

Figure 2: Invariant mass distribution for events with $\sum p_T > 700\,\text{GeV}$. The solid dots are the data and the histogram is the rescaled background prediction using Alpgen simulation. The error band on the background is the total uncertainty: statistical (negligible) and systematic uncertainties added in quadrature.

jets as well as electrons, photons and muons, and make no requirement on the particle types or their number other than there be at least three. The search is thus kept as general as possible. The invariant mass, M_{inv}, is calculated from all objects and including missing transverse energy.

An additional requirement is imposed on the scalar sum of transverse momenta of all reconstructed objects in an event: $\sum p_T > 700\,\text{GeV}$. This cut is useful for reducing the QCD $2 \to 2$ scattering processes characterised by a strong forward peak in the differential cross section, as it selects more centrally produced objects.

Since most of the objects passing the selections are jets, the dominant Standard Model background is QCD jet production. It is estimated using the MC generator Alpgen combined with Jimmy and Herwig. Since simulations can only approximate the true multi-jet cross section, the MC samples are normalised to the number of observed events in a nearby control region, where no new physics effects are expected. The predictions are then extrapolated to the signal region, hence relying only on the simulation of the shape of the differential cross section in mass. A control region in the range $300 < M_{\text{inv}} < 800\,\text{GeV}$ and $\sum p_T > 300\,\text{GeV}$ is chosen.

The QCD model uncertainties are estimated by taking the difference between the Alpgen and Pythia predictions, where the Pythia samples are renormalised in the control region in the same way. The M_{inv} distributions for data, as well as for the Alpgen and Pythia predictions are shown in Fig. 1. Further major systematic uncertainties are obtained from the variation of the control region, from the choice of the parton density functions (PDF) in the simulations, and from the jet energy scale uncertainty. The M_{inv} distribution for events with $\sum p_T > 700\,\text{GeV}$ for the data and for the simulation with its total uncertainty is shown in Fig. 2.

After all the event selections, 189 events are observed in the signal region, while the number

of background events is estimated to be $251 \pm 17(\text{stat.}) \pm 84(\text{syst})$. Using a Bayesian approach and assuming a flat prior p.d.f. over the cross section, an upper limit of 0.34 nb at the 95% confidence level is obtained for the cross section times signal acceptance.

For an estimate of a possible signal, black hole MC event samples are generated using the Blackmax and Charybdis programs. The samples are produced with an energy threshold equal to the fundamental scale of $M_D = 800\,\text{GeV}$ and six extra dimensions. Using the simulated acceptance value as an illustration, the upper limit on the production cross section for high invariant mass events above 800 GeV is 0.6 nb. This limit does not include systematic uncertainties in the signal acceptance which is expected to be large due to the lack of a well established physics model in the mass region near the gravity scale. At the mass threshold of 800 GeV, the most optimistic calculation for the black hole cross-section can give $\sim$60 nb [12]. The upper limit is well below this value, which illustrates the potential rejection power of this result on low scale gravity models.

References

[1] E. Feng, these proceedings.

[2] G. Aad *et al.* [ATLAS Collaboration], accepted by Phys. Rev. Lett. [arXiv:1008.2461].

[3] ATLAS Collaboration, conference note, ATLAS-CONF-2010-074.

[4] ATLAS Collaboration, conference note, ATLAS-CONF-2010-088.

[5] ATLAS Collaboration, conference notes, ATLAS-CONF-2010-065 and ATLAS-CONF-2010-066.

[6] N. Arkani-Hamed, S. Dimopoulos and G. R. Dvali, Phys. Lett. B **429** (1998) 263 [arXiv:hep-ph/9803315]; I. Antoniadis *et al.*, Phys. Lett. B **436** (1998) 257 [arXiv:hep-ph/9804398].

[7] T. Aaltonen *et al.* [CDF Collaboration], Phys. Rev. Lett. **101** (2008) 181602 [arXiv:0807.3132].

[8] V. M. Abazov *et al.* [D0 Collaboration], Phys. Rev. Lett. **101** (2008) 011601 [arXiv:0803.2137].

[9] T. Banks and W. Fischler, arXiv:hep-th/9906038; S. B. Giddings and S. D. Thomas, Phys. Rev. D **65** (2002) 056010 [arXiv:hep-ph/0106219]; S. Dimopoulos and G. L. Landsberg, Phys. Rev. Lett. **87** (2001) 161602 [arXiv:hep-ph/0106295].

[10] S. Dimopoulos and R. Emparan, Phys. Lett. B **526** (2002) 393 [arXiv:hep-ph/0108060]; D. M. Gingrich and K. Martell, Phys. Rev. D **78** (2008) 115009 [arXiv:0808.2512 [hep-ph]].

[11] K. Cheung and C. H. Chou, Phys. Rev. D **66** (2002) 036008 [arXiv:hep-ph/0205284]; E. J. Ahn, M. Cavaglia and A. V. Olinto, Phys. Lett. B **551** (2003) 1 [arXiv:hep-th/0201042].

[12] D. C. Dai *et al.*, Phys. Rev. D **77** (2008) 076007 [arXiv:0711.3012]; J. A. Frost *et al.*, JHEP **0910** (2009) 014 [arXiv:0904.0979]; D. M. Gingrich, Comp. Phys. Comm. **181** (2010) 1917 [arXiv:0911.5370].

Discovering SUSY in the first LHC run

Sven Heinemeyer

Instituto de Física de Cantabria (CSIC-UC), Santander, Spain

DOI: http://dx.doi.org/10.3204/DESY-PROC-2010-01/253

We analyze the potential of the first LHC physics run, assuming 1 fb^{-1} at $\sqrt{s} = 7$ TeV, to discover Supersymmetry (SUSY). The results are based on SUSY parameter fits following a frequentist approach. They include the experimental constraints from electroweak precision data, $(g-2)_\mu$, B physics and cosmological data. The two SUSY models under consideration are the constrained MSSM (CMSSM) with universal soft supersymmetry-breaking mass parameters, and a model with common non-universal Higgs mass parameters in the superpotential (NUHM1). We find that large parts of the regions preferred at the 68% C.L. are accessible to early LHC running.

1 Introduction

One of the main tasks of the LHC is to search for physics beyond the Standard Model (SM), where Supersymmetry (SUSY) is one of the favored ideas. The first physics run of the LHC is currently ongoing at $\sqrt{s} = 7$ TeV, aiming for 1 fb^{-1} until the end of 2011. Here we review the results from frequentist analyses [1, 2] of the parameter spaces of the constrained minimal supersymmetric extension of the Standard Model (CMSSM) — in which the soft SUSY-breaking scalar and gaugino masses are each constrained to universal values m_0 and $m_{1/2}$, respectively — and the NUHM1 — in which the soft SUSY-breaking contributions to the Higgs masses are allowed to have a different but common value. Both models have a common trilinear coupling A_0 at the GUT scale and $\tan\beta$ (the ratio of the two vacuum expectation values) as a low-energy input. A detailed list of references on the subject of frequentist (and bayesian) analyses can be found in Ref. [1].

2 Details of the fits

The results obtained in Refs. [1, 2] include various experimental results: B-physics observables (such as rates for BR($b \to s\gamma$) and BR($B_u \to \tau\nu_\tau$), and the upper limit on BR($B_s \to \mu^+\mu^-$)) as well as K-physics observables, precision electroweak data (such as the W boson mass and the anomalous magnetic moment of the muon, $(g-2)_\mu$), the bound on the lightest MSSM Higgs boson mass, M_h, and the cold dark matter (CDM) density (as inferred from astrophysical and cosmological data) assuming that this is dominated by the relic density of the lightest neutralino, $\Omega_\chi h^2$.

The fit is performed by using a global χ^2 likelihood function, which combines all theoretical

predictions with experimental constraints:

$$\chi^2 = \sum_i^N \frac{(C_i - P_i)^2}{\sigma(C_i)^2 + \sigma(P_i)^2} + \sum_i^M \frac{(f_{\mathrm{SM}_i}^{\mathrm{obs}} - f_{\mathrm{SM}_i}^{\mathrm{fit}})^2}{\sigma(f_{\mathrm{SM}_i})^2} + \chi^2(M_h) + \chi^2(\mathrm{BR}(B_s \to \mu\mu)) + \chi^2(\text{SUSY search limits}) \quad (1)$$

Here N is the number of observables studied, C_i represents an experimentally measured value (constraint), and each P_i defines a prediction for the corresponding constraint that depends on the supersymmetric parameters. The experimental uncertainty, $\sigma(C_i)$, of each measurement is taken to be both statistically and systematically independent of the corresponding theoretical uncertainty, $\sigma(P_i)$, in its prediction. We denote by $\chi^2(M_h)$ and $\chi^2(\mathrm{BR}(B_s \to \mu\mu))$ the χ^2 contributions from two measurements for which only one-sided bounds are available so far. Similarly, we include the lower limits from the direct searches for SUSY particles at LEP [3] as one-sided limits, denoted by "χ^2(SUSY search limits)" in Eq. (1). The experimental constraints used in our analyses are listed in Table 1 of Ref. [1]. Our statistical treatment of the CMSSM and NUHM1 makes use of a large sample of points (about 2.5×10^7) in the SUSY parameter spaces obtained with the Markov Chain Monte Carlo (MCMC) technique. Our analysis is entirely frequentist, and avoids any ambiguity associated with the choices of Bayesian priors.

The main computer code for our evaluations is the `MasterCode` [1,2,4–6], which includes the following theoretical codes. For the RGE running of the soft SUSY-breaking parameters, it uses `SoftSUSY` [7], which is combined consistently with the codes used for the various low-energy observables: `FeynHiggs` [8–11] is used for the evaluation of the Higgs masses and a_μ^{SUSY} (see also [12,13]), for the other electroweak precision data we have included a code based on [14,15], `SuFla` [16,17] and `SuperIso` [18,19] are used for flavor-related observables, and for dark-matter-related observables `MicrOMEGAs` [20] and `DarkSUSY` [21] are included. In the combination of the various codes, `MasterCode` makes extensive use of the SUSY Les Houches Accord [22, 23].

3 SUSY discovery potential of the first LHC run

For the parameters of the best-fit CMSSM point we find $m_0 = 60$ GeV, $m_{1/2} = 310$ GeV, $A_0 = 130$ GeV, $\tan\beta = 11$ and $\mu = 400$ GeV, yielding the overall $\chi^2/\mathrm{N}_{\mathrm{dof}} = 20.6/19$ (36% probability) and nominally $M_h = 114.2$ GeV. The corresponding parameters of the best-fit NUHM1 point are $m_0 = 150$ GeV, $m_{1/2} = 270$ GeV, $A_0 = -1300$ GeV, $\tan\beta = 11$ and $m_{h_1}^2 = m_{h_2}^2 = -1.2 \times 10^6$ GeV^2 or, equivalently, $\mu = 1140$ GeV, yielding $\chi^2 = 18.4$ (corresponding to a similar fit probability as in the CMSSM) and $M_h = 120.7$ GeV.

In Fig. 1 we display the best-fit value and the 68% and 95% likelihood contours for the CMSSM (upper plot) and the NUHM1 (lower plot) in the $(m_0, m_{1/2})$ plane, obtained as described above from a fit taking into account all experimental constraints. We also show exclusion contours for the hadronic search mode (jets plus missing energy) at CMS. The green (light gray) solid line shows the 95% C.L. exclusion contour for CMS for 1 fb^{-1} at $\sqrt{s} = 7$ TeV [24]. The black solid line shows the corresponding results for only 0.1 fb^{-1}. (Similar results hold for ATLAS.) One can see that with 1 fb^{-1} the best-fit points can be tested, together with a sizable part of the whole 68% C.L. preferred regions. In the case of the NUHM1 (lower plot) nearly the whole 68% C.L. region could be probed.

In conclusion, if the CMSSM or the NUHM1 (or a very similar SUSY model) were realized in nature, the first LHC physics run at $\sqrt{s} = 7$ TeV until the end of 2011 could reveal already

first signals of SUSY. On the other hand, no indication of SUSY-like signatures would already severly restrict these (kind of) GUT based models.

4 Acknowledgments

We thank O. Buchmüller, R. Cavanaugh, A. De Roeck, J. Ellis, H. Flächer, G. Isidori, K. Olive, F. Ronga and G. Weiglein with whom the results presented here have been obtained. Work supported in part by the European Community's Marie-Curie Research Training Network under contract MRTN-CT-2006-035505 'Tools and Precision Calculations for Physics Discoveries at Colliders' (HEPTOOLS).

References

[1] O. Buchmueller *et al.*, Eur. Phys. J. C **64** (2009) 391.

[2] O. Buchmueller *et al.*, JHEP **0809** (2008) 117.

[3] LEP Supersymmetry Working Group, see: `http://lepsusy.web.cern.ch/lepsusy/` .

[4] O. Buchmueller *et al.*, Phys. Lett. B **657** (2007) 87.

[5] O. Buchmueller *et al.*, Phys. Rev. D **81** (2010) 035009.

[6] See `http://cern.ch/mastercode` .

[7] B. C. Allanach, Comput. Phys. Commun. **143** (2002) 305.

[8] S. Heinemeyer, W. Hollik and G. Weiglein, Comput. Phys. Commun. **124** (2000) 76.
See `http://www.feynhiggs.de` .

[9] S. Heinemeyer, W. Hollik and G. Weiglein, Eur. Phys. J. C **9** (1999) 343.

[10] G. Degrassi *et al.*, Eur. Phys. J. C **28** (2003) 133.

[11] M. Frank *et al.*, JHEP **0702** (2007) 047.

[12] T. Moroi, Phys. Rev. D **53** (1996) 6565 [Erratum-ibid. D **56** (1997) 4424].

[13] S. Heinemeyer, W. Hollik and G. Weiglein, Phys. Rept. **425** (2006) 265.

[14] S. Heinemeyer *et al.*, JHEP **0608** (2006) 052.

[15] S. Heinemeyer, W. Hollik, A. Weber and G. Weiglein, JHEP **0804** (2008) 039.

[16] G. Isidori and P. Paradisi, Phys. Lett. B **639** (2006) 499.

[17] G. Isidori, F. Mescia, P. Paradisi and D. Temes, Phys. Rev. D **75** (2007) 115019, and references therein.

[18] F. Mahmoudi, Comput. Phys. Commun. **178** (2008) 745.

[19] D. Eriksson, F. Mahmoudi and O. Stal, JHEP **0811** (2008) 035.

[20] G. Belanger, F. Boudjema, A. Pukhov and A. Semenov, Comput. Phys. Commun. **176** (2007) 367; ibid. **149** (2002) 103; ibid. **174** (2006) 577.

[21] P. Gondolo *et al.*, New Astron. Rev. **49** (2005) 149.

[22] P. Skands *et al.*, JHEP **0407** (2004) 036.

[23] B. Allanach *et al.*, Comput. Phys. Commun. **180** (2009) 8.

[24] CMS Note-2010/008.

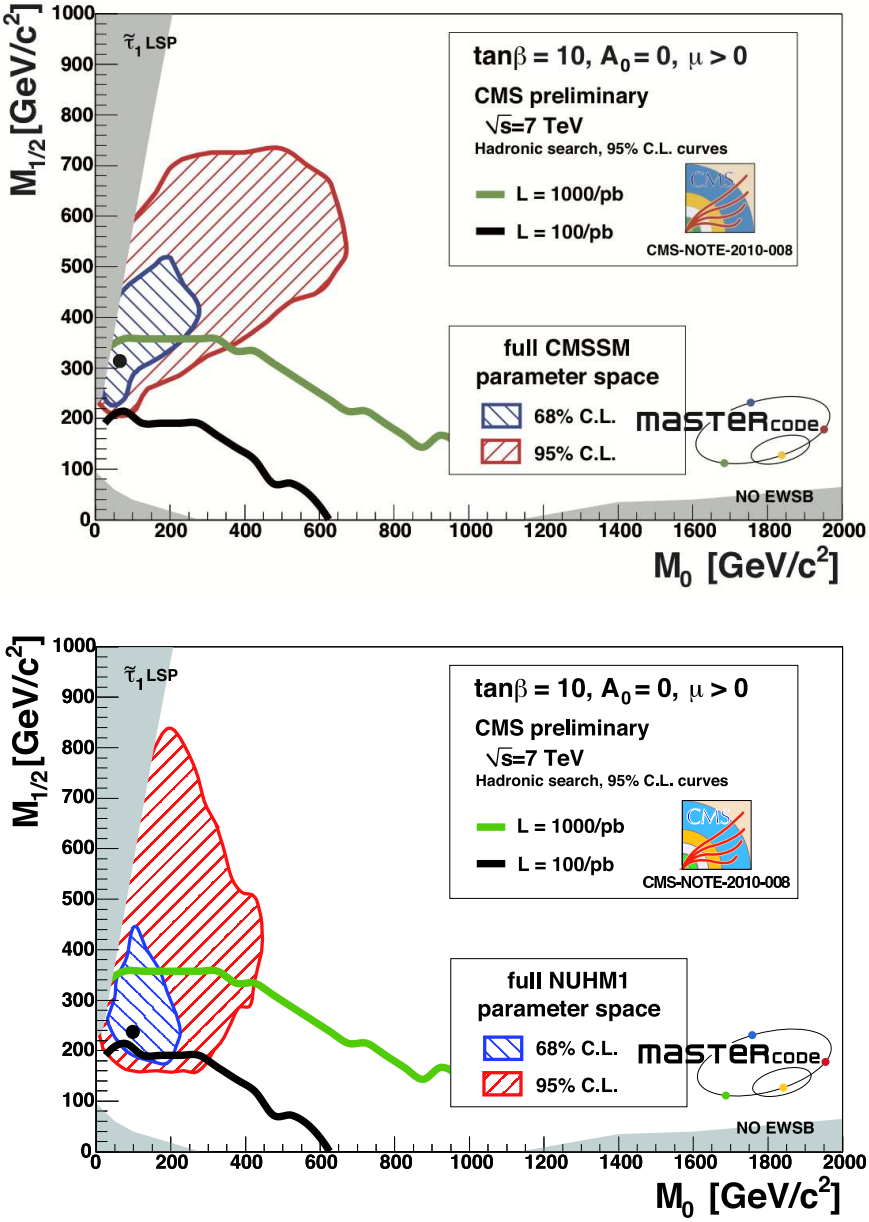

Figure 1: The $(m_0, m_{1/2})$ plane in the CMSSM (upper plot) and the NUHM1 (lower plot). The dark shaded area at low m_0 and high $m_{1/2}$ is excluded due to a scalar tau LSP, the light shaded areas at low $m_{1/2}$ do not exhibit electroweak symmetry breaking. Shown in both plots are the best-fit point, indicated by a filled circle, and the 68 (95)% C.L. contours from our fit as dark gray/blue (light gray/red) overlays, scanned over all $\tan\beta$ and A_0 values. The 95% C.L. exclusion curves (hadronic search channel) at CMS with 1 (0.1) fb^{-1} at 7 TeV center-of-mass energy is shown as green/light gray (black) solid curve.

Sparticle masses from transverse mass kinks at the LHC: The case of Yukawa unified SUSY GUTs

Diego Guadagnoli

Excellence Cluster Universe, Technische Universität München, Boltzmannstraße 2, D-85748 Garching, Germany

DOI: http://dx.doi.org/10.3204/DESY-PROC-2010-01/254

We pose the question of the performance of the LHC in measuring actual SUSY spectra (or their lightest part) in the example of Yukawa-unified SUSY GUTs. We choose two spectra, representative of two scenarios of SUSY breaking terms, and note that both of them are characterized by short decay chains. We thus take the so-called m_{T2}-kink method as our key strategy – since it does not rely on the presence of long decay chains – and discuss a procedure allowing to determine the whole lightest part of the SUSY spectra.

SUSY GUTs with Yukawa Unification

Introduction

The main motivations for supersymmetric (SUSY) Grand Unified Theories (GUTs), and, in their context, for third-generation Yukawa unification (YU), are well known, and will not be repeated here (see e.g. [1]). Concerning YU, it will suffice to say that, within this hypothesis, the large hierarchy given by m_t/m_b is explained as a hierarchy in the vevs of the two Higgs doublets used to give masses to fermions (i.e. $\tan\beta \equiv v_U/v_D \gg 1$), thereby allowing the Y_t and Y_b couplings to be both of order 1.

The more strictly phenomenological aspects of YU within SUSY GUTs may instead be summarized in the following main facts. In [2], the predictive power of the YU hypothesis was used to estimate the top mass, given the measured bottom and tau masses. It was realized that the bottom and tau masses undergo EW-scale, radiative corrections, proportional to the 'wrong' vev $v_U = v_D \tan\beta$. Hence these corrections will be large for large $\tan\beta$. In ref. [3] an 'opposite' strategy was therefore proposed: rather than using YU to predict quark masses, use their measured values – m_t had also been measured meanwhile – to learn about the allowed parameter space for the model, and make predictions for the SUSY spectrum. In this context, assuming GUT-scale universalities for the soft SUSY-breaking terms, one preferred region emerges [3]

$$-A_0 \approx 2\, m_{16}, \quad \mu, m_{1/2} \ll m_{16}, \tag{1}$$

with A_0, m_{16} and $m_{1/2}$ the universal sfermion trilinear, sfermion bilinear and gaugino bilinear soft terms, respectively, and μ the higgsino mass parameter. Quite interestingly the same relations (1) emerge as fixed-point solution from the attempt to build SUSY models with radiatively-driven inverted scalar mass hierarchy (ISMH) [4], i.e. light third generation and heavy first and second generation sfermions. ISMH is an appealing possibility to relieve at one

stroke the problem of fine tuning in the Higgs mass corrections, and of large flavor-changing neutral currents (FCNCs).

In more recent studies, SUSY GUTs with YU have been confronted with all the available low-energy data, using different techiques across the various studies, as well as different sets of low-energy data, and different assumed SUSY-breaking patterns. Our approach [5, 6, 7] has been to construct a χ^2 function out of EW observables, quark masses and FCNCs. This technique has the advantages of providing a global assessment of the model in a reparameterization-invariant way – what matters is the χ^2 minimum – and of exploiting at best the strong sensitivity of the high-energy parameters to the low-energy ones [8].

Two scenarios

From the findings of refs. [5, 6, 7], we picked up two representative scenarios. The two scenarios are as follows

S1: *SUSY GUTs with YU and universal GUT-scale soft terms [6]*[1]

The combined information from FCNCs favors values of $\tan\beta$ lower than O(50). Conversely, it is known [9] that m_b prefers $\tan\beta$ = O(50) – or else, close to 1, which is excluded by LEP. Hence this scenario is viable only advocating partial decoupling of the sfermion spectrum, the lightest mass exceeding 1 TeV. Relaxing $t-b-\tau$ YU to just $b-\tau$ YU allows to find a better compromise between the FCNC and m_b constraints, thereby somewhat lowering the lightest stop mass. Spectrum predictions are robust, and are summarized in the left column of table 1.

S2: *SUSY GUTs with YU and split trilinear soft terms at the GUT scale [7]*

With respect to scenario 1, trilinears are allowed to be split: $A_U \neq A_D$. Agreement with data clearly selects the region with large μ = O(m_{16}) and sizable $A_U - A_D$ splitting. In this region, the lightest stop (and the gluino) are required to be very close to their experimental bounds, i.e. are *very* light, and nonetheless all the FCNC tensions are relieved. Spectrum predictions are again robust, and are summarized in the right column of table 1.

Spectrum predictions			
S1, ref. [6]		S2, ref. [7]	
M_{h^0}	121	M_{h^0}	126
M_{H^0}	585	M_{H^0}	1109
M_A	586	M_A	1114
M_{H^+}	599	M_{H^+}	1115
$m_{\tilde{t}_1}$	783	$M_{\tilde{t}_1}$	192
$m_{\tilde{t}_2}$	1728	$m_{\tilde{t}_2}$	2656
$m_{\tilde{b}_1}$	1695	$m_{\tilde{b}_1}$	2634
$m_{\tilde{b}_2}$	2378	$m_{\tilde{b}_2}$	3759
$m_{\tilde{\tau}_1}$	3297	$m_{\tilde{\tau}_1}$	3489
$m_{\tilde{\chi}^0_1}$	59	$m_{\tilde{\chi}^0_1}$	53
$m_{\tilde{\chi}^0_2}$	118	$m_{\tilde{\chi}^0_2}$	104
$m_{\tilde{\chi}^+_1}$	117	$m_{\tilde{\chi}^+_1}$	104
$M_{\tilde{g}}$	470	$M_{\tilde{g}}$	399

Table 1: All masses are in units of GeV. Uppercase and lowercase masses stand for pole and respectively $\overline{\rm DR}$ masses.

From the table, it is evident that the main difference between the two scenarios is a stop respectively heavier and lighter than the gluino, whereas predictions are basically the same for $\tilde{\chi}^0_{1,2}$, $\tilde{\chi}^\pm_1$ and also $\tilde{g}$.

SUSY GUTs with YU at the LHC

At the 14 TeV LHC, the spectrum features described in the previous section imply that: *(1)* $\tilde{g}-\tilde{g}$ production is substantial in both scenarios (about 60 vs. 40% respectively); *(2)* $\tilde{t}_1-\tilde{t}_1$ production is large (40% !) in scenario 2 (and basically zero in the other); *(3)* $\tilde{\chi}^\pm_1-\tilde{\chi}^0_2$ associated

[1] Non-universality is allowed (and actually required) only for the Higgs soft terms (m_{H_u}, m_{H_d}).

production is also interesting in both scenarios (25 vs. 10%). Therefore, a suitable mass-determination strategy should be able to determine the masses of all these produced particles. In particular, noting that the $\tilde{g}$ and (for scenario 2) the $\tilde{t}_1$ are light, one can expect 2- or 3-steps decay chains, namely *short decay chains*. This points to the use of the M_{T2} variable as the main strategy for determining SUSY masses.

The M_{T2} event variable

The M_{T2} variable is best understood by shortly describing its precursor, the M_T variable. At the UA1 experiments, one could measure the W-boson mass from the decay mode $W \to \ell\nu$ by forming the variable [10]

$$M_T^2 = 2(E_T^\ell E_T^\nu - \vec{p}_T^{\,\ell}\vec{p}_T^{\,\nu}) \ .$$

Note in fact that $m_W^2 = (p_\ell + p_\nu)^2 = m_\ell^2 + m_\nu^2 + 2(E_T^\ell E_T^\nu \cosh(\eta_\ell - \eta_\nu) - \vec{p}_T^{\,\ell}\vec{p}_T^{\,\nu}) \geq M_T^2$, simply because $\cosh x \geq 1$. Here η: $\tanh\eta = p_z/E$ is the rapidity, in the usual HEP experimental definition. Therefore M_T provides, event by event, a lower bound on the m_W mass. The main point is that there are kinematical configurations whereby the bound is saturated, hence the endpoint of the m_T distribution equals (barring backgrounds) the m_W mass.

M_{T2} [11] is the two-decay-chains generalization of M_T. The event topology relevant for the applicability of M_{T2} is that of two produced particles Y_1 and Y_2 (e.g. $\tilde{g}\tilde{g}$) each decaying into a set of visible particles $V_{1,2}$, whose transverse invariant mass and transverse boost are supposed to be entirely reconstructed, plus an undetected particle (or set of particles), $\chi_{1,2}$. If the missing $\vec{p}_T$'s of the χ_i, $\vec{p}_T(\chi_i)$, were separately reconstructible, one could just construct two separate M_T variables. However, all one knows event by event is that $\vec{p}_T(\chi_1) + \vec{p}_T(\chi_2) =$ total $\vec{p}_T^{\,\rm miss}$, where the latter quantity can be inferred from the sum of the visible transverse momenta, because of momentum conservation. Therefore, the best one can say event by event is

$$M_{T2} \equiv \min_{\vec{p}_T(\chi_1)+\vec{p}_T(\chi_2)=\vec{p}_T^{\,\rm tot.miss}} \left\{ \max\left[M_T^2(\text{chain 1}), M_T^2(\text{chain 2}) \right] \right\} \leq m_Y^2 \ ,$$

where we have assumed mother particles $Y_1 = Y_2 = Y$, with mass m_Y.

Note that: *(1)* an event topology consisting of two decay chains, each with a final particle escaping detection, is actually a very useful one, for many Standard Model extensions (e.g. all those with a conserved Z_2 symmetry); *(2)* the inclusion of only transverse momentum components makes M_{T2} very suitable for hadron colliders, where the boost along the beam axis is unknown anyway; *(3)* at variance with the $W \to \ell\nu$ case, the missing-particle mass m_χ is not zero, it is not negligible, and it is unknown. Therefore M_{T2} is actually a function of trial values for m_χ. This functional dependence can actually be turned into an advantage. In fact, it was realized [12] that the maximum over the events of $M_{T2}(m_\chi)$ has a 'kink' (a discontinuity in the first derivative) at $\{m_Y^{\rm phys},\ m_\chi^{\rm phys}\}$. Hence the kink location permits a simultaneous measurement of both the Y and the χ masses!

Application to SUSY GUTs with YU

From the previous ideas, one can set up a strategy [13] to determine the whole lightest part of the SUSY spectrum for the two scenarios in table 1. This strategy can then be tested on events simulated at the 14 TeV LHC, including detector effects, in order to understand to which extent it is effective with real data. For the full analysis, the reader is referred to ref. [13]. The main results are also reported in table 2.

Here we will only shortly describe an example. Consider $\tilde{g}\tilde{g}$ production in scenario 2, followed by the decay chain

$$\tilde{g} \to W b \tilde{t}_1 \quad \text{with} \quad \tilde{t}_1 \to b \tilde{\chi}_1^\pm \quad \text{and} \quad \tilde{\chi}_1^\pm \to \ell \nu_\ell \tilde{\chi}_1^0 \ .$$

In 100/fb of data, one expects about 1.1 million such events. In the channel shown here, the mother particle, Y, is the gluino, and the escaping one, χ, is actually not only the $\tilde{\chi}_1^0$, but the $\tilde{\chi}_1^0$ plus the ν. For the event selection, one may: *(1)* trigger on $2W + 4b -$ jets $+ 2\ell + p_T^{\text{miss}}$; *(2)* apply suitable kinematical cuts on the obtained event sample, and a suitable jet-pairing scheme, in order to tame the combinatoric error (see [13] for details). Thereafter, one can *(3)* take *the whole* $\tilde{\chi}_1^\pm$*-initiated decay chain* as the escaping particle and construct M_{T2} accordingly. Plotting the maximum over the events of this M_{T2} shows indeed a discontinuity at the physical $m_{\tilde{g}} - m_{\tilde{\chi}_1^\pm}$ masses, whose fitted values are reported in table 2.

With the $\tilde{g}$ and $\tilde{\chi}_1^\pm$ masses determined this way, one can determine the $\tilde{t}_1$, $\tilde{\chi}_1^0$ and $\tilde{\chi}_2^0$ masses using simple endpoint methods. E.g., from $\tilde{t}_1\tilde{t}_1$, with $\tilde{t}_1 \to b\tilde{\chi}_1^\pm$ and $\tilde{\chi}_1^\pm \to qq'\tilde{\chi}_1^0$, one may determine $m_{\tilde{t}_1} - m_{\tilde{\chi}_1^0}$ from the endpoint of $M_{T,bqq'}$ and $m_{\tilde{\chi}_1^\pm} - m_{\tilde{\chi}_1^0}$ from the endpoint of $M_{T,qq'}$. A similar strategy can be worked out for scenario 1, with the caveat that, in this case, the $\tilde{t}_1$ is too heavy to be produced in non-negligible amounts, and its mass cannot be determined.

As demonstrated in the analysis (see [13]) and shown in table 2, our strategy allows to determine all of the lightest part of the SUSY spectra within 20 GeV of error.

Acknowledgments It is a pleasure to acknowledge Kiwoon Choi, Sang Hui Im and Chan Beom Park for the most pleasant collaboration. This work is supported by the DFG Cluster of Excellence 'Origin and Structure of the Universe'.

	Mass	Result (GeV)
S2	$m_{\tilde{g}}$	395 ± 16
	$m_{\tilde{\chi}_1^\pm}$	109 ± 17
	$m_{\tilde{\chi}_1^0}$	57 ± 17
	$m_{\tilde{\chi}_2^0}$	107 ± 18
	$m_{\tilde{t}_1}$	206 ± 17
S1	$m_{\tilde{g}}$	456 ± 15
	$m_{\tilde{\chi}_1^\pm}$	144 ± 20
	$m_{\tilde{\chi}_1^0}$	66 ± 16
	$m_{\tilde{\chi}_2^0}$	126 ± 16

Table 2: Mass determinations within our strategy, to be compared with table 1.

References

[1] D. Guadagnoli, arXiv:0810.0450 [hep-ph].

[2] L. J. Hall, R. Rattazzi and U. Sarid, Phys. Rev. D **50**, 7048 (1994). See also: R. Hempfling, Phys. Rev. D **49**, 6168 (1994); T. Blazek, S. Raby and S. Pokorski, Phys. Rev. D **52**, 4151 (1995).

[3] T. Blazek, R. Dermisek and S. Raby, Phys. Rev. Lett. **88**, 111804 (2002); T. Blazek, R. Dermisek and S. Raby, Phys. Rev. D **65**, 115004 (2002); See also: H. Baer and J. Ferrandis, Phys. Rev. Lett. **87**, 211803 (2001).

[4] J. A. Bagger *et al.*, Phys. Lett. B **473**, 264 (2000).

[5] M. Albrecht, W. Altmannshofer, A. J. Buras, D. Guadagnoli and D. M. Straub, JHEP **0710** (2007) 055.

[6] W. Altmannshofer, D. Guadagnoli, S. Raby and D. M. Straub, Phys. Lett. B **668** (2008) 385.

[7] D. Guadagnoli, S. Raby and D. M. Straub, JHEP **0910** (2009) 059.

[8] K. Tobe and J. D. Wells, Nucl. Phys. B **663**, 123 (2003).

[9] M. S. Carena, S. Pokorski and C. E. M. Wagner, Nucl. Phys. B **406**, 59 (1993); B. Ananthanarayan, K. S. Babu and Q. Shafi, Nucl. Phys. B **428**, 19 (1994).

[10] V. D. Barger, A. D. Martin and R. J. N. Phillips, Z. Phys. C **21** (1983) 99.

[11] C. G. Lester and D. J. Summers, Phys. Lett. B **463**, 99 (1999).

[12] W. S. Cho, K. Choi, Y. G. Kim and C. B. Park, Phys. Rev. Lett. **100**, 171801 (2008).

[13] K. Choi, D. Guadagnoli, S. H. Im and C. B. Park, arXiv:1005.0618 [hep-ph].

SUSY parameter determination

Takanori Kono for the Fittino Collaboration

Institut für Experimentalphysik, University of Hamburg, DESY, Notketraße 85, 22607 Hamburg, Germany

DOI: http://dx.doi.org/10.3204/DESY-PROC-2010-01/255

1 Introduction

Since March 2010, the Large Hadron Collider (LHC) started deliverying proton-proton collisions at the center-of-mass energy of 7 TeV and the experiments are accumulating data at a rapid pace. Evidence of physics beyond the Standard Model (SM) may be discovered in a few years. Once evidence of new physics is discovered at the LHC, we must understand the model of the new physics and determine its fundamental parameters. Supersymmetry (SUSY) is one of the most attractive models which may solve several remaining problems of SM such as the hierarchy problem or the missing dark matter candidate.

We investigate the prospects of determining SUSY parameters taking the minimal supergravity (mSUGRA) as the model at the SPS1a benchmark point [1]. This is well-motivated from current experimental contraints as we shall explain in the next section. We show results expected with 1 and 10 fb^{-1} of integrated luminosity at the LHC. Also, we point out that there is an ambiguity on the particle assignments in the cascade decay such as $\tilde{q} \to q\tilde{\chi}_2^0 \to q l^{\pm}\tilde{l}^{\mp} \to q l^{\pm} l^{\mp} \tilde{\chi}_1^0$ and show how it affects the interpretatoin of data and the parameter determination.

2 SUSY parameter fit with Fittino

The program Fittino [2] has been used for the study presented here. The program consists of a collection of fitting algorithms and statistical tools with an interface to external theory programs using the Les Houches Accord format [3]. This allows to include any model into the framework. For the calculation of obsevables, SPheno [4] and Mastercode [5] were used to calculate SUSY and low energy observables, respectively.

Parameter	Best fit value	SPS1a value
M_0	$76.2^{+79.2}_{-29.1}$ (GeV)	100
$M_{1/2}$	331.5 ± 86.6 (GeV)	250
A_0	383.8 ± 647	-100
$\tan\beta$	13.2 ± 7.2	10

Table 1: Best fit value of mSUGRA parameters from low energy measurements. Values of the SPS1a benchmark point are also shown for comparison.

All measurements performed at various high energy experiments (LEP, SLC, Tevatron and B-factories) have been successfully explained by SM and there is no evidence of SUSY so far. However, some observables are sensitive to the effects of SUSY via higher order corrections such as the anomalous magnetic moment of the muon, $(g-2)_\mu$, and the cold dark matter relic density, Ω_{CDM}, from cosmological measurements. We refer to these existing observables

as *low energy observables*. It is possible to set constraints on the allowed region in the SUSY parameter space using these observables. A fit to the mSUGRA model with $\mathrm{sgn}(\mu) = +1$ was performed with measurements at LEP, SLC and Tevatron as well as $(g-2)_\mu$ and Ω_{CDM}, in order to derive the allowed region in the mSUGRA parameter space and the best fit point with uncertainties. The complete list of observables used in the fit can be found elsewhere [6].

The best fit values for M_0, $M_{1/2}$, A_0 and $\tan\beta$ are shown in table 1. It was found that $(g-2)_\mu$ and Ω_{CDM} were the most effective to constrain the parameter space. The values for the SPS1a benchmark point is shown too for comparison. It is seen that the best fit values are consistent with the benchmark point.

3 Prospects with LHC data and decay chain ambiguity

As seen in the previous section, the SPS1a benchmark point lies very close to the current best fit values within the mSUGRA model. Therefore, the SPS1a benchmark point has been used for the investigation of the SUSY parameter determination at the LHC. In general, observables with exclusive final states are considered for the SUSY parameter determination as they can be related to SUSY particle masses easily than more inclusive measurements. One example is the decay chain $\tilde{q} \to q\tilde{\chi}_2^0 \to q l^\pm \tilde{l}_R^\mp \to q l^\pm l^\mp \tilde{\chi}_1^0$ following the squark or gluino production. From such a decay chain, it is possible to reconstruct the invariant mass distribution of the two leptons. It is known that the kinematic end-point of the distribution is related to masses of SUSY particles involved in the decay, so that they can be included in the fit with an explicit formula. In addition to the above decay chain, similar decay chains, $\tilde{q} \to q\tilde{\chi}_2^0 \to q\tau^\pm \tilde{\tau}_R^\mp \to q\tau^\pm\tau^\mp\tilde{\chi}_1^0$ and $\tilde{q} \to q\tilde{\chi}_4^0 \to q l^\pm \tilde{l}_L^\mp \to q l^\pm l^\mp \tilde{\chi}_1^0$ are considered in the fit in order to increase the sensitivity. The full list of possible measurements at the LHC and expected uncertainties are taken from previous studies [1, 6] which are based on detailed studies by the ATLAS and CMS collaborations.

When one uses these observables, it is usually assumed that the SUSY particles involved in a certain decay chain are known. However, in a typical decay chain, e.g. $\tilde{q} \to q\tilde{\chi}_2^0 \to q l^\pm \tilde{l}^\mp \to q l^\pm l^\mp \tilde{\chi}_1^0$, all SUSY particles in the decay chain are not directly detected. As the squark undergoes a cascade decay towards the lightest SUSY particle (LSP), one only detects SM particles and a possible missing transverse energy ($E_{\mathrm{T}}^{\mathrm{miss}}$) in the detector, and relates the kinematic endpoints to the corresponding SUSY particle masses. However, there is no guarantee that the assumptions on the particles in the decay chain is correct. This may lead to a misinterpretation of the measurement and a wrong determination of SUSY parameters. Under the assumption that the signature $q l^\pm l^\mp + E_{\mathrm{T}}^{\mathrm{miss}}$ was produced within the mSUGRA framework, it is reasonable to consider that several neutralinos and sleptons (either right- or left-handed) were involved in the decay chain. This leads to considering the decay chain $\tilde{q} \to q\tilde{\chi}_i^0 \to q l^\pm \tilde{l}_{L,R}^\mp \to q l^\pm l^\mp \tilde{\chi}_j^0$ with all possible combinations of neutralinos and sleptons.

Among the observables considered here, the following three decay chains may be interpreted with different particle assignments.

(a) $\tilde{q} \to q\tilde{\chi}_2^0 \to q l^\pm \tilde{l}_R^\mp \to q l^\pm l^\mp \tilde{\chi}_1^0$

(b) $\tilde{q} \to q\tilde{\chi}_2^0 \to q\tau^\pm \tilde{\tau}_R^\mp \to q\tau^\pm\tau^\mp\tilde{\chi}_1^0$

(c) $\tilde{q} \to q\tilde{\chi}_4^0 \to q l^\pm \tilde{l}_L^\mp \to q l^\pm l^\mp \tilde{\chi}_1^0$

Fits were performed taking these ambiguities into account. Toy fits were repeated by smearing the observables around the best fit point. Toy fits are usually used in order to evaluate uncertainties on fit parameters. Here, one may use the same technique to obtain the probability

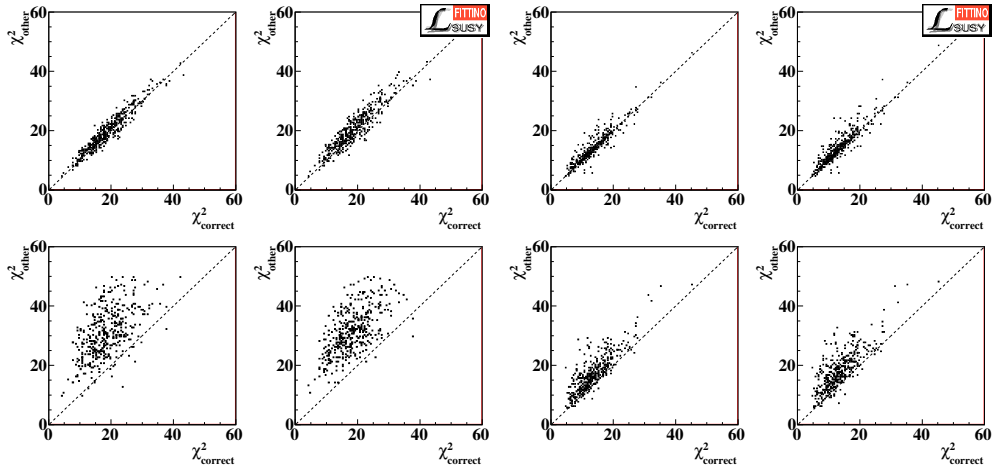

Figure 1: χ^2 correlation of the fit assuming (a) 10 fb^{-1} and (b) 1 fb^{-1} of luminoisty

that a wrong interpretation may have a smaller χ^2 than the correct interpretation, by comparing the χ^2 given by different interpretations. If such a probability is high, one can claim that the decay chain ambiguity must be considered seriously when interpreting the measurements. Figure 1 (a) shows the correlation of χ^2 between the correct model and the wrong interpretation ordered by the probability of having the lowest χ^2 among all interpretations considered assuming 10 fb^{-1} of luminosity at the LHC. Particle assignments considered in these cases and their probabilities of having the smallest χ^2 are given in table 2. In order to evaluate the results for 1 fb^{-1} of luminosity at the LHC, statistical uncertainties of the measurements were scaled according to the ratio of the luminosities while keeping the same values for systematic uncertainties. Results for 1 fb^{-1} of luminosity are shown in figure 1 (b) and table 3.

As tables 2 and 3 show, the probability of the wrong interpretation having smaller χ^2 reaches up to $\simeq 50\%$ and is bigger with larger statistical uncertainties on the measurements. In spite of performing a fit with a wrong interpretation, little differences in fitted parameters were observed in the case of 10 fb^{-1}. In case of 1 fb^{-1}, the fit results are rather unstable which indicates that better precision or more observables than considered here are necessary to have a reliable fit.

Table 2: Interpretation of the decay chain and the probability of it having the smallest χ^2 among other interpretations in the toy fit assuming 10 fb^{-1} of luminosity.

Interpretation of the decay chain	Probability (%)
Correct interpretation	69
(c) $\tilde{\chi}^0_3 \to l^\pm \tilde{l}^\mp_L \to l^\pm l^\mp \tilde{\chi}^0_2$	16
(c) $\tilde{\chi}^0_2 \to l^\pm \tilde{l}^\mp_R \to l^\pm l^\mp \tilde{\chi}^0_1$	12
(a) $\tilde{\chi}^0_3 \to l^\pm \tilde{l}^\mp_L \to l^\pm l^\mp \tilde{\chi}^0_1$, (b) $\tilde{\chi}^0_4 \to \tau^\pm \tilde{\tau}^\mp_R \to \tau^\pm l^\mp \tilde{\chi}^0_1$	3
(a) $\tilde{\chi}^0_3 \to l^\pm \tilde{l}^\mp_R \to l^\pm l^\mp \tilde{\chi}^0_1$, (b) $\tilde{\chi}^0_3 \to \tau^\pm \tilde{\tau}^\mp_R \to \tau^\pm l^\mp \tilde{\chi}^0_1$	< 0.1

Table 3: Interpretation of the decay chain and the probability of it having the smallest χ^2 among other interpretations in the toy fit assuming 1 fb^{-1} of luminosity.

Interpretation of the decay chain	Probability (%)
Correct interpretation	48
(a) $\tilde{\chi}_3^0 \to l^{\pm}\tilde{l}_R^{\mp} \to l^{\pm}l^{\mp}\tilde{\chi}_1^0$, (b) $\tilde{\chi}_3^0 \to \tau^{\pm}\tilde{\tau}_R^{\mp} \to \tau^{\pm}\tau^{\mp}\tilde{\chi}_1^0$	21
(a) $\tilde{\chi}_3^0 \to l^{\pm}\tilde{l}_L^{\mp} \to l^{\pm}l^{\mp}\tilde{\chi}_1^0$, (b) $\tilde{\chi}_4^0 \to \tau^{\pm}\tilde{\tau}_R^{\mp} \to \tau^{\pm}\tau^{\mp}\tilde{\chi}_1^0$	19
(a) $\tilde{\chi}_4^0 \to l^{\pm}\tilde{l}_R^{\mp} \to l^{\pm}l^{\mp}\tilde{\chi}_1^0$, (b) $\tilde{\chi}_3^0 \to \tau^{\pm}\tilde{\tau}_R^{\mp} \to \tau^{\pm}\tau^{\mp}\tilde{\chi}_1^0$	3.6
(a) $\tilde{\chi}_3^0 \to l^{\pm}\tilde{l}_L^{\mp} \to l^{\pm}l^{\mp}\tilde{\chi}_1^0$, (b) $\tilde{\chi}_4^0 \to \tau^{\pm}\tilde{\tau}_L^{\mp} \to \tau^{\pm}\tau^{\mp}\tilde{\chi}_1^0$	2.5

4 Conclusion

With the start of the LHC operation, evidence of SUSY may be discovered in the near future. The interpretation of experimental measurements and SUSY parameter determination are crucial for understanding the new physics model. Within the studied mSUGRA model, model parameters can be determined to a good precision with $\simeq 10$ fb^{-1} of luminosity at the LHC while the ambiguity in the particle assignment in the decay chain is not negligible while the differences in fitted parameters are modest.

References

[1] G. Weiglein *et al.* [LHC/LC Study Group], Phys. Rept. **426**, 47 (2006) [arXiv:hep-ph/0410364].

[2] P. Bechtle, K. Desch and P. Wienemann, Comput. Phys. Commun. **174** (2006) 47 [arXiv:hep-ph/0412012].

[3] B. Allanach *et al.*, Comput. Phys. Commun. **180** (2009) 8 [arXiv:0801.0045 [hep-ph]].

[4] W. Porod, Comput. Phys. Commun. **153** (2003) 275 [arXiv:hep-ph/0301101].

[5] O. Buchmueller *et al.*, Phys. Lett. B **657** (2007) 87 [arXiv:0707.3447 [hep-ph]].
O. Buchmueller *et al.*, JHEP **0809** (2008) 117 [arXiv:0808.4128 [hep-ph]],
O. Buchmueller *et al.*, Eur. Phys. J. C **64** (2009) 391 [arXiv:0907.5568 [hep-ph]],

[6] P. Bechtle, K. Desch, M. Uhlenbrock and P. Wienemann, Eur. Phys. J. C **66** (2010) 215 [arXiv:0907.2589 [hep-ph]].

CP-violation in SUSY cascades at the LHC

Jamie Tattersall[1], *Gudrid Moortgat-Pick*[2], *Krzysztof Rolbiecki*[1]

[1]IPPP, University of Durham, Durham DH1 3LE, UK
[2]II. Institut für Theoretische Physik, University of Hamburg,
Luruper Chaussee 149, 22761 Hamburg, Germany

DOI: http://dx.doi.org/10.3204/DESY-PROC-2010-01/256

We study the potential to observe CP-violating effects in SUSY cascade decay chains at the LHC. Asymmetries composed by triple products of momenta of the final state particles are sensitive to CP-violating effects. Due to large boosts that dilute the asymmetries, these can be difficult to observe. Extending the methods of momentum reconstruction we show that the original size of these asymmetries may be measurable. A study is done at the hadronic level with backgrounds to estimate the expected sensitivity at the LHC.

1 Introduction

The search for Supersymmetry (SUSY) is one of the main goals of present and future colliders since it is one of the best motivated extensions of the Standard Model (SM). An important feature of SUSY models is the possibility of incorporating new sources of CP violation that are required to accommodate the baryon asymmetry of the universe. A careful analysis of how to observe new CP-violating effects at the LHC will be required and in the following we discuss an example in the Minimal Supersymmetric Standard Model.

CP-odd observables are the unambiguous way of discovering hints of complex parameters in the underlying theory. One example of such observables are CP-sensitive asymmetries based on the exploitation of triple product correlations of momenta and/or spins of three final state particles with independent momentum, see also [1].

Here we examine the production of $\tilde{t}_1\tilde{t}_1^*$ at the LHC with the following decay chain, Fig. 2,

$$\tilde{t}_1 \to \tilde{\chi}_2^0 t, \qquad \tilde{\chi}_2^0 \to \tilde{\ell}\ell_N, \qquad \tilde{\ell} \to \tilde{\chi}_1^0 \ell_F, \qquad t \to bjj. \tag{1}$$

In this process [2] the main source of CP-violation comes from the phase of the top trilinear coupling $A_t = |A_t|\mathrm{e}^{\mathrm{i}\phi_{A_t}}$. As an observable we choose the T_N-odd triple product of momenta of the final state particles,

$$\mathcal{T} = \vec{p}_{\ell_N} \cdot (\vec{p}_W \times \vec{p}_t) \, . \tag{2}$$

Using this triple product one can construct a CP-odd asymmetry,

$$\mathcal{A}_T = \frac{N_{\mathcal{T}_+} - N_{\mathcal{T}_-}}{N_{\mathcal{T}_+} + N_{\mathcal{T}_-}} \, , \tag{3}$$

where $N_{\mathcal{T}_+}$ ($N_{\mathcal{T}_-}$) are the numbers of events for which $\mathcal{T}$ is positive (negative).

At the parton level, in the stop $\tilde{t}_1$ rest frame, the asymmetry can be as large as 15%, cf. Fig. 1(a). However, particles produced at the LHC get large, undetermined boosts that are a consequence of the internal proton structure. Due to these boosts the asymmetry is strongly diluted as can be seen by comparing Fig. 1(a) and Fig. 1(b). This makes the observation and analysis of CP-violating effects very difficult at the LHC. For further discussion of these effects and other studies of CP-violation in stop decays at the LHC see [3].

We show that a very useful tool in such an analysis is the reconstruction of momenta of all the particles involved in the process, including those escaping detection ($\tilde{\chi}_1^0$). Using this technique one can recover the large asymmetry present at the parton level by boosting back into the rest frame of the stop. Furthermore, we can heavily suppress both standard model and SUSY backgrounds using reconstruction. Therefore, we greatly increase the discovery potential and here we present the first hadronic study of momentum reconstruction in relation to CP-violation. The technique of momentum reconstruction for CP-violating observables was first presented in [4].

2 CP-violation in the laboratory frame

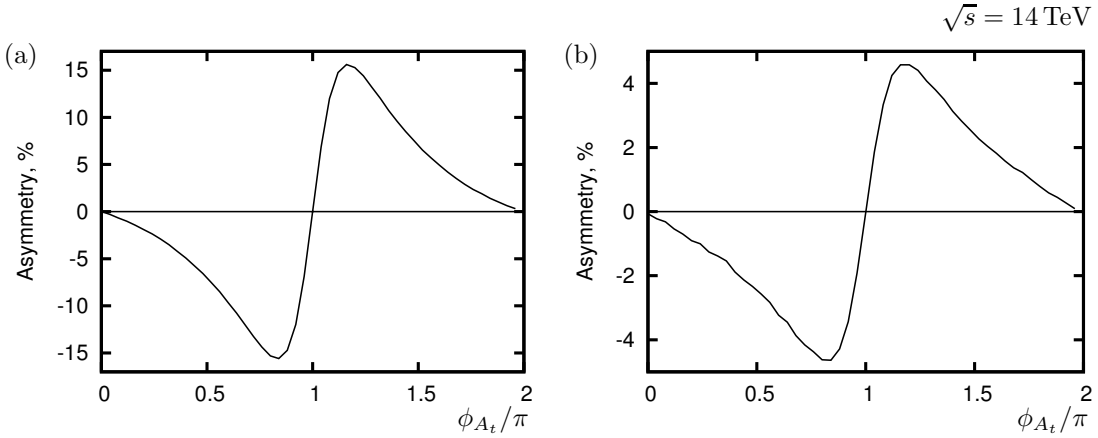

Figure 1: The asymmetry $\mathcal{A}_\text{T}$ as a function of ϕ_{A_t}, Eq. (3). (a) in the rest frame of $\tilde{t}_1$, (b) in the laboratory frame at the LHC at 14 TeV.

First we study the behaviour of the asymmetry after the inclusion of parton distribution functions (PDFs). Our observable, Eq. (3), is significantly reduced due to boosts compared with the asymmetry in the stop rest frame, where it is maximal, see Fig. 1(a). This is because a boosted frame can make the momentum vector of the lepton appear to come from the opposite side of the plane formed by W and t, hence changing the sign of the triple product, Eq. (2). Inclusion of PDFs reduce the asymmetry by about factor of 4 in our case. The maximum asymmetry is about $|\mathcal{A}_T| \simeq 4.5\%$ and if we use this asymmetry at the LHC it would be of limited statistical significance.

3 CP-violation with momentum reconstruction

In order to overcome the dilution factor due to PDFs, we investigate the possibility of reconstructing the momenta of the invisible particles ($\tilde{\chi}_1^0$) in the process on an event by event

basis [4, 5]. We perform the reconstruction at the hadronic level to verify the viability of the technique to the LHC.

For the decay chain of interest we can reconstruct the four unknown components of the $\tilde{\chi}_1^0$ momentum assuming me know the masses of the four particles involved in the cascade decay. We write down the four on-shell mass conditions,

$$m_{\tilde{\chi}_1^0} = (P_{\tilde{\chi}_1^0})^2, \quad (4)$$

$$m_{\tilde{\ell}} = (P_{\tilde{\chi}_1^0} + P_{\ell_F^+})^2, \quad (5)$$

$$m_{\tilde{\chi}_2^0} = (P_{\tilde{\chi}_1^0} + P_{\ell_F^+} + P_{\ell_N^+})^2, \quad (6)$$

$$m_{\tilde{t}_1} = (P_{\tilde{\chi}_1^0} + P_{\ell_F^+} + P_{\ell_N^+} + P_t)^2, \quad (7)$$

and solve the system.

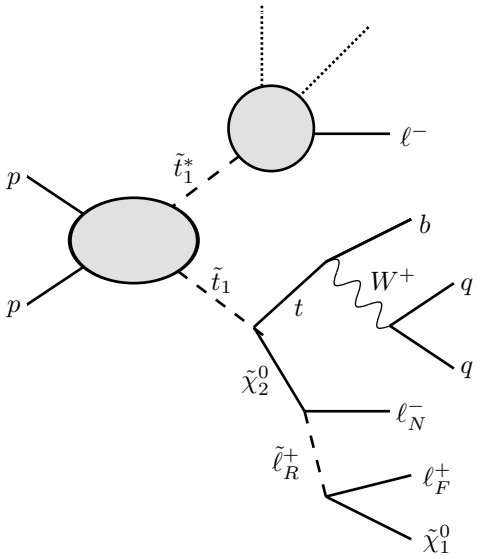

Figure 2: The process studied for momentum reconstruction.

Once we have the $\tilde{\chi}_1^0$ momentum we can trivially find the momentum of any other particle in the cascade decay. We can therefore find the momentum of the $\tilde{t}_1$ and boost all final state particles into this frame to recover the full asymmetry.

There is a complication in finding the $\tilde{\chi}_1^0$ momentum because if we solve Eq. (4-7) we see that we are left with a quadratic in $(P_{\tilde{\chi}_1^0})^2$. Consequently, we will have two viable solutions for the $\tilde{\chi}_1^0$ momentum but we cannot know which is correct. Since we do not have any additional constraints to pick the correct solution, we calculate the $\tilde{t}_1$ rest frame for both. However we only count those events that give the same sign for the triple product, Eq. (2). This guarantees that we take the correct sign for the triple product for the calculation of the asymmetry.

In addition, this method also significantly reduces the combinatorial background from wrong lepton or jet identification and both standard model and SUSY backgrounds [2]. For example, we need to correctly identify the near and far lepton in the cascade decay, Eq. 1, and our method is to try to perform reconstruction with both lepton assignments. Firstly, only a small subset of events with the wrong assignment will give real solutions for the $\tilde{\chi}_1^0$ momentum. Secondly, if the wrong assignment does satisfy the kinematical conditions, we only accept events where the sign of all triple products coincide. As one solution will have the true assignment we know the sign of the triple product will be correct and thus we will kill the combinatorial background.

Parameter	m_0	$m_{1/2}$	$\tan\beta$	sign(μ)	A_0
Value	65	210	5	+	0

Table 1: mSUGRA benchmark scenario.

To estimate the viability of this measurement at the LHC we study a mSUGRA scenario (Tab. 1) and produce fully hadronic events with a jet finder applied. We also apply realistic cuts for the LHC, implement experimental efficiencies (e.g. b-tagging). In addition, we require a top within a mass window to be reconstructed and include the most important standard model backgrounds. Within this scenario we find that the LHC should have sensitivity at 3-σ with $500\,\text{fb}^{-1}$ for $0.5\,\pi < \phi_{A_t} < 0.9\,\pi$.

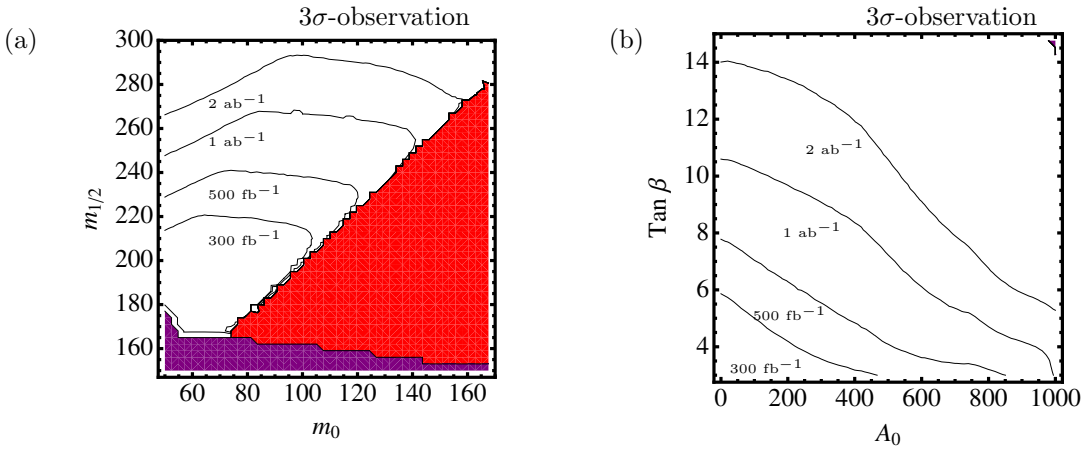

Figure 3: Minimum luminosity required for 3σ-discovery of CP-violation in $\tilde{t}_1\tilde{t}_1$ production at the LHC at 14 TeV. Purple (dark) area is ruled out by LEP direct detection and red (light) area has no two body decay $\tilde{\chi}_2^0 \to \tilde{\ell}^{\pm}\ell^{\mp}$. (a) $m_0, m_{1/2}$ plane, (b) $\tan\beta, A_0$ plane.

In Figs. 3(a, b) we see the effect of varying the mSUGRA parameters on the minimum luminosity required for a 3-σ observation at the LHC, assuming that the parton level asymmetry, $|\mathcal{A}_T| = 15\%$. We see that as $m_{1/2}$ is increased, Fig. 3(a), we require more luminosity due to an increased $\tilde{t}_1$ mass and hence smaller production cross section. An increase in both $\tan\beta$ and A_0 also produce a similar increase in the luminosity required for discovery. An increase in $\tan\beta$ reduces the $\tilde{\chi}_2^0 \to \tilde{\ell}^{\pm}\ell^{\mp}$ branching ratio while an increase in A_0 produces a smaller A_t that consequently reduces our sensitivity to the phase.

4 Acknowledgements

KR is supported by the EU Network MRTN-CT-2006-035505 (HEPTools). JT is supported by the UK Science and Technology Facilities Council (STFC).

References

[1] O. Kittel, arXiv:0904.3241 [hep-ph].

[2] G. Moortgat-Pick, K. Rolbiecki and J. Tattersall, arXiv:1008.2206 [hep-ph].

[3] A. Bartl, E. Christova, K. Hohenwarter-Sodek and T. Kernreiter, Phys. Rev. D **70** (2004) 095007 [arXiv:hep-ph/0409060]; P. Langacker, G. Paz, L. T. Wang and I. Yavin, JHEP **0707** (2007) 055 [arXiv:hep-ph/0702068]; J. Ellis, F. Moortgat, G. Moortgat-Pick, J. M. Smillie and J. Tattersall, *Eur. Phys. J.* **C60**, 633 (2009) [arXiv:0809.1607 [hep-ph]]; F. Deppisch and O. Kittel, JHEP **0909** (2009) 110 [Erratum-ibid. **1003** (2010) 091] [arXiv:0905.3088 [hep-ph]].

[4] G. Moortgat-Pick, K. Rolbiecki, J. Tattersall and P. Wienemann, JHEP **1001**, 004 (2010) [arXiv:0908.2631 [hep-ph]].

[5] K. Kawagoe, M. M. Nojiri and G. Polesello, *Phys. Rev.* **D71**, 035008 (2005) [arXiv:hep-ph/0410160]; H. C. Cheng, D. Engelhardt, J. F. Gunion, Z. Han and B. McElrath, *Phys. Rev. Lett.* **100**, 252001 (2008) [arXiv:0802.4290 [hep-ph]].

Missing energy commissioning in CMS and prospects for supersymmetry searches with 1 fb^{-1}

Robert Schöfbeck for the CMS Collaboration

Institute of High Energy Physics, Nikolsdorfergasse 18, Vienna, Austria

DOI: http://dx.doi.org/10.3204/DESY-PROC-2010-01/257

Supersymmetry may give rise to striking events that could be discovered early in LHC running. We discuss the prospects of discovery of search strategies based on the generic event signatures of high jet multiplicity and large missing transverse momentum. An important aspect of such searches is the commissioning of search variables with the first LHC data which we present in detail.

1 Introduction

The CMS detector [1] has nearly 4π solid angle coverage and is able to detect most species of particles produced in proton-proton (pp) collisions up to $|\eta| \approx 5$. Exceptions are neutrinos and hypothetical weakly interacting particles, which escape from the detector without leaving a trace. Their presence can still be inferred from the *missing transverse momentum* ($\vec{\not\!\!E}_T$), defined as the apparent imbalance of the component of the momentum in the plane perpendicular to the beam direction, and its magnitude is referred to as *missing transverse energy* ($\not\!\!E_T$).

$\not\!\!E_T$ is one of the most important variables for discriminating leptonic decays of W bosons from background events which do not contain neutrinos, such as QCD jet and Drell-Yan events. $\not\!\!E_T$ is also an important variable in any search for new particles that are weakly interacting or quasi-stable. Many beyond-the-standard-model scenarios, including Supersymmetry, predict events containing large $\not\!\!E_T$.

2 $\not\!\!E_T$ commissioning with early CMS data

$\not\!\!E_T$ is generally calculated as the magnitude of the negative vector sum of the momentum transverse to the beam axis of all final-state particles reconstructed in the detector. The most traditional and common algorithm uses energies deposited in calorimeter towers and assumes massless objects based on energies measured in the tower and angles defined by a vector from the reconstructed primary vertex of the event to the tower. CMS has implemented three types of algorithms to reconstruct $\not\!\!E_T$: (*i*) $\not\!\!E_T$ based on calorimeter energies (*Calo* $\not\!\!E_T$) [2], using the tower geometry of the hadron calorimeter, (*ii*) $\not\!\!E_T$ calculated by replacing the calorimeter tower energies matched to charged hadrons with their corresponding charged-track momenta (track-corrected $\not\!\!E_T$ or *Tc* $\not\!\!E_T$) [3], (*iii*) $\not\!\!E_T$ calculated using a complete particle-flow technique (*Pf* $\not\!\!E_T$) [4].

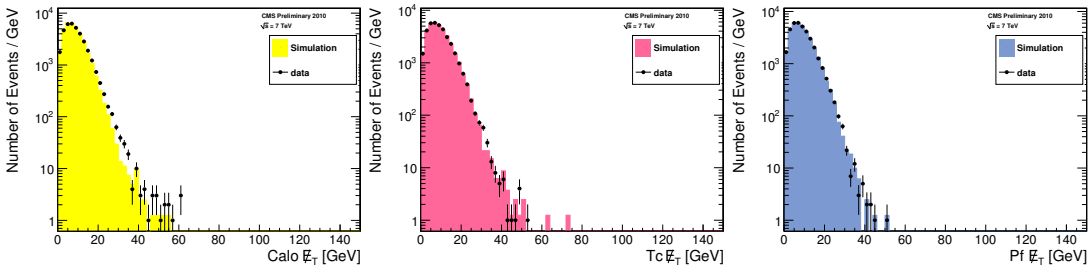

Figure 1: *Calo* $\not\!\!E_T$, *Tc* $\not\!\!E_T$ and *Pf* $\not\!\!E_T$ in a selection with two jets.

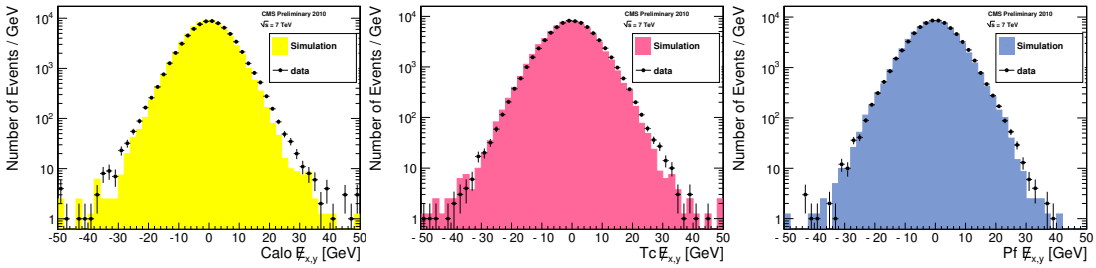

Figure 2: *Calo* $\not\!\!E_{x,y}$, *Tc* $\not\!\!E_{x,y}$ and *Pf* $\not\!\!E_{x,y}$ in a selection with two jets.

The data sets used for studies were collected since the end of March 2010 and correspond to an integrated luminosity of 272 μb^{-1}. The data samples were collected by the minimum-bias trigger and the dijet-selection requires two jets in the central rapidity range $|\eta| < 3$ passing the jet ID cuts and $p_T > 20$ or 10 GeV for the first and second hardest jet [5].

In Fig. 1 and Fig. 2 we show the $\not\!\!E_T$ and $\not\!\!E_{x,y}$ distributions for the three algorithms and note the good general agreement with simulation. The Monte Carlo distribution for Calo $\not\!\!E_T$ in Fig. 1 is somewhat narrower, consistent with the under-estimation of the $\not\!\!E_T$ resolution in the simulation [5]. The distributions in Fig. 2 have two entries per event; one for the x component and the other for the y component. As expected, they are roughly symmetric with respect to zero, and general agreement is observed between data and Monte Carlo distributions, although the data distributions are slightly wider, indicating worse $\not\!\!E_T$ resolution. This observed difference is primarily attributed to the imperfect response in the HCAL barrel and endcap regions. There is also a slight asymmetry in the $\not\!\!E_{x,y}$ distributions which is partially due to the non-uniform noise contributions in the ECAL endcap in the azimuthal angle.

3 Prospects for SUSY searches

The phenomenology of mSUGRA models [6, 7] has been studied extensively in the literature, partly because these models have the attractive feature that they can be specified by just four parameters and a sign:

$$m_0, m_{1/2}, \tan\beta, A_0, \mathrm{sign}(\mu) \tag{1}$$

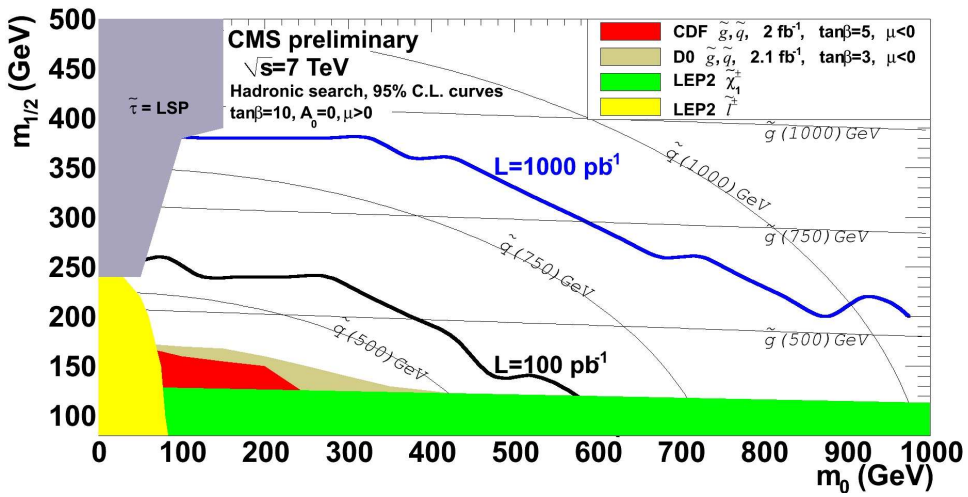

Figure 3: Estimated 95% C.L. exclusion limits for the all-hadronic SUSY search, expressed in mSUGRA parameter space.

where m_0 is the common mass of the scalars at the supersymmetric GUT scale, $m_{1/2}$ is the common gaugino mass, A_0 is the common soft trilinear SUSY breaking parameter, $\tan\beta \equiv v_u/v_d$ is the ratio of the two Higgs vacuum expectation values, and sign(μ) is the sign of Higgsino mass parameter. For the CMS sensitivity scans, we have chosen $A_0 = 0$, $\tan\beta = 3$ or 10, and sign(μ) to be positive. With these parameters fixed, the sensitivity curves are displayed in the plane of $m_{1/2}$ vs. m_0 in Fig. 3. The sensitivity curves are based on the expected signal yield, which is a function of position in mSUGRA parameter space (due to variation in both the cross section and in the efficiency), and the expected background (and its uncertainty), which is only a function of the cuts. No attempt was made to optimize the selection cuts as a function of position in mSUGRA space.

Figure 3 shows the 95% C.L. upper limit contours [8] for the all-hadronic search at two values of the integrated luminosity, 100 pb^{-1} and 1 fb^{-1}, for $\tan\beta = 10$ at $\sqrt{s} = 7$ TeV. Some aspects of this plot require care in interpretation. The exclusion regions for the CDF [9] measurement are defined for $\tan\beta = 5$, while those from D0 [10] are defined for $\tan\beta = 3$. These Tevatron searches are both based on jets + missing transverse momentum signatures using approximately 2 fb^{-1}. The LEP exclusion regions are based on searches for sleptons and charginos [11]. Preliminary CMS studies of the hadronic channel indicate that its sensitivity is only weakly dependent on the value of $\tan\beta$.

Figure 4 shows the 95% C.L. upper limit contours for the like-sign dilepton search, combining the $\mu^\pm\mu^\pm$, $\mu^\pm e^\pm$ and $e^\pm e^\pm$ channels. For comparison, we show the exclusion region from recent CDF and D0 trilepton analyses [12, 13]. Both CMS and Tevatron analyses assumed $\tan\beta = 3$ in evaluating the sensitivity curves. The peaks in the sensitivity curve at low $m_{1/2}$ and for $m_{1/2}$ 450 GeV reflect the rate of production of like-sign dileptons in mSUGRA models.

These results indicate that in the 7 TeV run, CMS should have sensitivity to regions of SUSY (mSUGRA) parameter space beyond the current Tevatron limits. Both of the channels discussed here (all-hadronic and like-sign dileptons) should be able to yield interesting sensitivities well before 1 fb^{-1}.

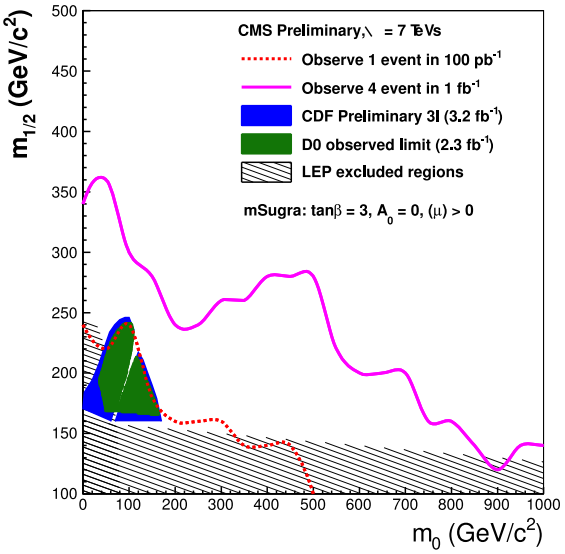

Figure 4: Estimated 95% C.L. exclusion limits for the like-sign dilepton SUSY search, expressed in mSUGRA parameter space. The expected background from the standard model at 100 pb^{-1} (1 fb^{-1}) is 0.4 (4.0) events; we have assumed an observed yield of 1 event (4 events) for the purpose of setting these exclusion limits.

References

[1] G. L. Bayatian *et al.* [CMS Collaboration], "CMS physics: Technical design report".

[2] CMS Collaboration, "Missing ET Performance in CM", CMS Physics Analysis Summary JME-07-001 (2007).

[3] CMS Collaboration, "Track-corrected Missing Transverse Energy in CM", CMS Physics Analysis Summary JME-09-010 (2009).

[4] CMS Collaboration, "Particle-Flow Event Reconstruction in CM", CMS Physics Analysis Summary PFT-09-001 (2009).

[5] CMS Collaboration, "Jet and MET Commissioning Results from 7 TeV Collission Data", CMS Detector Performance Summary DPS-2010-014.

[6] A. H. Chamseddine, R. L. Arnowitt and P. Nath, "Locally Supersymmetric Grand Unification", Phys. Rev. Lett. **49** (1982) 970.

[7] E. Cremmer, P. Fayet and L. Girardello, "Gravity Induced Supersymmetry Breaking And Low-Energy Mass Spectrum", Phys. Lett. B **122**, 41 (1983).

[8] J. Conway, CDF/Pub/Statistics/Public/6428 (2005).

[9] CDF Collaboration (T. Altonen et al.), Phys. Rev. Lett. 102, 121801 (2009); arXiv.org:0811.2512; the CDF exclusion region in the $m_{1/2}$ vs. m_0 plane appears in CDF Public Note 9229, March 2008.

[10] D0 Collaboration (V.M. Abazov et al.), Phys. Lett. B 660, 449 (2008); arXiv.org:0712.3805.

[11] LEPSUSYWG; ALEPH, DELPHI, L3, and OPAL Collaborations, note LEPSUSYWG/02-06.2, http://lepsusy.web.cern.ch/lepsusy.

[12] CDF Collaboration, CDF/PUB/EXOTIC/PUBLIC/9817 (2009).

[13] D0 Collaboration, V. Abazov et al., Phys. Lett. B 680, 34 (2009).

Drell-Yan production of heavy vectors in Higgsless models

Oscar Catà[1], *Gino Isidori*[1,2], *Jernej F. Kamenik*[3*]

[1]INFN, Laboratori Nazionali di Frascati, Via E. Fermi 40 I-00044 Frascati, Italy
[2]TUM Institute for Advanced Study, Technische Universität München, Arcisstr. 21, D-80333 München, Germany
[3]J. Stefan Institute, Jamova 39, P. O. Box 3000, 1001 Ljubljana, Slovenia

DOI: http://dx.doi.org/10.3204/DESY-PROC-2010-01/261

One or more heavy spin-1 fields may replace the Higgs boson in keeping perturbative unitarity up to a few TeV while at the same time account for the electroweak precision tests. We study the Drell-Yan production of heavy vector and axial-vector states in generic Higgsless models at hadron colliders. We analyse in particular the l^+l^-, WZ, and three SM gauge boson final states. In the l^+l^- case we show how present Tevatron data restricts the allowed parameter space of these models. The two and three gauge boson final states (especially WZ, WWZ, and WZZ) are particularly interesting in view of the LHC, especially for light axial-vector masses, and could shed more light on the role of spin-1 resonances in the electroweak precision tests.

1 Motivation

Experiments provide unambiguous indications that the SM gauge group is spontaneously broken $[SU(2)_L \times U(1)_Y \to U(1)_Q]$. One elementary $SU(2)_L$ scalar doublet with ϕ^4 potential is the most economical and simple choice. However it is not the only allowed possibility. So far only the ground state of this Lagrangian has been tested with good accuracy through the mass measurements of W and Z, $\langle\phi\rangle \equiv v = 246\text{GeV}$. Some dynamical sensitivity to the Higgs mechanism is obtained from electroweak precision observables (EWPO), which actually provide an indirect indication for a light Higgs, when the SM is regarded as an effective theory with a very high cut-off scale. But do we really need a fundamental Higgs field? EWPO indicate a spontaneous breaking of $SU(2)_L \times U(1)_Y$ where the breaking mechanism must respect, to a good accuracy, the custodial symmetry $[m_Z^2/m_W^2 \simeq 1 + (g'/g)^2]$. General formulation of the symmetry breaking mechanism in absence of a fundamental Higgs (or for large Higgs masses) can be done in terms of a Chiral Lagrangian

$$\mathcal{L}_\chi^{(2)} = \frac{v^2}{4}\text{Tr}[D_\mu U^\dagger D^\mu U]\,, \tag{1}$$

where the field $U = \exp(i\Pi/v)$ containing the broken symmetry generators transforms under the global $SU(2)_L \times SU(2)_R$ symmetry as $U \to g_R U g_L^\dagger$, while its covariant derivate under the

*Speaker

gauged $SU(2)_L \times U(1)_Y$ subgroup reads $D_\mu U = -ig' B_\mu U + igUW_\mu$. The spontaneous breaking of the global symmetry down to its vectorial part $SU(2)_{L+R}$ breaks the gauged subgroup down to $U(1)_Q$. The resulting EW chiral Lagrangian contains all the degrees of freedom we have directly probed in experiments. The naïve cut-off of the theory is dictated by the convergence of EW loops: $\Lambda_{NDA} = 4\pi v \approx 3\text{TeV}$. It perfectly describes particle physics up 3 TeV even beyond the tree level with only two drawbacks (which point towards the existence of new degrees of freedom below the naïve cut-off): (1) violation of unitarity in longitudinal $W_L W_L \to W_L W_L$ scattering (tree-level amplitude violates unitarity for center-of-mass energy $\sqrt{s} \approx 1\text{TeV}$); (2) a bad fit to EWPO S and T [1].

2 Introducing the Heavy Vectors

A natural alternative to Higgs-type mechanisms in curing the problem of unitarity in $WW \to WW$ scattering is represented by heavy vector fields. These are expected in many non-SUSY scenarios: techni-rho in technicolor or massive gauge bosons in 5-dimensional theories and hidden gauge models. The difficult task here is to cure at the same time unitarity and EWPO. It can be analysed in general terms by constructing an appropriate effective chiral Lagrangian with the heavy vector resonances (R) as new explicit d.o.f.

$$\mathcal{L}_\chi = \mathcal{L}_\chi^{(2)} + \mathcal{L}_{kin}(R, U, A_i; m_R) + \mathcal{L}_{int}(R, U, A_i; G_R, F_R, g_R)\,, \tag{2}$$

see ref. [2] for all parameter definitions and notation. We consider an effective theory based on the following two main assumptions [2]: (1) The (new) dynamics that breaks the SM EW symmetry is invariant under the global symmetry $SU(2)_L \times SU(2)_R$ and under the discrete parity P: $SU(2)_L \leftrightarrow SU(2)_R$. (2) One vector (V), or one vector + one axial-vector (V+A), both belonging to the adjoint representation of $SU(2)_{L+R}$ (triplets), are the only light fields below a cut-off $\Lambda = 2{-}3\,\text{TeV}$. An effective Lagrangian expansion can now be performed for these vector fields based on ordering of operators according to the standard derivative (momentum) expansion.

The tree level unitarity of WW scattering can be cured completely via the exchange of a single intermediate vector resonance provided the VW_LW_L coupling G_V takes on a particular value $G_V^2 = v^2/3$. Requiring the theory to be unitary only below the naive cut-off, the unitarity constraint is almost insensitive to the value m_V [2]. Also the leading contributions to S & T are generated by the exchange of single heavy fields. While S is affected already at the tree level, T only receives contributions at one-loop. It turns out there are two natural ways to accommodate the bounds when these leading order effects are taken into account. Either both V and A are light and almost degenerate, or only V is light, with a small VW_LW_T coupling F_V. In both cases EWPO and unitarity can be accommodated for specific choices of the free parameters ($F_{A,V}$, G_V). The main conclusion is however that we need *at least one relatively light vector field* [2] and it remains true even if both S and T are evaluated at the one-loop level [3].

3 Production of Heavy Vectors at Hadron Colliders

The main property of the vector fields is that the leading decay mode is into 2 longitudinal SM gauge bosons

$$\Gamma_V^+ \approx \Gamma_{WZ}^V = \frac{G_V^2 m_V^3}{48\pi v^4}[1+\mathcal{O}(g^2\epsilon^2)]\,, \quad \Gamma_V^0 \approx \Gamma_{WW}^V = \Gamma_{WZ}^V[1+\mathcal{O}(g^2\epsilon^2)]\,, \tag{3}$$

where $\epsilon = v^2/m_V^2$, resulting in typically narrow widths of 5(40) GeV at heavy vector masses of 0.5(1.0) TeV. Note also that the ZZ channel is forbidden at tree level and that the coupling of heavy vectors to SM fermions is highly suppressed

$$Br(V^0 \to q\bar{q}) \approx 3Br(V^0 \to \ell^+\ell^-) \approx \frac{6F_V^2 m_W^4}{G_V^2 m_V^4}\,, \tag{4}$$

which translates into 1.6(0.1)% at heavy vector mass of 0.5(1.0) TeV. The main differences, when discussing axial resonances compared to vector ones, is that their decays to pairs of longitudinal SM gauge bosons are forbidden by parity so that depending on phase space the leading decay modes can be to pairs of heavy vectors and SM gauge fields (governed by an independent VAW coupling g_A). This in turn leads to interesting phenomenology of three gauge boson final states.

The most general signature of Higgsless models is the appearance of the vector state in WW scattering [$pp \to V + jj(WW\,\text{fusion}) \to WW(WZ) + jj$]. It constitutes a model-independent link with the unitarity problem. However, this requires a difficult analysis and high statistics[4]. A potentially cleaner signal (if the resonances are not too heavy) is the Drell-Yan production of the resonances and subsequent decay into l^+l^-, 2 and 3 SM heavy gauge bosons [5]. These channels constitute a link to the contribution of the heavy vectors to EWPO. Given the narrow widths, for low masses the signals are quite large (see table 1). However, the leading decay

	$M = 500$ GeV	$M = 750$ GeV	$M = 1000$ GeV
$\sigma(pp \to V^+ \to X)_{\sqrt{s}=14\ \text{TeV}}$	11 pb	1.2 pb	0.23 pb
$\sigma(pp \to V^+ \to X)_{\sqrt{s}=10\ \text{TeV}}$	6.7 pb	0.7 pb	0.13 pb
$\sigma(pp \to V^+ \to X)_{\sqrt{s}=7\ \text{TeV}}$	4.2 pb	0.32 pb	0.06 pb

Table 1: Summary of the leading-order cross sections for the production of a light charged vector resonance in pp collisions at $\sqrt{s} = 14$ TeV, $\sqrt{s} = 10$ TeV and $\sqrt{s} = 7$ TeV . The results are obtained summing over all decay products in the mass range $|M_X - M_V| \leq 3\Gamma_V$, setting $F_V = 2G_V$, and fixing G_V from unitarity ($G_V = v/\sqrt{3}$). The results for different values of F_V can be obtained scaling the figures in the table by $F_V^2/(2G_V)^2$.

modes (2W, 3W) have low reconstruction efficiencies while the l^+l^- case is suppressed by the small $Br(R \to l^+l^-)$.

The l^+l^- state of the art is the analysis of the e^+e^- (and di-muon) final states in $p - \bar{p}$ collisions published by CDF [6] and D0[7]. Using the CDF e^+e^- data as normalization for the SM events (which takes into account all the relevant exp. efficiencies), we have produced an exclusion plot in the $F_V - m_V$ plane (see figure 4 in ref.[5]). The result is obtained under two

main assumptions: G_V is fixed by tree-level unitarity and $m_A \gg m_V$. Including the analysis of the di-muon channel removes all the areas, where an excess is seen in the electron-positron data. If, on the other hand, an excess at higher mass will become significant, we can hope to see a clear signal at the LHC (even with $1-2\,\mathrm{fb}^{-1}$). No huge peaks as with a sequential Z' are expected, but they should be clearly visible [5].

More prospective are two and three SM gauge boson final states. Some illustrative examples are shown on figures 6 – 8 in ref.[5], where we have used $F_V = 2G_V$, $F_A = F_V$ and G_V is fixed by unitarity, while $g_A = 1/2$. Note that the expected reconstructed signal will necessarily be further suppressed by typically low reconstruction efficiencies, e.g. for the purely leptonic channels $[WZ]BrZ_{lept} \times BrW_{lept} = 1.5\%$ while for $[WWZ]BrZ_{lept} \times BrW_{lept} \times BrW_{had} = 0.9\%$. Due to the typically sizable contribution of the intermediate vector resonance in the WWZ final state it is also worth looking at the WZ invariant- mass distribution.

4 Conclusions

Heavy vector fields, which replace the Higgs boson in maintaining perturbative unitarity up to LHC energies, are naturally expected in a wide class of Higgsless models. The most general signature of these models is the appearance of the lightest vector state in WW scattering (model-independent link with the unitarity problem). The Drell-Yan production of the new states is subject to larger uncertainties (see also [8]). For light $m_{V(A)}$ we could expect visible signals (even with low statistics), and the information could help to clarify the role of the heavy vectors in EWPO. The results in the e^+e^- channel from Tevatron are already providing significant information, while the 2 and 3 SM gauge boson final states seem to be quite promising and would deserve a more realistic study.

References

[1] M. E. Peskin and T. Takeuchi, Phys. Rev. Lett. **65**, 964 (1990); G. Altarelli and R. Barbieri, Phys. Lett. B **253**, 161 (1991).

[2] R. Barbieri, G. Isidori, V. S. Rychkov and E. Trincherini, Phys. Rev. D **78**, 036012 (2008).

[3] O. Catà and J. F. Kamenik, in preparation.

[4] A. Belyaev, arXiv:0711.1919 [hep-ph].

[5] O. Catà, G. Isidori and J. F. Kamenik, Nucl. Phys. B **822**, 230–244 (2009).

[6] T. Aaltonen *et al.* [CDF Collaboration], Phys. Rev. Lett. **102**, 031801 (2009); *ibid.* **102** , 091805 (2009).

[7] D0 Conf. Note 5923.

[8] R. Barbieri, A. E. Carcamo Hernandez, G. Corcella, R. Torre and E. Trincherini, JHEP **1003**, 068 (2010).

Flavour physics

B Physics (Experiment)

Michal Kreps

KIT, Wolfgang-Gaede-Straße 1, 77131 Karlsruhe, Germany

DOI: http://dx.doi.org/10.3204/DESY-PROC-2010-01/25

In the past few years flavor physics made an important transition from the work on confirming the standard model of particle physics to the phase of search for effects of new physics beyond the standard model. In this paper we review the current state of the physics of b-hadrons with an emphasis on results with sensitivity to new physics.

1 Introduction

The beginning of b-physics dates back to 1964 when the decay of the long-lived kaon to two pions and thus CP-violation was observed [1]. It did not take very long until a theoretical explanation of CP-violation was proposed. In their famous work, Kobayashi and Maskawa showed that with four quarks there is no reasonable way to include CP-violation [2]. In addition they proposed several models to explain CP-violation in the kaon system, amongst which the six quark model got favored over time.

The explanation of CP-violation in the six quark model of Kobayashi and Maskawa builds on the idea of quark mixing introduced by Cabibbo. The quark mixing introduces a difference between the eigenstates of the strong and weak interactions. CP-violation requires a complex phase in order to provide a difference between a process and its charge conjugate. In the four quark model, the quark mixing is described by a 2×2 unitary matrix. With only four quarks, states can always be rotated in order to keep the mixing matrix real and thus four quark mixing cannot accommodate the CP-violation. Other arguments, which we are not going to discuss here, prevent also the suitable inclusion of the CP-violation in other parts of the theory. With the extension to six quarks, the mixing matrix becomes a 3×3 unitary matrix, called the Cabibbo-Kobayashi-Maskawa matrix, V_{CKM}. In this case there is no possibility to rotate away all phases and one complex phase always remains in the matrix. This complex phase of V_{CKM} provides CP-violation in the standard model. The idea has two important implications: First, in addition to the three quarks known in the early 1970's and the predicted charm quark, it postulates the existence of two additional quarks, called bottom and top. Second, despite the tiny CP-violation in the kaon system, the proposed mechanism predicts large CP-violation in the B-system. It took almost three decades, but both predictions have been confirmed experimentally, first by discovering the bottom quark in 1977 [3], second by the top quark discovery in 1995 [4, 5], and finally by the measurement of large CP-violation in the B^0-system in 2001 [6, 7].

In order to test the Kobayashi-Maskawa mechanism of CP-violation many measurements are performed. Their main aim is to determine V_{CKM} with the highest possible precision. Tests are often presented in the form of the so-called unitarity triangle. It follows from the

unitarity requirement of V_{CKM}. The product of the two columns of the matrix has to be zero in the standard model. As the elements of the matrix are complex numbers, this requirement graphically represents a triangle in the complex plane. In the last decade flavor physics moved towards the search for inconsistencies which would indicate the presence of new physics. We omit the charm mixing and CP-violation prospects of starting experiments which are discussed elsewhere in these proceedings. Here we concentrate on the big picture with some emphasis on tensions in various measurements performed by the *BABAR*, Belle, CDF, CLEO-c and DØ experiments.

2 Sides of the unitarity triangle

Looking to the unitarity triangle there are two sets of quantities one can determine, namely angles and sides. In this section we will discuss the status of the determination of sides. They are determined by the V_{td}, V_{ub} and V_{cb} elements of V_{CKM}. To determine those quantities, two principal measurements are used. The first is the measurement of the B^0 oscillation frequency which determines V_{td}. The second is the measurement of the branching fraction of semileptonic B decays, which can be translated to V_{ub} or V_{cb}. As there are no recent results on B mixing, we concentrate on semileptonic decays and the determination of V_{ub} and V_{cb}.

The determination of V_{ub} and V_{cb} is based on the $b \to u\,l\,\nu$ and $b \to c\,l\,\nu$ transitions. The advantage of semileptonic transitions is that all soft QCD effects are contained in a single form factor. In general two complementary approaches exist. The first one is inclusive measurements, where one tries to measure the inclusive rate of $B \to X_{(c,u)}\,l\,\nu$ with $X_{(c,u)}$ denoting any possible hadron containing a charm or an up quark. The second approach uses exclusive measurements where one picks up a well defined hadron like D^* in the case of V_{cb} measurement. The two approaches are complementary; with the inclusive approach being theoretically clean at first order, while the exclusive approach is much cleaner in the experiment, but more difficult in theory. In addition, part of the good properties of the inclusive approach on the theory side is destroyed by the necessity of kinematic requirements on the experimental side. As one needs good control over the background in those measurements, it is practically the domain of e^+e^- B-factories running at the $\Upsilon(4S)$ resonance.

Coming to the current status, determinations of V_{cb} as well as V_{ub} have some issues and inconsistencies [8]. On the one hand, in the inclusive determination of V_{cb} the fit to all information has consistently a too small χ^2. On the other hand, in the exclusive determination using $B \to D^*l\,\nu$ decays, different measurements are not fully consistent with $\chi^2/ndf = 56.9/21$. This inconsistency is due to the differences between the Belle and *BABAR* results rather than inconsistence between old and new measurements. The world average determined from the inclusive measurement is $V_{cb} = (41.5 \pm 0.44 \pm 0.58) \times 10^{-3}$, from $B \to D\,l\,\nu$ we obtain $V_{cb} = (39.4 \pm 1.4 \pm 0.9) \times 10^{-3}$, and from $B \to D^*l\,\nu$ we obtain $V_{cb} = (38.6 \pm 0.5 \pm 1.0) \times 10^{-3}$. Obviously, despite the tension in the experimental information from $B \to D^*l\,\nu$ decays, the two exclusive determinations agree with each other, but the inclusive approach yields a value which is about $2.3\,\sigma$ higher than that from the exclusive determinations.

While the determination of V_{ub} in principle is the same as the determination of V_{cb}, in practice it is much more difficult due to the smallness of the $b \to u\,l\,\nu$ branching fraction compared to that of $b \to c\,l\,\nu$. The $b \to c\,l\,\nu$ decay in this case is a significant background. The kinematic selection to reduce this background destroys the possibilities of the theory for precise and reliable calculations. On the inclusive determination side, there are several groups

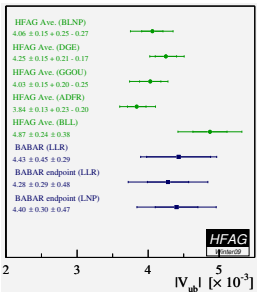

Figure 1: Summary of different inclusive determinations of V_{ub} from semileptonic $b \to u\,l\,\nu$ decays [8].

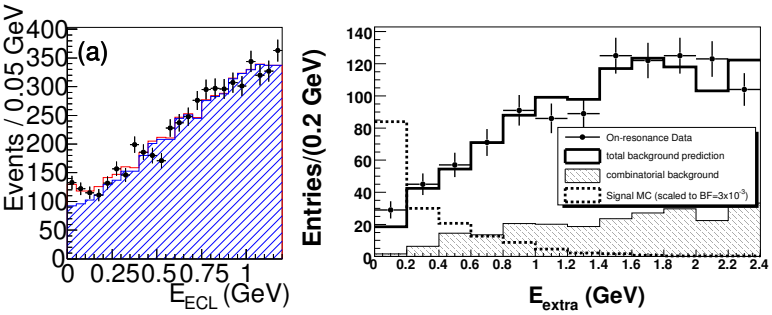

Figure 2: Distribution of the remaining energy in $B \to \tau\,\nu$ searches using semileptonic tag at Belle (left) and fully hadronic tag at *BABAR* (right).

which perform fits to the experimental data of inclusive decays. On the exclusive determination side, the *BABAR* experiment provides new results on $B \to \pi\,l\,\nu$ and $B \to \rho\,l\,\nu$. Using their partial branching fraction in different momentum transfer regions together with lattice QCD calculations they derive $|V_{ub}| = (2.95 \pm 0.31) \times 10^{-3}$ [9], which is about $2\,\sigma$ below the inclusive determinations. If this persists, we have another discrepancy in the sides of the unitarity triangle.

Another way of accessing V_{ub} is to use $B^+ \to \tau\,\nu$ leptonic decays which proceed through weak annihilation. In the standard model its rate is given by the expression

$$BF = \frac{G_F^2 m_B}{8\pi}\, m_l^2 \left(1 - \frac{m_l^2}{m_B^2}\right)^2 f_B^2 |V_{ub}|^2 \tau_B\,, \tag{1}$$

where all quantities except for f_B^2 and V_{ub} are well known. Typically one takes f_B^2 and V_{ub} as input from other measurements and puts constraints on new physics. Alternatively one can take the measured branching fraction together with the prediction for f_B^2 and extract V_{ub}. B-factories recently provided evidence for this decay. Both, Belle and *BABAR* reconstruct one B in a semileptonic or a fully hadronic decay, called tagged, together with identified charged products of the τ decay. In such events, all what should be remaining are neutrinos and therefore one expects zero additional energy in the event. In Fig. 2 we show examples of the distribution of additional energy. The Belle experiment sees evidence on the level of $3.5\,\sigma$ in both tags [10, 11], while the *BABAR* experiment obtains an excess of about $2.2\,\sigma$ [12, 13]. The world average of the branching fraction of $(1.73 \pm 0.35) \times 10^{-4}$ is a little higher than the SM prediction of $(1.20 \pm 0.25) \times 10^{-4}$ and yields a value of V_{ub} which is in some tension with other determinations.

The result of the $B^+ \to \tau\,\nu$ branching fraction brings up the question whether the theory prediction from lattice QCD for f_B^2 is correct. One way to test predictions is to turn to the charm sector where we expect smaller contributions from new physics. The decay $D_s^+ \to \tau^+\nu$ is a usual testing ground for calculations. The branching fraction is given by the same formula as for $B^+ \to \tau\,\nu$, replacing f_B^2 and V_{ub} by their appropriate counterparts. The branching fraction for $D_s^+ \to \tau^+\nu$ was measured by the CLEO, *BABAR* and Belle experiments and there used to be some discrepancy between the prediction for f_{D_s} and its value extracted from the $D_s^+ \to \tau^+\nu$ data. A summary of the evolution of this discrepancy is shown in Fig. 3 [14]. The current

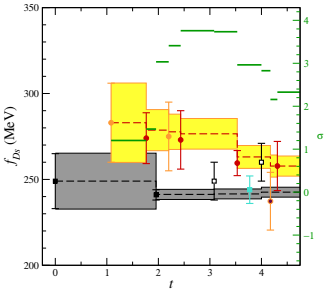

Figure 3: Comparison of the predicted f_{D_s} with experimental results. The circles denote experimental values with the yellow band showing the average. The squares show the prediction and the gray area the theory average. The green lines denote the difference between theory and experiment in Gaussian σ. The time t is measured in years since June 2005.

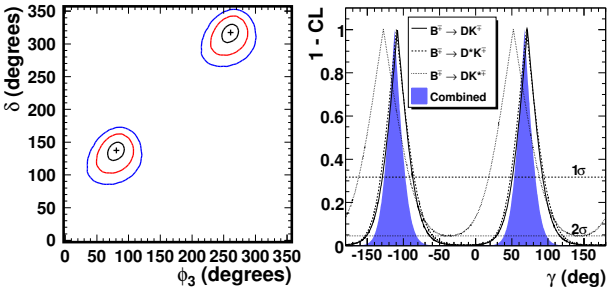

Figure 4: Confidence regions in the plane of the strong phase δ and the CKM angle γ/ϕ_3 from the Belle experiment (left) and 1-CL for the CKM angle γ from the *BABAR* experiment (right). In the left plot, the contours correspond to 1, 2 and 3 standard deviations. In the right plot, separate contours for the decays $B^+ \to D^0 K^+$, $B^+ \to D^{*0} K^+$, and $B^+ \to D^0 K^{*+}$ and a combination of all are shown.

situation is not too critical anymore as the discrepancy went down from $4\,\sigma$ to $2\,\sigma$. With this we conclude the discussion of sides of the unitarity triangle, where despite a lot of experimental work and large progress several tensions remain.

3 Angles of the unitarity triangle

The angles of the unitarity triangle are defined as

$$\alpha = \arg\left(-V_{td}V_{tb}^*/V_{ud}V_{ub}^*\right), \quad (2)$$
$$\beta = \arg\left(-V_{cd}V_{cb}^*/V_{td}V_{tb}^*\right), \quad (3)$$
$$\gamma = \arg\left(-V_{ud}V_{ub}^*/V_{cd}V_{cb}^*\right). \quad (4)$$

As they are given by the phases of complex numbers, their determination is possible only through measurements of CP-violation. Here we omit the determination of the angle α, briefly mention the status of the angle β, and concentrate on the angle γ which received most of the new experimental information.

The angle β is practically given by the phase of V_{td}. One of the processes where this CKM matrix element enters is the B^0 mixing. Its best determination comes from the measurement of CP-violation due to the interference of decays with and without mixing to a common final state. Using decays to the $c\,\bar{c}$ resonance with a neutral kaon *BABAR* extracts $\sin 2\beta = 0.687 \pm 0.028 \pm 0.012$ using the final dataset [15]. The latest measurement from Belle gives $\sin 2\beta = 0.642 \pm 0.031 \pm 0.017$ [16]. It is worth to note that both experiments are still statistically limited.

The determination of the angle γ provides important information for tests of physics beyond the standard model. It is determined from the interference of tree level $b \to c$ and $b \to u$ transitions and thus has small sensitivity to new physics. While several different decays are suggested for the determination, all current experimental information comes from $B^+ \to D^0 K^+$.

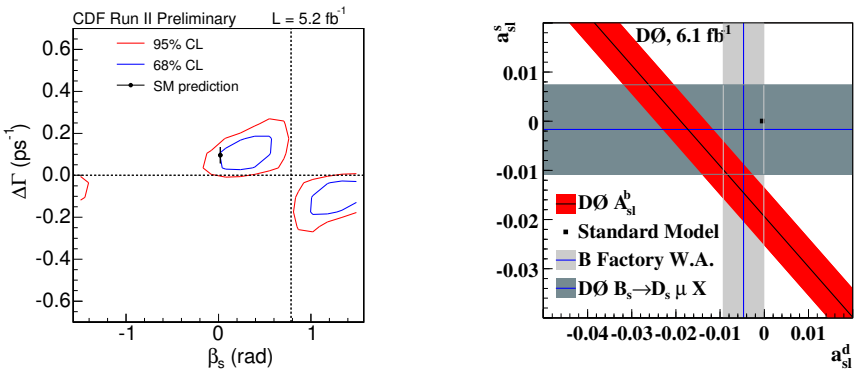

Figure 5: The $\Delta\Gamma_s$-β_s confidence regions in $B_s \to J/\psi\,\phi$ decays from the CDF experiment using 5.2 fb^{-1} of data (right). Latest results on the flavor specific asymmetry in semileptonic B_s decays from the DØ experiment (right).

In those decays, the $b \to c$ transition provides the $B^+ \to D^0 K^+$ decay while the $b \to u$ transitions yields the $B^+ \to \bar{D}^0 K^+$ final state. Thus measurements of the CP-violation in the final states which are common to D^0 and $\bar{D}^0$ is needed. Three different approaches are currently used: The first one uses the Cabibbo-favored decay $\bar{D}^0 \to K^-\pi^-$ with the doubly Cabibbo-suppressed decay $D^0 \to K^-\pi^+$ [17, 18]. The second method uses Cabibbo-suppressed D^0 decays to final states like $\pi^+\pi^-$ and K^+K^- [19]. The third approach uses a Dalitz plot analysis of $D^0 \to K_s\pi^+\pi^-$ [20]. The main limitation is that the rates are small and up to now there was no significant measurement of CP-violation in those decays. Recently the Belle and *BABAR* experiments announced an approximate $3.5\,\sigma$ evidence for CP-violation in $B^+ \to D^0 K^+$ decays with $D^0 \to K_s\pi^+\pi^-$ [21, 22]. The extracted confidence regions on the angle γ are shown in Fig. 4. The Belle experiment extracts $\gamma = (78^{+11}_{-12} \pm 4 \pm 9)^\circ$ and *BABAR* obtains $\gamma = (68 \pm 14 \pm 4 \pm 3)^\circ$.

4 B_s sector

The CP-violation in the B_s meson sector is currently the most exciting and most widely discussed topic in relation to new physics. Two results, which in many models of new physics are related, are the measurement of the CP-violation in $B_s \to J/\psi\,\phi$ decays and the flavor specific asymmetry in semileptonic B_s decays.

The origin of the first one is in the interference of the decays with and without B_s mixing. The standard model predicts only tiny CP-violation which comes from the fact that all entering CKM matrix elements are almost real. The previous results from the two Tevatron experiments showed about 1.5-1.8 σ deviation from the standard model [23, 24], with their combination being $2.2\,\sigma$ away. Recently, the CDF collaboration updated its result with more data and a few improvements, which yield better constraints on the CP-violation in $B_s \to J/\psi\,\phi$. The resulting 2-dimensional $\Delta\Gamma_s$-β_s contour is shown in Fig. 5. Overall, the CDF experiment now observes a better agreement between the data and the standard model with a difference of about $0.8\,\sigma$. More details on this update can be found in [25].

The second measurement we present here is the measurement of the flavor specific asymmetry in semileptonic b-hadron decays. In the standard model, as well as in a large class of

new physics models, this quantity is predicted to be small. It can be generated either by direct CP-violation or by an asymmetry in the mixing rate between b- and $\bar{b}$-mesons. Typically, direct CP-violation is zero as we talk about the most allowed decay amplitude $b \to c\,l\,\nu$ which would need a second contribution to interfere with. As it is not easy to construct a model where a second amplitude with reasonable size exists, typically the direct CP-violation is predicted to be zero. The effect of different mixing rates is small for the B^0 due to the small decay width difference and it is small in the standard model for the B_s due to the small phase involved. The DØ experiment announced a new measurement this year, with a highly improved treatment of systematic uncertainties. They measure $A^b_{fs} = (-96 \pm 25 \pm 15) \times 10^{-4}$ which is significantly different from the standard model expectation of $A^b_{fs} = (-2.3^{+0.5}_{-0.6}) \times 10^{-4}$ [26]. If this result is confirmed, it is a clear sign of physics beyond the standard model. For more details see [27].

5 Rare decays

Rare FCNC transitions are best known outside the flavor physics community for searches of physics beyond standard model. The prime example is the rare $B_s \to \mu^+\mu^-$ decay, where previous results could put strong constraints on some new physics models, even with limits which are far from the standard model expectations. The standard model prediction for the branching fraction of $B_s \to \mu^+\mu^-$ is $(3.6 \pm 0.3) \times 10^{-9}$ [28]. The main difficulty is in suppressing and controlling the background. The search for this decay is dominated by the Tevatron experiments. Recently, the DØ experiment updated its result using 6.1 fb^{-1} of data yielding an upper limit on the branching fraction of 5.2×10^{-8} at 95% C.L. [29]. The best limit at this moment comes from the CDF experiment using 3.7 fb^{-1} of data: 4.3×10^{-8} at 95% C.L. [30]. Those are about an order of magnitude above the standard model prediction.

Another example of a FCNC rare process which generates a lot of excitement these days is a class of decays governed by the $b \to s\,l^+l^-$ quark level transition with l being a charged lepton. The decays $B^{0,\pm} \to K^{0,\pm}\mu^+\mu^-$ and $B^{0,\pm} \to K^{*0,\pm}\mu^+\mu^-$ have already been observed. Recently, the CDF experiment observed also the decay $B_s \to \phi\,\mu^+\mu^-$ with an approximate $6.3\,\sigma$ significance using 4.4 fb^{-1} of data [31]. The measured branching fraction is $(1.44 \pm 0.33 \pm 0.46) \times 10^{-6}$. As those decays proceed even in the standard model through more than one amplitude, there is a rich phenomenology of interferences. From the interference effects, the forward-backward asymmetry of the muons as a function of dimuon invariant mass is the one which is responsible for the excitement. It has been measured in the Belle [32], *BABAR* [33] and CDF [31] experiments and we show the results in Fig. 6. While not statistically significant, all three experiments show some departure in the same direction from the standard model. It is going to be interesting to follow future measurements of this quantity.

6 Conclusions

Globally, except for the flavor specific asymmetry in semileptonic b-decays, there is no significant discrepancy in the global picture of CP-violation. However, there are a few discrepancies which are worth to be followed in the future. In Fig. 7 we show the global status of the CKM fit [34]. Another determination [35] provides a similar picture. Both groups see an approximate $2.5\,\sigma$ improvement of the fit if either the constraint from $B \to \tau\,\nu$ or $\sin 2\beta$ is removed from the fit. Other small discrepancies are in V_{ub} and in the CP-violation parameter ϵ_K in the kaon system.

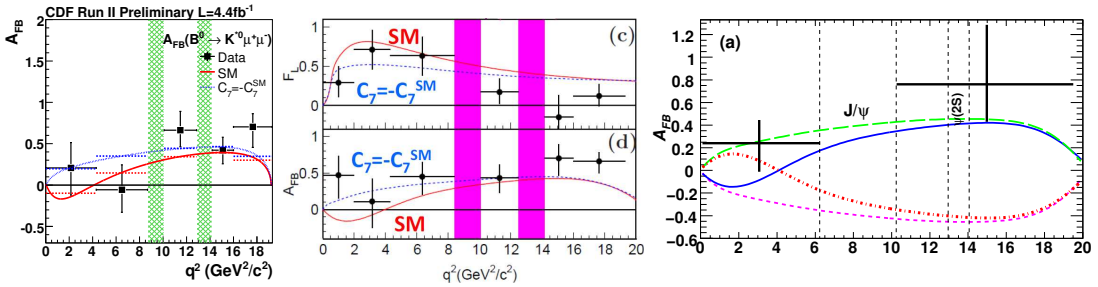

Figure 6: The forward-backward asymmetry of the muon in $B \to K^* \mu^+ \mu^-$ decays as a function of the dimuon invariant mass from CDF (left), Belle (middle) and *BABAR* (right). The points represent measurement, the red line in the CDF and Belle cases and the blue line in the *BABAR* result show the standard model prediction and the other curves represent different beyond the standard model scenarios. The areas without data points correspond to the charmonium regions which are excluded from the analysis.

Within the limited space we could not discuss the charm quark sector, which has strong potential. Its status and prospects at the time of the conference can be found in [36]. The prospects of the LHC in the bottom quark sector were discussed in several contributions, the most relevant one with respect to this work being [37]. With large expectations the whole community is positive about future interesting results and the importance of flavor physics for discovering and/or understanding physics beyond standard model.

Acknowledgments

The author would like to thank the organizers for the kind invitation to the conference and would like to acknowledge support from the Bundesministerium für Bildung und Forschung, Germany.

References

[1] J. H. Christenson, J. W. Cronin, V. L. Fitch and R. Turlay, Phys. Rev. Lett. **13** (1964) 138.

[2] M. Kobayashi and T. Maskawa, Prog. Theor. Phys. **49** (1973) 652.

[3] S. W. Herb *et al.*, Phys. Rev. Lett. **39** (1977) 252.

[4] S. Abachi *et al.* [D0 Collaboration], Phys. Rev. Lett. **74** (1995) 2422 [arXiv:hep-ex/9411001].

[5] F. Abe *et al.* [CDF Collaboration], Phys. Rev. Lett. **74** (1995) 2626 [arXiv:hep-ex/9503002].

[6] B. Aubert *et al.* [*BABAR* Collaboration], Phys. Rev. Lett. **86** (2001) 2515 [arXiv:hep-ex/0102030].

[7] K. Abe *et al.* [Belle Collaboration], Phys. Rev. Lett. **87** (2001) 091802 [arXiv:hep-ex/0107061].

[8] E. Barberio *et al.* [Heavy Flavor Averaging Group], arXiv:0808.1297 [hep-ex] and online update at http://www.slac.stanford.edu/xorg/hfag.

[9] B. Aubert *et al.* [*BABAR* Collaboration], arXiv:1005.3288 [hep-ex].

[10] K. Ikado *et al.* [Belle Collaboration], Phys. Rev. Lett. **97** (2006) 251802 [arXiv:hep-ex/0604018].

[11] I. Adachi *et al.* [Belle Collaboration], arXiv:0809.3834 [hep-ex].

[12] B. Aubert *et al.* [*BABAR* Collaboration], Phys. Rev. D **77** (2008) 011107 [arXiv:0708.2260 [hep-ex]].

[13] B. Aubert *et al.* [*BABAR* Collaboration], Phys. Rev. D **81** (2010) 051101 [arXiv:0809.4027 [hep-ex]].

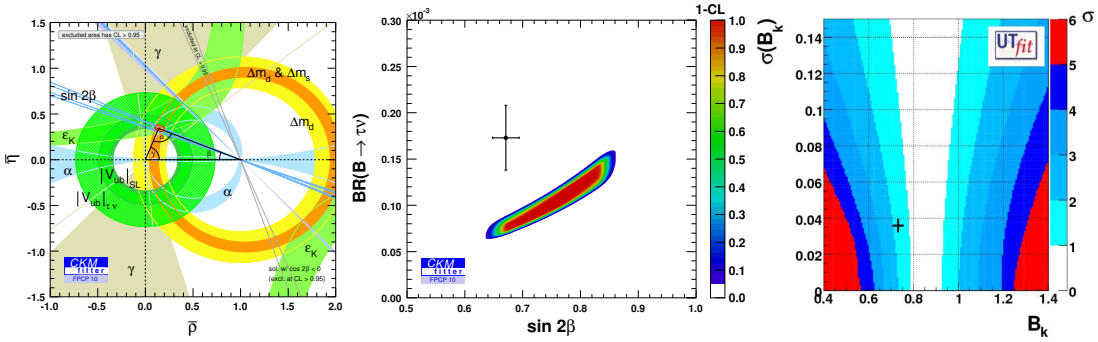

Figure 7: The global status of the unitarity triangle fit from the CKMFitter group (left), the graphical representation of the $B \to \tau\,\nu$ versus $\sin 2\beta$ disagreement (middle) and the situation with indirect and direct determinations of the parameter proportional to ϵ_K from the UTFit group (right). In the middle plot, colored confidence regions show the expectation for the $B \to \tau\,\nu$ branching fraction from the fit where two quantities are excluded while the point shows experimental results. In the right plot, the colored areas show the confidence regions of B_K from the fit without constraint from the CP-violation in the kaon system. The cross represents the experimental measurement of the quantity.

[14] A. S. Kronfeld, arXiv:0912.0543 [hep-ph].

[15] B. Aubert *et al.* [*BABAR* Collaboration], Phys. Rev. **D79** (2009) 072009. [arXiv:0902.1708 [hep-ex]].

[16] K. -F. Chen *et al.* [Belle Collaboration], Phys. Rev. Lett. **98** (2007) 031802. [hep-ex/0608039]

[17] D. Atwood, I. Dunietz, A. Soni, Phys. Rev. Lett. **78** (1997) 3257-3260. [hep-ph/9612433].

[18] D. Atwood, I. Dunietz, A. Soni, Phys. Rev. **D63** (2001) 036005. [hep-ph/0008090].

[19] M. Gronau, D. London., Phys. Lett. **B253** (1991) 483-488.

[20] A. Giri, Y. Grossman, A. Soffer *et al.*, Phys. Rev. **D68** (2003) 054018. [hep-ph/0303187].

[21] P. del Amo Sanchez *et al.* [*BABAR* Collaboration], Submitted to: Phys.Rev.Lett.. [arXiv:1005.1096 [hep-ex]].

[22] A. Poluektov *et al.* [The Belle Collaboration], Phys. Rev. **D81** (2010) 112002. [arXiv:1003.3360 [hep-ex]].

[23] The CDF Collaboration, CDF Public Note 9458.

[24] V. M. Abazov *et al.* [D0 Collaboration], Phys. Rev. Lett. **101** (2008) 241801. [arXiv:0802.2255 [hep-ex]].

[25] E. Puschel, in these proceedings; The CDF Collaboration, CDF Public Note 10206.

[26] A. Lenz, U. Nierste, JHEP **0706** (2007) 072. [hep-ph/0612167].

[27] I. Bertram, in these proceedings; V. M. Abazov *et al.* [D0 Collaboration], arXiv:1005.2757 [hep-ex].

[28] A. J. Buras, Prog. Theor. Phys. **122** (2009) 145-168. [arXiv:0904.4917 [hep-ph]].

[29] V. M. Abazov *et al.* [D0 Collaboration], arXiv:1006.3469 [hep-ex].

[30] The CDF Collaboration, CDF Public Note 9892.

[31] The CDF Collaboration, CDF Public Note 10047.

[32] J. -T. Wei *et al.* [BELLE Collaboration], Phys. Rev. Lett. **103** (2009) 171801. [arXiv:0904.0770 [hep-ex]].

[33] B. Aubert *et al.* [*BABAR* Collaboration], Phys. Rev. **D79** (2009) 031102. [arXiv:0804.4412 [hep-ex]].

[34] J. Charles *et al.* [CKMfitter Group Collaboration], Eur. Phys. J. **C41** (2005) 1-131. [hep-ph/0406184] and updates at http://ckmfitter.in2p3.fr.

[35] M. Ciuchini *et al.*, JHEP **0107** (2001) 013 [arXiv:hep-ph/0012308] and updates at http://www.utfit.org.

[36] T. Mannel, in these proceedings.

[37] G. Conti, in these proceedings.

Flavour theory and the LHC era

Andrzej J. Buras

Physik-Department, Technische Universität München, D-85748 Garching, Germany
TUM Institute of Advanced Study, Lichtenbergstr. 2a, D-85748 Garching, Germany

DOI: http://dx.doi.org/10.3204/DESY-PROC-2010-01/26

This decade should make a significant progress towards the Theory of Flavour and the main goal of this talk is to transfer this belief to my colleagues in the particle physics community. Indeed a significant part of this decade could turn out to be the Flavour Era with participation of the LHC, Belle II, Super-Flavour-Facility and dedicated Kaon and lepton flavour violation experiments. Selected superstars of flavour physics listed below will play a prominent role in these events. In this writeup the leading role is played by the *prima donna* of 2010: CP violation in B_s system.

1 Introduction

In our search for a fundamental theory of elementary particles we need to improve our understanding of flavour [1, 2]. This is clearly a very ambitious goal that requires the advances in different directions as well as continuos efforts of many experts day and night, as depicted with the help of a "Flavour Clock" in Figure 1.

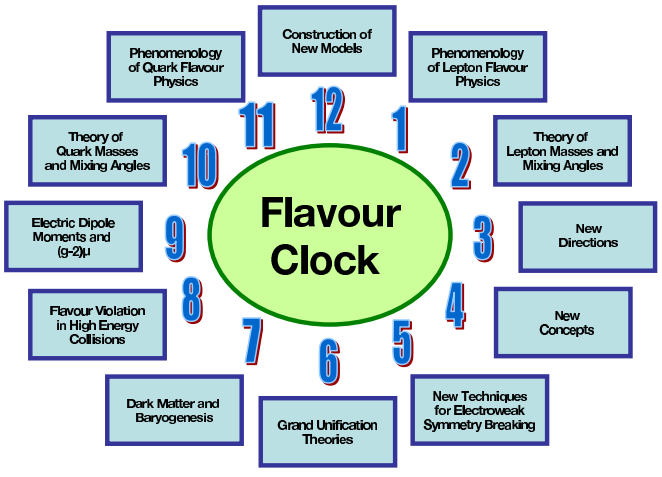

Figure 1: Working towards the Theory of Flavour around the Flavour Clock.

Despite the impressive success of the CKM picture of flavour changing interactions [3] in which also the GIM mechanism [4] for the suppression of flavour changing neutral currents (FCNC) plays a very important role, there are many open questions of theoretical and experimental nature that should be answered before we can claim to have a theory of flavour. Among the basic questions in flavour physics that could be answered in the present decade are the following ones:

1. What is the fundamental dynamics behind the electroweak symmetry breaking that very likely plays also an important role in flavour physics?

2. Are there any new flavour symmetries that could help us to understand the existing hierarchies of fermion masses and the hierarchies in the quark and lepton flavour violating interactions?

3. Are there any flavour violating interactions that are not governed by the SM Yukawa couplings? In other words, is Minimal Flavour Violation (MFV) the whole story?

4. Are there any additional *flavour violating* CP-violating (CPV) phases that could explain certain anomalies present in the flavour data and simultaneously play a role in the explanation of the observed baryon-antibaryon asymmetry in the universe (BAU)?

5. Are there any *flavour conserving* CPV phases that could also help in explaining the flavour anomalies in question and would be signalled in this decade through enhanced electric dipole moments (EDMs) of the neutron, the electron and of other particles?

6. Are there any new sequential heavy quarks and leptons of the 4th generation and/or new fermions with exotic quantum numbers like vectorial fermions?

7. Are there any elementary neutral and charged scalar particles with masses below 1 TeV and having a significant impact on flavour physics?

8. Are there any new heavy gauge bosons representing an enlarged gauge symmetry group?

9. Are there any relevant right-handed (RH) weak currents that would help us to make our fundamental theory parity conserving at short distance scales well below those explored by the LHC?

10. How would one successfully address all these question if the breakdown of the electroweak symmetry would turn out to be of a non-perturbative origin?

An important question is the following one: will some of these questions be answered through the interplay of high energy processes explored by the LHC with low energy precision experiments or are the relevant scales of fundamental flavour well beyond the energies explored by the LHC and future colliders in this century? The existing tensions in some of the corners of the SM and still a rather big room for new physics (NP) contributions in rare decays of mesons and leptons and CP-violating observables including in particular EDMs give us hopes that indeed several phenomena required to answer at least some of these questions could be discovered in this decade.

2 Superstars of flavour physics in 2010-2015

In this decade we will be able to resolve the short distance scales by more than an order of magnitude, extending the picture of fundamental physics down to scales $5 \cdot 10^{-20}$m with the help of the LHC. Further resolution down to scales as short as 10^{-21}m or even shorter scales should be possible with the help of high precision experiments in which flavour violating processes will play a prominent role.

As far as high precision experiments are concerned a number of selected processes and observables will in my opinion play the leading role in learning about the NP in this new territory. This selection is based on the sensitivity to NP and theoretical cleanness. The former can be increased with the increased precision of experiments and the latter can improve with the progress in theoretical calculations, in particular the non-perturbative ones like the lattice simulations.

My superstars for the coming years are as follows:

- The mixing induced CP-asymmetries in B_s and B_d decays to CP-eigenstates like $\psi\phi$ and $\phi\phi$, respectively. Denoting them as usual by $S_F(B_q)$ with F being the final state, in particular $S_{\psi\phi}(B_s)$ is very important as that is tiny in the SM and subject to large NP contributions: $S_{\psi\phi} \approx 0.04$. The asymmetry $S_{\phi\phi}(B_s)$ is also important. It is also very strongly suppressed in the SM and is sensitive to NP similar to the one explored through the departure of $S_{\phi K_S}(B_d)$ from $S_{\psi K_S}(B_d)$ [5].
- The rare decays $B_{s,d} \to \mu^+\mu^-$ that could be enhanced in certain NP scenarios by an order of magnitude with respect to the SM values.
- The angle γ of the unitarity triangle (UT) that can be precisely measured through tree level decays.
- $B^+ \to \tau^+\nu_\tau$ that is sensitive to charged Higgs particles.
- The rare decays $K^+ \to \pi^+\nu\bar{\nu}$ and $K_L \to \pi^0\nu\bar{\nu}$ that belong to the theoretically cleanest decays in flavour physics.
- Numerous angular symmetries and asymmetries in $B \to K^* l^- l^-$.
- Lepton flavour violating decays like $\mu \to e\gamma$, $\tau \to e\gamma$, $\tau \to \mu\gamma$, decays with three leptons in the final state and $\mu - e$ conversion in nuclei.
- Electric dipole moments of the neutron, the electron, atoms and leptons.
- Anomalous magnetic moment of the muon $(g-2)_\mu$ that indeed seems to be "anomalous" within the SM even after the inclusion of radiative corrections.
- The ratio $\varepsilon'/\varepsilon_K$ in $K_L \to \pi\pi$ decays which is known experimentally within 10% and which should gain in importance in this decade due to improved lattice calculations. ε' parametrizes the direct CP violation in these decays, while ε_K describes the size of indirect CP violation.

Clearly, there are other stars in flavour physics but I believe that the ones above will play the crucial role in our search for the theory of flavour. Having experimental results on these decays and observables with sufficient precision accompanied by improved theoretical calculations will

exclude several presently studied models reducing thereby our exploration of short distance scales to a few avenues.

In the rest of this presentation I will discuss some of these decays in the context of the basic questions in flavour physics listed previously. In particular we will collect a number of messages on NP which result from the recent and not so recent model independent studies and detailed analyses of concrete numerous beyond the SM models (BSM). In this context the role of correlations between various observables implying various patterns of flavour violation characteristic for various concrete models should be strongly emphasized. Recent reviews can be found in [1, 2]. In the context of $B_{s,d}$-mixing and related NP see a very detailed recent analysis in [6].

3 Beyond the Standard Model (BSM)

During the last 35 years several extensions of the SM have been proposed and analyzed in the rich literature. In particular in the last 10 years, after the data on $B_{d,s}$ decays, $B^0_{d,s} - \bar{B}^0_{d,s}$ mixing and related CP violation improved considerably and the bounds on lepton flavour violating decays became stronger, useful model independent analyses of FCNC processes could be performed. Moreover several extensive analyses of the full spectrum of flavour violating processes in the context of specific BSM scenarios have been published.

3.1 Minimal Flavour Violation

Among the model independent approaches in flavour physics the most prominent role is played by MFV [7, 8] in which flavour violation including CP violation originates entirely from the SM Yukawa couplings. This approach naturally suppresses FCNC processes to the level observed experimentally even in the presence of new particles with masses of a few hundreds GeV. It also implies specific correlations between various observables, which are most stringent in the so-called constrained MFV (CMFV) [8] in which only the SM operators are assumed to be relevant. Basically MFV reduces to CMFV when only one Higgs doublet is present.

A particularly interesting set-up is obtained introducing flavour-blind CPV phases compatible with the MFV symmetry principle [9, 10, 11, 12, 13].

As recently shown in [14], the general formulation of the MFV hypothesis with flavour-blind CPV phases (FBPh) applied to a general two Higgs doublet model is very effective in suppressing FCNCs to a level consistent with experiments, leaving open the possibility of sizable non-standard effects also in CPV observables. In what follows we will call this model 2HDM$_{\overline{\rm MFV}}$ with the "bar" on MFV indicating the presence of FBPhs. As discussed in [14], the 2HDM$_{\overline{\rm MFV}}$ can accommodate a large CP-violating phase in B_s mixing, as hinted by CDF and D0 data [15, 16, 17], while ameliorating simultaneously the observed anomaly in the relation between ϵ_K and $S_{\psi K_S}$ [18, 19].

On general grounds, it is natural to expect that FBPhs contribute also to CPV flavour-conserving processes, such as the EDMs. Indeed, the choice adopted in [7] to assume the Yukawa couplings as the unique breaking terms of both the flavour symmetry and the CP symmetry, was motivated by possibly too large effects in EDMs with generic FBPhs. This potential problem has indeed been confirmed by the recent model-independent analysis in [20].

In [21] the correlations between EDMs and CP violation in $B_{s,d}$ mixing in 2HDM$_{\overline{\rm MFV}}$ including FBPhs in Yukawa interactions and the Higgs potential have been studied in detail. It

has been shown that in both cases the upper bounds on EDMs of the neutron and the atoms do not forbid sizable non-standard CPV effects in B_s mixing. However, if a large CPV phase in B_s mixing will be confirmed, this will imply hadronic EDMs very close to their present experimental bounds, within the reach of the next generation of experiments, as well as $Br(B_{s,d} \to \mu^+\mu^-)$ typically largely enhanced over its SM expectation. The two flavour-blind CPV mechanisms can be distinguished through the correlation between $S_{\psi K_S}$ and $S_{\psi\phi}$ that is strikingly different if only one of them is relevant. Which of these two CPV mechanisms dominates depends on the precise values of $S_{\psi\phi}$ and $S_{\psi K_S}$, as well as on the CKM phase (as determined by tree-level processes). Current data seems to show a mild preference for a *hybrid* scenario where both these mechanisms are at work. I will be a bit more explicit about this result below.

3.2 Beyond Minimal Flavour Violation

There is a number of explicit BSM models that introduce new sources of flavour violation and CP violation beyond those present in the MFV framework discussed above. Among them the Littlest Higgs Model with T-parity (LHT), the Randall-Sundrum model without and with custodial protection (RSc), various supersymmetric flavour models, Z'-models, models with vectorial new quarks, the SM extended by the fourth sequential generation of quarks and leptons (SM4) and multi-Higgs doublet models are the ones in which most extensive flavour analyses have been performed. Most of them have been reviewed in some details in [1], where the relevant references can be found. I will concentrate in this presentation on very recent developments and will only recall some of the most interesting results of these older analyses if necessary.

During the second half of 2009 and also in 2010 the flavour analyses in the framework of the 2HDM with and without MFV and also the SM4 became popular. The 2HDM$_{\overline{\rm MFV}}$ has been already briefly discussed above. The SM4 introduces three new mixing angles s_{14}, s_{24}, s_{34} and two new phases in the quark sector and can still have a significant impact on flavour phenomenology. Most recent extensive analyses of FCNC processes in the SM4 can be found in [22, 23, 24, 25]. More about it later.

Next, let me mention an effective theory approach in which the impact of RH currents in both charged- and neutral-current flavour-violating processes has been analysed [26]. While RH currents are present in several supersymmetric flavour models, in RS models and of course in left-right symmetric models based on the gauge group $SU(2)_L \times SU(2)_R \times U(1)_{B-L}$ (see [27, 28] for most recent papers), the recent phenomenological interest in these models originated in tensions between inclusive and exclusive determinations of the elements of the CKM matrix $|V_{ub}|$ and $|V_{cb}|$. It could be that these tensions are due to the underestimate of theoretical and/or experimental uncertainties. Yet, it is a fact, as pointed out and analyzed recently in particular in [29, 30, 31], that the presence of RH currents could either remove or significantly weaken some of these tensions, especially in the case of $|V_{ub}|$. Implications of this setup for other observables, in particular FCNC processes without specifying the fundamental theory in detail but only assuming its global symmetry and the pattern of its breakdown have been analyzed in [26]. As we will see this approach can be considered as a minimal flavour violating scenario in the RH sector and will be called RHMFV in what follows. I will return to the results of this work below.

Finally, recent studies of flavour violating processes in models for fermion masses and mixings [32, 33, 34], indicate that a full theory of flavour has to involve at a certain level non-MFV interactions.

4 Waiting for signals of NP in FCNC processes

4.1 General remarks

The last decade has established that flavour-changing and CPV processes in $B_{s,d}$ and K systems are on the whole well described by the SM. The same applies to electroweak precision tests. This implies automatically tight constraints on flavour-changing phenomena beyond the SM and a potential problem for a natural solution of the hierarchy problem and other problems listed in the Introduction, several of which require the presence of NP not far from the electroweak scale.

It is evident from various model-independent studies that NP at the TeV scale must have a non-generic flavour structure in order to satisfy existing constraints. Moreover, in order to avoid fine tuning of parameters, natural protection mechanisms suppressing FCNCs generated by NP are required. In addition to MFV and GIM, RS-GIM, T-parity in Littlest Higgs models, alignment and degeneracy, most familiar from supersymmetric models and generally flavour symmetries (abelian and non-abelian) have been invented for this purpose. Last but certainly not least, custodial symmetries, like the ones related to the Higgs system and relevant for electroweak precision tests, can be used to suppress specific flavour-violating neutral gauge boson couplings.

It should be emphasized that only protection mechanisms that are stable under radiative corrections can be considered as solutions to flavour problems and considerations of protection mechanisms only at tree level are insufficient. In this context let us recall that the standard assignment of the $SU(2)_L \times U(1)_Y$ quark charges, identified long ago by Glashow, Iliopoulos, and Maiani (GIM) [4], forbids tree-level flavour-changing couplings of the quarks to the SM neutral gauge bosons. This mechanism is only violated at the loop level and the FCNC processes are strongly suppressed by the products of CKM elements and mass splittings of quarks or leptons carrying the same electric charge. Only in processes involving the top quark exchanges is GIM strongly broken but in a calculable manner and the pattern of this breakdown seems to agree with experiment although the tests of this pattern have to be still very much improved.

In the case of only one Higgs doublet, namely within the SM, this structure is effective also in eliminating possible dimension-four FCNC couplings of the quarks to the Higgs field. While the $SU(2)_L \times U(1)_Y$ assignment of quarks and leptons can be considered as being well established, much less is known about the Higgs sector of the theory. In the presence of more than one Higgs field the appearance of tree-level FCNC is not automatically forbidden by the standard assignment of the $SU(2)_L \times U(1)_Y$ fermion charges: additional conditions have to be imposed on the model in order to guarantee a sufficient suppression of FCNC processes [35, 36]. The absence of renormalizable couplings contributing at the tree level to FCNC processes, in multi-Higgs models, goes under the name of Natural Flavour Conservation (NFC) hypothesis.

It has been pointed out recently [14] that the MFV hypothesis is more stable in suppressing FCNCs than the hypothesis of NFC alone when quantum corrections are taken into account. Indeed the NFC hypothesis is usually based on a $U(1)_{PQ}$ symmetry that has to be broken in order to avoid massless scalars. NFC can also be enforced by a Z_2 symmetry. However, it turns out that also this symmetry is insufficient to protect FCNCs when radiative corrections are considered. On the other hand MFV hypothesis based on continuous flavour symmetries is more powerful. Thus 30 years after the seminal papers of Glashow, Weinberg and Paschos, the hypothesis of NFC can be replaced by the more powerful and more general hypothesis of MFV. Other recent interesting analyzes of 2HDMs can be found in [37, 38, 39, 40].

4.2 Three strategies in waiting for NP in flavour physics

Particle physicists have been waiting eagerly for a solid evidence of NP for the last 30 years. Except for neutrino masses, the BAU and dark matter, no clear signal emerged so far. While waiting several strategies for finding NP have been developed. They can be divided roughly into three classes.

4.2.1 Precision calculations within the SM

Here basically the goal is to calculate the background to NP coming from the known dynamics of the SM. At first sight this approach is not very exciting. Yet, in particular in flavour physics, where the signals of NP are generally indirect, this approach is very important. From my point of view, being involved more than one decade in calculations of higher order QCD corrections [41], I would claim that for most interesting decays these perturbative and renormalization group improved calculations reached already the desired level. The most advanced NNLO QCD calculations have been done for $B \to X_s\gamma$, $K^+ \to \pi^+\nu\bar{\nu}$, $B \to X_s l^+ l^-$ and recently for ε_K [42]. See also the two loop electroweak contributions to $K \to \pi\nu\bar{\nu}$ [43].

The main progress is now required from lattice groups. Here the main goals for the coming years are more accurate values of weak decay constants $F_{B_{d,s}}$ and various $\hat{B}_i$ parameters relevant for $B_{d,s}$ physics. For $K^0 - \bar{K}^0$ mixing the relevant parameter $\hat{B}_K$ is now known with an accuracy of 4% [44]. An impressive achievement. Let us hope that also the parameters B_6 and B_8, relevant for ε'/ε will be known with a similar accuracy within this decade.

Clearly further improvements on the hadronic part of two-body non-leptonic decays is mandatory in order to understand more precisely the direct CP violation in $B_{s,d}$ decays.

4.2.2 The bottom-up approach

In this approach one constructs effective field theories involving only light degrees of freedom including the top quark in which the structure of the effective Lagrangians is governed by the symmetries of the SM and often other hypothetical symmetries. This approach is rather powerful in the case of electroweak precision studies and definitely teaches us something about $\Delta F = 2$ transitions. However, except for the case of MFV and closely related approaches based on flavour symmetries, the bottom-up approach ceases, in my view, to be useful in $\Delta F = 1$ decays, because of very many operators that are allowed to appear in the effective Lagrangians with coefficients that are basically unknown [45]. In this approach then the correlations between various $\Delta F = 2$ and $\Delta F = 1$ observables in K, D, B_d and B_s systems are either not visible or very weak, again except MFV, CMFV or closely related approaches. Moreover the correlations between flavour violation in low energy processes and flavour violation in high energy processes to be studied soon at the LHC is lost. Again MFV belongs to a few exceptions.

4.2.3 The top-down approach

My personal view shared by some of my colleagues is that the top-down approach is more useful in flavour physics. Here one constructs first a specific model with heavy degrees of freedom. For high energy processes, where the energy scales are of the order of the masses of heavy particles one can directly use this "full theory" to calculate various processes in terms of the fundamental parameters of a given theory. For low energy processes one again constructs the low energy theory by integrating out heavy particles. The advantage over the previous approach is that

now the coefficients of the resulting local operators are calculable in terms of the fundamental parameters of this theory. In this manner correlations between various observables belonging to different mesonic systems and correlations between low energy and high-energy observables are possible. Such correlations are less sensitive to the free parameters than separate observables and represent patterns of flavour violation characteristic for a given theory. These correlations can in some models differ strikingly from the ones of the SM and of the MFV approach.

4.3 Anatomies of explicit models

Having the last strategy in mind my group at the Technical University Munich, consisting dominantly of diploma students, PhD students and young post–docs investigated in the last decade flavour violating processes with the emphasis put on FCNC processes, in the following models: CMFV, MFV, MFV-MSSM, Z'-models, general MSSM, a model with a universal flat 5th dimension, the Littlest Higgs model (LH), the Littlest Higgs model with T-parity (LHT), SUSY-GUTs, Randall-Sundrum model with custodial protection (RSc), flavour blind MSSM (FBMSSM), three classes of supersymmetric flavour models with the dominance of left-handed currents (δLL model), the dominance of right-handed currents (AC model) and models with equal strength of left- and right-handed currents (RVV2 and AKM models), the last comments applying only to the NP part. This year we have analyzed the SM4, the 2HDM$_{\overline{\rm MFV}}$ and finally quark flavour mixing with RH currents in an effective theory approach RHMFV. These analyses where dominated by quark flavour physics, but in the case of the LHT, FBMSSM, supersymmetric flavour models and the SM4 lepton flavour violation has also been studied in detail.

As a partial review of this work appeared already in [1] with various correlations presented in Figures 5 - 11 of that paper I will not discuss them in detail here. In [1] numerous references (301) to our papers and studies by other groups can be found. The detailed discussion of the supersymmetric flavour models (δLL, AC, RVV2, AKM) can be found in [32].

The "DNA" of flavour physics effects for the most interesting observables constructed in [32] and extended by the recent results obtained in the SM4 is presented in Table 1. This table only indicates whether large, moderate or small NP effects in a given observable are still allowed in a given model but does not exhibit correlations between various observables characteristic for a given model. Such correlations can be found in [1] and original papers quoted there. I will summarize the most striking ones later on.

4.4 ε_K-anomaly and related tensions

It has been pointed out in [19] that the SM prediction for ε_K implied by the measured value of $S_{\psi K_S} = \sin 2\beta$, the ratio $\Delta M_d/\Delta M_s$ and the value of $|V_{cb}|$ turns out to be too small to agree well with experiment. This tension between ε_K and $S_{\psi K_S}$ has been pointed out from a different perspective in [18]. These findings have been confirmed by a UTfitters analysis [46]. The CKMfitters having a different treatment of uncertainties find less significant effects [6].

The main reasons for this tension are on the one hand a decreased value of the relevant non-perturbative parameter $\hat{B}_K = 0.724 \pm 0.008 \pm 0.028$ [44] resulting from unquenched lattice calculations and on the other hand the decreased value of ε_K in the SM arising from a multiplicative factor, estimated first to be $\kappa_\varepsilon = 0.92 \pm 0.02$ [19]. This factor took into account the departure of ϕ_ε from $\pi/4$ and the long distance (LD) effects in $\mathrm{Im}\Gamma_{12}$ in the $K^0 - \bar{K}^0$ mixing. The recent inclusion of LD effects in $\mathrm{Im}M_{12}$ modified this estimate to $\kappa_\varepsilon = 0.94 \pm 0.02$ [47]. Very recently

	AC	RVV2	AKM	δLL	FBMSSM	LHT	RSc	4G
$D^0 - \bar{D}^0$	★★★	★	★	★	★	★★★	?	★★
ϵ_K	★	★★★	★★★	★	★	★★	★★★	★★
$S_{\psi\phi}$	★★★	★★★	★★★	★	★	★★★	★★★	★★★
$S_{\phi K_S}$	★★★	★★	★	★★★	★★★	★	?	★★
$A_{\rm CP}\,(B \to X_s\gamma)$	★	★	★	★★★	★★★	★	?	★
$A_{7,8}(K^*\mu^+\mu^-)$	★	★	★	★★★	★★★	★★	?	★★
$B_s \to \mu^+\mu^-$	★★★	★★★	★★★	★★★	★★★	★	★	★★★
$K^+ \to \pi^+\nu\bar{\nu}$	★	★	★	★	★	★★★	★★★	★★★
$K_L \to \pi^0\nu\bar{\nu}$	★	★	★	★	★	★★★	★★★	★★★
$\mu \to e\gamma$	★★★	★★★	★★★	★★★	★★★	★★★	★★★	★★★
$\tau \to \mu\gamma$	★★★	★★★	★	★★★	★★★	★★★	★★★	★★★
$\mu + N \to e + N$	★★★	★★★	★★★	★★★	★★★	★★★	★★★	★★★
d_n	★★★	★★★	★★★	★★	★★★	★	★★★	★
d_e	★★★	★★★	★★	★	★★★	★	★★★	★
$(g-2)_\mu$	★★★	★★★	★★	★★★	★★★	★	?	★

Table 1: "DNA" of flavour physics effects for the most interesting observables in a selection of SUSY and non-SUSY models. ★★★ signals large NP effects, ★★ visible but small NP effects and ★ implies that the given model does not predict sizable NP effects in that observable. From [32].

also NNLO-QCD corrections to the QCD factor η_{ct} in ε_K [42] have been calculated enhancing the value of ε_K by 3%. Thus while in [19] the value $|\varepsilon_K|_{\rm SM} = (1.78 \pm 0.25)\cdot 10^{-3}$ has been quoted and with the new estimate of LD effects and new input one finds $|\varepsilon_K|_{\rm SM} = (1.85 \pm 0.22)\cdot 10^{-3}$, including NNLO corrections gives the new value

$$|\varepsilon_K|_{\rm SM} = (1.92 \pm 0.25)\cdot 10^{-3}, \tag{1}$$

significantly closer to the experimental value $|\varepsilon_K|_{\rm exp} = (2.23 \pm 0.01)\cdot 10^{-3}$. This result is compatible with [42, 6] although the central value in (1) is sensitive to the input parameters, in particular the value of $\sin 2\beta$.

Consequently, the ε_K-anomaly softened considerably but it is still alive. Indeed, the $\sin 2\beta = 0.74 \pm 0.02$ from UT fits is visibly larger than the experimental value $S_{\psi K_S} = 0.672 \pm 0.023$. The difference is even larger if one wants to fit ε_K exactly: $\sin 2\beta \approx 0.80$ [18, 19].

One should also recall the tension between inclusive and exclusive determinations of $|V_{cb}|$ with the exclusive ones in the ballpark of $3.5 \cdot 10^{-3}$ and the inclusive ones typically above $4.0 \cdot 10^{-3}$.

As discussed in [18, 19] a small negative NP phase φ_{B_d} in $B_d^0 - \bar{B}_d^0$ mixing would solve some

of these problems. Indeed we have then

$$S_{\psi K_S}(B_d) = \sin(2\beta + 2\varphi_{B_d})\,, \qquad S_{\psi\phi}(B_s) = \sin(2|\beta_s| - 2\varphi_{B_s})\,, \tag{2}$$

where the corresponding formula for $S_{\psi\phi}$ in the presence of a NP phase φ_{B_s} in $B_s^0 - \bar{B}_s^0$ mixing has also been given. With a negative φ_{B_d} the true $\sin 2\beta$ is larger than $S_{\psi K_S}$, implying a higher value on $|\varepsilon_K|$, in reasonable agreement with data and a better UT-fit. This solution would favour the inclusive value of $|V_{ub}|$.

Now with a universality hypothesis of $\varphi_{B_s} = \varphi_{B_d}$ [48, 19], a negative φ_{B_d} would automatically imply an enhanced value of $S_{\psi\phi}$ which in view of $|\beta_s| \approx 1^\circ$ amounts to roughly 0.04 in the SM. However, in order to be in agreement with the experimental value of $S_{\psi K_S}$ this type of NP would imply $S_{\psi\phi} \leq 0.25$.

The universality hypothesis of $\varphi_{B_s} = \varphi_{B_d}$ in [48, 19] was clearly ad hoc. Recently, in view of the enhanced value of $S_{\psi\phi}$ at CDF and D0 a more dynamical origin of this relation has been discussed by other authors and different relations between these two phases corresponding still to a different dynamics have been discussed in the literature. Let us elaborate on this topic in more detail.

4.5 Facing an enhanced CPV in B_s mixing

Possibly the most important highlight in flavour physics in 2008, 2009 [15] and even more in 2010 was the enhanced value of $S_{\psi\phi}$ measured by the CDF and D0 collaborations, seen either directly or indirectly through the correlations with various semi-leptonic asymmetries. While in 2009 and in the spring of 2010 [16], the messages from Fermilab indicated good prospects for $S_{\psi\phi}$ above 0.5, the recent messages from ICHEP 2010 in Paris, softened such hopes significantly [17]. Both CDF and D0 find the enhancement by only one σ. Yet, this does not yet preclude $S_{\psi\phi}$ above 0.5, which would really be a fantastic signal of NP. But $S_{\psi\phi}$ below 0.5 appears more likely at present. Still even a value of 0.2 would be exciting as in the SM one has $S_{\psi\phi} \approx 0.04$. Let us hope that the future data from Tevatron and in particular from the LHCb, will measure this asymmetry with sufficient precision so that we will know to which extent NP is at work here. One should also hope that the large CPV in the dimuon CP asymmetry from D0, which triggered new activities, will be better understood. I have nothing to add here at present and can only refer to numerous papers [39, 49, 50, 6, 51].

Leaving the possibility of $S_{\psi\phi} \geq 0.5$ still open but keeping in mind that also $S_{\psi\phi} \leq 0.25$ could turn out to be the final value, let us investigate how different models would face these two different results and what kind of dynamics would be behind these two scenarios.

4.5.1 $S_{\psi\phi} \geq 0.5$

Such large values can be obtained in the RSc model due to KK gluon exchanges and also heavy neutral KK electroweak gauge boson exchanges. In the supersymmetric flavour model with the dominance of right-handed currents like the AC model, double Higgs penguins constitute the dominant NP contributions responsible for $S_{\psi\phi} \geq 0.5$, while in the RVV2 model where NP left-handed current contributions are equally important, also gluino boxes are relevant. On the operator level, it is LR *scalar* operator which is primarly responsible for this enhancement.

Interestingly the SM4 having only $(V-A)*(V-A)$ operators is also capable in obtaining high values of $S_{\psi\phi}$ [22, 23, 25] but not as easily as the RSc, AC and RVV2 models. The lower scales of NP in the SM4 relative to the latter models and the non-decoupling effects of t'

compensate to some extent the absene of LR scalar operators. In the LHT model where only $(V-A)*(V-A)$ operators are present and the NP enters at higher scales than in the SM4, $S_{\psi\phi}$ above 0.5 is out of reach [52].

All these models contain new sources of flavour and CP violation and it is not surprising that in view of many parameters involved large values of $S_{\psi\phi}$ can be obtained. The question then arises whether strongly enhanced values of this asymmetry would uniquely imply new sources of flavour violation beyond the MFV hypothesis. The answer to this question is as follows:

- In models with MFV and FBPhs set to zero, $S_{\psi\phi}$ remains indeed SM-like.
- In supersymmetric models with MFV and non-vanishing FBPhs and in the FBMSSM, at both small and large $\tan\beta$, the supersymmetry constraints do not allow values of $S_{\psi\phi}$ visibly different from the SM value [32, 50]
- In the 2HDM$_{\overline{\rm MFV}}$ in which at one-loop both Higgs doublets couple to up- and down-quarks, the interplay of FBPh with the CKM matrix allows to obtain $S_{\psi\phi} \geq 0.5$ while satisfying all existing constraints [14].

In the presence of a large $S_{\psi\phi}$ the latter model allows also for a simple and unique softening of the ε_K-anomaly and of the tensions in the UT analysis if the FBPh in the Yukawa interactions are the dominant source of new CPV. In this case the NP phases φ_{B_s} and φ_{B_d} are related through

$$\varphi_{B_d} \approx \frac{m_d}{m_s}\varphi_{B_s} \approx \frac{1}{17}\varphi_{B_s}, \tag{3}$$

in visible contrast to the hypothesis $\varphi_{B_s} = \varphi_{B_d}$ of [48, 19]. Thus in this scenario, the large values of φ_{B_s} required to obtain values of $S_{\psi\phi}$ above 0.5 imply a unique small shift in $S_{\psi K_S}$ that allows to lower $S_{\psi K_S}$ from 0.74 down to 0.70, that is closer to the experimental value 0.672 ± 0.023. This in turn implies that it is $\sin 2\beta = 0.74$ and not $S_{\psi K_S} = 0.67$ that should be used in calculating ε_K resulting in a value of $\varepsilon_K \approx 2.0 \cdot 10^{-3}$ within one σ from the experimental value. The direct Higgs contribution to ε_K is negligible because of small masses $m_{d,s}$. We should emphasize that once φ_{B_s} is determined from the data on $S_{\psi\phi}$ by means of (2), the implications for ε_K and $S_{\psi K_S}$ are unique. It is remarkable that such a simple set up allows basically to solve all these tensions provided $S_{\psi\phi}$ is sufficiently above 0.5. The plots of ε_K and $S_{\psi K_S}$ versus $S_{\psi\phi}$ in [14] show this very transparently.

4.5.2 $S_{\psi\phi} \approx 0.25$

Yet, as signalled recently by CDF and D0 data [17], $S_{\psi\phi}$ could be smaller. In this case all non-MFV models listed above can reproduce such values and in particular this time also the LHT model [52] and another supersymmetric flavour model (AKM) analysed by us stay alive [32].

Again MSSM-MFV cannot reproduce such values. On the other hand the 2HDM$_{\overline{\rm MFV}}$ can still provide interesting results. Yet as evident from the plots in [14] the FBPh in Yukawa interactions cannot now solve the UT tensions. Indeed the relation in (3) precludes now any interesting effects in ε_K and $S_{\psi K_S}$: $S_{\psi\phi}$ and the NP phase φ_{B_s} are simply too small. Evidently, this time the relation

$$\varphi_{B_d} = \varphi_{B_s} \tag{4}$$

would be more appropriate.

Now, the analyses in [49, 50] indicate how such a relation could be obtained within the 2HDM$_{\overline{\rm MFV}}$. This time the FBPh in the Higgs potential are at work, the relation in (4) follows and the plots of ε_K and $S_{\psi K_S}$ versus $S_{\psi\phi}$ are strikingly modified: the dependence is much stronger and even moderate values of $S_{\psi\phi}$ can solve all tensions. This time not scalar LR operators but scalar LL operators are responsible for this behaviour.

Presently it is not clear which relation between φ_{B_s} and φ_{B_d} fits best the data but the model independent analysis of [49] indicates that φ_{B_s} should be significantly larger than φ_{B_d}, but this hierarchy appears to be smaller than in (3). Therefore as pointed out in [21] in the 2HDM$_{\overline{\rm MFV}}$ the best agreement with the data is obtained by having these phases both in Yukawa interactions and the Higgs potential, which is to be expected in any case. Which of the two flavour-blind CPV mechanisms dominates depends on the value of $S_{\psi\phi}$, which is still affected by a sizable experimental error, and also by the precise amount of NP allowed in $S_{\psi K_S}$.

Let us summarize the dynamical picture behind an enhanced value of $S_{\psi\phi}$ within 2HDM$_{\overline{\rm MFV}}$. For $S_{\phi\phi} \geq 0.7$ the FBPh in Yukawa interactions are expected to dominate. On the other hand for $S_{\phi\phi} \leq 0.25$ the FBPh in the Higgs potential are expected to dominate the scene. If $S_{\psi\phi}$ will eventually be found somewhere between 0.3 and 0.6, a hybrid scenario analyzed in [21] would be most efficient although not as predictive as the cases in which only one of these two mechanism is at work.

4.6 Implications of an enhanced $S_{\psi\phi}$

4.6.1 Preliminaries

Let us then assume that indeed $S_{\psi\phi}$ will be found to be significantly enhanced over the SM value. The studies of different observables in different models allow then immediately to make some concrete predictions on a number of observables which makes it possible to distinguish different models. This is important as $S_{\psi\phi}$ alone is insufficient for this purpose.

In view of space limitations I will discuss here only the implications for $B_{s,d} \to \mu^+\mu^-$ and $K \to \pi\nu\bar{\nu}$ decays, which we declared to be the superstars of the coming years. Subsequently I will make brief comments on a number of other superstars: EDMs, $(g-2)_\mu$, lepton flavour violation and ε'/ε.

4.6.2 $S_{\psi\phi} \geq 0.5$ scenario

The detailed studies of several models in which such high values of $S_{\psi\phi}$ can be attained imply the following pattern:

- In the AC model and the 2HDM$_{\overline{\rm MFV}}$, $Br(B_{s,d} \to \mu^+\mu^-)$ will be automatically enhanced up to the present upper limit of roughly $3 \cdot 10^{-8}$ from CDF and D0. The double Higgs penguins are responsible for this correlation [14, 21, 32].

- In the SM4 this enhancement will be more moderate: up to $(6-9)\cdot 10^{-9}$, that is a factor of 2-3 above the SM value [23, 25].

- In the non-abelian supersymmetric flavour model RVV2, $Br(B_{s,d} \to \mu^+\mu^-)$ can be enhanced up to a few 10^{-8} but it is not uniquely implied due to the pollution of double-Higgs contributions through gluino boxes, that disturbs the correlation present in the AC model [32].

- In the RSc, $Br(B_{s,d} \to \mu^+\mu^-)$ is SM-like independently of the value of $S_{\psi\phi}$ [53]. If the custodial protection for Z flavour violating couplings is removed values of 10^{-8} are possible [53, 54].

The question then arises what kind of implications does one have for $Br(B_d \to \mu^+\mu^-)$. Our studies show that

- The 2HDM$_{\overline{\rm MFV}}$ implies automatically an enhancement of $Br(B_d \to \mu^+\mu^-)$ with the ratio of these two branching ratios governed solely by $|V_{td}/V_{ts}|^2$ and weak decay constants.

- This familiar MFV relation between the ratio of these two branching ratios $Br(B_{s,d} \to \mu^+\mu^-)$ and $(|V_{ts}|/|V_{td}|)^2$ is strongly violated in non-MFV scenarios like AC and RVV2 models and as seen in Fig. 5 of [1] taken from [32] for a given $Br(B_s \to \mu^+\mu^-)$ the range for $Br(B_d \to \mu^+\mu^-)$ can be large with the values of the latter branching ratios being as high as $5 \cdot 10^{-10}$.

- Interestingly, in the SM4, large $S_{\psi\phi}$ accompanied by large $Br(B_s \to \mu^+\mu^-)$ precludes a large departure of $Br(B_d \to \mu^+\mu^-)$ from the SM value $1 \cdot 10^{-10}$ [25].

We observe that simultaneous consideration of $S_{\psi\phi}$ and $Br(B_{s,d} \to \mu^+\mu^-)$ can already help us in eliminating some NP scenarios. Even more insight will be gained when $Br(K^+ \to \pi^+\nu\bar{\nu})$ and $Br(K_L \to \pi^0\nu\bar{\nu})$ will be measured:

- First of all the supersymmetric flavour models mentioned above predict by construction tiny NP contributions to $K \to \pi\nu\bar{\nu}$ decays. This is also the case of the 2HDM$_{\overline{\rm MFV}}$.

- In the RSc model significant enhancements of both branching ratios are generally possible [53, 54] but not if $S_{\psi\phi}$ is large. Similar comments would apply to the LHT model where the NP effects in $K \to \pi\nu\bar{\nu}$ can be larger than in the RSc [52]. However, the LHT model has difficulties to reproduce a very large $S_{\psi\phi}$ and does not belong to this scenario.

- Interestingly, in the SM4 large $S_{\psi\phi}$, $Br(K^+ \to \pi^+\nu\bar{\nu})$ and $Br(K_L \to \pi^0\nu\bar{\nu})$ can coexist with each other [25].

4.6.3 $S_{\psi\phi} \approx 0.25$ scenario

In this scenario many effects found in the large $S_{\psi\phi}$ scenario are significantly weakend. Prominent exceptions are

- In the SM4, $Br(B_s \to \mu^+\mu^-)$ is not longer enhanced and can even be suppressed, while $Br(B_d \to \mu^+\mu^-)$ can be significantly enhanced [25].

- The branching ratios $Br(K^+ \to \pi^+\nu\bar{\nu})$ and $Br(K_L \to \pi^0\nu\bar{\nu})$ can now be strongly enhanced in the LHT model [52] and RSc model [53, 54] with respect to the SM but this is not guaranteed.

These patterns of flavour violations demonstrate very clearly the power of flavour physics in distinguishing different NP scenarios.

4.7 EDMs, $(g-2)_\mu$ and $Br(\mu \to e\gamma)$

These observables are governed by dipole operators but describe different physics as far as CP violation and flavour violation is concerned. EDMs are flavour conserving but CP-violating, $\mu \to e\gamma$ is CP-conserving but lepton flavour violating and finally $(g-2)_\mu$ is lepton flavour conserving and CP-conserving. A nice paper discussing all these observables simultaneously is [55].

In concrete models there exist correlations between these three observables of which EDMs and $\mu \to e\gamma$ are very strongly suppressed within the SM and have not been seen to date. $(g-2)_\mu$ on the other hand has been very precisely measured and exhibits a 3.2σ departure from the very precise SM value (see [56] and references therein). Examples of these correlations can be found in [32, 57]. In certain supersymmetric flavour models with non-MFV interactions the solution of the $(g-2)_\mu$ anomaly implies simultaneously d_e and $Br(\mu \to e\gamma)$ in the reach of experiments in this decade.

Here I would like only to report on correlations between $S_{\psi\phi}$ and the EDMs of the neutron, Thallium and Mercury atoms within the $2\text{HDM}_{\overline{\text{MFV}}}$. The significant FBPhs required to reproduce the enhanced value of $S_{\psi\phi}$ in this model, necessarily imply large EDMs in question. As a recent detailed analysis in [21] shows the present upper bounds on the EDMs do not forbid sizable non-standard CPV effects in B_s mixing. However, if a large CPV phase in B_s mixing will be confirmed, this will imply hadronic EDMs very close to their present experimental bounds, within the reach of the next generation of experiments.

4.8 News on right-handed currents

One of the main properties of the Standard Model regarding flavour violating processes is the left-handed structure of the charged currents that is in accordance with the maximal violation of parity observed in low energy processes. Yet, the SM is expected to be only the low-energy limit of a more fundamental theory in which parity could be a good symmetry implying the existence of RH charged currents. Prominent examples of such fundamental theories are left-right symmetric models on which a rich literature exists. We have also seen that several NP models that we discussed contain RH currents.

The recent phenomenological interest in the RH currents in general, and not necessarily in the context of a given left-right symmetric model as done recently in [27, 28], originated in tensions between inclusive and exclusive determinations of the elements of the CKM matrix $|V_{ub}|$ and $|V_{cb}|$. In particular it has been pointed out [29, 30, 31], that the presence of RH currents could either remove or significantly weaken some of these tensions, especially in the case of $|V_{ub}|$.

Assuming that RH currents provide the solution to the problem at hand, there is an important question whether the strength of the RH currents required for this purpose is consistent with other flavour observables and whether it implies new effects somewhere else that could be used to test this idea more globally.

In order to answer this question an effective theory approach for the study of RH currents has been proposed in [26]. In this approach the central role is played by a left-right symmetric flavour group $SU(3)_L \times SU(3)_R$, commuting with an underlying $SU(2)_L \times SU(2)_R \times U(1)_{B-L}$ global symmetry and broken only by two Yukawa couplings. The model contains a new unitary matrix V_R controlling flavour-mixing in the RH sector and can be considered as the minimally flavour violating generalization to the RH sector. Thus bearing in mind that this model contains

non-MFV interactions from the point of view of the standard MFV hypothesis that includes only LH charged currents, we will call this model RHMFV.

A detailed analysis of this setup in [26] shows that the general structure of V_R can be determined, under plausible assumptions, from the existing tree level decays in the K and B_d systems and FCNC processes. The presence of $(V-A)*(V+A)$ operators, whose contributions are strongly enhanced through renormalization group effects and in the case of ε_K also through chiral enhancement of their matrix elements, plays here an important role. The resulting V_R differs significantly from the CKM matrix.

As already stated above the RHMFV model goes beyond the MFV framework and new CPV phases in the RH sector allow for sizable enhancement of $S_{\psi\phi}$ and solution of the ε_K-anomaly as well as of the $|V_{ub}|$-problem. The resulting "true" value of $\sin 2\beta = 0.77 \pm 0.05$ is much larger than the measured value of $S_{\psi K_S} = 0.672 \pm 0.023$. Usually this problem would be solved through a negative new phase φ_{B_d}, however the ε_K constraint does not allow in this model for a non-negligible value of this phase. It appears then that the simultaneous explanation of the $|V_{ub}|$-problem, of large $S_{\psi\phi}$ and of the data on $S_{\psi K_S}$ is problematic through RH currents alone. Similarly in this simple setup the $B_{s,d} \to \mu^+\mu^-$ constraints eliminate the possibility of removing the known anomaly in $Z \to b\bar{b}$.

On top of it, the constraint from $B \to X_s l^+ l^-$ precludes $B_s \to \mu^+\mu^-$ to be close to its present experimental bound. Moreover NP effects in $B_d \to \ell^+\ell^-$ are found generally smaller than in $B_s \to \ell^+\ell^-$. Contributions from RH currents to $B \to \{X_s, K, K^*\}\nu\bar{\nu}$ and $K \to \pi\nu\bar{\nu}$ decays can still be significant. Most important, the deviations from the SM in these decays would exhibit a well-defined pattern of correlations.

4.9 Waiting for precise predictions of ε'/ε

The flavour studies of the last decade have shown that provided the hadronic matrix elements of QCD-penguin and electroweak penguin operators will be known with sufficient precision, ε'/ε will play a very important role in constraining NP models. We have witnessed recently an impressive progress in the lattice evaluation of $\hat{B}_K$ that elevated ε_K to the group of observables relevant for precision studies of flavour physics. Hopefully this could also be the case of ε'/ε already in this decade.

5 Summary

We are at the beginning of a new decade which certainly will bring us first more detailed insights into the physics at short distance scales $10^{-19} - 10^{-21}$m. The interplay of high energy collider results with the flavour precision experiments will allow us to make important steps towards a New Standard Model of which Flavour Theory will be a prominent part. For the time being we have to wait for the first big discoveries at the LHC and at other machines around the world. In particular we look forward to the full performance of the flavour superstars. These notes hopefully demonstrate that we will have a lot of fun with flavour physics in this decade.

Acknowledgements

I would like to thank the organizers for inviting me to such a pleasant conference and all my collaborators for exciting time we spent together exploring the short distance scales with the

help of flavour violating processes. In particular thanks go to Monika Blanke and Stefania Gori for reading carefully the manuscript of this paper. This research was partially supported by the Cluster of Excellence 'Origin and Structure of the Universe' and by the German 'Bundesministerium für Bildung und Forschung' under contract 05H09WOE.

References

[1] A. J. Buras, PoS E **PS-HEP2009** (2009) 024 [arXiv:0910.1032 [hep-ph]].

[2] G. Isidori, Y. Nir and G. Perez, arXiv:1002.0900 [hep-ph]; O. Gedalia and G. Perez, arXiv:1005.3106 [hep-ph].

[3] N. Cabibbo, Phys. Rev. Lett. **10** (1963) 531. M. Kobayashi and T. Maskawa, Prog. Theor. Phys. **49** (1973) 652.

[4] S. L. Glashow, J. Iliopoulos and L. Maiani, Phys. Rev. D **2** (1970) 1285.

[5] R. Fleischer and M. Gronau, Phys. Lett. B **660** (2008) 212 [arXiv:0709.4013 [hep-ph]].

[6] A. Lenz *et al.*, arXiv:1008.1593 [hep-ph]; ckmfitter.in2p3.fr

[7] G. D'Ambrosio, G. F. Giudice, G. Isidori and A. Strumia, Nucl. Phys. B **645** (2002) 155 [arXiv:hep-ph/0207036].

[8] A. J. Buras, P. Gambino, M. Gorbahn, S. Jager and L. Silvestrini, Phys. Lett. B **500** (2001) 161 [arXiv:hep-ph/0007085]. A. J. Buras, Acta Phys. Polon. B **34** (2003) 5615 [arXiv:hep-ph/0310208].

[9] A. L. Kagan, G. Perez, T. Volansky and J. Zupan, Phys. Rev. D **80** (2009) 076002 [arXiv:0903.1794 [hep-ph]].

[10] G. Colangelo, E. Nikolidakis and C. Smith, Eur. Phys. J. C **59** (2009) 75 [arXiv:0807.0801 [hep-ph]].

[11] L. Mercolli and C. Smith, Nucl. Phys. B **817** (2009) 1 [arXiv:0902.1949 [hep-ph]].

[12] P. Paradisi and D. M. Straub, Phys. Lett. B **684** (2010) 147 [arXiv:0906.4551 [hep-ph]].

[13] J. R. Ellis, J. S. Lee and A. Pilaftsis, Phys. Rev. D **76** (2007) 115011 [arXiv:0708.2079 [hep-ph]].

[14] A. J. Buras, M. V. Carlucci, S. Gori and G. Isidori, arXiv:1005.5310 [hep-ph].

[15] T. Aaltonen *et al.* [CDF Collaboration], Phys. Rev. Lett. **100** (2008) 161802 [arXiv:0712.2397 [hep-ex]]. V. M. Abazov *et al.* [D0 Collaboration], Phys. Rev. Lett. **101** (2008) 241801 [arXiv:0802.2255 [hep-ex]].

[16] V. M. Abazov *et al.* [D0 Collaboration], Phys. Rev. D **82** (2010) 032001 [arXiv:1005.2757 [hep-ex]]. V. M. Abazov *et al.* [D0 Collaboration], Phys. Rev. Lett. **105** (2010) 081801 [arXiv:1007.0395 [hep-ex]].

[17] T. Aaltonen *et al.* [CDF Collaboration], CDF public notes, 9458, 10206. V. M. Abazov *et al.* [D0 Collaboration], D0 Conference note 6098.

[18] E. Lunghi and A. Soni, Phys. Lett. B **666** (2008) 162 [arXiv:0803.4340 [hep-ph]].

[19] A. J. Buras and D. Guadagnoli, Phys. Rev. D **78**, 033005 (2008) [arXiv:0805.3887 [hep-ph]]; Phys. Rev. D **79** (2009) 053010 [arXiv:0901.2056 [hep-ph]].

[20] B. Batell and M. Pospelov, arXiv:1006.2127 [hep-ph].

[21] A. J. Buras, G. Isidori and P. Paradisi, arXiv:1007.5291 [hep-ph].

[22] W. S. Hou, M. Nagashima and A. Soddu, Phys. Rev. D **72** (2005) 115007 [arXiv:hep-ph/0508237]. Phys. Rev. D **76** (2007) 016004 [arXiv:hep-ph/0610385].

[23] A. Soni, A. K. Alok, A. Giri, R. Mohanta and S. Nandi, Phys. Lett. B **683** (2010) 302 [arXiv:0807.1971 [hep-ph]]. A. Soni, A. K. Alok, A. Giri, R. Mohanta and S. Nandi, arXiv:1002.0595 [hep-ph].

[24] M. Bobrowski, A. Lenz, J. Riedl and J. Rohrwild, Phys. Rev. D **79** (2009) 113006 [arXiv:0902.4883 [hep-ph]]. O. Eberhardt, A. Lenz and J. Rohrwild, arXiv:1005.3505 [hep-ph].

[25] A. J. Buras, B. Duling, T. Feldmann, T. Heidsieck, C. Promberger and S. Recksiegel, arXiv:1002.2126 [hep-ph]; JHEP **1007** (2010) 094 [arXiv:1004.4565 [hep-ph]]. A. J. Buras, B. Duling, T. Feldmann, T. Heidsieck and C. Promberger, arXiv:1006.5356 [hep-ph].

[26] A. J. Buras, K. Gemmler and G. Isidori, arXiv:1007.1993 [hep-ph].

[27] A. Maiezza, M. Nemevsek, F. Nesti and G. Senjanovic, arXiv:1005.5160 [hep-ph].

[28] D. Guadagnoli and R. N. Mohapatra, arXiv:1008.1074 [hep-ph].

[29] A. Crivellin, Phys. Rev. D **81** (2010) 031301 [arXiv:0907.2461 [hep-ph]].

[30] C. H. Chen and S. h. Nam, Phys. Lett. B **666** (2008) 462 [arXiv:0807.0896 [hep-ph]].

[31] R. Feger, V. Klose, H. Lacker, T. Lueck and T. Mannel, arXiv:1003.4022 [hep-ph].

[32] W. Altmannshofer, A. J. Buras, S. Gori, P. Paradisi and D. M. Straub, Nucl. Phys. B **830** (2010) 17 [arXiv:0909.1333 [hep-ph]].

[33] Z. Lalak, S. Pokorski and G. G. Ross, arXiv:1006.2375 [hep-ph].

[34] E. Dudas, G. von Gersdorff, J. Parmentier and S. Pokorski, arXiv:1007.5208 [hep-ph].

[35] S. L. Glashow and S. Weinberg, Phys. Rev. D **15** (1977) 1958.

[36] E. A. Paschos, Phys. Rev. D **15** (1977) 1966.

[37] F. J. Botella, G. C. Branco and M. N. Rebelo, Phys. Lett. B **687** (2010) 194 [arXiv:0911.1753 [hep-ph]].

[38] A. Pich and P. Tuzon, Phys. Rev. D **80** (2009) 091702 [arXiv:0908.1554 [hep-ph]]. M. Jung, A. Pich and P. Tuzon, arXiv:1006.0470 [hep-ph].

[39] B. A. Dobrescu, P. J. Fox and A. Martin, Phys. Rev. Lett. **105** (2010) 041801 [arXiv:1005.4238 [hep-ph]].

[40] C. B. Braeuninger, A. Ibarra and C. Simonetto, Phys. Lett. B **692** (2010) 189 [arXiv:1005.5706 [hep-ph]].

[41] A. J. Buras, arXiv:hep-ph/9806471.

[42] J. Brod and M. Gorbahn, arXiv:1007.0684 [hep-ph].

[43] J. Brod, M. Gorbahn and E. Stamou, arXiv:1009.0947 [hep-ph].

[44] D. J. Antonio *et al.* [RBC Collaboration and UKQCD Collaboration], Phys. Rev. Lett. **100** (2008) 032001 [arXiv:hep-ph/0702042]. C. Aubin, J. Laiho and R. S. Van de Water, Phys. Rev. D **81** (2010) 014507 [arXiv:0905.3947 [hep-lat]]. T. Bae *et al.*, arXiv:1008.5179 [hep-lat].

[45] B. Grzadkowski, M. Iskrzynski, M. Misiak and J. Rosiek, arXiv:1008.4884 [hep-ph].

[46] See the talk by Cecilia Tarantino at ICHEP 2019 and www.utfit.org

[47] A. J. Buras, D. Guadagnoli and G. Isidori, Phys. Lett. B **688** (2010) 309 [arXiv:1002.3612 [hep-ph]].

[48] P. Ball and R. Fleischer, Eur. Phys. J. C **48** (2006) 413 [arXiv:hep-ph/0604249].

[49] Z. Ligeti, M. Papucci, G. Perez and J. Zupan, arXiv:1006.0432 [hep-ph].

[50] K. Blum, Y. Hochberg and Y. Nir, arXiv:1007.1872 [hep-ph].

[51] C. W. Bauer and N. D. Dunn, arXiv:1006.1629 [hep-ph]. N. G. Deshpande, X. G. He and G. Valencia, arXiv:1006.1682 [hep-ph]. D. Choudhury and D. K. Ghosh, arXiv:1006.2171 [hep-ph]. C. H. Chen, C. Q. Geng and W. Wang, arXiv:1006.5216 [hep-ph]. P. Ko and J. h. Park, arXiv:1006.5821 [hep-ph]. S. F. King, arXiv:1006.5895 [hep-ph]. Y. Bai and A. E. Nelson, arXiv:1007.0596 [hep-ph]. J. Kubo and A. Lenz, arXiv:1007.0680 [hep-ph]. C. Berger and L. M. Sehgal, arXiv:1007.2996 [hep-ph]. B. Dutta, Y. Mimura and Y. Santoso, arXiv:1007.3696 [hep-ph]. S. Oh and J. Tandean, arXiv:1008.2153 [hep-ph].

[52] M. Blanke, A. J. Buras, B. Duling, S. Recksiegel and C. Tarantino, Acta Phys. Polon. B **41** (2010) 657 [arXiv:0906.5454 [hep-ph]].

[53] M. Blanke, A. J. Buras, B. Duling, K. Gemmler and S. Gori, JHEP **0903** (2009) 108 [arXiv:0812.3803 [hep-ph]]. M. Blanke, A. J. Buras, B. Duling, S. Gori and A. Weiler, JHEP **0903** (2009) 001 [arXiv:0809.1073 [hep-ph]].

[54] M. Bauer, S. Casagrande, U. Haisch and M. Neubert, arXiv:0912.1625 [hep-ph].

[55] J. Hisano, M. Nagai, P. Paradisi and Y. Shimizu, JHEP **0912** (2009) 030 [arXiv:0904.2080 [hep-ph]].

[56] J. Prades, Acta Phys. Polon. Supp. **3** (2010) 75 [arXiv:0909.2546 [hep-ph]].

[57] W. Altmannshofer, A. J. Buras and P. Paradisi, Phys. Lett. B **669** (2008) 239 [arXiv:0808.0707 [hep-ph]].

Review of charm physics: a theory perspective

Thomas Mannel

Theoretische Physik 1, Universität Siegen, 57068 Siegen, Germany

DOI: http://dx.doi.org/10.3204/DESY-PROC-2010-01/228

1 Introduction: why charm?

Charm physics has attracted significant and renewed attention due to new observations. On one hand, there has been convincing evidence of D-$\overline{D}$ mixing, paving the road to interesting weak interaction effects and maybe even to some new physics, on the other hand, a large number of narrow states is observed in the mass region of the J/ψ, which hints at some interesting effects in strong interaction physics of charmonia-like systems.

In this micro-review I will focus only on the electroweak and "new physics" aspects of charm physics; the spectroscopy of the new states cannot (yet?) be analyzed from fundamental QCD, and hence it is difficult at present to arrive at some conclusion concerning the QCD part of the standard model from these spectroscopic data.

From the flavour point of view the charm quark offers several unique possibilities. The flavour structure of the standard model, encoded in the fermion masses and in the CKM and PMNS mixing matrices, is quite peculiar. Strange and bottom physics test this flavour structure in a very similar way, since both are "down-type" quarks. Charm physics offers a possibility to test the flavour physics of the "up-type" quarks which has to be investigated as well in order to have a full test of the flavour structure.

One important observation in flavour physics is the strong suppression of flavour-changing neutral currents (FCNC's), which is implemented in the standard model by the Glashow-Iliopoulos-Maiani (GIM) mechanism [1]. GIM ensures that tree-level FCNC's are absent, implying also that FCNC's induced by loop diagrams yield finite results. In case of degenerate quark masses the standard model would have an additional flavour symmetry, which would protect it from any FCNC, even at loop level. This flavour symmetry is broken by the mass differences of the up-type quarks and of the down type quarks, and hence all FCNC's in the standard model are proportional to $(m_{u_i}^2 - m_{u_j}^2)$ or $(m_{d_i}^2 - m_{d_j}^2)$.

Thus, for the bottom and the strange quarks we have as an estimate, including a loop factor

$$\text{GIM-Suppression} \propto \text{CKM Factor}\, \frac{1}{16\pi^2}\, \frac{m_t^2 - m_u^2}{M_W^2} \tag{1}$$

indicating that the GIM mechanism is weakened by the large top mass. For this reason FCNC effects can appear at an observable level for strange and bottom quarks; in particular, the observation of B-$\overline{B}$ mixing in 1987 by ARGUS here at DESY [2] was the first hint at a large top mass, since for a lighter top quark these oscillations could not have been observed.

However, for charm the role of the up- and down-type quarks is interchanged. The corresponding GIM factor becomes

$$\text{GIM-Suppression} \propto \text{CKM Factor}\,\frac{1}{16\pi^2}\frac{m_b^2-m_d^2}{M_W^2} \tag{2}$$

resulting in a heavy suppression factor $\sim m_b^2/M_W^2$. Thus the SM contributions to up-type FCNC's like $c \to u$, $t \to c$ etc are in general tiny.

In turn, this opens an interesting new window to new physics, since the standard model "pollution" in these processes is small and the relative strength of a possible new physics contribution will thus be enhanced

$$\left(\frac{\text{New Physics Signal}}{\text{Standard Model noise}}\right)_{\text{up-type}} > \left(\frac{\text{New Physics Signal}}{\text{Standard Model noise}}\right)_{\text{down-type}}$$

assuming that a new physics contribution does not exhibit a GIM-like structure.

The only alternative possibility to investigate up-type flavour physics is by processes involving the top quark. However, due to the large mass and its lifetime, which is small compared to typical times for the formation of a hadron from quark constituents, the physics of the top quark is completely different. In particular, there is no formation of top hadrons such that e.g. T-$\overline{T}$ oscillations will not be possible. Hence the charm quark offers the unique possibility to study up-type quark flavour physics.

2 "Bread and butter" charm physics

A large portion of charm flavour physics is related to standard proceses involving the $\Delta C = \pm 1$ effective interaction. As in all quark flavour physics, the problem consists of calculating the hadronic matrix elements of operators formulated in terms of quarks and gluons. Since the charm quark mass is only about 1.2 GeV, it is a borderline case for the application of heavy quark expansions, since $\Lambda_{\rm QCD}/m_c \sim 0.3 - 0.4$.

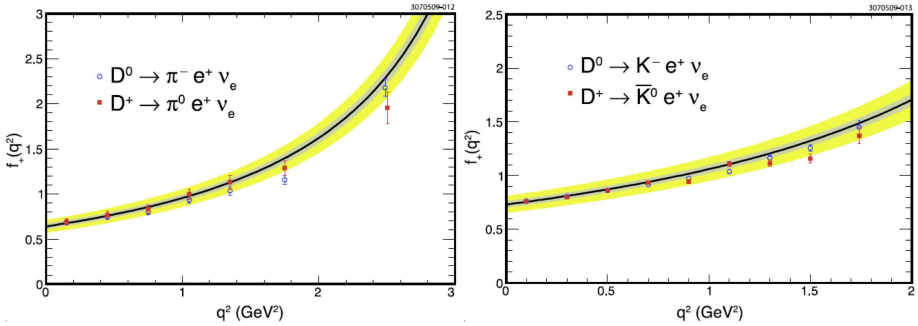

Figure 1: Data and theory predictions for exclusive semileptonic D decays [5].

Semileptonic decays are easier to treat and, in particular for exclusive decays, precises data has been taken e.g. at CLEO-c and the B facotries. The non-perturbative methods that may be used to calculate the necessary form factors are either lattice calculation [3] or (finite mass)

QCD sum rules. As an example, we show the results of a QCD sum rule estiamate [4]. Once the non-perturbative input is fixed, the data may be used for an independent extraction of V_{cd} and V_{cs}.

The extraction of the CKM elements proceeds through the measurement of the exclusive decays $D \to \pi\ell\bar{\nu}_\ell$ and $D \to K\ell\bar{\nu}_\ell$. The differential rate in the limit of vanishing final state masses reads

$$\frac{d\Gamma(D \to \pi\ell\nu)}{dq^2} = \frac{G_F^2|V_{cd}|^2}{24\pi^3} p_\pi^3 |f_+(q^2)|^2 \tag{3}$$

which is expressed in terms of the form factor f_+.

Fig. 1 shows the data for the form factor f_+ for the decays $D \to \pi\ell\bar{\nu}_\ell$ and $D \to K\ell\bar{\nu}_\ell$. in comparison with the theoretical prediction. Based on a QCD sum rule claculation one may extract a value for V_{cd}; we obtain $V_{cd} = 0.225 \pm 0.005 \pm 0.003^{+0.016}_{-0.012}$[4]. Note that this value is competitive with the value based on neutrino-antineutrino interactions [6].

Charmed hadrons have a large number of noneptonic decays due to the sizable mass of the charm quark. However, these decays are even more difficult to compute as the corresponding B decays, heavy mass expansion methods will not work as well here. While two body decays may be treated by the standard factorization assumption, the three and even four body decays are of interest for CP violation studies.

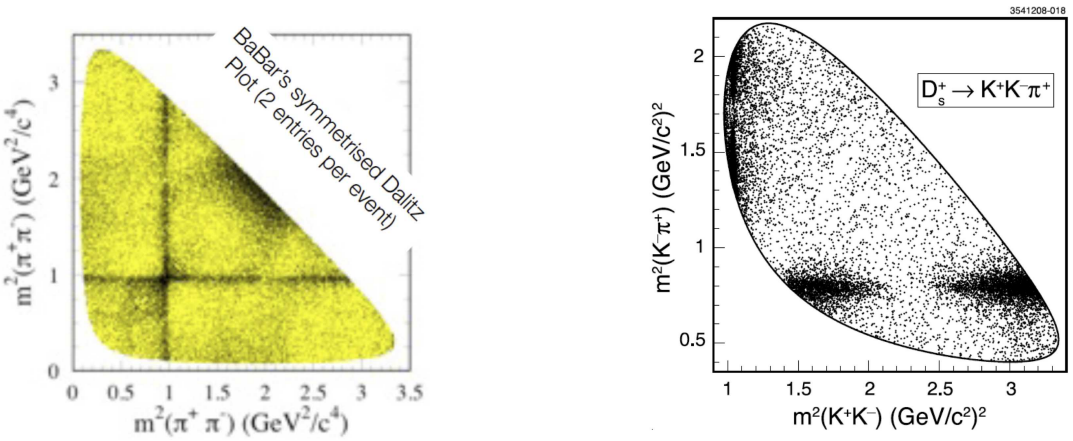

Figure 2: Dalitz distributions for three-body decays of the D meson.

Fig. 2 shows data for multiparticle final states from BaBar [7] and CLEO-c [8] for the decay $D_s \to \pi\pi\pi$ and $D_s \to KK\pi$ as examples for the quality of the present data. The resonance structures due the ρ, K^* and ϕ resonances are clearly visible; however a quantitative description of the Dalitz distrbutions is still difficult. However, as we shall see below, one may still define intresting observables with respect to CP violation studies.

3 Charm mixing

A special case for a FCNC is the $\Delta C = \pm 2$ interaction leading to the mixing of D^0 and $\overline{D}^0$. Thus in general, the charm eigenstates D^0 and $\overline{D}^0$ are not the same as the mass eigenstates

due to this interaction. Rather, the two mass eigenstates $D_{1/2}$ are superpositions of the two according to

$$|D_{1,2}\rangle = p|D^0\rangle \pm q|\overline{D}^0\rangle \quad \text{with} \quad |p|^2 + |q|^2 = 1 \tag{4}$$

In general, the two mass eigenstates have different mass eigenvalues as well as a different width. The mixing parameters are defined as

$$x = \frac{m_1 - m_2}{\Gamma} \quad y = \frac{\Gamma_1 - \Gamma_2}{2\Gamma} \quad \text{with} \quad \Gamma = \frac{1}{2}(\Gamma_1 + \Gamma_2) \tag{5}$$

In the standard model, the $\Delta C = \pm 2$ interaction is mediated at the quark level by the box diagrams shown in Fig. 3. However, only the b-quark contribution becomes an effectively local interaction, while the d and the s contributions contain long distance pieces. Unfortunately, unlike in the case of B-$\bar{B}$ oscillations, the purely short distance piece is suppressed by the small CKM factor $(V_{cb}V_{ub}^*)^2$ while the long distance parts are proportional to $(V_{cs}V_{us}^*)^2$ and $(V_{cd}V_{ud}^*)^2$ and hence do not suffer from a strong CKM suppression. However, as has been pointed out in eq.(2), there is still a factor m_s^2/M_W^2 aside from the CKM factors, and hence we expect in general only small D^0-$\overline{D}^0$ mixing.

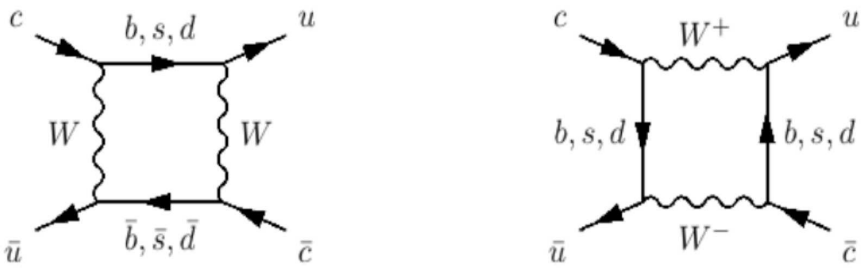

Figure 3: Quark level diagrams for D^0-$\overline{D}^0$ mixing

The long distance effects originating from the intermediate s and d quarks correspond in the hadronic world to common decay channels of the D and the $\overline{D}$; an example is shown in Fig. 4

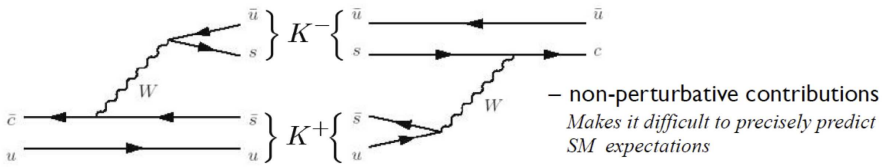

Figure 4: Example for a long distance contribution to D^0-$\overline{D}^0$ mixing

The long distance contributions are diffcult to estimate, and hence there is a substantial theoretical uncertainty in the calculation of x and y in the standard model. The typical results cover a range of $|x| \sim \mathcal{O}(10^{-3\cdots-2})$, $|y| \sim \mathcal{O}(10^{-3\cdots-2})$ [9]. The basis of these calculations are either an exclusive ansatz by summing over the possible common decay modes $D \to [K\pi/\pi\pi/\pi\rho/...] \to \overline{D}$

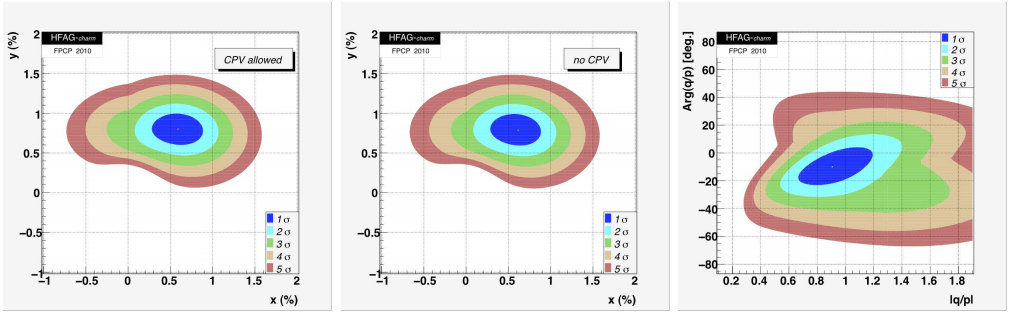

Figure 5: HFAG average for x and y

or by employing an operator product expansion which yields a series in inverse powers of the charm mass.

Charm mixing has attracted a lot of attention recently due to some experimental evidence. Fig. 5 shows the HFAG average [10] of the various data, ruling out the no-mixing case at a level of 5 σ. The most recent analyses yield $x = (0.59 \pm 0.20)\%$, $y = (0.80 \pm 0.13)\%$, $|p/q| = 0.91^{+0.19}_{-0.16}$ and $\arg(p/q) = -0.175^{+0.162}_{-0.152}$ rad, and hence there is evidence for D-$\overline{D}$ mixing. However, up to now there is no single 5 σ measurement.

From the theoretical side, the interpretation of these results is difficult due to long distance effects. A scenario where $|x| > 1\%$ and $|x| \gg |y|$ could be interpreted as a manifestion of new physics, however, this seems to be ruled out by the present data, which lie well within the standard-model expectations. However, due to the substantial hadronic uncertainties it may still contain a large new-physics contribution; a precise prediction within the standard model clearly requires a theoretical breakthrough in our ability to calculate hadronic matrix elements.

Although it is difficult to obtain a theory prediction for x and y, it is still of practical importance to know the values of these parameters, since the mixing opens the road to the possibility of time dependent CP asymmetries.

4 CP violation and new physics

Due to the small CKM angles between the first and third as well as between the second and the third family charm physics is mainly "two family" physics. Hence, in the standard model, the "pollution" of the third family is small and thus also all CP violating effects are small: There are no weak phases (and hence no CP violation) neither in Cabibbo allowed nor in doubly Cabibbo suppressed decays, and in singly Cabibbo suppressed decays the weak phase is of the order λ^4 where $\lambda \sim 0.2$ is the Wolfenstein parameter.

A direct CP violation usually occurs through an interference of two amplitudes with different CP phases. In the standard model this is the interference of a tree and a penguin diagram as shown in Fig. 6. It is well known that the resulting CP asymmetries are proportional to the strong phase difference of the two amplitudes and hence a quantitative estimate normally suffers from hadronic uncertainties.

However, due to the presence of D-$\overline{D}$ mixing the time evolution generates a phase difference $\sim \Delta m_D\, t$ where $\Delta m_D \propto x$ is the mass difference in the neutral D system. With respect to the

CP asymmetry, this phase difference acts like a strong phase and hence D-$\overline{D}$ oscillations offer a new window to measure CP asymmetries.

The time dependent CP asymmetry due to the small values of x and y may be written as

$$\mathcal{A}_{\rm CP}(t) = [x \sin\phi_{\rm CP} + y\,\epsilon_{\rm CP}\cos\phi_{\rm CP}]\left(\frac{t}{\tau}\right) \tag{6}$$

where $\phi_{\rm CP}$ is the weak phase of the D-$\overline{D}$ mixing amplitude, and $\epsilon_{\rm CP}$ corresponds to the parameter ϵ know from the kaon system and τ is the average lifetime. In the standard model we have $x, y \sim 1\%$ and $\phi_{\rm CP}, \epsilon_{\rm CP} \sim 10^{-3}$ and hence $\mathcal{A}_{\rm CP,SM}(t \sim \tau) = 10^{-5}$. Clearly such a small CP asymmetry is an exprimental challenge; in turn, if a sizable effect would turn up it would immediately imply the presence of new physics. In any case, channels like $D^0(t) \to K_s\phi, K^+K^-, \pi^+\pi^-, K^+\pi^-$ are interesting places to look for a CP asymmetry.

The ultimate tool for CP violation studies is to use the phase space distributions of multi-particle final states [11]. In general, local asymmetries can be expected to be larger than integrated ones, and one can also rely on relative normalizations instead of absolute ones. Furthermore, a phase space distribution may also give some hint on the nature of a possible new physics effect. The sensitivity and definitions of appropriate observables is currently under study.

Fig. 7 shows the current status of CP violation in charm decays [12] . There is no indication of an effect, however, we may expect that the uncertainties will reduce significantly in the near future.

5 FCNC decays

Rare FCNC decays are mediated by quark transitons of the form $c \to u + \gamma$ or $c \to u + \ell^+ + \ell^-$. At the quark level, these decays are supressed by the GIM mechanism, but there are also large long distance contributions, which are hard to calculate and which are several orders of magnitude larger than the short distance pieces.

The $c \to u + \gamma$ transitions at the quark level correspond to the decays $D_{(s)} \to \gamma + K^*/\rho/\omega/\phi$. The short distance piece mediated by the electromagnetic penguin diagram analgous to the one

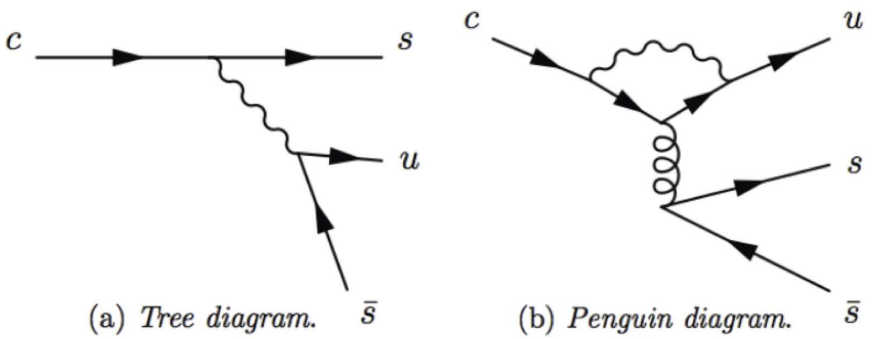

Figure 6: Tree and penguin diagrams for charm

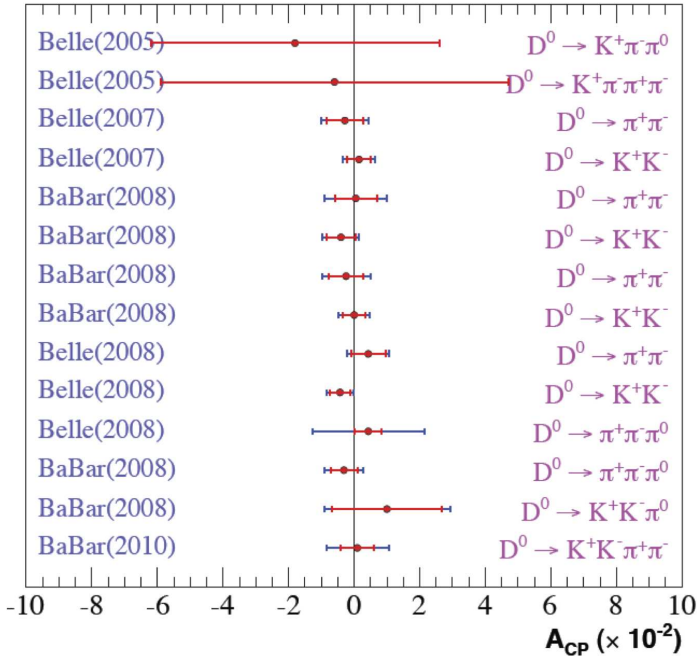

Figure 7: Current status of Charm CP measurements.

shown in Fig. 6 (b) yields a very small contribution of the order of BR $\sim$ few $\times 10^{-8}$ reflecting the GIM suppression. However, an estimate of the long distance contribution yields much larger branching ratios of the order $\mathrm{BR}(D^0 \to K^*\gamma) \sim 10^{-5} - 10^{-4}$ and $\mathrm{BR}(D^0 \to \rho\gamma) \sim 10^{-6} - 10^{-5}$ with a substantial uncertainty.

Any "new physics" in this case would appear through a local, penguin-like contribution of similar structure as the short distance operators. Unless this has an enormous coefficient that overwhelms even the long-distance contribution, this will be hard to identify. Again a theoretical breakthrough would be needed in the calculation of hadronic matrix elements before a convincing case for new physics in theses decays can be constructed.

The situation is not much different for the $c \to u + \ell^+ + \ell^-$ case. The decays $D_{(s)} \to \ell^+\ell^- + K^*/\rho/\omega/\phi$ are also dominated by long distance contributions, e.g. $\mathrm{BR}(D^0 \to \pi/\rho + \ell^+\ell^-) \sim 10^{-6}$ which is again three orders of magnitude larger than the short distance piece. However, the additional information contained in the lepton mass- and energy spectra my help to construct a new physics case.

Finally, purely leptonic FCNC modes may be good candidates for a search at LHC, while the mode $D^0 \to \gamma\gamma$ will be a challenge at any hadron machine. However, from the theoretical side, the mode $D^0 \to \gamma\gamma$ also has long distance contributions which are not well under control, which in turn pollute some of the interesting modes such as $D^0 \to \mu^+\mu^-$. Standard model estimates yield a small braching ratio, $\mathrm{BR}(D^0 \to \mu^+\mu^-) \sim 10^{-12}$.

References

[1] S. L. Glashow, J. Iliopoulos and L. Maiani, Phys. Rev. D **2** (1970) 1285.

[2] H. Albrecht *et al.* [ARGUS Collaboration], Phys. Lett. B **192**, 245 (1987).

[3] C. Aubin *et al.* [Fermilab Lattice Collaboration and MILC Collaboration and HPQCD Collab], Phys. Rev. Lett. **94** (2005) 011601 [arXiv:hep-ph/0408306].

[4] A. Khodjamirian, C. Klein, T. Mannel and N. Offen, Phys. Rev. D **80** (2009) 114005 [arXiv:0907.2842 [hep-ph]].

[5] Figure taken from the talk of K. Ecklund at "Flavour Physics and CP Violation 2010", Torino, Italy, May 2010, http://agenda.infn.it/getFile.py/access?contribId=22&resId=0&materialId=slides&confId=2635

[6] C. Amsler *et al.* [Particle Data Group], Phys. Lett. B **667**, 1 (2008).

[7] B. Aubert *et al.* [BABAR Collaboration], Phys. Rev. D **79** (2009) 032003 [arXiv:0808.0971 [hep-ex]].

[8] R. E. Mitchell *et al.* [CLEO Collaboration], Phys. Rev. D **79** (2009) 072008 [arXiv:0903.1301 [hep-ex]].

[9] For a review, see the talk by A. Lenz at "Open Charm @ PANDA", Mainz, November 2009, http://www.kph.uni-mainz.de/Dateien/03_lenz.pdf

[10] *Heavy Flavour Averaging Group*, http://www.slac.stanford.edu/xorg/hfag/

[11] I. Bediaga, I. I. Bigi, A. Gomes, G. Guerrer, J. Miranda and A. C. d. Reis, Phys. Rev. D **80** (2009) 096006 [arXiv:0905.4233 [hep-ph]].

[12] Figure taken from the talk of M. Martinelli at "Flavour Physics and CP Violation 2010", Torino, Italy, May 2010, http://agenda.infn.it/getFile.py/access?contribId=35&resId=1&materialId=slides&confId=2635

An Updated Measurement of the B_s^0 Mixing Phase $\sin(2\beta_s)$ at CDF

Elisa Pueschel for the CDF Collaboration

Carnegie Mellon University, 5000 Forbes Ave, Pittsburgh, PA 15213, USA

DOI: http://dx.doi.org/10.3204/DESY-PROC-2010-01/231

The phase of B_s^0 mixing (β_s) is extremely sensitive to new physics amplitudes and is still largely unconstrained experimentally. CDF reports the latest update of the $\sin(2\beta_s)$ measurement using $B_s^0 \to J/\psi\phi$ decays reconstructed in 5.2 fb^{-1} of data.

1 Introduction

The decay $B_s^0 \to J/\psi\phi$ presents a theoretically clean system in which to attempt indirect detection of new physics. The B_s^0 meson can decay directly to the $J/\psi\phi$ final state, as shown in the left diagram in Fig. 1. It can also mix into a $\bar{B}_s^0$ meson via a box diagram, as shown in the right diagram in Fig. 1, before decaying to the final state.

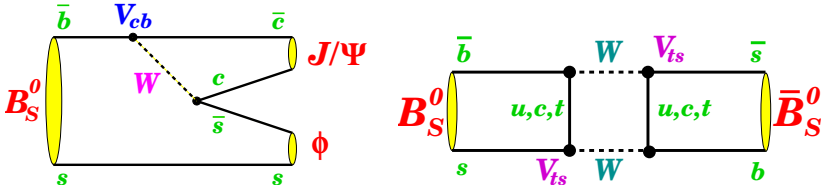

Figure 1: The B_s^0 meson can decay to $J/\psi\phi$ directly (left), or can mix to a $\bar{B}_s^0$ meson before decaying (right).

The mixing box diagram presents an interfering amplitude that can produce CP violation in this system, as well as providing a loop diagram in which new physics could participate. Should a non-standard model heavy particle be exchanged in the mixing box diagram, the CP violation produced by the interference between the direct decays and decays via mixing could be altered from the standard model expectation [1].

Neutral meson mixing occurs when a meson's mass and flavor eigenstates are not identical. This introduces several observables, including Δm_s, the mass difference between the mass eigenstates and also the mixing oscillation frequency, and $\Delta\Gamma_s$, the decay width difference between the mass eigenstates. Additionally, there exists a CP phase ϕ_s, which is expected to be close to zero in the standard model.

Although other mixing observables are measured, the determination of the CP violating phase β_s is the primary goal of this analysis. The phase is associated with the CP violation that occurs in the interference between the direct decay and decay via mixing amplitudes in

$B_s^0 \to J/\psi\phi$ decays. The phase β_s is defined in terms of elements of the Cabibbo-Kobayashi-Maskawa matrix as $\beta_s \equiv arg(-V_{ts}V_{tb}^*/V_{cs}V_{cb}^*)$, the smallest angle of the unitarity triangle produced by the second and third columns of the CKM matrix. The phase is expected to be quite small in the standard model, $\beta_s \approx 0.02$. Should new physics contributions produce an additional large CP violating phase, ϕ_s^{NP}, the new phase would dominate both β_s and ϕ_s.

2 Analysis Strategy

The decay $B_s^0 \to J/\psi\phi$ is a pseudoscalar decay to two vector particles. The angular momenta of the vector particles sum to produce three angular momentum final states. Two of the angular momentum states, the S and D waves, are CP even, while the P wave is CP odd. An angular analysis is required to determine the relative proportion of CP even to CP odd in the final state and measure β_s. This is done using the transversity basis, which describes a set of CP pure final state amplitudes. Three transversity angles, θ, ϕ, and ψ are also defined [2]. The linear polarization of the vector particles produce the time dependent amplitudes $A_\perp(t)$, $A_{||}(t)$, and $A_0(t)$. The amplitudes $A_\perp(t)$ and $A_{||}(t)$ are transversely polarized and CP odd and even, respectively, while $A_0(t)$ is longitudinally polarized and CP even. Information about the initial amplitudes is encoded in the strong phases $\delta_{||} \equiv (A_{||}(0)A_0^*(0))$ and $\delta_\perp \equiv (A_\perp(0)A_0^*(0))$.

The measurement of $\sin(2\beta_s)$ begins with the reconstruction of $B_s^0 \to J/\psi(\to \mu^+\mu^-)\phi(\to K^+K^-)$ events. The final state angular distributions are analyzed to extract the relative CP odd and CP even contributions. An angular analysis alone can be used to determine β_s, but sensitivity to $\sin(2\beta_s)$ is improved by taking into account whether the B meson was a B_s^0 or $\bar{B}_s^0$ at production. This requires flavor tagging algorithms that tag the B meson's initial flavor by tracks produced in association with the meson (same-side), or the decay products of the other half of the $b\bar{b}$ quark pair from which the reconstructed meson originated (opposite-side). The flavor tagging information is combined with the angular analysis into an un-binned maximum likelihood fit. The likelihood fit is used to extract all parameters of interest: most importantly $\sin(2\beta_s)$, but also $\Delta\Gamma$, the B_s^0 lifetime $\tau(B_s^0)$, the transversity amplitudes and the strong phases.

An additional consideration made in this update of the $\sin(2\beta_s)$ measurement is the possibility of the $B_s^0 \to J/\psi\phi$ signal being contaminated by non-resonant $B_s^0 \to J/\psi K^+K^-$ or $B_s^0 \to J/\psi f_0(980)$ [3]. In order to account for possible contamination, the likelihood is extended to fit for non-resonant contributions in the ϕ mass range. Both states are modeled with flat invariant mass distributions and flat phases with respect to the dominant P wave in the ϕ mass region used for the fit, an assumption that was validated with realistic Monte Carlo. A mass integration was performed over the ϕ mass window, as a K^+K^- mass-dependent fit was beyond the current scope of the analysis.

Before inclusion of non-resonant contributions, an exact symmetry under the transformation $(\beta_s, \Delta\Gamma, \delta_\perp, \delta_{||})$ to $(\pi/2-\beta_s, -\Delta\Gamma, \pi-\delta_\perp, 2\pi-\delta_{||})$ is present in the likelihood. This produces an ambiguity in the measurement of β_s, with two valid solutions in the space of β_s, $\Delta\Gamma$ and the strong phases. Should a substantial non-resonant contribution exist, it would interfere with the dominant P wave and break the symmetry in the likelihood, removing the ambiguity.

3 Data Selection and Calibration

This measurement relies on CDF's tracking subsystems for mass and spatial resolution, and on the particle identification subsystems for selection and tagging. Over 5 fb^{-1} of data from

a di-muon trigger were used. Backgrounds were suppressed using an artificial neural network trained on kinematic quantities such as the p_T of tracks and decay particles, and the vertex probability for decay particles. The cut on the neural network output was chosen by minimizing the β_s errors on pseudo-experiments. The final selection produced a signal sample of ∼6500 $B_s^0 \to J/\psi\phi$ events.

The flavor tagging algorithms employed in this measurement are developed on high statistics Monte Carlo samples, and their power must be calibrated to the relevant data samples. In the case of opposite side tagging, opposite side fragmentation products are used to tag the b or $\bar{b}$. The opposite fragmentation behavior is independent of the species of the reconstructed meson, and self-tagging $B^+ \to J/\psi K^+$ decays can be used to determine a tagging dilution scale factor.

The same side tracks used for tagging are dependent on the species of the associated B meson at production, thus the dilution scale factor must be determined on B_s^0 meson decays. An amplitude scan in the mixing frequency Δm_s was performed. The probability was normalized such that the amplitude should be unity at the true value of Δm_s. The measured amplitude relates the measured to the predicted tagging dilution. This measurement was performed using $B_s^0 \to D_s^- \pi^+$ and $B_s^0 \to D_s^- (3\pi)^+$ decays. The measured value of the amplitude at its maximum value is $\mathcal{A} = 0.94 \pm 0.15$ (stat) $\pm$ 0.13 (syst). The measured value of the mixing frequency is $\Delta m_s = 17.79 \pm 0.07$ ps^{-1}, well consistent with the world average.

4 Results

Fit projections were used to check the fit performance for the proper time distribution and the transversity angle distributions. The fit projection for the proper time is shown in Fig. 2. The lifetime distributions are different for the heavy and light B_s^0 mass eigenstates, enabling the measurement of $\Delta\Gamma$. The fit projections for the three transversity angles also show good agreement between the fit and the data distributions.

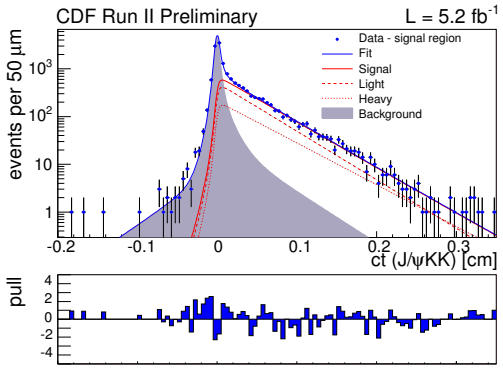

Figure 2: The B_s^0 meson's proper time fit projection. The lifetime distributions for the heavy and light mass eigenstates are denoted by the dashed red lines.

The likelihood shows biases (particularly for β_s) and non-Gaussian behaviors when β_s is allowed to float in the fit. When β_s is fixed to zero, the likelihood is well-behaved, making it possible to quote values for the remaining parameters of interest. The results are the following:

$$
\begin{aligned}
c\tau_s &= (458.7 \pm 7.5\ (\text{stat.}) \pm 3.6\ (\text{syst.}))\ \mu\text{m} \\
\Delta\Gamma &= (0.075 \pm 0.035\ (\text{stat.}) \pm 0.010\ (\text{syst.}))\ ps^{-1} \\
|A_\parallel(0)|^2 &= 0.231 \pm 0.014\ (\text{stat}) \pm 0.015\ (\text{stat}) \\
|A_0(0)|^2 &= 0.524 \pm 0.013\ (\text{stat}) \pm 0.015\ (\text{syst}) \\
\delta_\perp &= 2.95 \pm 0.65\ (\text{stat}) \pm 0.07\ (\text{syst}).
\end{aligned}
$$

For the fit with β_s floating, a profile likelihood ordering technique was used to guarantee coverage at the 68% and 95% confidence levels. The final contour in the $\beta_s - \Delta\Gamma$ plane is shown in the left plot in Fig. 3. The p-value at the standard model point was calculated to be 44%, indicating a good consistency with the standard model expectation. The right plot in Fig. 3 shows the one dimensional β_s confidence interval. The p-value at the standard model point for this case is 31%. In both the two dimensional and one dimensional confidence regions, the two solutions for β_s are of nearly identical depth, because the measured non-resonant contamination was too small to break the symmetry of the likelihood. The non-resonant K^+K^-/f_0 fraction is measured to be less than 6.7% at the 95% confidence level.

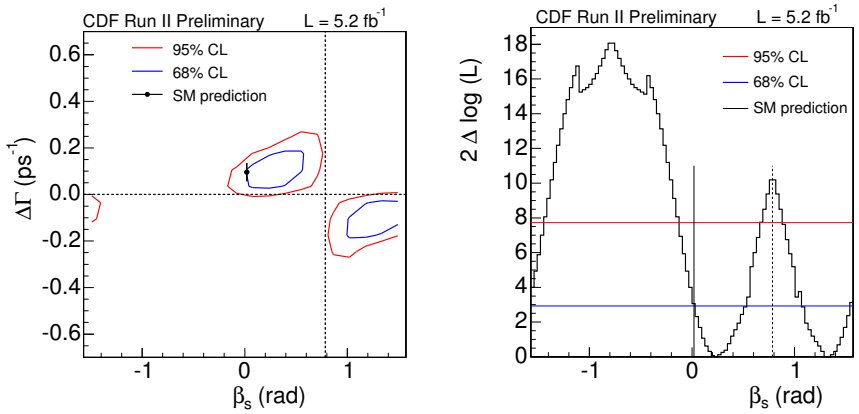

Figure 3: Confidence regions in the $\beta_s - \Delta\Gamma$ plane (left) and β_s (right).

This latest measurement of CP violation in $B_s^0 \to J/\psi\phi$ decays on 5.2 fb^{-1} of data shows improvement in the errors on β_s and the decay width difference $\Delta\Gamma$, as well as greater consistency with the standard model expectation. It is expected that CDF will double its data sample by the end of Run II, allowing an even more precise determination of $\sin(2\beta_s)$.

References

[1] I. Dunietz, R. Fleischer and U. Nierste, Phys. Rev. D **63** (2001) 114015.

[2] A. S. Dighe, I. Dunietz and R. Fleischer, Eur. Phys. J. C **6** (1999) 647.

[3] S. Stone, L. Zhang, [arXiv:hep-ph/0812.2832].

Towards the measurement of the J/ψ cross section at $\sqrt{\mathrm{s}} = 7\,\mathrm{TeV}$ in LHCb

Julien Cogan for the LHCb Collaboration

CPPM/IN2P3, Marseille, France

DOI: http://dx.doi.org/10.3204/DESY-PROC-2010-01/224

The J/ψ production in inelastic collisions at a centre-of-mass energy of $\sqrt{s} = 7\,\mathrm{TeV}$ is studied with the LHCb detector. Using the data collected between April and June 2010 at the Large Hadron Collider, LHCb will measure the p_T differential cross section in the region $p_\mathrm{T} \in [0; 10]\,\mathrm{GeV}/c$ integrating over the rapidity range $y \in [2.5; 4]$. The ongoing analysis should lead to a first measurement with an accuracy better than 15% ignoring the effect of the unknown J/ψ polarization.

1 Introduction

The measurement of heavy quark production in hadron colliders allows probing the spectrum and dynamics of the partons of the colliding hadrons. In particular, the study of heavy quark-antiquark resonances (quarkonia), such as the $c\bar{c}$ bound state J/ψ, is interesting because these states have large production cross sections and can be produced in different spin configurations. Although J/ψ production was studied by several experiments in the past, the underlying production mechanism is still not yet completely understood.

In the comparison between experimental J/ψ observables and theoretical computations one should take into account the fact that there are three major sources of J/ψ production in pp collisions:

- direct J/ψ production,
- feed-down J/ψ from other heavier prompt charmonium states like χ_{c1} or χ_{c2},
- J/ψ from b-hadron decay chains, possibly through heavier charmonium intermediate decays.

The first two sources will be called prompt J/ψ in the following. The third source will be abbreviated as J/ψ from b.

As a first measurement with early LHC data, LHCb aims at measuring the production cross sections of J/ψ and of J/ψ from b, as a function of the J/ψ transverse momentum p_T integrating over the rapidity range $y \in [2.5; 4]$ in the pp centre-of-mass frame. The J/ψ are reconstructed in the decay mode $\mathrm{J}/\psi \to \mu^+\mu^-$ and J/ψ from b-hadron decays are separated from prompt J/ψ using the J/ψ pseudo-propertime. The status of this analysis is reported here.

2 The LHCb detector and dataset

The study reported here uses data collected at the LHC at a centre-of-mass energy of 7 TeV between April and June 2010 with low pile-up conditions. This data sample corresponds to about $14\,\mathrm{nb}^{-1}$ of pp collisions. The LHCb detector is a forward detector described in detail in [1]. The analysis makes use of all LHCb detector components, except the RICH detectors. For all data included in the analysis the VELO detector was at its closed nominal position.

3 Monte-Carlo simulation

Monte Carlo samples were generated at a centre-of-mass energy of 7 TeV using a software based on the PYTHIA generator [2]. Prompt J/ψ production processes activated in PYTHIA are the Leading Order Color Singlet and Color Octet processes. Their implementation and the parameters used are described in detail in [3].

4 Selected J/ψ

4.1 J/ψ selection

In this preliminary analysis, the J/ψ candidates are formed from a pair of long tracks[1] of opposite charge with p_{T} larger than 700 MeV/c, which are required to be well reconstructed both in the tracking detectors and in the the muon stations. Both tracks must be identified as muons and of good track fit quality ($\chi^2/ndof < 4$). The two muons are required to originate from a common vertex, and only candidates giving a good quality vertex ($\chi^2/ndof < 15$) are kept. The invariant mass distribution of the muon pairs passing this selection is shown in Fig. 1.

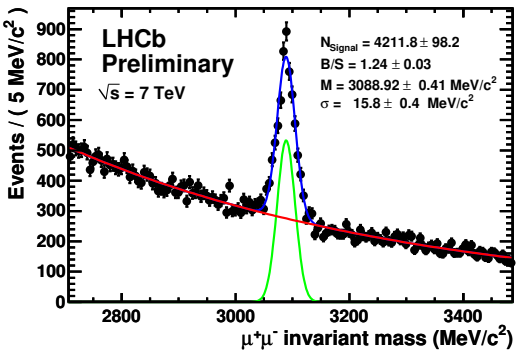

Figure 1: $\mu^+\mu^-$ invariant mass distribution

[1] A track is defined as long if it has hits reconstructed in the vertex detector and in the main tracking stations after the dipole magnet

4.2 Raw spectra

The transverse momentum and rapidity distributions of the selected J/ψ is plotted in Fig. 2, showing a softer p_{T} spectrum in the data than the one used in our simulation.

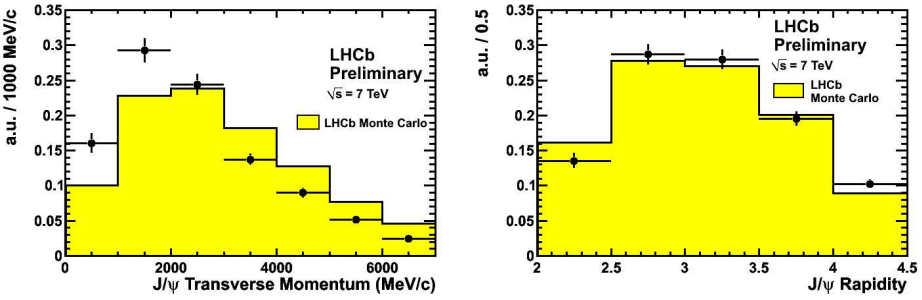

Figure 2: Transverse momentum (left) and rapidity (right) spectra for selected J/ψ (dots) and simulation (filled histogram)

4.3 Distinction between prompt J/ψ and J/ψ from b

J/ψ from b tend to be far from the primary vertex. They are separated from prompt J/ψ which are produced immediately at the primary vertex by exploiting the J/ψ proper time in the z direction. The z axis is defined along the beam axis in the LHCb frame, and is oriented from the VELO to the Muon detector. The discriminating variable (J/ψ pseudo propertime) is defined as:

$$t_z(\mathrm{J}/\psi) = \frac{d_z \times M_{\mathrm{J}/\psi}}{p_z} \tag{1}$$

where d_z is the distance along the z-axis between the J/ψ decay vertex and the primary vertex from which it originates ; p_z is the J/ψ momentum in the z direction and $M_{\mathrm{J}/\psi}$ is the nominal J/ψ mass.

The obtained distribution for J/ψ candidates is shown in Fig. 3. The plot on the right, obtained after subtracting the background using the sidebands, shows a clear signal from B hadron decays.

5 Towards the cross section determination

The cross section σ is defined as:

$$\sigma = \frac{N\left(\mathrm{J}/\psi \to \mu^+\mu^-\right)}{\mathcal{L} \times \epsilon \times \mathcal{B}\left(\mathrm{J}/\psi \to \mu^+\mu^-\right)}, \tag{2}$$

where $N\left(\mathrm{J}/\psi \to \mu^+\mu^-\right)$ is the number of observed J/$\psi \to \mu^+\mu^-$, ϵ is the J/ψ detection efficiency, $\mathcal{L}$ the integrated luminosity, and $\mathcal{B}\left(\mathrm{J}/\psi \to \mu^+\mu^-\right)$ the branching fraction of the J/$\psi \to \mu^+\mu^-$ decay.

The determination of the quantities entering Eq. 2 is ongoing. The luminosity will be determined with a 10% uncertainty using measurements of the beam profiles that exploit the high

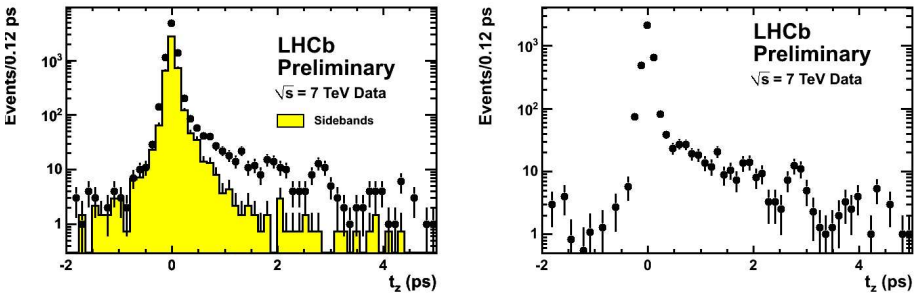

Figure 3: Left : Pseudo propertime distribution for candidates in signal (dots) and sidebands regions (filled histogram); right : pseudo proper time for signal events after sideband subtraction.

precision of the LHCb VELO. The detection efficiency factorizes the geometrical acceptance, the reconstruction and selection efficiency, and the trigger efficiency. For this first measurement, it will be estimated from simulation. The unknown J/ψ polarization yields to large uncertainties (up to 20%) on the geometrical acceptance that will be studied using simulation. The remaining systematic uncertainties will be assigned using data driven methods and are expected to be kept below 15% in total.

6 Conclusion

With a sample of $\sim 14\,\mathrm{nb}^{-1}$ of pp collisions, LHCb will measure the production cross sections of prompt J/ψ and of J/ψ from b, as a function of the J/ψ transverse momentum p_{T} integrating over the rapidity range $y \in [2.5; 4]$ in the pp centre-of-mass frame. The analysis is ongoing and shows excellent prospects. It should allow to measure the total cross section in the region $p_{\mathrm{T}} \in [0; 10]\,\mathrm{GeV}/c$ and $y \in [2.5; 4]$ with an accuracy better than 15% ignoring the effect of the unknown J/ψ polarization.

References

[1] A. Alves *et al.* [The LHCb collaboration], JINST **3** (2008) S08005

[2] T. Sjöstrand, S. Mrenna and P. Z. Skands, hep-ph/0603175, JHEP 05 (2006) 026.

[3] M. Bargiotti and V. Vagnoni, CERN-LHCb-2007-042.

b and c physics with early ATLAS data

Nir Amram for the ATLAS Collaboration

Tel Aviv University, Tel-Aviv 69978, Israel
CERN CH-1211, Genve 23, Switzerland

DOI: will be assigned

Studies of the first $J/\psi \to \mu^+\mu^-$ and $D^{*\pm}$, $D^{\pm}$ and $D_s^{\pm}$ observations using the ATLAS detector, in 7 TeV proton-proton collisions at the LHC, is reported.

1 Introduction

Production of charm mesons is one of the first hard processes to be measured at the LHC. Study of the J/ψ resonance and a D^* meson signatures with early Large Hadron Collider (LHC) [1] data is one of the first goals of the ATLAS [2, 3] physics programme. Measuring the J/ψ production and properties in ATLAS is a crucial step both for understanding the detector performance and for performing measurements of various B-physics channels.

In this note we present the first studies on the J/ψ resonance of the di-muon decay channel and $D^{*\pm}$, $D^{\pm}$, $D_s^{\pm}$ with the ATLAS detector using data collected in $\sqrt{s} = 7$ TeV proton-proton collisions at the LHC. The former study corresponds to an integrated luminosity of 6.4 ± 1.3 nb^{-1} and the latter to 0.37 nb^{-1}.

2 Properties of the $J/\psi \to \mu^+\mu^-$ signal

Invariant mass distributions are studied for di-muon pairs. In all cases Inner Detector (ID) [4] track parameters are used to calculate the properties of the J/ψ candidates.

An unbinned maximum-likelihood fit is used to extract the J/ψ mass and the number of J/ψ signal candidates from the data. The number of signal events N_{sig} and background events N_{bck} is calculated in the mass interval of $m_{J/\psi} \pm 3\sigma_m$.

In Figure 1 (left plot) the invariant mass for all oppositely charged muon pairs passing vertexing is shown. In the same figure, the fit function to the prompt J/ψ Monte Carlo (MC) samples, normalised to the number of signal events observed, is also shown. The fit results from data and MC are summarised in Table 1.

The invariant mass resolution depends on the pseudorapidities of the two muon tracks. In order to investigate further the measured properties of J/ψ candidates found in different regions of the detector, the candidates are divided into three categories: both muons in the barrel ($\eta < 1.05$) detector (BB); one muon in the endcap ($\eta \geq 1.05$) and one in the barrel (EB); both muons in the endcap (EE). The same mass fit is performed on each of these categories.

As expected, due to material effects, the mass width when both muons are in the endcap region is $\sim$2.5 times greater than when both muons are in the barrel. This behavior is also well reproduced in the MC.

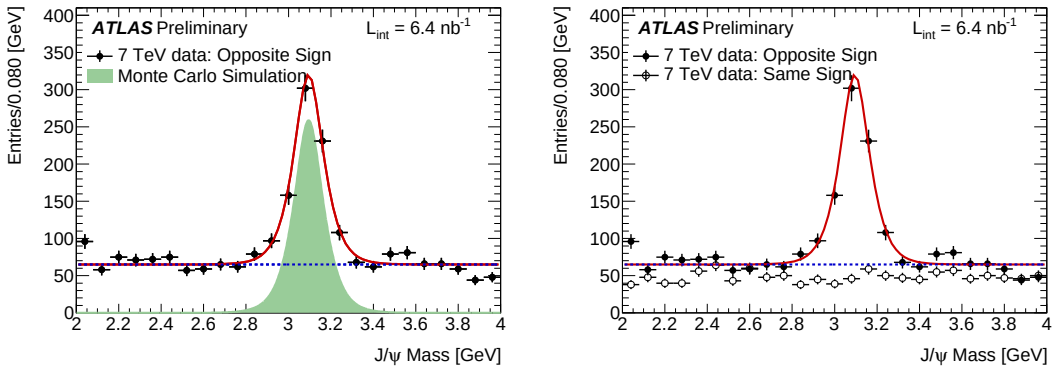

Figure 1: Invariant mass distribution of reconstructed $J/\psi \to \mu^+\mu^-$ candidates. Comparison of data to MC (left) and opposite-sign to same-sign di-muon pairs (right). The points with error bars are data. The solid line is the result of maximum likelihood unbinned fit to all di-muon pairs in the mass window 2–4 GeV and the dashed line is the result for the background of the same fit. The result of the fit to the prompt J/ψ MC is represented by solid area. Same sign combinations in open circles.

		$m_{J/\psi}$, GeV	σ_m, MeV	N_{sig}	N_{bck}
all	data	3.095 ± 0.004	82 ± 7	612 ± 34	332 ± 9
	MC	3.098 ± 0.001	74 ± 0.4		
BB	data	3.097 ± 0.005	36 ± 6	69 ± 9	8 ± 1
	MC	3.098 ± 0.001	37 ± 0.7		
EB	data	3.089 ± 0.008	66 ± 12	88 ± 11	34 ± 3
	MC	3.097 ± 0.001	53 ± 0.8		
EE	data	3.095 ± 0.006	88 ± 9	437 ± 31	324 ± 10
	MC	3.098 ± 0.001	82 ± 0.5		

Table 1: Summary of fit results to mass distributions of $J/\psi \to \mu^+\mu^-$ candidates. The number of background events is given in the range $m_{J/\psi} \pm 3\sigma_m$. The same fit is applied to prompt J/ψ MC data. Results for data before vertexing are shown for comparison.

The current analysis has access to very low p_{T} J/ψ candidates producing soft p_{T} muon tracks, which are nevertheless detected in the Muon Spectrometer (MS) [5]. Muons with enough energy to cross the calorimeters reach the MS mainly in the forward region (where $p >> p_T$). As a consequence, the J/ψ candidates in this momentum regime have preferentially high rapidity.

3 Reconstruction of Charm Mesons

$D^{*\pm}$, $D^{\pm}$ and D_s^+ charm mesons were reconstructed in the range of transverse momentum $p_T(D^{(*)}) > 3.5$ GeV and pseudorapidity $|\eta(D^{(*)})| < 2.1$. Charm-meson candidates were reconstructed using tracks measured in the ATLAS inner tracking detector. We exploit the hard nature of charm fragmentation with the selections $p_T(D^*) > 3.5\ GeV$, $p_T(K,\pi) > 1.0\ GeV$, and $p_T(D^*)/\Sigma E_T > 0.02$, where ΣE_T is the total transverse energy in the detector.

The dE/dx particle identification was not used since it is not effective in the kinematic ranges utilized for the charm-meson reconstruction. Instead, kaon and pion masses were assumed in turn for each tracking term.

$D^{*\pm}$ mesons were identified using the decay channel $D^{*+} \to D^0\pi_s^+ \to (K^-\pi^+)\pi_s^+$. The top left plot in Fig. 2 shows the mass difference $\Delta M = M(K\pi\pi_s) - M(K\pi)$ distribution for the $D^{*\pm}$ candidates which satisfy $1.83 < M(K\pi) < 1.90$ GeV. A clear signal is seen at the nominal value of $M(D^{*+}) - M(D^0)$. The top right plot in Fig. 2 shows the $M(K\pi)$ distribution for the $D^{*\pm}$ candidates which satisfy $144 < \Delta M < 147$ MeV. A clear signal of the D^0 mass is measured with 2100 events to be $1865.5 \pm 1.4\ MeV$, in agreement with the PDG world average [6].

$D^{\pm}$ mesons were reconstructed from the decay $D^+ \to K^-\pi^+\pi^+$. Figure 2 shows the $M(K\pi\pi)$ distribution (bottom left) for the $D^{\pm}$ candidates after all cuts. A clear signal of the D^+ mass is measured with 1667 events to be $1871.8 \pm 1.1\ MeV$, in agreement with the PDG value. The width of the signal is in agreement with the MC expectation.

$D_s^{\pm}$ mesons were reconstructed from the decay $D_s^+ \to \phi\pi^+$ with $\phi \to K^+K^-$. The bottom right plot in Fig. 2 shows the $M(KK\pi)$ distribution for the $D_s^{\pm}$ candidates with $M(KK)$ within ± 6 MeV of the nominal ϕ mass. A clear signal of the D_s^+ mass is measured with 326 events to be $1971.5 \pm 4.6 MeV$, in agreement with the PDG value. A smaller signal is expected around the nominal D^+ mass from the decay $D^+ \to \phi\pi^+$ with $\phi \to K^+K^-$.

4 Summary and conclusions

The decay $J/\psi \to \mu\mu$ is observed in ATLAS data using combined information from the muon spectrometer and the inner detector. A clear peak in the data is seen with an integrated luminosity of $6.4 \pm 1.3\mathrm{nb}^{-1}$. The peak has been fitted using an unbinned maximum likelihood method; this yields an overall mean of 3.095 ± 0.004 GeV, which is in agreement with the PDG value for the J/ψ mass within statistical uncertainty. The signal resolution is 82 ± 7 MeV, in line with Monte Carlo expectations. The mass resolution varies with the pseudorapidity of the muons, as expected, and this variation is in agreement with Monte Carlo within statistical uncertainty. We conclude by stating that the final number of observed $J/\psi \to \mu\mu$ decays was 612 ± 34, over a background of 332 ± 9 candidates.

Clean $D^{*\pm}$, $D^{\pm}$ and $D_s^{\pm}$ signals have been reconstructed with the ATLAS detector using $1.4\,\mathrm{nb}^{-1}$ of integrated luminosity. The fitted mass values were found to be in agreement with their PDG world averages while the observed invariant mass resolution agrees with MC expectations.

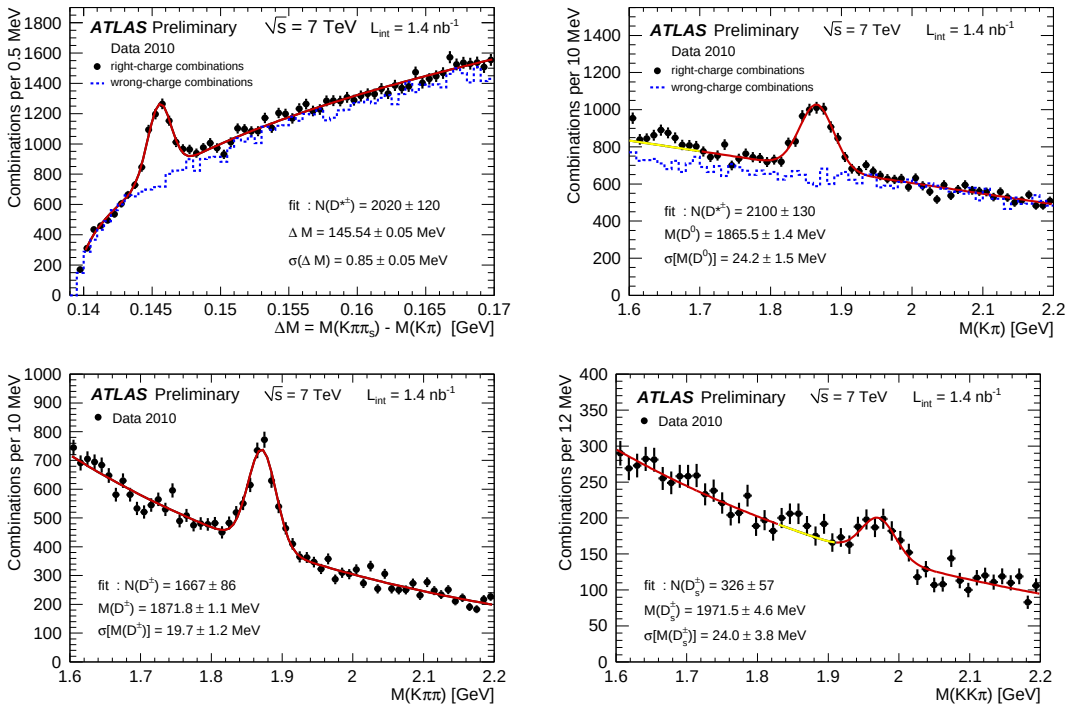

Figure 2: The distribution of the mass difference, $\Delta M = M(K\pi\pi_s) - M(K\pi)$ (top left) and the $M(K\pi)$ distribution for the $D^{*\pm}$ candidates (top right). The $M(K\pi\pi)$ distribution for the $D^{\pm}$ candidates (bottom left). The $M(KK\pi)$ distribution for the $D_s^{\pm}$ candidates (bottom right). The dashed histograms show the distributions for wrong-charge combinations. The solid curves represent fit results.

These studies confirm the high performance of the ATLAS detector for precision tracking measurements.

References

[1] L. Evans and P. Bryant, *LHC machine*, JINST **3** (2008) S08001.

[2] ATLAS Collaboration, G. Aad et al., *The ATLAS Experiment at the CERN Large Hadron Collider*, JINST **3** (2008) S08003.

[3] C. Clement, *ATLAS first physics results*, in *Proceedings of Physics at the LHC 2010*. 2010.

[4] ATLAS Collaboration, *ATLAS inner detector: Technical Design Report. Vol. 1*, Tech. Rep. CERN-LHCC-97-16, CERN, Geneva, Apr, 1997.

[5] ATLAS Collaboration, *The ATLAS Muon Spectrometer Technical Design Report*, Tech. Rep. CERN-LHCC-97-22, CERN, Geneva, Mar, 1997.

[6] PDG Collaboration, C. Amsler et al., *Review of Particle Physics*, Phys. Lett. **B667** (2008) 1.

Results and prospects for di-muon final states at LHCb

Justine Serrano for the LHCb Collaboration

Centre de physique des particules de Marseille, 163 avenue de Luminy, Marseille, France

DOI: http://dx.doi.org/10.3204/DESY-PROC-2010-01/227

Final states of rare decays with di-muons have a very high trigger efficiency in LHCb and will provide some of the most promising analyses for new physics. With the 2010 data from the LHC the focus will be on the search for the decays $B_s \to \mu^+\mu^-$ and $D^0 \to \mu^+\mu^-$ as well as a first angular analysis of $B_d \to K^*\mu^+\mu^-$. The first data collected by LHCb have been used to start the validation of some key aspects of these analyses. In this context, the LHCb capabilities in constraining new physics models through the studies of rare decays are discussed.

1 Introduction

Decays of heavy flavour mesons which proceed via flavor changing neutral currents (FCNC) are forbidden at the tree level in the Standard Model (SM). As a consequence, they are heavily suppressed and form an excellent probe to search for new physics (NP) as virtual new particles can enter in the loop processes. Rare decays with di-muons in the final state are of particular interest for LHCb as they have a very high trigger efficiency. Here, the LHCb potential for the search of new physics in $B_s \to \mu^+\mu^-$, $D^0 \to \mu^+\mu^-$ and $B_d \to K^*\mu^+\mu^-$ is discussed. The first data collected by LHCb (about 14 nb^{-1}) at a center-of-mass energy of 7 TeV, have been used to start the validation of the key aspects of these analyses. In particular, the performance of the muon trigger, muon identification, tracking and vertexing has been demonstrated using mainly $J/\psi \to \mu^+\mu^-$ and $K_s \to \pi^+\pi^-$ samples.

2 Search for $B_s \to \mu^+\mu^-$

The helicity suppressed $B_s \to \mu^+\mu^-$ decay is due to very rare loop diagrams in the SM and its branching ratio (BR) is expected to be extremely small: $(3.6 \pm 0.4) \times 10^{-9}$ [1] but NP models such as for example supersymmetry could enhance it up to several orders of magnitude. The current best limits are achieved by CDF [2], BR$< 3.6 \times 10^{-8}$ at 90% confidence level (CL) (3.7 fb^{-1}), and D0 [3], BR$< 5.1 \times 10^{-8}$ at 95% CL (6.1 fb^{-1}). The LHCb event selection for this decay is based on a loose preselection to reject most of the background, followed by a multidimensional analysis based on three variables: the $\mu^+\mu^-$ invariant mass, and two likelihood variables, one describing the particle identification information and the second describing the geometrical information of the decay (impact parameter significance of the muons, B_s proper time, impact parameter of the B_s, distance of closest approach between the two muons, muon

isolation). The last step of the analysis consists of using a normalisation channel to derive the BR. Several $B_{u,d}$ channels are envisaged as $B_d \to K^+\pi^-$ or $B_u \to J/\psi\, K^+$. The use of these decays introduces a systematic uncertainty due to the poorly known hadronization rate ratio $f_{u,d}/f_s$ which can become dominant at high statistics [4]. A new method has been proposed recently to derive this ratio from data [5].

To validate the different analysis steps, a sample of more than 3500 $J/\psi \to \mu^+\mu^-$ events has been selected in the data. The $\mu^+\mu^-$ invariant mass resolution found is 16 MeV/c^2, which, given the fact that the tracking and alignement is not yet fully calibrated, is promising for the $B_s \to \mu^+\mu^-$ study. Same sign events have also been used to subtract background from data and study J/ψ distributions like the vertex χ^2 or the muon transverse momentum. The geometrical likelihood function has been validated using $K_s \to \pi\,\pi$ and $D^0 \to k\,\pi$ decays. A good agreement between data and simulation is visible. In the future, $B_{d,s} \to h\,h'$ decays, h and h' being charged kaons or pions, will be used as they are kinematically closer to the $B_s \to \mu^+\mu^-$ decay. Finally, the nominal preselection has been applied to data. The amount of

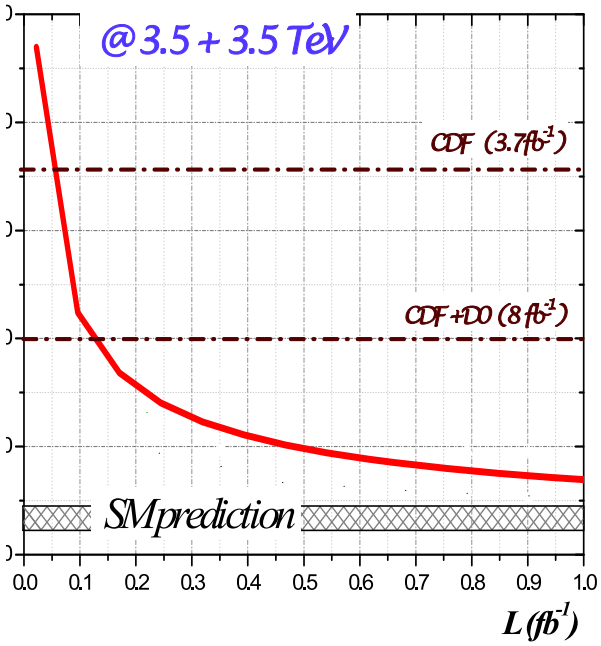

Figure 1: Exclusion limit at 90% CL for the measurement of BR($B_s \to \mu^+\mu^-$) at LHCb.

background found is well reproduced by the simulation.[1] The work done so far with the first data indicates that LHCb is in good shape to do physics analyses and that we can be confident in MC expectations. Figure 1 shows the expected BR exclusion at a confidence level of 90% as a function of the integrated luminosity up to 1 fb^{-1}. LHCb can improve the current Tevatron limit with 0.1 fb^{-1} and will be able to exclude BR up to twice the SM prediction with the 2010/2011 data.

[1] These background events are not in the sensitive region and would be rejected by the geometrical likelihood.

3 Search for $D^0 \to \mu^+\mu^-$

$D^0 \to \mu^+\mu^-$ is a very rare decay as the SM predicts a branching ratio of 3×10^{-13} [6]. However, in the Minimal Supersymmetric Standard Model (MSSM) with conserved R-parity it can be enhanced up to 10^{-6}. The current best limit has been obtained by Belle [7]: $\mathrm{BR}(D^0 \to \mu^+\mu^-) < 1.4 \times 10^{-7}$ at 90% CL.

The analysis strategy in LHCb is very similar to the search for $B_s \to \mu^+\mu^-$. A loose selection is applied to look for $D^* \to D^0\pi$, $D^0 \to \mu^+\mu^-$, followed by a multivariate analysis based on kinematic and geometrical variables. The normalization is done with respect to the $D^0 \to \pi\,\pi$ channel. With 0.1 fb^{-1}, LHCb will be able to improve the Belle limit down to 4×10^{-8} at 90% CL.

4 Study of the $B_d \to K^*\mu^+\mu^-$ decay channel

The decay $B_d \to K^*\mu^+\mu^-$ is fully described by three decay angles Θ_L, Θ_K and ϕ, and the di-muon invariant mass q^2. The angular distribution of this decay gives access to a number of observables sensitive to NP [8]. Among these observables, the forward-backward asymmetry A_{FB} in the $\mu^+\mu^-$ rest frame as a function q^2 is of interest, in particular the q^2 value where A_{FB} crosses zero, s_0. The value of s_0 can be precisely predicted in the SM thanks to the cancellation of the hadronic uncertainties at this point, and NP could give a sizeable deviation to this prediction.

LHCb is expected to collect 1400 events for 1 fb^{-1} with a background to signal ratio of 0.2, to be compared with the $\mathcal{O}(100)$ events analysed by Babar, Belle and CDF each [9]. Two methods have been developed for LHCb to measure s_0. The first one uses a binned counting analysis and a linear fit to A_{FB} around the crossing region, while the second one is based on a fit of the forward and backward distributions separately. Both methods give a sensitivity on s_0 of about 0.5 GeV^2 for 2 fb^{-1}. The LHCb sensitivity is also illustrated in Fig. 2 for 0.1 fb^{-1} (left) and 1 fb^{-1} (right) of data.

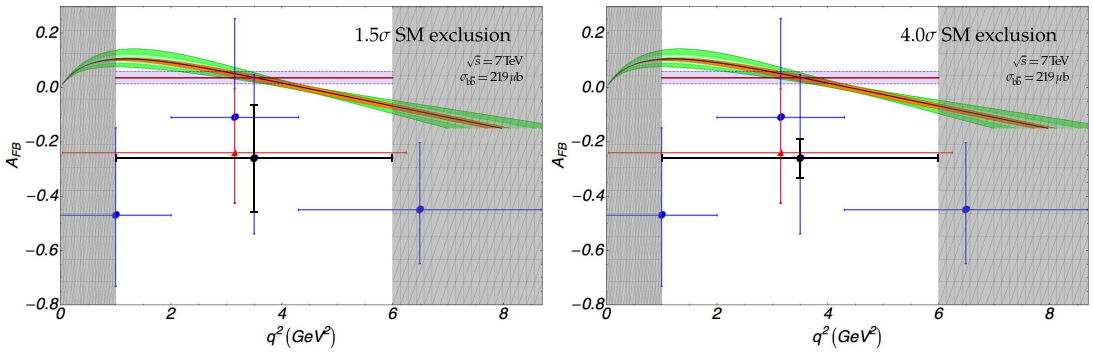

Figure 2: Precision with which A_{FB} can be determined at LHCb from 0.1 fb^{-1} (left) and 1 fb^{-1} of data. The SM prediction is shown as a line surrounded by a grey area (theoretical uncertainty). The blue (dark grey) ellipses correspond to the Belle measurement, the red (light grey) triangle to the Babar measurement and the black circle is the LHCb expectation assuming the Belle A_{FB} central value in the region from 1 to 6 GeV^2.

References

[1] A. J. Buras, PoS E **PS-HEP2009** (2009) 024 [arXiv:0910.1032 [hep-ph]].

[2] T. Aaltonen *et al.* [CDF Collaboration], Phys. Rev. Lett. **100** (2008) 101802 [arXiv:0712.1708 [hep-ex]].

[3] V. M. Abazov *et al.* [D0 Collaboration], arXiv:1006.3469 [hep-ex].

[4] The LHCb Collaboration, arXiv:0912.4179 [hep-ex].

[5] R. Fleischer, N. Serra and N. Tuning, arXiv:1004.3982 [hep-ph].

[6] G. Burdman, E. Golowich, J. L. Hewett and S. Pakvasa, Phys. Rev. D **66** (2002) 014009 [arXiv:hep-ph/0112235].

[7] M. Petric [BELLE collaboration], arXiv:1005.5445 [hep-ex].

[8] W. Altmannshofer, P. Ball, A. Bharucha, A. J. Buras, D. M. Straub and M. Wick, JHEP **0901** (2009) 019 [arXiv:0811.1214 [hep-ph]]. F. Kruger and J. Matias, Phys. Rev. D **71** (2005) 094009 [arXiv:hep-ph/0502060]. U. Egede, T. Hurth, J. Matias, M. Ramon and W. Reece, JHEP **0811** (2008) 032 [arXiv:0807.2589 [hep-ph]].

[9] B. Aubert *et al.* [BABAR Collaboration], Phys. Rev. D **79** (2009) 031102 [arXiv:0804.4412 [hep-ex]]. J. T. Wei *et al.* [BELLE Collaboration], Phys. Rev. Lett. **103** (2009) 171801 [arXiv:0904.0770 [hep-ex]]. [CDF Collaboration], CDF note 10047.

Prospects for CP violation at LHCb

Géraldine Conti for the LHCb Collaboration

EPFL, 1015 Lausanne, Switzerland

DOI: http://dx.doi.org/10.3204/DESY-PROC-2010-01/232

The determination of the CP-violating phase $\Phi_s^{J/\psi\phi}$ in a flavour-tagged, time-dependent, angular analysis of the decay $B_s^0 \to J/\psi\phi$ is one of the key goals of the LHCb experiment. Its small value predicted in the Standard Model could be significantly enhanced by New Physics contributions. The CKM unitarity triangle angle γ will also be measured precisely, both in modes where tree-level processes dominate and where loop diagrams are significant. Comparison of the two sets of results will be a sensitive probe for New Physics. Here, we will review the prospects for the determinations of $\Phi_s^{J/\psi\phi}$ and γ using 2 fb^{-1} of data at $\sqrt{s}$ =7 TeV [1].

1 Introduction

1.1 The LHCb experiment

The LHCb experiment at the LHC is dedicated to B physics [2]. Its goal is to make precision measurements of CP violation in B decays, which could lead to indirect discoveries of New Physics. The LHCb detector is a single-arm forward spectrometer, which is expected to see at the nominal luminosity an integrated $b\bar{b}$ cross-section of 500 μb, corresponding to $\sim 10^{12}$ $b\bar{b}$ pairs per year. Until now (June 1st, 2010), the LHCb experiment has collected $\sim$ 14 nb^{-1} of data at 7 TeV.

1.2 CKM angles β_s and γ

In the Standard Model, the source of CP violation arises from a complex phase in the CKM matrix. The CKM matrix can be represented by six unitarity triangles, from which four parameters are needed to describe the CKM matrix, the β, γ, β_K and β_s angles [3]. Two of these angles are of interest in this paper. First, the β_s angle will be linked to the study of the CP-violating phase in $B_s^0 \to J/\psi\phi$ decays. From global fits to experimental data, it is predicted to be $2\beta_s = (0.0360^{+0.0020}_{-0.0016})$ rad [3]. Second, the γ angle will be precisely measured at LHCb. Current experimental constraints give $\gamma = 73^{+22\circ}_{-25}$ [3].

2 CP-violating phase in $B_s^0 \to J/\psi\phi$

2.1 Phenomenology

B_s^0 mesons can decay into $J/\psi\phi$ through tree and penguin processes driven by $\bar{b} \to \bar{c}c\bar{s}$ quark level transitions. The tree diagram dominates with a single weak phase $\Phi_D = \arg(V_{cs}V_{cb}^*)$.

Before decaying into $J/\psi\phi$, B_s^0 mesons can also oscillate into $\bar{B}_s^0$ through box diagrams, with a mixing phase Φ_M. The interference between the two paths to $J/\psi\phi$ gives rise to the CP-violating phase $\Phi_s^{J/\psi\phi} = \Phi_M - 2 \cdot \Phi_D$. In the Standard Model, $\Phi_s^{J/\psi\phi}$ is equal to $-2\beta_s$, hence it is predicted to be very small. However, new particles could contribute to the B_s^0 -$\bar{B}_s^0$ box diagram and have the potential to modify $\Phi_s^{J/\psi\phi}$ significantly from its expectation.

$B_s^0 \to J/\psi\phi$ is a pseudo-scalar to vector-vector decay. Due to total angular momentum conservation, the final state is an admixture of CP-even (ℓ=0,2) and CP-odd (ℓ=1) states, ℓ being the orbital angular momentum between J/ψ and ϕ. An angular analysis of the decay products is required to disentangle statistically between the final states with the two different CP eigenvalues. The decay product angles $\Omega = \{\theta, \varphi, \psi\}$ in the transversity basis are defined in [1].

2.2 Analysis strategy

$\Phi_s^{J/\psi\phi}$ is obtained by fitting the theoretical expressions of the differential decay rates $d\Gamma/d\Omega$ to data as a function of proper time and the transversity angles (the detailed theoretical expressions can be found in [1]).

The flavour specific $B^0 \to J/\psi K^{*0}$ and $B_u \to J/\psi K^+$ channels will be used as control channels to estimate the mistag rates and check the proper time resolution. The $B^0 \to J/\psi K^{*0}$ channel will also be used to validate the angular acceptances corrections and the fit procedure, by comparing the fitted values of the amplitudes and the strong phase differences with those already obtained by other experiments [4, 5].

In its 14 nb^{-1} data sample, LHCb has started collecting $B_s^0 \to J/\psi\phi$, $B^0 \to J/\psi K^{*0}$ and $B_u \to J/\psi K^+$ candidates. An untagged sample will be studied first. Once the tagging is calibrated and a good proper time resolution achieved, a simplified one-angle time-dependent tagged analysis integrated over $\cos(\psi)$ and φ will be performed, before the three-angle analysis.

2.3 Sensitivity studies

An expected performance for the $\Phi_s^{J/\psi\phi}$ measurement at the LHCb experiment is shown in Figure 1 for different integrated luminosities, for an LHC centre of mass energy of 7 TeV.

The lines above and below the sensitivity curve indicate uncertainties coming from the $b\bar{b}$ cross-section and the visible branching ratio of $B_s^0 \to J/\psi\phi$. It has to be noted that the value used for the $\sigma(b\bar{b})$ is rather conservative, at least with respect to the value given by Pythia of 0.457 μb. The Standard Model prediction of $2\beta_s$, 0.0368, bounded by its uncertainties, is also drawn. The black line shows the combined CDF/D⊘ uncertainty scaled to 16 fb^{-1}.

With an integrated luminosity of 2 fb^{-1}, the statistical uncertainty on $\Phi_s^{J/\psi\phi}$, $\sigma(\Phi_s^{J/\psi\phi})$, is expected to be ~ 0.07.

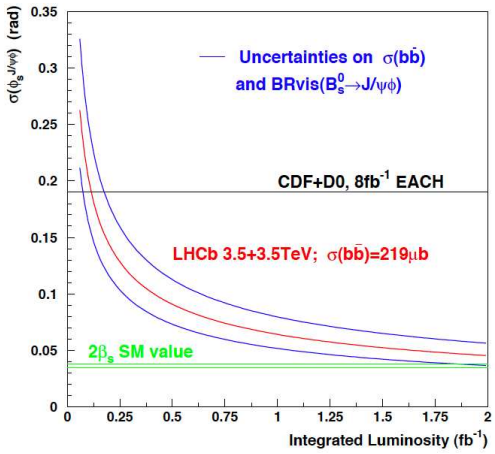

Figure 1: Statistical uncertainty on $\Phi_s^{J/\psi\phi}$ versus the integrated luminosity at an LHC centre of mass energy $\sqrt{s} = 7$ TeV.

3 γ from tree processes

The measurement at tree level of γ can be performed using several different B decays, using either direct CP violation or time-dependent effects. Three methods that will be used at LHCb (ADS/GLW, GGSZ and time-dependent studies) are explained in the following. A global fit to all the measurements at tree level will allow to obtain the best sensitivity to γ. It is foreseen to be $\sim 7^\circ$ with 1 fb^{-1} of data at 7 TeV. Already with 100 pb^{-1}, LHCb will be able to improve some B-factory measurements.

3.1 $B^{\pm(0)} \to D(hh)K^{\pm(*0)}$ decays with ADS/GLW method

γ is extracted through the interference between the amplitudes of $B^{\pm(0)} \to D(hh)K^{\pm(*0)}$ decays, with D representing a D^0 or a $\bar{D}^0$. The final states hh used in the GLW method are CP eigenstates ($f_D = K^+K^-$ or $\pi^+\pi^-$). In the ADS method, the D decays to doubly Cabibbo favoured and suppressed states $f_D = K^\pm\pi^\mp$.

Combining the ADS and GLW modes results in a total of six rates (four ADS, two GLW), with five parameters. These are the CP-violating weak phase γ, the ratio $r_{B^{\pm(0)}}$ between the magnitude of the two tree amplitudes, the CP-conserving strong phase difference $\delta_{B^{\pm(0)}}$ between $B^{+(0)}$ and $B^-(\bar{B}^0)$, the ratio $r_{K\pi}$ between the favoured and suppressed D decay tree diagrams and the D decay strong phase difference $\delta_{K\pi}$. The last parameter can be constrained using external measurements made at CLEO-c [6].

In the neutral B meson case, both trees are colour-suppressed. The sensitivity is enhanced as r_{B^0}, governing the size of the asymmetry, is bigger than $r_{B^\pm}$ of the charged B meson case. However, signal rates are lower for the neutral B meson case than for the charged one.

The sensitivity to γ can be improved by adding a Dalitz plot analysis of the neutral $B^0 \to D\pi^-K^+$ decay mode [7] or taking into account the ADS $B^\pm \to D(K\pi\pi\pi)K^\pm$ decay mode.

3.2 $B^\pm \to D(K^0_S\pi^+\pi^-)K^\pm$ decays with GGSZ (Dalitz) method

The GGSZ (Dalitz) method is applied to the three-body $D \to K^0_S\pi^+\pi^-$ decays. γ is extracted here through the difference in densities observed in the Dalitz planes of $D \to K^0_S\pi^+\pi^-$ coming from $B^\pm \to DK^\pm$ decays. The extraction of γ is performed either by using a model-dependent unbinned fit or a model-independent binned fit, where the bins are determined by δ_D coming from external measurements [1].

3.3 Time-dependent $B^0_s \to D_sK$ and $B^0 \to D^\pm\pi^\mp$ decays

In the time-dependent analysis of the flavour tagged $B^0_s \to D_sK$, the B^0_s mesons can decay directly or oscillate first. The interference between the two paths to the same final state is sensitive to $\gamma - \Phi_M$. Φ_M is the B^0_s meson mixing phase, which will be determined from the study of $B^0_s \to J/\psi\phi$ decays.

The time-dependent CP asymmetries in $B^0 \to D^\pm\pi^\mp$ allow $\gamma + 2\beta$ to be measured. As β is already well measured [3], γ can be determined from these asymmetries. On the way to γ, the first ($B^0 \to D^+\pi^- + B^+ \to D^0\pi^+$) candidates have been recorded in real data.

4 γ from loop processes

γ is extracted through the combined measurement of the $B^0_d \to \pi^+\pi^-$ and $B^0_s \to K^+K^-$ CP asymmetries. The invariance of the strong interaction under the d and s quarks exchange (U-spin symmetry) is assumed. Depending on the U-spin scenario chosen, the sensitivity to γ for 2 fb^{-1} of data at 14 TeV is $\sim 7-10^\circ$ (numbers not available for 1 fb^{-1} at 7 TeV).

The time-dependent asymmetry for neutral B mesons decaying into a CP eigenstate f is :

$$A_{CP}(t) = \frac{\Gamma(\bar{B}^0_{d/s}(t) \to f) - \Gamma(B^0_{d/s}(t) \to f)}{\Gamma(\bar{B}^0_{d/s}(t) \to f) + \Gamma(B^0_{d/s}(t) \to f)} = \frac{-C_{CP}\cos\Delta m t + S_{CP}\sin\Delta m t}{\cosh\frac{\Delta\Gamma}{2}t - A^{\Delta\Gamma}_{CP}\sinh\frac{\Delta\Gamma}{2}t} \quad (1)$$

where $\Gamma(\bar{B}^0_{d/s}(t) \to f)$ and $\Gamma(B^0_{d/s}(t) \to f)$ are the decay rates of the initial $\bar{B}$ and B states respectively. Δm and $\Delta\Gamma$ are the mass and width differences between the two mass eigenstates.

The C_{CP} and S_{CP} terms can be written in terms of the γ angle, for both $B^0_d \to \pi^+\pi^-$ and $B^0_s \to K^+K^-$ decays. In each case, these terms also depend on two hadronic parameters d and θ, which parameterize the magnitude and phase of the penguin-to-tree amplitude ratio respectively. A total of four equations with five unknowns (d,d',θ,θ',γ) is obtained. To solve the system, the U-spin symmetry is used ($d = d'$ and $\theta = \theta'$). Weaker assumptions can also be made, as for example keeping only the $d = d'$ constraint. An even weaker assumption on the U-spin symmetry is $\xi = d'/d = [0.8, 1.2]$ without any constraint on the phases θ and θ' [8].

5 Conclusions

From the $\sim$14 nb^{-1} sample collected up to now by the LHCb detector at $\sqrt{s}$ =7 TeV, first candidates relevant to the measurements of the CP-violating weak phases $\Phi_s^{J/\psi\phi}$ and γ have been selected. With 1 fb^{-1} of data taken at $\sqrt{s}$ =7 TeV, sensitivites of $\sigma(\Phi_s^{J/\psi\phi}) \sim 0.07$ and $\sigma(\gamma) \sim 7^\circ$ (tree level) are expected from Monte Carlo studies. Both measurements will improve our knowledge about CP-violation and potentially lead to an indirect discovery of New Physics.

6 Acknowledgments

The author would like to thank Marta Calvi, Tim Gershon and Olivier Leroy for their invaluable suggestions in the preparation of the presentation and the present document.

References

[1] The LHCb Collaboration, LHCb-PUB-2009-029 (2009).

[2] The LHCb Collaboration, J. Inst. A 3 S08005 (2008).

[3] Amsler C. et al. (Particle Data Group), Phys. Rev. Lett. B 667 (2008) 1.

[4] The Babar Collaboration, PRD-RC 76, 031102 (2007).

[5] The CDF Collaboration, Public note 8950 (2007).

[6] J. L. Rosner et al. (CLEO Collaboration), Phys. Rev. Lett 100, 221801 (2008).

[7] T. Gershon, Phys. Rev. D79:051301 (2009) [arXiv:0810.2706].

[8] J. Nardulli, arXiv:hep-ex/0807.1670v1.

Heavy ion physics

Heavy ion collisions: puzzles and hopes

Jean-Paul Blaizot

IPhT-CEA Saclay, 91191 Gif-sur-Yvette cedex, France

DOI: http://dx.doi.org/10.3204/DESY-PROC-2010-01/28

This talk is a brief summary of some theoretical issues in the field of hot and dense QCD matter and ultra-relativistic heavy ion collisions.

1 Introduction

The study of ultra-relativistic heavy ion collisions offers the possibility to address several fundamental questions about the state of matter at very high temperature and density, or about the structure of the wave-function of a nucleus at asymptotically high energy. The reason why this second issue appears in the context of heavy ion collisions is related to the need to understand how dense and hot matter is produced there, and this requires a good knowledge of the nuclear wave-functions, and in particular of their small x partons. This feature contributes to bring together the fields of "small x" physics and that of ultra-relativistic heavy ions, with the common goal of studying QCD in regimes of large parton densities.

The extreme situations alluded to the above are believed to bring simplicity to the theoretical description of the systems under study. The naive picture of the quark-gluon plasma belongs to such asymptotic idealizations: as a natural consequence of the QCD asymptotic freedom, one expects indeed hadronic matter to turn at high temperature and density into a gas of quarks and gluons whose free motion is only weakly perturbed by their interactions. However, the data that have been collected over the last decade at RHIC [1] suggest that the temperature reached in present nuclear collisions is presumably not high enough, or is attained for too short a period of time to lead to such an idealized state of matter. The data rather provide evidence that the quark-gluon plasma produced in RHIC collisions is strongly coupled, and behaves as a "perfect liquid" rather than an ideal gas.

The origin of the strongly coupled character of the quark-gluon plasma is one of the several "puzzles" that RHIC is leaving us with, one that I shall briefly address in this talk. The "hopes" mentioned in the title of the talk reflect of course the exciting perspectives opened by the LHC: many of the questions left open by RHIC will be, hopefully, clarified there, and, perhaps, the high energies available at the LHC will be sufficient to produce the ideal quark-gluon plasma.

2 The QCD phase diagram

The study of dense and hot matter is not directly concerned with the properties of individual, elementary, particles, as is traditionally the case in particle physics. Rather, one is interested in the behavior of collections of large numbers of such particles, and in the various "phases" in which such systems may exist. Properties of QCD matter (matter made of quarks and gluons)

can be studied as a function of various control parameters, the most relevant ones (because they are directly accessible experimentally) being the temperature and the baryonic chemical potential.

Simple considerations allow us to draw the main features of the phase diagram. A basic property of QCD is the confinement of color charges: at low density and temperature quarks and gluons combine into color singlet hadrons that make up hadronic or nuclear matter. When the density, or the temperature, become high enough quarks and gluons start to play a dominant role in the thermodynamics, leading possibly to a transition to a phase of matter where color is "deconfined". Chiral symmetry (an exact symmetry of QCD when quark masses vanish) is spontaneously broken in the hadronic world, but is expected to be restored at high temperature and density. At large baryon chemical potentials, a rich structure appears in the phase diagram, yet largely unexplored (for a recent review see e.g. [3, 4]). Among the salient features, let us mention the emergence of color supraconductivity at large density, the possible existence of a critical point, as well a a possible new phase of "quarkyonic" matter whose existence has been conjectured recently on the basis of large N_c arguments [5].

3 The ideal baryonless quark-gluon plasma

There are at least two good reasons to focus on the case of baryon-free matter: i) the baryonless quark-gluon plasma is that for which we can do the most elaborate calculations from first principles, using in particular lattice gauge theory; ii) this is likely the state of matter created in the early stages of nucleus-nucleus collisions in the central rapidity region.

The QCD asymptotic freedom

QCD is "asymptotically free", which means that the interactions between quarks and gluons become weak when the typical energy scale (Q) involved is large compared to Λ_{QCD}. The strong coupling constant "runs", according to the (one-loop) formula $\alpha_s = \frac{g^2}{4\pi} \approx 1/\ln(Q/\Lambda_{QCD})$. Because the natural scale in thermodynamical functions is $Q \simeq 2\pi T$, this formula leads us to expect that matter becomes simple when $T \gg \Lambda_{QCD}$: it turns into an ideal gas of quarks and gluons. Weak coupling calculations (based on resummed QCD perturbation theory), that reproduce lattice results for temperatures greater than 2.5 to 3 T_c [6], suggest that the dominant effect of interactions is to turn (massless) quarks and gluons into weakly interacting (massive) quasiparticles. The thermodynamic functions such as the pressure, the entropy density or the energy density, all go to their corresponding Stefan-Boltzmann values at high temperature. This is confirmed by new lattice calculations that can probe arbitrarily large temperatures, and which demonstrate the approach to the Stefan-Boltzmann limit in a convincing way, in good agreement with weak coupling calculations [7].

The cross-over between hadronic matter and the quark-gluon plasma

Most recent lattice calculations indicate that the transition from the hadronic world to the quark gluon plasma is not a phase transition proper, but a smooth crossover [8], extending over a range of temperatures of the order of 20 to 30 MeV. This implies in particular that there is no unique way to define the "transition temperature" T_c: it depends somewhat on how it is measured. Thus one may define the "chiral transition temperature" as the location of the

peak in the chiral susceptibility, and this may differ from the "deconfinement temperature" measured for instance by the inflexion point in the Polyakov loop expectation value (note that this terminology is not meant to imply the existence of "two" transitions !). Independently of this basic ambiguity, some discrepancy remains as to the precise temperature location of the transition region [9, 10], but this is being resolved [11].

Between T_c and $\sim 3T_c$, there is a significant deviation between the energy density ϵ, and $3P$, where P is the pressure. The quantity $\epsilon - 3P$, which equals the trace of the energy momentum tensor, would vanish (for massless quarks) if it were not for the fact that the QCD coupling runs and depends on the temperature. The finite value of $\epsilon - 3P$ is related to the so-called QCD scale anomaly. It is appreciable only for $T \lesssim 3T_c$, and below T_c it receives contributions from the massive hadrons. This region between T_c and $3T_c$, is a difficult region where the physics is not well understood, but for which much theoretical effort is needed, since this is presumably the region where the quark-gluon plasma produced at RHIC spends most of its existence. Among the important open questions, one concerns the fate, in this region, of the quasiparticles that dominate the thermodynamics at higher temperature.

4 From the "ideal gas" to the "perfect liquid"

We shall examine now some of the RHIC results (see the talk by R. Bellwied for a more exhaustive presentation [2]), focusing on a few which suggest in the most convincing way that matter produced at RHIC is strongly interacting.

Matter is opaque to the propagation of jets

This is seen in several ways. First by looking at the correlations among the produced particles, and observing that in most central Au-Au collisions, the usual companion of a jet, expected at 180 degrees from the trigger jet, is absent [12]. Another view of the same physics is obtained by studying the so-called nuclear modification factor, a ratio that summarizes the deviation from what would be obtained if the nucleus-nucleus collision was an incoherent superposition of nucleon-nucleon collisions. The attenuation which persists at fairly large transverse momentum is usually discussed in terms of the energy loss of the leading parton in the dense medium [13]. This energy loss is found to be large and difficult to account for in a perturbative scheme (see e.g. [14] for a recent discussion).

Matter flows like a fluid

If nucleus-nucleus collisions were simple superpositions of nucleon-nucleon collisions, the produced particles would have isotropic distributions, irrespective of the shape of the collision zone in the transverse plane. However, if the interactions among the produced particles are sufficiently strong to bring the system close to local equilibrium, then a collective motion emerges: strong pressure gradients are induced by the anisotropy of the initial interaction zone, leading to anisotropic momentum distributions[15]. This so-called elliptic flow has been observed at RHIC, and is a beautiful evidence of collective behavior and (at least partial) thermalization of the produced matter.

The quark-gluon plasma as a perfect fluid

The hydrodynamical calculations that are used to analyze the flow data require a short equilibration time and a relative low viscosity, i.e. a ratio of viscosity to entropy density lower than about 0.4 [16]. Such a low value points to the fact that matter is strongly interacting, since the ratio of viscosity to entropy density would be much larger in a weakly interacting system. In fact, the "measured" value is not too different from that obtained in some gauge theories that can be solved exactly at strong coupling: $\eta/s = 1/4\pi \approx 0.08$ [17], a value that has been conjectured to be a lower bound [18]. The small value of η/s obtained for the quark-gluon plasma found at RHIC is what has motivated its qualification as a "perfect liquid".

5 Is the quark-gluon plasma strongly coupled ?

The opacity of matter, the elliptic flow, and the small value of η/s are measurements that contribute to build a picture of the quark-gluon plasma as a strongly coupled system.

The ideal strongly coupled quark-gluon plasma

In fact, the RHIC data have produced a complete shift of paradigm in the field, suggesting a new ideal system that can be used as a reference system: the strongly coupled quark-gluon plasma (sQGP). This was made possible by a theoretical breakthrough that allows one to perform calculations in some strongly coupled gauge theories, using the so-called AdS/CFT correspondence, a mapping between a strongly coupled gauge theory and a weakly coupled (i.e. classical) gravity theory. This correspondence has led to the detailed calculations of many properties of strongly coupled non abelian plasmas (for a recent review see [19]). Among the successes of this approach, let us recall the exact results for the entropy density $s/s_0 = 3/4$, and for the viscosity to entropy density ratio $\eta/s = 1/4\pi$ that we have just mentioned.

A puzzling situation: weakly or strongly coupled ?

The interpretation of RHIC data in terms of a strongly coupled quark-gluon plasma leads to a somewhat puzzling situation. There is indeed no evidence that in the transition region the QCD coupling constant becomes so huge that weak coupling techniques (with appropriate resummations) are meaningless. And we know that for temperatures above $3T_c$ such calculations account well for lattice data. Besides, the description of the early stages of nucleus-nucleus collisions in terms of the color glass condensate (see below) relies heavily on weak coupling concepts.

A possible way out this paradoxical situation is to acknowledge the coexistence, within the quark-gluon plasma, of degrees of freedom with different wavelengths, and whether these degrees of freedom are weakly or strongly coupled depends crucially on their wavelengths: short wavelengths can be weakly coupled, whereas long wavelengths are always strongly coupled. It is also worth recalling here that non perturbative features may arise in a system from the cooperation of many degrees of freedom, or strong classical fields, making the system strongly interacting while the elementary coupling strength remains small. An illustration is provided next.

6 High density partonic systems

The wave function of a relativistic system describes a collection of partons, mostly gluons, whose number grows with the energy of the system: this is because each gluon acts as a color source that can radiate other gluons when the system is boosted to higher energy (then x, the typical momentum fraction, decreases). This phenomenon has been well established at HERA [20]. One expects, however, that the growth of the gluon density eventually "saturates" when non linear QCD effects start to play a role. The existence of such a saturation regime has been predicted long ago, but it is only during the last decade that equations providing a dynamical description of this regime have been obtained (for recent reviews, see [21, 22, 23]).

The onset of saturation is characterized by a particular momentum scale, called the saturation momentum Q_s, given by $Q_s^2 \approx \alpha_s(Q_s^2) xG(x, Q_s^2)/\pi R^2$, where R is the transverse size of the system. Partons in the wave function have different transverse momenta k_T. Those with $k_T > Q_s$ are in a dilute regime; those with $k_T < Q_s$ are in the saturated regime. Note that at saturation, naive perturbation theory breaks down, even though $\alpha_s(Q_s)$ may be small if Q_s is large: the saturation regime is a regime of weak coupling, but large density. In fact, at saturation, the number of partons occupying a small disk of radius $1/Q_s$ in the transverse plane is proportional to $1/\alpha_s$, a large number if α_s is small. In such conditions classical field approximations become relevant to describe the nuclear wave-functions. This observation is at the basis of the McLerran-Venugopalan model [24]. The color glass formalism provides a more complete physical picture, allowing in particular a complete description of the evolution of the wave function as a function of energy [21, 22, 23].

The saturation momentum increases as the gluon density increases. This increase of the gluon density may come from the decrease of x with increasing energy ($Q_s^2 \sim x^{-0.3}$), or from the additive contributions of several nucleons in a nucleus, $xG_A(x, Q_s^2) \propto A$, and hence $Q_s^2 \propto \alpha_s A^{1/3}$, where A is the number of nucleons in the nucleus. Thus, the saturation regime sets in earlier (i.e., at lower energy) in collisions involving large nuclei than in those involving protons. In fact, the parton densities in the central rapidity region of a Au-Au collision at RHIC are not too different from those measured in deep inelastic scattering at HERA. In a nucleus-nucleus collision, most partons that play a direct role in particle production have momenta of the order of Q_s. A very successful phenomenology based on the saturation picture has been developped at RHIC (see e.g. [23, 25, 26] for recent reviews). However, understanding how the quark-gluon plasma is produced, i.e., understanding the detailed mechanisms by which partonic degrees of freedom get freed and subsequently interact to lead to a thermalized system, remains a challenging problem.

By selecting particular kinematics, one may reach lower values of x. Thus, for instance, the study of dA collisions at RHIC, in the fragmentation region of the deuteron, gives access to a regime of small x values in the nucleus, where quantum evolution could be significant. Indeed, very exciting results have been obtained in this regime [27], which have been interpreted as evidence of saturation (see e.g. [28, 23]). In particular, the disappearance of di-hadron correlations at forward rapidity, which has been observed recently [29], has a natural interpretation in terms of saturation. This result is potentially very important as it may represent the first direct evidence of large parton density effects [30].

7 Conclusion

The field of ultra-relativistic heavy ion collisions has undergone spectacular progress in the last decade, both theoretically and experimentally. Progress in understanding the behavior of QCD in the regime of large parton densities has contributed to bring together the field of small x physics, and that of heavy ions, and has led to very exciting developments. Other, somewhat unexpected, developments took place, such as the intrusion of string theoretical techniques and the use of the AdS/CFT duality in order to study strongly coupled plasmas. But, to a large extent, experiments continue to drive the field. As I have indicated, RHIC has produced a vast amount of high quality data which have forced us to revise our concepts, and left us with a number of puzzles. We can be confident that many of these puzzles will be clarified by the forthcoming experiments at the Large Hadon Collider.

References

[1] RHIC collaborations "white papers", Nucl. Phys. **A757** (2005).

[2] R. Bellwied, these proceedings.

[3] P. Braun-Munzinger and J. Wambach, arXiv:0801.4256 [hep-ph].

[4] K. Fukushima and T. Hatsuda, arXiv:1005.4814 [hep-ph].

[5] L. McLerran and R. D. Pisarski, Nucl. Phys. A **796** (2007) 83 [arXiv:0706.2191 [hep-ph]].

[6] J. P. Blaizot, E. Iancu and A. Rebhan, Phys. Rev. D **63** (2001) 065003 [arXiv:hep-ph/0005003]; Nucl. Phys. A698 (2002) 404.

[7] G. Endrodi, Z. Fodor, S. D. Katz and K. K. Szabo, PoS **LAT2007** (2007) 228 [arXiv:0710.4197 [hep-lat]].

[8] Y. Aoki, G. Endrodi, Z. Fodor, S. D. Katz and K. K. Szabo, Nature **443** (2006) 675 [arXiv:hep-lat/0611014].

[9] Z. Fodor, PoS **LAT2007** (2007) 011 [arXiv:0711.0336 [hep-lat]].

[10] A. Bazavov *et al.*, Phys. Rev. D **80** (2009) 014504 [arXiv:0903.4379 [hep-lat]].

[11] S. Borsanyi, Z. Fodor, C. Hoelbling, S. D. Katz, S. Krieg, C. Ratti and K. K. Szabo [Wuppertal-Budapest Collaboration], arXiv:1005.3508 [hep-lat].

[12] J. Adams *et al.* [STAR Collaboration], Phys. Rev. Lett. **91** (2003) 072304 [arXiv:nucl-ex/0306024].

[13] Y. Akiba [PHENIX Collaboration], Nucl. Phys. A **774** (2006) 403 [arXiv:nucl-ex/0510008].

[14] A. Majumder, J. Phys. G **34** (2007) S377 [arXiv:nucl-th/0702066].

[15] J. Y. Ollitrault, Phys. Rev. D **46**, 229 (1992).

[16] M. Luzum and P. Romatschke, Phys. Rev. C **78**, 034915 (2008) [Erratum-ibid. C **79**, 039903 (2009)] [arXiv:0804.4015 [nucl-th]].

[17] G. Policastro, D. T. Son and A. O. Starinets, Phys. Rev. Lett. **87** (2001) 081601 [arXiv:hep-th/0104066].

[18] P. Kovtun, D. T. Son and A. O. Starinets, Phys. Rev. Lett. **94** (2005) 111601 [arXiv:hep-th/0405231].

[19] S. S. Gubser, arXiv:0907.4808 [hep-th].

[20] S. Chekanov *et al.* [ZEUS Collaboration], Phys. Rev. D **67**, 012007 (2003) [arXiv:hep-ex/0208023].

[21] E. Iancu and R. Venugopalan, arXiv:hep-ph/0303204.

[22] H. Weigert, Prog. Part. Nucl. Phys. **55**, 461 (2005) [arXiv:hep-ph/0501087].

[23] J. Jalilian-Marian and Y. V. Kovchegov, Prog. Part. Nucl. Phys. **56** (2006) 104 [arXiv:hep-ph/0505052].

[24] L. D. McLerran and R. Venugopalan, Phys. Rev. D **49** (1994) 2233 [arXiv:hep-ph/9309289].

[25] F. Gelis, E. Iancu, J. Jalilian-Marian and R. Venugopalan, arXiv:1002.0333 [hep-ph].

[26] T. Lappi, arXiv:1003.1852 [hep-ph].

[27] I. Arsene *et al.* [BRAHMS Collaboration], Phys. Rev. Lett. **93** (2004) 242303 [arXiv:nucl-ex/0403005].

[28] D. Kharzeev, Y. V. Kovchegov, and K. Tuchin, *Phys. Lett.* B599:23–31, 2004.

[29] E. Braidot [STAR Collaboration], arXiv:1005.2378 [hep-ph].

[30] J. L. Albacete and C. Marquet, arXiv:1005.4065 [hep-ph].

Heavy ion physics with the ATLAS detector

Helena Santos for the ATLAS Collaboration

LIP, Av. Elias Garcia 14-1, 1000-149 Lisboa, Portugal

DOI: http://dx.doi.org/10.3204/DESY-PROC-2010-01/233

The ATLAS experiment will participate in the heavy ion program of the Large Hadron Collider (LHC), for which the main goal is to create strong interacting matter under extreme energy density and temperature conditions. Evidence from SPS and RHIC data suggests that in such extreme conditions matter undergoes a phase transition from ordinary hadronic matter to a plasma of quarks and gluons, the QGP. The large acceptance, high granularity calorimeters, silicon tracking detectors, and muon spectrometers assure that ATLAS can handle such a challenging program.

1 Introduction

Pb+Pb collisions at the LHC are expected to produce a QGP with energy densities 2–3 times (or even more) larger than at RHIC, with larger initial temperatures (by a factor of 2) and longer lifetimes (the order of 1.5). To carry on this program, the ATLAS [1] experiment has a large detector acceptance, as shown in Figure 1, with full azimuthal coverage and 10 units of pseudo-rapidity, not taking into account the very forward detectors which will play a major role in the heavy ion program. In Pb+Pb collisions, the detector is especially suited to study jets and photons. Concerning jets, the large acceptance and fine segmentation allows full reconstruction and a detailed study of their properties. For photons, the fine segmentation of the first layer of the electromagnetic calorimeter allows for separation of direct photons from those originating from π^0 and η decays. This is a unique strength of the ATLAS detector at the LHC.

2 Global observables

The day-one physics will be devoted to establish the global features of the heavy ion program. The collisions centrality is characterized event-by-event by the impact parameter, b, which is intrinsically related to the geometry of the collision and so to the number of collisions and the number of excited participating nucleons. A strong correlation between these variables and the energy deposited in the ATLAS calorimeters is expected. Figure 2 (left plot) demonstrates how well ATLAS reconstructs the transverse energy over the whole pseudorapidity range in central collisions, b=2 fm, taking into account correction factors for acceptance cracks and energy depositions by particles which originate from re-interactions in the detector material. Measurements of the inclusive charged particle density will be essential and few days of data taking will help establish which physics scenarios can be ruled out using the measured multiplicities [2]. The middle plot of Figure 2 shows the capabilities of ATLAS to reconstruct $dN_{ch}/d\eta$ in central collisions. The estimated errors are 10-15%.

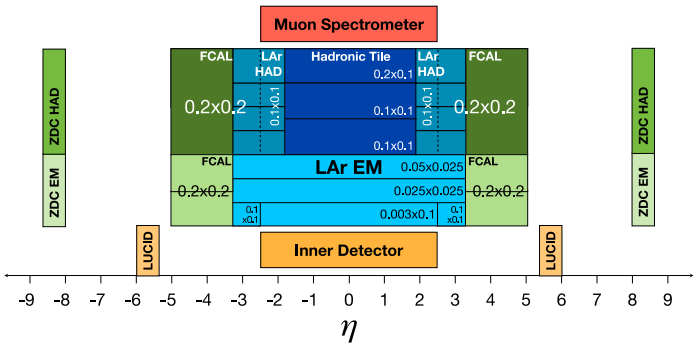

Figure 1: The pseudo-rapidity coverage of the various components of the ATLAS detector.

One observable that gives insight into the very earliest phase of the collisions is the elliptic flow, which arises when two colliding nuclei do not overlap totally. In such a case, the initial spatial anisotropy leads to a final state elliptical asymmetry in momentum space with respect to the reaction plane. The variable v_2 is the second Fourier coefficient of the particle azimuthal distribution with respect to the reaction plane and measures the elliptical shape of the particle's momentum distribution in the transverse plane. Figure 2 (right plot) shows v_2 as a function of the transverse momentum for mid-central events. Three methods to measure elliptic flow are applied to the simulated data – event plane, two-particle correlations and Lee-Yang Zeros [3, 4]. All three fail at the very low p_T due the presence of fake tracks in this momentum range. The Lee-Yang Zeros method, however, shows the best performance and is less sensitive to non-flow effects.

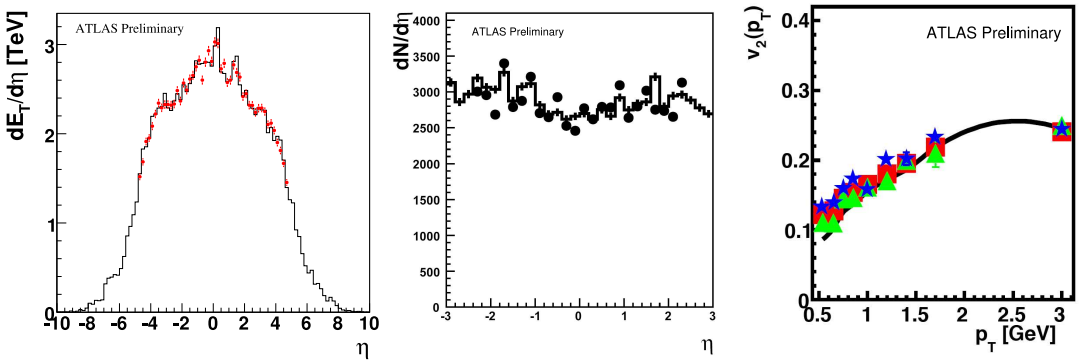

Figure 2: Left and middle: comparison of the reconstructed $dE_T/d\eta$ and $dN_{ch}/d\eta$ distributions (points) with the true distributions (histograms) for central events with b = 2.3 fm. Right: p_T dependence of the reconstructed v_2 from the event plane method (squares), two-particle correlations (stars) and the Lee-Yang Zeros method (triangles) for mid-central events, b=7 fm.

3 Jets

One of the most important topics of the LHC heavy ion program will be the jet suppression measurements [5, 6]. Jets reconstruction in Pb+Pb collisions is challenging due to the large underlying event. Thus, methods have been developed to subtract it by removing the averaged transverse energy, estimated far enough from the seeded jet signal, as well as to identify and reject fake jets [7, 8]. Figure 3 compares the reconstructed jet spectrum with the input one, and the fake jet spectrum as a function of the transverse energy. Even without correcting for efficiency and energy resolution, the reconstructed spectrum matches the input one above 80 GeV quite well. The background at low E_T is suppressed by two orders of magnitude. At 70 GeV the reconstruction efficiency is about 70%, the resolution is approximately 25% and the background is negligible.

4 Direct photons

The design of the ATLAS electromagnetic calorimeter is optimal for direct photon identification [1]. As seen in Figure 4, the first layer has a very fine longitudinal segmentation along the η direction, allowing to disentangle direct photons from π^0 and η photon decays. This is a unique feature of ATLAS and rather important because direct photons are not affected by the strong interacting medium and so they can be used as a reference for jet suppression measurements [5]. Also the energy scale determination will benefit because the p_T-balance of di-jet correlations is of limited use due to the expected energy loss in the QGP and the fluctuations of the large underlying event. The left plots of Figure 4 show the reconstructed energy deposition in the strip layers as a function of the strip cluster size, $\Delta\eta$, for direct photons and for π^0s embedded in HIJING central events. The energy of a single photon is concentrated across a few strips with a single maximum at the middle, whereas a cluster from a π^0 decay is distributed across more strips.

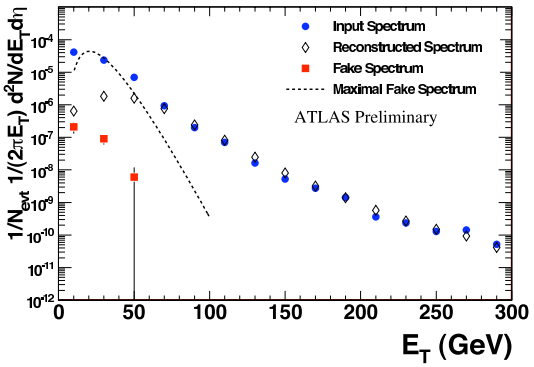

Figure 3: Input, raw reconstructed and fake spectra for cone jets in central ($dN_{ch}/d\eta$=2650) Pb+Pb collisions. The reconstructed spectrum is not corrected for efficiency and energy resolution. Dashed line represents the absolute fake jet rate from HIJING events prior to background jet rejection.

5 Heavy ions run in 2010

The first heavy ion run at the LHC is scheduled for November and December of 2010. The CM energy will be 2.76 TeV/nucleon pair, a factor 2 smaller than the nominal one. The peak luminosity will be 2 orders of magnitude smaller, 1–2x10^{25}. Taking into account the total inelastic Pb+Pb cross section, 7.7 barns, an interaction rate of 80-160 Hz is expected. Some

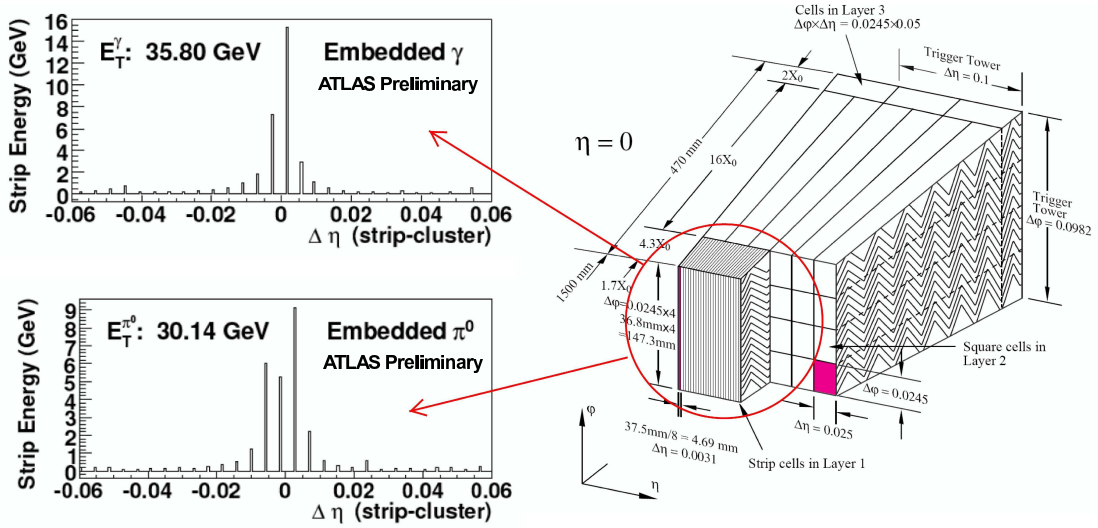

Figure 4: The reconstructed energy deposition in the strip layers around the direction of (top left) a single photon and a single π^0 (bottom left), both embedded in a central Pb+Pb event. On the right the sketch of a barrel module with the different layers is shown, with the fine granularity in η of the first layer being enhanced.

advantages of these low rates can be exploited, namely in triggering. In principle, depending on how large events will be, no Level-1 rejection is needed and the High Level Trigger will work in transparent mode. Beyond minimum bias, the Level-1 trigger will be used to find regions of interest concerning rare signals, namely jets, muons, and ultra-peripheral collisions. Even with low to moderate luminosity, 50 Hz written to tape will amount to two million Pb+Pb events per day.

In conclusion, ATLAS is fully prepared to collect and analyze the first heavy ion data.

6 Acknowledgments

This work was supported in part by FCT, UE, COMPETE, and QREN under the contract Project CERN/FP/109323/2009.

References

[1] The ATLAS Collaboration, G. Add et al., JINST 3, S08003 (2008).
[2] B. B. Back et al. PHOBOS Collaboration, Phys. Rev. C74, 021902 (2006a).
[3] S. Wang et al., Phys. Rev. C44, 1091 (1991) and references therein.
[4] R. S. Bhalerao, N. Borghini, and J. Y. Ollitrault, 4 Phys. Lett. B580, 157 (2004).
[5] S.S. Adler et al. PHENIX Collaboration, Phys. Rev. C75, 024909 (2007a).
[6] J. Adams et al. STAR Collaboration, Phys. Rev. Lett. 91, 072304 (2003).
[7] N. Grau for the ATLAS Collaboration, J. Phys. G: Nucl. Part. Phys. 35, 104040 (2008).
[8] N. Grau, B.A. Cole, W.G. Holzmann, M. Spousta and P. Steinberg for the ATLAS Collaboration, arXiv:0810.1219.

Posters

Unnatural Origin of Fermion Masses for Technicolor

Matti Antola[1], *Matti Heikinheimo*[2]*, *Francesco Sannino*[3], *Kimmo Tuominen*[4]

[1]Department of Physics and Helsinki Institute of Physics, P.O.Box 64, FI-000140, University of Helsinki, Finland
[2]Department of Physics, P.O.Box 35, FI-000140, University of Jyväskylä and Helsinki Institute of Physics, P.O.Box 64, FI-000140, University of Helsinki, Finland
[3]CP[3]-Origins, Campusvej 55, DK-5230 Odense M, Denmark
[4]CP[3]-Origins, Campusvej 55, DK-5230 Odense M, Denmark and Helsinki Institute of Physics, P.O.Box 64, FI-000140, University of Helsinki, Finland

DOI: http://dx.doi.org/10.3204/DESY-PROC-2010-01/heikinheimo

We explore the scenario in which the breaking of the electroweak symmetry is due to the simultaneous presence and interplay of a dynamical sector and an unnatural elementary Higgs. Here the elementary Higgs represents the sector responsible for fermion masses. Our goal is to investigate the interplay between the technicolor sector and the sector giving masses to the SM fermions, and this simple model works as a well defined framework that permits perturbative calculations.

The idea of bosonic technicolor was originally pioneered in a series of papers by Simmons [1], Kagan and Samuel [2] and Carone and Georgi [3, 4]. More recently this type of model has been investigated also in [5]. It was noted that these models permit to write renormalizable Yukawa interactions with ordinary fermions replacing the extended technicolor dynamics. In comparison to the earlier works we have:

- Included all dimension four operators with at most one mixing between the two scalar sectors.
- Provided an extensive scan of the parameters of the model.
- Updated the comparison with measurements.
- We linked the dynamical sector with models of (Ultra) Minimal Walking technicolor [6, 7, 8, 9].

We start with the following Lagrangian:

$$\mathcal{L}_{UTC} = \mathcal{L}_{SM}\Big|_{\text{Higgs}=0} + \mathcal{L}_{TC} + \mathcal{L}_{\text{Higgs}} + \mathcal{L}_{\text{Yukawa}} \ . \tag{1}$$

The TC-sector has no direct couplings with the SM fermions, but the elementary Higgs has Yukawa couplings with both the SM- and technifermions, encoded in $\mathcal{L}_{\text{Yukawa}}$. We construct

*Speaker

a low energy effective theory, where both the composite and the elementary scalar sector are described by a linear Lagrangian. The composite field is written as

$$M = \frac{1}{\sqrt{2}}\left(sI_{2\times 2} + 2i\pi_M\right) \propto Q_L \bar{Q}_R, \quad \langle s\rangle \equiv f, \tag{2}$$

where f is the technipion decay constant, and the elementary Higgs field as

$$H = \frac{1}{\sqrt{2}}\left(hI_{2x2} + 2i\pi_H\right), \quad \langle h\rangle \equiv v\ . \tag{3}$$

The Higgs Lagrangian is then given by

$$\mathcal{L}_{\rm Higgs} = \frac{1}{2}Tr\left[DH^\dagger DH\right] - V_H,\ V_H = \frac{1}{2}m_H^2 Tr\left[H^\dagger H\right] + \frac{\lambda_H}{4!}Tr^2\left[H^\dagger H\right]. \tag{4}$$

The technicolor sector is taken to be the Next to Minimal Walking Technicolor (NMWT) model [7], consisting of two techniflavors in the two-index symmetric representation of $\mathrm{SU}(3)_{\rm TC}$.

The techniquark Yukawa term

$$-\bar{Q}_L H Y_Q Q_R, \tag{5}$$

breaks the $(\mathrm{SU}(2)_{\rm L}\times\mathrm{SU}(2)_{\rm R})^2$ global symmetry of the model down to $\mathrm{SU}(2)_{\rm R}\times\mathrm{U}(1)_{\rm R}$. As the techniquarks form the chiral condensate, this term yields a linear term in the elementary scalar Lagrangian that will generate a vacuum expectation value for the Higgs, regardless of the sign of the original mass term m_H^2. When constructing the effective Lagrangian that mixes the technicolor sector with the elementary scalar, we include all dimension four operators with at most one mixing between the two scalar sectors. Applying Georgi's generalized naive dimensional analysis [10] we arrive at the following Lagrangian for the TC-sector and its coupling with the elemantary Higgs:

$$\begin{aligned}
\mathcal{L}_{TC} - \bar{Q}_L H Y_Q Q_R \quad &\rightarrow \quad \frac{1}{2}\mathrm{Tr}\left[DM^\dagger DM\right] + \frac{1}{2}(c_3/\alpha)\mathrm{Tr}\left[DM^\dagger DHY_Q\right] - V_M \\
V_M \quad &= \quad \frac{1}{2}m_M^2\mathrm{Tr}\left[M^\dagger M\right] + \frac{\lambda_M}{4!}\mathrm{Tr}^2\left[M^\dagger M\right] \\
&\quad -\frac{1}{2}(\alpha c_1)f^2\mathrm{Tr}\left[M^\dagger H Y_Q\right] - \frac{1}{24}(\alpha c_2)\mathrm{Tr}\left[M^\dagger M\right]\mathrm{Tr}\left[M^\dagger H Y_Q\right] \\
&\quad -\frac{1}{24}(c_4/\alpha)\mathrm{Tr}\left[H^\dagger H\right]\mathrm{Tr}\left[M^\dagger H Y_Q\right] + \text{h.c.}
\end{aligned} \tag{6}$$

Here $c_1 \ldots c_4$ are order one dimensionless real coefficients and $\alpha = \Lambda/f$, where Λ is the mass of the lowest lying vector resonance of the theory, is taken to be greater than one.

The above Lagrangian is diagonalized, and the physical propagating fields are given by a non unitary transformation from the original fields, due to the kinetic mixing term. In unitary gauge, the particle spectrum consists of two SM Higgs -like scalars and three massive pions, while three massless pions have been eaten to become the longitudinal degrees of freedom of the weak gauge bosons.

We perform an extensive scan of the parameters of the model, not restricting to any special case for the mass parameter of the fundamental scalar, as opposed to earlier work on models of this type. We constrain the parameters via direct search limits and electroweak and flavor precision tests. The mass patterns for the two scalars, passing all the electroweak and flavor

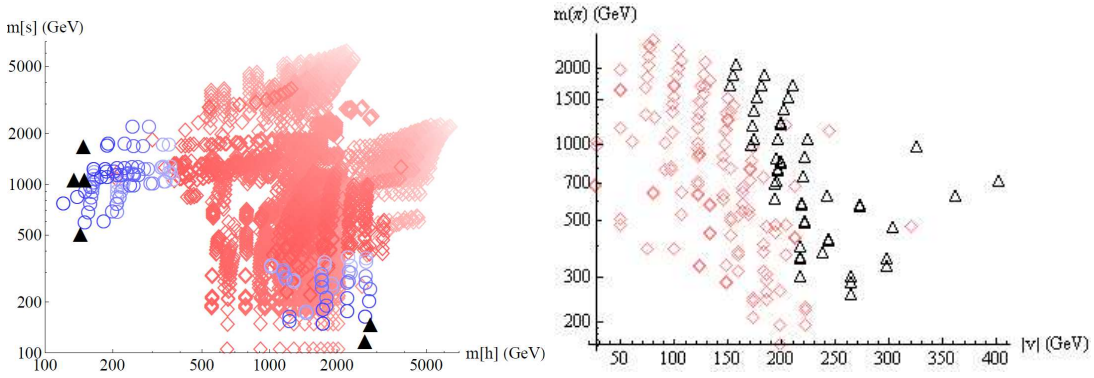

Figure 1: Left: The masses of the scalar particles. The black triangles are allowed by all data, blue circles are less favored by the electroweak precision data and red diamonds are ruled out. Right: The mass of the technipions, as a function of the vacuum expectation value of the elementary scalar. The black triangles are allowed and the read diamonds are ruled out.

tests as well as direct search limits, are shown as black triangles in the left panel of figure 1. Blue circles are less favored by the electroweak precision data and the red diamonds are ruled out. Our model thus predicts the existence of one light and one heavy Higgs-like scalar. The right panel of the figure shows as black triangles the allowed mass of the technipions, as a function of the vacuum expectation value of the elementary scalar. We see that the technipion mass is not very well constrained by the electroweak precision data, ranging from a few hundred GeV to a few TeV.

We find that the model is viable in the light of all existing experimental data and can be seen as a stepping stone towards a well defined extension of the SM featuring a complete solution to both the origin of spontaneous breaking of the electroweak symmetry and the mass of any SM fermion.

References

[1] E. H. Simmons, Nucl. Phys. B **312**, 253 (1989).

[2] A. Kagan and S. Samuel, Phys. Lett. B **270**, 37 (1991).

[3] C. D. Carone and E. H. Simmons, Nucl. Phys. B **397**, 591 (1993) [arXiv:hep-ph/9207273]; C. D. Carone and H. Georgi, Phys. Rev. D **49**, 1427 (1994) [arXiv:hep-ph/9308205].

[4] C. D. Carone, E. H. Simmons and Y. Su, Phys. Lett. B **344**, 287 (1995) [arXiv:hep-ph/9410242].

[5] A. R. Zerwekh, arXiv:0907.4690 [hep-ph].

[6] F. Sannino and K. Tuominen, Phys. Rev. D **71**, 051901 (2005) [arXiv:hep-ph/0405209].

[7] D. D. Dietrich, F. Sannino and K. Tuominen, Phys. Rev. D **72**, 055001 (2005) [arXiv:hep-ph/0505059]; D. D. Dietrich, F. Sannino and K. Tuominen, Phys. Rev. D **73**, 037701 (2006) [arXiv:hep-ph/0510217].

[8] D. D. Dietrich and F. Sannino, Phys. Rev. D **75**, 085018 (2007) [arXiv:hep-ph/0611341]. T. A. Ryttov and F. Sannino, Phys. Rev. D **76**, 105004 (2007) [arXiv:0707.3166 [hep-th]].

[9] T. A. Ryttov and F. Sannino, Phys. Rev. D **78**, 115010 (2008) [arXiv:0809.0713 [hep-ph]].

[10] H. Georgi, Phys. Lett. B **298** (1993) 187 [arXiv:hep-ph/9207278].

Collider signatures related to quark flavour violation in the MSSM

Björn Herrmann

DESY, Notketraße 85, 22607 Hamburg, Germany

in collaboration with A. Bartl, M. Bruhnke, H. Eberl, K. Hidaka, W. Majerotto and W. Porod

DOI: http://dx.doi.org/10.3204/DESY-PROC-2010-01/herrmann

In the Standard Model (SM), the only source of flavour violation are the Yukawa interactions and the resulting rotation from the gauge to the mass eigenstates of the fermions. In consequence, all quark-flavour violating (QFV) interactions can be parametrized in terms of the CKM-matrix. Among the numerous extensions of the SM, Supersymmetry (SUSY) and in particular the Minimal Supersymmetric Standard Model (MSSM) is among the most popular and best-studied ones. Postulating a superpartner with opposite statistics for each of the SM particles, it cures the hierarchy problem by stabilizing the Higgs mass, leads to gauge coupling unification, and includes interesting candidates for the cold dark matter observed in our Universe. Although it is clear that SUSY must be broken at the electroweak scale, there is no theoretical consensus about the exact breaking mechanism. One therefore introduces so-called soft-breaking terms in the SUSY Lagrangian.

One of the open questions related to the breaking mechanism concerns the flavour structure of the theory. The hypothesis of minimal flavour violation (MFV) assumes that flavour violation is the same as in the SM. Then, all QFV interactions (e.g. the squark-quark-chargino vertex) are again parameterized through the CKM-matrix. However, new sources of flavour violation can appear in SUSY models, especially if they are embedded in larger frameworks such as grand unified theories. This non-minimal flavour violation (NMFV) allows then for non-diagonal – i.e. flavour-violating – entries in the mass matrices of the sfermions that are not related to the CKM-matrix any more. These entries are conveniently considered as additional free parameters at the electroweak scale and can imply a different phenomenology as compared to the case of MFV. For a review on flavour violation in the MSSM see, e.g., Ref. [1]. Details on the parametrization of NMFV in the MSSM can also be found in Refs. [2, 3, 4, 5].

The studies discussed in the following focus on NMFV in the sector of squarks. Analogous arguments hold for sleptons, where the CKM-matrix is replaced by the PMNS-matrix. Moreover, the present analyses are based on flavour-mixing between the second and third generation and within the right-right sector of the squark mass matrices, which are least constrained by experimental measurements. The benchmark scenario SPS1a' [6], which serves as input for many experimental studies, is taken as reference point within the framework of minimal supergravity. The observed features are, however, present in wide ranges of the MSSM parameter space and also for variations of other QFV entries in the mass matrices.

Experimental limits from a large variety of rare decays, meson oscillations, or other precision measurements put strong constraints on the QFV elements of the squark mass matrices. Most

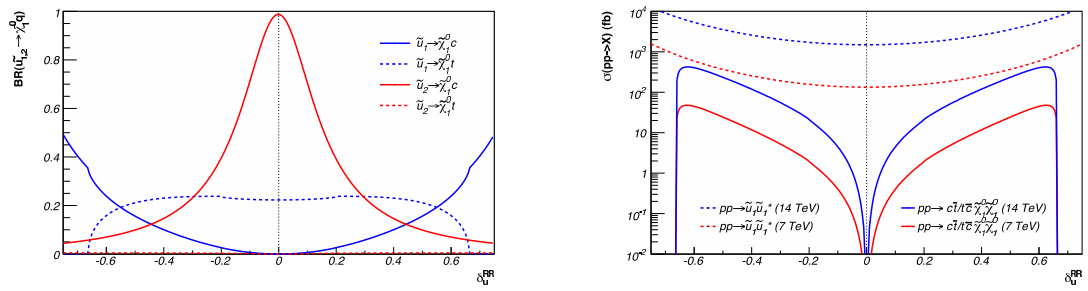

Figure 1: Branching ratios (left) of the two lightest up-type squarks and production cross-sections (right) of the discussed NMFV-signature for squark generation mixing between the second and third generations.

important in the context of QFV are the decays $b \to s\gamma$ and $b \to s\mu\mu$ as well as the observable ΔM_{B_s} related to B-meson oscillations. In the present study, all relevant constraints have explicitly been taken into account at the 95% confidence level and combined with the theoretical error estimate where available. Detailed discussions of the resulting allowed regions are given in Refs. [2, 3, 4, 5, 7, 8].

The physical mass spectrum of the squarks strongly depends on the introduced flavour-violating elements of the mass matrices [2, 4, 5, 7, 8]. In particular, the mass splitting between the involved mass eigenstates is increased with increasing flavour mixing. At the same time, the flavour content of the different squarks is modified. For example, the lightest up-type squark is a pure stop-mixture in the case of MFV, but receives sizeable charm-admixtures for larger values of the corresponding non-diagonal entries in the mass matrix. Vice versa, the charm content of the second-lightest squark is then exchanged for a stop-admixture.

The modified mass spectrum and flavour contents alter the decay modes of the squarks. In particular, new channels can be opened when introducing NMFV-elements in the mass matrices [4, 5]. The left panel of Fig. 1 shows the example of the fermionic decays of the two lightest up-type squarks into neutralinos. Here and in the following, the variables δ_u^{RR} and δ_d^{RR} parametrize the mixing (in the right-right sector) between the second and third generation up- and down-type squarks, respectively. The non-diagonal elements of the squark mass matrix are normalized to the diagonal ones according to Refs. [4, 5]. For a wide range of the NMFV-parameter, at least three of the branching ratios are simultaneously large, which may lead to important QFV effects in collider experiments [4].

In particular, they can give rise to sizeable event rates for the signal

$$pp \to \tilde{u}_{1,2}\tilde{u}^*_{1,2} \to c\bar{t}\ (t\bar{c})\ \tilde{\chi}^0_1\tilde{\chi}^0_1,$$

where the neutralinos give rise to missing transverse energy ($E_T^{\rm miss}$). While this process is practically not realized in the MSSM with MFV or in the Standard Model, allowing for NMFV can lead to rather sizeable cross-sections already for a moderate amount of additional flavour-mixing, as can be seen in the right panel of Fig. 1. The expected number of signal events at the LHC would be up to about 20.000 (10) for an integrated luminosity of 100 fb^{-1} (1 fb^{-1}) at $\sqrt{s} = 14$ TeV (7 TeV) [4].

Concerning the detectibility, top-quark identification is necessary to distinguish the proposed signal from top-antitop production including missing energy. The most crucial point for flavour-

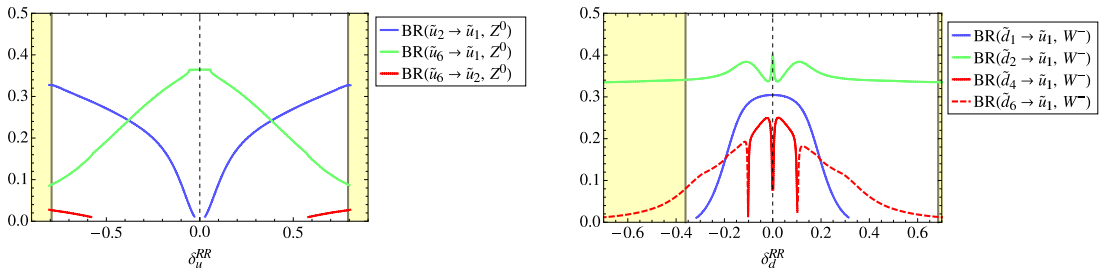

Figure 2: Typical NMFV-signatures related to squarks decaying into Z- or W-bosons for generation mixing between the second and third generations.

mixing between the second and third generation would be efficient charm-tagging. Otherwise, one should rather search for the signature $jet + (anti)top + E_T^{\text{miss}}$ [4].

Another type of NMFV-signature at colliders is connected to the bosonic decay modes of the squarks [5]. As for the fermionic case discussed above, new channels can be opened when allowing for new flavour-mixing entries in the mass matrices. Fig. 2 shows the example for decays of selected squarks into Z- or W-bosons and an up-type squark. Assuming MFV, only one squark can decay into the final state $\tilde{u}_1 Z^0$ in the given example. For increasing non-minimal flavour-mixing, as discussed above, a second mass eigenstate obtains a sizeable stop-content. At the same time, the mass of the lightest squark $\tilde{u}_1$ is decreasing so that the new decay channel $\tilde{u}_6 \to \tilde{u}_1 Z^0$ is opened [5].

Similar arguments hold for the decay of squarks into W-bosons. Here, two modes are present for MFV, while additional channels become possible already for moderate flavour-violating entries. If it will be possible to observe squarks at the LHC and to reconstruct their decays modes, the observation of such a signature would exclude the hypothesis of MFV [5].

In summary, despite the strong constraints from experimental data, NMFV can lead to new signatures in collider experiments that can challenge the hypothesis of MFV. Here, this has been shown for the benchmark scenario SPS1a'. The given conclusions hold, however, for wide ranges of the MSSM parameter space [4, 5]. The presented results are a clear call for detailed Monte-Carlo studies including background reactions and detector simulation. Such studies will in particular be necessary to identify the regions of parameter space where the proposed signatures are observable.

References

[1] F. del Aguila *et al.*, Eur. Phys. J. C57: 183 (2008).

[2] T. Hurth and W. Porod, JHEP 0908: 067 (2009).

[3] A. Bartl, K. Hidaka, K. Hohenwarter-Sodek, T. Kernreiter, W. Majerotto and W. Porod, Phys. Lett. B679: 260 (2009).

[4] A. Bartl, H. Eberl, B. Herrmann, K. Hidaka, W. Majerotto, W. Porod, arXiv:1007.5483 [hep-ph].

[5] M. Bruhnke, B. Herrmann and W. Porod, accepted for publication in JHEP, arXiv:1007.2100 [hep-ph].

[6] J. A. Aguilar-Saavedra *et al.*, Eur. Phys. J. C46: 43 (2006).

[7] G. Bozzi, B. Fuks, B. Herrmann and M. Klasen, Nucl. Phys. B787: 1-52 (2007).

[8] B. Fuks, B. Herrmann and M. Klasen, Nucl. Phys. B810: 266-299 (2008).

ATLAS high-level calorimeter trigger algorithms performance with first LHC *pp* collisions

Pavel Ježˇ for the ATLAS Collaboration

Niels Bohr Institute, Blegdamsvej 17, 2100 Copenhagen, Denmark

DOI: http://dx.doi.org/10.3204/DESY-PROC-2010-01/jez

After the commissioning phase with beams at SPS injection energy (450 GeV), the LHC [1] recently started the physics program with 7 TeV collisions. Consequently, the ATLAS detector [2] also entered its operation phase recording these collisions.

The task of the ATLAS trigger is to select 200 events out of 40 millions every second. It starts with the hardware-based trigger, the Level 1 (L1), which finds Regions of Interest (RoI's) using coarse information from the fast muon chamber or calorimeter. These RoI's are used as starting points for the two software based trigger levels: the Level 2 (L2), which operates only in the RoI's but uses full detector granularity, and the Event Filter (EF), which can explore the whole detector using full granularity information. The L2 and the EF are altogether referred to as the High Level Trigger (HLT) system. The L1 output rate is roughly 75 kHz with a latency of 2.5 μs. At L2, the output rate is decreased to 3 kHz with 40 ms latency and finally the EF output is 200 Hz and the time budget is roughly 4 s per event.

All trigger algorithms share a common data preparation step, optimized for fast processing. During the initial data taking period while the nominal luminosity is not attained, the trigger system accepts most of the incoming events and the bulk of the selection is performed only by the L1. The HLT is functional, but its decision is used for event rejection only when the maximum recording rate is reached. The trigger menus are composed of several signature subtriggers specialized in selecting different event types. Those using calorimeter data are presented in this paper.

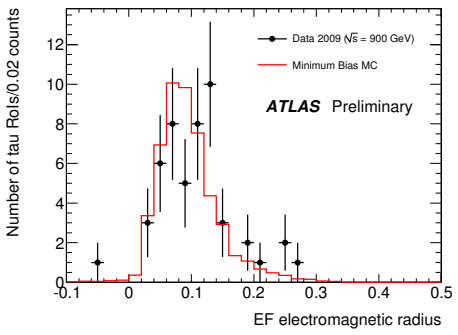

Figure 1: Candidate τ jet EM radius distribution at EF. Dots are 2009 collision data, solid line is MC expectation.

For example, the τ trigger is designed to select hadronic decays of the τ lepton, characterized by the presence of 1 or 3 $\pi^{\pm}$ accompanied by a ν and possibly π^0's. At L1, the τ trigger uses the electromagnetic (EM) and hadronic calorimeter to find transverse energy (E_T) deposits which pass the threshold (lowest is 5 GeV). At L2, selection criteria are applied using tracking and calorimeter based information. This takes advantage of calorimeter cluster confinement and low track multiplicity to discriminate τ's from the multi-jet background. Exploiting the same characteristics, the EF uses different selection criteria for single-prong (1 $\pi^{\pm}$) and multi-prong (3 $\pi^{\pm}$) decays in more refined algorithms which are almost identical to the offline reconstruction algorithms.

The distributions of the important observables obtained from data during 2009 have been compared with the non-diffractive minimum bias Monte Carlo and show reasonable agreement given the limited statistics. Fig. 1 presents a measure of the shower lateral size in the EM calorimeter (EM radius) calculated by the EF as the energy-weighted average cell distance from the cluster barycenter (obtained after weighting the position of each cell by its energy). It is an important discriminating variable because τ jets are more confined than QCD jets. Note that in all figures the MC has been normalized by the number of entries in data sample.

The ATLAS jet trigger is based on the selection of high hadronic E_T depositions. If a L1 jet candidate passes a given E_T threshold (lowest is 5 GeV), the L2 jet trigger continues by requesting calorimeter data around the L1 jet RoI position and runs an iterative cone algorithm with fixed radius. The EF jet algorithm is based on the offline reconstruction algorithm using calorimeter towers projecting towards the collision centre.

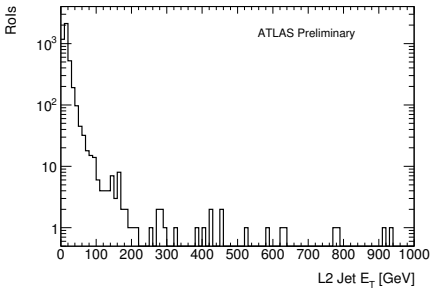

Figure 2: Transverse energy of jets measured at L2 in 900 GeV collisions.

The most important variable for the jet trigger is the transverse energy. The E_T measured in both the EM and the hadronic calorimeter is added up to obtain the jet trigger E_T. The distribution of the jet E_T obtained at L2 is presented in Fig. 2. Some clearly unphysical jets (with more than half the beam energy) are related to the detector noise. Jet clean-up procedures are being established by the collaboration to deal with such issues.

The aim of the e/γ trigger is to select events with electrons or photons in the final state. At L1, a threshold is set on minimal E_T deposit in the electromagnetic calorimeter (the lowest was 3 GeV in the commissioning period). At L2, fast algorithms for calorimeter reconstruction are run and fast tracking is used to reconstruct electron L2 objects. Already at this level it is possible to use the fine granularity of the first layer of the EM calorimeter to distinguish between primary and secondary γ's coming from π^0. At the EF, reconstruction algorithms very similar to those used offline are applied.

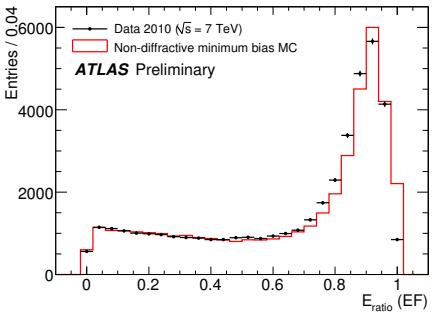

Figure 3: Distribution of photon E_{ratio} at EF. Dots are 7 TeV collision data, solid line is MC expectation.

Nice agreement with Monte Carlo expectation is observed with both 900 GeV and 7 TeV collisions. An important e/γ shower shape variable is called E_{ratio}, which is the fractional difference between the first and second highest energetic cell in the first calorimeter layer (Fig. 3 shows its distribution). For single γ's it peaks around 1, while for γ pairs from π^0 decays it is close to 0.

The ATLAS detector can be triggered also by events with considerable missing E_T or with a large amount of total E_T deposited in the calorimeters. That could play a crucial role in new physics discoveries such as dark matter candidates. The vector (missing E_T) and scalar (total E_T) sum of E_T are computed at L1 from all calorimeter elements. At L2, missing E_T is computed by adding the vector and scalar sums of all reconstructed muon momenta to the calorimetric measurement done at L1. Note that L2 is presently not configured to access L2

energy measurements due to strong network restrictions to read-out the whole detector at the full L2 input rate. At the EF, the total E_T and missing E_T are again recalculated with more precise input from the whole detector. Like for the other calorimeter triggers, no significant deviation from the MC expectation was observed in collision data. Figure 4 presents the comparison of minimum bias Monte Carlo and missing E_T measured at the EF from 7 TeV collisions. More details about the missing E_T trigger performance can be found in [3].

In order to guarantee the quality of the information provided at the trigger level, automatic monitoring is performed with respect to the information obtained offline. One of the most important tests is the comparison of energy of the clusters produced by the EF to the clusters produced by the offline code. Those checks verify that the cell and cluster calculations are compatible at both levels despite the different choice of algorithms or parameters.

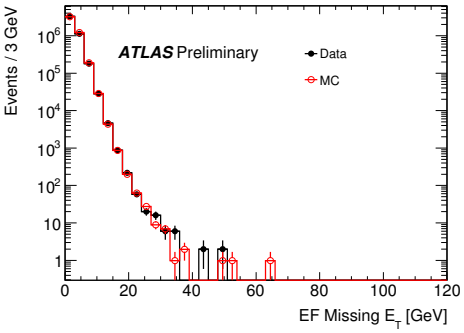

Figure 4: Distribution of missing E_T at EF. Dots are 7 TeV collision data, solid line is MC expectation.

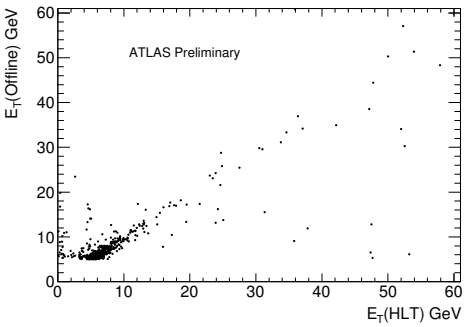

Figure 5: Correlation of the EF and offline E_T obtained from 900 GeV data.

The correlation of the E_T of e/γ clusters calculated at the EF and during offline reconstruction is presented on Fig. 5. Note that several off-diagonal candidates with low offline E_T and high EF E_T would not pass offline quality cuts which are used to declare the EM cluster to be an electron or photon candidate. More analyses are ongoing to produce even more HLT/offline compatible results.

The studies presented in this paper demonstrated that calorimeter HLT algorithms are under control. Key observables behave comparable to MC studies and ongoing comparison with offline performance shows no important bias caused by those algorithms. Furthermore, time requirements were evaluated to be within the required operational constraints and all algorithms proved their robustness during the many hours long LHC runs. A comprehensive summary of the calorimeter HLT performance as well as further references can be found in [4].

Recently, many of the algorithms (especially from e/γ and τ triggers) were switched to perform active selection of events during runs with higher luminosity.

References

[1] L. Evans and P. Bryant, JINST **3** (2008) S08001.
[2] G. Aad *et al.* [ATLAS Collaboration], JINST **3** (2008) S08003.
[3] G. Aad *et al.* [ATLAS Collaboration], ATLAS-CONF-2010-026.
[4] G. Aad *et al.* [ATLAS Collaboration], ATLAS-CONF-2010-030.

Three-loop predictions for the light Higgs mass in the MSSM

Philipp Kant

Humboldt-Universität zu Berlin, Newtonstr. 15, 12489 Berlin

DOI: http://dx.doi.org/10.3204/DESY-PROC-2010-01/kant

The Minimal Supersymmetric Extension of the Standard Model (MSSM) features a light Higgs boson, the mass M_h of which is predicted by the theory. Given that the LHC will be able to measure the mass of a light Higgs with great accuracy, a precise theoretical calculation of M_h yields an important test of the MSSM. In order to deliver this precision, we present three-loop radiative corrections of $\mathcal{O}\left(\alpha_t\alpha_s^2\right)$ and provide a computer code that combines our results with corrections to M_h at lower loop orders that are available in the literature.

1 Introduction

The Higgs sector of the Minimal Supersymmetric Extension of the Standard Model (MSSM) consists of a two-Higgs doublet model, which is tightly constrained by supersymmetry. In particular, the quartic terms of the Higgs potential are completely fixed by the gauge couplings. Thus, it is possible to describe the MSSM Higgs sector through only two new (with respect to the Standard Model) parameters, which are usually taken to be the mass M_A of the pseudoscalar Higgs and the ratio $\tan\beta = \frac{v_2}{v_1}$ of the vacuum expectation values of the Higgs doublets. In particular, M_h, the mass of the light scalar Higgs boson, can be predicted, and at the tree-level only these two parameters enter the prediction, leading to an upper bound of $M_h \leq M_Z$. However, M_h is sensitive to virtual corrections to the Higgs propagator that shift this upper bound significantly. These virtual corrections depend on all the supersymmetry breaking parameters. This sensitivity to virtual corrections, combined with the great precision with which the Large Hadron Collider (LHC) will be able to measure the mass of a light Higgs, allows M_h to be used as a precision observable to test supersymmetric models – assuming that the theoretical uncertainties are suffiently small and under control.

Consequently, the one- and two-loop corrections to M_h have been studied extensively in the literature (see, for example [1, 2, 3, 4, 5, 6, 7, 8]). The remaining uncertainty has been estimated to be about $3 - 5\,\text{GeV}$ [10, 9]. Recently, also three-loop corrections have become available. The leading- and next-to-leading terms in $\ln(M_{SUSY}/M_t)$, where M_{SUSY} is the typical scale of SUSY particle masses, have been obtained in [11]. Motivated by the observation that the contributions from loops of top quarks and their superpartners, the stops, are dominant at the one- and two-loop level, we have calculated three-loop SUSY-QCD corrections to these diagrams. These corrections are of $\mathcal{O}\left(\alpha_t\alpha_s^2\right)$, where α_t is the coupling of the Higgs to the top quarks. A first result has been obtained in [12]. There, we assumed that all the superpartners had approximately the same mass. This restriction has been dropped recently in [13].

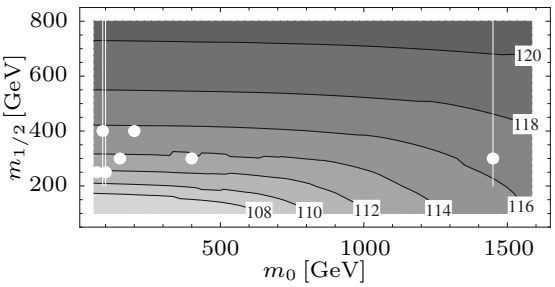

Figure 1: Prediction for the value of M_h (in GeV) for MSUGRA scenario with $\tan\beta = 10$, $A_0 = 0$, as evaluated by H3M. The white lines and points indicate the benchmark scenarios of [19].

2 Organisation of the calculation

A major difficulty in obtaining the results of [13] was the presence of many different mass scales – the masses m_t of the top quark, $m_{\tilde{g}}$ of the gluino, $m_{\tilde{t}_{1,2}}$ of the stops and $m_{\tilde{q}}$ of the partners of the light quarks – in the three-loop propagator diagrams. Assuming that there is a distinct hierarchy between these masses, they can be disentangled by the method of asymptotic expansions [14], yielding an expansion of the diagrams in small mass ratios and logarithms of mass ratios. Working in the effective potential approximation, we set the external momentum flowing through the Higgs propagator to zero and are left with tadpole integrals with a single mass scale, which are known and implemented in the FORM [15] program MATAD [16].

However, as the masses of the superpartners are not known, it is not clear which hierarchy one should assume. We solve this by computing the diagrams for many different hierarchies. Then, when given a point in the MSSM parameter space, we choose whichever hierarchy fits best and evaluate M_h using the calculation in the chosen hierarchy. To choose the best hierarchy and to estimate the error introduced by the asymptotic expansion, we compare, at the two-loop level, our expanded result with the result of [7], which contains the full mass dependence.

For convenience, we have written the MATHEMATICA package H3M [17], which automatically performs the choice of the best fitting hierarchy and provides a SUSY LES HOUCHES interface to our calculation. This allows to perform parameter scans as in Fig. 1. In order to get a state-of-the art prediction for M_h, we include all available contributions to M_h at the one- and two-loop level that are implemented in FEYNHIGGS [18]. For details on the usage and inner workings of the program, we refer to [13].

3 Estimating the theoretical uncertainty

We observe that the dependence of M_h on the renormalisation prescription, which is often used as a guesstimate for the uncertainty due to unknown higher order corrections, reduces drastically when one goes from two to three loops. But since we also find that the size of the three-loop corrections can be of the order of one to two GeV, which is rather large given that the two-loop corrections are only about a factor of two larger, we prefer to be conservative in our estimation of the theoretical uncertainty. Assuming a geometric progression of the perturbative series, we get for MSUGRA scenarios an uncertainty due to missing higher order corrections of 100 MeV to 1 GeV, depending on the value of $m_{1/2}$. The parametric uncertainty due to α_s, m_t

and $m_{\tilde{t}_{1,2}}$ is of the same order of magnitude. The uncertainty introduced by the expansion in mass ratios amounts to at most 100 MeV [13].

4 Conclusions

We present a calculation of the $\mathcal{O}\left(\alpha_t\alpha_s^2\right)$ corrections to M_h, shifting the value of M_h by about 1 GeV. We provide a computer code combining our results with corrections from lower loop orders, thus enabling a state-of-the-art prediction of M_h. Our calculation lowers the theoretical uncertainty due to missing higher orders to the same magnitude as the parametric uncertainty.

This work was supported by the DFG through SFB/TR 9 and by the Helmholtz Alliance "Physics at the Terascale".

References

[1] R. Hempfling and A. H. Hoang, Phys. Lett. B **331**, 99 (1994) [hep-ph/9401219]. H. E. Haber, R. Hempfling and A. H. Hoang, Z. Phys. C **75**, 539 (1997) [hep-ph/9609331].

[2] R.J. Zhang, Phys. Lett. B **447**, 89 (1999) [hep-ph/9808299]; J.R. Espinosa and R.J. Zhang, JHEP **0003**, 026 (2000) [hep-ph/9912236]; Nucl. Phys. B **586**, 3 (2000) [hep-ph/0003246].

[3] S. Heinemeyer, W. Hollik and G. Weiglein, Phys. Rev. D **58**, 091701 (1998) [hep-ph/9803277]. Phys. Lett. B **440**, 296 (1998) [hep-ph/9807423]. Eur. Phys. J. C **9**, 343 (1999) [hep-ph/9812472].

[4] A. Pilaftsis and C. E. Wagner, Nucl. Phys. B **553**, 3 (1999) [hep-ph/9902371]. M. Carena, J. R. Ellis, A. Pilaftsis and C. E. Wagner, Nucl. Phys. B **586**, 92 (2000) '[hep-ph/0003180], Nucl. Phys. B **625**, 345 (2002) [hep-ph/0111245].

[5] M. Carena et al, Nucl. Phys. B **580**, 29 (2000) [hep-ph/0001002].

[6] J. R. Espinosa and I. Navarro, Nucl. Phys. B **615**, 82 (2001) [hep-ph/0104047].

[7] G. Degrassi, P. Slavich and F. Zwirner, Nucl. Phys. B **611**, 403 (2001) [hep-ph/0105096], A. Brignole, G. Degrassi, P. Slavich and F. Zwirner, Nucl. Phys. B **631**, 195 (2002) [hep-ph/0112177], Nucl. Phys. B **643**, 79 (2002) [hep-ph/0206101].

[8] S. P. Martin, Phys. Rev. D **67** (2003) 095012 [arXiv:hep-ph/0211366].

[9] B. C. Allanach, A. Djouadi, J. L. Kneur, W. Porod and P. Slavich, JHEP **0409** (2004) 044 [arXiv:hep-ph/0406166].

[10] G. Degrassi, S. Heinemeyer, W. Hollik, P. Slavich and G. Weiglein, Eur. Phys. J. C **28**, 133 (2003) [arXiv:hep-ph/0212020].

[11] S. P. Martin, Phys. Rev. D **75** (2007) 055005 [arXiv:hep-ph/0701051].

[12] R. V. Harlander, P. Kant, L. Mihaila and M. Steinhauser, Phys. Rev. Lett. **100** (2008) 191602 [Phys. Rev. Lett. **101** (2008) 039901] [arXiv:0803.0672 [hep-ph]].

[13] P. Kant, R. V. Harlander, L. Mihaila and M. Steinhauser, arXiv:1005.5709 [hep-ph].

[14] V. A. Smirnov, Springer Tracts Mod. Phys. **177** (2002) 1.

[15] J. A. M. Vermaseren, arXiv:math-ph/0010025.

[16] M. Steinhauser, Comput. Phys. Commun. **134** (2001) 335 [arXiv:hep-ph/0009029].

[17] `http://www-ttp.particle.uni-karlsruhe.de/Progdata/ttp10/ttp10-23`

[18] M. Frank, T. Hahn, S. Heinemeyer, W. Hollik, H. Rzehak and G. Weiglein, JHEP **0702** (2007) 047 [arXiv:hep-ph/0611326]. S. Heinemeyer, W. Hollik and G. Weiglein, Eur. Phys. J. C **9** (1999) 343 [arXiv:hep-ph/9812472]. S. Heinemeyer, W. Hollik and G. Weiglein, Comput. Phys. Commun. **124** (2000) 76 [arXiv:hep-ph/9812320].

[19] B. C. Allanach *et al.*, in *Proc. of the APS/DPF/DPB Summer Study on the Future of Particle Physics (Snowmass 2001)* ed. N. Graf, Eur. Phys. J. C **25** (2002) 113 [arXiv:hep-ph/0202233].

Alignment of the ATLAS Inner Detector tracking system

Thomas Loddenkoetter for the ATLAS Collaboration

Physikalisches Institut, Nuallee 12, 53115 Bonn, Germany

DOI: http://dx.doi.org/10.3204/DESY-PROC-2010-01/loddenkoetter

Modern tracking systems like the ATLAS Inner Detector (ID) have intrinsic resolutions that by far exceed the assembly precision. For an accurate description of the real geometry one has to obtain corrections to the nominal positions. This alignment task is crucial for efficient track reconstruction as well as for precise momentum measurement and vertex reconstruction.

The criteria for the required alignment precision at ATLAS are that the resolutions of the track parameters should not decrease by more than 20% due to alignment effects and that the systematic error on the W mass should be below < 15 MeV [1].

The ID [1][2] consists of three sub-components: the Pixel Detector (Pixel), the Semi-Conductor Tracker (SCT) and the Transition Radiation Tracker (TRT). The Pixel is a silicon pixel detector consisting of three cylindrical barrel layers and three disks in each end-cap. Its intrinsic resolution is $10 \times 115\ \mu m^2$ ($R\phi \times z$), leading to a required alignment precision of $7 \times 100\ \mu m^2$.

The SCT is a silicon strip detector with four barrel layers and nine disks per end-cap. The intrinsic resolution of the SCT is $17 \times 580\ \mu m^2$ ($R\phi \times z$), the target precision for alignment is $12 \times 200\ \mu m^2$. Pixel and SCT together consist of about 5800 modules in total.

The TRT consists of straw-like polyamide drift tubes with a diameter of 4 mm. The barrel is divided into three rings of 32 modules each, containing in total 73 layers of straws. Each end-cap consists of 160 disks of radially oriented straws. The TRT has an intrinsic resolution of 130 µm ($R\phi$ only), the target alignment precision is 30 µm.

To achieve the alignment goals, various tools are available. Already during the detector installation, *assembly and survey measurements* were performed, yielding a precision of up to O(100 µm). These measurements serve as a starting point or external constraint for other methods [3].

The SCT is equipped with a *Frequency Scanning Interferometry (FSI)* [4] system that measures deformations of the SCT with an extremely high precision of O(1 µm). Its purpose is to monitor the stability of the alignment with time. The FSI is not fully integrated in the alignment software yet.

The tool for ultimate alignment precision is *track-based alignment* which uses particle tracks to determine the alignment by examining residuals between the reconstructed hits in the detector and the intercept of the track trajectory in the module, estimated by the track fit. Several million high-p_T tracks are needed in order to reach the desired precision.

The algorithms used by ATLAS are based on minimizing the track χ^2 or on centering residual distributions by examining their mean values.

The alignment can be performed at different levels of granularity. This *alignment level* defines the "alignable structures" i.e. the substructures of the ID to which individual alignment constants are assigned. Each alignable structure has six degrees of freedom (dof), corresponding to six alignment parameters (three translations and three orientations). For the ID alignment, several alignment levels are implemented: Level 1 treats the whole Pixel as well as SCT and TRT barrel and end-caps as alignable structures, which makes 42 dof, on level 2 all ID subcomponents are split up into their barrel layers/modules and end-cap disks/layers (1146 dof). Finally, on level 3, all single sensors are aligned individually (Pixel and SCT only, about 36000 dof). Furthermore, several intermediate levels are defined that all follow the assembly structures of the detectors. For a full ID alignment, the alignment chain is run iteratively at different levels.

The baseline algorithm for track-based alignment at ATLAS is the Global χ^2 [5]. Tracks are fitted simultaneously, minimizing a global χ^2 w.r.t. all track and alignment parameters at the same time. The χ^2 definition is given in Eq. 1, where $\mathbf{r_j}$ is the vector of residuals of a track, $\boldsymbol{\tau_j}$ and $\mathbf{a}$ denote the track and alignment parameters, respectively, and V is the covariance matrix.

$$\chi^2 = \sum_{tracks} \mathbf{r_j}^T(\boldsymbol{\tau_j}, \mathbf{a})(V^{-1})_j \mathbf{r_j}(\boldsymbol{\tau_j}, \mathbf{a}) \qquad \longrightarrow \qquad \frac{d(\chi^2)}{d(\boldsymbol{\tau_j}, \mathbf{a})} \stackrel{!}{=} 0 \tag{1}$$

For minimization, the derivatives of χ^2 w.r.t. all $\boldsymbol{\tau_j}$ and $\mathbf{a}$ are required to be 0 at the same time. This leads to a linear system of N linear equations, represented by an N×N matrix, where N is the number of dofs. This can be solved by different techniques. At low granularity, the full diagonalization of the matrix is possible. All eigenmodes of the system and their eigenvalues are then known. At full granularity, a fast solution is more suitable and can be achieved with matrix conditioning. In this case the eigenvectors and -values are unknown. Also the statistical errors on alignment parameters cannot be calculated then.

Unfortunately, the χ^2 minimization is normally not sufficient for a proper alignment. The reason are the *weak modes*, which are solutions of the alignment that leave the residuals (almost) invariant, but may bias the track parameters and therefore are a source of systematics. In the χ^2 algorithm they appear as eigenmodes with very small eigenvalues, to which the algorithm is therefore insensitive. Typically, weak modes correspond to systematic deformations of the whole detector. To deal with weak modes, various measures can be taken.

The most important is to prevent the alignment from introducing weak modes. At low granularity, when the eigenmodes are known, this can be done by cutting away those modes with the lowest eigenvalues. At high granularity, when the eigenmodes are unknown, one can apply a *soft mode cut*, i.e. constrain the system by appropriately conditioning the matrix in a way that weak modes get suppressed.

Of course, cutting away or suppressing weak modes is not enough, as the real detector may contain such deformations. Aligning these requires extra steps. As weak modes are often connected to certain track topologies, a good measure is to mix tracks with different topologies, e.g. collision tracks, cosmics and beam halos. Effectively, this reduces the number of weak modes

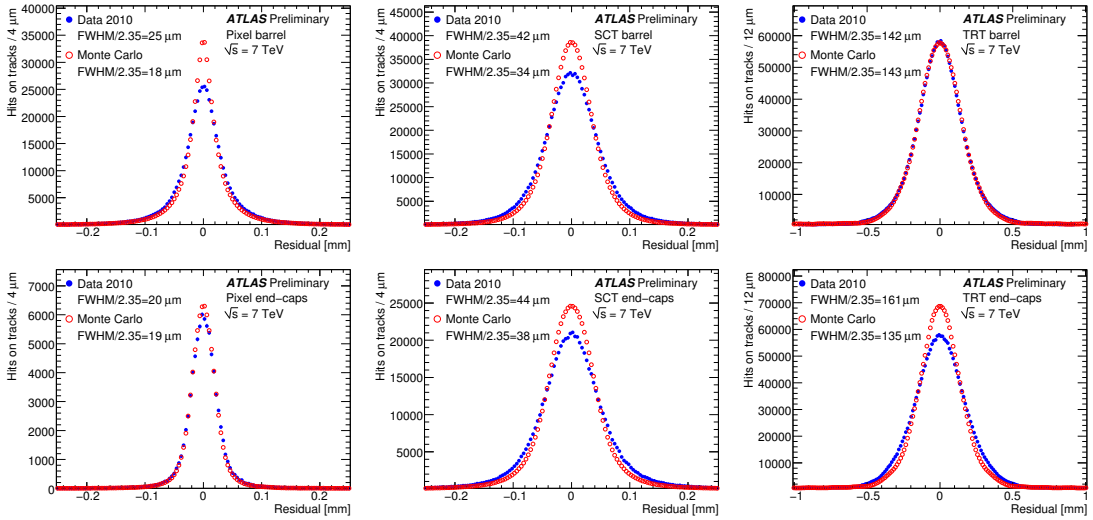

Figure 1: Unbiased residual distributions in local x coordinate for barrel and end caps of Pixel, SCT and TRT. Data points are for 7 TeV collision data from 2010 with the current alignment (dark dots) and for a simulation with perfect alignment (light circles). The simulated distributions are normalized to the number of entries in the data. The "Full Width Half-Maximum" of the distributions divided by 2.35 are quoted.

of the system. Vertex or beam spot constraints have a similar effect. Finally, one can examine quantities that *are* affected by weak modes, like invariant mass distributions of resonances etc.

Figure 1 shows the results for 7 TeV data from 2010 with the current alignment (dark dots) and for a simulation with perfect alignment (light circles). The unbiased residual distributions in the most sensitive local coordinate are presented for all sub-detectors. Tracks used for the plots were required to have $p_T > 2$ GeV and number of silicon hits ≥ 6. For these low-momentum tracks, the width of the residual distribution is larger than the intrinsic "per-hit" accuracy of the detectors due to the contribution from multiple scattering to the track parameter errors.

In the TRT end-caps the measured resolution w.r.t. the simulation is significantly worse than in the barrel. This is due to the fact that the TRT end-cap geometry did not allow for as detailed cosmic ray studies as the barrel and the Pixel and the SCT. Further commissioning of the TRT end-caps is required to achieve performance similar to that of the barrel.

References

[1] [ATLAS Collaboration], 1997, CERN-LHCC-97-16/17.

[2] G. Aad *et al.* [ATLAS Collaboration], JINST **3** (2008) S08003.

[3] T. Golling, 2006, ATL-INDET-PUB-2006-001.

[4] P. A. Coe, D. F. Howell and R. B. Nickerson, Measur. Sci. Tech. **15** (2004) 2175.
S. M. Gibson *et* al., 2005, Optics and lasers in engineering *43* 815-831

[5] P. Bruckman, A. Hicheur and S. J. Haywood, 2005, ATL-INDET-PUB-2005-002.

Forward Λ_b production in pp collisions at LHC

Gennady I. Lykasov, Denis A. Artemenkov, Vadim A. Bednyakov
JINR, Dubna, 141980, Moscow region, Russia

DOI: http://dx.doi.org/10.3204/DESY-PROC-2010-01/lykasov

As is well known, there are successful phenomenological approaches for describing the soft hadron-nucleon, hadron-nucleus and nucleus-nucleus interactions at high energies based on the Regge theory and the $1/N$ expansion in QCD, for example the quark-gluon string model (QGSM) [1] and the dual parton model (DPM) [2]. In this paper we present the results on the beauty baryon production, in particular Λ_b, in pp collisions at LHC energies and small p_t within the QGSM to find the information on the Regge trajectories of the bottom ($b\bar{b}$) mesons and the fragmentation functions (FF) of all the quarks and diquarks to this baryon. Actually, these results are the predictions for the LHC experiments.

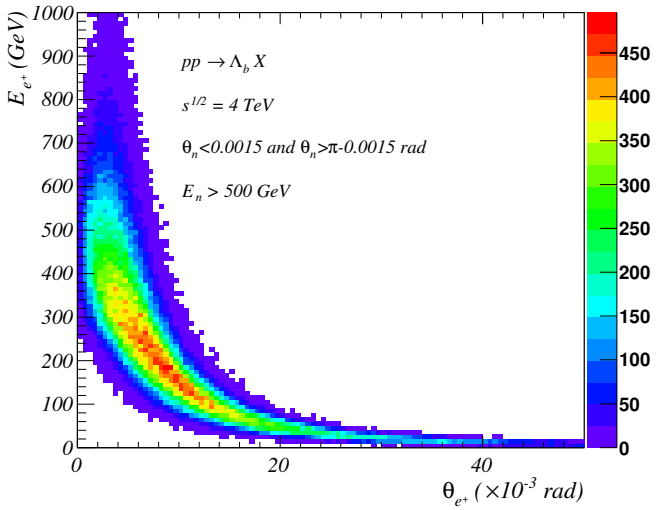

Figure 1: The distribution over θ_{e^+} and E_{e^+} in the inclusive process $pp \to \Lambda_b X \to J/\psi\,\Lambda^0 X \to e^+e^-n\,\pi^0 X$ at $\sqrt{s} = 4\,\text{GeV}$. The rate of the events is about 4.6 percent (13.8 nb).

The detailed calculations and the predictions on these reactions are presented in [3, 4], where it is shown that all the observables are very sensitive to the value of intercept $\alpha_\Upsilon(0)$ of the $\Upsilon(b\bar{b})$ Regge trajectory. The upper limit of our results is reached at $\alpha_\Upsilon(0) = 0$, when this Regge trajectory as a function of the transfer t is nonlinear. Using the hadron detector at the CMS and the TOTEM one could register the decay $\Lambda_b^0 \to J/\psi\,\Lambda^0 \to \mu^+\mu^-\pi^-p$ by detecting two muons and one proton emitted forward. However, the acceptance of the muon detector is $10^\circ \le \theta_\mu \le 170^\circ$ [5], where, according to our calculations, the fraction of these events is too low.

On the other hand, the electromagnetic calorimeter at the CMS is able to measure the dielectron pairs e^+e^- in the acceptance about $1^\circ \leq \theta_{e(e^+)} \leq 179^\circ$ [6]. Fig. 1 illustrates that the electrons and positrons produced from the J/ψ decay are emitted at very small scattering angles, mainly at $\theta_e < 16\,\text{mrad}$. The rate of these events, when the neutrons are emitted at $\theta_n < 1.5\,\text{mrad}$ and $E_n > 500\,\text{GeV}$, is about 4.6 percent (13.8 nb). In Fig. 2 the two-dimensional distribution over E_p and θ_p for the reaction $pp \to \Lambda_b X \to J/\psi\,\Lambda^0 X \to e^+e^-p\,\pi^-X$ is presented. The rate of these events is about 0.74 percent (2.22 nb). This could be reliable using the TOTEM together with the CMS [7].

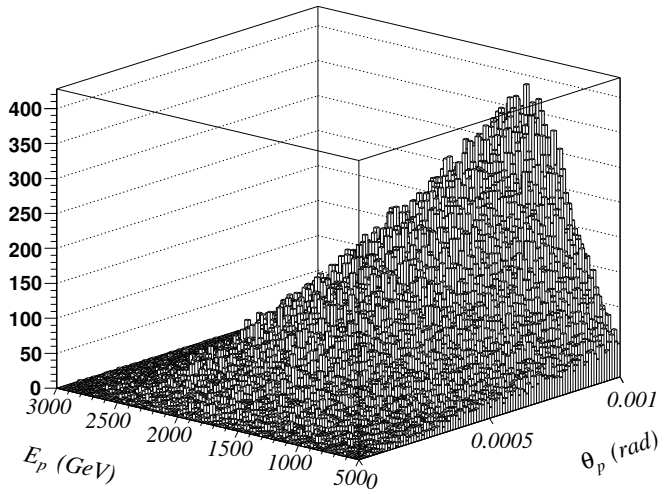

Figure 2: The two-dimensional distribution over θ_p and E_p in the inclusive process $pp \to \Lambda_b X \to J/\psi\,\Lambda^0 X \to e^+e^-p\,\pi^-X$ at $\sqrt{s} = 10\,\text{TeV}$ at $\alpha_\Upsilon(0) = 0$, when $E_p \geq 500\,\text{GeV}$ and $\theta_p \leq 1\,\text{mrad}$. The rate of these events is about 0.74 percent (2.22 nb).

The ATLAS is able also to detect e^+e^- by the electromagnetic calorimeter in the interval $1^\circ \leq \theta_{e(e^+)} \leq 179^\circ$ [5] and the neutrons emitted forward at the angles $\theta_n \leq 0.1\,\text{mrad}$ [8]. In Fig. 3 we present the prediction for the reaction $pp \to \Lambda_b X \to J/\psi\,\Lambda^0 X \to e^+e^-n\,\pi^0 X$, that could be reliable at the ATLAS experiment. The rate of these events is about 0.015 percent (45 pb).

The TOTEM [9] together with the CMS might be able to measure the channel $\Lambda_b \to J/\psi\,\Lambda^0 \to e^+e^-\pi^-p$ (the integrated cross-section is about 0.2–0.3 μb at $\alpha_\Upsilon(0) = 0$ and smaller at $\alpha_\Upsilon(0) = -8$). The T2 and T1 tracking stations of the TOTEM apparatus have their angular acceptance in the intervals $3\,\text{mrad} < \theta < 10\,\text{mrad}$ (corresponding to $6.5 > \eta > 5.3$) and $18\,\text{mrad} < \theta < 90\,\text{mrad}$ (corresponding to $4.7 > \eta > 3.1$) respectively, and could thus detect 42% of the muons from the J/ψ decay. In the same angular intervals, 36% of the π^- and 35% of the protons from the Λ^0 decay are expected. According to a very preliminary estimate [7], protons with energies above 3.4 TeV emitted at angles smaller than 0.6 mrad could be detected in the Roman Pot station at 147 m from IP5 [9, 7]. In the latter case, the reconstruction of the proton kinematics may be possible, whereas the trackers T1 and T2 do not provide any momentum or energy information. Future detailed studies are to establish the full event topologies with all correlations between the observables in order to assess whether the signal events can be identified and separated from backgrounds. These investigations should also

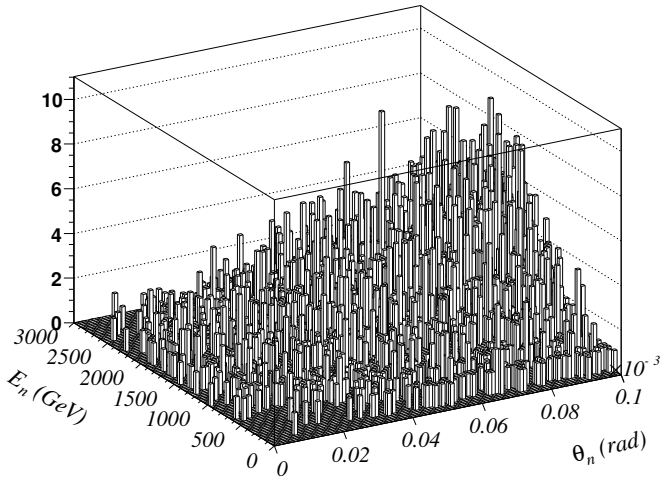

Figure 3: The two-dimensional distribution over θ_p and E_p in the inclusive process $pp \to \Lambda_b X \to J/\psi\, \Lambda^0 X \to e^+e^- n\, \pi^0 X$ at $\sqrt{s} = 10\,\text{TeV}$ at $\alpha_\Upsilon(0) = 0$, when $\theta_p \leq 0.1\,\text{mrad}$. The rate of these events is about 0.015 percent (45 pb).

include the CMS calorimeters HF and CASTOR which cover the same angular ranges as T1 and T2 respectively [7].

Acknowledgments

We are very grateful to V. V. Lyubushkin for a help in the MC calculations. We also thank M. Deile, P. Grafström, and N. I. Zimin for extremely useful help related to the possible experimental check of the suggested predictions at the LHC and the preparation of this paper. We are also grateful to D. Denegri, K. Eggert, A. B. Kaidalov, and M. Poghosyan for very useful discussions. This work was supported in part by the Russian Foundation for Basic Research grant N: 08-02-01003.

References

[1] A. B. Kaidalov and K. A. Ter-Martirosyan, Phys. Lett. B **116** (1982) 489, [arXiv:hep-ph/0909.5061].

[2] A. Capella, U. Sukhatme, C. I. Tan and J. Tran Than Van Phys. Rep. **236** (1994) 225, [arXiv:hep-ph/0909.5061].

[3] G. I. Lykasov, V. V. Lyubushkin and V. A. Bednyakov, Nucl. Phys. [Proc. Suppl.] **198** (2010) 165 [arXiv:hep-ph/0909.5061].

[4] V. A. Bednyakov, G. I. Lykasov and V. V. Lyubushkin, arXiv:hep-ph/1005.0559.

[5] ATLAS Collaboration, Technical Design Report, ATLAS-TDR-017,CERN-LHCC-2005-022.

[6] CMS Collaboration J. Phys. G: Nucl. Part. Phys. **34** (2007) 995.

[7] M. Deile, Private communication; H. Niewiadomski, TOTEM-NOTE, **002** (2009).

[8] ATLAS Collaboration, Letter of Intent "Zero Degree Calorimeters".

[9] TOTEM Collaboration, Technical Design Report, (2004),CERN-LHCC-2004-002; Addendum CERN-LHCC-2004-020, "The Totem Experiment At The CERN Large Hadron Collider", JINST **3**2008 S08007.

On the phenomenology of a two-Higgs-doublet model with maximal CP symmetry at the LHC – synopsis and addendum

M. Maniatis[1], *A. von Manteuffel*[2], *O. Nachtmann*[1]

[1]Institut für Theoretische Physik, Universität Heidelberg, Philosophenweg 16, 69120 Heidelberg, Germany
[2]Institut für Theoretische Physik, Universität Zürich, Winterthurerstr. 190, 8057 Zürich, Switzerland

DOI: http://dx.doi.org/10.3204/DESY-PROC-2010-01/maniatis

Predictions for LHC physics are given for a two-Higgs-doublet model having four generalized CP symmetries. In this *maximally-CP-symmetric model* (MCPM) the first fermion family is, at tree level, uncoupled to the Higgs fields and thus massless. The second and third fermion families have a very symmetric coupling to the Higgs fields. But through the electroweak symmetry breaking a large mass hierarchy is generated between these fermion families, that is, we find roughly what is observed in Nature. In this paper we present a short outline of the model and extend a former study by the predictions at LHC for a center-of-mass energy of 7 TeV.

1 Introduction

Extending the Standard Model (SM) Higgs sector to two Higgs doublets, φ_1, φ_2, gives the two-Higgs-doublet model (THDM). Many properties of THDMs turn out to have a simple geometric meaning if we introduce gauge invariant bilinears [1, 2],

$$K_0 = \varphi_1^\dagger\varphi_1 + \varphi_2^\dagger\varphi_2, \qquad \mathbf{K} = \begin{pmatrix} K_1 \\ K_2 \\ K_3 \end{pmatrix} = \begin{pmatrix} \varphi_1^\dagger\varphi_2 + \varphi_2^\dagger\varphi_1 \\ i\varphi_2^\dagger\varphi_1 - i\varphi_1^\dagger\varphi_2 \\ \varphi_1^\dagger\varphi_1 - \varphi_2^\dagger\varphi_2 \end{pmatrix}. \tag{1}$$

In terms of these bilinears K_0, $\mathbf{K}$, the most general THDM Higgs potential reads

$$V = \xi_0 K_0 + \boldsymbol{\xi}^{\mathrm{T}}\mathbf{K} + \eta_{00}K_0^2 + 2K_0\boldsymbol{\eta}^{\mathrm{T}}\mathbf{K} + \mathbf{K}^{\mathrm{T}}E\mathbf{K} \tag{2}$$

with parameters ξ_0, η_{00}, 3-component vectors $\boldsymbol{\xi}$, $\boldsymbol{\eta}$ and a 3×3 matrix $E = E^{\mathrm{T}}$, all real.

Generalised CP transformations (GCPs) are defined by [5, 6, 7]

$$\varphi_i(x) \to U_{ij}\,\varphi_j^*(x'), \qquad i,j = 1,2\,, \qquad x' = (x^0, -\mathbf{x}) \tag{3}$$

with U an arbitrary unitary 2×2 matrix and $U = \mathbb{1}_2$ corresponds to the standard CP transformation. In terms of the bilinears this reads [3, 4]

$$K_0(x) \to K_0(x'), \qquad \mathbf{K}(x) \to \bar{R}\,\mathbf{K}(x') \tag{4}$$

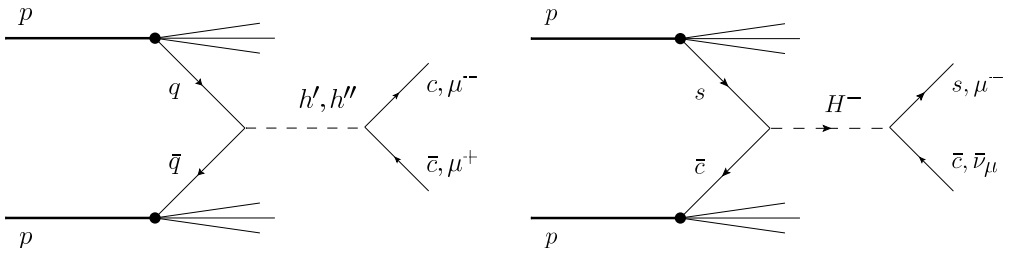

Figure 1: Feynman diagrams for the Drell–Yan type Higgs-boson production and decay reactions which are enhanced in the MCPM ($q = c, s$).

with an improper rotation matrix $\bar{R}$. Requiring $\bar{R}^2 = \mathbb{1}_3$ leads to two types of GCPs. In K space: (i) $\bar{R} = -\mathbb{1}_3$, point reflection, (ii) $\bar{R} = R^{\mathrm{T}}\, \bar{R}_2\, R$, reflection on a plane ($R \in SO(3)$), where $\bar{R}_2 = \mathrm{diag}(1, -1, 1)$ is in K space a reflection on the 1–3 plane.

While the CP transformations of type (ii) are equivalent to the standard CP transformation, the point reflection transformation of type (i) is quite different and turns out to have very interesting properties. Motivated by this geometric picture of generalised CP transformations, the most general THDM invariant under the point reflection (i) has been studied in [8, 9, 10]. The corresponding potential has to obey the conditions $\boldsymbol{\xi} = \boldsymbol{\eta} = 0$,

$$V_{\mathrm{MCPM}} = \xi_0\, K_0 + \eta_{00}\, K_0^2 + \mathbf{K}^{\mathrm{T}}\, E\, \mathbf{K}\,. \tag{5}$$

This model is, besides the point reflection symmetry of type (i), invariant under three GCPs of type (ii). We call this model therefore maximally CP symmetric model, MCPM. Requiring also maximally CP symmetric Yukawa couplings we find that at least two fermion families are necessary in order to have non-vanishing fermion masses. That is, we find a reason for family replication in the MCPM. Furthermore, requiring absence of large flavor changing neutral currents it was shown that the Yukawa couplings are completely fixed. For instance for the lepton sector we get the Yukawa couplings

$$\mathscr{L}_{\mathrm{Yuk}} = -\sqrt{2}\frac{m_\tau}{v}\left\{\bar{\tau}_R\, \varphi_1^\dagger \begin{pmatrix}\nu_\tau \\ \tau\end{pmatrix}_L - \bar{\mu}_R\, \varphi_2^\dagger \begin{pmatrix}\nu_\mu \\ \mu\end{pmatrix}_L\right\} + h.c. \tag{6}$$

The physical Higgs-boson fields are denoted by ρ', h', h'', and $H^\pm$.

Let us briefly summarize the essential properties of the MCPM: There are 5 physical Higgs particles, three neutral ones, ρ', h', h'', and a charged Higgs-boson pair $H^\pm$. Under the standard CP transformation, ρ' and h' are even, while h'' is odd. The ρ' boson couples exclusively to the third (τ, t, b) family, ρ' behaves like the SM Higgs boson. The Higgs bosons h', h'', $H^\pm$ couple exclusively to the second (μ, c, s) family with strengths proportional to the masses of the third generation fermions. The first (e, u, d) family is uncoupled to the Higgs bosons. For further details we refer to [8].

2 Predictions for hadron colliders

Since the Yukawa couplings of the h', h'', $H^\pm$ Higgs bosons to the second fermion family are proportional to the third-fermion-family masses we have large cross sections for Drell–Yan type

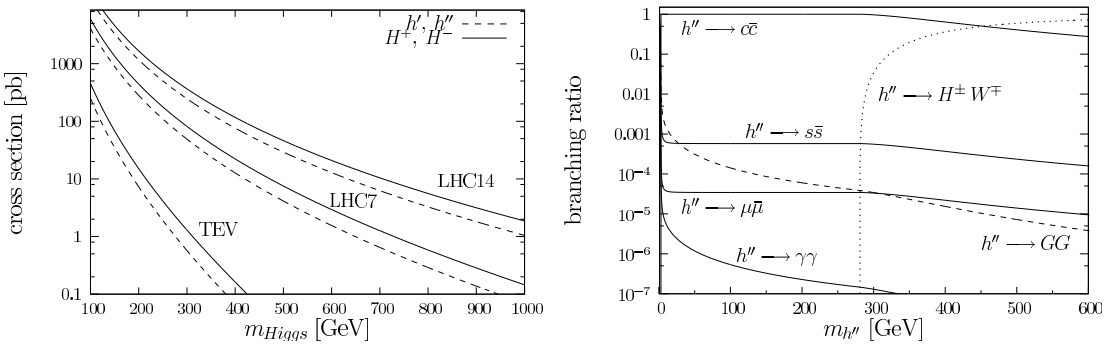

Figure 2: left: total cross section of Drell–Yan type Higgs boson production at TEVATRON and LHC. right: branching ratios of the CP odd h'' Higgs boson, where a mass of $m_{H^\pm} = 200$ GeV is assumed.

Higgs-boson production, that is, Higgs-boson production in quark–antiquark annihilation. For the same reason we have large decay rates of these Higgs bosons to the second generation fermions. In Figure 1 we show the diagrams for these production and decay reactions in pp collisions. In [9] the cross sections were computed for Drell-Yan Higgs-boson production at the TEVATRON and the LHC for center-of-mass energies of 1.96 TeV and 14 TeV, respectively. In [10] radiative effects were considered. Here we add the cross sections for a center-of-mass energy of 7 TeV at LHC, which is currently available. The corresponding total cross sections for the Drell–Yan production of the h', h'', $H^\pm$ bosons are shown in Figure 2. In this figure we also recall the branching ratios of the h'' boson decays. As an example consider Higgs-boson masses h', h'', $H^\pm$ of 200 GeV where we get very large total production cross sections, around 850 pb, for LHC7. These Higgs bosons decay mainly into light c and s quarks. However, tagging of c and s-quarks in the detectors is at least challenging. Channels involving muons should be more easily accessible experimentally. With the branching ratio of 3×10^{-5} into μ-pairs, we predict about 25 μ events from a 200 GeV h' (h'') at LHC7 for 1 fb^{-1} integrated luminosity. For further details of the calculations we refer to [8, 9, 10].

References

[1] F. Nagel, PhD thesis, Heidelberg (2004) `http://www.slac.stanford.edu/spires/find/hep/www?irn=6461018`.

[2] M. Maniatis, A. von Manteuffel, O. Nachtmann and F. Nagel, Eur. Phys. J. C **48**, 805 (2006)

[3] C. C. Nishi, Phys. Rev. D **74** 036003 (2006)

[4] M. Maniatis, A. von Manteuffel and O. Nachtmann, Eur. Phys. J. C **57** (2008) 719

[5] T. D. Lee and G. C. Wick, Phys. Rev. **148**, 1385 (1966).

[6] G. Ecker, W. Grimus and W. Konetschny, Nucl. Phys. B **191** (1981) 465,

[7] G. Ecker, W. Grimus and H. Neufeld, Nucl. Phys. B **247** (1984) 70,

[8] M. Maniatis, A. von Manteuffel and O. Nachtmann, Eur. Phys. J. C **57** (2008) 739

[9] M. Maniatis and O. Nachtmann, JHEP **05** (2009) 028

[10] M. Maniatis and O. Nachtmann, JHEP **04** (2010) 027

Performance of the ATLAS liquid argon calorimeter

Zhaoxia Meng on behalf of the ATLAS Liquid Argon Calorimeter Group

Institute of Physics, Academia Sinica, TW-Taipei 11529, Taiwan.
Also at School of Physics, Shandong University, Jinan, P.R.China.

DOI: http://dx.doi.org/10.3204/DESY-PROC-2010-01/meng

The liquid argon calorimeter (LAr) [1] of the ATLAS detector [2] measures energy deposited by particles produced in p-p collisions at the CERN Large Hadron Collider (LHC). Figure 1 illustrates the LAr system. It consists of the electromagnetic calorimeter (EM), the hadronic end-cap (HEC) and the forward calorimeter (FCAL). The material utilized for collecting signal is liquid argon. The absorber consists of lead in the EM, copper in the HEC and the first layer of the FCAL and tungsten alloy in the outer two layers of the FCAL. Copper electrodes, electronic boards and various support structures constitute additional material in the calorimeter.

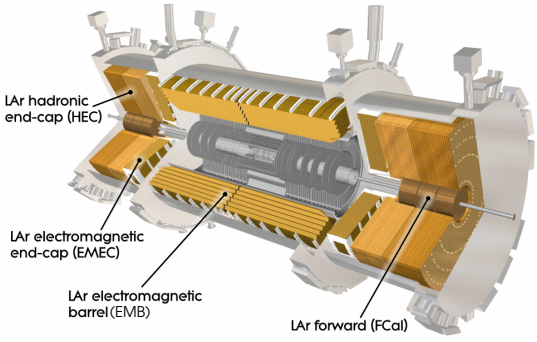

Figure 1: Schematic view of the liquid argon calorimeter system.

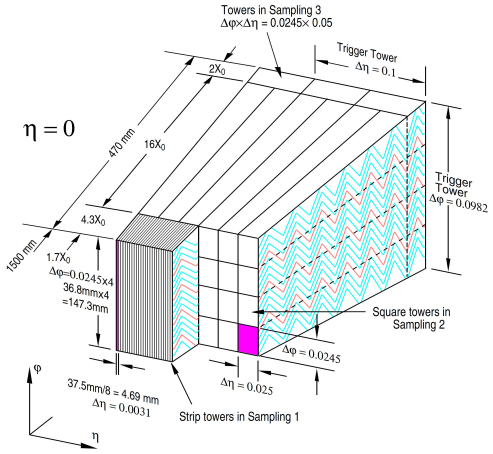

Figure 2: Readout granularity of the EM calorimeter.

The LAr is a sampling calorimeter with fine granularity, especially in the first EM layer, large coverage in $|\eta|$, up to $|\eta| = 4.9$, and full coverage in ϕ. Figure 2 illustrates the granularity of the EM calorimeter [3]. The design energy resolutions for each LAr sub-detector are listed in Table 1.

Ionization electrons are produced by passage of charged particles. They drift to electrodes and produce electrical currents proportional to the energy deposited. The currents have triangular shapes that are amplified, shaped and then sampled $N_{samples}$ (default is 5) times every 25 ns. Each sample is then digitized. The triangular signal has a $\sim$1 ns rise time and several

hundreds ns decay time (T_{drift}). The drift time in the barrel region of the calorimeter has a constant value ∼460 ns. Smaller values in the end-caps reflect gap width decreasing with $|\eta|$ [4].

The ionization signal shape can be predicted by modeling of the electronic readout chain. The ionization signal shape is predicted by describing the signal propagation and the response of the electronic readout, that are determined or tuned by the calibration system [4]. A calibration pulse of precisely known amplitude is injected into each cell through the same path as seen through the ionization pulse so probing the electrical and readout properties of each cell. Figure 3 illustrates the agreement of the measured signal shape and the predicted one. The difference is less than 4% [5].

	Resolution
EM Barrel	$\frac{\sigma_E}{E} = \frac{10\%}{\sqrt{E}} \bigoplus 0.7\%$
EM End-Cap	$\frac{\sigma_E}{E} = \frac{10\%}{\sqrt{E}} \bigoplus 0.7\%$
HEC	$\frac{\sigma_E}{E} = \frac{50\%}{\sqrt{E}} \bigoplus 3\%$
FCAL	$\frac{\sigma_E}{E} = \frac{100\%}{\sqrt{E}} \bigoplus 10\%$

Table 1: Design energy resolutions of the LAr calorimeters.

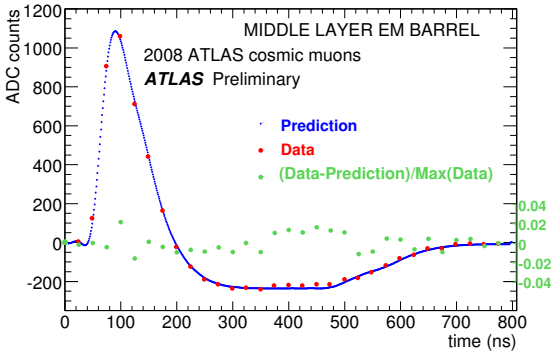

Figure 3: Typical ionization pulse shape in the EM barrel.

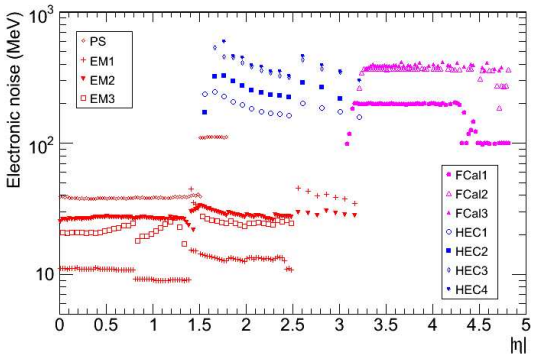

Figure 4: Electronic noise at cell level as a function of $|\eta|$ for each longitudinal layer of the calorimeter.

The individual cell energy is reconstructed from the digitized signal according to the formula:

$$E_{cell} = F_{\mu A \to MeV} \times F_{DAC \to \mu A} \times \left(\frac{M_{phys}}{M_{cali}}\right)^{-1} \times G \times A\,, \qquad (1)$$

where A is the amplitude in ADC counts, G represents the gain, $\frac{M_{phys}}{M_{cali}}$ is a correction for the difference of the maxima between the injected and the ionization pulses, $F_{DAC \to \mu A}$ converts current in DAC units to μA and $F_{\mu A \to MeV}$ converts current to energy.

Pedestal, gains and noise are parameters used in the energy reconstruction. Their determination is very important since they affect signal to background ratio and energy resolution.

Pedestal is obtained from runs taken without any beam or calibration pulse injection. Average pedestal is computed for each cell in every run. Gains are obtained from calibration runs. In these runs, a set of fixed current DAC is injected into each cell N times, in which M≤N events are triggered, sampled and digitized. Average response of the M events for each sample is calculated and used to reconstruct the maximum amplitude of the pulse. Gains are obtained by fitting the maximum amplitude as a function of DAC. Stability of the pedestal and gain

studied during 6 months in 2009 shows good results. The largest variation of pedestal is 10 MeV from the medium gain in the FCAL. The relative variation of the gain is within 0.3% [5].

Electronic noise (σ_{noise}) as a function of η obtained from randomly triggered events is shown in Figure 4. The noise ranges from 10 to 50 MeV in the EM calorimeter, and from 100 to 500 MeV in the HEC and the FCAL where the size of cells is much larger than that in the EM calorimeter.

The readout clock of each LAr cell must be synchronized to the LHC bunch crossing in order to reconstruct correct energy for every event. Alignment of timing-in for all the LAr cells within 1 ns is required. Measurements of the timing alignment performed in different data taking periods show that the LAr cells are in time as required.

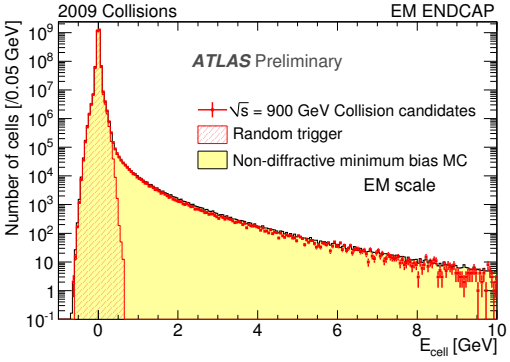

Figure 5: Cell energy distribution for collision events in the EM end-cap calorimeter.

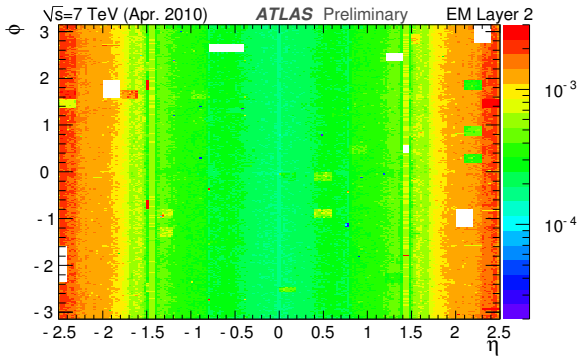

Figure 6: Cell occupancy map in the EM calorimeter with 7 TeV collision data.

Since the delivery of collision data started in 2009, various performance studies have been done. Figure 5 illustrates the cell energy distributions in the EM end-caps. Random trigger events record mainly cell noise. Good agreement between the data and simulated signal due to collision events is observed. Figure 6 illustrates the occupancy map for the second layer of the EM calorimeter. Cell energy larger than 5 σ_{noise} is plotted. White rectangles correspond to the ∼1.3% dead readout channels [5].

In addition to the studies of LAr performance discussed above, the temperature uniformity and contamination of the liquid argon were also checked. The measured values are all consistent with design. No extra contribution has been found to global resolution constant term [5].

References

[1] ATLAS liquid argon calorimeter: Technical design report, The ATLAS Collaboration, CERN-LHCC-96-41 (1996) [http://cdsweb.cern.ch/record/331061?ln=pt]

[2] G Aad et al, "The ATLAS Experiment at the CERN Large Hadron Collider, The ATLAS Collaboration" JINST 3 (2008) S08003 [http://cdsweb.cern.ch/record/1125884]

[3] Calorimeter Performance Technical Design Report, The ATLAS Collaboration [http://atlas.web.cern.ch/Atlas/TDR/caloperf/caloperf.html]

[4] G.Aad et al., Drift Time Measurement in the ATLAS Liquid Argon Electromagnetic Calorimeter using Cosmic Muons, The ATLAS Collaboration, Accepted by EPJC [http://arxiv.org/abs/1002.4189]

[5] G.Aad et al., Readiness of the ATLAS Liquid Argon Calorimeter for LHC Collisions, The ATLAS Collaboration, Accepted by EPJC [http://arxiv.org/abs/0912.2642]

Neutral MSSM Higgs and Z boson associated production at the LHC

Caesar P. Palisoc[1], *Bernd A. Kniehl*[2]

[1]National Institute of Physics, University of the Philippines, Diliman, Queson City 1101, Philippines
[2]II. Institut für Theoretische Physik, Universität Hamburg, Luruper Chaussee 149, 22761 Hamburg, Germany

DOI: http://dx.doi.org/10.3204/DESY-PROC-2010-01/palisoc

We study the associated hadroproduction of a neutral Higgs and a Z Boson within the minimal supersymmetric standard model (MSSM). We calculate the partonic cross sections for producing CP-odd neutral Higgs boson plus Z boson analytically to lowest order. To LO, the contributing partonic cross sections include tree-level quark-antiquark ($q\overline{q}$) annihilation and one-loop gluon-gluon (gg) fusion, which proceeds via quark and squark loops. The cross sections are expressed in terms of helicity amplitudes. We present cross sections as functions of the Higgs mass and $\tan\beta$ assuming LHC experimental conditions.

We focus on the hadronic production of a neutral CP-odd MSSM Higgs boson in association with a Z boson. We describe and list the lowest order contribution to the hadronic production cross section and explore the phenomenological consequence under experimental conditions of the LHC.

We present the LO cross sections of the partonic subprocesses $q\overline{q} \to ZA^0$ and $gg \to ZA^0$ in the MSSM. We work in the parton model of QCD with $n_f = 5$ active quark flavors $q = u, d, s, c, b$, which we take to be massless. However, we retain the b-quark Yukawa couplings at their finite values, in order not to suppress possibly sizeable contributions. The various couplings v_{Zqq}, a_{Zqq}, $g_{\phi qq}$, $g_{h^0A^0Z}$, $g_{H^0A^0Z}$, g_{h^0ZZ}, and g_{H^0ZZ} are readily available in the literature.

Considering the generic partonic subprocess $ab \to ZA^0$, we denote the four-momenta of the incoming partons, a and b, and the outgoing Z and A^0 bosons by p_a, p_b, p_Z, and p_{A^0}, respectively, and define the partonic Mandelstam variables as $s = (p_a + p_b)^2$, $t = (p_a - p_Z)^2$, and $u = (p_b - p_Z)^2$. The on-shell conditions read $p_a^2 = p_b^2 = 0$, $p_Z^2 = m_Z^2 = z$, and $p_{A^0}^2 = m_{A^0}^2 = h$. Four-momentum coservation implies that $s + t + u = z + h$. Furthermore, we have $sp_T^2 = tu - zh = N$, where p_T is the absolute value of transverse momentum common to the Z and A^0 bosons in the center-of-mass (c.m.) frame.

The differential cross section for the tree-level $b\overline{b}$ annihilation may be generically written as

$$\begin{aligned}\frac{d\sigma}{dt}\left(b\bar{b} \to ZA^0\right) &= \frac{G_F^2 c_w^4 z}{3\pi s}\left[\lambda|S|^2 - 4sp_T^2\left(\frac{1}{t}+\frac{1}{u}\right)g_{A^0bb}a_{Zbb}\Re S\right.\\ &\left. + g_{A^0bb}^2\left(v_{Zbb}^2 T_+ + a_{Zbb}^2 T_-\right)\right], \qquad (1)\end{aligned}$$

where G_F is the Fermi constant, $\lambda = s^2+z^2+h^2-2(sz+zh+hs)$, and $S = g_{h^0A^0Z}g_{h^0bb}\mathcal{P}_{h^0}(s)+$

$g_{H^0A^0Z}g_{H^0bb}\mathcal{P}_{H^0}(s)$, $T_\pm = 2 \pm 2 + 2p_T^2\left[z\left(\frac{1}{t}\pm\frac{1}{u}\right)\mp\frac{2s}{tu}\right]$. Here, $\mathcal{P}_X(s) = \frac{1}{s-m_X^2+im_X\Gamma_X}$ is the propagator function of particle X, with mass m_X and total decay width Γ_X.

We express the quark and squark one-loop contributions to the gg fusion in terms of helicity amplitudes. We label the helicity states of the two gluons and the Z boson in the partonic c.m. frame by $\lambda_a = -1/2, 1/2, \lambda_b = -1/2, 1/2$, and $\lambda_Z = -1, 0, 1$. The helicity amplitudes of the quark and squark triangle contributions read

$$\begin{aligned}
\mathcal{M}^{\triangle}_{\lambda_a\lambda_b 0} &= 8i\sqrt{\frac{\lambda}{z}}(1+\lambda_a/\lambda_b)\sum_q m_q\left(g_{h^0A^0Z}g_{h^0qq}\mathcal{P}_{h^0}(s)+g_{H^0A^0Z}g_{H^0qq}\mathcal{P}_{H^0}(s)\right)F_\triangle\left(s,m_q^2\right),\\
\tilde{\mathcal{M}}^{\triangle}_{\lambda_a\lambda_b 0} &= -2i\sqrt{\frac{\lambda}{z}}(1+\lambda_a/\lambda_b)\sum_{\tilde{q}_i}\left(g_{h^0A^0Z}g_{h^0\tilde{q}_i\tilde{q}_i}\mathcal{P}_{h^0}(s)+g_{H^0A^0Z}g_{H^0\tilde{q}_i\tilde{q}_i}\mathcal{P}_{H^0}(s)\right)\tilde{F}_\triangle\left(s,m_{\tilde{q}_i}^2\right).
\end{aligned}$$

where $F_\triangle(s,m_q^2) = 2+(4m_q^2-s)C^{00}_{qqq}(s)$, and $\tilde{F}_\triangle(s,m_{\tilde{q}_i}^2) = 2+4m_{\tilde{q}_i}^2C^{00}_{\tilde{q}_i\tilde{q}_i\tilde{q}_i}(s)$ are the quark and squark triangle form factors, respectively, and $C^{00}_{qqq}(s) = C_0(0,0,m_q^2,m_q^2,m_q^2)$ is the scalar three-point function. As for the quark box contribution, all twelve helicity combinations contribute. Due to Bose symmetry, they are related by $\mathcal{M}^{\square}_{\lambda_a\lambda_b\lambda_Z}(t,u) = (-1)^{\lambda_Z}\mathcal{M}^{\square}_{\lambda_b\lambda_a\lambda_Z}(u,t)$, $\mathcal{M}^{\square}_{\lambda_a\lambda_b\lambda_Z}(t,u) = \mathcal{M}^{\square}_{-\lambda_a-\lambda_b-\lambda_Z}(t,u)$. Keeping $\lambda_Z = \pm1$ generic, we thus only need to specify four expressions. These read

$$\begin{aligned}
\mathcal{M}^{\square}_{++0} &= -\frac{8i}{\sqrt{z\lambda}}\sum_q g_{A^0qq}a_{Zqq}m_q\left[F^0_{++}+(t\leftrightarrow u)\right],\\
\mathcal{M}^{\square}_{+-0} &= -\frac{8i}{\sqrt{z\lambda}}\sum_q g_{A^0qq}a_{Zqq}m_q\left[F^0_{+-}+(t\leftrightarrow u)\right],\\
\mathcal{M}^{\square}_{++\lambda_Z} &= -4i\sqrt{\frac{2N}{s}}\sum_q g_{A^0qq}a_{Zqq}m_q\left[F^1_{++}-(t\leftrightarrow u)\right],\\
\mathcal{M}^{\square}_{+-\lambda_Z} &= -4i\sqrt{\frac{2N}{s}}\sum_q g_{A^0qq}a_{Zqq}m_q\left[F^1_{+-}-(t\leftrightarrow u,\lambda_Z\to-\lambda_Z)\right].
\end{aligned}\tag{2}$$

The quark box form factors, $F^{|\lambda_Z|}_{\lambda_a\lambda_b}$, are functions of s,t,u, and depend on the scalar three- and four-point function. They are quite lengthy to be included here. We recall that $\tilde{\mathcal{M}}_{\lambda_a\lambda_b\lambda_Z} = 0$.

The differential cross section of $gg\to ZA^0$ is then given by

$$\frac{d\sigma}{dt}(gg\to ZA^0) = \frac{\alpha_s^2(\mu_r)G_F^2m_W^4}{256(4\pi)^3s^2}\sum_{\lambda_a,\lambda_b,\lambda_Z}\left|\mathcal{M}^{\triangle}_{\lambda_a\lambda_b\lambda_Z}+\mathcal{M}^{\square}_{\lambda_a\lambda_b\lambda_Z}+\tilde{\mathcal{M}}^{\triangle}_{\lambda_a\lambda_b\lambda_Z}\right|^2,\tag{3}$$

where $\alpha_s(\mu_r)$ is the strong-coupling constant at renormalization scale μ_r. Due to Bose symmetry, the right-hand side of Eq. (3) is symmetric in t and u.

We are now in a position to explore the phenomenological implications of our results. The SM input parameters for our numerical analysis are taken to be $G_F = 1.16637\times10^{-5}$ GeV^{-2}, $m_W = 80.398$ GeV, $m_Z = 91.1876$ GeV, $m_t = 171.3$ GeV , and $\overline{m}_b(\overline{m}_b) = 4.20$ GeV [1]. We adopt the LO proton PDF set CTEQ6L1 [2]. We evaluate $\alpha_s(\mu_r)$ and $m_b(\mu_r)$ from the LO formulas, which may be found, *e.g.*, in Eqs. (23) and (24) of Ref. [3], respectively, with $n_f = 5$ quark flavors and asymptotic scale parameter $\Lambda^{(5)}_{QCD} = 165$ MeV [2]. We identify the

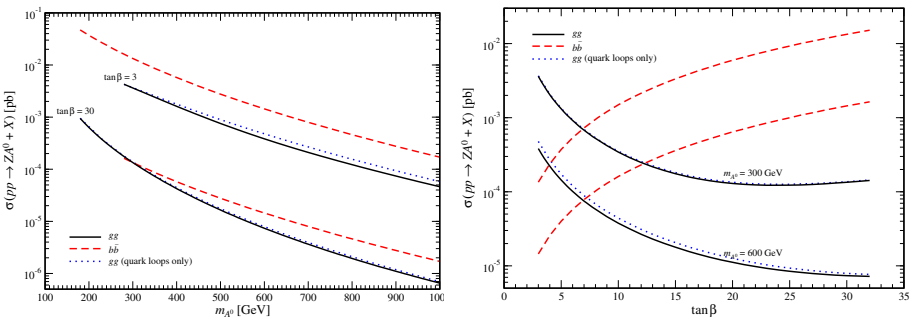

Figure 1: Total cross sections σ (in fb) of the $p\overline{p} \to ZA^0 + X$ via $b\overline{b}$ annihilation (dashed lines) and gg fusion (solid lines) at the LHC as functions of m_{A^0} for $\tan\beta = 3$ and 30, and as functions of $\tan\beta$ for $m_{A^0} = 300$ GeV and 600 GeV. The dotted lines correspond to gg fusion originating from quark loops only.

renormalization and factorization scales with the $Z\phi$ invariant mass $\sqrt{s}$. We vary $\tan\beta$ and m_{A^0} in the ranges $3 < \tan\beta < 32 \approx m_t/m_b$ and 180 GeV $< m_{A^0} <$ 1 TeV, respectively. As for the GUT parameters, we choose $m_{1/2} = 150$ GeV, $A = 0$, and $\mu < 0$, and tune m_0 so as to be consistent with the desired value of m_{A^0}. All other MSSM parameters are then determined according to the SUGRA-inspired scenario as implemented in the program package SUSPECT [4]. We do not impose the unification of the τ-lepton and b-quark Yukawa couplings at the GUT scale, which would just constrain the allowed $\tan\beta$ range without any visible effect on the results for these values of $\tan\beta$. We exclude solutions which do not comply with the present experimental lower mass bounds of the sfermions, charginos, neutralinos, and Higgs bosons [1].

Figure 1 shows the fully integrated cross sections of $pp \to ZA^0 + X$ at the LHC as functions of m_{A^0} for $\tan\beta = 3$ and 30, and as functions of $\tan\beta$ for $m_{A^0} = 300$ GeV and 600 GeV, with c.m. energy $\sqrt{S} = 14$ TeV. We note that the SUGRA-inspired MSSM with our choice of input parameters does not permit $\tan\beta$ and m_{A^0} to be simultaneously small, due to the experimental lower bound on the selectron mass [1]. This explains why the curves for $\tan\beta = 3$ only start at $m_{A^0} \approx 280$ GeV, while those for $\tan\beta = 30$ already start at $m_{A^0} \approx 180$ GeV. The $b\overline{b}$-annihilation contribution (dashed lines), which originates from the Yukawa-enhanced amplitudes, and the total gg-fusion contributions (solid lines), corresponding to the coherent superposition of quark and squark loop amplitudes, are given separately. It shows that the $b\overline{b}$-annihilation dominates at large to moderate values of $\tan\beta$. On the other hand, the gg-fusion dominates at small values of $\tan\beta$. We note further that the squark loop contribution, although minimal, tend to decrease the total gg-fusion contribution.

References

[1] Particle Data Group, C. Amsler *et al.*, Phys. Lett. B **667**, 1 (2008).

[2] J. Pumplin, D. R. Stump, J. Huston, H.-L. Lai, P. Nadolsky, and W.-K. Tung, JHEP **0207**, 012 (2002) [arXiv:hep-ph/0201195].

[3] B. A. Kniehl, Z. Phys. C **72**, 437 (1996) [arXiv:hep-ph/9403386].

[4] A. Djouadi, J. L. Kneur, and G. Moultaka, Comput. Phys. Commun. **176**, 426 (2007) [arXiv:hep-ph/0211331].

Performance of the ATLAS inner detector trigger algorithms in p-p collisions at $\sqrt{s} = 900$ GeV and $\sqrt{s} = 7$ TeV

Andrea Ferretto Parodi for the ATLAS Collaboration

DESY, Notkestraße 85, 22607 Hamburg, Germany

DOI: http://dx.doi.org/10.3204/DESY-PROC-2010-01/ferrettoparodi

The ATLAS inner detector trigger algorithms have been running online during data taking with proton-proton collisions at the Large Hadron Collider (LHC) in December 2009 and spring 2010 at the centre-of-mass energies of 900 GeV and 7 TeV.

The inner detector [1] is the ATLAS subdetector closest to the interaction point and provides precise tracking and momentum measurement of particles created in the collisions. It is composed of the pixel detector (silicon pixels), the semiconductor tracker (SCT, silicon stereo strips) and the transition radiation tracker (TRT, straw drift tubes). The whole detector is immersed in a 2 T solenoid magnetic field.

The ATLAS trigger [1], designed to reject uninteresting collision events in real time, performs the online event selection in three stages, called Level-1 (L1), Level-2 (L2) and event filter (EF). L1 is hardware based and has access to summary event informations from the calorimeters and the muon spectrometer, and defines one or more regions of interest (RoIs), geometrical regions of the detector, identified by η and ϕ coordinates, containing interesting physics objects. L2 and the EF (globally called high level trigger, HLT) are software based and can access information from all subdetectors, including the inner detector. RoI based reconstruction reduces the data access (to $\sim 2\%$ of the entire event) and also the processing time by performing the reconstruction only in the region relevant for the trigger decision. Globally, the ATLAS trigger reduces the acquisition rate to about 200 Hz, down from a proton-proton bunch crossing rate of 40 MHz.

HLT tracking algorithms run on a farm of commercial CPUs, and their basic task is to reconstruct trajectories of charged particles, used for the definition of many trigger items (high p_T leptons, tracks coming from τ decays, jets or B-hadrons decays) and for the determination of the online beam spot (more details in the following). L2 is based on fast custom algorithms, while the EF is based on offline tools, adapted to take into account trigger requirements.

Performance of the HLT algorithms in terms of tracking efficiency is measured w.r.t. offline reconstructed tracks, requiring a one-to-one geometrical best matching ($\Delta R = \sqrt{\Delta\eta^2 + \Delta\phi^2}$) of a reconstructed online track with an offline one. For this kind of study, only reconstructed tracks passing a set of selection criteria are considered: at least 1 pixel hit and 6 SCT clusters, $|\eta| < 2.5$, $|z_0| < 200$ mm, $|d_0| < 1.5$ mm (both impact parameters z_0 and d_0 are calculated w.r.t. the reconstructed offline primary vertex).

The data used in the following for these performance studies are taken from LHC stable beam collisions with inner detector components and magnetic solenoid fully operational. In addition,

comparisons between data and non-diffractive minimum bias Monte Carlo (MC) simulated events are presented.

The RoI selection mode previously described is designed to work with higher energy physics objects, while data taken at $\sqrt{s} = 900$ GeV contain mostly soft events. At this stage, there was not enough statistics of collected tracks from an RoI-based trigger. Therefore, during 900 GeV collisions the HLT algorithms worked in *full scan* mode, retrieving data from the whole inner detector. This mode of operation is adopted for the beam spot determination and for online selection of B-physics decay channels.

Comparisons between the number of Si hits w.r.t. MC/offline and efficiency vs p_T for 900 GeV collisions data are shown in Fig. 1–4 for both L2 and EF algorithms.

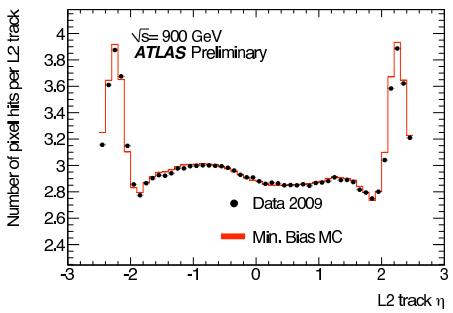

Figure 1: Average number of pixel hits per L2 track (data and MC).

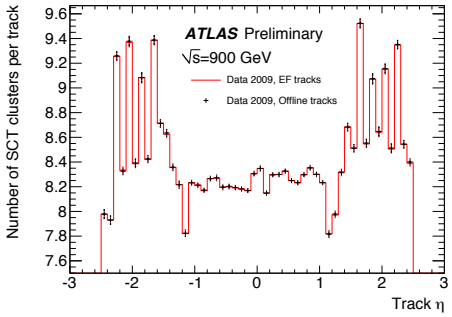

Figure 2: Average number of SCT hits per EF track (data and offline).

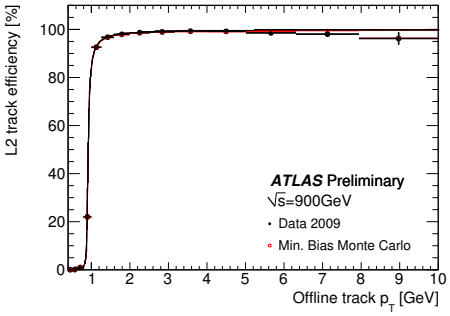

Figure 3: L2 tracking efficiency vs p_T w.r.t. offline (data and MC).

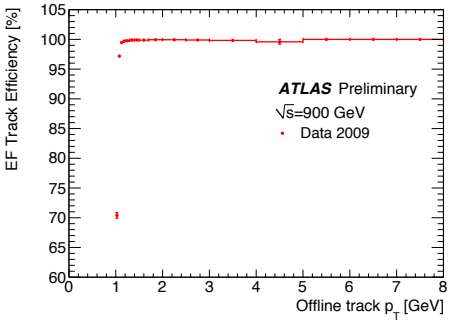

Figure 4: EF tracking efficiency vs p_T w.r.t. offline (data).

Figure 1 and Fig. 2 show an excellent agreement between data and MC/offline; complementary plots of L2 SCT hits and EF pixel hits are not presented, but show agreement at the same level. Figure 3 and Fig. 4 prove very good tracking efficiency w.r.t. offline. Figure 3 shows also excellent agreement between data and MC performance. More detailed results about 900 GeV tracking performance can be found in [2].

For the previously discussed reasons, collision data taken at $\sqrt{s} = 7$ TeV, with increased luminosity, represent the first opportunity to test the performance of RoI-based selections with real data.

In the following, the tracking efficiencies for muon and jet selections are presented. The track reconstruction for muons and jets starts from different RoIs ($\Delta\eta$, $\Delta\phi = 0.2$ and $\Delta\eta$,

$\Delta\phi = 0.4$, respectively). For muons, the reconstructed tracks are then matched to the muon spectrometer, while for jets a precise estimate of the track parameters at the perigee is crucial to identify tracks coming from secondary vertices for jet flavour tagging purposes.

Figures 5–6 show the muon and jet tracking efficiencies vs p_T during collision data taking at $\sqrt{s} = 7$ TeV. In both selections the HLT tracking algorithms show a very good reconstruction efficiency.

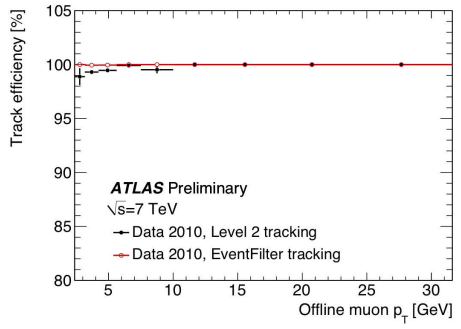

Figure 5: L2 and EF muon tracking efficiency vs p_T w.r.t. offline.

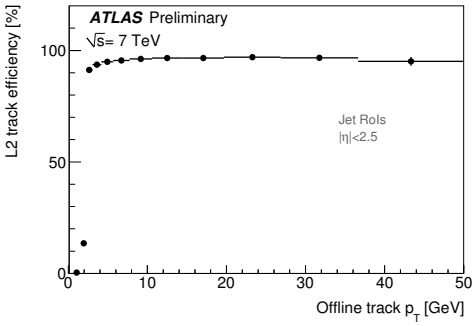

Figure 6: L2 jet tracking efficiency vs p_T w.r.t. offline.

As already mentioned, L2 tracking is used in the online determination of the beam spot, i.e. the transverse position of the LHC luminous region, crucial for all the selections which require a precise estimate of the interaction point (jet flavour tagging, monitoring of beam profile). L2 algorithms allow for an estimation of the beam spot mean position using the transverse distribution of online reconstructed primary vertices. Online primary vertices are obtained by fitting together all the L2 tracks reconstructed in full scan mode.

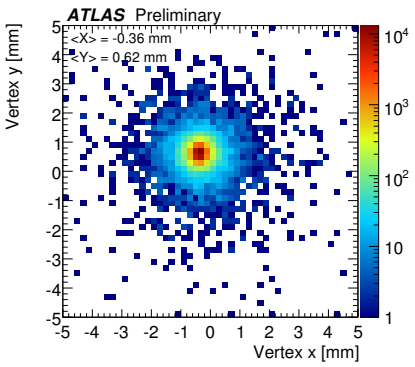

Figure 7: xy-distribution of the online L2 vertices.

Figure 7 shows the xy-distribution of online primary vertices during collision data taking at $\sqrt{s} = 7$ TeV: beam spot mean position and width are extracted by a gaussian fit of this distribution. Excellent agreement has been observed w.r.t. offline beam spot measurements.

ATLAS HLT algorithms have been successfully run online at the LHC since December 2009, at a centre-of-mass energy of 900 GeV and 7 TeV: it was shown that performance studies w.r.t offline tracks and MC simulations are in excellent agreement. Moreover, the performance of reconstructing tracks in the trigger system has been studied over time and changing beam conditions, producing very encouraging results. Furthermore, L2 tracks have been used to determine online the position of the LHC luminous region.

References

[1] ATLAS Collaboration, "The ATLAS Experiment at the CERN Large Hadron Collider," JINST 3 (2008) S08003.

[2] ATLAS Collaboration, "Performance of the ATLAS Inner Detector Trigger algorithms in p-p collisions at $\sqrt{s} = 900$ GeV," ATLAS-CONF-2010-014 (2010).

MSSM Higgs Boson Production via Gluon Fusion

Margarete Mühlleitner[1], *Heidi Rzehak*[1]*, *Michael Spira*[2]

[1]KIT, ITP, Wolfgang-Gaede-Str. 1, 76128 Karlsruhe, Germany
[2]Paul Scherrer Institut, 5232 Villigen PSI, Switzerland

DOI: http://dx.doi.org/10.3204/DESY-PROC-2010-01/rzehak

One major task at the LHC is the search for Higgs bosons. In the Minimal Supersymmetric Standard Model (MSSM), the cross section of the production process of Higgs bosons via gluon fusion, $gg \to h, H$, yields the largest values for a wide range of the MSSM parameters. This process is loop-induced where, in the MSSM, the coupling of the Higgs boson to the gluons is not only mediated by top and bottom quark loops as in the Standard Model (SM) but also by the corresponding squark loops (see Fig. 1). For large $\tan\beta$, which denotes the ratio of the two vacuum expectation values of the two complex Higgs doublets introduced in the MSSM, the coupling of bottom quarks to the Higgs bosons is enhanced. Therefore, for large $\tan\beta$, also bottom quark as well as bottom squark loops contribute sizeably to the gluon fusion cross section.

Pure QCD and Supersymmetric QCD Contributions

The pure QCD corrections to quark and squark loops (see Fig. 1 (b)) have been calculated at next-to-leading order taking into account the full mass dependence [1]. An increase of the cross section by up to 100% has been found. Theses corrections can be approximated by the limit of very heavy top quark and squarks with an accuracy of 20% – 30% for small $\tan\beta$ [2] (for large $\tan\beta$ also bottom quark and squark loops have to be taken into account). In the heavy top quark mass limit — without squark effects — the next-to-next-to-leading order (NNLO) QCD corrections have been calculated which resulted in an increase of 20% – 30% of the cross section [3]. At NNLO finite top quark mass effects (no squarks) have been discussed and found to be below the scale uncertainty [4]. Estimates of the next-to-next-to-next-to-leading order (N^3LO) corrections indicate an improved convergence [5].

The supersymmetric (SUSY) as well as the pure QCD contributions, taking into account gluino as well as gluon contributions (see Fig. 1 (c) as well as (b)), have been calculated in the heavy top quark, top squark and gluino limit [6]. The size of the next term in the mass expansion indicates that this is a good approximation for the lightest MSSM Higgs boson for small and moderate $\tan\beta$ values. Most recently, also the pure and the SUSY QCD contributions to the bottom quark and squark loops have been calculated based on an asymptotic expansion in the squark and gluino masses which are assumed to be much heavier than the bottom quark and the Higgs boson [7].

The pure and the SUSY QCD corrections have been calculated including the mass dependence of all particles and also the bottom quark and squark contributions [8]. This calculation

*Speaker

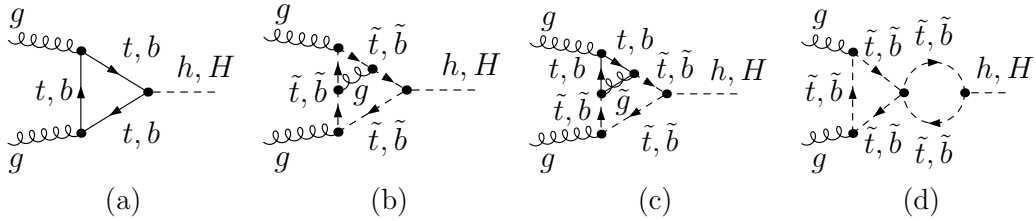

Figure 1: Sample diagrams which contribute to the gluon fusion process at (a) leading order and (b), (c), (d) next to leading order.

has shown that the heavy mass limit is a good approximation for small and moderate $\tan\beta$. Also, it was pointed out that the contributions from the squark quartic couplings (see Fig. 1 (d)) as well as from the gluinos can be sizeable.

This leads us to a conceptional problem: On the one hand if the supersymmetric relations between the parameters are kept intact the gluinos do not decouple. To be more precise, for heavy gluinos, the results of the form factors depend logarithmically on the gluino mass $M_{\tilde{g}}$. On the other hand the decoupling theorem says that heavy fields decouple at low momenta (except for renormalization effects) [9].

Decoupling of the Gluinos

Assuming vanishing squark mixing, for scales *above* the gluino mass, the coupling of the light CP-even Higgs boson to quarks λ_Q and the coupling of the same Higgs boson to squarks $\lambda_{\tilde{Q}}$ can be expressed as

$$\lambda_Q = g\,\frac{m_Q}{v} \quad \text{and} \quad \lambda_{\tilde{Q}} = 2\,g\,\frac{m_Q^2}{v} \tag{1}$$

where $v = (v_1^2 + v_2^2)^{\frac{1}{2}} \approx 246$ GeV and v_i is the i$^{\text{th}}$ Higgs vacuum expectation value. m_Q denotes the top quark mass and g is a normalization factor of the Higgs coupling to a quark pair with respect to the SM. Obviously, the symmetry relation between λ_Q and $\lambda_{\tilde{Q}}$ in Eq. 1 is intact. For the evaluation of λ_Q and $\lambda_{\tilde{Q}}$ at a different scale the corresponding renormalization group equations (RGE) can be used. In the assumed case of scales *above* the gluino mass, the RGE for $2\,\frac{v}{g}\,\lambda_Q^2$ and for $\lambda_{\tilde{Q}}$ are the same.

For scales *below* the gluino mass, the gluino decouples from the RGE and the RGE for $2\,\frac{v}{g}\,\lambda_Q^2$ and for $\lambda_{\tilde{Q}}$ differ. The symmetry relation between λ_Q and $\lambda_{\tilde{Q}}$ is broken.

At the scale of the gluino mass the proper matching yields a finite threshold contribution for the evolution from the gluino mass scale to smaller scales. The logarithmic behaviour of the matching relation is given by the solution of the RGE for smaller scales.

If the decoupling of the gluino is taken into account in the RGE the gluino also decouples from the theory as it should according to the decoupling theorem (for more details, see [10]).

Genuine SUSY QCD Contributions

In Fig. 2, first results of the calculation of the genuine SUSY QCD contributions to the bottom quark and squark amplitudes are shown in terms of the form factor C^b_{SUSY} normalized to

the bottom quark form factor A_b^{Higgs}:

$$A_b^{\text{Higgs}}(1 + C^b_{\text{SUSY}}\frac{\alpha_s}{\pi}) \,. \qquad (2)$$

The parameters are chosen as follows: The sfermion mass parameter $M_{\text{SUSY}} = 800$ GeV, the gluino mass $M_{\tilde{g}} = 1.0$ TeV, the gaugino mass parameter $M_2 = 500$ GeV, the Higgs superfield mixing parameter $\mu = 2.0$ TeV, $\tan\beta = 30$ and the trilinear coupling chosen in the $\overline{\text{MS}}$ scheme as $A_b = -1.133$ TeV. The SUSY QCD contributions with the full mass dependence (solid lines) are sizeable and can be roughly approximated using a correct bottom Yukawa coupling. This approximation is referred to as Δ_b approximation (dashed lines). It is important to choose the renormalization carefully. Using the trilinear coupling A_b in the $\overline{\text{MS}}$ scheme is one reasonable choice (for further details, see [11]).

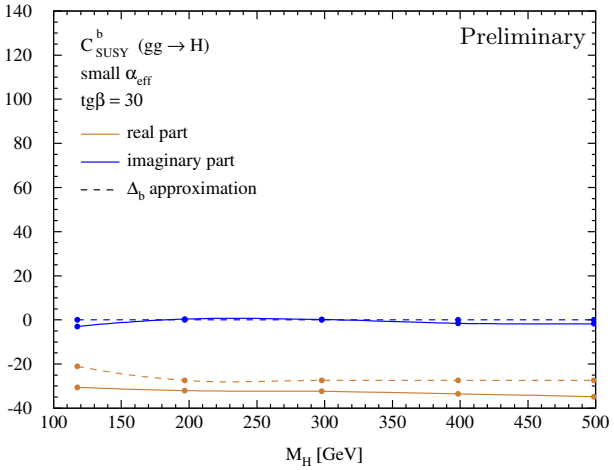

Figure 2: The genuine SUSY QCD contributions in terms of the form factor C^b_{SUSY} normalized to the bottom quark form factor: Real part in orange (light gray), imaginary part in blue (dark gray). The result with the full mass dependence (solid) is compared to the one in the Δ_b approximation (dashed).

References

[1] D. Graudenz, M. Spira, P.M. Zerwas, Phys. Rev. Lett. **70** (1993) 1372; M. Spira, A. Djouadi, D. Graudenz, P.M. Zerwas, Phys. Lett. **B318** (1993) 347; Nucl. Phys. **B453** (1995) 17; C. Anastasiou, S. Beerli, A. Daleo, Z. Kunszt, JHEP **0701** (2007) 082; U. Aglietti, R. Bonciani, G. Degrassi, A. Vicini, JHEP **0701** (2007) 021; R. Bonciani, G. Degrassi, A. Vicini, JHEP **0711** (2007) 095; M. Mühlleitner, M. Spira, Nucl. Phys. **B790** (2008) 1.

[2] A. Djouadi, M. Spira, P.M. Zerwas, Phys. Lett. **B264** (1991) 440; S. Dawson, Nucl. Phys. **B359** (1991) 283; R.P. Kauffman, W. Schaffer, Phys. Rev. **D49** (1994) 551; S. Dawson, R. Kauffman, Phys. Rev. **D49** (1994) 2298; S. Dawson, A. Djouadi, M. Spira, Phys. Rev. Lett. **77** (1996) 16; M. Krämer, E. Laenen, M. Spira, Nucl. Phys. **B511** (1998) 523.

[3] R.V. Harlander, W.B. Kilgore, Phys. Rev. Lett. **88** (2002) 201801; JHEP **0210** (2002) 017; C. Anastasiou, K. Melnikov, Nucl. Phys. **B646** (2002) 220; Phys. Rev. **D67** (2003) 037501; V. Ravindran, J. Smith, W.L. van Neerven, Nucl. Phys. **B665** (2003) 325.

[4] R.V. Harlander, K.J. Ozeren, Phys. Lett. **B679** (2009) 467; JHEP **0911** (2009) 088; A. Pak, M. Rogal, M. Steinhauser, Phys. Lett. **B679** (2009) 473; JHEP **1002** (2010) 025; R. V. Harlander, H. Mantler, S. Marzani, K. J. Ozeren, Eur. Phys. J. C **66** (2010) 359.

[5] S. Catani, D. de Florian, M. Grazzini, P. Nason, JHEP **0307** (2003) 028; S. Moch, A. Vogt, Phys. Lett. **B631** (2005) 48; V. Ravindran, Nucl. Phys. **B746** (2006) 58; Nucl. Phys. **B752** (2006) 173.

[6] R.V. Harlander, M. Steinhauser, Phys. Lett. **B574** (2003) 258, Phys. Rev. **D68** (2003) 111701; JHEP **0409** (2004) 066; R.V. Harlander, F. Hofmann, JHEP **0603** (2006) 050; G. Degrassi, P. Slavich, Nucl. Phys. **B805** (2008) 267.

[7] G. Degrassi, P. Slavich, arXiv:1007.3465 [hep-ph].

[8] C. Anastasiou, S. Beerli, A. Daleo, Phys. Rev. Lett. **100** (2008) 241806.

[9] T. Appelquist, J. Carazzone, Phys. Rev. **D11** (1975) 2856.

[10] M. Mühlleitner, H. Rzehak, M. Spira, JHEP **0904** (2009) 023.

[11] M. Mühlleitner, H. Rzehak, M. Spira, PoS **RADCOR2009** (2010) 043, arXiv:1001.3214 [hep-ph].

Inclusive and associated b-quark production in the Regge limit of QCD

Bernd A. Kniehl[1], *Vladimir Saleev*[2], *Alexandera Shipilova*[2*]

[1]Institut für Theoretische Physik, Universität Hamburg, Luruper Chaussee 149, 22761 Hamburg, Germany
[2]Samara State University, Ak. Pavlova Street 1, 443011 Samara, Russia

DOI: http://dx.doi.org/10.3204/DESY-PROC-2010-01/shipilova

The study of b-jet production at high-energy colliders is of great interest for the test of perturbative quantum chromodynamics (QCD). The presence of a heavy b quark, with mass $m_b \gg \Lambda_{\rm QCD}$, where $\Lambda_{\rm QCD}$ is the asymptotic scale parameter of QCD, in such processes guarantees a large momentum transfer that keeps the strong-coupling constant small $\alpha_s(m_b) \lesssim 0.1$.

The total center-of-mass energy at the Tevatron, $\sqrt{S} = 1.96$ TeV in Run II, sufficiently exceeds the scale μ of the relevant hard processes, so that $\sqrt{S} \gg \mu \gg \Lambda_{\rm QCD}$. In this regime, the contributions to the production cross section from subprocesses involving t-channel exchanges of partons (gluons and quarks) may become dominant. Then, the off-shell properties of the incoming partons can no longer be neglected, and t-channel partons become Reggeized. In this so-called quasi-multi-Regge kinematics (QMRK), the particles (multi-Regge) or groups of particles (quasi-multi-Regge) produced in the collision are strongly separated in rapidity. For the inclusive b-jet production, this implies that a single b quark is produced in the central region of rapidity, while other particles, including a $\bar{b}$ quark, are produced at large rapidities. In the case of $b\bar{b}$ pair and $b\gamma$ associated production in the central rapidity region, we also assume that there are no other particles in this region, so that these particles are considered as quasi-multi-Regge pairs. The QMRK approach [1] is particularly appropriate for this kind of high-energy phenomenology. It is based on an effective quantum field theory implemented with the non-Abelian gauge-invariant action including fields of Reggeized gluons [2] and quarks [3].

First, we investigate inclusive single b-jet production in $p\bar{p}$ collisions. To leading order (LO) in the QMRK approach, there is only one partonic subprocess, $Q_b + R \to b(k)$ [4], where R and Q_b are the Reggeized gluon and b quark (with four-momentum k), respectively. At next-to-leading order (NLO), the main contribution arises from the partonic subprocess $R + R \to b + \bar{b}$, where the b and $\bar{b}$ quarks are produced close in rapidity, and its squared amplitude was obtained in Ref. [5]. In Fig. 1(a), the preliminary data presented by the CDF Collaboration [6] are compared with our predictions. Throughout all our analysis, the renormalization and factorization scales are chosen to be $\mu = \xi k_T$, where $1/2 \le \xi \le 2$, and the resulting theoretical uncertainties are indicated as shaded bands. In Fig. 1(a), we observe that the contribution due to LO subprocess greatly exceeds the one due to NLO subprocess and practically exhausts the full result. It nicely agrees with the CDF data throughout the entire k_T range.

*Speaker

In our analysis, we adopt the Kimber-Martin-Ryskin prescription [7] for unintegrated parton distribution functions (PDFs), using as input the Martin-Roberts-Stirling-Thorne collinear PDFs of the proton [8].

$b\bar{b}$-dijet production receives contributions from both subprocess $R + R \to b + \bar{b}$ and the annihilation of a Reggeized quark-antiquark pair, $Q_q + \bar{Q}_q \to b + \bar{b}$, where $q = u, d, s, c, b$. The induced vertex of the latter was obtained in Ref. [3] and the squared amplitudes in Ref. [9]. The CDF data [10] as distributions in the leading-jet (jet with the maximal transverse energy) transverse energy E_{1T}, the dijet invariant mass $M_{b\bar{b}}$, and the azimuthal separation angle $\Delta\phi$ are compared with our QMRK predictions in Figs. 1(b)–(d), where the two LO contributions are shown separately along with their superpositions. We observe that the total QMRK predictions nicely describe all the three measured cross section distributions. The contributions due to Reggeized gluon fusion dominate for $E_{1T} \lesssim 200$ GeV and $M_{b\bar{b}} \lesssim 300$ GeV and over the whole $\Delta\phi$ range considered. The peak near $\Delta\phi = 0.4$ in Fig. 1(d) arises from the isolation cone condition $R_{\rm cone} = \sqrt{\Delta y^2 + \Delta\phi^2} > 0.4$.

At last, there are two mechanisms of photon-associated b-quark production: direct photon production via the LO partonic subprocess in the QMRK $Q_b + R \to b + \gamma$ [11], and the fragmentation of final-state partons into photons. In Figs. 1(e)–(f), we observe that the contribution due to direct photon production greatly exceeds the one due to photon production by fragmentation, by about of one order of magnitude at $k_{T\gamma} > 40$ GeV and by about a factor 5 at $k_{T\gamma} \approx 30$ GeV. The direct photon contribution practically exhausts the full result. It nicely agrees with the D0 data [12] throughout the entire $k_{T\gamma}$ range considered.

The work of B.A.K. was supported in part by BMBF Grant No. 05H09GUE, by DFG Grant No. KN 365/7–1, and by HGF Grant No. HA 101. The work of V.A.S. and A.V.S. was supported in part by the Federal Agency for Education of the Russian Federation under Contract No. P1338. The work of A.V.S. was also supported in part by the International Center of Fundamental Physics in Moscow and the Dynastiya Foundation.

References

[1] V. S. Fadin, L. N. Lipatov, Nucl. Phys. B **406** (1993) 259; Nucl. Phys. B **477** (1996) 767 [arXiv:hep-ph/9602287].

[2] L. N. Lipatov, Nucl. Phys. B **452** (1995) 369 [arXiv:hep-ph/9502308].

[3] L. N. Lipatov, M. I. Vyazovsky, Nucl. Phys. B **597** (2001) 399 [arXiv:hep-ph/0009340].

[4] V. A. Saleev, Phys. Rev. D **78** (2008) 034033 [arXiv:0807.1587v1[hep-ph]]; Phys. Rev. D **78** (2008) 114031 [arXiv:0812.0946v1[hep-ph]].

[5] V. A. Saleev, D. V. Vasin, Phys. Lett. B **605** (2005) 311 [arXiv:hep-ph/0411109].

[6] T. Aaltonen [CDF Collaboration], CDF note 8418 (2006), URL: `http://www-cdf.fnal.gov/physics/new/qcd/QCD.html`.

[7] M. A. Kimber, A. D. Martin, M. G. Ryskin, Phys. Rev. D **63** (2001) 114027 [arXiv:hep-ph/0101348].

[8] A. D. Martin, R. G. Roberts, W. J. Stirling, R. S. Thorne, Phys. Lett. B **531** (2002) 216 [arXiv:hep-ph/0201127].

[9] B. A. Kniehl, V. A. Saleev, A. V. Shipilova, Phys. Rev. D **81** (2010) 094010 [arXiv:1003.0346v2[hep-ph]].

[10] T. Aaltonen [CDF Collaboration], CDF note 8939 (2007), URL: `http://www-cdf.fnal.gov/physics/new/qcd/QCD.html`.

[11] V. A. Saleev, in Proc. of the XVII International Workshop on DIS and Related Topics, Madrid, Spain, 2009, `http://dx.doi.org/10.3360/dis.2009.103`.

[12] V. Abazov [D0 Collaboration], Phys. Rev. Lett. **102** (2009) 192002 [arXiv:0901.0739v2[hep-ex]].

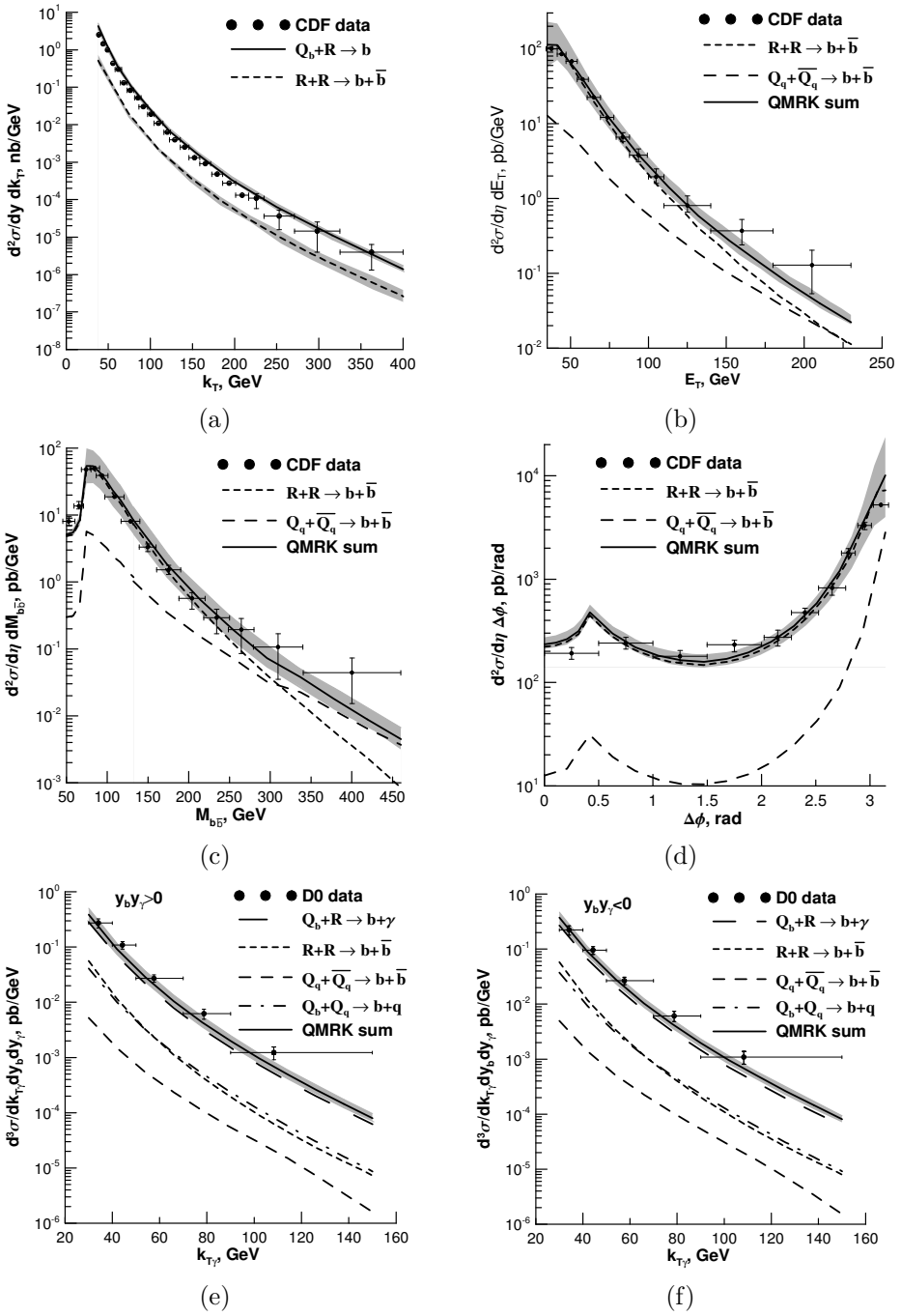

Figure 1: The distribution in (a) transverse momentum of inclusive single b-jet hadroproduction [6], the ones in (b) leading-jet transverse energy, (c) dijet invariant mass, and (d) azimuthal separation angle of inclusive $b\bar{b}$-dijet hadroproduction [10], and the ones in transverse momentum of $b\gamma$ hadroproduction [12] for (e) $y_b y_\gamma > 0$ and (f) $y_b y_\gamma < 0$ are compared with the QMRK predictions.

Physics potential of the CMS CASTOR forward calorimeter

Dmytro Volyanskyy for the CMS Collaboration
DESY, Notketraße 85, 22607 Hamburg, Germany

DOI: http://dx.doi.org/10.3204/DESY-PROC-2010-01/volyanskyy

The CASTOR calorimeter is a detector covering the very forward region of the CMS experiment at the LHC. It surrounds the beam pipe with 14 longitudinal modules each of which consisting of 16 azimuthal sectors and allows to reconstruct shower profiles, separate electrons and photons from hadrons and search for phenomena with anomalous hadronic energy depositions. The physics program that can be performed with this detector includes a large variety of different QCD topics. In particular, the calorimeter is supposed to contribute to studies of low-x parton dynamics, diffractive scattering, multi-parton interactions and cosmic ray related physics in proton-proton and heavy-ion collisions. The physics capabilities of this detector are briefly summarized in this paper.

1 Detector overview

The CASTOR (Centauro And STrange Object Reseacrh) detector is located at a distance of 14.4 m from the CMS interaction point right behind the Hadronic Forward (HF) calorimeter and the T2, a tracking station of the TOTEM experiment, covering the pseudorapidity region $-6.6 < \eta < -5.2$. This is a quartz-tungsten Cerenkov sampling calorimeter. That is, it is made of repeating layers (arranged in a sandwich structure) of quartz and tungsten plates. The former is used as the active material because of its radiation hardness, while the latter serves as the absorber medium providing the smallest possible shower size. The signal in CASTOR is produced when charged shower particles pass through the quartz plates with the energy above the Cerenkov threshold (190 keV for electrons). The generated Cerenkov light is then collected by air-code light guides, which are transmitting it further to photo-multipliers tubes PMTs. These devices produce signals proportional to the amount of light collected. As can be seen in Figure 1, the detector plates are tilted at 45° w.r.t. the beam axis to maximaize the Cerenkov light output in the quartz. The CASTOR detector is a compact calorimeter with the physical size of

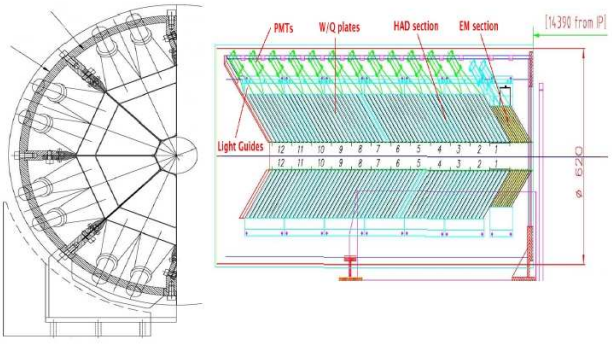

Figure 1: *Sketch of the CASTOR calorimeter: front view (left) and longitudinal cross section (right).*

about 65 cm × 36 cm × 150 cm and having no segmentation in η. It is embedded into a skeleton, which is made of stainless steel. The detector consists of 14 longitudinal modules, each of which comprises 16 azimuthal sectors that are mechanically organized in two half calorimeters. First 2 longitudinal modules form the electromagnetic section, while the other 12 modules form the hadronic section. In the electromagnetic section, the thicknesses of the tungsten and quartz plates are 5.0 and 2.0 mm, respectively. The corresponding thicknesses in the hadronic section are twice as large as in the electromagnetic section. With this design, the diameter of the showers of electrons and positrons produced by hadrons is about one cm, which is an order of magnitude smaller than in other types of calorimeters. The detector has a total depth of 10.3 interaction lengths and includes 224 readout channels. It should be noted that the final CASTOR design is the result of three test beam campaigns and numerous Monte Carlo simulations. After the completion of the detector construction in the spring of 2009, the calorimeter has been successfully installed and commissioned in the summer of 2009.

2 The CASTOR physics capabilities

Because of its pseudorapidity coverage, CASTOR significantly expands the CMS capability to investigate physics processes occurring at very low polar angles and so, providing a valuable tool to study low-x QCD, diffractive scattering, multi-parton interactions and underlying event structure. Another CASTOR objective is to search for exotic objects with unusual longitudinal shower profile, several of which have been observed in cosmic ray experiments.

2.1 Low-x QCD

A study of QCD processes at a very low parton momentum fraction $x = p_{\text{parton}}/p_{\text{hadron}}$ is a key to understand the structure of the proton, whose gluon density is poorly known at very low values of x. At the LHC the minimum accessible x in proton-proton (pp) collisions decreases by a factor of about 10 for each 2 units of rapidity. This implies that a process with a hard scale of $Q \sim 10$ GeV and within the CASTOR acceptance can probe quark densities down $x \sim 10^{-6}$ [1], that has never been achieved before. Such processes include the production of forward jets and Drell-Yan electron pairs. The latter occurs via the $qq \rightarrow \gamma^* \rightarrow e^+e^-$ reaction within the acceptance of CASTOR and TOTEM-T2 station, whose usage is essential for detecting these events. Measurements of Drell-Yan events can also be used to study QCD saturation effects – the effects of rising of the gluon density in the proton with decreasing values of x, that have been firstly observed at HERA. It was found that the Drell-Yan production cross section is suppressed roughly by a factor of 2 when using a PDF with saturation effects compared to one without. Another way to constrain the parton distribution function (PDF) of the proton at low x is provided by measuring forward jets in CASTOR that will enable to probe the parton densities down 10^{-6}. Moreover, this allows to gain information on the full QCD evolution to study high order QCD reactions. Apart from that, it has been found that a BFKL like simulation, for which the gluon ladder is ordered in x, predicts more hard jets in the CASTOR acceptance than the DGLAP model that assumes strong ordering in the transverse momentum k_{T} and random walk in x. Therefore, measurements of forward jets in CASTOR can be used as a good tool to distinguish between DGLAP and non-DGLAP type of QCD evolution. Furthermore, CASTOR in combination with HF can be used to measure Mueller-Navalet dijet events, which are characterized by two jets with similar p_{T} but large rapidity separation. By measuring Mueller-Navalet dijets in CASTOR one can probe BFKL-like dynamics and small-x evolution.

2.2 Diffraction

A good way to study the perturbative QCD and the hadron structure is provided by diffractive pp interactions (where one or both the colliding protons stay intact) via measurements of the cross sections for diffractive W, Z, jet or heavy quark productions. The CASTOR calorimeter is, in particular, a very useful tool to measure the single-diffractive productions of W and dijets in pp collisions ($pp \to pX$ reaction, where X is either a W boson or a dijet system). These are hard diffractive processes that are sensitive to the quark and gluon content of the low-x proton PDFs, correspondingly. A selection of such events can be performed using the multiplicity distributions of tracks in the central tracker and calorimeter towers in HF plus CASTOR exploiting the fact that diffractive events on average have lower multiplicity in the central region and in the "gap side" than non-difractive ones. Feasibility studies to detect the single-diffractive productions of W [2] and dijets [3] have shown that the diffractive events peak in the regions of no activity in HF and CASTOR.

2.3 Multi-parton interactions and underlying event structure

Measurements of energy deposits in the CASTOR acceptance should significantly improve our understanding of the multi-parton interactions (MPI) and underlying event (UE) structure. The latter is an unavoidable background to most collider observables, whose understanding is essential for precise measurements at the LHC. It consists of particles arising from the beam-beam remnants and from MPI. The MPI arise in the region of small-x where parton densities are large so that the likelihood of more than one parton interaction per event is high. According to all QCD models, the larger the collision energy the greater the contribution from MPI to the hard scattering process. However, this dependence is currently weakly known. Measurements of the forward energy flow by means of CASTOR will allow to discriminate between different MPI models, which vary quite a lot. Furthermore, measurements of forward particle production in pp and Pb-Pb collisions at LHC energies with CASTOR should help to significantly improve the existing constraints on ultra-high energy cosmic ray models.

3 Conclusion

The CASTOR calorimeter is a valuable CMS subcomponent allowing to perform a very rich physics program. The detector is fully integrated in the CMS readout and currently take collision data. Its first physics results are currently under preparation.

4 Acknowledgments

I am very thankful to Hannes Jung, Kerstin Borras and many other colleagues working in the CMS forward physics community for fruitful discussions, suggestions and encouragements.

References

[1] *CMS and TOTEM Collaborations.* CERN/LHCC 2006-039/G-124 (2006).

[2] *CMS Collaboration.* CERN CMS-PAS-DIF-07-002 (2007).

[3] *CMS Collaboration.* CERN CMS-PAS-FWD-08-002 (2008).

The sensitivity of the ATLAS detector to the Standard Model Higgs boson in the four lepton final state

Craig Wiglesworth for the ATLAS Collaboration

Department of Physics, University of Liverpool, United Kingdom

DOI: http://dx.doi.org/10.3204/DESY-PROC-2010-01/wiglesworth

The Higgs boson is the only particle in the Standard Model (SM) that has not yet been discovered. Although its mass (m_H) is a free parameter, direct searches at the Large Electron Positron collider have set a lower limit on m_H of 114.4 GeV at 95% confidence level (CL) [1]. In addition, ongoing searches at the Tevatron have excluded the range $162 < m_H < 166$ GeV at 95% CL [2]. Assuming the overall validity of the SM, a global fit to precision electroweak data provides an indirect upper limit on m_H of 157 GeV at 95% CL [3].

The analyses described here were performed using detailed simulations of the ATLAS detector response to proton-proton collisions at a centre-of-mass energy of 14 TeV. Further details of the analyses can be found in [4].

The $H \to ZZ^{(*)} \to 4l$ channel is an important channel in the search for the SM Higgs boson as it provides one of the cleanest experimental signatures. In the range of m_H values considered, the dominant background to this channel is the $pp \to ZZ^{(*)} \to 4l$ continuum. Below about 200 GeV, where one of the Z bosons in the signal channel is produced off-shell, the $pp \to Zb\bar{b}$ and $pp \to t\bar{t}$ processes also contribute.

The online selection of candidate $H \to ZZ^{(*)} \to 4l$ events is performed either by single lepton or double lepton triggers. The offline event selection requires that the candidate events have at least four leptons that can be coupled into pairs of same flavour and opposite charge. The $4l$ invariant mass resolution is improved by 10% to 17% when applying a Z boson mass constraint to one (or both if $m_H > 200$) of the lepton pairs. The resulting 4μ invariant mass distribution in simulated signal events for $m_H = 130$ GeV is shown in Figure 1. A similar distribution is also observed for the $4e$ invariant mass.

The calorimeter isolation, track isolation and transverse impact parameter significance of the leptons in the candidate events are discriminating variables in the rejection of the $pp \to Zb\bar{b}$ and $pp \to t\bar{t}$ background processes. The track (calorimeter) isolation variable is defined as the total transverse momentum (total energy) deposit around the lepton, normalised to the transverse momentum of the lepton. The impact parameter significance is the transverse impact parameter of the lepton with respect to the primary vertex, divided by the corresponding measurement error. The $4l$ invariant mass distributions in simulated signal and background events after all event selection criteria are shown in Figure 2.

The signal significance is determined using two different approaches. In the first approach, the number of signal and background events are counted within a mass window of $m_H \pm 2\sigma$,

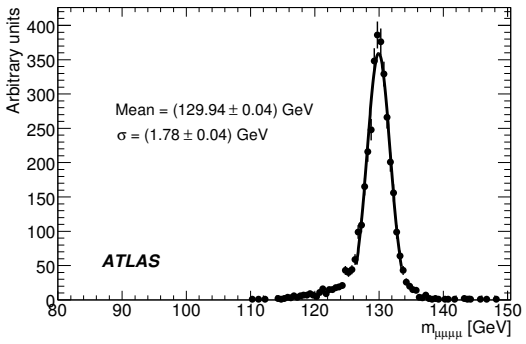

Figure 1: The 4μ invariant mass distribution in simulated signal events for $m_H = 130$ GeV.

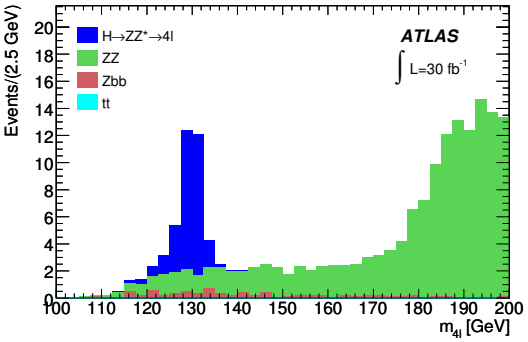

Figure 2: The $4l$ invariant mass distributions in simulated signal and background events after all event selection criteria for $m_H = 130$ GeV.

where σ is the experimental $4l$ invariant mass resolution. The significance is then calculated using Poissonian statistics without consideration of systematic uncertainties. In the second approach, the signal and background contributions are extracted from a fit to the $4l$ invariant mass distribution. The signal significance and exclusion limits are then calculated using a profile likelihood ratio method in which systematic uncertainties are taken into account. The 3% to 5% uncertainty on the signal selection efficiency is dominated by the experimental uncertainties relating to lepton reconstruction performance. The expected signal significance for an integrated luminosity of 30 fb^{-1} and the luminosity required for an exclusion at 95% CL in the $H \to ZZ^{(*)} \to 4l$ channel are shown in Figure 3 and Figure 4, respectively.

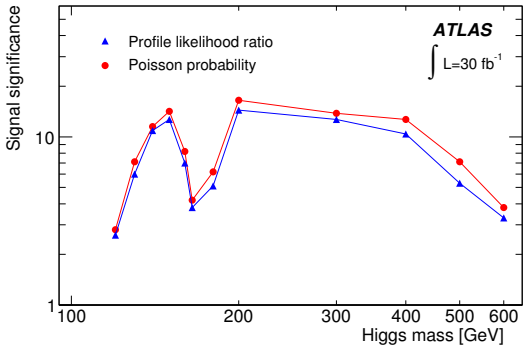

Figure 3: The expected signal significance for an integrated luminosity of 30 fb^{-1}.

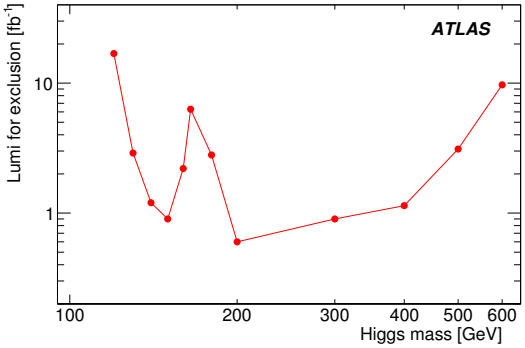

Figure 4: The luminosity required for an exclusion at 95% CL.

The $H \to ZZ^{(*)} \to 4l$ channel is combined with other important decay channels ($H \to W^+W^-$, $H \to \gamma\gamma$ and $H \to \tau^+\tau^-$) to provide a single measure of the significance of a discovery or an exclusion limit for various m_H values [4]. The expected combined discovery significances for an integrated luminosity of 10 fb^{-1} and the combined exclusion limits for an integrated luminosity of 2 fb^{-1} are shown in Figure 5 and Figure 6, respectively.

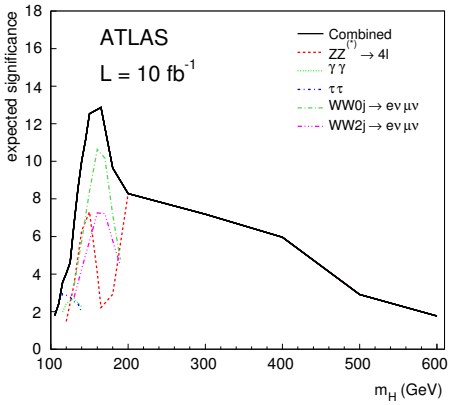

Figure 5: The expected combined discovery significances for an integrated luminosity of 10 fb^{-1}.

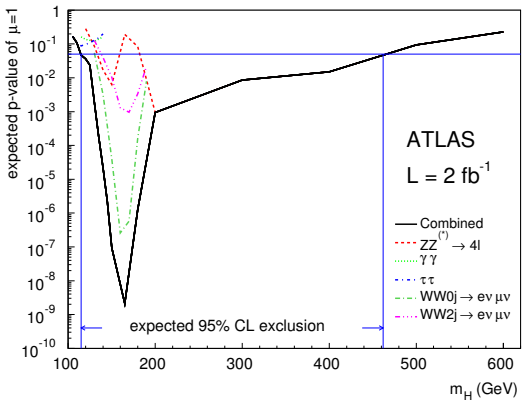

Figure 6: The expected combined exclusion limits for an integrated luminosity of 2 fb^{-1}.

With an integrated luminosity of 30 fb^{-1}, the expected sensitivity of the ATLAS detector to the discovery of the SM Higgs boson in the $H \to ZZ^{(*)} \to 4l$ channel alone is at the 5σ level or greater in the mass range $130 < m_H < 500$ GeV, with the exception of the region around 160 GeV where the branching ratio for $H \to ZZ^*$ decays is suppressed due to the opening of the phase space for the decay into two on-shell W bosons. With an integrated luminosity of 10 fb^{-1}, the expected combined sensitivity of the ATLAS detector to the discovery of the SM Higgs boson in the combination of channels is at the 5σ level or greater in the mass range $130 < m_H < 430$ GeV. For $m_H > 200$ GeV, the $H \to ZZ^{(*)} \to 4l$ channel will play a key role in the discovery or exclusion of the SM Higgs boson.

References

[1] R. Barate *et al.* [LEP Working Group for Higgs boson searches and ALEPH Collaboration], Phys. Lett. B **565** (2003) 61 [arXiv:hep-ex/0306033].

[2] T. Aaltonen *et al.* [CDF and D0 Collaborations], Phys. Rev. Lett. **104** (2010) 061802 [arXiv:1001.4162 [hep-ex]].

[3] J. Alcaraz [ALEPH Collaboration and CDF Collaboration and D0 Collaboration], arXiv:0911.2604 [hep-ex].

[4] G. Aad *et al.* [The ATLAS Collaboration], CERN-OPEN-2008-020.

Tile calorimeter at work in the collision era

Tibor Zenis on behalf of the ATLAS Tile Calorimeter Group

Comenius University in Bratislava, Safarikovo namestie 6, 818 06 Bratislava 16, Slovakia

DOI: http://dx.doi.org/10.3204/DESY-PROC-2010-01/zenis

1 Detector description

The Tile Calorimeter [1] is the central region hadronic calorimeter (Fig. 1 left) of the ATLAS experiment [2] at the CERN Large Hadron Collider.

The Tile Calorimeter is a sampling calorimeter using steel as absorber and scintillator plates as active medium. It is divided into a 5.8 m long central barrel and two 2.6 m long extended barrel cylinders, each having an inner radius 2.28 m and an outer radius of 4.25 m.

Each of the cylinders is composed of 64 azimuthal modules subtending $\Delta\phi = 0.1$. The Tile scintillator plates are placed perpendicular to the colliding beam axis, and are radially staggered in depth. The structure is periodic along the beam axis. Two sides of the scintillating tiles are read out by wave-length shifting (WLS) fibers into two separate photomultipliers (PMTs).

By the grouping of WLS fibers to specific PMTs, modules are segmented in pseudorapidity η and in radial depth. The resulting typical cell dimensions are $\Delta\eta \times \Delta\phi = 0.1 \times 0.1$.

This segmentation defines a quasi-projective tower structure. Altogether, Tile Calorimeter comprises 4672 read-out cells, each equipped with two PMTs that receive light from opposite sides of the tiles.

The Tile Calorimeter together with the central liquid argon electromagnetic calorimeter will measure the energy of particle jets and contribute to the determination of the missing transverse energy of events in the pseudorapidity range $|\eta| < 1.7$.

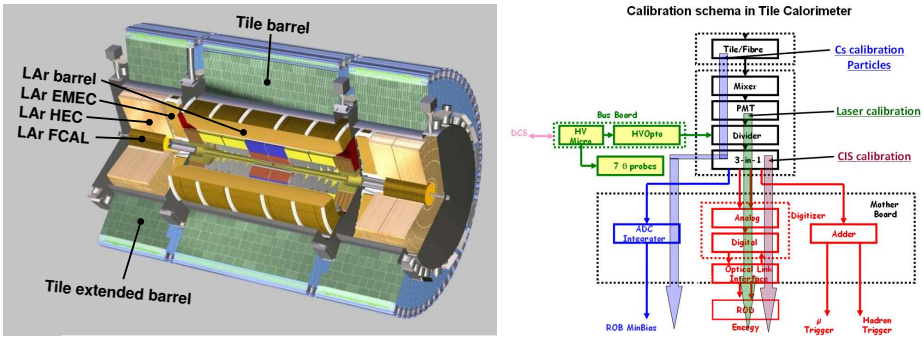

Figure 1: Left: View of the central part of ATLAS detector showing the tile calorimeter (tile barrel in center, tile extended barrels in side regions) surrounding the different segments of the liquid argon (LAr) calorimeter. Right: Calibration scheme in the tile calorimeter: Cs radioactive source, laser pulses, charge injection system.

2 Calibration

The Tile Calorimeter is equipped with a system that allows to monitor and to calibrate each stage of the read-out system exploiting different signal sources (Fig. 1 right).

The Charge Injection System sends charge pulses to each electronic channel. The system is designed to calibrate the read-out electronic system across all PMTs of the calorimeter at accuracy of 1 %. The Laser system provides light to all PMTs. It is designed to calibrate and monitor the response of the PMTs with a precision better than 0.5 %. The radioactive Cesium source ^{137}Cs moves through all Tile Calorimeter cells by a hydraulic system. The Cesium calibration system allows to obtain a uniformity of the cell response at the level of 0.3 %. [3]

3 Cosmic muons and splash events

The Tile Calorimeter response to cosmic and test-beam muons was used to measure the performance of the detector. The electromagnetic scale of the Tile Calorimeter modules was validated with the precision of 3 % using muons. Good agreement between data and Monte Carlo (MC) in test-beam and cavern muon data was observed.

The time offsets of the Tile Calorimeter cells were measured with cosmic muons and single beam data. The results agree within a precision of 1 ns.

In the splash events the LHC beam hits a completely closed collimator 140 m far from the center of the ATLAS and secondary particles penetrate all ATLAS detectors. The Tile Calorimeter cells timing after time-of-flight correction was validated (Fig. 2 left) and RMS = 0.45 ns was achieved for cells with proper time calibration.

4 Collisions

The distribution of the Tile Calorimeter cell response was compared with collision data at 7 TeV, 2.36 TeV, 900 GeV, minimum bias MC and randomly triggered events (Fig. 2 right). Good agreement between data and MC was observed.

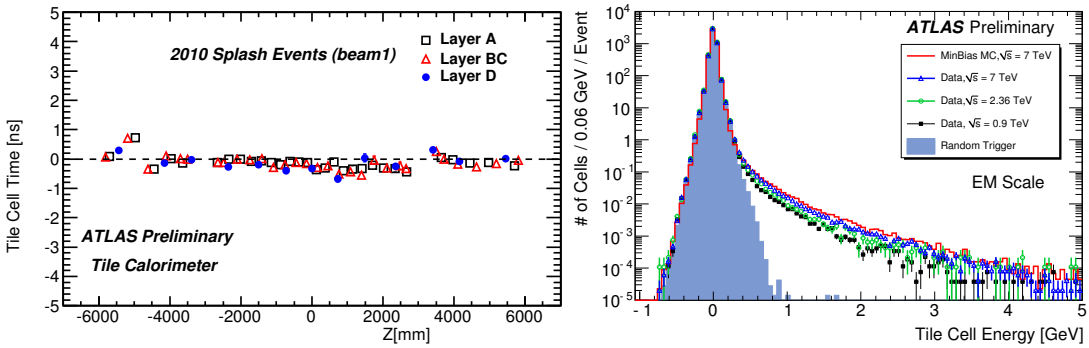

Figure 2: Left: The average cell time as a function of the cell Z (along beam axis) coordinate. Timing corrections based on the time of flight had been applied. Right: Energy of the tile calorimeter cells. The distributions from collision data at 7 TeV, 2.36 TeV, and 0.9 TeV are superimposed with Pythia minimum bias Monte Carlo and randomly triggered events.

The Tile Calorimeter cell response uniformity as a function of pseudorapidity η and azimuthal angle ϕ was compared between collision events at 7 TeV and non-diffractive minimum bias MC events (Fig. 3). A nice match between MC and data was seen.

The online signal reconstruction by the ROD/DSP Optimal Filtering Non Iterative reconstruction [4] was validated with the collision events as well as out of time events. It was shown that linearity of online algorithm is within a few percent in the significant time range $[-10, 10]$ ns.

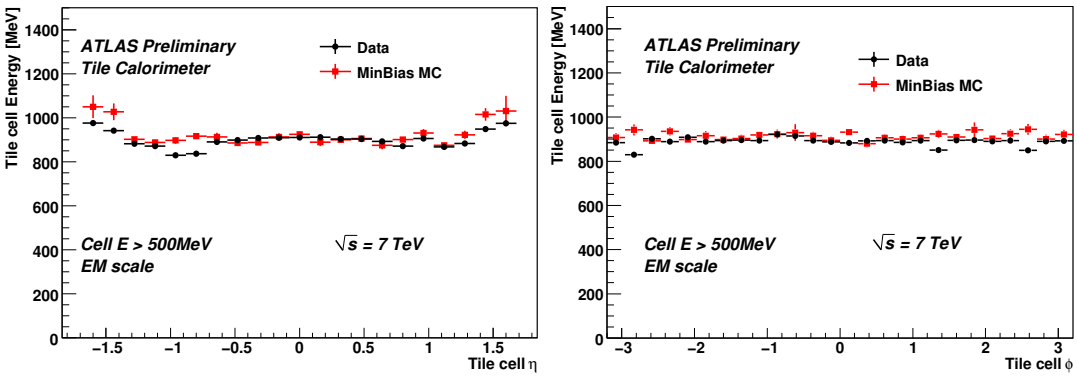

Figure 3: Tile calorimeter cell response uniformity as a function of pseudorapidity (left) and azimuthal angle (right) for 7 TeV collision and MC events.

5 Conclusion

The performance of the Tile Calorimeter has been measured and monitored using calibration data, random triggered data, cosmic muons, splash events and collision events.

The results of these studies give important information that assess the uniformity, the stability and the resolution of the energy measurements and, in general, the quality of the data description as given by the simulation of the Tile Calorimeter detector.

The performance and the quality of understanding the Tile Calorimeter is demonstrated. The detector is ready to detect hadrons, jets and to measure the missing transverse energy.

Acknowledgements

I acknowledge the support from the Ministry of Education of the Slovak Republic.

References

[1] [ATLAS Collaboration], "ATLAS tile calorimeter: Technical design report," CERN-LHCC-96-42.

[2] G. Aad *et al.* [ATLAS Collaboration], "The ATLAS Experiment at the CERN Large Hadron Collider," JINST **3** (2008) S08003.

[3] [The ATLAS Collaboration], "Readiness of the ATLAS Tile Calorimeter for LHC collisions," to be submitted to EPJC, (2010)

[4] A. Valero, "The ATLAS TileCal Read-Out Drivers Signal Reconstruction," ATL-TILECAL-PROC-2009-004, http://cdsweb.cern.ch/record/1223960

Recent performance results with the ATLAS Muon Spectrometer

Giovanni Zevi Della Porta for the ATLAS Muon Collaboration

Harvard University, Cambridge, MA 02138, United States of America

DOI: http://dx.doi.org/10.3204/DESY-PROC-2010-01/zevidellaporta

The ATLAS Muon Spectrometer (MS) is used to trigger on muons and reconstruct their tracks. It is composed of two sets of air-core superconducting toroidal magnets embedded in three layers of precision chambers and three layers of trigger chambers. Monitored Drift Tubes (MDT) and Cathode Strip Chambers (CSC) measure the bending coordinate (η) with a point resolution of respectively 80 and 60 μm. Resistive Plate Chambers (RPC) in the Barrel ($|\eta| < 1$) and Thin Gap Chambers (TGC) in the Endcap ($1 < |\eta| < 2.7$) also provide the second coordinate (ϕ) and the trigger signal (up to $|\eta| < 2.4$), with a point resolution around 1 cm.

Different types of muon tracks can be reconstructed using different combinations of subdetectors. Stand-alone tracks are based only on MS hits. The MS hits are used to form local straight segments, which are combined to form a curved track. The track parameters are then extrapolated, accounting for energy loss in the calorimeters, to the Interaction Point. Combined tracks are formed by matching a stand-alone track with an Inner Detector (ID) track, improving the precisionon of the track parameters, especially at low momenta. Tagged tracks are built from extrapolated ID tracks by looking for either a segment in the MS or energy depositions compatible with an isolated muon in the calorimeters. They are designed to increase tracking efficiency for low momentum muons or muons traversing uninstrumented areas (cracks).

The first set of performance studies on which we report is based on a large sample of RPC-triggered cosmic-ray events crossing the MS Barrel, recorded in the fall of 2009. Of these events, 48 million were collected without a toroidal B-field. For 21 million events the B-field was at nominal value (with a field integral between 2 and 8 Tm) in order to study momentum resolution and tracking efficiency.

Chamber alignment and sagitta resolution are studied using cosmic-ray tracks collected without magnetic field. The segment sagitta is defined as the distance from the Middle-station segment to the straight line connecting the segments in the Inner and Outer stations. The segment sagitta distribution for each sector is fitted to a double Gaussian (see Fig. 1(a)). The mean of the narrow Gaussian is used for track-based alignment of the spectrometer, while the sigma corresponds to the sagitta resolution. The sagitta resolution is parametrized into two separate components: multiple scattering and intrinsic resolution, respectively dominating at high and low momenta. Using the solenoidal magnetic field of the Inner Detector to determine the momentum of the muon tracks, the intrinsic component of the sagitta resolution is isolated and found to be between 80 and 100 μm.

The hit residual distribution, track reconstruction efficiency and momentum resolution are studied using curved tracks collected with the solenoidal B-field at its nominal value, and are found to be very close to the design specifications for the MS. The hit residual is defined as

the distance between a reconstructed track and the position (drift radius) of its individual hits. The residual distribution for stand-alone tracks crossing three MDT chambers is found to be 104 μm, consistent with the measured sagitta resolution. The efficiency of track reconstruction is obtained by calculating the fraction of ID cosmic-ray tracks which are also reconstructed in the MS. The reconstruction efficiency for stand-alone tracks crossing two or more MDT chambers matches with the cosmic simulation, averaging 95% (see Fig. 1(b)).

To measure the momentum resolution of the MS without requiring a comparison with the ID, the top and bottom sections of a cosmic-ray track traversing the whole detector are compared. The momentum resolution is the width of the fitted distribution of relative p_T differences ($\Delta p_T/p_T$) between the top and bottom halves of the track. Fitting the momentum resolution against the momentum of the tracks (see Fig. 1(c)) allows the extraction of its three components: energy loss correction (P_0), multiple scattering (P_1), and intrinsic resolution (P_2). Extrapolating the fitted function to 1 TeV momenta gives a resolution of $11 \pm 2\%$ for tracks crossing small MDT chambers and $25 \pm 2\%$ for tracks crossing large ones. The difference between small and large chambers is due to the difference in integrated magnetic field along the muon paths. The design goal for 1 TeV muon tracks is a p_T resolution of approximately 10%.

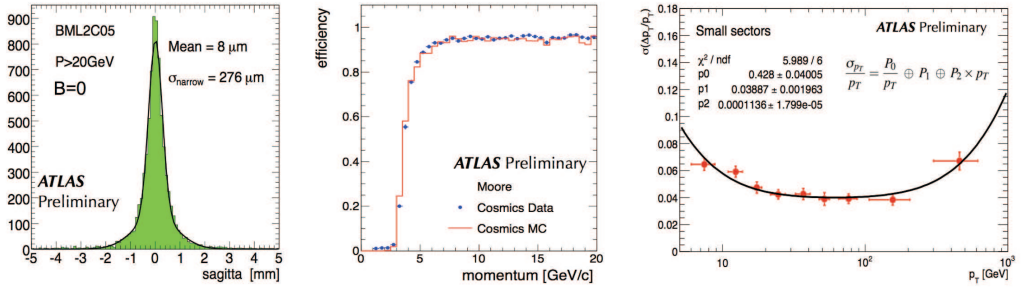

(a) (b) (c)

Figure 1: Performance results from a study of cosmic-ray tracks in the MS Barrel. A segment sagitta distribution (a), the reconstruction efficiency as a function of momentum for stand-alone tracks (b), and the p_T resolution as a function of p_T for small MDT sectors (c).

The second set of performance studies discussed here is for the most part based on the first 0.6 nb^{-1} of 7 TeV pp collisions triggered using the ATLAS Minimum Bias Trigger Scintillators. The hardware performance of the MS during these collision runs was good, with very low fractions of dead or noisy channels (0.3% for MDT, 1.5% for CSC, 2.7% for RPC, 1.2% for TGC), and the performance of the muon tracking chambers matches well our expectation from Monte-Carlo. Some basic distributions are shown, for both data and simulation, in figures 2(a) to 2(f). Here the Monte-Carlo is normalized to the number of events in the data. Using a larger dataset (6.4 nb^{-1}), the efficiency of the muon triggers relative to the tracking efficiency was measured by comparing triggered tracks with reconstructed tracks in the minimum-bias sample. The geometrical acceptance of the RPC trigger is around 80%, setting a limit for its relative efficiency, while the TGC efficiency reaches its plateau above 90% (see Figs. 2(g) and 2(h)).

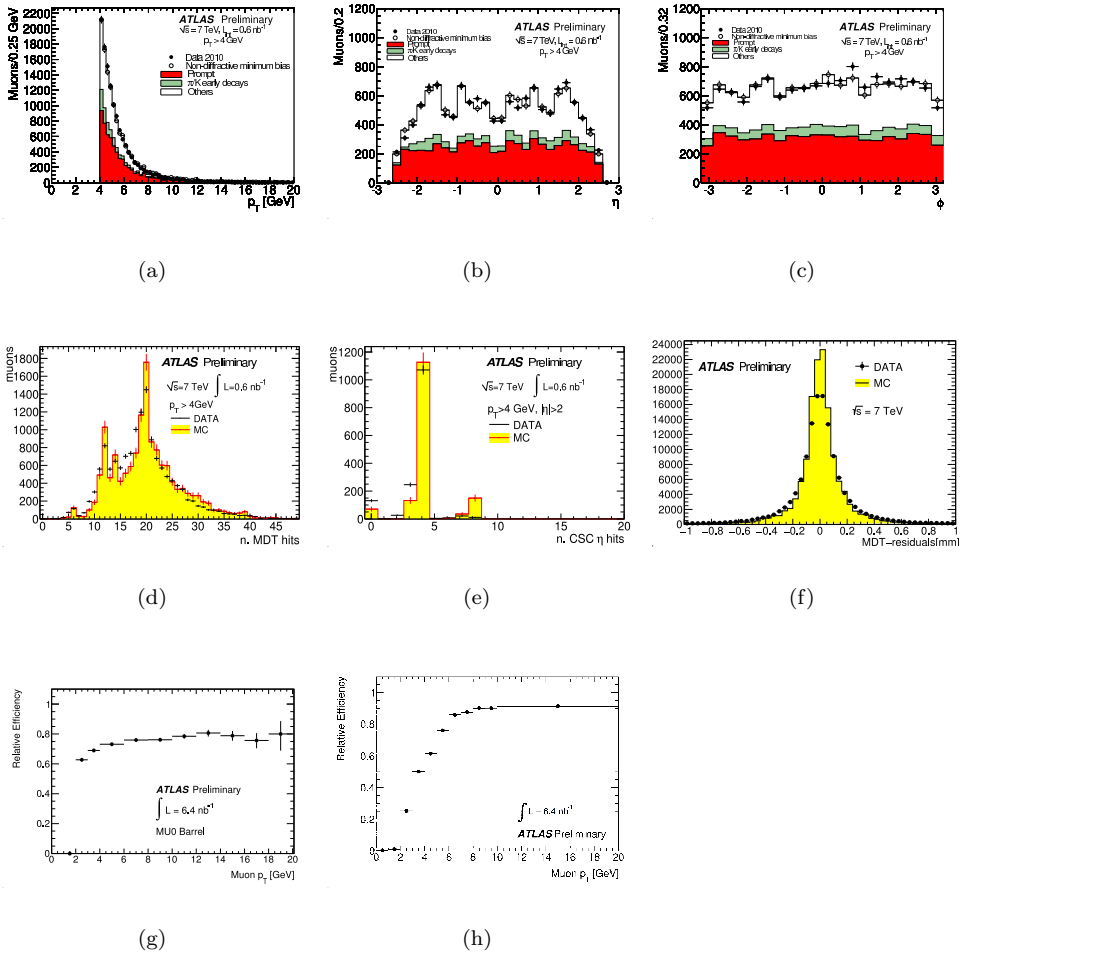

(a) (b) (c)

(d) (e) (f)

(g) (h)

Figure 2: Basic distributions obtained from collision muons compared to simulation: track p_T (a), η (b), and ϕ (c), number of MDT (d) and CSC (e) hits per combined track match the Monte-Carlo prediction well. The two peaks in (d) correspond to tracks crossing two and three chambers, respectively. The hit residual distribution (f) is slightly wider in data than in the simulation due to an underestimation of the material in the MS. (g) and (h): RPC and TGC trigger efficiencies for the lowest trigger threshold (MU0) relative to combined tracks.

References

[1] The ATLAS Collaboration, *Muon Performance in Minimum Bias pp Collision Data at* $\sqrt{s} = 7$ TeV *with ATLAS*. ATL-CONF-2010-036 (2010).

[2] The ATLAS Collaboration, *Preliminary studies for the measurement of the inclusive muon spectrum in pp collisions at* $\sqrt{s} = 7$ TeV *with the ATLAS detector*. ATL-CONF-2010-035 (2010).

[3] The ATLAS Collaboration, *First observation of the* $J/\psi \to \mu\mu$ *resonance in ATLAS pp collisions at* $\sqrt{s} = 7$ TeV. ATL-CONF-2010-045 (2010).

List of Authors

Alioli, Simone, 204
Amram, Nir, 358
Antola, Matti, 385
Artemenkov, Denis A., 400

Banfi, Andrea, 186
Bednyakov, Vadim A., 400
Benedetti, Daniele, 246
Biesiada, Jedrzej, 164
Blaizot, Jean-Paul, 373
Bonato, Alessio, 43
Brandt, Gerhard, 157
Broz, Michal, 219
Buras, Andrzej J., 325

Catà, Oscar, 311
Cerati, Giuseppe B., 214
Cogan, Julien, 354
Conti, Géraldine, 366
Cornelissen, Thijs, 67

Dainese, Andrea, 97
Demaria, Natale, 34
Dermíšek, Radovan, 279
DeViveiros, Pier-Olivier, 190

Espinosa, Jose R., 267

Feng, Eric, 241
Ferretto Parodi, Andrea, 412

Gallo, Elisabetta, 173
Gehrmann, Thomas, 134
Gelmini, Graciela B., 261
Gieseke, Stefan, 194
Gouzevitch, Maxime, 237
Grabowska-Bold, Iwona, 87
Graziano, Alberto, 271
Grojean, Christophe, 267
Guadagnoli, Diego, 295

Halyo, Valerie, 107
Heikinheimo, Matti, 385
Heinemeyer, Sven, 275, 291
Herrmann, Björn, 388
Heuer, Rolf-Dieter, 3
Hoepfner, Kerstin, 284
Höche, Stefan, 199

Isidori, Gino, 311

Jež, Pavel, 391
Jenni, Peter, 10

Kamenik, Jernej F., 311
Kant, Philipp, 394
Kerschen, Nicolas, 227
Khoze, Valery A., 275
Kniehl, Bernd A., 409, 418
Kono, Takanori, 299
Krasny, Mieczyslaw Witold, 250
Krauss, Frank, 199
Kreps, Michal, 317

Lamont, Mike, 15
Lee, Yen-Jie, 160
Lendermann, Victor, 288
Loddenkoetter, Thomas, 397
Lunardon, Marcello, 51
Lykasov, Gennady I., 400

Mühlleitner, Margarete, 267, 415
Maciuc, Florin, 39
Mackeprang, Rasmus, 91
Mager, Magnus, 55
Maire, Antonin, 168
Maniatis, Markos, 403
Mannel, Thomas, 342
Manteuffel, Andreas von, 403
Marco, Emanuele Di, 232
Meng, Zhaoxia, 406

Miśkowiec, Dariusz, 177
Mitsuka, Gaku, 29
Moortgat-Pick, Gudrid, 303

Nachtmann, Otto, 403

Palisoc, Caesar P., 409
Plätzer, Simon, 194
Potrap, Igor, 47
Pueschel, Elisa, 350

Röhr, Christian, 194
Radicci, Valeria, 59
Roland, Benoît, 223
Rolbiecki, Krzysztof, 303
Ryskin, Misha G., 275
Rzehak, Heidi, 415

Saleev, Vladimir, 418
Sannino, Francesco, 385
Santos, Helena, 379
Schöfbeck, Robert, 307
Schneider, Olivier, 119
Schukraft, Jürgen, 23
Schönherr, Marek, 199
Scodellaro, Luca, 71
Serrano, Justine, 362
Servant, Géraldine, 254
Seymour, Michael H., 147
Shipilova, Alexandera, 418
Siegert, Frank, 199
Siodmok, Andrzej, 194
Spira, Michael, 415

Tackmann, Kerstin, 63
Tasevsky, Marek, 275
Tattersall, Jamie, 303
Thom, Julia, 128
Torassa, Ezio, 181
Tuominen, Kimmo, 385

Volyanskyy, Dmytro, 421

Warsinsky, Markus, 209
Weiglein, Georg, 275
Wiedner, Dirk, 79
Wiglesworth, Craig, 424

Xíng, Fúnaì, 83

Yurkewicz, Adam, 75

Zenis, Tibor, 427
Zevi Della Porta, Giovanni, 430